12-2016

Synthesis and performance of novel supramolecular tools for single-particle cryogenic electron microscopy and drug and gene delivery

Kyle J. Wright
Purdue University

SYNTHESIS AND PERFORMANCE OF NOVEL SUPRAMOLECULAR TOOLS FOR SINGLE-PARTICLE CRYOGENIC ELECTRON MICROSCOPY AND DRUG AND GENE DELIVERY

VOLUME I

A Dissertation

Submitted to the Faculty

of

Purdue University

by

Kyle J. Wright

In Partial Fulfillment of the

Requirements for the Degree

of

Doctor of Philosophy

December 2016

Purdue University

West Lafayette, Indiana

Graduate School Form 30
(Updated 11/20/2014)

PURDUE UNIVERSITY
GRADUATE SCHOOL
Thesis/Dissertation Acceptance

This is to certify that the thesis/dissertation prepared

By Kyle J. Wright

Entitled SYNTHESIS AND PERFORMANCE OF NOVEL SUPRAMOLECULAR TOOLS FOR SINGLE-PARTICLE CRYOGENIC ELECTRON MICROSCOPY AND DRUG AND GENE DELIVERY

For the degree of Doctor of Philosophy

Is approved by the final examining committee:

David H. Thompson

Chengde Mao

Jonathan Wilker

Wen Jiang

To the best of my knowledge and as understood by the student in the Thesis/Dissertation Agreement, Publication Delay, and Certification/Disclaimer (Graduate School Form 32), this thesis/dissertation adheres to the provisions of Purdue University's "Policy on Integrity in Research" and the use of copyrighted material.

David H. Thompson

Approved by Major Professor(s): _____

_____

Approved by: Timothy Zwier 11/30/2016

Head of the Department Graduate Program Date

To my family and friends, Thank you all.

ACKNOWLEDGMENTS

I would like to thank my research advisor Prof. David H. Thompson for his patience and guidance throughout the course of my studies. It has been a great experience working and learning in an independent and positive research environment.

I would like to express gratitude to my graduate committee members, Prof. Chengde Mao and Prof. Jonathan Wilker for their guidance during the course of my graduate work. Thanks to Prof. Wen Jiang for participation in my final defense committee.

I would like to thank all of my past and current coworkers in the Thompson research group for their feedback and critical discussion on research projects and for helping contribute to a positive work environment. I would like to specially thank Dr. Seok-Hee Hyun for his guidance and help during the development of my scientific skills and constant technical expertise throughout my Ph.D. studies. I would like to thank all of the undergraduate researchers with whom I have had the pleasure of working.

Finally, I would like to thank my family and especially my parents, Joe and Nancy Wright, for their constant support and guidance throughout.

TABLE OF CONTENTS

Page

Page

Page

Page

LIST OF TABLES

LIST OF FIGURES

Figure Page

Figure Page

Figure Page

Figure Page

Appendix Figure Page

Appendix Figure Page

Appendix Figure Page

Appendix Figure Page

Appendix Figure Page

Appendix Figure Page

Appendix Figure Page

Appendix Figure Page

Appendix Figure Page

LIST OF SCHEMES

Scheme Page

Scheme Page

ABSTRACT

Wright, Kyle J. Ph.D., Purdue University, December 2016. Synthesis and Performance of Novel Supramolecular Tools for Single-Particle Cryogenic Electron Microscopy and Drug and Gene Delivery. Major Professor: David H. Thompson.

High-resolution biomacromolecular structure elucidation is fundamentally important to structure-based drug design and basic research into complex biochemical processes. Cryo-EM is an emerging alternative to XRD and NMR that is complementary in many ways relative to XRD and NMR. Materials approaches to cryo-EM are anticipated to greatly facilitate the cryo-EM process, allowing progress toward a more high-throughput application of cryo-EM to address challenges in structural biology.

Various affinity-based approaches inspired by approaches previously introduced for 2D crystallization were developed for facilitation of cryo-EM. A library of affinity lipopolymer constructs were synthesized consisting of lipopolymers of various PEG molecular weights conjugated to lipids displaying varied affinity or covalently-active moieties at their distal termini. Modified-EM grids with stabilized lipid coatings were then used to capture His_6-T7 bacteriophage and His_6-RplL from cell lysates, purified His_8-GFPuv, and nanodisc embedded His_6-$MalFGK_2$. Graphene-oxide-NTA-based affinity grids were fabricated via covalent modification of graphene-oxide and monolayer

fabrication on a Langmuir trough. These monolayers were characterized by AFM, SEM, and evaluated for specific capture of his-tagged protein targets. These materials were also used to capture his_6-GroEL from clarified cell lysates and used to generate a cryo-EM dataset yielding a map with a gold standard resolution of 8.1 Å. A library of polyrotaxanes based on PEG, α-CD and various endcaps and rotaxanation methods was synthesized. Several of these compounds were further modified with NTA moieties to impart affinity interactions on the tubular polyrotaxane templates which might be used for isolation of proteins and assisted cryo-EM. The laterally- and rotationally-mobile NTA-CD ligating groups enabled the capture of his-tagged proteins of substantially different sizes and facilitated their imaging via AFM, cryo-TEM, and TEM. This material may greatly facilitate cryo-EM analysis of his-tagged proteins by concentrating them into large and readily detectable clusters that enables projection images of the protein structure in all possible 3D orientations.

. Several families of diblock copolymer-based drug and gene delivery systems were also developed utilizing organocatalytic ring-opening polymerization (ROP) catalyzed by common amidine and guanidine bases. A library of mPEG-b-polycarbonate pendant polymers was synthesized and evaluated as part of a non-viral gene delivery system. The diblock copolymers showed the ability to form nanoparticles, typically 100-250 nm in size, with slightly positive surface zeta-potentials, effectively condensed pDNA at N/P ratios above 10, and showed comparable transfection efficiencies to Lipofectamine-2000 in HeLa Cells. Organocatalytic ROP was also utilized to synthesize small libraries of mPEG-b-poly(ε-caprolactone), mPEG-b-poly(trimethylene carbonate) and mPEG-b-poly(lactide-co-glycolide) diblock copolymers including a novel collagen-binding

peptide-diblock copolymer conjugate (SILY-PEG-b-PCL) utilizing organocatalytic ROP from a heterobifunctional PEG derivative. A facile and widely applicable synthetic procedure for the synthesis of cyclic amino-acid-N-carboxyanhydride monomers for synthesis of polypeptides utilizing tetrahydrofuran (THF) as solvent was developed and used to synthesize a small library of some novel and previously reported NCA monomers in superior yield and purity.

CHAPTER ONE:
MATERIALS APROACHES TO FACILITATION OF SINGLE PARTICLE CRYO-EM

1.1 High-Resolution Biomacromolecular Structure Elucidation

High resolution structural information is a valuable asset for studies of biological systems and processes including: cellular trafficking and infrastructure, enzymatic processes, interactions between multiprotein complexes and infectious particles[1], as well as for structure-based, or rational, drug design efforts[2]. X-ray crystallography (XRD), and nuclear magnetic resonance (NMR)-based methods account for the majority of published biomacromolecular structures[3] to date (Table 1.1). Although tens of thousands of protein structures have been solved at or near atomic resolution, there are many targets of interest as pharmaceutical leads or for basic research, such as integral membrane proteins (IMP), which have not been solved with sufficient resolution to enable structure-based drug design or adequate conformational information.

Structure-based drug design and high-throughput screening are the main tools used for identification of new pharmaceutical lead compounds. High-throughput screening involves the production and testing of very large libraries of compounds against an appropriate cell type or disease model to determine bioactivity and efficacy. Once an active compound is discovered, the process may be further refined by testing against a library of structurally-related compounds. In the case of structure-based drug design[2b], where approaches like molecular docking are used to design ligands and

estimate binding affinities, high resolution structural information often dictates accuracy and validity of results or even the ability to engage in this effort at all. Bakheet et al.[2a] estimate that 57% of human drug targets are IMP's (Figure 1.1). Thus, facilitation of novel structure-based drug design will require high resolution structural information on these types of biomacromolecules.

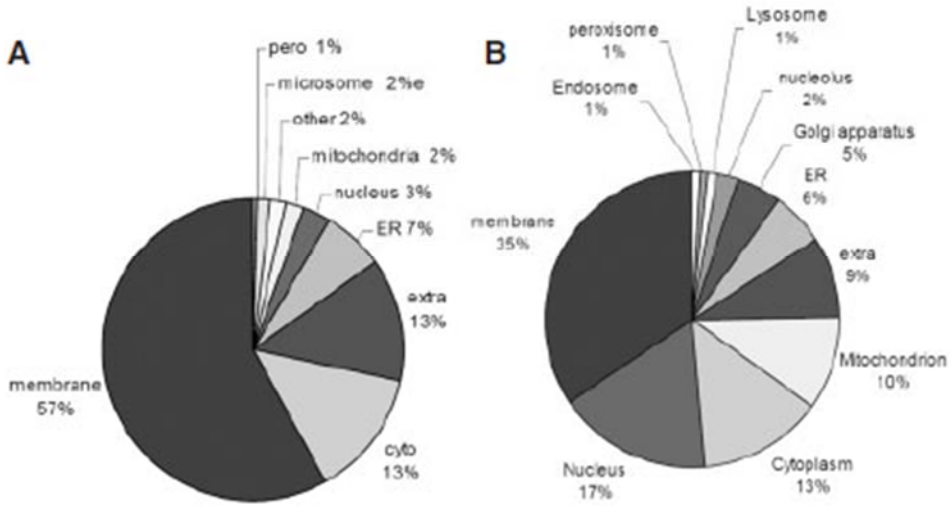

Figure 1.1 Sub-Cellular Locations of Proteins. (A) Drug targets and (B) Non-drug targets[2a].

A thorough structural understanding of biological systems is highly advantageous and often essential for progress in theoretical or applied efforts relating to the system of interest. Dynamic processes and complex multiprotein interactions are particularly informed through high-resolution structural information. For example, Chang et al.[1] have elucidated information regarding the mechanism by which some viruses package and

release their genome during infection via asymmetric single-particle cryo-EM reconstruction.

Table 1.1 Statistics of PDB Entries by Experimental Method (Nov. 8, 2016).

Experimental Method	Proteins	Nucleic Acids	Protein:NA Complexes	Other	Total
X-Ray	103,269	1,776	5,286	4	110,335
NMR	10,188	1,180	237	8	11,613
EM	877	30	302	0	1,209
Hybrid	92	3	2	1	98
Other	178	4	6	13	201

1.1.1 X-Ray Crystallography

XRD is currently the most widely used and cost-effective method for determination of protein structures (Table 1.1). The combination of electron density map information obtained from x-ray diffraction patterns of high quality protein crystals with known protein amino acid sequence allows for determination of the protein's three-dimensional structure (Figure 1.2A). X-ray crystallography (XRD) is based on observation of x-ray diffraction patterns from large well-ordered 3D crystals[4]. Protein crystals are typically grown from supersaturated solutions of the protein. Supersaturation is usually induced via addition of inorganic salts (e.g. $(NH_4)_2SO_4$, NaCl, KCl, $CaCl_2$, etc.), volatile organic solvents (e.g. ethanol, acetonitrile, acetone, etc.), or polymers (e.g. polyethylene glycol (PEG)) as precipitants to concentrate the protein solution. Crystal formation is limited to cases where strong intermolecular contacts can be made to form an extended lattice. Proteins often show complex phase diagrams, are highly sensitive to solution conditions (e.g. pH, salinity, temperature, etc.), and may be difficult to obtain in

high purity due to proteolytic degradation or limitations in removal of occult impurities. The protein crystallization process is often approached by varying experimental variables (e.g. pH, salinity, temperature, precipitant, humidity, etc.) systematically across a wide parameter space using different crystallization methods. Generally, the highest quality protein crystals, that is, those that are the most well-ordered, are obtained when the nucleation and crystal growth steps are kinetically well separated[5].

Proteins may also have a high degree of conformational flexibility, which can produce misfolded states. As a result, each molecule has regions on its surface that vary from particle to particle, which impedes stabilization from intermolecular contacts and impairs crystallization. This might be a result of a hinge between domains or other flexible motifs. Proteins are also typically difficult to concentrate under mild conditions and tend to form crystals that are fragile due to high water content. The larger and more structurally irregular the macromolecular complex is, the less likely it is that it will form crystals such that the contact area is large in comparison with the total area of the molecular assembly itself[6].

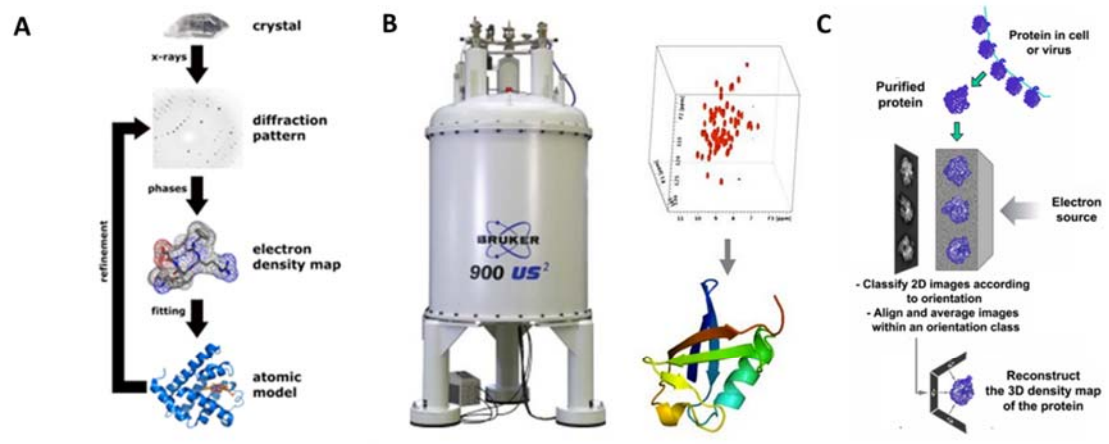

	X-Ray Crystallography	Protein-NMR	Single -Particle Cryo-EM
Sample	sample must be crystallized	labeled with a stable NMR-active isotope	sample is frozen in its native state
MW range	any size molecule	practical size limit is ~50 kDa	best suited for >200 kDa proteins and complexes
Advantages	crystallization process is slow and best suited for stable proteins	best suited for studying protein structural dynamics	near-atomic resolution fast sample prep

Figure 1.2 High Resolution Tools in Structural Biology[7]. (A) X-ray crystallography (XRD). (B) Nuclear magnetic resonance spectroscopy (NMR). (C) Single-particle cryo-EM.

Other molecules may be unstable to crystallization conditions or be more likely to precipitate due to denaturation. Lipid membranes are also likely to impede crystallization due to their dynamic nature. IMP's and some viruses fall into this class. IMP's are generally not amenable to crystallization and there is no guarantee that they will crystallize in their native conformation[8]. Often, crystallization efforts and structural studies of IMP's may involve focusing on partial structures. Also, crystallization happens over an extended time span, thus, dynamic events that happen on short time scales do not lend themselves to study by XRD. In crystallography, many conditions are often investigated. This requires a large quantity of sample, which is often impractical.

Crystallization also requires a highly pure sample. Since many samples are not amenable to extensive purification, crystallization may be impossible. Furthermore, extensive handling of human infectious particles is highly undesirable, but unavoidable during crystallographic screening.

1.1.2 Nuclear Magnetic Resonance (NMR)

NMR-based techniques involve multidimensional NMR either in solution, or in the solid-state[9]. Unlike XRD, NMR does not require crystallization and the sample is examined in solution. Protein-NMR relies on 2D Nuclear Overhauser Enhancement Spectroscopy (NOESY) to observe interactions between proximal hydrogen atoms of the polypeptide chain (less than 5 Å apart). Proteins isotopically labeled with ^{15}N- and ^{13}C-enriched amino acids are used to aid resolutions of overlapping peaks in multi-dimensional NOESY spectra. The combination of large numbers of NOE proximity relationships along with knowledge of the protein sequence allow for elucidation of the 3D structure of the protein (Figure 1.2B).

The foundations of NMR structural analysis rely on high quality NMR spectra recorded with good sensitivity and spectral resolution[7b]. These limitations become harder to overcome with increasing molecular weight). This is due to low sensitivity and line broadening due to rapid transverse spin relaxation and extensive signal overlap due to highly complex spectra. Most published structures of biomolecules studied by NMR have molecular weights less than 25 kDa[9]. Isotopic labeling has been employed to overcome

this problem[10], but this process is very time-consuming and requires extensive biochemical manipulation[11].

NMR structural studies of biomolecules require a very concentrated sample (~1mM). This means that a large amount of highly purified material is required. This is impractical in many cases and highly concentrated solutions are incompatible with many targets due to aggregation or denaturation. Frequently, NMR is used as a complement to low resolution crystal structures. Artificial conditions and sample preparation mean that there is no guarantee of native conformation from NMR structures.

1.1.3 Electron Microscopy

Electron microscopy is an emerging tool for the elucidation of high resolution structural information. Electron diffraction has long been successfully used to determine 3D structures of 2D crystalline samples up to a resolution of 1.9 Å[12]. Cryo-electron microscopy in combination with single-particle 3D reconstruction, collectively referred to as cryo-EM, has played an increasingly important role in determination of 3D structures up to subnanometer resolution[13]. Currently the highest obtained resolution from cryo-EM is the 2.2 Å structure of E. coli β-galactosidase in complex with the cell-permeant inhibitor phenethyl-β-D-thiogalactopyranoside (PETG) (Figure 1.3).

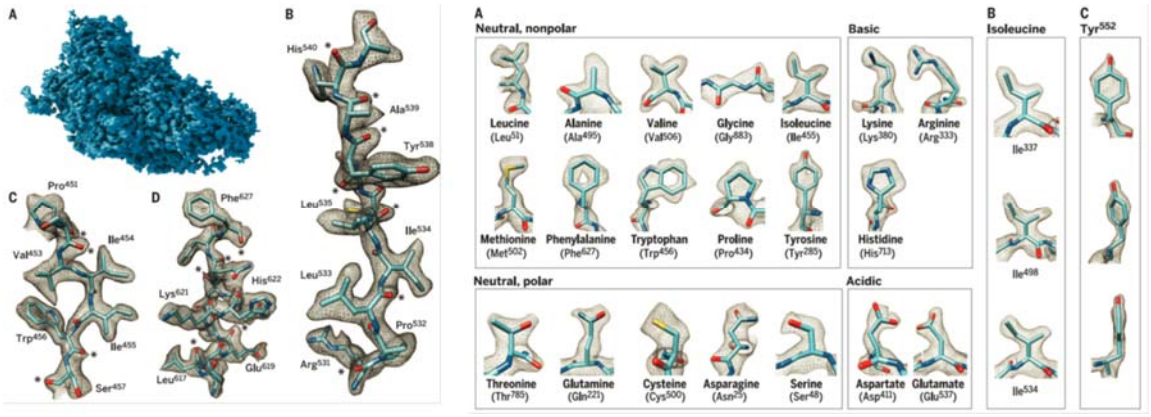

Figure 1.3. 2.2 Å Structure of β-Galactosidase-PETG Reported by Bartesaghi et. al[13a].

Observation of multi-protein interactions is essential for fundamental understanding of biochemistry and cell biology, but, like IMP's, structural studies of large macromolecular machines are rarely attainable using XRD or NMR-based methods. This is largely due to the size, irregular shape, and flexibility of these species. For example, a large macromolecular protein machine, the proteasome[14] has recently been a subject of structural study due to the link between the ubiquitin-proteasome pathway[15] and its relation to the mitotic cycle and oncogenesis[16]. The intact complex, referred to as the 26S Proteasome, along with the ubiquitin-conjugating system comprises the ubiquitin-proteasome system[16], which is the major extralysosomal pathway for intracellular protein degradation in eukaryotes. Like IMP's, large macromolecular complexes like the proteasome are impractical for study by XRD or NMR. Recently, efforts have focused on cryo-electron microscopy (cryo-EM)[17].

1.2 Single-Particle Cryo-EM

Three dimensional structure determinations based on cryogenic electron microscopy (cryo-EM) have become a common tool to structural biologists in recent years[12, 18]. The technique has become more viable for high-resolution structure elucidation due to advances in instrumentation[19], experimental techniques, and improved software for single-particle reconstruction[12, 20] that is more accessible and more powerful. As a result, the number of protein structures solved by cryo-EM has increased steadily since 2007 (Figure 1.4).

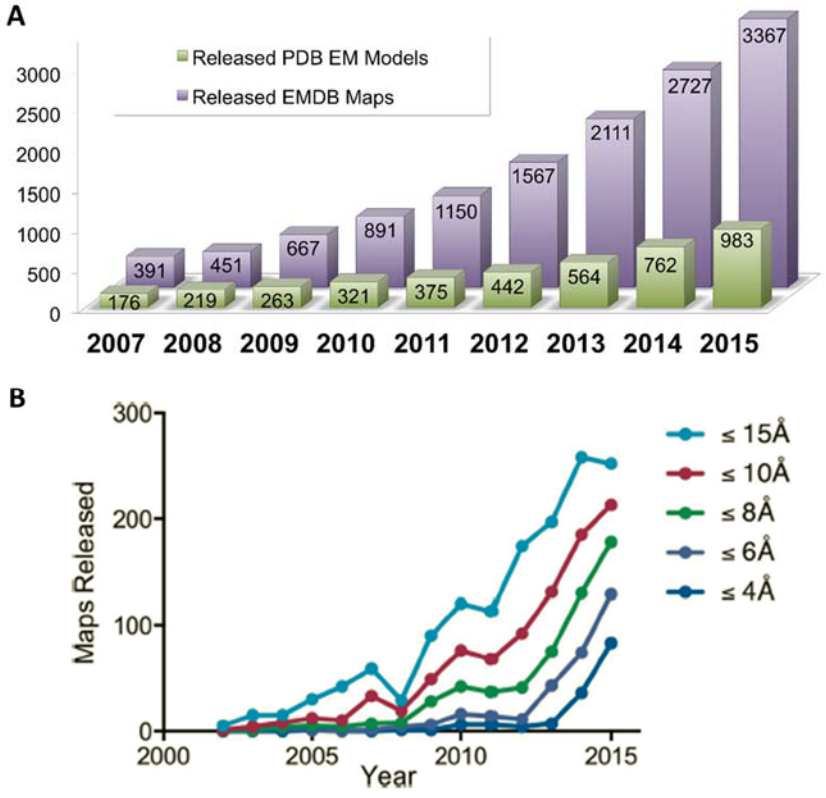

Figure 1.4 Growth of Structures Solved by Cryo-EM. (A) Growth of structures solved by cryo-EM since 2007 based on PDB and EMDB entries. (B) Growth of structures submitted to the PDB since 2002 by resolution[21].

Cryo-EM tends to generate higher resolution structures when the target is high molecular weight or consists of symmetrical multi-protein subunits. As a result, many of the first cryo-EM structures were viral particles. These targets are generally challenging for XRD and are too large for NMR. As cryo-EM develops as a technique, access to high-resolution structural information on these targets is expected to reveal new insights for biology and drug design (Figure 1.5).

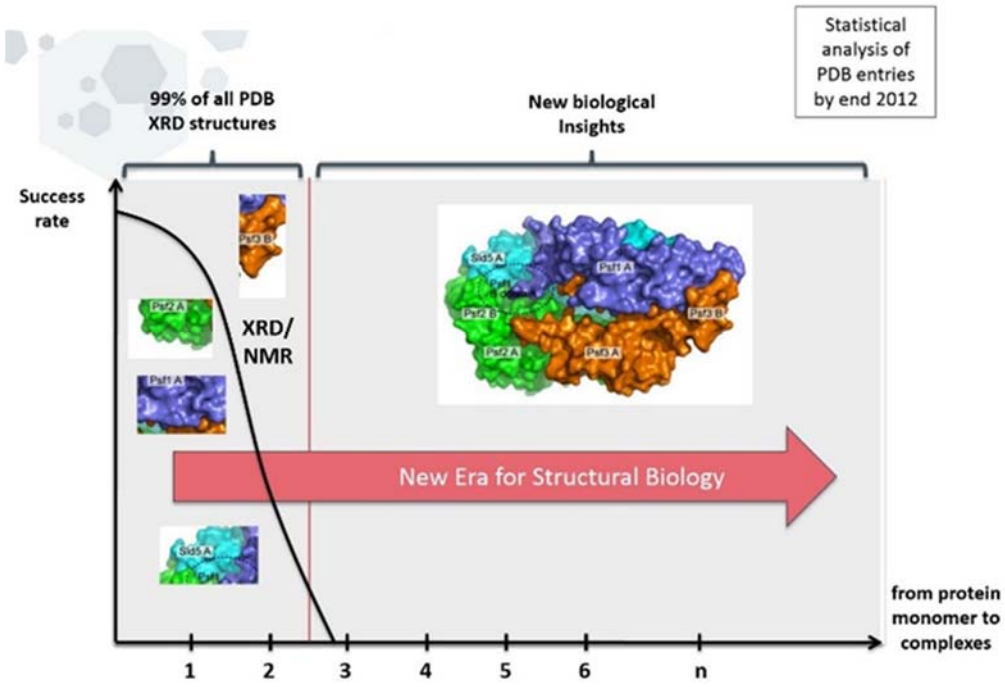

Figure 1.5 Added Value of Cryo-EM in Structural Biology[22].

In cryo-EM, highly pure samples are preferable although, moderately pure samples are tolerable depending on imaging conditions due to particle selection during image processing. Generally, a cryo-EM based project begins with isolation and

purification of the particle of interest (Figure 1.6). Cryo-EM sample preparation involves the application of a solution of the purified particle to a TEM grid. This solution is wicked away, allowed to dry shortly, and then flash-frozen in a solution of liquid ethane cooled with liquid nitrogen forming a thin layer of vitreous ice containing imbedded particles (Figure 1.7). An advantage of cryo-EM is that a relatively small amount of sample is required to collect a significant amount of data. One can take several micrographs from a single grid which requires only about 5 μL of sample at moderate concentrations. Since samples are flash frozen, relatively delicate samples are applicable to cryo-EM since the particles are preserved in a layer of vitreous ice. Also, events that happen on small time-scales may be observed since flash-freezing of the sample effectively preserves a snapshot of molecular conformations at the time of freezing. These advantages are particularly desirable for observing interactions between macromolecules or observing large delicate samples.

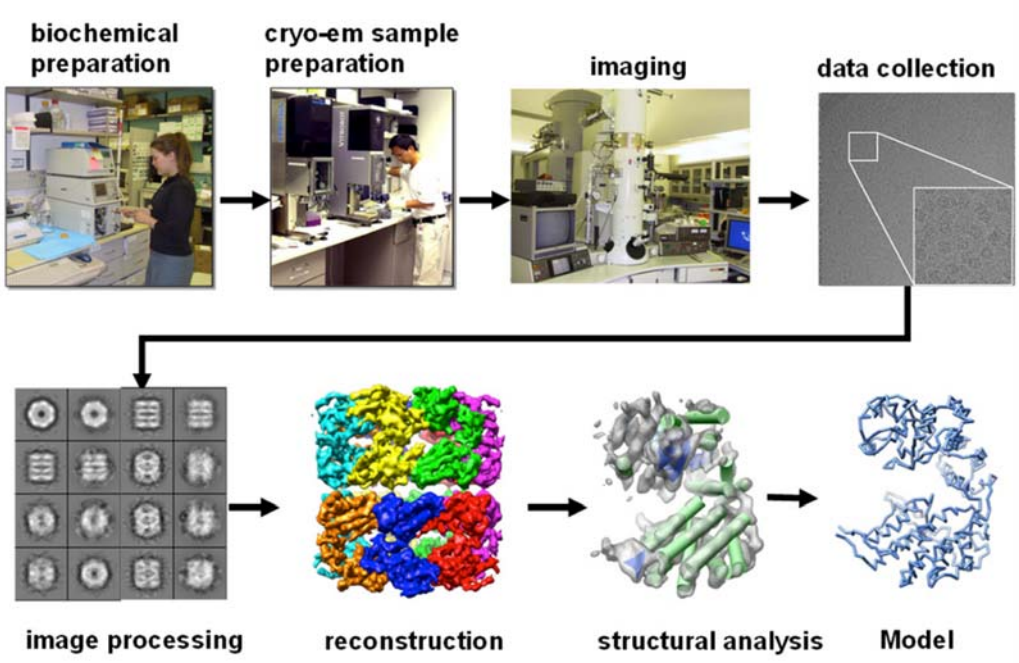

Figure 1.6 Pipeline in Biological Cryo-EM.

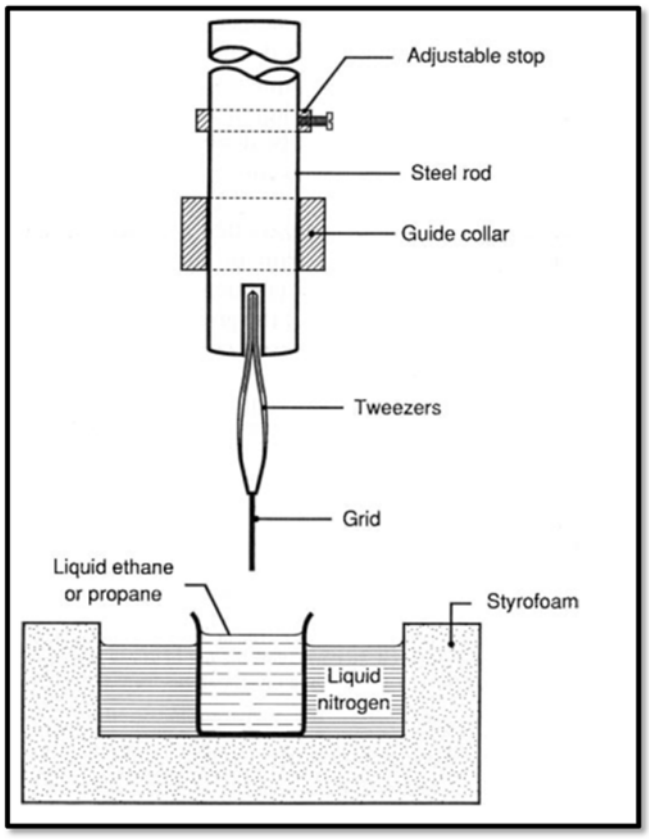

Figure 1.7 Vitrification Process During Cryo-EM Sample Preparation.

This sample is then imaged under low dose conditions to prevent sample degradation due to radiation damage. Radiation damage is one of the major drawbacks of electron optics applied to organic and biological systems. Primary events result in the formation of reactive species such as free radicals, which then undergo a secondary chemical event that promotes structural denaturation. Accumulated electrons also lead to the phenomenon known as charging, in which areas of accumulated charge distort the electron optics and lead to aberrations.

In traditional transmission electron microscopy, stains are used to improve contrast. These stains are composed of heavy metal salts. This is because contrast is mostly due to phase contrast in EM, which increases with increasing Z (atomic number). Higher Z elements scatter electrons mote effectively, which leads to high contrast in areas where the high Z elements are localized. In cryo-EM, typically no stains are used although the technique has been applied[23]. An absence of staining is preferable, since staining can lead to deformation, and phase contrast from protein atoms is necessary if atomic-scale resolution is the ultimate goal of the study.

2D particle projection images are then analyzed using reconstruction software to derive a reconstructed 3D image of the particle. One limitation of cryo-EM is the large number of particles necessary for a high resolution 3D structure to be obtained. The number depends on the geometry, size, and conformational flexibility of the particle, but tens of thousands of particles may be required. For example, a 6 Å structure of the molecular chaperone GroEL was obtained from 39,085 particles selected from 42 micrographs[24].

1.2.1 3D Reconstruction of Biomacromolecules and Complexes

Reconstruction strategies often involve geometrical averaging of particle orientations during 3D reconstruction, which simplifies the process. In fact, 3D reconstruction is generally more easily accomplished for highly symmetrical particles, but is theoretically applicable to any particle geometry (Figure 1.8). Structural studies of the Epsilon-15 virus by cryo-EM have determined the viral capsid structure at 4.5 Å

imposing icosahedral symmetry[25] while the structure was solved at 20 Å using an asymmetric approach[26]. Cryo-EM has been frequently employed for studies of virus structure due to the high symmetry of these particles.

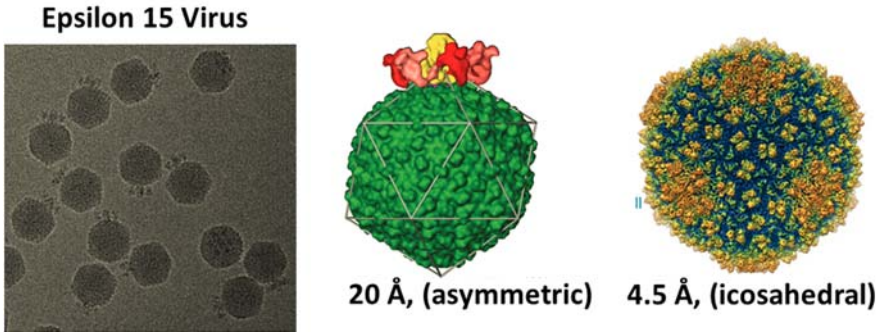

Figure 1.8 Importance of Symmetry in Cryo-EM. 20 Å asymmetric reconstruction[24] and 4.5 Å icosahedral reconstruction[23] of Epsilon-15 virus.

The 3D reconstruction process depends on the method and varies from different developers and software. Generally, particles are selected manually using an image processing program. Most reconstruction software packages contain all of the necessary tools for a reconstruction project. More recently, automated particle selection programs have been developed to simplify the process[27]. However, automated particle selection often falls short of manual particle selection because automated programs tend to pick anomalies, and distorted particles. Including anomalous particles in a reconstruction data set can dramatically limit the minimum attainable resolution of the reconstruction. This also points out that conformational flexibility is not desirable in cryo-EM studies. As a result, manual particle selection is sometimes necessary. For reconstruction to be successful, the particle needs to be represented by many particles in many different

rotational orientations. This can be an issue since it has been noted that some particles adopt preferred orientations during cryo-EM sample preparation. For example, the molecular chaperone GroEL is a barrel shaped protein and particle images of the protein on its side are much more prevalent in micrographs than images of the two ends of the protein[23b, 28].

The particles are grouped into classes of similar orientation. The basic principle of 3D reconstruction involves Fourier transform of the 2D projection images of the 3D particle. These 2D Fourier transforms can then be combined in Fourier space to produce the 3D Fourier-space representation of the phase contrast from cryo-EM imaging. This can then undergo Fourier inversion to give the real-space 3D reconstruction.

Cryo-EM has become more popular and more viable in recent years due to advances in electron microscope technology as well as reconstruction algorithms[29] and software[30]. Development of software for reconstructions involving more diverse particle symmetries[20c] and more user friendly software[20a, 20b, 30b] are among the many developments of late in cryo-EM software development. In particular, much effort has centered around accurate determination of the contrast transfer function (CTF) that corrects the 2D images for the experimental out of focus distance, accurate determination of the relative orientation of individual particles, and the use of larger particle sets. This has led to routine reconstructions of suitable targets at 10 Å resolution, which is expected to continue to improve to in the near future.

Cryo-EM shows a great deal of promise for biomacromolecular structure elucidation, especially at moderate resolution and hybrid methods, which combine EM-based studies of fragile complexes with XRD or NMR analyses of individual components

are promising but laborious processes[7a, 31]. In many ways cryo-EM is a complementary technique to XRD and NMR. It works well for large fragile targets, provides a very good mimic of the targets native environment, and studies require a very small amount of pure material. To push EM-based structure determination further, materials approaches need to be invented that can facilitate cryo-EM-based 3D reconstruction.

1.3 Materials Approaches to Single-Particle Cryo-EM

Materials methods have previously been applied to structural studies focusing on electron microscopy-based structure determination. The concept of interfacial templating was first applied to 2D crystallography and the techniques were later applied to cryo-EM to expand the scope of cryo-EM in terms of expanding practical targets for cryo-EM and allowing for observation of dynamic events that would not otherwise be observed under conventional cryo-EM sample preparation and imaging conditions.

1.3.1 2D Crystallization of Proteins at Lipid Interfaces

Electron diffraction has regularly been successfully used to determine 3D structures of 2D crystalline samples up to a resolution of 1.9 Å[12]. For compounds with convoluted topologies and internal degrees of freedom which are unable to form ordered diffraction-quality 3D crystals, 1D and 2D templating approaches have been developed by orienting the protein with respect to the interface and limiting 2D diffusion. 1D and 2D substrates like lipid lamellar phases, lipid monolayers, and lipid cubic phases have been used to produce 2D crystals of both soluble proteins and IMP's. These interfaces

provide large surface areas for protein adsorption, can be utilized with a wide variety of lipid conjugates allowing for tunable binding interactions, and are compatible with microfluidic interfaces.

2D crystals grown at interfaces are only a single molecular layer in thickness, making them extremely challenging for analysis by conventional XRD. If the 2D crystals are analyzed by tilt-series electron crystallography, the reconstructed volume invariably contains the "missing cone" defect due to practical limitations of projecting the electron beam through the sample at high tilt angles. 1D substrates allow for analysis by helical reconstruction[32], however, this method requires strict control of the 1D substrate diameter, which is often impractical and is dependent on the nature of the substrate.

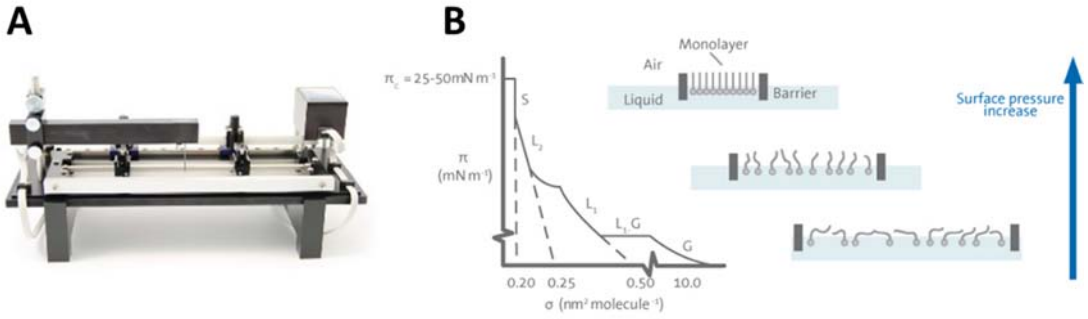

Figure 1.9 Lipid Monolayer Formation Using a Langmuir Trough[33]. (A) A typical Langmuir trough setup. (B) Pressure-area isotherm relationship to 2D lipid phase.

Most interfacial templating approaches have focused on lipid monolayer-based substrates[5]. Lipid monolayer-based approaches involve formation of a monolayer film at the air-water interface. This is typically accomplished by spreading an organic solution of the lipids on a Langmuir trough (Figure 1.9A). As the solvent evaporates, the lipids form

a monolayer at the air-water interface with the polar head groups orient toward the aqueous subphase and the hydrophobic lipid tails orient toward the air where they can interact through dispersion forces with the lipid chains of neighboring molecules. The monolayer film can then be compressed allowing for phase control of the lipid monolayer. As the monolayer is compressed, the lipids form 2D gas-, fluid-, or solid-state films at the air-water interface (Figure 1.9B).

If the protein of interest is present in the aqueous subphase, it can become concentrated at the surface of the Langmuir trough if it possesses an affinity for the lipids of the substrate. Thus, the general consideration for 2D crystallization is the generation of an interface that can produce enrichment of the protein at the interface. The combined elevated protein concentration, enhanced protein alignment, and fluid dynamics of the film, which allows for lateral mobility, contribute to the formation of 2D crystals. By designing the lipid components to have specific interactions with the protein of interest, samples of lower purity may be acceptable for 2D crystallization.

2D crystallization typically involves simple experimental protocols, and a wide range of monolayer compositions may be utilized to take advantage of specific tunable monolayer properties.

1.3.2 Interfacial Templating

The first effort of this type was reported by Kornberg[34] and coworkers who used antibody-based affinity interactions to concentrate protein targets on affinity lipid monolayer surfaces (Figure 1.10A). In this example, a monolayer of DNP-modified phasphatidylethanolamine (PE) lipid (Figure 1.11A) in a mixed monolayer of 1:1 DNP-

PE and PC was used to produce 2D crystals of anti-DNP IgG through the specific DNP-antibody interaction. This ligand affinity technique was later adapted to structural characterization of RNA polymerase II through electrostatic interaction with cationic-lipid-containing monolayers, 2D crystallization of streptavidin on monolayers containing biotinylated lipids, and 2D crystallization of DNA gyrase on monolayers containing an ATP-lipid conjugate[5]. Many different material interfaces have been employed utilizing interactions from electrostatics to coordination complexation to highly specific ligand-receptor type interactions[5, 35]. Many of these interactions are based on methods developed for affinity purification of biomolecules[36].

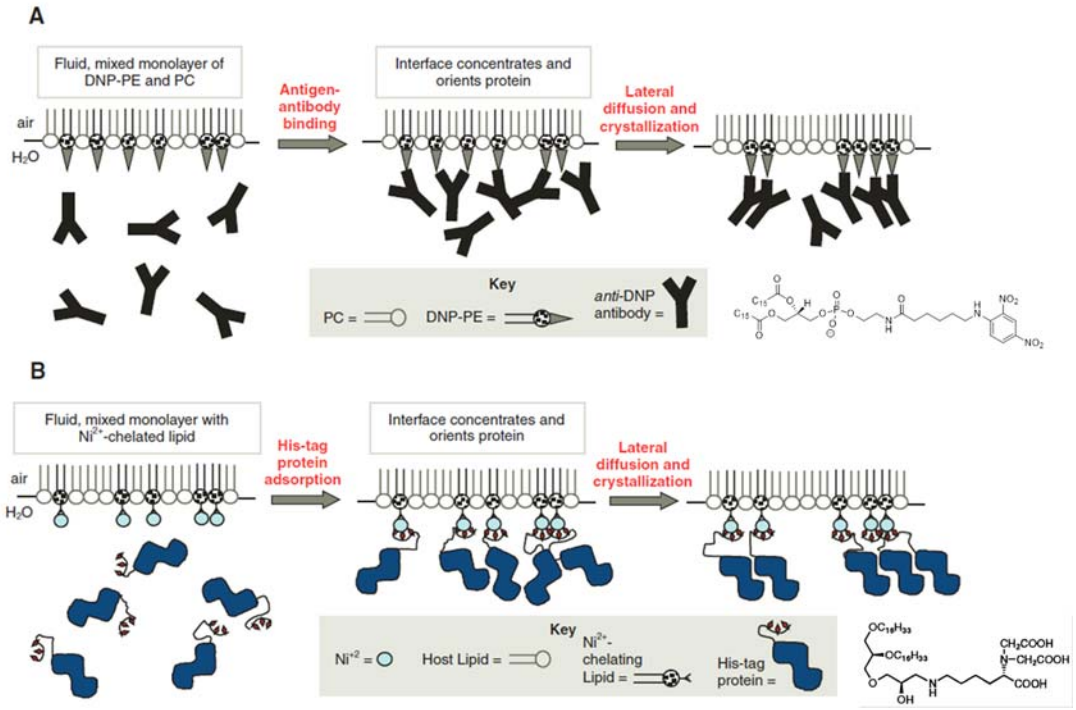

Figure 1.10 Conceptual Models of 2D Crystallization: (A) The original Uzgiris and Kornberg model using an antigenic lipid (DNP-PE), to concentrate anti-DNP antibodies at the air-water interfaces[34]. (B) Application of IMAC chemistry to induce 2D crystallization of recombinant histidine-tagged proteins[37].

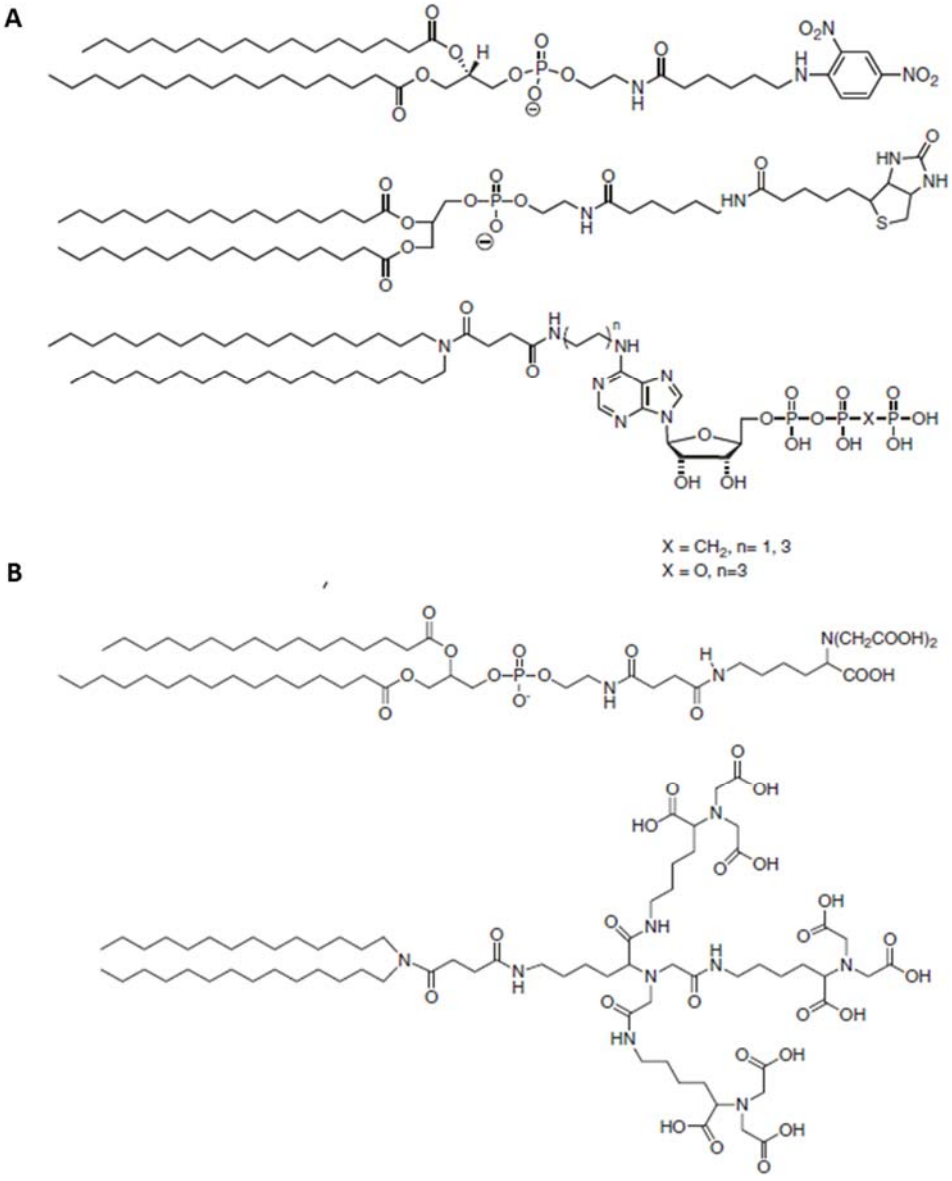

Figure 1.11 Molecular Structures of Some Lipids Used for 2D Crystallization Studies. (A) some ligand-lipid conjugates utilized for ligand-specific immobilization and crystallization and (B) some NTA-lipids synthesized for IMAC-based immobilization and crystallization of histidine-tagged proteins.

The interfacial templating approach to 2D crystallization was later adapted to incorporate affinity interactions from immobilized metal affinity chromatography (IMAC) chemistry (Figure 1.10B). These approaches generally rely on affinity interaction between nitrilotriacetic acid- (NTA) or iminodiacetic acid- (IDA)-lipid conjugates with divalent metal ions (e.g. Ni(II), Cu(II), Co(II), etc.) and a genetically engineered histidine tag (his-tag) of the protein of interest. Thompson and coworkers[37] used a nitriloltriacetic acid (NTA) containing mixed monolayer to capture and orient N-terminal his-tagged Moloney murine leukemia virus capsids forming 2D crystals for 2D electron crystallography. A similar approach was used to analyze HIV-1 capsid by 2D electron crystallography on NTA-lipid-containing surfaces[38]. Several NTA-containing lipids have been reported (Figure 1.11B). NTA forms a tetradentate complex with many divalent metal ions like Ni(II), Cu(II), etc.[39] This leaves two vacant coordination sites for an oligo-histidine tag (his-tag) to bind (Figure 1.12). Equilibrium constants K_D of 10^{-7} M for the his_6:protein:M^{2+} and $8x10^{-13}$ M for NTA:Ni^{2+} have been reported[39-40].

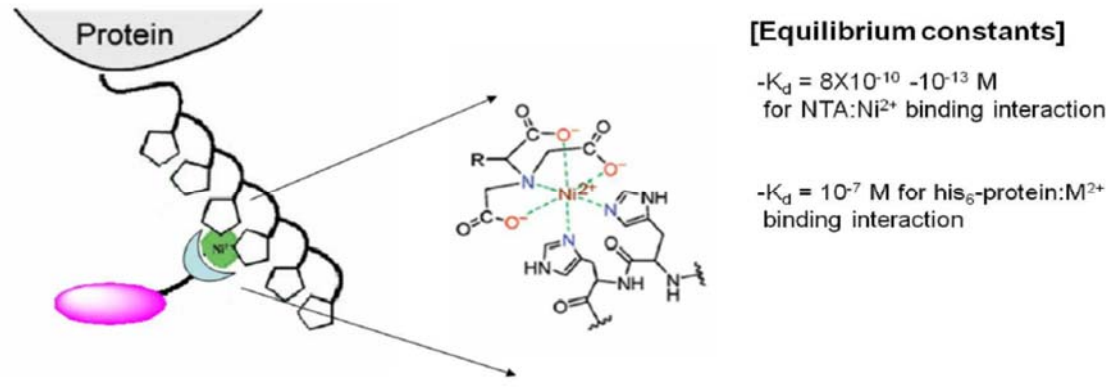

Figure 1.12 Binding Interaction of NTA:Ni^{2+}:His_6 in IMAC Chemistry[41].

Zhou et al. introduced the site-hopping concept for 2D crystallization of his-tagged proteins[42]. This concept involves substrates composed of acylated cyclodextrins (CD). These compounds formed stable monolayers exposing the CD cavity. CD cavities have varying binding affinity for various small molecular guests[43]. The second component of the system consists of an NTA-conjugate of a specific molecule possessing binding affinity for the CD cavity. By mixing the NTA-conjugate with the his-tagged protein of interest, a transient interaction with the monolayer is established. This approach may allow for more favorable kinetics of nucleation with respect to crystal growth due to the enhanced lateral mobility of protein at the 2D surface (Figure 1.13).

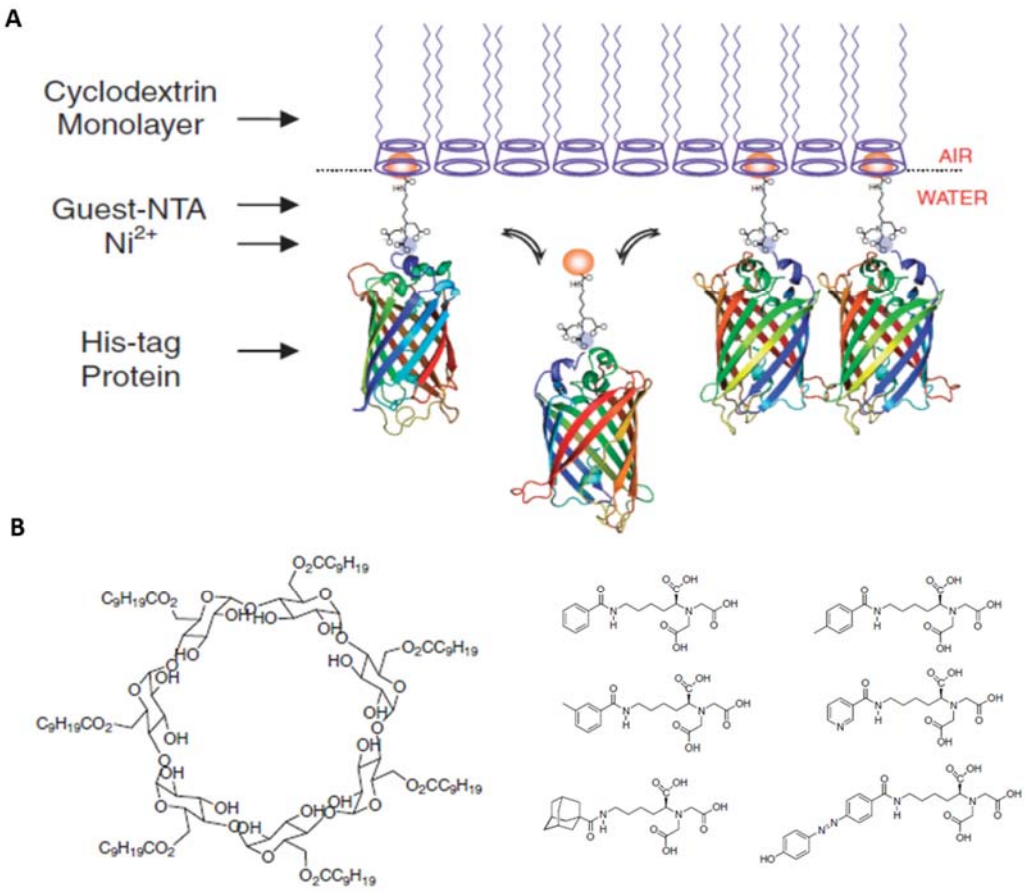

Figure 1.13 Site-Hopping Concept for 2D Crystallization Using Acylated-Cyclodextrin-Based Monolayers. (A) Site-Hopping concept for 2D Protein Crystallization. (B) Molecular structures of β-CD-lipid and some guest-NTA compounds.

1.3.3 The Affinity Grid

As cryo-EM became a more reliable and high-resolution tool, it was natural that the 2D crystallization strategy was adapted to address sample requirements for cryo-EM. By using TEM grids modified with 2D monolayer surfaces, the same affinity interactions could be utilized to generate diffuse bound particles for cryo-EM as opposed to 2D crystals. This approach allows for single-step purification and grid preparation and may allow for cryo-EM analysis of challenging samples (e.g. low concentration, transient

intermediates, etc.) and ultimately allow cryo-EM to become a more high-throughput technique.

1.3.3.1 Lipid Monolayer-Based Affinity Grids

The first direct application of the techniques of interfacial templating developed and implemented for 2D crystallization were first applied to cryo-EM when Kelly et al. developed the concept of monolayer purification[44] and the affinity grid[45]. The method involves the transfer of a mixed monolayer of lipids doped with a lipid with an NTA chelator head (Figure 1.14A) followed by capture and imaging of the adsorbed his-tagged proteins. An adaptation of this method utilizing a his-tagged adaptor protein bound to specific antibodies for the protein of interest has also been reported (Figure 1.14B)[46]. The affinity grids were reported to be shelf-stable for several months and able to capture and prepare samples for cryo-EM within minutes.

These materials were used to capture his-tagged rpl3, the human homolog of the E. coli 50 S ribosomal subunit rplC with or without associated RNA depending on sample preparation protocols. Cryo-EM data obtained using the modified grids were used to generate reconstructions of the 50 S ribosomal subunit, the 70 S ribosome and the 30 S ribosomal subunit from images from the same sample. This demonstrates the utility of this approach for study of dynamic processes within living systems that would be unobtainable if the target of interest is subjected to conventional sample preparation, particularly chromatographic purification. These materials were also shown to be stable in the presence of glycerol and detergents. This property was exploited to capture his-tagged aquaporin-9 (AQP9) from detergent-solubilized membrane fractions of sf9 insect

cells. This example demonstrates the utility of this approach for isolation of an IMP, a limitation for conventional cryo-EM.

Although this approach has shown several advantageous properties for cryo-EM, there are still several limitations to this approach. The monolayers are relatively unstable and tend to degrade in film quality following consecutive washes. The close proximity of the NTA moiety to the 2D surface allows relatively little rotational mobility for targets that contain a single his-tag. This limitation may lead to orientational bias and overall lower possible resolution for targets with only a single his-tag. The presence of antibody may lead to lower resolution or conformational changes relative to the native protein structure. Furthermore, the low electrical conductivity of the lipid monolayer may lead to charging effects. In order to address these limitations, novel affinity grids composed of lipopolymers[47] and based on graphene-oxide[48] have been designed and evaluated for cryo-EM. More recently, Sharma et al[49]. used the affinity grid approach to show that PKC βII binds to the small ribosomal subunit (40S) and interacts with RACK1, a seven bladed β-propeller protein present on the 40S and binds to two different regions close to blades 3 and 4 of RACK1. This study was a step toward understanding the molecular framework of PKC βII-RACK1 interaction and its role in translation.

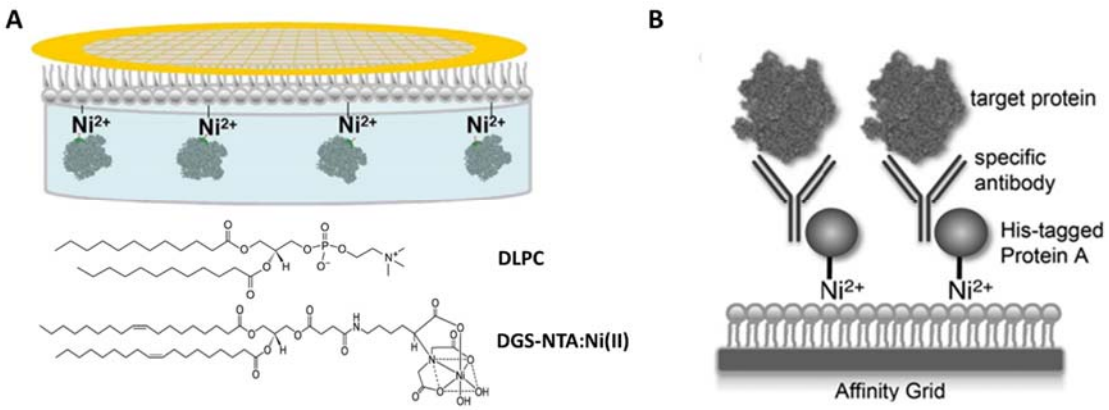

Figure 1.14 The Affinity Grid Approach to Cryo-EM. (A) affinity grids approach based on IMAC chemistry[45] and (B) alternate approach enabling capture of non-his-tagged proteins[46].

1.3.3.2 Antibody-Based Affinity Grids

In another interesting variant of the affinity grid concept, Yu et al. introduced the antibody-based affinity grid and the concept of cryo-SPIEM. This technique applied the traditional concept of solid-phase immune electron microscopy (SPIEM) to cryo-EM[50]. This approach involves direct non-covalent modification of carbon-coated TEM grids with antibodies. This approach was used to isolate and generate 3D reconstructions of native protein targets from pure samples and cellular lysates.

1.3.4 Other Approaches

In a particularly interesting example, Sigworth and coworker have developed a novel spherical reconstruction algorithm that allowed for determination of the BK potassium channel at 30 Å resolution as an IMP imbedded in a tethered proteoliposome formulation (Figure 1.15). This method allowed for moderate resolution reconstruction of an IMP,

which has previously eluded efforts by XRD by building off of an existing platform that had been developed to grow 2D streptavidin crystals at biotinylated lipid interfaces which can then be transferred to TEM grids[51]. The method highlights the flexibility of cryo-EM-based reconstruction.

The channel was reconstituted into liposomes doped with PEG-ylated lipids bearing a biotin at their termini. EM grids were prepared and a monolayer 2D crystal of streptavidin was transferred to the grid. The grids were then treated with the liposome formulation and imaged. Images were collected of the protein imbedded in the liposome[29]. This case required the development of a novel spherical reconstruction algorithm[20c], which illustrates the inherent challenges and flexibility of cryo-EM software development.

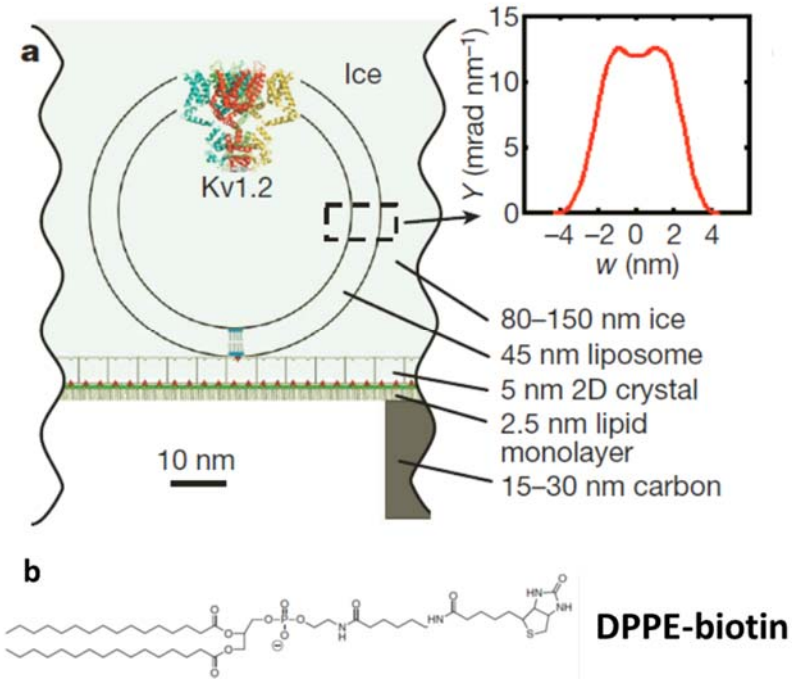

Figure 1.15 The Proteoliposome-Based Approach Developed by Sigworth et al[27].

Finally, Turberfield and coworkers[52] recently have described the use of two-dimensional DNA templates for site-specific scaffolding of G-protein-coupled membrane receptor complexes for SPA, however, the resolution possible with these templates is not yet known.

1.4 Conclusions

High-resolution biomacromolecular structure elucidation is fundamentally important to structure-based drug design and basic research into complex biochemical processes. XRD and NMR account for the majority of the reported protein structures on the protein data Bank (PDB). Cryo-EM is an emerging alternative to XRD and NMR that

is complementary in terms of sample applicability relative to XRD and NMR. TEM grid modification approaches originally developed for 2D crystallization studies have been applied to cryo-EM to extend the breadth of the technique. The affinity grid concept based on IMAC chemistry and antibody interactions has been used to isolate cryo-EM samples directly from cellular lysates or purified samples. Further exploration of this approach should continue to allow for application of the cryo-EM technique to challenging samples and targets that may not be readily amenable to XRD, NMR, or traditional cryo-EM samples preparation techniques. This could allow for access to high-resolution structural data on targets that are not currently accessible furthering molecular therapeutic and basic biochemical research efforts.

1.5 References

1. Chang, J.; Weigele, P.; King, J.; Chiu, W.; Jiang, W., Cryo-EM Asymmetric Reconstruction of Bacteriophage P22 Reveals Organization of its DNA Packaging and Infecting Machinery. *Structure* **2006,** *14* (6), 1073-82.

2. (a) Bakheet, T. M.; Doig, A. J., Properties and Identification of Human Protein Drug Targets. *Bioinformatics* **2009,** *25* (4), 451-7; (b) Mandal, S.; Moudgil, M.; Mandal, S. K., Rational Drug Design. *Eur J Pharmacol* **2009,** *625* (1-3), 90-100; (c) Gschwend, D. A.; Good, A. C.; Kuntz, I. D., Molecular Docking Towards Drug Discovery. *J Mol Recogn: JMR* **1996,** *9* (2), 175-86.

3. Grey, J. L. Thompson, D. H., Challenges and Opportunities for New Protein Crystallization Strategies in Structure-Based Drug Design. *Exp Op Drug Disc* **2010,** *5* (11), 1039-1045.

4. Hernandez-Santoyo, A., Difficult Macromolecular Structures Determined Using X-Ray Diffraction Techniques. *Protein Pept Lett* **2012,** *19* (7), 770-7.

5. Thompson, D. H.; Zhou, M. K.; Grey, J.; Kim, H. K., Design, Synthesis, and Performance of NTA-Modified Lipids as Templates for Histidine-Tagged Protein Crystallization. *Chem Lett* **2007,** *36* (8), 956-975.

6. Krissinel, E.; Henrick, K., Inference of Macromolecular Assemblies from Crystalline State. *J Mol Biol* **2007,** *372* (3), 774-97.

7. (a) Rossmann, M. G.; Morais, M. C.; Leiman, P. G.; Zhang, W., Combining X-Ray Crystallography and Electron Microscopy. *Structure* **2005,** *13* (3), 355-62; (b) Wider, G.; Wuthrich, K., NMR Spectroscopy of Large Molecules and Multimolecular Assemblies in Solution. *Curr Opin Struct Biol* **1999,** *9* (5), 594-601.

8. (a) Fujiyoshi, Y., Electron Crystallography for Structural and Functional Studies of Membrane Proteins. *J Electron Microsc* **2011,** *60 Suppl 1*, S149-59; (b) Wisedchaisri, G.; Reichow, S. L.; Gonen, T., Advances in Structural and Functional Analysis of Membrane Proteins by Electron Crystallography. *Structure* **2011,** *19* (10), 1381-93.

9. Renault, M.; Cukkemane, A.; Baldus, M., Solid-State NMR Spectroscopy on Complex Biomolecules. *Angew Chem* **2010,** *49* (45), 8346-57.

10. Ito, Y.; Selenko, P., Cellular Structural Biology. *Curr Opin Struct Biol* **2010,** *20* (5), 640-8.

11. McIntosh, L. P.; Dahlquist, F. W.; Redfield, A. G., Proton NMR and NOE Structural and Dynamic Studies of Larger Proteins and Nucleic Acids Aided by Isotope Labels: T4 lysozyme. *J Biomol Struct Dyn* **1987,** *5* (1), 21-34.

12. Zhou, Z. H., Towards Atomic Resolution Structural Determination by Single-Particle Cryo-Electron Microscopy. *Curr Opin Struct Biol* **2008,** *18* (2), 218-28.

13. (a) Alberto Bartesaghi, A. M., Soojay Banerjee, Doreen Matthies, Xiongwu Wu, Jacqueline L. S. Milne, Sriram Subramaniam, 2.2 Å Resolution Cryo-EM Structure of β-Galactosidase in Complex with a Cell-Permeant Inhibitor. *Science* **2015,** *348* (6239); (b) Banerjee, S.; Bartesaghi, A.; Merk, A.; Rao, P.; Bulfer, S. L.; Yan, Y.; Green, N.; Mroczkowski, B.; Neitz, R. J.; Wipf, P.; Falconieri, V.; Deshaies, R. J.; Milne, J. L.; Huryn, D.; Arkin, M.; Subramaniam, S., 2.3 A Resolution Cryo-EM Structure of Human p97 and Mechanism of Allosteric Inhibition. *Science* **2016,** *351* (6275), 871-5.

14. Baumeister, W.; Walz, J.; Zuhl, F.; Seemuller, E., The Proteasome: Paradigm of a Self-Compartmentalizing Protease. *Cell* **1998,** *92* (3), 367-380.

15. Hasselgren, P. O.; Fischer, J. E., The Ubiquitin-Proteasome Pathway - Review of a Novel Intracellular Mechanism of Muscle Protein Breakdown During Sepsis and Other Catabolic Conditions. *Ann Surg* **1997,** *225* (3), 307-316.

16. Orlowski, R. Z., The Role of the Ubiquitin-Proteasome Pathway in Apoptosis. *Cell Death Differ* **1999,** *6* (4), 303-313.

17. Iwanczyk, J.; Sadre-Bazzaz, K.; Ferrell, K.; Kondrashkina, E.; Formosa, T.; Hill, C. P.; Ortega, J., Structure of the Blm10-20 S Proteasome Complex by Cryo-Electron Microscopy. Insights Into the Mechanism of Activation of Mature Yeast Proteasomes. *J Mol Biol* **2006,** *363* (3), 648-59.

18. (a) Jiang, W.; Ludtke, S. J., Electron Cryomicroscopy of Single Particles at Subnanometer Resolution. *Curr Opin Struct Biol* **2005,** *15* (5), 571-7; (b) Glaeser, R. M., Electron Microscopy of Biological Specimens in Liquid Water. *Biophys J* **2012,** *103* (1), 163-4; author reply 165-6; (c) Zhang, X.; Settembre, E.; Xu, C.; Dormitzer, P. R.; Bellamy, R.; Harrison, S. C.; Grigorieff, N., Near-Atomic Resolution Using Electron Cryomicroscopy and Single-Particle Reconstruction. *Proc Natl Acad Sci U S A* **2008,** *105* (6), 1867-72.

19. Cheng, Y.; Grigorieff, N.; Penczek, P. A.; Walz, T., A Primer to Single-Particle Cryo-Electron Microscopy. *Cell* **2015,** *161* (3), 438-49.

20. (a) Tang, G.; Peng, L.; Baldwin, P. R.; Mann, D. S.; Jiang, W.; Rees, I.; Ludtke, S. J., EMAN2: An Extensible Image Processing Suite for Electron Microscopy. *J Struct Biol* **2007,** *157* (1), 38-46; (b) Hohn, M.; Tang, G.; Goodyear, G.; Baldwin, P. R.; Huang, Z.; Penczek, P. A.; Yang, C.; Glaeser, R. M.; Adams, P. D.; Ludtke, S. J., SPARX, a New Environment for Cryo-EM Image Processing. *J Struct Biol* **2007,** *157* (1), 47-55; (c) Jiang, Q. X.; Chester, D. W.; Sigworth, F. J., Spherical Reconstruction: a Method for Structure Determination of Membrane Proteins from Cryo-EM Images. *J Struct Biol* **2001,** *133* (2-3), 119-31.

21. Subramaniam, S. W. K., and Henderson, R. CryoEM at IUCrJ: a New Era. *IUCrJ* **2016,** *3* (1), 3-7.

22. Wohlfarth, T., The Role of Cryo-TEM for Structural Biology – Part I. **2010**.

23. (a) Adrian, M.; Dubochet, J.; Fuller, S. D.; Harris, J. R., Cryo-Negative Staining. *Micron* **1998,** *29* (2-3), 145-60; (b) De Carlo, S.; Boisset, N.; Hoenger, A., High-Resolution Single-Particle 3D Analysis on GroEL Prepared by Cryo-Negative Staining. *Micron* **2008,** *39* (7), 934-43.

24. Ludtke, S. J.; Chen, D. H.; Song, J. L.; Chuang, D. T.; Chiu, W., Seeing GroEL at 6 A Resolution by Single Particle Electron Cryomicroscopy. *Structure* **2004,** *12* (7), 1129-36.

25. Jiang, W.; Baker, M. L.; Jakana, J.; Weigele, P. R.; King, J.; Chiu, W., Backbone Structure of the Infectious Epsilon15 Virus Capsid Revealed by Electron Cryomicroscopy. *Nature* **2008,** *451* (7182), 1130-4.

26. Jiang, W.; Chang, J.; Jakana, J.; Weigele, P.; King, J.; Chiu, W., Structure of Epsilon15 Bacteriophage Reveals Genome Organization and DNA Packaging/Injection Apparatus. *Nature* **2006,** *439* (7076), 612-6.

27. (a) Sorzano, C. O.; Recarte, E.; Alcorlo, M.; Bilbao-Castro, J. R.; San-Martin, C.; Marabini, R.; Carazo, J. M., Automatic Particle Selection from Electron Micrographs Using Machine Learning Techniques. *J Struct Biol* **2009,** *167* (3), 252-60; (b) Zhu, Y.; Carragher, B.; Glaeser, R. M.; Fellmann, D.; Bajaj, C.; Bern, M.; Mouche, F.; de Haas, F.; Hall, R. J.; Kriegman, D. J.; Ludtke, S. J.; Mallick, S. P.; Penczek, P. A.; Roseman, A. M.; Sigworth, F. J.; Volkmann, N.; Potter, C. S., Automatic Particle Selection: Results of a Comparative Study. *J Struct Biol* **2004,** *145* (1-2), 3-14.

28. (a) Ludtke, S. J.; Baker, M. L.; Chen, D. H.; Song, J. L.; Chuang, D. T.; Chiu, W., De Novo Backbone Trace of GroEL from Single Particle Electron Cryomicroscopy. *Structure* **2008,** *16* (3), 441-8; (b) Ludtke, S. J.; Jakana, J.; Song, J. L.; Chuang, D. T.; Chiu, W., A 11.5 A Single Particle Reconstruction of GroEL Using EMAN. *J Mol Biol* **2001,** *314* (2), 253-62.

29. Wang, L.; Sigworth, F. J., Structure of the BK Potassium Channel in a Lipid Membrane from Electron Cryomicroscopy. *Nature* **2009,** *461* (7261), 292-5.

30. (a) Ludtke, S. J., 3-D structures of Macromolecules Using Single-Particle Analysis in EMAN. *Methods Mol Biol* **2010,** *673*, 157-73; (b) Ludtke, S. J.; Baldwin, P. R.; Chiu, W., EMAN: Semiautomated Software for High-Resolution Single-Particle Reconstructions. *J Struct Biol* **1999,** *128* (1), 82-97.

31. Rossmann, M. G., Fitting Atomic Models Into Electron-Microscopy Maps. *Acta Crystallographica. Section D, Biological Crystallography* **2000,** *56* (Pt 10), 1341-9.

32. (a) Dang, T. X.; Farah, S. J.; Gast, A.; Robertson, C.; Carragher, B.; Egelman, E.; Wilson-Kubalek, E. M., Helical Crystallization on Lipid Nanotubes: Streptavidin as a Model Protein. *J Struct Biol* **2005,** *150* (1), 90-9; (b) Dang, T. X.; Milligan, R. A.; Tweten, R. K.; Wilson-Kubalek, E. M., Helical Crystallization on Nickel-Lipid Nanotubes: Perfringolysin O as a Model Protein. *J Struct Biol* **2005,** *152* (2), 129-39.

33. Dynarowicz-Latka, P.; Dhanabalan, A.; Oliveira, O. N., Modern Physicochemical Research on Langmuir Monolayers. *Adv Colloid Interfac* **2001,** *91* (2), 221-293.

34. Uzgiris, E. E.; Kornberg, R. D., Two-Dimensional Crystallization Technique for Imaging Macromolecules, with Application to Antigen-Antibody-Complement Complexes. *Nature* **1983,** *301* (5896), 125-9.

35. Kang, E.; Park, J. W.; McClellan, S. J.; Kim, J. M.; Holland, D. P.; Lee, G. U.; Franses, E. I.; Park, K.; Thompson, D. H., Specific Adsorption of Histidine-Tagged Proteins on Silica Surfaces Modified with Ni2+/NTA-Derivatized Poly(ethylene glycol). *Langmuir* **2007,** *23* (11), 6281-8.

36. Waugh, D. S., Making the Most of Affinity Tags. *Trends Biotechnol* **2005,** *23* (6), 316-320.

37. Barklis, E.; McDermott, J.; Wilkens, S.; Schabtach, E.; Schmid, M. F.; Fuller, S.; Karanjia, S.; Love, Z.; Jones, R.; Rui, Y.; Zhao, X.; Thompson, D., Structural Analysis of Membrane-Bound Retrovirus Capsid Proteins. *EMBO J* **1997,** *16* (6), 1199-213.

38. Barklis, E.; McDermott, J.; Wilkens, S.; Fuller, S.; Thompson, D., Organization of HIV-1 Capsid Proteins on a Lipid Monolayer. *J Biol Chem* **1998,** *273* (13), 7177-80.

39. Lata, S.; Reichel, A.; Brock, R.; Tampe, R.; Piehler, J., High-Affinity Adaptors for Switchable Recognition of Histidine-Tagged Proteins. *J Am Chem Soc* **2005,** *127* (29), 10205-15.

40. Tinazli, A.; Tang, J.; Valiokas, R.; Picuric, S.; Lata, S.; Piehler, J.; Liedberg, B.; Tampe, R., High-Affinity Chelator Thiols for Switchable and Oriented Immobilization of Histidine-Tagged Proteins: a Generic Platform for Protein Chip Technologies. *Chemistry* **2005,** *11* (18), 5249-59.

41. Schmitt, J.; Hess, H.; Stunnenberg, H. G., Affinity Purification of Histidine-Tagged Proteins. *Mol Biol Rep* **1993,** *18* (3), 223-30.

42. Zhou, M. K. H., S.; Franses, J.; Kim, J. M.; Thompson, D. H.,, Synthesis and Self-Assembly Properties of Acylated Cyclodextrins and Nitrilotriacetic Acid (NTA)-Modified Inclusion Ligands for Interfacial Protein Crystallization. *Suprmol Chem* **2005,** *17* (1-2), 101-111.

43. Irie, T.; Uekama, K., Pharmaceutical Applications of Cyclodextrins. III. Toxicological Issues and Safety Evaluation. *J Pharm Sci* **1997,** *86* (2), 147-62.

44. Kelly, D. F.; Dukovski, D.; Walz, T., Monolayer Purification: a Rapid Method for Isolating Protein Complexes for Single-Particle Electron Microscopy. *Proc Natl Acad Sci U S A* **2008,** *105* (12), 4703-8.

45. Kelly, D. F.; Abeyrathne, P. D.; Dukovski, D.; Walz, T., The Affinity Grid: a Pre-Fabricated EM Grid for Monolayer Purification. *J. Mol. Biol.* **2008,** *382* (2), 423-33.

46. Kelly, D. F.; Dukovski, D.; Walz, T., Strategy for the Use of Affinity Grids to Prepare Non-His-Tagged Macromolecular Complexes for Single-Particle Electron Microscopy. *J. Mol. Biol.* **2010,** *400* (4), 675-81.

47. Benjamin, C. J.; Wright, K. J.; Hyun, S. H.; Krynski, K.; Yu, G.; Bajaj, R.; Guo, F.; Stauffacher, C. V.; Jiang, W.; Thompson, D. H., Nonfouling NTA-PEG-Based TEM Grid Coatings for Selective Capture of Histidine-Tagged Protein Targets from Cell Lysates. *Langmuir* **2016,** *32* (2), 551-9.

48. Christopher J. Benjamin, K. J. W., Scott C. Bolton, Seok-Hee Hyun, Kyle Krynski, Mahima Grover, Guimei Yu, Fei Guo, Tamara L. Kinzer-Ursem, Wen Jiang & David H. Thompson, Selective Capture of Histidine-tagged Proteins from Cell Lysates Using TEM grids Modified with NTA-Graphene Oxide. *Sci Rep* **2016,** *6* (32500), 1-11.

49. Gyanesh Sharmaa, J. P., Sanchaita Das, Robert Grassucci, Robert Langlois,; Cheri M. Hampton, D. F. K., Amedee des Georges, Joachim Frank, Affinity Grid-Based Cryo-EM of PKC Binding to RACK1 on the Ribosome. *J Struct Biol* **2013,** *181*, 190-194.

50. (a) Yu, G.; Li, K.; Jiang, W., Antibody-Based Affinity Cryo-EM Grid. *Methods* **2016,** *100*, 16-24; (b) Yu, G.; Vago, F.; Zhang, D.; Snyder, J. E.; Yan, R.; Zhang, C.; Benjamin, C.; Jiang, X.; Kuhn, R. J.; Serwer, P.; Thompson, D. H.; Jiang, W., Single-Step Antibody-Based Affinity Cryo-Electron Microscopy for Imaging and Structural Analysis of Macromolecular Assemblies. *J Struct Biol* **2014,** *187* (1), 1-9.

51. Han, B. G.; Walton, R. W.; Song, A.; Hwu, P.; Stubbs, M. T.; Yannone, S. M.; Arbelaez, P.; Dong, M.; Glaeser, R. M., Electron Microscopy of Biotinylated Protein Complexes Bound to Streptavidin Monolayer Crystals. *J Struct Biol* **2012,** *180* (1), 249-53.

52. Selmi, D. N.; Adamson, R. J.; Attrill, H.; Goddard, A. D.; Gilbert, R. J.; Watts, A.; Turberfield, A. J., DNA-Templated Protein Arrays for Single-Molecule Imaging. *Nano Lett* **2011,** *11* (2), 657-60.

CHAPTER TWO:
DEVELOPMENT OF NON-FOULING AFFINITY LIPOPOLYMER-BASED AFFINITY GRIDS FOR SINGLE PARTICLE CRYO-EM

2.1 Introduction

Single-particle cryogenic electron microscopy (cryoEM) is a rapidly advancing method of protein structure elucidation that is now capable of producing structures with resolutions approaching 2.2 Å, provided that thousands of single particle images can be collected.[1] At present, this is achieved by collecting and class averaging images from many different carbon-coated grid preparations that randomly adsorb and present the protein target in multiple orientations for cryoEM imaging. Since many protein target candidates exist in low copy number, may be highly labile, and/or are derived from infectious agents that are in low supply, there is significant motivation for the development of new sample preparation methods to improve the throughput and predictability of this technique.

Lipid monolayers have been used to concentrate proteins at interfaces for structure determination, as first described by Uzgiris and Kornberg.[2] Subsequent affinity monolayer developments explored a variety of affinity lipid-ligand interactions such as biotin-streptavidin, ATP lipid-ATP binding protein, Ni^{2+}:nitrilotriacetic acid (NTA)-hexahistidine-tagged (His_6-tag) protein, or Cu^{2+}:iminodiacetic acid-His_6-tag protein.[3] Many of these efforts were focused on the development two-dimensional crystallization

methods using nitriloltriacetic acid (NTA)-modified lipid conjugates,[4] with some cases showing the potential of NTA lipids for structure elucidation with resolutions in the 10 – 25Å regime.[4b]

NTA lipid monolayers were extended to the realm of single-particle cryo-EM by Walz and coworkers, with the structures for 50S ribosomal subunits,[5] transferrin-transferrin receptor complex,[6] and human RNA polymerase II[7] reported using a commercially available NTA lipid conjugate, 1,2-dioleoyl-*sn*-glycero-3-[((N-(5-amino-1-carboxypentyl)iminodiacetic acid)succinyl] (DGS-NTA), in mixed monolayers with 1,2-lauroyl-*sn*-glycero-3-phosphocholine (DLPC). This report also extended this technique to the retrieval of protein targets from cell lysates;[6a, 7] however, the potential of the approach is currently limited by the low stability,[5] non-specific fouling,[6a] and preferred orientation[8] limitations of DGS-NTA:DLPC monolayers.

2.2 Design of Novel Non-Fouling Affinity Grids

Herein, a novel system was developed to address these challenges by depositing non-fouling PEG-lipid[9] coatings containing common affinity ligands like NTA[3, 4e, 4f, 10] onto TEM grids.[11] These coatings are prepared by compression of lipid films generated using a Langmuir trough whose capture ligand surface density and PEG mushroom-brush conformational state can be controlled by initial film composition and applied surface pressures prior to deposition onto the EM grid. Brush conformation methoxypolyethylene glycol (mPEG) coatings are highly non-fouling,[12] thereby enabling the application of cell lysates directly onto the grid and removal of the non-specifically bound material in

subsequent buffer washing steps (Figure 2.1). Since the moiety bearing the affinity interaction exists at terminus of the lipopolymer, it is anticipated that this approach will allow for increased rotational degrees of freedom allowing for the potential of decreased sample orientation bias. In addition to the reduced sample quantity demands required for cryoEM analysis, the shortened sample processing times also limit the opportunities for proteolytic degradation and/or protein unfolding of the His_6-target that may occur during standard sample processing protocols.

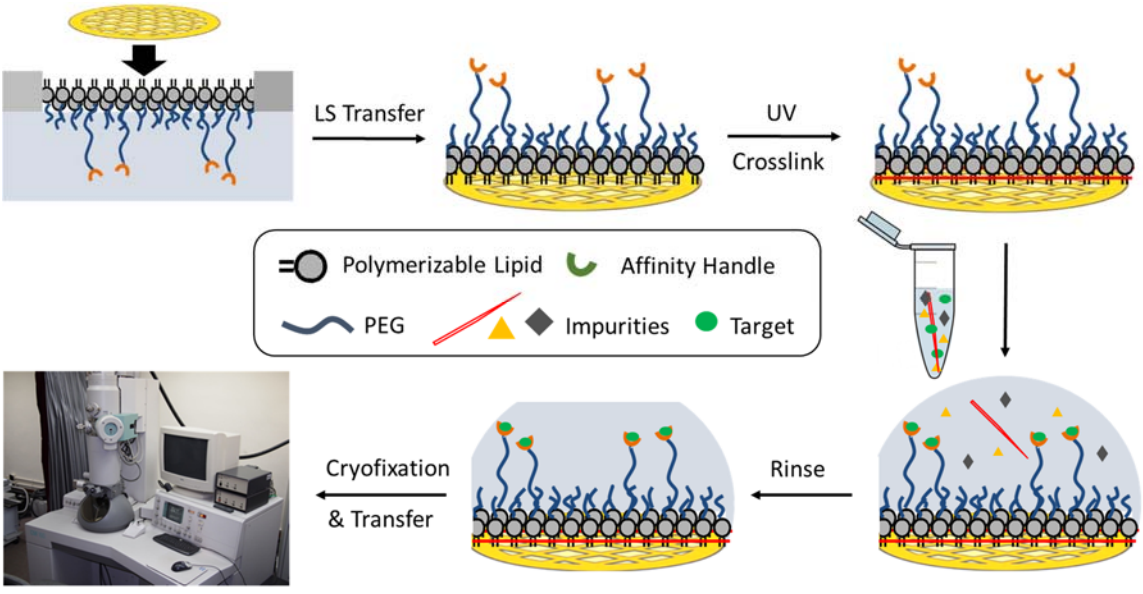

Figure 2.1 Conceptual Diagram Showing Lipopolymer-Based Affinity Grid Fabrication and Affinity Capture from Crude Cell Lysates.

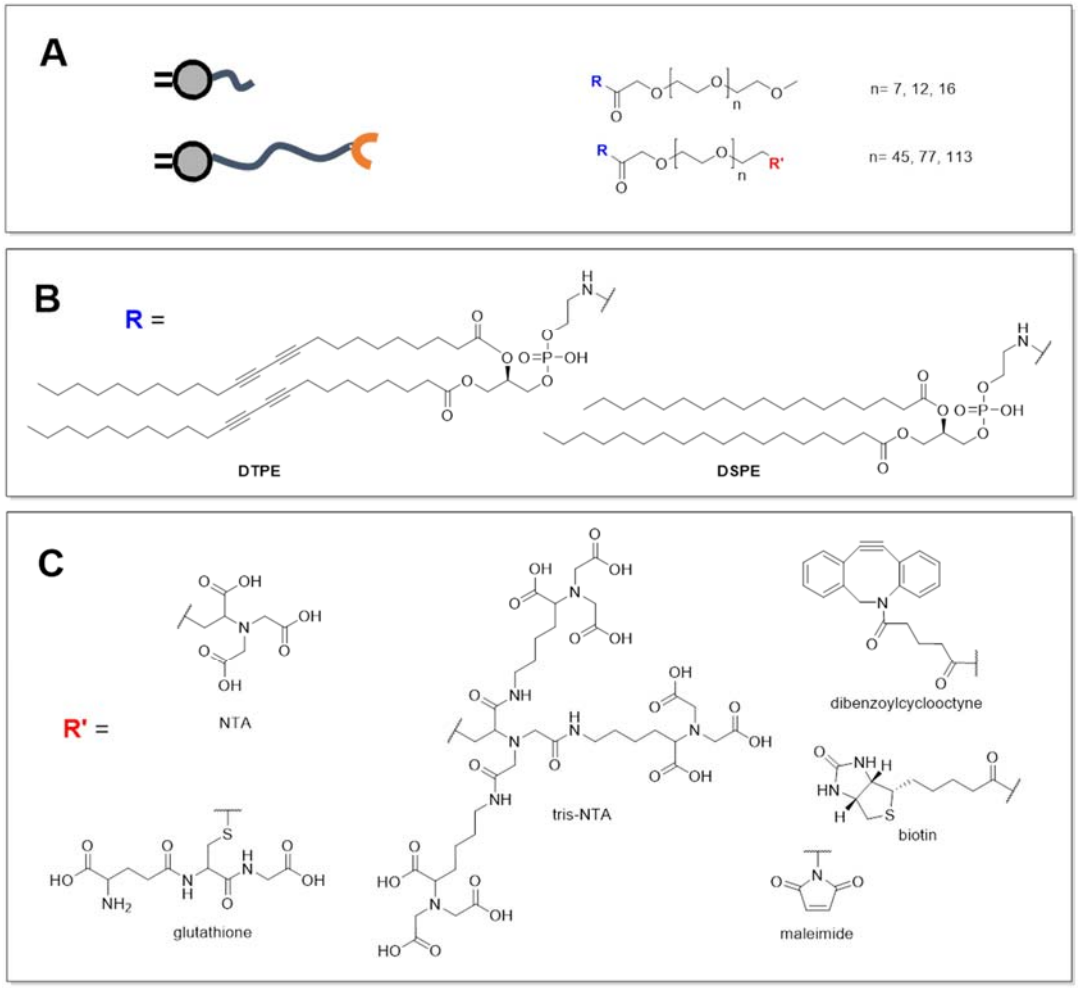

Figure 2.2 Chemical Structures of Targeted Affinity Lipopolymer Library. (A) Targeted PEG molecular weights. (B) Lipid structures. (C) affinity moieties and reactive termini.

A small library of affinity lipopolymer constructs was designed to maintain the essential monolayer purification capability while incorporating a surface PEG brush, to prevent non-specific adsorption, and a polymerizable lipid component which undergoes topochemical polymerization[13] upon exposure to UV light forming a more stable substrate for affinity grid sample preparation. Structures of the targeted library are depicted in Figure 2.2. Like the original approach introduced by Walz[14], our approach

consists of a mixed monolayer film consisting of two lipopolymer components. The first component is an mPEG-PE-lipid conjugate where the PE-lipid is either 1,2-(tricosa-10',12'-diynoyl)-*sn*-glycero-3-phosphoethanolamine (DTPE) or – 1,2-(distearoyl)-*sn*-glycero-3-phosphoethanolamine (DSPE) and the mPEG is relatively low molecular weight (e.g. ~350-750 Da). This component is designed to function as the non-fouling brush component of the monolayer, preventing non-specific adsorption and typically composes 90-99 % of the molar lipid concentration of the monolayer. When DTPE is the lipid component, a topochemical polymerization[13, 15], induced by UV light (Figure 2.3), may be utilized to produce a conjugated 2D polymer, which should be more stable than a lipid monolayer and may allow for charge dissipation during electron imaging, which may lead to defects[16] and lower overall possible resolution during 3D reconstruction of affinity grid-based cryo-EM.

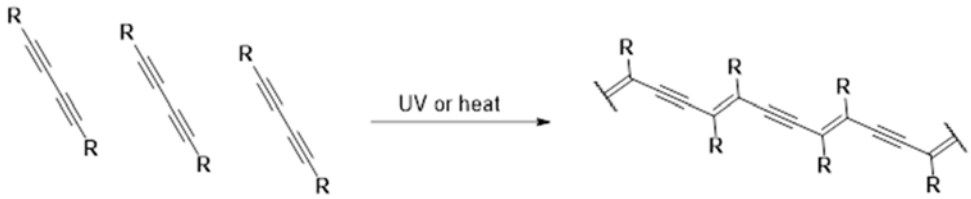

Figure 2.3 Topochemical Polymerization of Diacetylenic Lipids[13].

The minor component of the lipopolymer-based affinity grid approach is similar, but is composed of a higher molecular weight polymer (2-5 kDa) whose persistence length is significantly longer than the major component. The lipids utilized are either DTPE or DSPE. The distal terminus of this component is designed to incorporate various

affinity chemistries and covalently-active functionalities to enable selective capture of a wide range of targets using the lipopolymer-based affinity grid concept. NTA and tris-NTA are useful for capture of his-tagged proteins using IMAC[17] chemistry, glutathione is a useful handle for affinity purification of glutathione-S-transferase- (GST)-tagged proteins[18], biotin may be utilized to take advantage of its affinity interaction with avidin- or streptavidin-fusions[19] or for characterizing IMP's via the proteoliposome-based spherical reconstruction approach to cryo-EM introduced by Sigworth and Wang[20].

The proposed materials are designed to be formulated into monolayers using a Langmuir trough. Since the relative molar compositions of the monolayer are completely tunable, relative particle surface density can be tuned to yield optimal particle spacing for 3D reconstruction and automated particle selection[21].

2.3 Synthesis and Characterization of Affinity Lipopolymer Constructs

2.3.1 Synthesis of Functional mPEG Derivatives

A small library of functional mPEG derivatives (Scheme 2.1) was synthesized following modified protocols previously reported for end group modification of higher molecular weight bifunctional PEG[22]. mPEG of various molecular weight (~350-5,000 Da) **1a-e** was converted to the mesylate (**2a-e**) via treatment with methansulfonyl chloride in dichloromethane (DCM) in the presence of triethylamine with average yields of 90-99 %. The mesylates were converted to azide-terminal-mPEG (**3a-e**) via S_N2 displacement by sodium azide in N,N-dimethylformamide (DMF) in 83-95 % average

yield. Reduction using hydrogen gas (1 atm) and 10 mol % palladium on carbon (Pd/C) support in ethyl acetate (EtOAc) gave the terminal amine (**4a-e**) in 82-94 % average yields.

Carboxyl-terminal mPEG were obtained via Jones oxidation of **1a-e**, giving **5a-e** in 89-94 % average yields. Conversion was determined via TLC analysis combined with staining with bromocresol green to verify oxidation. An alternative route to amine terminal mPEG through an aldehyde-terminal intermediate was also utilized. The aldehyde-terminal mPEG derivatives were obtained via Albright-Goldman oxidation of **1a-e** to give **6a-e** in 89-94 % average yield. The aldehyde-terminal mPEG were then converted to the amine **7a-e** via reductive amination mediated by sodium cyanoborohydride and ammonia in methanol in 90-98 % overall yield. Reported yields are given as percent recovery. Polymers were purified via extractions and precipitation into diethyl ether depending on the polymer molecular weight (PEG with molecular weight < ~2 kDa exists as an oil or liquid and cannot be precipitated). For lower molecular weight polymers, TLC and TLC staining was utilized to monitor conversion to determine optimal reaction times. The efficiency of conversion for Jones oxidation is near complete[22b]. Conversions reported for the Albright-Goldman and reductive amination protocols are 78-86 %[22b].

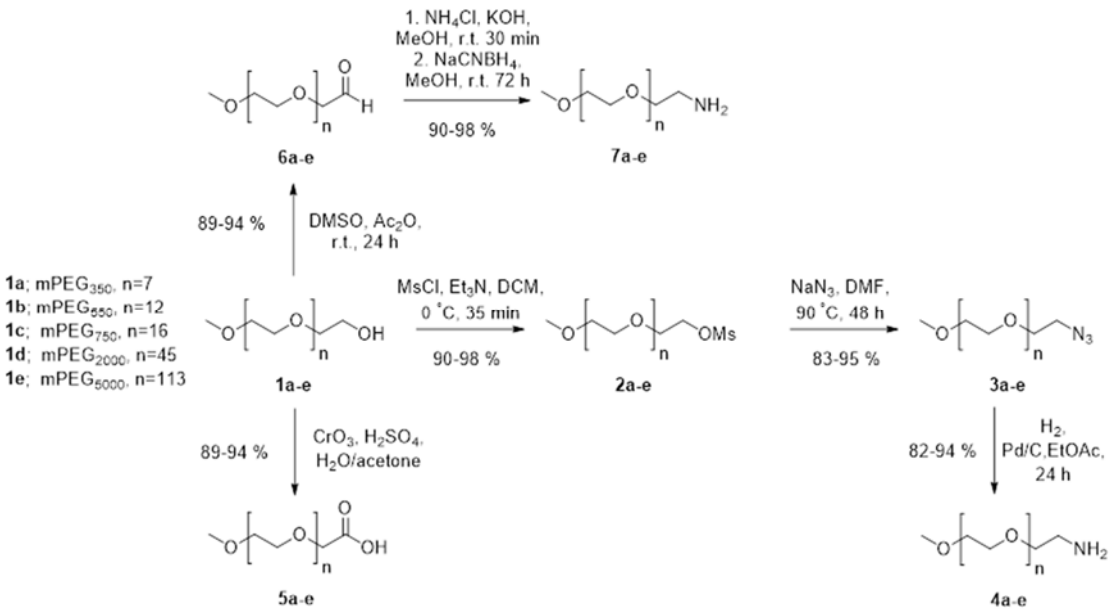

Scheme 2.1 Synthesis of Functional mPEG Derivatives.

2.3.2 Synthesis of mPEG-Lipid Conjugates

mPEG-lipid conjugates were synthesized via a two-step process (Scheme 2.2). Carboxyl terminal mPEG **5a** was converted to the active N-hydroxysuccinimidyl ester **8** mediated by N-ethyl-N'-(3-dimethylaminopropyl)-carbodiimide (EDC) and N-hydroxysuccinimide (NHS) in the presence of diisopropylethylamine (DIEA) in DMF. Compound **8** was obtained in 84.4 % yield. Direct coupling of the carboxyl-terminal polymer and PE lipid was not performed in order to avoid activation of the phosphate groups of the lipids. The lipid conjugates **9a-c** were synthesized via NHS-displacement upon treatment of the active ester of PEG with the phosphoethanolamine lipid in the presence of base. After chromatographic purification, mPEG conjugates of DTPE (**9a**),

DSPE (**9b**) and DPPE (**9c**) were synthesized. The lipid conjugates were obtained in varying yields from 31.1-72.3 %.

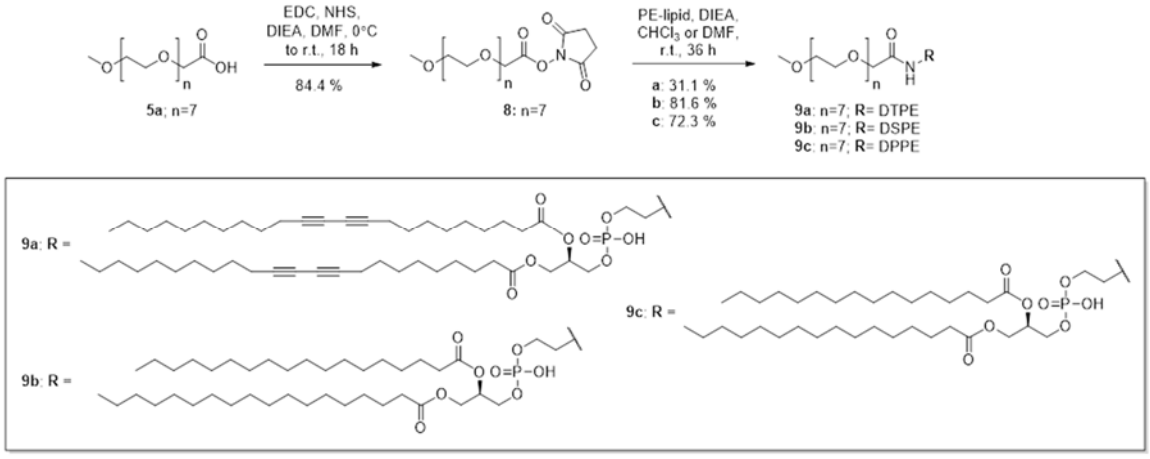

Scheme 2.2 Synthesis of mPEG-Lipid Conjugates.

2.3.3 Synthesis of Biotin-PEG-lipids

Biotin terminal lipopolymers (**11a-b**) were synthesized via treatment of commercial heterobifunctional biotin-PEG-NHS **10** with the phosphoethanolamine lipid (Scheme 2.3). After chromatographic purification, conjugates of DTPE (**11a**) and DSPE (**11b**) were synthesized in 75.3 and 56.4 % yield, respectively. In this case, PEG molecular weight was (~2.0 kDa).

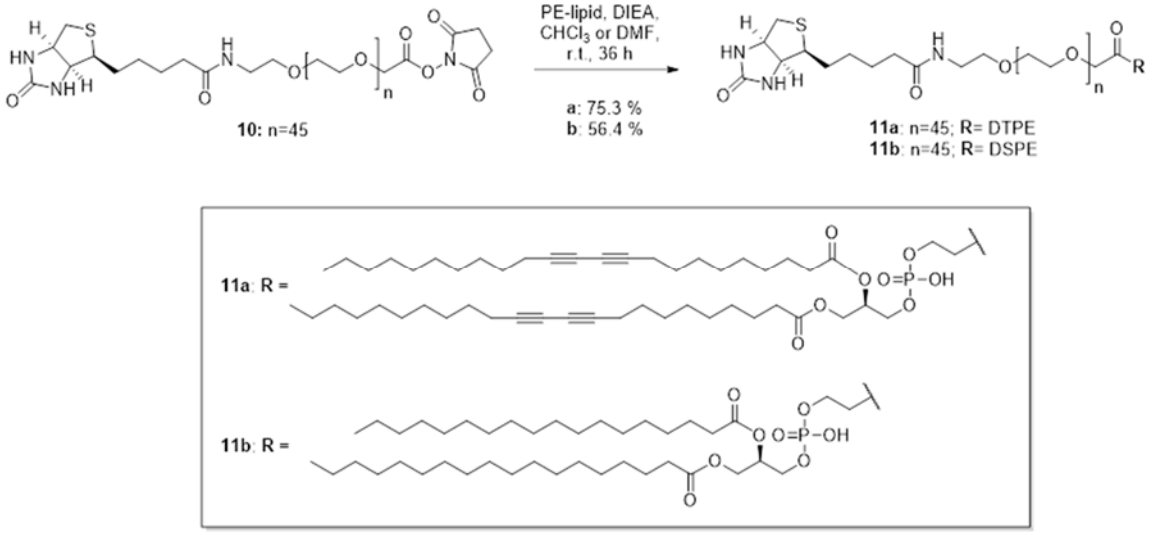

Scheme 2.3 Synthesis of Biotin-PEG-Lipids.

2.3.4 Synthesis of Functional t-butyl-NTA and tris-NTA Derivatives

A small library of functional t-butyl-protected NTA and tris-NTA derivatives were also prepared (Scheme 2.4). The protocols used to synthesize these materials were based on previously reported protocols with modification[23].

H-Lys(Z)-OH (**12)** was converted to the t-butyl ester **13** by transesterification of t-butyl acetate catalyzed by perchloric acid in 78.7 % yield. Compound **13** was then dialkylated by t-butyl bromoacetate in the presence of DIEA in DMF to give Compound **14** in 84.4 % yield after chromatographic purification. Compound **14** was debenzylated by reductive hydrogenation on palladium on carbon support to give Compound **15** in 99.7 % yield. Carboxyl-NTA **16** was synthesized from Compound **15** via acylation by succinic anhydride in the presence of organic base in DCM in 99.7 % yield after chromatographic purification. Alkyne-NTA derivative **17** was synthesized from Compound **16** via EDC-

mediated coupling with propargylamine in the presence of N-hydroxybenzotriazole (HOBt) and DIEA in DMF in 88.5 % yield after chromatographic purification.

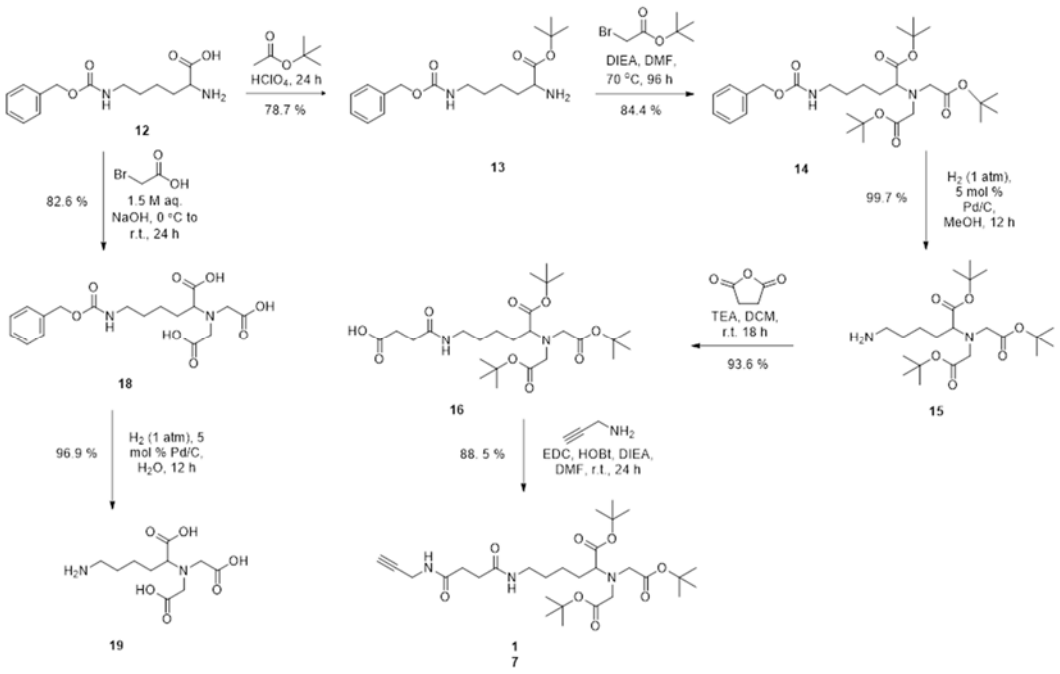

Scheme 2.4 Synthesis of Functional t-butyl-NTA Derivatives.

Z-protected NTA derivative **18** was synthesized via direct dialkylation of Compound **12** by bromoacetic acid in aqueous sodium hydroxide solution to give Compound **18** in 96.3 % yield without chromatographic purification**.** Compound **18** may also be converted to the fully deprotected lysine-NTA derivative **19** via hydrogenation using palladium on carbon under 1 atm of hydrogen gas in aqueous solution in 96.3 % yield.

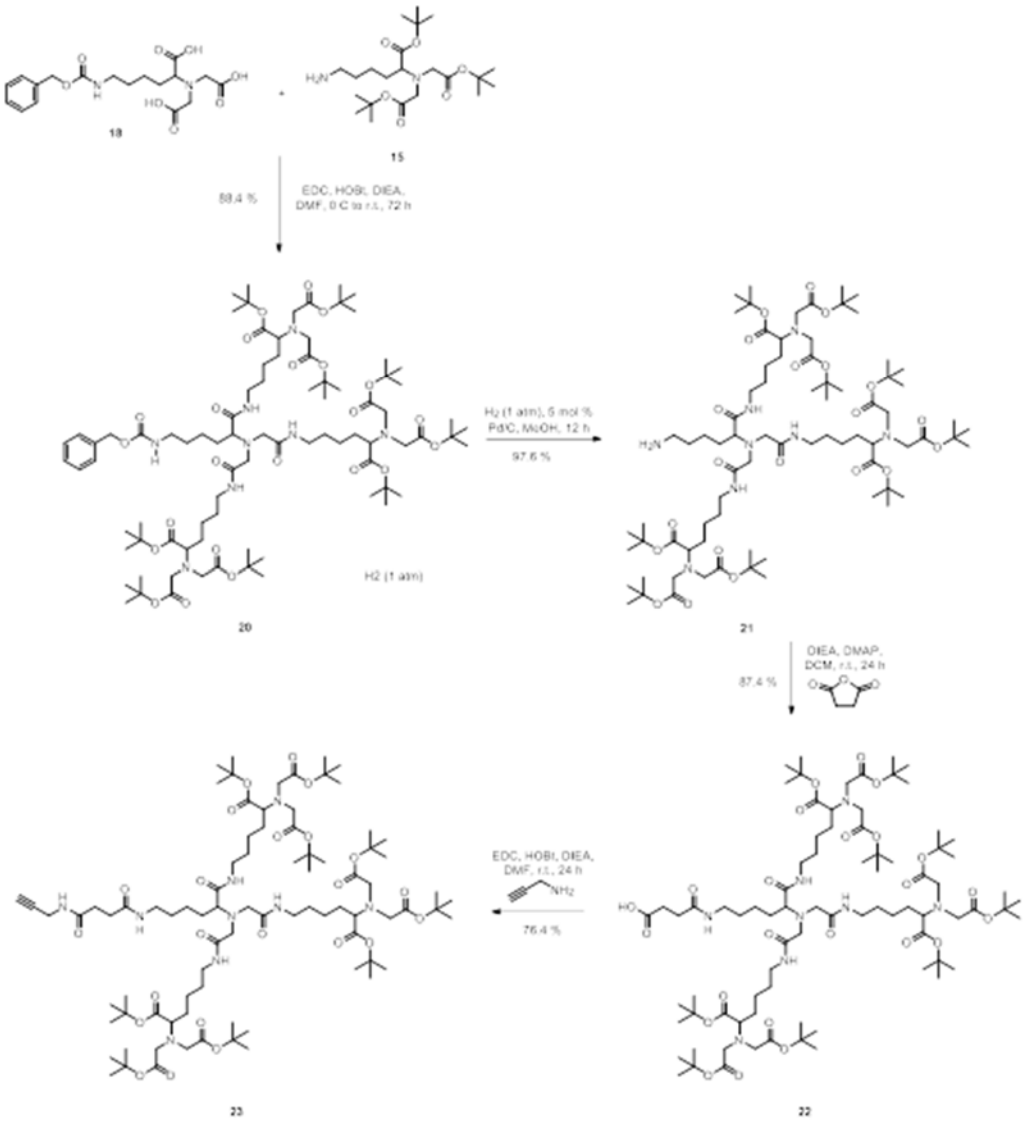

Scheme 2.5 Synthesis of Functional t-butyl-tris-NTA Derivatives.

Z-protected tris-NTA **20** was synthesized by EDC coupling of Compounds **15** and **18** in the presence of HOBt and DIEA in DMF in 88.4 % yield after chromatographic purification. Hydrogenation of **20** by Pd/C under 1 atm of hydrogen gas gave **21** in 97.6 % yield. A similar functionalization strategy to generate carboxyl- and alkynyl-

functional-NTA derivatives was also employed for tris-NTA. Compound **21** was converted to a carboxyl-functional derivative via acylation by succinic anhydride in the presence of base in DCM to give Compound **22** in 87.4 % yield after chromatographic purification. Compound **22** was then converted to an alkynyl derivative via EDC-mediated coupling with propargylamine in the presence of HOBt and DIEA in DMF to give Compound **23** in 76.4 % yield after chromatographic purification (Scheme 2.5).

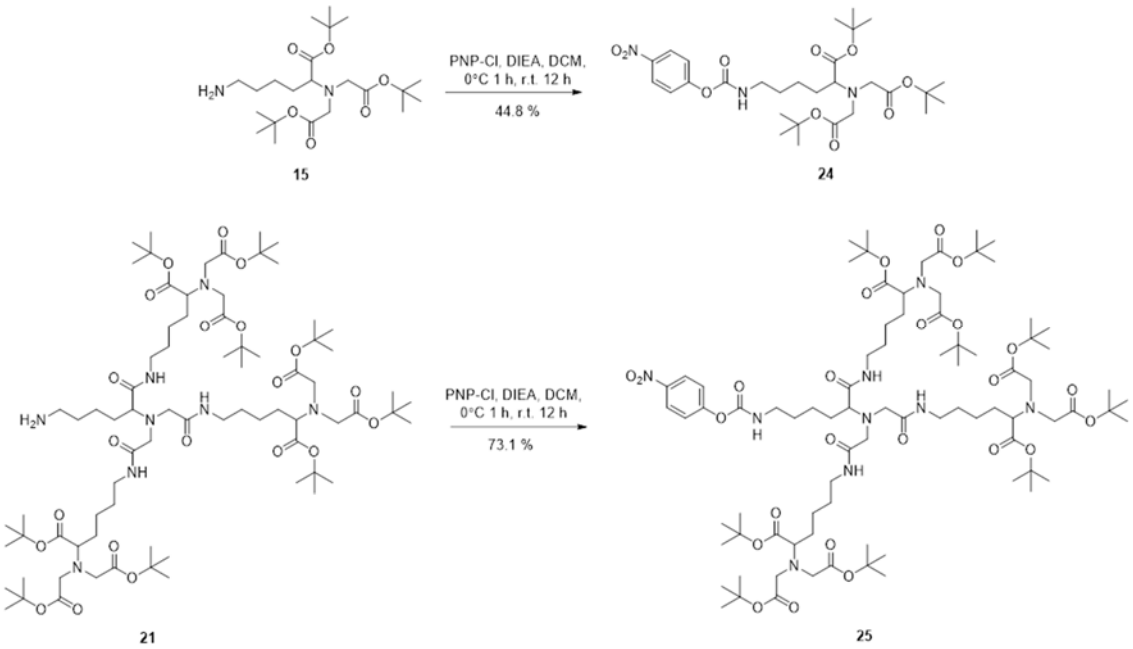

Scheme 2.6 Synthesis of PNP-Activated t-butyl-Protected NTA and tris-NTA Derivatives.

Reactive p-nitrophenyl carbamate derivatives of Compounds **15** and **21** were synthesized via treatment of the respective primary amines with p-nitrophenyl chloroformate in the presence of DIEA in DCM to give Compounds **24** and **25** in 44.8 % and 73.1 % yields, respectively, after chromatographic purification (Scheme 2.6).

2.3.5 Initial Synthesis of DTPE-PEG-NTA.

Initial efforts to synthesize NTA-terminal lipopolymers were only moderately successful due to low overall yield and side reactions associated with DTPE. Commercial heterobifunctional PEG derivative **26** containing t-butyl carbamate (Boc) and N-hydroxysuccinimidyl-ester termini was used to acylate DTPE in the presence of base in DCM under dark conditions. Lipopolymer conjugate **27** was obtained in 87.8 % yield after chromatographic purification. Removal of Boc was effected by treatment with trifluoroacetic acid (TFA) in DCM in the presence of triethylsilane as a cation scavenger to give **28** in 91.3 % yield. Treatment of **28** with p-nitrophenylcarbamate **24** in the presence of base in DCM gave Compound **29** in 26.9 % yield after chromatographic purification. Compound **29** was then treated with TFA and triethylsilane in DCM to give Compound **30** in 62.1 % yield.

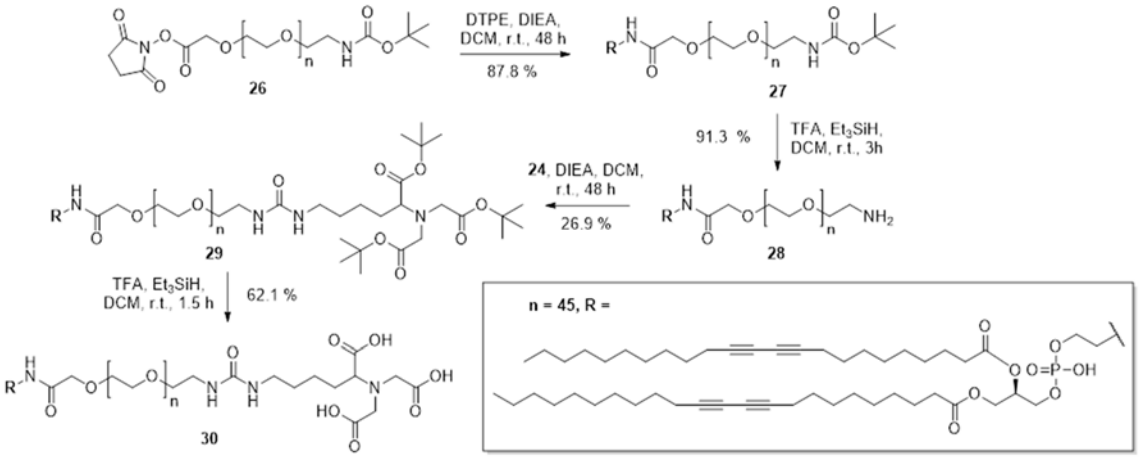

Scheme 2.7 Initial Synthesis of DTPE-PEG-NTA.

2.3.6 Synthesis of Thiol-Functional NTA and tris-NTA Derivatives.

When working with polymers, small changes in end group or conjugation of a small-molecule tend to cause little change in the retention-factor of the product relative to the starting material. Thus, reactions that are highly efficient are best. For synthesizing affinity lipopolymer constructs, a synthetic pathway was designed that utilized thiol-maleimide chemistry as the final step in the pathway to conjugate various affinity moieties. Although thiol-containing derivatives of NTA have been synthesized and reported[24] by groups in the past, the synthetic routes to these compounds are unnecessarily complicated, use starting materials uncommon to other NTA synthetic routes and the target compounds are quite hydrophobic since they have long alkyl chains as tethers between the NTA and thiol functionalities.

A simpler synthesis that utilizing t-butyl-protected-lysine-NTA derivative **15** and S-trityl-3-mercaptopropionic acid **32** as starting materials was devised where a global TFA-mediated deprotection could yield the fully deprotected **34** (Scheme 2.8). 3-Mercaptopropionic acid **31** was trityl-protected via treatment with trityl chloride in DCM to give **32** in 93.2 % yield. Coupling between Compounds **15** and **32** was accomplished by EDC-mediated coupling in the presence of HOBt and DIEA in DMF to give Compound **33** in 53.4 % yield after chromatographic purification. Global deprotection was effected by treatment of Compound **33** with TFA in the presence of triethylsilane in DCM to give Compound **34** in 92.7 % yield.

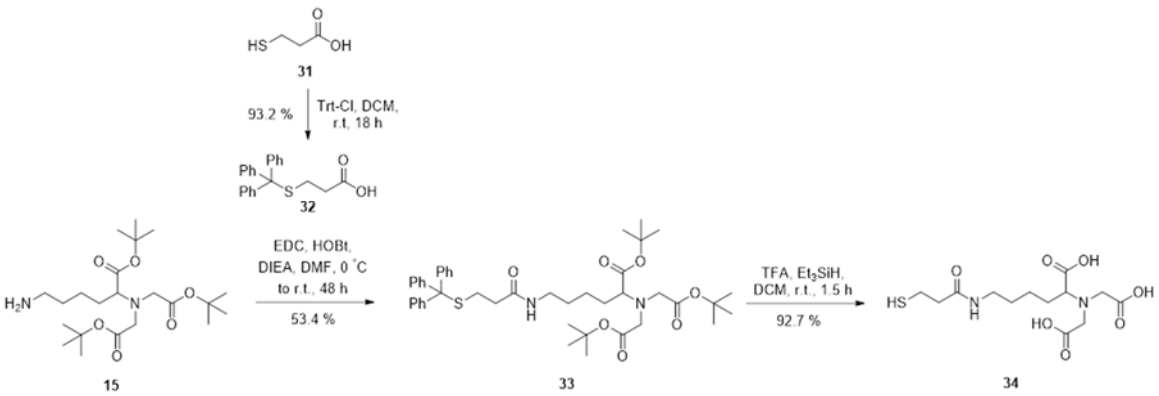

Scheme 2.8 Synthesis of Thiol-NTA.

Following a similar strategy, with a global TFA-mediated deprotection as the final step a thiol-containing derivative of tris-NTA was synthesized. Tris-NTA is used for affinity interaction with his-tagged protein in the same way as NTA, but tris-NTA has much higher binding affinities for his-tags (nM) as compared to NTA (μM).

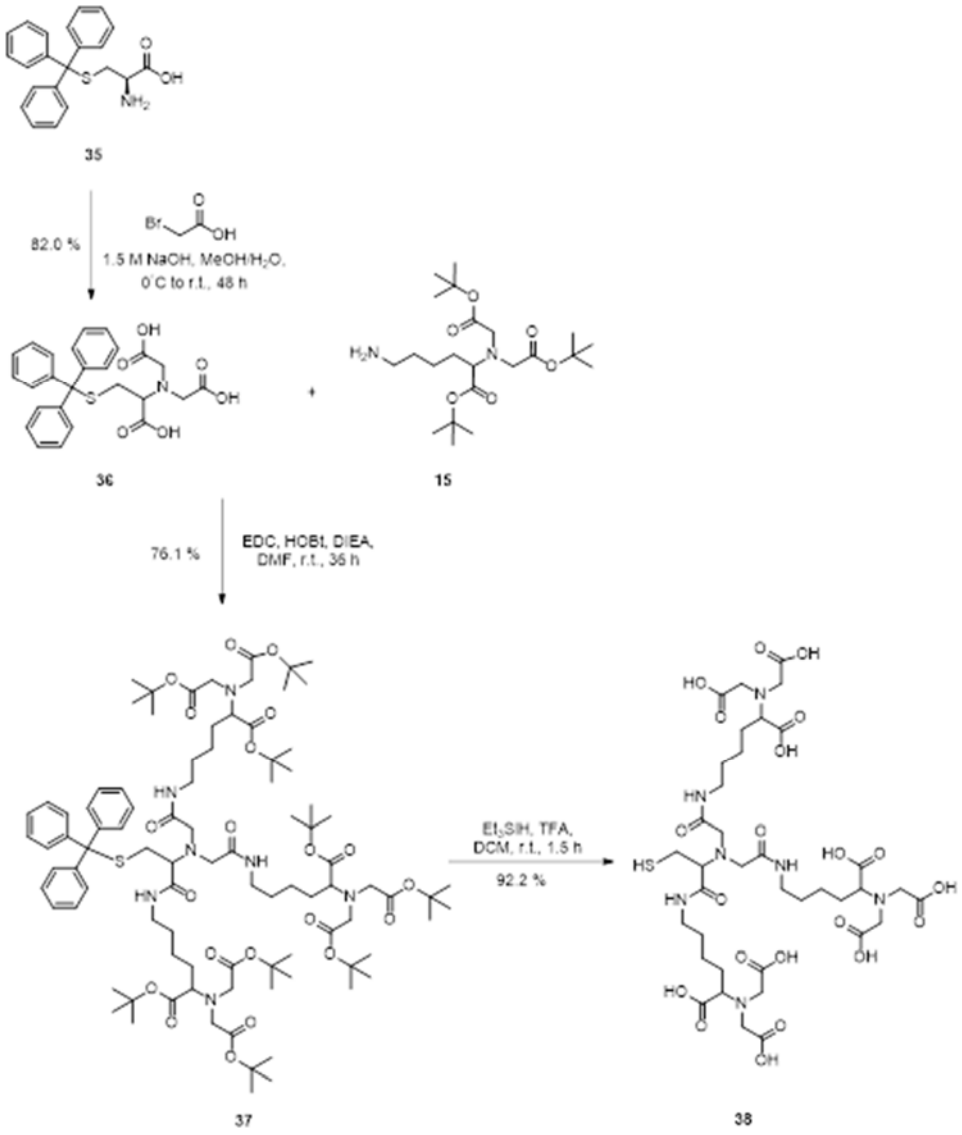

Scheme 2.9 Synthesis of Thiol-tris-NTA.

S-Trityl-L-cysteine (**35**) was dialkylated under basic conditions by bromoacetic acid in a mixture of water and methanol to give Compound **36** in 82.0 % yield. EDC-mediated coupling between Compounds **36** and **15** in the presence of HOBt and DIEA in DMF gave Compound **37** in 76.1 % yield after chromatographic purification. Global

deprotection of Compound **37** by TFA in the presence of triethylsilane in DCM gave Compound **38** in 92.2 % yield. Both Compounds **34** and **38** were highly water soluble, making them suitable for aqueous conjugation reactions (Scheme 2.9).

2.3.7 Synthesis of DSPE-PEG-Maleimide and DSPE-PEG-NTA.

A mild synthesis of NTA-containing lipopolymer was accomplished using thiol-maleimide Michael-addition chemistry (Scheme 2.10). Commercial heterobifunctional PEG Compounds **39a-b** containing maleimide- and N-hydroxysuccinimidyl ester-terminal functionalities was conjugated to DSPE in the presence of DIEA in chloroform to give Compounds **40a-b** in 43.4 % and 30.1 %, respectively after chromatographic purification. Thiol-NTA derivative **34** was then conjugated to the lipopolymer via Michael-addition in the presence of triethylamine (TEA) in DMF to give **41a-b** in 89.8 % and 53.3 % yields, respectively

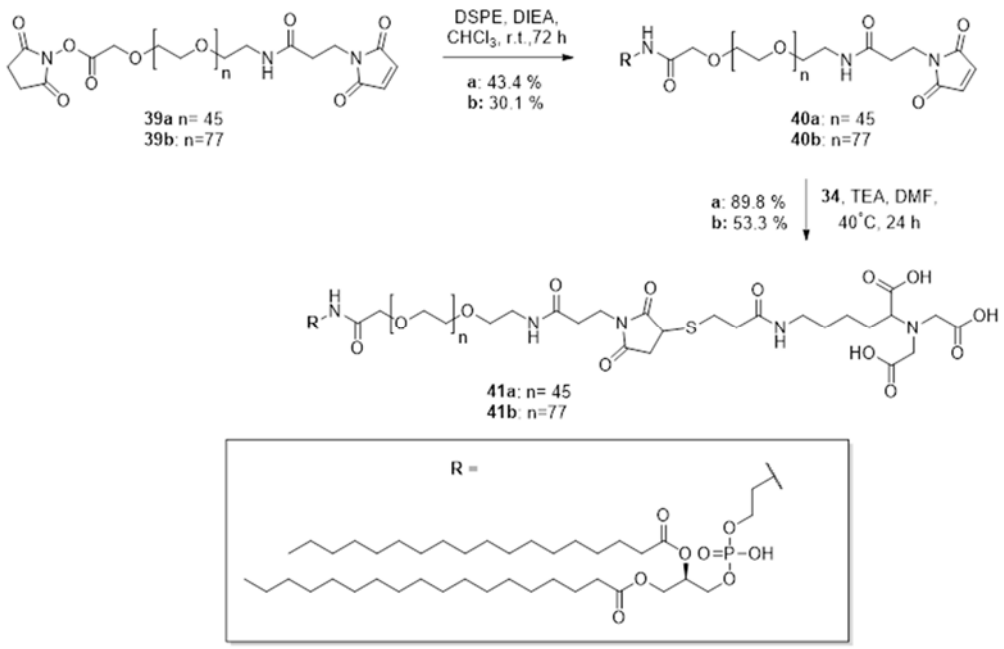

Scheme 2.10 Synthesis of DSPE-PEG-Maleimide and DSPE-PEG-NTA.

An alternative synthetic pathway to DSPE-PEG-maleimide was also utilized, but the overall yield of 45.8 % over three steps was only slightly improved over the single-step direct conjugation of the phosphoethanolamine-containing lipid to the heterobifunctional PEG derivative, maleimide-PEG-NHS (Scheme 2.11). This pathway utilized the Diels-Alder adduct formation between 2.5-dimethylfuran and maleimide[25], which is subject to thermodynamic control. Compound **39a** and 2.5-dimethylfuran were mixed at 40 °C to form the Diels-Alder adduct **42**. Compound **42** was then conjugated to DSPE in the presence of DIEA in chloroform to give **43** in 75.8 % yield. The Retro-Diels-Alder reaction was effected by heating isolated Compound **43** in toluene at 80 °C to give Compound **44** in 61.5 % yield.

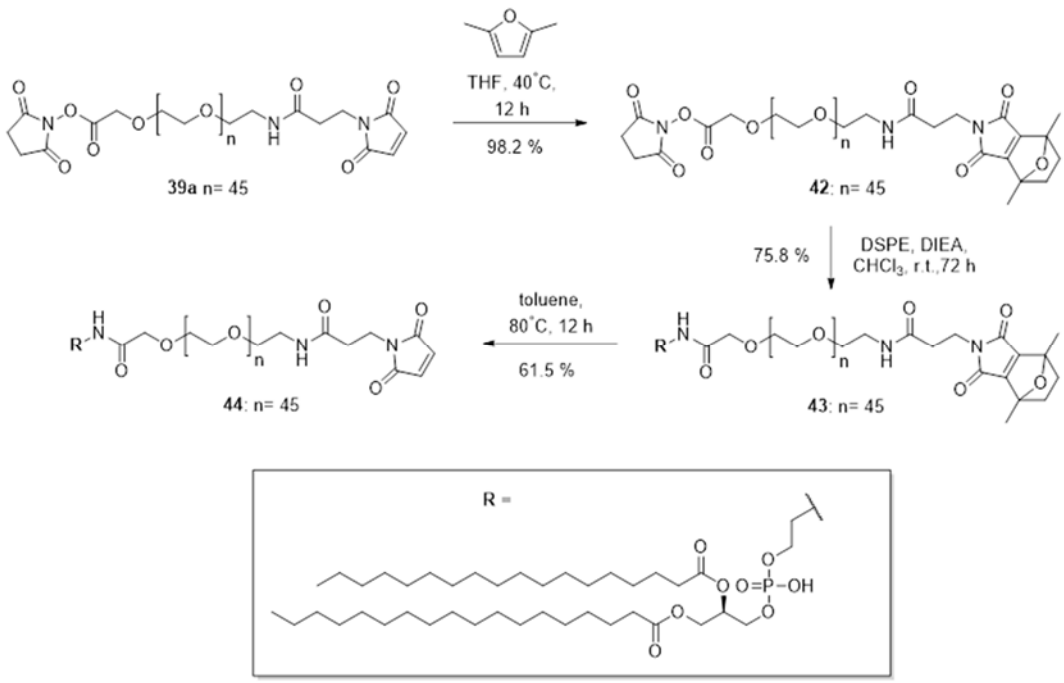

Scheme 2.11 Alternative Synthesis of DSPE-PEG-Maleimide Utilizing Diels-Alder as a Protection Strategy.

2.3.8 Synthesis of DSPE-PEG-tris-NTA

A similar strategy for the synthesis of Compound **41** was employed to generate tris-NTA-terminal lipopolymer construct (Scheme 2.12). Compounds **40a-b** were conjugated to thiol-containing tris-NTA construct **38** via Michael addition in the presence of TEA in DMF to give **45a-b** in 87.7 % and 40.2 % yield, respectively.

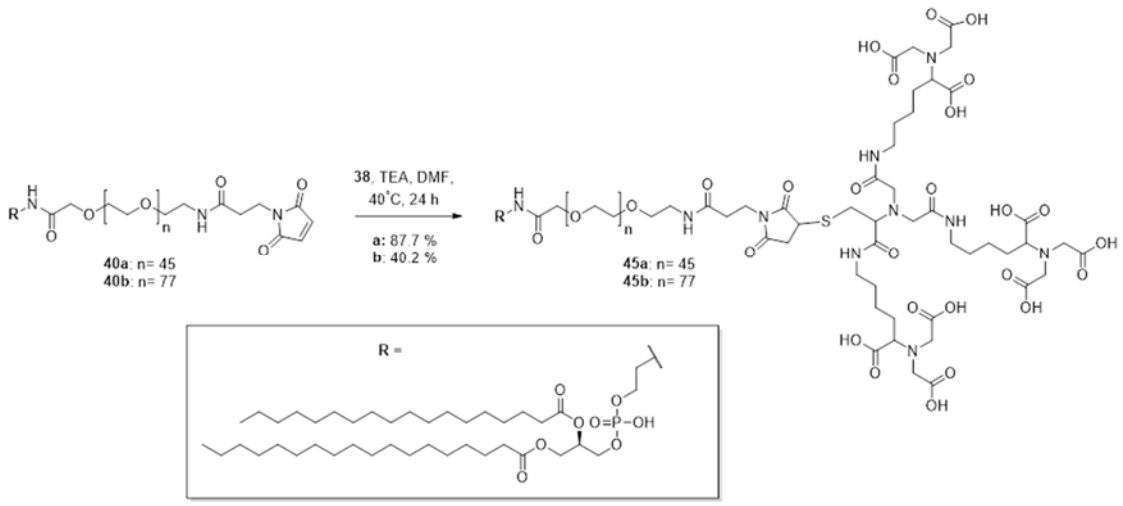

Scheme 2.12 Synthesis of DSPE-PEG-tris-NTA.

2.3.9 Synthesis of DSPE-PEG-Glutathione

A similar approach was used to generate a lipopolymer conjugate of glutathione. Glutathione-S-transferase (GST) binds glutathione with high affinity and can be engineered as a fusion protein with a target protein of interest[26]. Therefore, glutathione-terminal lipopolymer constructs may be useful for cryo-EM analysis of protein targets that bind glutathione or can be engineered to be GST-tagged. Compound **40a** was coupled to L-glutathione via Michael addition in the same manner as the thiol-NTA and thiol-tris-NTA derivatives. Compound **46** was obtained in 93.1 % yield.

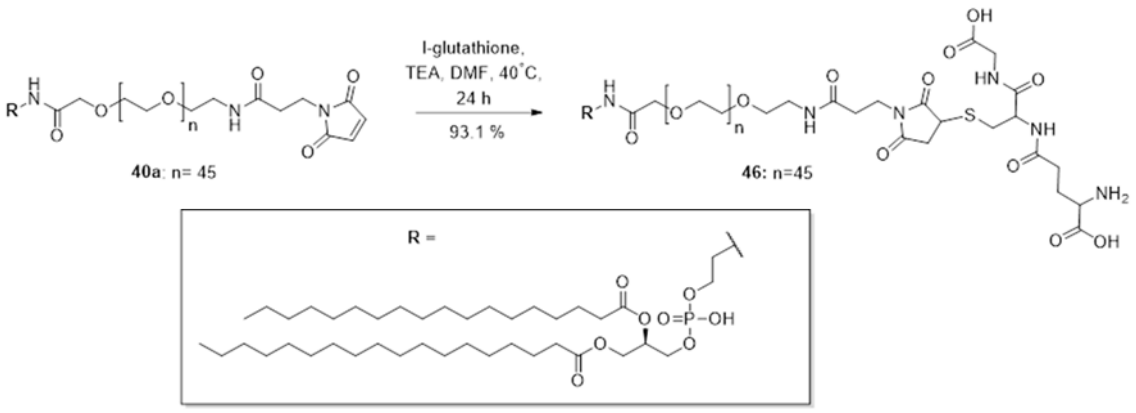

Scheme 2.13 Synthesis of DSPE-PEG-Glutathione.

2.4 Performance of PEG-NTA-Based Affinity Grids

Langmuir-Schaefer deposition of a mixed monolayer containing two synthetic polymerizable lipids – 1,2-(tricosa-10',12'-diynoyl)-*sn*-glycero-3-phosphoethanolamine-N (methoxypolyethylene glycolamide 350) (**9a**, mPEG350-DTPE) and either 1,2-(tricosa-10',12'-diynoyl)-*sn*-glycero-3-phosphoethanolamine-N-[(5-amido-1-carboxypentyl)iminodiacetic acid]polyethylene glycolamide 2000) (**30**, NTA-PEG2000-DTPE) or 1,2-distearoyl–*sn*-glycerol-3-phosphoethanolamine-N-[(5-amido-1-carboxypentyl)iminodiacetic acid]polyethylene glycolamide 2000) (**41a**, NTA-PEG2000-DSPE) – prior to treatment with a 10 min, 254 nm light exposure was used to prepare stabilized affinity monolayers supported on carbon coated EM grids. These grids were then used to capture His_6-T7 bacteriophage and His_6-RplL from cell lysates, as well as purified histidine-tagged green fluorescent protein (His_8-GFP) and nanodisc embedded His_6-$MalFGK_2$. Findings indicate that polymerized NTA lipid monolayers are capable of capturing His_6-protein targets in a manner that controls their areal densities, while

efficiently blocking non-specific adsorption and limiting film degradation upon prolonged detergent exposure.

2.4.1 Affinity Lipopolymer Monolayer Formation and Characterization

$CHCl_3$ stock solutions of the lipid mixtures were prepared, spread at the air-water interface at 20 °C, a 5 min incubation period allowed for evaporation of the solvent, and the films compressed at a rate of 10 $Å^2$/molecule until collapse at 30 mN/m – 35 mN/m for the mixed monolayers and 40 mN/m for pure mPEG350-DTPE monolayers. The pressure-area isotherms shown in Figure 2.4 for 1:99 and 5:95 NTA-PEG2000-DTPE:mPEG350-DTPE lipid mixtures displayed gradually increasing surface pressures upon film compression, except that the onset of surface pressure occurred at larger molecular areas as the NTA-PEG2000-DTPE composition in the film increased. We attribute this observation to the displacement of surface-adsorbed NTA-PEG2000 from the air-water interface as previously described[27] for mixed mPEG2000-lipid monolayers. As this desorption process progresses, the majority component, mPEG350, undergoes a mushroom-brush regime transition upon compression to 30 mN/m while the NTA-PEG2000 fraction remains in the mushroom configuration. The extension of the PEG2000 polymer mushroom conformation from the surface of the film can be calculated by $L_o = \alpha N(\alpha/D)^{2/3}$, where L_o = the length of PEG graft, α = length of PEG monomer (3.5 Å), N = number of ethylene glycol units in the PEG chain (i.e., 45), and D = the distance between grafting sites. For a lipid film containing 1% NTA-PEG2000-DTPE, the grafting site separation is estimated to be 47 Å and the L_o = 2.8 nm. Fully

compressed 5:95 NTA-PEG2000-DTPE:mPEG350-DTPE monolayers are estimated to have a grafting site separation of 9.4 Å and a NTA-PEG2000 graft extension of 8.2 nm. As the lipid film is compressed below 113 $Å^2$/molecule, the mPEG350 fraction enters the brush regime, while the NTA-PEG2000 polymer chain accommodates further compression by extending farther away from the air-water interface in a concentration-dependent manner. Consequently, a longer NTA-PEG was prepared for these studies since it would confer greater conformational freedom to the immobilized histidine-tagged target and present it in a greater diversity of possible orientations for cryoEM single particle analysis.

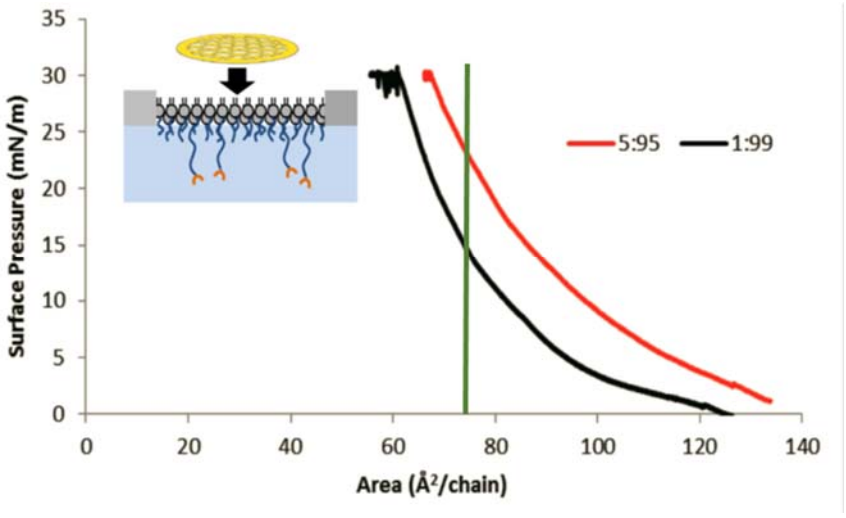

Figure 2.4 Pressure-Area Isotherm for 1:99 (black) and 5:95 (red) NTA-PEG2000-DSPE:mPEG350-DTPE Monolayers at 20 °C. The mushroom to brush regime is estimated to be approximately 75 $Å^2$/molecule (green line) for mPEG350-DTPE-rich monolayers.

Since the lipid films typically collapsed at surface pressures above 30 mN/m, the monolayers were compressed to 30 mN/m prior to Langmuir-Schaefer (LS) transfer onto carbon-coated grids that were not subjected to glow discharge before LS deposition. This method produced transfer ratios between 0.89 – 0.97 for the LS deposition step. Photopolymerization of the lipid monolayer was initiated by placing the grids ~6 – 8 cm from a handheld UV lamp and irradiated for 10 min. Grid performance as a function of varied irradiation time suggested that a 10 min exposure was most favorable.

After monolayer film transfer onto 400 mesh grids and staining with freshly prepared 1% $UO_2(OAc)_2$, TEM images revealed the presence of large continuous areas exceeding 900 μm^2 in size that were punctuated by much smaller zones of higher contrast (Figure 2.5). We infer from these findings that the large area regions were monolayer films with occasional, interspersed domains of bilayer and trilayer films arising from partial monolayer collapse during compression that were preserved by the photopolymerization process. Sufficiently large areas of the grid were coated by stabilized monolayer film structures to make them suitable for negative stain and cryoEM studies; however, the multi-layer sections of the film were helpful for monitoring the stability of the film in the presence of detergents as described below.

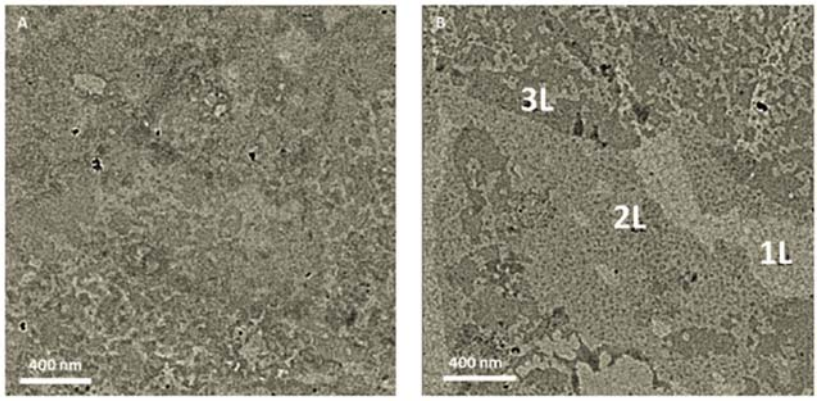

Figure 2.5 Characterization of Affinity Lipopolymer Monolayers by TEM. (A) Negative Stain TEM Images of Grids Coated with 1:99 NTA-PEG2000-DSPE:mPEG350-DTPE Monolayers. (B) Some sections of the monolayer-coated grid display areas with stepwise contrast that is suggestive of monolayer (1L), bilayer (2L) and trilayer (3L) lipid films. Scale bar: 400 nm.

2.4.2 Evaluation of Affinity Lipopolymer Non-Fouling Properties

The anti-fouling properties of the mPEG350 brush layer within the stabilized monolayer coating was probed qualitatively using fluorescence microscopy analysis of His_8-GFPuv adsorption onto these modified surfaces. Wide field and line scan fluorescence microscopy analysis revealed that glow discharged bare amorphous carbon surfaces possessed nearly 20-fold greater fluorescence intensities after exposure to His_8-GFPuv than grids bearing mPEG350 brush regime coatings (>8000 RFU and ~400 RFU, respectively; Figure 2.6). Our data shows that the fluorescence distribution was uniform over both types of surfaces, however, in rare instances there were small variations in fluorescence observed. In those cases, we attribute the areas of decreased fluorescence to grid regions with an incomplete carbon coating, whereas zones of substantially increased fluorescence were ascribed to incomplete LS transfer of the brush layer mPEG350-DTPE. We infer from these findings that non-specific binding of protein on the brush

regime mPEG350-DTPE coated grids is much lower than that of glow discharged bare carbon films due to the combined effects of molecular weight, polymer hydration, excluded volume, elastic restoration, and grafting density on the surface that enhance the antifouling properties of the mPEG coating.[12b, 28] In some cases, low molecular weight PEG polymers such as mPEG350 display greater antifouling properties than their higher molecular weight counterparts since the shorter PEG chains are better able to form a more densely packed layer.[29] Based on these findings, we concluded that brush regime mPEG350-DTPE monolayers, deposited onto a carbon coated surface by LS transfer, would be a good candidate for blocking non-specific adsorption of macromolecules onto EM grid surfaces. To test this assumption, we conducted a comparative study between DLPC monolayers and mPEG350-DTPE stabilized monolayers, both deposited via LS transfer, using bare carbon grids as a control.

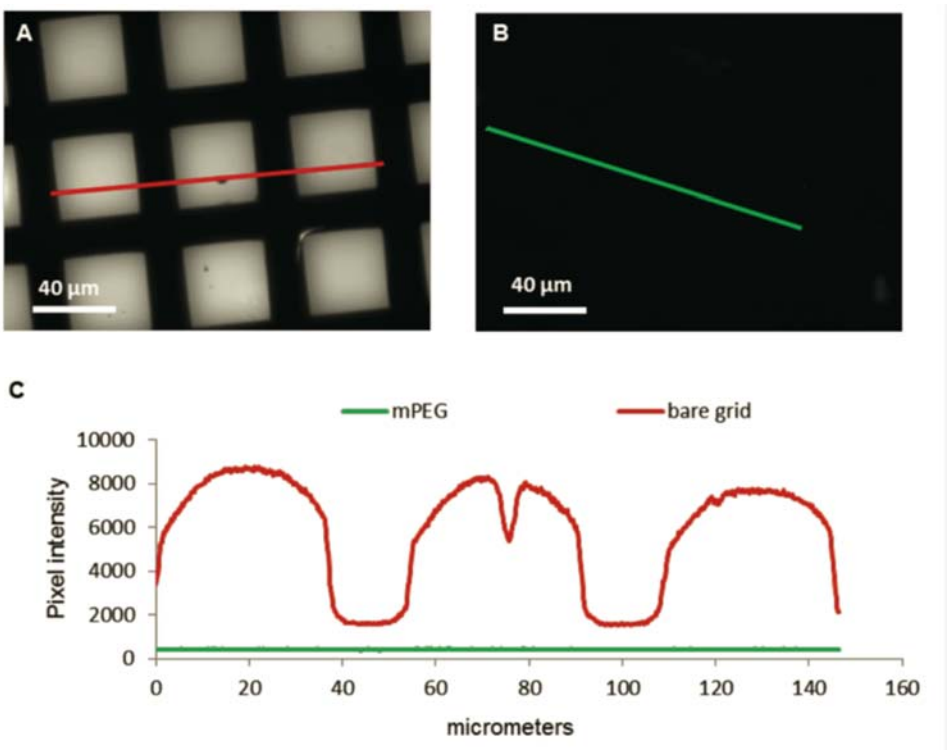

Figure 2.6 Fluorescence Microscopy of Uncoated and Stabilized Monolayer-Coated TEM Grids. Fluorescence microscopy analysis of EM grids exposed to 2.0 mg/mL His_8-GFPuv for 2 min, followed by three MilliQ water rinses to remove unbound protein. (A) Bare carbon coated grids (glow discharged) and (B) 100% mPEG350-DTPE coated grids prepared by compression to the brush regime of mPEG350, LS transfer onto carbon coated grids, and photopolymerization as described in the Experimental Section. (C) Line scans of the regions highlighted in (A) and (B), showing CCD pixel intensity as a function of position along the grid using the same protein source, protein deposition time, rinsing conditions, and fluorescence imaging settings. Substantially lower His_8-GFPuv fluorescence was found on the mPEG350-DTPE coated grids than in the bare carbon coated grids. The abrupt reduction in pixel intensity centered at 76 µm in the bare carbon surface line scan is attributed to an absence of carbon coating on this section of the TEM grid.

His_8-GFPuv capture on grids bearing stabilized 1:99 and 5:95 Ni^{2+}:NTA-PEG2000-DTPE:mPEG350-DTPE monolayers was first demonstrated by fluorescence microscopy. Wide-field fluorescence images (Figure 2.6) of Ni^{2+}:NTA-PEG2000-DTPE:mPEG350-DTPE modified grids reveal a non-uniform, concentration-dependent

GFP fluorescence. Some spots of bright fluorescence, suggestive of GFP aggregation, were also observed. The observed pixel intensities in the fluorescence line scan analyses were higher for the grids bearing a 5:95 Ni^{2+}:NTA-PEG2000-DTPE:mPEG350-DTPE coating than the grids coated with a 1:99 monolayer. In both cases, the bound His_8-GFPuv could be removed from the grid surface after a brief 5 min exposure to either 500 mM imidazole or 150 mM EDTA to remove Ni^{2+} from the His_8:Ni^{2+}:NTA complex to enable elution of the immobilized protein target from stabilized, Ni^{2+} activated 1:99 and 5:95 Ni^{2+}:NTA-PEG2000-DTPE:mPEG350-DTPE monolayers. These findings indicate that His-tag targets can be captured in an NTA concentration-dependent manner, with higher NTA loadings producing greater target protein concentrations on TEM coated with stabilized, Ni^{2+}-activated NTA-PEG2000-DTPE:mPEG350-DTPE monolayers.

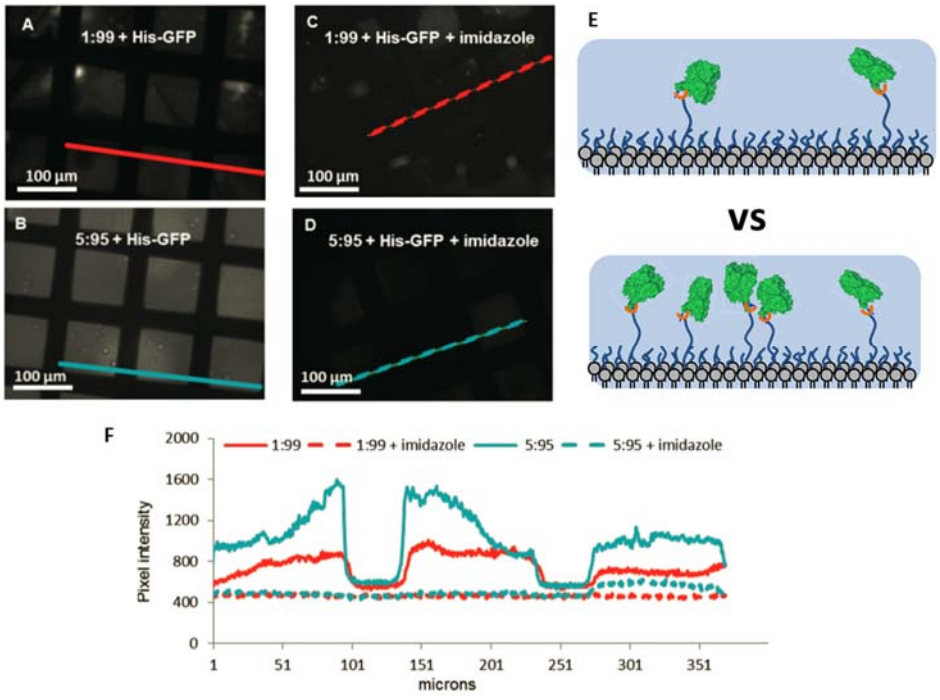

Figure 2.7 Fluorescence Microscopy of TEM Grids Coated with Stabilized NTA-PEG2000-DSPE:mPEG350-DTPE Monolayers. Fluorescence microscopy analysis of EM grids coated with 1:99 or 5:95 NTA-PEG2000-DSPE:mPEG350-DTPE after compression to the brush regime of mPEG350, LS transfer onto carbon coated grids, photopolymerization, and Ni^{2+} activation as described in the Experimental Section. The grids were then exposed to 2.0 mg/mL His_8-GFPuv for 2 min, followed by three MilliQ water rinses to remove unbound protein. (A) Appearance of 1:99 coating before and (C) after 500 mM imidazole, pH 7.2 treatment. (B) Appearance of 5:95 coating before and (D) after 500 mM imidazole, pH 7.2 treatment. (E) Cartoon illustrating varying surface density of bound target with varying monolayer composition. (F) Line scans of the regions highlighted in (A) - (D), showing CCD pixel intensity as a function of position along the grid using the same protein source, protein deposition time, rinsing conditions, and fluorescence imaging settings.

Purified His_6-T7 bacteriophage (10^{11} – 10^{12} particles/mL) was used to probe the non-specific adsorption properties of DLPC and mPEG350-DTPE stabilized monolayer-coated grids at higher resolution, with carbon coated, glow-discharged grids serving as a control. The sample precipitated on grids lacking modified DLPC or mPEG350 monolayers (Figure 2.8A). We identified virus-like particles on these grids, as shown in

Figure 2.8A (inset); however, the poor sample quality produced on unmodified, glow-discharged grids made accurate quantification of adsorbed virus particles impossible. Therefore, we only quantified virus adsorption onto DLPC and mPEG350 modified grids, as discrete particles could be discerned in both cases. DLPC coated grids were found to decrease the amount of T7 that was adsorbed to the grid relative to bare carbon grids (Figure 2.8B), indicating that interactions between T7 bacteriophage and the DLPC monolayer are not as favorable. Nonetheless, a significant amount of occult debris remained on the DLPC monolayer coated grids. Grids coated with mPEG350-DTPE stabilized monolayers; however, displayed a greatly reduced accumulation of both T7 and debris (Figure 2.8C). The appearance of the virus particles in these samples included round-like objects as well as more familiar hexagonal projections of the mature icosahedral form of the virus. The T7 phage particle here represents the immature form where an absence of mature capsid shell protein gives results in the rounded appearance of these particles.[30] The low abundance of T7 phage particles in this image highlights the antifouling opportunities of these PEGylated surfaces. Quantitative comparisons of the T7 particle densities on DLPC and mPEG350 monolayers revealed an accumulation of ~110 particle/1 μm^2, and 5 particle/1 μm^2, respectively. We infer from these findings that mPEG350-DTPE stabilized monolayers are the most effective toward blocking non-specific adsorption of T7 bacteriophage (Figure 2.8D). Low magnification images of purified T7 deposited onto both DLPC and mPEG-DTPE stabilized monolayer coated grids reveal a substantially lower background in the case of mPEG350-DTPE coated grids (Figure 2.8E and 2.8F).

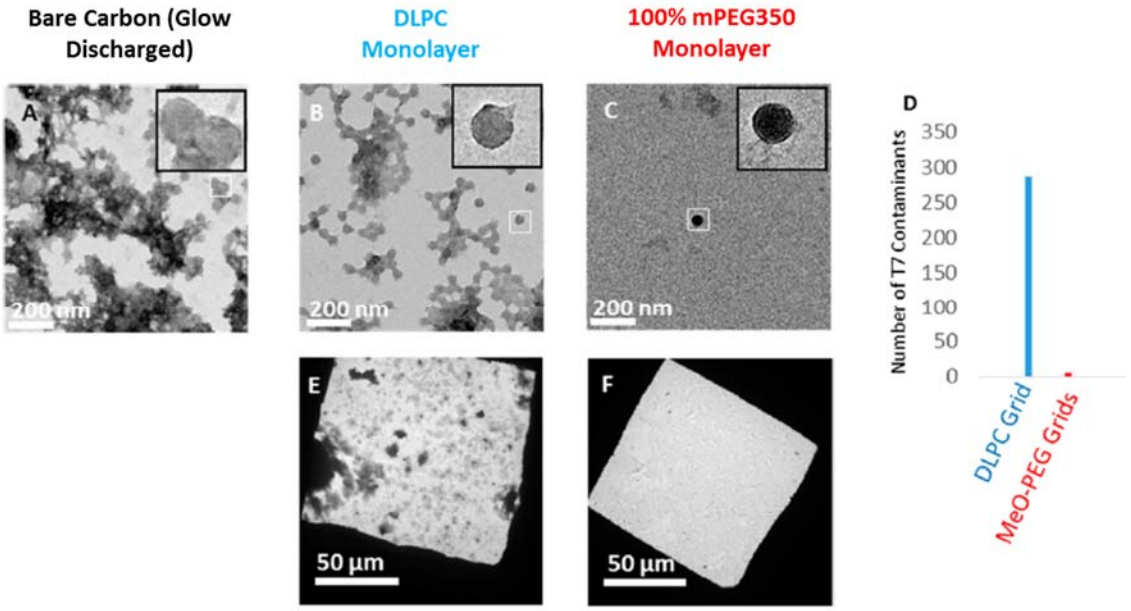

Figure 2.8 Comparative Performance of Uncoated (bare carbon, glow-discharge), DLPC, and mPEG350-DTPE Coated Grids Toward Non-Specific Protein Adsorption (i.e., lacking NTA groups to promote specific binding). The capacity of these grids to reject non-specific protein adsorption was tested by negative stain TEM analysis using His_6-T7 bacteriophage in purified form or within cell lysates. (A) Purified His_6-T7 bacteriophage on glow-discharged bare carbon grid; (B) purified His_6-T7 bacteriophage on 100% DLPC monolayer coated grid; (C) His_6-T7 bacteriophage on stabilized 100% mPEG350-DTPE monolayer coated grid; (D) number of non-specific contaminants adsorbed from purified His_6-T7 bacteriophage solution onto bare carbon grids (blue), DLPC coated grids (red), and mPEG350-DTPE coated grids (green) as determined by counting 60 randomly selected fields across 3 different grids for each grid type; (E) His_6-T7 bacteriophage in cell lysate applied to 100% DLPC coated grid; and (F) His_6-T7 bacteriophage in cell lysate applied to stabilized 100% mPEG350-DTPE coated grid.

2.4.3 Affinity Capture of His-Tagged Proteins Using Affinity Lipopolymers Grids

After evaluating the capacity of these grids to inhibit non-specific adsorption, we next turned our attention to their ability to direct affinity-guided interactions with NTA-modified grids. First, we used fluorescence microscopy to monitor His_8-GFPuv capture on grids bearing stabilized 1:99 and 5:95 Ni^{2+}:NTA-PEG2000-DTPE:mPEG350-DTPE monolayers. Wide-field fluorescence images (Figure 2.7) of Ni^{2+}:NTA-PEG2000-DTPE:mPEG350-DTPE modified grids reveal a non-uniform, concentration-dependent GFP fluorescence. Occasional spots of bright fluorescence, suggestive of GFP aggregation, were also observed. The observed average pixel intensities in the fluorescence line scan analyses were higher for the grids bearing a 5:95 Ni^{2+}:NTA-PEG2000-DTPE:mPEG350-DTPE coating than the grids coated with a 1:99 monolayer. In both cases, the bound His_8-GFPuv could be removed from the grid surface after a brief 5 min exposure to either 500 mM imidazole or 150 mM EDTA to remove Ni^{2+} from the His_8:Ni^{2+}:NTA complex to enable elution of the immobilized protein target from stabilized, Ni^{2+} activated 1:99 and 5:95 Ni^{2+}:NTA-PEG2000-DTPE:mPEG350-DTPE monolayers. These findings indicate that histidine-tagged targets can be captured in an NTA concentration-dependent manner, with higher NTA loadings producing greater target protein concentrations on TEM grids coated with stabilized, Ni^{2+}-activated NTA-PEG2000-DTPE:mPEG350-DTPE monolayers.

Affinity capture of His_6-T7 bacteriophage from cell lysates was then tested by negative stain and cryoelectron microscopy using grids modified with mPEG350-DTPE stabilized monolayers, Ni^{2+}:NTA-PEG2000-DTPE:mPEG350-DTPE stabilized monolayers, and Ni^{2+}:NTA-PEG2000-DTPE:mPEG350-DTPE stabilized monolayers

rinsed with 500 mM imidazole after lysate exposure (Figure 2.9). In the presence of mPEG350-DTPE stabilized monolayers, we observed minimal binding of His_6-T7 bacteriophage and very low levels of debris from the lysate onto the grid (Figure 2.9A). Background adsorption of non-T7 phage debris is highlighted in the inset of this image. In some cases, T7 particles were not observed on the brush polymer surface even at low magnification, suggesting a complete blockage of non-specific adsorption. Grids bearing Ni^{2+}-charged 1:99 NTA-PEG2000-DTPE:mPEG350-DTPE stabilized monolayers were capable of capturing His_6-T7 bacteriophage from cell lysate while limiting the background adsorption of undesired non-target cellular components (Figure 2.9B). It is worth noting that T7 viral particles often give mixed results of negative-stain and positive-stained particles since uranyl salts may positively stain packaged nucleic acid within the capsid structure.[31] Exposure of these samples to 500 mM imidazole led to greatly decreased surface adsorption of His_6-T7 bacteriophage, suggesting that the interaction of phage particles with the supported NTA-lipid monolayer is Ni^{2+} specific (Figure 2.9C). We attribute the occurrence of the few remaining particles to either non-specific adsorption to uncoated grid regions or particles that are avidly bound due to multivalent interactions between the phage particles and the NTA-PEG grafted surface. To compensate for particle capture efficiency limitations in samples prepared for cryogenic imaging[5] due to unfavorable kinetics and/or modest ligand-receptor affinities,[32] we examined 1:99 and 5:95 Ni^{2+}:NTA-PEG2000-DTPE:mPEG350-DTPE stabilized monolayer coated grids to determine whether the areal density of NTA ligands had a detectable influence on His_6-T7 bacteriophage capture efficiency. Using identical sample processing methods and incubation times, we qualitatively observed an increase in particle surface density with

increasing Ni^{2+}:NTA-PEG2000-DTPE composition (unpublished data). Since this comparison was not performed in a side-by-side manner between 1:99 and 5:95 Ni^{2+}:NTA-PEG2000-DTPE:mPEG350-DTPE stabilized monolayers with the same lysate, it is conceivable that these findings may be the result of different virus titers in the His_6-T7 bacteriophage preparations. Nonetheless, these findings are consistent with the His_8-GFPuv experiments described above (Figure 2.7) showing that higher surface concentrations of affinity capture lipid produces greater areal densities of immobilized target on the NTA-modified surface, with the 5:95 Ni^{2+}:NTA-PEG2000-DTPE:mPEG350-DTPE stabilized monolayer coated grids being more suitable for cryoEM sample preparation (Figure 2.9D). The immobilization of both mature and immature T7 phage from lysate samples **(**Figure 2.9F) highlights the potential of rapid purification using affinity grids for the study of dynamic processes, which may not be possible when visualizing purified samples generated using standard TEM sample preparations.

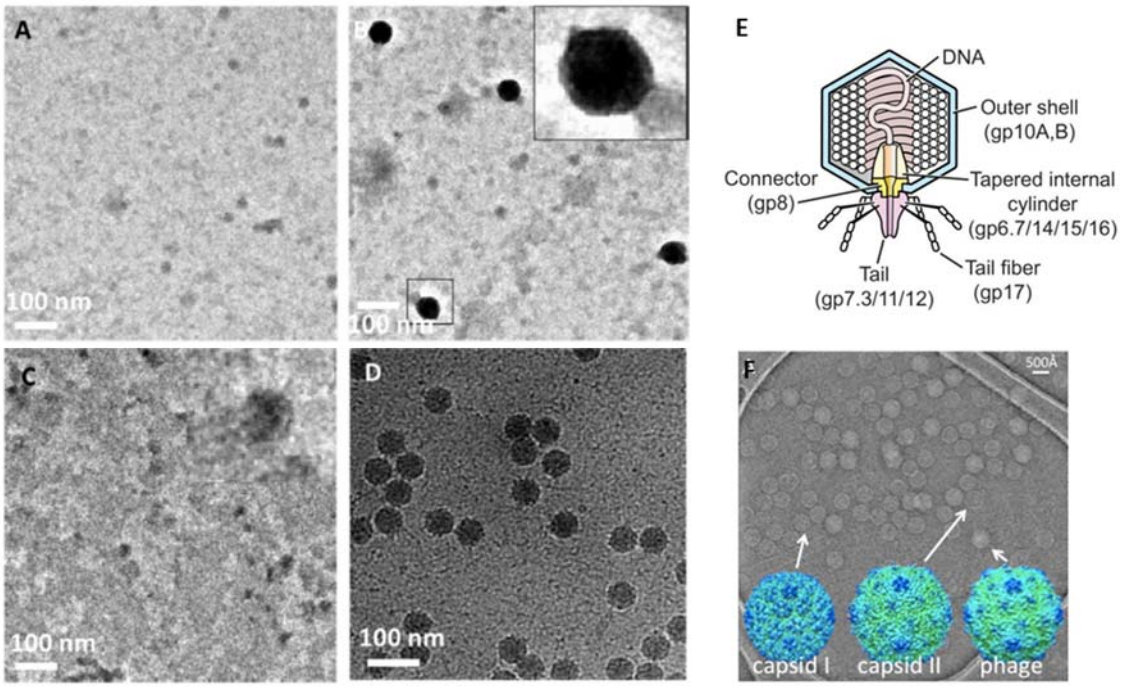

Figure 2.9 Effect of NTA Surface Density on His-T7 Bacteriophage Captured from Cell Lysates Using Negative Stain and Cryo-EM Analysis. (A) Negative stain TEM appearance of grid coated with stabilized 100% mPEG350-DTPE monolayer after 2 min exposure to cell lysate containing His-T7 bacteriophage; (B) same as in (A), except that the grid was coated with stabilized 1:99 Ni^{2+}:NTA-PEG2000-DSPE:mPEG350-DTPE monolayer; (C) same as in (B), except that the grid was rinsed with 500 mM imidazole, pH = 7.4 after the 2 min lysate exposure step; and (D) cryoEM appearance of grid coated with stabilized 5:95 Ni^{2+}:NTA-PEG2000-DSPE:mPEG-350-DTPE monolayer after 2 min exposure to cell lysate containing His-T7 bacteriophage. (E) Schematic of T7 bacteriophage organization and structure. (F) Cryo-EM image of his-T7 bacteriophage revealing different stages of maturation.

We next demonstrated the capture of the 50S *E. coli* ribosomal subunit,[5] His_6-RplL, directly from cell lysates onto grids coated with Ni^{2+}:NTA-PEG2000-DTPE:mPEG350-DTPE stabilized monolayers. Negative stain EM images of His_6-RplL lysate deposited onto grids coated with mPEG350-DTPE stabilized monolayers showed no appreciable target-specific adsorption onto the grid (Figure 2.10A). After LS deposition of 1:99 Ni^{2+}:NTA-PEG2000-DTPE:mPEG350-DTPE stabilized monolayers

onto the grids, particles consistent with the size and various shapes of the 50S subunit were observed on the grid surface (Figure 2.10B). When 500 mM imidazole was added to samples containing the captured ribosomal particles on 1:99 Ni^{2+}:NTA-PEG2000-DTPE:mPEG350-DTPE stabilized monolayers, the previously adsorbed particles were eluted from the surface of the TEM grid (Figure 2.10C), consistent with the expectation that the interaction of His_6-RplL with the surface of the grid is Ni^{2+} specific. Using the same sample preparation procedure, cryo-EM analysis revealed the capture of His_6-RplL from *E. coli* lysates (Figure 2.10D) as crown-like projections in some images (Figure 5D). These have frequently been reported and are attributed to the 50S ribosomal subunit. The earliest reported TEM images of ribosomes were small, featureless bumps on the grid surface;[33] however, more powerful tools eventually led to the revelation of several features in the ribosomal units such as ‘crown-like’ and ‘duck-like’ projections for the 50S and 30S subunits, respectively.[34] Since the RplL protein carries the hexahistidine tag on the 50S subunit in our construct, we identified many more of these particles bound to the grid than the 30S subunit. Crown-like projections are clearly seen from the side view of the 50S particle with a central protuberance, a ridge, a stalk, and two groove-like features.

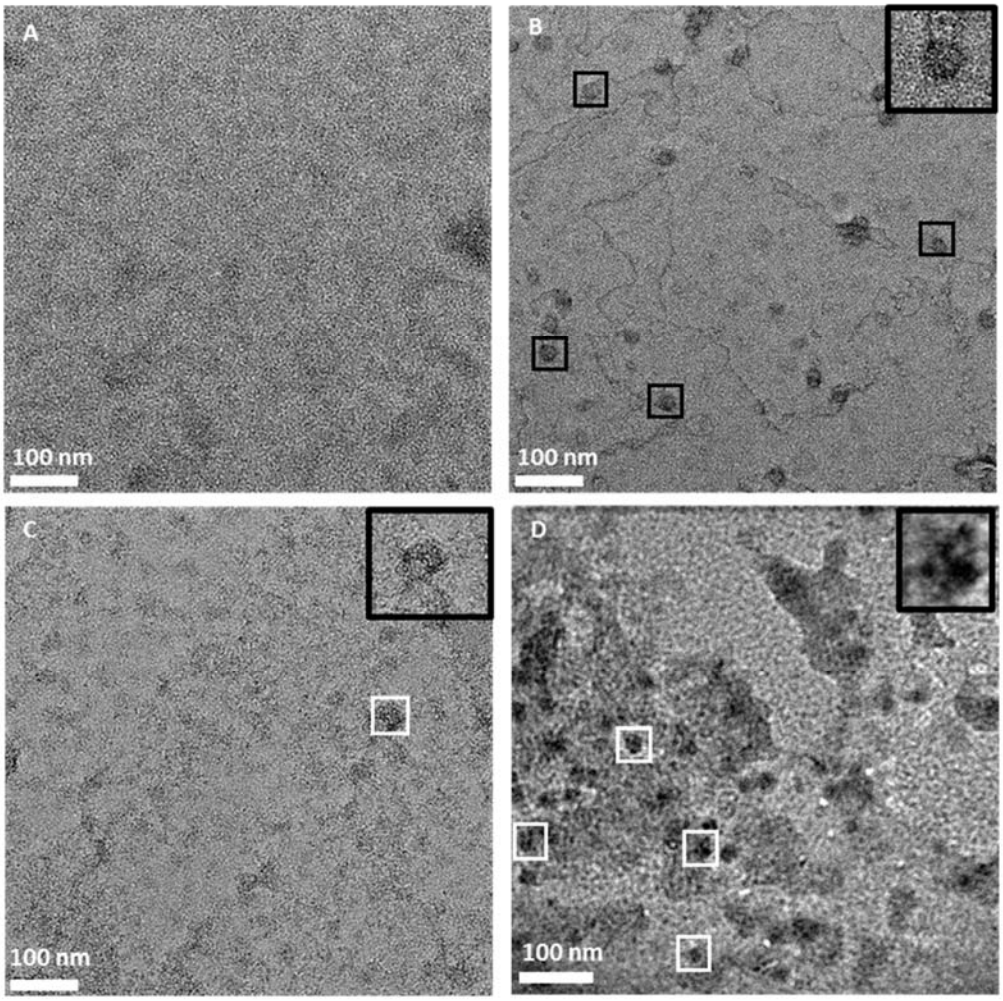

Figure 2.10 Affinity Capture of His-RplL from Cell Lysates onto Stabilized Ni^{2+}:NTA-PEG2000-DTPE:mPEG-350-DTPE Monolayer Coated Grids. (A) Negative stain TEM of grid coated with stabilized 100% mPEG350-DTPE after 2 min exposure to cell lysate containing His-RplL; (B) negative stain TEM of grid coated with 1:99 Ni^{2+}:NTA-PEG2000-DSPE:mPEG350-DTPE after 2 min exposure to cell lysate containing His-RplL; (C) same as in (B), except that the grid was rinsed with 500 imidazole, pH=7.4 after the 2 min exposure to cell lysate containing His-RplL; and (D): cryoEM image of grid coated with stabilized 5:95 Ni^{2+}:NTA-PEG2000-DSPE:mPEG-350-DTPE monolayer after 2 min exposure to cell lysate containing His-RplL.

A key design feature of these stabilized affinity coatings is their utilization of two different types of poly(ethylene glycol)-modified lipids, one high molar ratio brush layer

short segment to block non-specific adsorption and facilitate stabilization via photopolymerization (i.e., mPEG350-DTPE) and a second low molar ratio component to enable multiple orientations of the captured protein target to avoid preferred orientations at the monolayer interface and provide a more representative single particle reconstruction analysis data set. We tested this hypothesis by preparing dozens of TEM grids bearing stabilized Ni^{2+}:NTA-PEG2000-DSPE:mPEG350-DTPE coatings that had been treated with His_6-RplL containing lysates. CryoEM evaluation of these grids confirmed that the NTA-PEG2000 tether is capable of both capturing and presenting multiple orientations of the bound His_6-RplL target as demonstrated by the overlay of the known 50S subunit and 70S complex structures in different rotational configurations onto the corresponding EM images shown in Figures 2.11A-D.

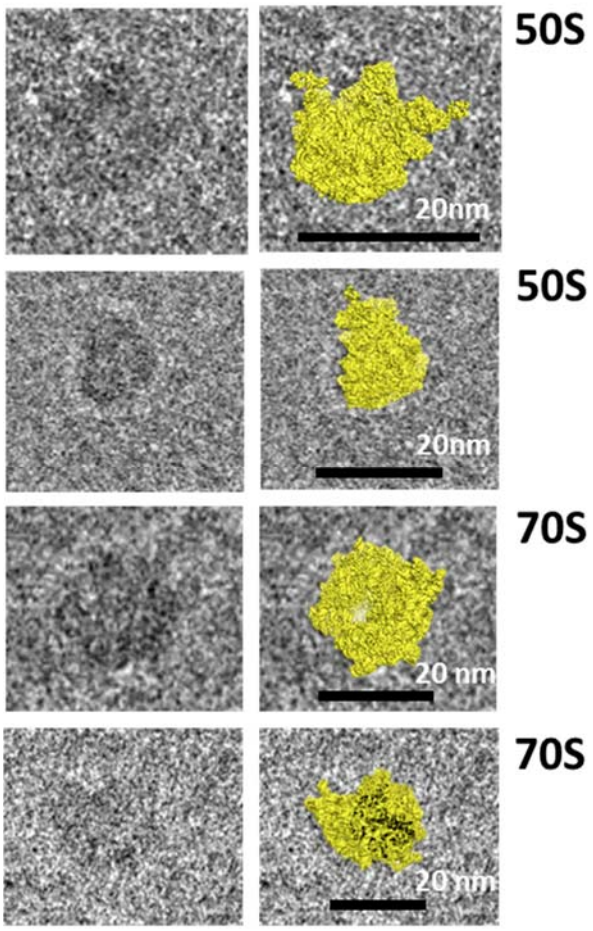

Figure 2.11 Cryo-EM Images and Conformational Overlay Showing Representative Views of His-tag RplL from Cell Lysates onto Stabilized 5:95 Ni^{2+}-NTA-PEG2000-DSPE:mPEG350-DTPE Monolayer Coated Grids. (A, B) Projections of different ribosomal large subunit (50S) orientations onto corresponding cryo-EM images; (C, D): projections of different full ribosomal (70S) particle orientations onto corresponding cryoEM images.

Membrane scaffold proteins (MSP) have become an increasingly popular tool for stabilizing membrane protein dispersions since it provides a platform in which the local environment of solubilized membrane proteins resemble the natural environment of the lipid bilayer in cells.[35] MSP are used to corral lipids and membrane proteins within disk-like structures containing a lipid bilayer interior that can host reconstituted membrane

proteins for structure analysis by electron microscopy,[36] protein modification studies,[37] and protein activation analysis.[38] We used the purified hexahistidine-tagged maltose transporter, His_6-$MalFGK_2$, solubilized in MSP lipid nanodisc, for evaluating their affinity capture properties on NTA-modified stabilized affinity grids. Although His-tag MSP can be used for affinity purification,[39] we used a His_6-$MalFGK_2$ construct for nanodisc reconstitution to ensure that only nanodisc containing His_6-$MalFGK_2$ are surface immobilized. We found that mPEG350-DTPE stabilized monolayer coated grids treated with His_6-$MalFGK_2$ nanodisc appeared to have fewer particles bound to the grid surface (Figure 2.12A) than the grids coated with 1:99 Ni^{2+}:NTA-PEG2000-DTPE:mPEG350-DTPE stabilized monolayers (Figure 2.12B). Treatment of the His_6-$MalFGK_2$-immobilized grids with 500 mM imidazole produced a decrease in MSP nanodisc binding to the surface (Figure 2.12C), further suggesting that the interaction between nanodisc solubilized His_6-$MalFGK_2$ and the NTA-modified surface is Ni^{2+} specific. High magnification images of nanodisc solubilized His_6-$MalFGK_2$ immobilized onto 5:95 Ni^{2+}:NTA-PEG2000-DTPE:mPEG350-DTPE stabilized monolayers (Figure 2.12D) reveal a set of disc-like features in the size range of other lipid nanodisc dispersions (7 – 13 nm in diameter).[40] Although the His_6-$MalFGK_2$ within the MSP nanodiscs is not directly observed due to its small size relative to the nanodiscs, the fact that these features elute with 500 mM imidazole strongly corroborates the assumption that they contain His_6-$MalFGK_2$. In addition, our images show predominantly top/bottom views of the particles, i.e., a disk-like appearance in TEM micrographs (Figure 2.12D), suggesting that a longer PEG spacer is needed to collect a greater number of side views for this solubilized target.

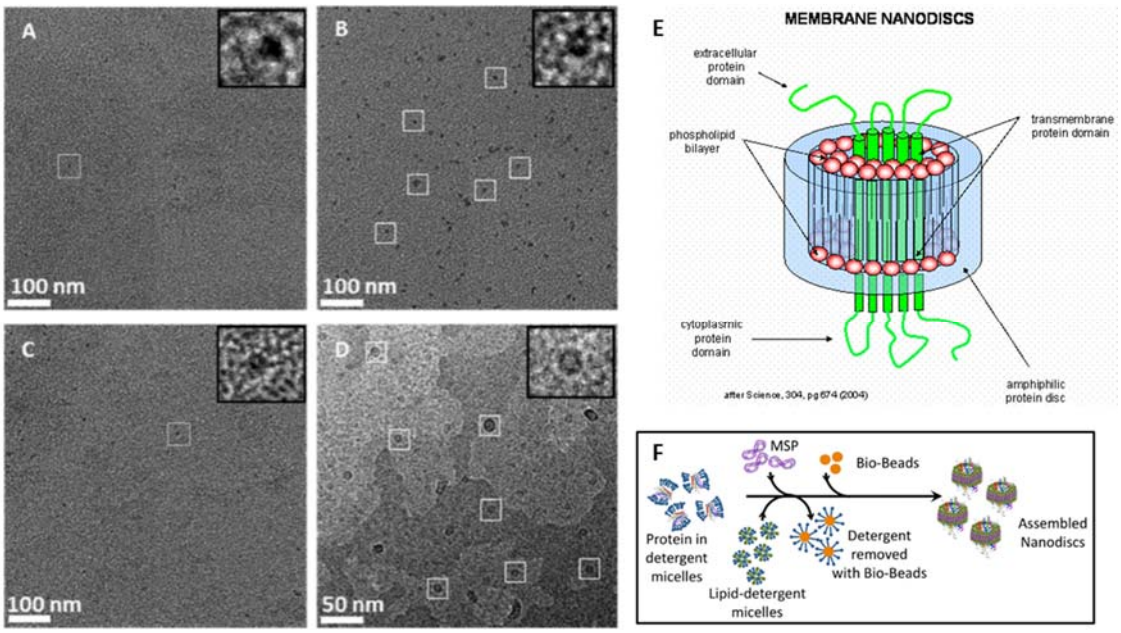

Figure 2.12 Affinity Capture of MSP Nanodisc Containing Purified His_6-$MalFGK_2$. (A) Negative stain TEM of stabilized 100% mPEG350-DTPE monolayer-coated grid after treatment with His-$MalFGK_2$ in nanodiscs; (B) negative stain TEM of His-$MalFKG_2$ in nanodisc captured on stabilized 1:99 Ni^{2+}:NTA-PEG2000-DSPE:mPEG350-DTPE monolayer-coated grid; (C) same as in (B), except that the grid was rinsed with 500 mM imidazole, pH = 7.4 after the His-$MalFGK_2$ in nanodisc exposure step; and (D) cryoEM of His-$MalFGK_2$ in nanodisc captured on stabilized 5:95 Ni^{2+}:NTA-PEG2000-DSPE:mPEG-350-DTPE monolayer-coated grid. (E) Schematic of MSP nanodisc 3D structure. (F) Schematic illustration of preparation of MSP nanodisc from detergent solubilized protein.

2.4.4 Affinity Lipopolymer Grid Stability Against Detergent Exposure

In order to test the durability of the stabilized monolayers toward detergent exposure, the modified grids were treated with either 0.03% Triton X-100 (CAC = 0.015%), 0.014% Tween 20 (CAC = 0.0072%), or 0.5% CHAPS (CMC=0.49%) solutions for varying periods of time before TEM observation. Lipid monolayers adsorbed to solid substrates display better detergent resistance than lipid bilayers that are prone to disruption via lipid flip-flop.[41] Initial encounter of detergents with the outer

bilayer leaflet results in fluidization and lipid flip-flop from the inner leaflet to the outer leaflet, eventually leading to complete solubilization of the bilayer structure.[41b] Inhibition of flip-flop due to adsorption of a highly compressed monolayer onto the solid carbon substrate inhibits flip-flop processes, leading to improved detergent resistance.

Despite some evidence of enhanced detergent resistant of supported DLPC monolayers, prior attempts to produce TEM grids coated with mixed Ni^{2+}:NTA-DSG:DPLC monolayers showed that their exposure to harsher detergents such as Triton X-100, Tween-20, and CHAPS led to monolayer solubilization.[5] We tested the detergent resistance of our stabilized Ni^{2+}:NTA-PEG2000-DTPE:mPEG350-DTPE monolayer coatings under conditions where DLPC monolayers failed by using 0.03% Triton X-100 (CMC = 0.015%), 0.014% Tween 20 (CMC = 0.0072%), or 0.5% CHAPS (CMC = 0.49%) at 5, 15, and 30 min exposures to the detergent solutions. Negative stain TEM observation of the coatings after detergent exposure indicated that stabilized Ni^{2+}:NTA-PEG2000-DTPE:mPEG350-DTPE monolayer coatings remain intact after 30 minutes of incubation with Triton X-100, Tween-20, and CHAPS (Figure 2.13). In the case of Triton X-100, some holes in the monolayer were occasionally observed, but none were apparent in grids treated with Tween 20 or CHAPS. The capacity of these coatings to immobilize purified His_6-T7 bacteriophage after detergent exposure for 20 min indicated that a modest reduction in phage binding to the grid occurred, however, the immobilized His_6-T7 bacteriophage particles were bound specifically as indicated by their ability to be removed by elution with 500 mM imidazole.

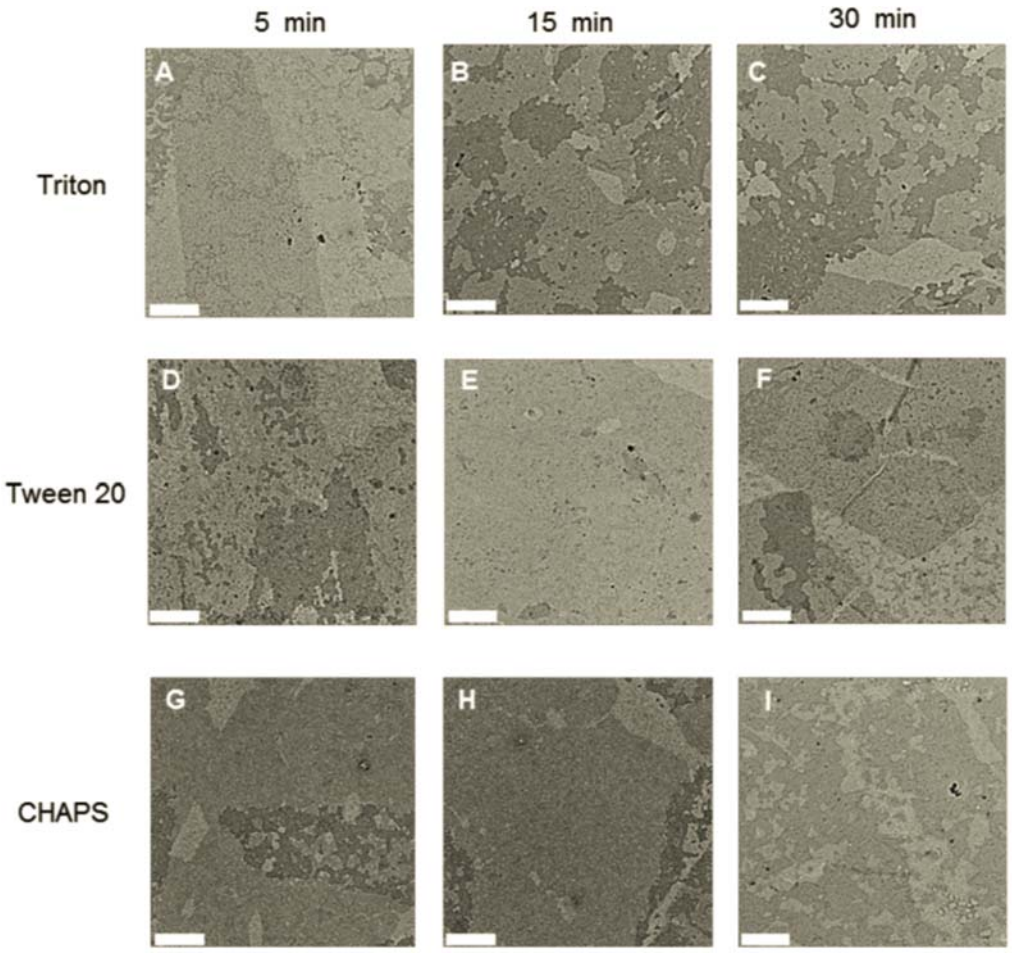

Figure 2.13 Negative Stain TEM Images of TEM Grids Coated with 1:99 NTA-PEG2000-DSPE:mPEG350-DTPE After Exposure to Different Detergents. Negative stain TEM analysis of EM grids coated with 1:99 NTA-PEG2000-DSPE:mPEG350-DTPE after compression to the brush regime of mPEG350, LS transfer onto carbon coated grids, photopolymerization, and exposure to different detergent solutions for varying periods of time prior to TEM analysis. (A – C): A 0.03% Triton X-100 solution (10 μL) was placed in contact with the grids for (A) 5, (B) 15, or (C) 30 min. (D – F): A 0.014% Tween 20 solution (10 μL) was placed in contact with the grids for (D) 5, (E) 15, or (F) 30 min. (G – I): A 0.5% CHAPS solution (10 μL) was placed in contact with the grids for (G) 5, (H) 15, or (I) 30 min. The scale bars in all images are 400 nm. A defocus of > 10 μm was used to improve visualization of the monolayer film coatings.

Fluorescence microscopy analysis of detergent-treated Ni^{2+}:NTA-PEG2000-DTPE:mPEG350-DTPE monolayers revealed that the stabilized Ni^{2+} lipid monolayer coatings retained their ability to capture His_8-GFPuv. Pixel intensity data was collected over the entire fluorescence image (Figure 2.14) to best represent the overall specific capture capacity of the coating, regardless of whether it had been detergent compromised or not. In the case of Triton X-100 exposed samples, the fluorescence was occasionally enhanced near the grid edges, possibly as a result of solubilized or damaged monolayer near the center of the grid holes that were unable to capture His_8-GFPuv in those regions. We did not see this phenomenon with either CHAPS- or Tween 20-treated surfaces. These grids exhibited a uniform distribution of His_8-GFPuv fluorescence over the grid holes until the surfaces were treated with 500 mM imidazole to displace the immobilized protein. Despite the limitations of these stabilized Ni^{2+}:NTA-PEG2000-DTPE:mPEG350-DTPE monolayer coatings toward prolonged Triton X-100 exposure, our data indicates that histidine-tagged proteins can be reversibly immobilized even after detergent exposure. We infer from these findings that both the integrity of the stabilized lipid monolayer and the specific affinity capture of the grids remains intact after exposure to detergents that has proven detrimental to previously reported mixed Ni^{2+}:NTA-DGS:DLPC monolayers.[5]

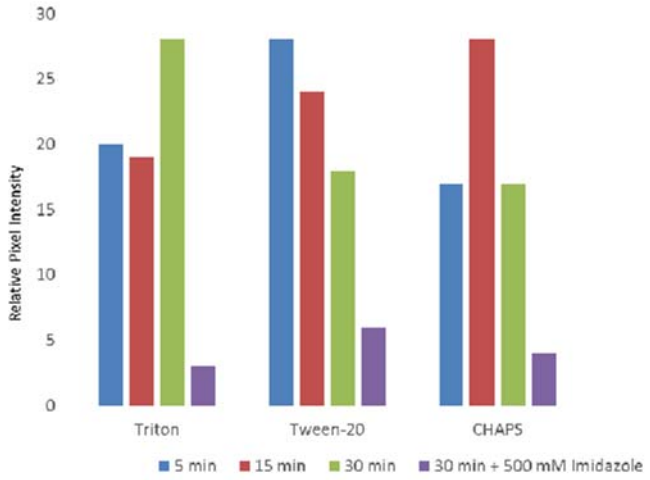

Figure 2.14 Effect of Detergent Exposure on 1:99 Ni^{2+}:NTA-PEG2000-DSPE:mPEG350-DTPE Stabilized Monolayer Affinity Grids as Determined by Fluorescence Microscopy Using His_8-GFP as a probe for NTA Monolayer Retention.

2.5 Conclusions

A library of affinity lipopolymer constructs was synthesized consisting of lipopolymers of various PEG molecular weights conjugated to DTPE or DSPE as lipid anchors and NTA, tris-NTA, biotin and glutathione as affinity moieties or maleimide as a covalent functionality. This strategy is expected to be effective for specific capture of other targets of interest by varying the composition of the PEG terminus. Specific targets to expand the library include dibenzocycloctynyl and other specific ligands. This strategy may also be useful for screening of a molecular drug target by incorporating the drug target into the affinity lipopolymer constructs.

Langmuir-Schaefer transfer of compressed, mixed lipid monolayers containing Ni^{2+}:NTA-PEG2000:mPEG350 head groups in 1:99 and 5:95 molar ratios are capable of capturing His-tag protein targets from cell lysates with controllable areal densities and low degrees of non-specific protein adsorption. Photopolymerization of the mPEG350-DTPE

component in these monolayers by irradiating for 10 min at 254 nm produced EM grids with stabilized lipid coatings that were used to then used to capture His_6-T7 bacteriophage and His_6-RplL from cell lysates, purified His_8-GFPuv, and nanodisc embedded His_6-$MalFGK_2$. Our data indicate that the crosslinked lipid coating maintains the non-fouling properties of the monolayer and provides multiple orientations of the captured target on the surface, while also affording greater mechanical and detergent resistance than previously reported for EM grid-supported DLPC monolayers.

2.6 Future Directions

To further advance this project, we are interested in the synthesis of novel lipopolymer constructs with terminal moieties which impart specificity for binding or covalent reaction with a specific target or class of targets. For instance, by generating a library of lipopolymer drug conjugates, a screening array could be constructed for simultaneous identification and structural characterization by cryo-EM. This could be a powerful new approach for drug discovery. As another example, dibenzocycloctynyl-lipopolymer conjugate **47** could allow for selective capture of azide-containing targets. We are interested in exploring affinity grid performance with polymer conjugates of other types of lipids which may provide better monolayer performance. We are also interested in exploring the relation of parameters like PEG molecular weight, lipid composition and modification of other surfaces to affinity grid performance, as well.

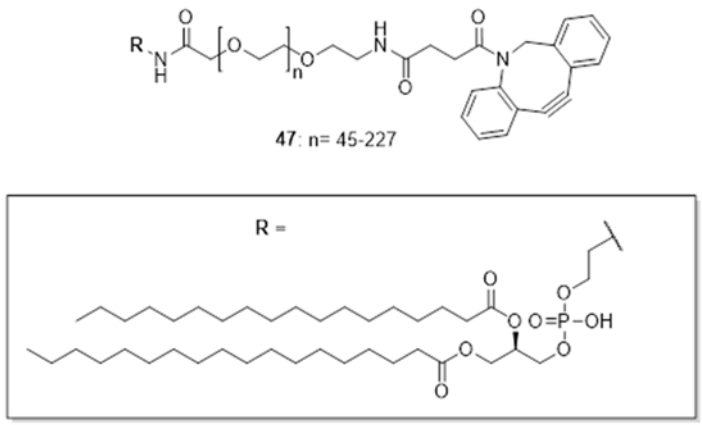

Figure 2.15. Proposed Affinity Lipopolymer for Immobilization of Azide-Containing Targets, DSPE-PEG-DBCO.

2.7 Experimental Methods

All reactions were carried out under a blanket of N_2 or argon gas. Reaction progress was monitored by thin-layer chromatography (TLC) analysis. TLC spots were visualized either by UV light (254nm), exposure by ninhydrin staining, staining with phosphomolybdic acid (PMA), staining by bromocresol green, or by staining with I_2. Flash column chromatography was carried out using 230-400 mesh silica gel and analytical grade solvents. Solvents were purchased from Mallinckrodt/Baker and used without further purification unless noted. Toluene was purchased from Fisher. mPEG polymers were from Sigma-Aldrich and were purified before use via precipitation N-(3-dimethylaminopropyl)-N'-ethylcarbodiimide hydrochloride (EDC), N^{ε}-((benzyloxy)carbonyl)-l-lysine (H-Lys(Z)-OH) and H-Cys(Trt)-OH were purchased from Advanced Chemtech. Heterobifunctional PEG derivatives were purchased from JenKem Technology USA. 1,2-Distearoyl-*sn*-glycero-3-phosphoethanolamine (DSPE) and 1,2-(tricosa-10',12'-diynoyl)-*sn*-glycero-3-phosphoethanolamine (DTPE) were purchased

from Avanti Polar Lipids. All other chemicals were purchased from Sigma Aldrich and used without further purification. Dichloromethane (DCM), and toluene were distilled from CaH_2. Triethylamine (TEA) was distilled from CaH_2 and stored over BaO. Tetrahydrofuran (THF) was distilled from sodium-benzophenone ketyl. α-methoxy-polyethylene glycol (mPEG350) was purchased from Sigma Aldrich and purified by azeotropic drying with toluene. Jones' reagent (1.25 M in CrO_3) was prepared by dissolving 17.5 g CrO_3 in 125 mL water plus 16 mL conc. H_2SO_4.

^{1}H and ^{13}C nuclear magnetic resonance (NMR) spectra were recorded on either a Bruker AV500HD (500MHz) or a Bruker ARX400 spectrometer (400 MHz). Chemical shifts are reported in ppm relative to the residual solvent peaks as internal standard

2.7.1 Synthesis of Affinity Lipopolymer Constructs

mPEG-mesylate (2a-e). mPEG was dried azeotropically with toluene several times and dried *in vacuo* for 18 hours. As a representative reaction, mPEG (6.00 g) was dissolved in DCM (85 mL) and triethylamine (1.5 equiv.) was added. The solution was cooled to 0 °C in an ice bath and methansulfonyl chloride (MsCl, 1.1 equiv.) was added dropwise over 10 minutes. The reaction was stirred for an additional 30 minutes at 0 °C. The solution was transferred to a separatory funnel with an additional 50 mL DCM. The solution was washed with 100 mL ice water followed by 100 mL 5 % HCl solution. The organic solution was dried with anhydrous sodium sulfate and concentrated in vacuo. For mPEG < 2.0 kDa the oily residue was further dried *in vacuo*. For mPEG > 2.0 kDa, the oily residue was precipitated into cold diethyl ether (500-800 mL), filtered and dried *in vacuo*. Yield: (90-98 %); TLC: R_f= 0.66 (3:17 MeOH:DCM) for mPEG350.

mPEG-azide (3a-e). mPEG-mesylate **2a-e** (6.69 g) was dissolved in DMF (150 mL) and sodium azide (10.0 equiv.) was added. The solution was stirred for 90 °C for 48 hours. DMF was evaporated *in vacuo*. The residue was dissolved in DCM ((200 mL), filtered and washed with deionized water (150 mL) twice. The aqueous washes were extracted with DCM (100 mL) twice each and the organic extracts were combined with the original organic solution and concentrated *in vacuo*. For mPEG < 2.0 kDa the oily residue was further dried *in vacuo*. For mPEG > 2.0 kDa, the oily residue was precipitated into cold diethyl ether (500-800 mL), filtered and dried *in vacuo.* Yield: (83-95 %); TLC: R_f= 0.63 (3:17 MeOH:DCM) for mPEG350.

mPEG-amine (4a-e). mPEG-azide **3a-e** (5.52 g) was dissolved in ethyl acetate (50 mL) and 10% palladium on carbon (wet type) was added via spatula. The flask was equipped with a three-way adapter and a hydrogen balloon. The flask was evacuated and purged with hydrogen three times and stirred vigorously under 1 atm hydrogen atmosphere for 24 hours at ambient temperature. The solution was gravity filtered through celite and concentrated *in vacuo*. For mPEG < 2.0 kDa the oily residue was further dried *in vacuo*. For mPEG > 2.0 kDa, the oily residue was precipitated into cold diethyl ether (500-800 mL), filtered and dried *in vacuo.* Yield: (82-94 %); TLC: R_f= 0.06 (3:17 MeOH:DCM) for mPEG350.

mPEG-carboxylic acid (5a-e). Jones oxidation was used to produce carboxylic acid-terminal mPEG**.** As a representative reaction, mPEG (5.00 g) was dissolved in 280 mL acetone. Jones' Reagent (1.1 equiv) was added to a 500 mL round bottom flask and the mPEG solution was added to this flask dropwise over 1 h via addition funnel. The

resulting solution was stirred at 20 °C for 1 h before quenching the excess Jones reagent with a few mL of iPrOH. The resulting green precipitate was removed by decantation of the liquid solution. The volatiles were removed under reduced pressure and the residue dissolved in 150 mL H_2O. The aqueous phase was extracted with DCM (4 x 120 mL). Depending of mPEG molecular weight, it may be necessary to add MeOH (100-200 mL) to effect phase separation. The organic layers were combined and dried over anhydrous Na_2SO_4, filtered, and evaporated under reduced pressure. For mPEG < 2.0 kDa, the oily residue was dried *in vacuo*. For mPEG > 2.0 kDa, the oily residue was precipitated into cold diethyl ether (500-800-mL), filtered and dried *in vacuo*. TLC analysis was used to verify conversion using bromocresol green stain. Yield: (89-94 %); TLC: R_f= 0.26 (3:17 MeOH:DCM) for mPEG350; ^{1}H NMR for mPEG350 (400 MHz, $CDCl_3$): δ 3.35 (s 3H), 3.4-3.8 (m 30H), 4.01 (s 2H), 10.1-12.2 (br 1H).

mPEG-aldehyde (6a-e). Albright-Goldman oxidation was used to oxidize terminal hydroxyl-moieties of mPEG to aldehyde groups. mPEG **1a-e** was dissolved in a mixture of dimethyl sulfoxide (DMSO) and acetic anhydride (Ac_2O) (5 mL of 3:2 DMSO:Ac_2O for every 1 mmol of alcohol). This solution is prepared beforehand at least 24 hours before reaction. The solution was stirred for 24 hours at ambient temperature. The solution was concentrated *in vacuo*. For mPEG < 2.0 kDa the oily residue was further dried *in vacuo*. For mPEG > 2.0 kDa, the oily residue was precipitated into cold diethyl ether (500-800 mL) 2-3 times, filtered and dried *in vacuo.* Yield: (89-94 %).

mPEG-amine (7a-e). An alternative synthesis of amine-terminal mPEG was developed utilizing reductive amination. mPEG-aldehyde **6a-e** (7.31 g), ammonium chloride (10.0 equiv.) and potassium hydroxide (3.3 equiv) were dissolved in anhydrous MeOH (25 mL). This solution was stirred for 30 min. A solution of sodium cyanoborohydride (10.0 equiv.) in anhydrous MeOH (10 mL) was added and the solution was stirred under argon at ambient temperature for 24 hours. The solution was poured into 100 mL of deionized water and extracted with DCM (100 mL) four times. The organic extracts were dried over anhydrous sodium sulfate and concentrated *in vacuo*. For mPEG < 2.0 kDa the oily residue was further dried *in vacuo*. For mPEG > 2.0 kDa, the oily residue was precipitated into cold diethyl ether (500-800 mL), filtered and dried *in vacuo.* Yield: (90-98 %); TLC: R_f= 0.04 (3:17 MeOH:DCM) for mPEG350.

mPEG350-NHS (8). Compound **5a** (274 mg, **0**.753 mmol), and NHS (217 mg, 1.885 mmol) were dissolved in 15 mL DCM and the resulting solution was cooled in an ice bath. EDC (173 mg, 0.902 mmol) was then added followed by DIEA (393 µL, 2.259 mmol), and the solution was stirred while slowly warming from 4 to 20 °C over 18 hours. Volatiles were removed under reduced pressure and the residue was dissolved in 50 mL DCM. The organic filtrate was washed with 50 mL H_2O twice before combining and extracting the aqueous phase with DCM (2 x20 mL). The combined organic phases were dried over anhydrous Na_2SO_4 before removing the solvent under reduced pressure and purifying the residue by flash chromatography on silica (3:17 MeOH:DCM). Yield: 230 mg (84.4 %); TLC: R_f= 0.66 (3:17 MeOH:DCM); ^{1}H NMR (400 MHz, $CDCl_3$): δ 2.65 (s 4H), 3.35 (s 3H), 3.4-3.8 (m 30H), 4.01 (s 2H).

mPEG350-DTPE (9a). Compound **3** (100 mg, 0.210 mmol) and DTPE (183 mg, 0.210 mmol) were dissolved in DMF (5 mL) in a 100 mL round bottom flask covered in aluminum foil. DIEA (37 μL) was added and the solution was stirred at 20 °C for 36 hours in the dark under N_2. The volatiles were removed under reduced pressure and the residue was purified by chromatography on silica (3:17 MeOH:DCM). Yield: 82 mg (31.1%); TLC: R_f= 0.29 (3:17 MeOH:DCM). ^{1}H NMR (400 MHz, $CDCl_3$): δ 0.88 (t 6H), 1.25-1.35 (m 44H), 1.49 (m 8H), 2.22 (m 8H), 2.53 (br 2H), 2.61 (br 2H), 3.36 (s 3H), 3.54-4.32 (m, 40H), 512 (br 1H), 7.64 (br 1H).

mPEG350-DSPE (9b). Compound **3** (100 mg, 0.210 mmol) and DSPE (157 mg, 0.210 mmol) were dissolved in chloroform (10 mL) in a 100 mL round bottom flask. DIEA (154 μL) was added and the solution was stirred at 20 °C for 36 hours under N_2. The volatiles were removed under reduced pressure and the residue was purified by chromatography on silica (3:17 MeOH:DCM). Yield: 173.2 mg (81.6%); TLC: R_f= 0.24 (3:17 MeOH:DCM). ^{1}H NMR (400 MHz, $CDCl_3$) δ 4.48 – 4.33 (m, 1H), 4.33 – 4.05 (m, 4H), 3.91 – 3.69 (m, 5H), 3.64 (s, 52H), 3.37 (s, 6H), 3.07 (s, 2H), 2.95 (s, 2H), 2.71 (d, *J* = 48.6 Hz, 7H), 2.33 (s, 1H), 1.24 (s, 22H), 0.87 (t, *J* = 15.3 Hz, 6H).

mPEG350-DPPE (9c). Compound **3** (61.0 mg, 0.13 mmol) and DPPE (100 mg, 0.14 mmol) were dissolved in chloroform (5 mL) in a 100 mL round bottom flask. DIEA (92 μL) was added and the solution was stirred at 20 °C for 36 hours under N_2. The volatiles were removed under reduced pressure and the residue was purified by chromatography on silica (3:17 MeOH:DCM). Yield: 108.8 mg (72.3 %); TLC: R_f= 0.21 (3:17

MeOH:DCM). ^{1}H NMR (400 MHz, $CDCl_3$) δ 5.20 (s, 1H), 4.36 (d, *J* = 13.7 Hz, 1H), 4.16 (s, 1H), 4.01 (s, 2H), 3.94 (s, 3H), 3.65 (d, *J* = 13.0 Hz, 18H), 3.54 (d, *J* = 5.8 Hz, 2H), 3.47 (s, 1H), 3.38 (d, *J* = 13.5 Hz, 3H), 2.86 (s, 1H), 2.27 (s, 3H), 1.56 (s, 4H), 1.23 (s, 40H), 0.86 (t, *J* = 6.5 Hz, 6H).

DTPE-PEG2K-biotin (11a). Biotin-PEG2K-NHS (**10**, 163 mg) and DTPE (52 mg) were combined in an oven-dried 100 mL round bottom flask equipped with a rubber septum and magnetic stir bar covered in aluminum foil. The solids were dissolve in 5 mL chloroform and 26 μL DIEA was added. The solution was stirred under nitrogen for 36 hours. The volatiles were removed under reduced pressure and the residue was purified by chromatography on silica (1:4 MeOH:DCM). Yield: 146 mg (75.3 %); TLC: R_f= 0.38 (1:4 MeOH:DCM). ^{1}H NMR (400 MHz, $CDCl_3$) δ 6.49 (s, 1H), 5.84 (s, 1H), 5.20 (s, 1H), 4.52 (s, 1H), 4.35 (s, 3H), 4.07 (d, *J* = 57.5 Hz, 11H), 3.63 (s, 343H), 3.10 (d, *J* = 32.1 Hz, 6H), 2.90 (d, *J* = 17.2 Hz, 3H), 2.82 – 2.55 (m, 4H), 2.52 – 2.03 (m, 19H), 1.68 (s, 12H), 1.57 – 1.08 (m, 91H), 0.87 (s, 6H).

DSPE-PEG2K-biotin (11b). Biotin-PEGK-NHS (**10**, 200 mg) and DSPE (66 mg) were combined in an oven-dried 100 mL round bottom flask equipped with a rubber septum and magnetic stir bar. The solids were dissolve in 10 mL chloroform and 34 μL DIEA was added. The solution was stirred under nitrogen for 36 hours. The volatiles were removed under reduced pressure and the residue was purified by chromatography on silica (1:4 MeOH:DCM). Yield: 150 mg (56.4 %); TLC: R_f= 0.43 (1:4 MeOH:DCM). ^{1}H NMR (400 MHz, $CDCl_3$) δ 6.59 (s, 1H), 6.13 (s, 1H), 5.46 (s, 1H), 5.28 (s, 4H), 5.16 (s, 1H), 4.56 – 4.43 (m, 1H), 4.41 – 4.24 (m, 2H), 4.11 (s, 2H), 3.97 (s, 5H), 3.62 (s,

207H), 3.13 (s, 1H), 2.99 (s, 2H), 2.93 – 2.81 (m, 1H), 2.81 – 2.57 (m, 1H), 2.36 – 2.06 (m, 6H), 1.79 – 1.61 (m, 4H), 1.60 – 1.50 (m, 4H), 1.41 (d, J = 6.9 Hz, 8H), 1.35 (d, J = 6.5 Hz, 5H), 1.23 (s, 55H), 0.96 – 0.73 (m, 6H).

tert-Butyl N^6-((benzyloxy)carbonyl)-L-lysinate (13). N^{ε}-((benzyloxy)carbonyl)-L-lysine (22.46 g, 80.11 mmol) was mixed with t-butyl acetate (270 mL) in a 500 mL round bottom flask and concentrated $HClO_4$ (10.0 mL) added to this mixture, producing a clear solution. This solution was stirred for 24 hours before extracting with 120 mL 5% HCl nine times. The aqueous extracts were combined and the pH was adjusted to about 12 via addition of 33 % NaOH solution. The aqueous solution was extracted with diethyl ether (4 x 240 mL). The ether extracts were combined and dried over anhydrous $MgSO_4$. The ether was then filtered and concentrated under reduced pressure and dried under a 50 μm vacuum overnight giving a colorless oil. Yield: 21.20 g (78.7 %). ^{1}H NMR (400 MHz, $CDCl_3$): δ 1.30 (s 9H), 1.23-1.50 (m 8H), 2.99 (t 2H), 3.11 (t (1H), 4.91 (s 2H), 5.61 (br 1H), 7.14-7.16 (m 5H). ^{13}C NMR (101 MHz, $CDCl_3$): δ 175.18, 156.34, 142.38, 136.60, 128.31, 127.88, 108.60, 80.74, 77.46, 77.14, 76.82, 66.29, 54.66, 40.66, 34.36, 31.08, 29.53, 27.90, 22.64.

Di-t-Butyl 2,2'-((6-(((benzyloxy)carbonyl)amino)-1-(t-butoxy)-1-oxohexan-2-yl)azanediyl)diacetate (14). *N*$^{\varepsilon}$-Benzyloxycarbonyl-L-lysine-t-butyl ester (**13**, 13.921 g, 41.38 mmol) was dissolved in DMF (80 mL) prior to the addition of t-butyl bromoacetate (18.34 mL, 24.21 g, 124.12 mmol) and DIEA (25.23 mL, 18.72 g, 144.85 mmol) by syringe. The solution was stirred under N_2 at 70 °C for 96 hours. The solvent was

evaporated under reduced pressure and the residue was extracted with 200 mL of ethyl acetate and filtered. The ethyl acetate extract was purified by flash chromatography on silica (4:1 hexane:EtOAc) to give **14** as a slightly yellow oil. Yield: 27.37 g (84.4 %); TLC: R_f = 0.18 (4:1 hexane:EtOAc); ^{1}H NMR ($CDCl_3$): δ 1.25-1.50 (m 6H), 1.30 (s 18H), 1.32 (s 9H), 3.04 (m 2H), 3.16 (t 1H), 3.33 (q 4H), 4.93 (s 2H), 5.39 (br 1H), 7.15-7.19 (m 5H). ^{13}C NMR (101 MHz, $CDCl_3$) δ 172.07, 170.41, 156.32, 136.69, 128.15, 127.79, 127.64, 80.70, 80.33, 77.54, 77.22, 76.90, 66.03, 64.91, 60.04, 53.62, 40.56, 29.93, 29.02, 27.97, 27.86, 27.73, 22.80, 20.71, 13.97.

Di-t-butyl 2,2'-((6-amino-1-(tert-butoxy)-1-oxohexan-2-yl)azanediyl)diacetate (15). Compound **14 (**9.84 g, 17.4 mmol) was dissolved in MeOH (90 mL) in a 500 mL round bottom flask. To this solution was added 40 mg of 10% Pd/C. The flask was evacuated and purged with H_2 three times and then stirred for 12 hours under 1 atm H_2. The heterogeneous solution was then filtered through a pad of Celite, with further washing of the Celite cake with 50 mL MeOH. The filtrate was concentrated under reduced pressure to give **15** as a clear oil. Yield: 7.52 g (99.7 %); TLC: R_f = 0.02 (4:1 hexane:EtOAc); ^{1}H NMR ($CDCl_3$): δ 1.29 (s 18H), 1.30 (s 9H) 1.1-1.5 (m 6H), 2.63 (t 2H), 3.16 (t 1H), 3.30 (q 4H), 3.96 (br 3H)^{13}C NMR (101 MHz, $CDCl_3$) δ 172.05, 170.46, 80.78, 80.42, 77.41, 77.09, 76.77, 64.94, 53.52, 49.54, 40.90, 31.09, 30.09, 27.95, 27.87, 22.91.

4-((5-(Bis(2-(tert-butoxy)-2-oxoethyl)amino)-6-(tert-butoxy)-6-oxohexyl)amino)-4-oxobutanoic acid (16). Compound **15** (1.00 g, 2.32 mmol) and succinic anhydride (0.418 g, 4.18 mmol) were combined in an oven-dried 250 mL round bottom flask equipped with a rubber septum and magnetic stir bar. The solids were dissolved in DCM (20 mL)

and TEA (1.62 mL, 11.61 mmol) was added. The reaction was stirred at ambient temperature for 18 hours. The solution was concentrated and dissolved in 50 mL ethyl acetate. This solution was washed with 5% HCl (30 mL) twice. The organic phase was concentrated and purified by flash chromatography using a gradient of 1:1 hexane ethyl acetate to 1:1 hexane ethyl acetate. The pure fractions were combined and dried *in vacuo* to give **16** as a colorless oil. Yield: 1.15 g (93.6 %); TLC: R_f = 0.28 (1:1 hexane:EtOAc). ^{1}H NMR (400 MHz, $CDCl_3$) δ 7.40 (d, *J* = 114.3 Hz, 2H), 6.96 (s, 1H), 3.46 – 3.24 (m, 6H), 3.23 – 2.97 (m, 3H), 2.54 (t, *J* = 6.4 Hz, 2H), 2.44 (d, *J* = 6.1 Hz, 2H), 1.79 – 1.46 (m, 3H), 1.34 (d, *J* = 6.2 Hz, 29H), 1.28 (d, *J* = 6.3 Hz, 3H).

Di-tert-butyl 2,2'-((1-(tert-butoxy)-1-oxo-6-(4-oxo-4-(prop-2-yn-1-ylamino)butanamido)hexan-2-yl)azanediyl)diacetate (17). Compound **16** (1.15 g, 2.17 mmol) and propargylamine (131 mg, 2.38 mmol) and HOBt (322 mg, 2.38 mmol) were combined in an oven-dried 250 mL round bottom flash equipped with a rubber septum and magnetic stir bar. The solids were dissolved in DMF (8 mL) and EDC (457 mg, 2.38 mmol) was added followed by DIEA (1.15 mL, 6.50 mmol). The reaction was stirred for 24 hours at ambient temperature. The solution was diluted with 90 mL DCM and washed with 5 % HCl (50 mL) twice. The organic phase was dried over anhydrous sodium sulfate and concentrated *in vacuo*. The residue was purified via flash chromatography using a gradient of 4:1 hexane:EtOAc to 1:1 hexane:EtOAc. Pure fractions were combined and dried *in vacuo* to give Compound **17** as a clear oil. Yield: 1.09 g (88.5 %); TLC: R_f = 0.35 (1:1 hexane:EtOAc). ^{1}H NMR (400 MHz, $CDCl_3$) δ 8.03 (s, 1H), 7.12 (d, *J* = 4.9

Hz, 1H), 3.48 – 3.26 (m, 5H), 3.26 – 3.06 (m, 3H), 2.94 (s, 1H), 2.52 (dd, *J* = 15.3, 10.9 Hz, 3H), 1.91 – 1.66 (m, 1H), 1.66 – 1.48 (m, 4H), 1.36 (d, *J* = 6.1 Hz, 34H).

2,2'-((5-(((Benzyloxy)carbonyl)amino)-1-carboxypentyl)azanediyl)diacetic acid (18). Compound **12** (10.00 g, 35.67 mmol) was dissolved in 1.5 M NaOH and cooled to 0 °C in an ice bath. Bromoacetic acid was also dissolved in 67 mL of 1.5 M NaOH and cooled to 0 °C in an ice bath. The bromoacetic acid solution was added to the solution of Compound **12** and the solution was allowed to warm to ambient temperature and stirred for an additional 24 hours. The solution was heated to 50 °C and stirred for 2 hours. The solution was cooled back to 0 °C and the pH was adjusted to 2-3 using conc. HCl. The precipitate was filtered and dried *in vacuo* to give Compound **18** as a white crystalline solid. Yield: 11.67 g (82.6 %). ^{1}H NMR (400 MHz, DMSO-*d*$_6$) δ 12.51 (s, 0H), 7.68 – 7.06 (m, 6H), 4.98 (s, 2H), 3.55 – 3.38 (m, 4H), 3.31 (t, *J* = 7.4 Hz, 1H), 2.94 (s, 2H), 2.53 – 2.40 (m, 0H), 1.58 (s, 1H), 1.52 (s, 1H), 1.46 – 1.30 (m, 3H), 1.25 (s, 1H). ^{13}C NMR (101 MHz, DMSO) δ 190.15, 174.86, 174.14, 156.95, 138.18, 129.22, 128.60, 76.17, 65.99, 65.20, 54.27, 40.56, 40.35, 40.14, 30.20, 23.88.

2,2'-((5-Amino-1-carboxypentyl)azanediyl)diacetic acid (19). Compound **18** (2.90 g, 2.27 mmol) was dissolved in deionized water (50 mL) and 10 mL 1.5 M NaOH was added to dissolve the material in an oven-dried 250 mL round bottom flask. Palladium on carbon was added and the flask was equipped with a three-way adapter and a hydrogen balloon. The flask was evacuated and purged with hydrogen. The reaction was stirred vigorously under 1 atm hydrogen for 12 hours. The heterogeneous solution was filtered through Celite to remove catalyst and the pH was adjusted to 2 via addition of conc. HCl

and the white precipitate was concentrated using a rotary evaporator and isolated via filtration. Compound **19** was obtained as a white crystalline solid. Yield: 1.92 g (96.9 %). ^{1}H NMR (400 MHz, D_2O) δ 3.21 – 2.91 (m, 1H), 2.85 (t, *J* = 6.9 Hz, 0H), 2.45 (t, *J* = 7.0 Hz, 0H), 1.43 (q, *J* = 7.4 Hz, 0H), 1.39 – 1.23 (m, 0H), 1.23 – 0.97 (m, 0H).

Z-Lys-tris-NTA-OtBu (20). Compounds **15** (15.531 g, 36.07 mmol), **18** (2.67 g, 7.23 mmol) and HOBt (4.38 g, 32.46 mmol) were added to an oven-dried 250 mL round bottom flask equipped with a rubber septum and a magnetic stir bar. The contents were dissolved in DMF (240 mL) and cooled down to 0 °C in an ice bath. EDC (8.30 g, 43.29 mmol) was added followed by DIEA (12.57 mL, 72.14 mmol) and the solution was allowed to warm to ambient temperature and stirred for 72 hours. The solution was diluted with EtOAc and filtered then concentrated and purified via flash chromatography using 5:95 MeOH:DCM giving Compound **20** as a yellow oil. Yield: 2.57 g (88.4 %); TLC: R_f = 0.40 (5:95 MeOH:DCM). ^{1}H NMR (500 MHz, $CDCl_3$) δ 7.47 (d, *J* = 18.4 Hz, 3H), 7.32 – 7.15 (m, 5H), 5.24 (s, 1H), 4.98 (s, 2H), 3.44 – 3.32 (m, 11H), 3.30 (d, *J* = 5.0 Hz, 2H), 3.27 (d, *J* = 4.5 Hz, 2H), 3.23 – 3.01 (m, 13H), 2.97 (d, *J* = 6.9 Hz, 1H), 1.73 (s, 1H), 1.63 – 1.50 (m, 7H), 1.50 – 1.40 (m, 13H), 1.40 – 1.11 (m, 99H). ^{13}C NMR (126 MHz, $CDCl_3$) δ 172.20, 172.15, 171.42, 170.65, 170.62, 170.10, 156.44, 136.70, 128.36, 127.89, 81.00, 80.64, 77.43, 76.92, 66.29, 64.94, 57.97, 56.19, 53.70, 41.86, 40.49, 39.16, 30.13, 29.87, 29.48, 29.18, 28.62, 28.06, 24.34, 24.13, 23.28, 23.00.

H_2N-Lys-tris-NTA-OtBu (21). Compound **20 (**0.420 g, 0.26 mmol) was dissolved in MeOH (50 mL) in a 250 mL round bottom flask. To this solution was added 10% Pd/C. The flask was evacuated and purged with H_2 three times and then stirred for 12 hours

under 1 atm H_2. The heterogeneous solution was then filtered through a pad of Celite, with further washing of the Celite cake with 50 mL MeOH. The filtrate was concentrated under reduced pressure to give **21** as a clear yellow oil. Yield: 0.380 g (97.6 %); TLC: R_f = 0.03 (EtOAc).

HO_2C-Lys-tris-NTA-OtBu (22). Compound **21** and succinic anhydride were combined in an oven dried 50mL round bottom flask equipped with a rubber septum and a magnetic stir bar. DCM (5 mL) was added and TEA (37 µL) was added via syringe. The solution was stirred for 18 hours at ambient temperature. The contents were concentrated and purified via flash chromatography using 5:95 MeOH:DCM as eluent to give Compound **22** as a slightly yellow oil. Yield: 0.146 g (87.4 %); TLC: R_f = 0.39 (5:95 MeOH:DCM). ^{1}H NMR (400 MHz, $CDCl_3$) δ 3.42 (s, 1H), 3.24 (d, *J* = 15.3 Hz, 1H), 1.51 (d, *J* = 10.5 Hz, 4H), 1.44 (d, *J* = 6.4 Hz, 21H).

Alkyne-Lys-tris-NTA-OtBu (23). Compound **22** (139 mg, 0.09 mmol), HOBt (58.6 mg, 0.43 mmol), and propargylamine (56 µL, 0.87 mmol) were combined in an oven dried 50 mL round bottom flask equipped with a magnetic stir bar and rubber septum. DCM (5mL) was added and the solution was cooled to 0 °C in an ice bath. EDC (83 mg, 0.43 mmol) was added followed by DIEA (77µL, 0.43 mmol) and the solution was allowed to warm to ambient temperature and stirred for 24 hours. The contents were concentrated and purified via flash chromatography using 5:95 MeOH:DCM as eluent to give Compound **22** as a slightly yellow oil. Yield: 0. g (76.4 %); TLC: R_f = 0.32 (5:95 MeOH:DCM). ^{1}H NMR (400 MHz, $CDCl_3$) δ 8.13 (d, *J* = 12.8 Hz, 1H), 7.65 (s, 1H), 7.56 (s, 1H), 7.36 – 7.04 (m, 3H), 4.14 – 3.86 (m, 2H), 3.60 (d, *J* = 3.5 Hz, 2H), 3.60 –

3.33 (m, 17H), 3.33 – 2.98 (m, 18H), 2.84 (s, 4H), 2.49 (s, 2H), 2.37 – 2.09 (m, 3H), 1.96 (s, 2H), 1.87 – 0.98 (m, 150H), 0.96 – 0.60 (m, 6H).

Di-tert-butyl-2,2'-((1-(tert-butoxy)-6-(((4-nitrophenoxy)carbonyl)amino)-1-oxohexan-2-yl)azanediyl)diacetate (24). p-Nitrophenyl chloroformate (PNP-Cl, 0.552 g, 2.74 mmol) was dissolved into 20 mL DCM in a 100 mL round bottom flask equipped with a stir bar and addition funnel and was cooled to 4 °C in an ice bath. Compound **15** (0.983 g, 2.28 mmol) in 20 mL DCM was added to the addition funnel. The system was evacuated and flashed with nitrogen gas. The solution of **15** was added over a one hour period at 4 °C and stirred for an additional 12 hours warming to room temperature. The solution was concentrated in vacuo and purified by flash chromatography using 4:1 hexane:EtOAc as eluent. Yield: 0.609 g (44.8 %).; TLC: R_f= 0.24 (4:1 hexanes:EtOAc); ^{1}H NMR ($CDCl_3$): δ 1.38 (s 18H), 1.40 (s 9H), 1.18-1.59 (m 6H), 3.18-3.29 (m 3H), 3.40 (q 4H), 6.09 (br 1H), 7.24 (d 2H, J = 9 Hz), 8.14 (d 2H, J = 9 Hz); MS (ESI+). Expected: 596.68 [M+H]; Found 596.59 ([M+H], 618.54 [M+Na].

PNP-tris-NTA-OtBu (25). PNP-Cl (0.060 g, 0.30 mmol) was dissolved into 15 mL DCM in a 100 mL round bottom flask equipped with a stir bar and addition funnel and was cooled to 4 °C in an ice bath. Compound **21** (0.372 g, 0.25 mmol) in 10 mL DCM was added to the addition funnel. The system was evacuated and flashed with nitrogen gas. The solution of **21** was added over a one-hour period at 4 °C and stirred for an additional 12 hours warming to room temperature. The solution was concentrated in vacuo and purified by flash chromatography using EtOAc as eluent. Yield: 0.302 g (73.1 %).; TLC: R_f= 0.31 (EtOAc); ^{1}H NMR ($CDCl_3$): δ 1.35 (s 54H), 1.38 (s 27H), 110-1.68

(m 18H), 3.09-3.37 (m 9H), 3.42 (q 12H), 6.14 (br 3H), 7.24 (d 2H, J = 9 Hz), 8.13 (d 2H, J = 9 Hz); MS (ESI+). Expected: 1665.01 [M+H]; Found 1666.45 ([M+2H], 1667.44 ([M+3H]), 1689.39 [M+Na].

NHBoc-PEG2000-DTPE (27). NHS-PEG2K-NHBoc (**26**, 190 mg, 0.095 mmol) and DTPE (82.8 mg, 0.095 mmol) were dissolved in DCM (10 mL) in a 25 mL round bottom flask with stir bar. DIEA (83 μL, 0.474 mmol) was added and the flask was evacuated, flushed with nitrogen and covered with aluminum foil. The solution was stirred at ambient temperature for 48 hours in the dark. Volatiles were evaporated and purified by flash chromatography on silica using an eluting system of DCM and MeOH starting with 95:5 then 90:10 then 85:15. Fractions containing product were combined and dried in vacuo to give **27**. Yield: 0.209 g (87.8 %).; TLC: R_f= 0.72 (80:20 DCM:MeOH); ^{1}H NMR ($CDCl_3$): δ 0.88 (m 6H), 1.23-1.49 (m 50H), 1.42 (s 9H), 2.21 (m 8H), 2.66 (t 4H), 3.26-3.96 (m 180 H), 4.11-4.12 (m 2H), 4.33-4.36 (m 2H), 5.17 (br 1H).

NH_2-PEG2000-DTPE (28). Compound **27** (209 mg, 0.076 mmol) and triethylsilane (200 μL, 1.25 mmol) was dissolved in 30 % TFA in DCM solution (20 mL) and stirred for 1.5 hours under ambient temperature and atmosphere. Volatiles were removed *in vacuo* and the residue was evaporated with 15 mL DCM twice more. The product was dried *in vacuo* and used without further purification. Yield: 0.191 g (91.3 %).; TLC: R_f= 0.56 (80:20 DCM:MeOH).

NTA-(OtBu)3-PEG2000-DTPE (29). Compound **28** (95.5 mg, 0.034 mmol) and Compound **24** (205 mg, 0.344 mmol) were dissolved in DCM (5 mL) in a 25 mL round

bottom flask with stir bar covered in aluminum foil. The flask was evacuated and flushed with nitrogen. DIEA (60 μL, 0.348 mmol) was added and the solution stirred for 48 hours at ambient temperature under a nitrogen atmosphere in the dark. Volatiles were evaporated under reduced pressure and the product was purified by flash chromatography on silica using a gradient of DCM:MeOH as eluent starting with 90:10 moving to 85:15 then finally 80:20. Fractions containing product were pooled, concentrated and dried *in vacuo* to give Compound **29**. Yield: 29.0 mg (26.9 %).; TLC: R_f= 0.65 (80:20 DCM:MeOH).

NTA-PEG2000-DTPE (30). Compound **29** (29 mg, 0.009 mmol) and triethylsilane (100 μL, 0.625 mmol) were dissolved in 30% TFA in DCM solution (10 mL) in a 25 mL round bottom flask with stir bar covered in aluminum foil. The solution was stirred under ambient temperature and atmosphere for 1.5 hours in the dark. Volatiles were evaporated and the residue was dissolved in 5mL PBS buffer (pH = 7.2) plus 5 mL MeOH. The solution was extracted with $CHCl_3$ (3x8 mL). The organic extracts were dried over anhydrous Na_2SO_4, filtered, concentrated and dried *in vacuo* to give Compound **30**. Yield: 18.0 mg (62.1 %).; TLC: R_f= 0.01 (80:20 DCM:MeOH).

***S*-Trityl-3-mercaptopropionic acid (32).** 3-Mercaptopropionic acid (**31**, 6.00 g, 56.5 mmol) was dissolved in DCM (50 mL) in a 250 mL round bottom flask. Trityl chloride (17.34 g, 62.2 mmol) in DCM (30 mL) was added dropwise to this solution over 1 hour before stirring for an additional 12 h. The white precipitate was filtered and washed with diethyl ether (2 x 50 mL) and dried under a 50 μm vacuum to give a fine white powder.

Yield: 18.25 g (93%); ^{1}H NMR (400 MHz, $CDCl_3$): δ 2.25 (t, 2H, J = 8 Hz), 2.47 (t, 2H, J = 8 Hz), 7.2-7.3 (m, 9H), 7.43 (d, 6H).

Di-t-butyl 2,2'-((1-(t-butoxy)-1-oxo-6-(3-(tritylthio)propanamido)hexan-2-yl)azanediyl)diacetate (33). Compound **32** (1.46 g, 4.19 mmol) and Compound **15** (1.80 g, 4.19 mmol) were dissolved in DMF (100 mL) in a 250 mL round bottom flask. This solution was cooled on an ice bath before addition of EDC (0.962 g, 5.02 mmol), HOBt (0.678 g, 5.02 mmol), and 1.86 mL of DIEA (1.35 g, 10.4 mmol). The solution was stirred under Ar for 48 hours while allowing the mixture to gradually warm from 4 → 20 °C. The DMF was evaporated under reduced pressure and the residue was dissolved in EtOAc (80 mL). This solution was washed with H_2O (2 x 100 mL) before combining the aqueous phases and back extracting with EtOAc (100 mL). The EtOAc layers were combined and dried over anhydrous Na_2SO_4. The solvent was evaporated and the residue purified by flash chromatography on silica using 1:1 hexane:EtOAc as eluent yielding **33** as a colorless oil. Yield: 1.70 g (53.4 %).; TLC: R_f= 0.54 (1:1 hexane:EtOAc); ^{1}H NMR ($CDCl_3$): δ 1.22-1.61 (m 6H), 1.39 (s 18H), 1.43 (s 9H), 2.09 (t 2H), 2.46 (t 2H), 3.11 (m 2H), 3.25 (t 1H), 3.43 (m 4H), 5.98 (br 1H), 7.14-7.4 (m 15H). ^{13}C NMR (126 MHz, $CDCl_3$) δ 172.39, 170.92, 170.73, 144.77, 129.59, 127.88, 126.61, 81.10, 80.73, 77.39, 77.14, 76.88, 66.66, 64.92, 53.91, 39.19, 35.36, 29.83, 28.41, 28.23, 28.16, 27.77, 22.89.; MS (ESI+). Expected: 762.02 [M+H]; Found 762.71.

2,2'-((1-Carboxy-5-(3-mercaptopropanamido)pentyl)azanediyl)diacetic acid (34). Compound **33** (0.800 g, 1.05 mmol) was dissolved in DCM (10 mL), followed by addition of Et_3SiH (0.367 g, 3.16 mmol) and 2-mercaptoethanol (.246 g, 3.15 mmol). This solution was cooled on an ice bath before addition of TFA (15 mL) dropwise over 10 min. The solution was stirred for 1 h at 4 °C before removal of the volatiles under reduced pressure. Diethyl ether (20 mL) and 4 drops of concentrated HCl were added to the residue before decanting the organic phase and repeating the process two more times. Toluene (30 mL) was then added to the residue and evaporated under reduced pressure three times to give Compound **34** as a white powder. Yield: 0.327 g (92.7 %); ^{1}H NMR (500 MHz, DMSO-d6) δ 3.50 (q, J = 16.6, 15.4 Hz, 4H), 3.34 (d, J = 7.3 Hz, 1H), 2.99 (s, 2H), 2.92 – 2.76 (m, 1H), 2.70 – 2.55 (m, 2H), 2.47 (d, J = 13.4 Hz, 2H), 2.33 (d, J = 7.1 Hz, 1H), 2.27 – 2.06 (m, 1H), 1.70 – 1.45 (m, 2H), 1.36 (s, 3H), 1.23 (d, J = 15.3 Hz, 3H), 1.13 (t, J = 17.8 Hz, 1H). 13C NMR (126 MHz, DMSO) δ 174.15, 173.35, 170.40, 64.75, 53.73, 40.28, 39.95, 39.61, 38.74, 31.17, 29.56, 29.25, 23.54, 20.44.

2,2'-((1-Carboxy-2-(tritylthio)ethyl)azanediyl)diacetic acid (36). H-Cys(Trt)-OH (1.00 g, 4.73 mmol) was dissolved in 30 mL 1.5 KOH in MeOH in a 100 mL round bottom flask. Bromoacetic acid (2.760 g, 19.86 mmol) was dissolved in 10 mL 1.5 M KOH in MeOH and 10 mL deionized water. The two separate solutions were cooled to 0 °C in an ice bath and the bromoacetic acid solution wat added to the solution of H-Cys(Trt)-OH and the solution was stirred at ambient temperature for 48 hours under argon. The solution was stirred at 50 °C for 3 hours. The solution was concentrated *in vacuo* and precipitated via the addition of conc. HCl. The precipitate was filtered and recrystallized

from acidic water. Yield:2.27 g (82.0 %); ^{1}H NMR (500 MHz, DMSO-d6) δ 7.30 (d, J = 3.7 Hz, 12H), 7.28 – 7.00 (m, 4H), 3.32 – 3.09 (m, 4H), 2.87 (t, J = 7.5 Hz, 1H), 2.82 (s, 0H), 2.55 (dd, J = 13.0, 6.9 Hz, 1H), 2.51 – 2.45 (m, 1H), 2.32 (dd, J = 13.0, 8.1 Hz, 1H). 13C NMR (126 MHz, DMSO) δ 173.88, 173.15, 144.96, 129.63, 128.47, 127.14, 66.61, 65.93, 54.40, 40.46, 40.13, 39.96, 39.46, 32.73.

Trt-Cys-tris-NTA-OtBu (37). Compound **36** (0.511 g, 1.07 mmol), Compound **15** (2.295 g, 5.33 mmol) and HOBt (0.735 g, 4.80 mmol) were combined in an oven-dried 100 mL round bottom flask equipped with a magnetic stir bar and rubber septum. The contents were dissolved in 25 mL DMF and cooled to 0 °C in an ice bath. EDC (1.226 g, 6.40 mmol) followed by DIEA (1.857 mL, 10.66 mmol) were added and the solution was allowed to warm to room temperature and stir for 36 hours at ambient temperature. The solution was concentrated *in vacuo* and the residue was purified by flash chromatography using a gradient of 1:1 hexane:EtOAc to 3:7 hexane:EtOAc to give Compound **37** as a slightly yellow oil. Yield: 1.392 g (76.1 %).; TLC: R_f= 0.42 (1:1 hexane:EtOAc); ^{1}H NMR (500 MHz, $CDCl_3$) δ 7.32 (d, *J* = 8.1 Hz, 6H), 7.19 (t, *J* = 7.6 Hz, 7H), 7.13 (t, *J* = 7.3 Hz, 3H), 3.45 – 3.29 (m, 13H), 3.25 – 3.15 (m, 6H), 1.55 (d, *J* = 6.8 Hz, 8H), 1.48 – 1.26 (m, 96H). 13C NMR (126 MHz, CDCl3) δ 172.22, 171.14, 170.62, 170.55, 144.47, 127.90, 126.71, 81.03, 80.66, 80.48, 77.42, 77.17, 76.91, 67.24, 65.85, 65.30, 64.95, 55.69, 53.67, 53.56, 39.36, 39.19, 34.62, 31.57, 31.45, 30.35, 29.88, 29.43, 28.17, 28.08, 23.49, 23.06.

11-(2-((5-(Bis(carboxymethyl)amino)-5-carboxypentyl)amino)-2-oxoethyl)-2,20-bis(carboxymethyl)-10-(mercaptomethyl)-9,13-dioxo-2,8,11,14,20-pentaazahenicosane-1,3,19,21-tetracarboxylic acid (38). Compound **37** (1.392 g, 0.81 mmol) was dissolved in DCM (20 mL) and triethylsilane (1.94 mL, 12.16 mmol) was added. TFA (20 mL) was added and the solution was stirred at ambient temperature for 1.5 hours under a stream of nitrogen. Volatiles were removed *in vacuo*. DCM (80 mL) was added and evaporated *in vacuo* to remove excess TFA. The residue was trituriated with diethyl ether to remove triphenylmethyl by-products. The residue was suspended in deionized water and lyophilized to give Compound **38** as a white powder. Yield: 0.725 g (92.2 %).; ^{1}H NMR (500 MHz, DMSO-d_6) δ 3.63 – 3.41 (m, 12H), 3.36 (dt, J = 13.0, 6.5 Hz, 5H), 3.29 – 3.15 (m, 3H), 3.15 – 2.94 (m, 6H), 2.77 – 2.61 (m, 1H), 1.71 – 1.57 (m, 3H), 1.52 (d, J = 8.4 Hz, 4H), 1.47 – 1.31 (m, 11H), 1.30 – 1.16 (m, 4H). ^{13}C NMR (126 MHz, DMSO) δ 174.14, 173.38, 65.37, 64.81, 55.83, 53.76, 40.47, 40.30, 40.13, 39.97, 39.80, 39.63, 39.46, 38.87, 29.58, 29.26, 28.20, 23.59, 15.63.

Maleimide-PEG-DSPE (40a). DSPE (0.072 g, 0.096 mmol) and NHS-PEG2K-maleimide (**39a**, 0.200 g, 0.095 mmol) were dissolved in $CHCl_3$ (15 mL) in a 50 mL round bottom flask with stir bar and DIEA (0.062g, 0.480) mmol was added via syringe. The flask was evacuated and flushed with nitrogen and stirred for 72 hours at ambient temperature. The volatiles were evaporated under reduced pressure and the residue purified by flash chromatography on silica using a gradient starting with 85:15 DCM:MeOH and increasing in polarity to 80:20 DCM:MeOH. Yield: 0.118 g (43.4 %).; TLC: R_f= 0.48 (4:1 DCM:MeOH); ^{1}H NMR ($CDCl_3$): δ 0.84 (t 6H), 1.15-1.40 (m 64H),

2.24 (m 4H), 2.48 (t 2H) 2.99 (m 2H), 3.37-4.10 (m 180 H), 3.80-3.96 (m 4H), 4.12 (m 2H), 4.34 (d 2H), 5.17 (m 1H), 6.27 (br 1H), 6.67 (s 1H), 7.38 (br 1H).

Maleimide-PEG-DSPE (40b). DSPE (0.094 g, 0.13 mmol) and NHS-PEG3.4K-maleimide (**39b**, 0.400 g, 0.12 mmol) were dissolved in $CHCl_3$ (10 mL) in a 50 mL round bottom flask with stir bar and DIEA (0.074 g, 0.57 mmol) was added via syringe. The flask was evacuated and flushed with nitrogen and stirred for 72 hours at ambient temperature. The volatiles were evaporated under reduced pressure and the residue purified by flash chromatography on silica using a gradient starting with 85:15 DCM:MeOH and increasing in polarity to 80:20 DCM:MeOH. Yield: 0.146 g (30.1 %).; TLC: R_f= 0.49 (4:1 DCM:MeOH); ^{1}H NMR (400 MHz, $CDCl_3$) δ 4.00 – 3.87 (m, 1H), 3.61 (s, 25H), 3.52 – 3.45 (m, 1H), 2.34 – 2.16 (m, 1H), 1.61 – 1.48 (m, 1H), 1.39 (d, J = 6.9 Hz, 1H), 1.33 (d, J = 6.6 Hz, 1H), 1.21 (s, 9H), 0.84 (t, J = 6.8 Hz, 1H).

NTA-PEG2K-DSPE (41a). Compounds **40a** (20.0 mg, 0.007 mmol) and **34** (18.0 mg, 0.051 mmol) were dissolved in DMF (4 mL) in a 25 mL round bottom flask with stir bar. TEA (15.0 µL, 0.119 mmol) was added and the flask was evacuated and flushed with nitrogen. The solution was stirred at 40 °C for 24 hours monitoring the consumption of starting material by TLC. Volatiles were removed *in vacuo* at 45 °C and the residue was dissolved in 6 mL PBS buffer (pH = 7.2) plus 4 mL MeOH. This solution was extracted with $CHCl_3$ (3x15 mL). The organic extracts were combined and dried over anhydrous Na_2SO_4, filtered and concentrated *in vacuo* to give **41a**. Yield: 21.2 mg (a: 89.8 %; b: 53.3 %).; TLC: R_f= 0.0 (4:1 DCM:MeOH); ^{1}H NMR ($CDCl_3$): δ 0.84 (t 6H), 1.15-1.40 (m 64H), 2.25 (s 4H), 2.28-2.32 (m 2H), 2.48-2.53 (m 2H), 2.75-2.78 (m 4H), 2.48-3.7

(m 180H), 3.70 (s 4H), 3.88 (br 2H), 4.00 (br 2H), 4.16 (br 2H), 4.37-4.40 (br 1H), 5.30 (s 1H), 6.96 (s 1H).

NTA-PEG3.4K-DSPE (41b). Compounds **40b** (49.0 mg, 0.01 mmol) and **34** (21.0 mg, 0.05 mmol) were dissolved in DMF (5 mL) in a 25 mL round bottom flask with a stir bar. TEA (16.4 μL, 0.09 mmol) was added and the flask was evacuated and flushed with nitrogen. The solution was stirred at 40 °C for 24 hours monitoring the consumption of starting material by TLC. Volatiles were removed *in vacuo* at 45 °C. the residue was dissolved in 6 mL PBS buffer (pH = 7.2) plus 4 mL MeOH. This solution was extracted with $CHCl_3$ (3x15 mL). The organic extracts were combined and dried over anhydrous Na_2SO_4, filtered and concentrated *in vacuo* to give **41b**. Yield: 28.6 mg (53.3 %); ^1H NMR (500 MHz, $CDCl_3$) δ 7.26 (s, 1H), 4.02 (d, J = 12.0 Hz, 1H), 3.82 – 3.74 (m, 1H), 3.63 (s, 55H), 3.54 – 3.46 (m, 1H), 2.50 (d, J = 29.9 Hz, 1H), 2.30 (d, J = 7.9 Hz, 1H), 2.24 (s, 1H), 1.70 – 1.65 (m, 1H), 1.59 (s, 3H), 1.43 (s, 2H), 1.37 (s, 3H), 1.24 (s, 18H), 0.87 (s, 6H).

NHS-PEG2K-MAL-2/5-dimethylfuran adduct (42). NHS-PEG2K-maleimide (0.200 g, 0.10 mmol) was added to an oven-dried 50 mL round bottom flask equipped with a magnetic stir bar and rubber septum. The solid material was dissolved in toluene (10 mL) and 2.5 dimethylfuran (2.50 mL g, 23.14 mmol) was added. The solution was heated to 40 °C and stirred under nitrogen for 12 hours. The solution was concentrated, precipitated into 200 mL diethyl ether and filtered to give Compound **42** as a white powder. Yield: 151.7 mg (98.2 %); 1H NMR (400 MHz, $CDCl_3$) δ 6.23 (s, 1H), 6.10 (s, 1H), 4.43 (s,

2H), 3.55 (s, 182H), 3.37 (s, 2H), 3.30 (s, 1H), 3.12 (s, 1H), 2.78 (s, 4H), 2.73 (s, 4H), 2.29 (s, 2H), 2.20 (d, J = 8.2 Hz, 1H), 2.10 (s, 1H), 1.68 (s, 3H), 1.59 (s, 2H).

DSPE-PEG2K-MAL-2/5-dimethylfuran adduct (43). Compound **42** (0.200 g, 0.10 mmol) and DSPE (0.079 g, 0.11 mmol) were dissolved in chloroform (5 mL) in an oven-dried 50 mL round bottom flask equipped with magnetic stir bar and rubber septum. DIEA (95 μL, 0.53 mmol) was added and the solution was stirred for 72 hours at ambient temperature. The volatiles were evaporated under reduced pressure and the residue purified by flash chromatography on silica using a gradient starting with 85:15 DCM:MeOH and increasing in polarity to 80:20 DCM:MeOH. Yield: 0.182 g (75.8 %).; TLC: R_f= 0.17 (95:5 DCM:MeOH); ^{1}H NMR (400 MHz, $CDCl_3$) δ 4.12 (dd, *J* = 11.9, 6.7 Hz, 1H), 3.98 – 3.87 (m, 5H), 3.79 (dd, *J* = 8.5, 5.0 Hz, 1H), 3.61 (s, 182H), 3.46 – 3.42 (m, 2H), 3.38 (q, *J* = 5.8 Hz, 3H), 3.18 (s, 1H), 3.00 (s, 2H), 2.78 (s, 1H), 2.62 (s, 1H), 2.29 – 2.16 (m, 4H), 1.74 (s, 1H), 1.65 (s, 1H), 1.54 (q, *J* = 9.3, 8.0 Hz, 4H), 1.39 (d, *J* = 7.3 Hz, 7H), 1.33 (d, *J* = 6.7 Hz, 7H), 1.21 (s, 61H), 0.84 (t, *J* = 6.8 Hz, 6H).

DSPE-PEG2K-MAL (44). Compound **43** was dissolved in toluene (20 mL) and heated at 80 °C for 12 hours under argon. The solution was concentrated *in vacuo* and redissolved in DCM (40 mL). This solution was filtered through a pad a Celite and activated carbon. The product **44** was precipitated into diethyl ether (200 mL), filtered and dried *in vacuo*. Yield: 0.112 g (61.5 %).; TLC: R_f= 0.69 (4:1 DCM:MeOH); ^{1}H NMR (400 MHz, $CDCl_3$) δ 7.40 (s, 1H), 7.26 (s, 2H), 6.68 (s, 1H), 6.33 (s, 1H), 5.20 (s, 1H), 4.35 (d, J = 10.8 Hz, 1H), 4.18 – 4.09 (m, 1H), 3.97 (s, 4H), 3.80 (d, J = 7.5 Hz, 2H), 3.61 (s, 182H), 3.44 (s, 2H), 3.38 (s, 3H), 3.00 (s, 2H), 2.58 – 2.43 (m, 2H), 2.24 (s, 3H), 1.55

(s, 4H), 1.42 (t, J = 7.8 Hz, 7H), 1.35 (d, J = 6.6 Hz, 7H), 1.22 (s, 48H), 0.85 (t, J = 6.6 Hz, 6H).

Tris-NTA-PEG2000-DSPE (45a). Compounds **40a** (20.0 mg, 0.01 mmol) and **38** (48.0 mg, 0.05 mmol) were dissolved in DMF (5 mL) in a 25 mL round bottom flask with a stir bar. TEA (35 μL, 0.22 mmol) was added and the flask was evacuated and flushed with nitrogen. The solution was stirred at 40 °C for 24 hours monitoring the consumption of starting material by TLC. Volatiles were removed *in vacuo* at 45 °C. the residue was dissolved in 6 mL PBS buffer (pH = 7.2) plus 4 mL MeOH. This solution was extracted with $CHCl_3$ (3x15 mL). The organic extracts were combined and dried over anhydrous Na_2SO_4, filtered and concentrated *in vacuo* to give **45a**. Yield: 23.6 mg (87.8 %); ^1H NMR (400 MHz, $CDCl_3$) δ 6.95 (s, 2H), 5.30 (s, 1H), 5.22 (t, J = 5.6 Hz, 1H), 4.12 (s, 1H), 4.00 (s, 3H), 3.87 (s, 2H), 3.82 (d, J = 6.8 Hz, 3H), 3.64 (s, 182H), 3.49 – 3.43 (m, 4H), 3.40 (s, 3H), 3.08 (s, 7H), 2.98 – 2.87 (m, 6H), 2.81 – 2.72 (m, 8H), 2.52 (d, J = 6.8 Hz, 4H), 2.36 – 2.26 (m, 6H), 2.24 (s, 5H), 1.88 (s, 2H), 1.65 – 1.48 (m, 11H), 1.46 – 1.40 (m, 3H), 1.29 (d, J = 32.8 Hz, 81H), 0.86 (d, J = 7.1 Hz, 16H).

Tris-NTA-PEG3.4K-DSPE (45b). Compounds **40b** (49.0 mg, 0.01 mmol) and **38** (57.0 mg, 0.06 mmol) were dissolved in DMF (5 mL) in a 25 mL round bottom flask with stir bar. DIEA (16.4 μL, 0.09 mmol) was added and the flask was evacuated and flushed with nitrogen. The solution was stirred at 40 °C for 24 hours monitoring the consumption of starting material by TLC. Volatiles were removed *in vacuo* at 45 °C and the residue was dissolved in 6 mL PBS buffer (pH = 7.2) plus 4 mL MeOH. This solution was extracted with $CHCl_3$ (3x15 mL). The organic extracts were combined and dried over anhydrous

Na_2SO_4, filtered and concentrated *in vacuo* to give **45b**. Yield: 24.3 mg (40.2 %); ^{1}H NMR (500 MHz, $CDCl_3$) δ 6.93 (s, 4H), 5.36 (dt, *J* = 10.7, 5.2 Hz, 1H), 5.21 (t, *J* = 5.2 Hz, 1H), 4.35 (d, *J* = 11.8 Hz, 1H), 4.15 (dd, *J* = 11.3, 7.0 Hz, 2H), 4.09 – 3.94 (m, 6H), 3.87 (s, 3H), 3.83 – 3.77 (m, 3H), 3.64 (s, 309H), 2.71 (s, 1H), 2.49 (s, 4H), 2.29 (d, *J* = 7.5 Hz, 9H), 2.24 (s, 7H), 1.88 (s, 3H), 1.59 (s, 20H), 1.51 – 1.43 (m, 13H), 1.37 (s, 35H), 1.25 (s, 146H), 0.90 – 0.80 (m, 50H).

Glutathione-NTA-PEG2K-DSPE (46). Compound **40b** (20.0 mg, 0.01 mmol) and L-glutathione (15.4 mg, 0.05 mmol) were dissolved in DMF (5 mL) in a 25 mL round bottom flask with a stir bar. DIEA (16.4 μL, 0.09 mmol) was added and the flask was evacuated and flushed with nitrogen. The solution was stirred at 40 °C for 24 hours monitoring the consumption of starting material by TLC. Volatiles were removed *in vacuo* at 45 °C and the residue was dissolved in 6 mL PBS buffer (pH = 7.2) plus 4 mL MeOH. This solution was extracted with $CHCl_3$ (3x15 mL). The organic extracts were combined and dried over anhydrous Na_2SO_4, filtered and concentrated *in vacuo* to give Compound **46**. Yield: 20.3 mg (93.1 %); ^{1}H NMR (400 MHz, $CDCl_3$) δ 7.41 (d, J = 8.8 Hz, 2H), 7.19 (d, J = 6.9 Hz, 1H), 6.95 (s, 1H), 5.20 (s, 1H), 4.20 – 4.08 (m, 1H), 4.00 (d, J = 5.7 Hz, 5H), 3.64 (s, 182H), 3.05 (s, 1H), 2.50 (s, 3H), 2.36 – 2.16 (m, 6H), 1.71 – 1.50 (m, 9H), 1.31 (d, J = 50.7 Hz, 81H), 1.02 – 0.63 (m, 31H).

2.7.2 Cell Lysate Preparation

The ASKA library, a complete *E. coli* K-12 ORF archive in which over 4000 bacterial proteins have been cloned into pCA24N expression vectors, was used**.** Each protein coding ORF has an N-terminal His_6 and a C-terminal green fluorescence protein (GFP); each protein coding ORF is also available without the GFP fusion (which are the strains used in these studies). Cells containing the RplL gene overexpression vector were grown to OD = 0.6 in 100 mL of LB broth using a 37 °C shaker/incubator and induced with a final concentration of 1.0 mM IPTG before allowing to grow for an additional 4 h. After centrifugation, the supernatant was discarded before resuspending the cell pellet in lysis buffer (20 mM Tris, 10 mM $MgCl_2$, 100 mM KCl, pH=7.4, 100 µg aprotinin, 174 µg PMSF, 500 µg lysozyme) and incubation for 20 min. The cell membranes were disrupted by sonication (35 pulses, 1 sec/pulse at 75 W) before centrifugation of the suspension at 11,000 g for 10 min. The supernatant containing His_6-RplL was diluted 10-fold before application to the TEM grid for analysis.

Purified C-terminal His_6-tag gp10 (capsid protein) of T7 bacteriophage was typically produced at a concentration of ~1 x 10^{12} particles/mL. BL21 bacteria cells in 1 mL of LB media were grown to OD = 0.8 before addition of T7 bacteriophage (1.0 µL, 1.0X10^{12} particles/mL) to the culture and shaking at 37 °C for 1 h. After centrifugation of the cells, the supernatant was used directly for TEM grid analysis.

2.7.3 His_8-GFP Purification

A glycerol stock of *E. coli* cells, transformed with the His_8-GFPuv pT7-7 plasmid, was shaken at 37 °C overnight before addition to 250 mL of LB media with shaking at 37 °C until an OD_{600} of 0.7 was reached. Then, a 1.0 M stock solution of isopropyl-β-D-thiogalactopyranoside (IPTG) was added, bringing the final concentration to 1.0 mM, before shaking continually at 37 °C for an additional 5 h. The cells were then centrifuged at 11,000 g for 10 min, the supernatant discarded, and the pellet re-suspended in 10 mL of lysis buffer (50 mM NaH_2PO_4, 100 mM NaCl, pH = 8.0, 100 µg aprotinin, 174 µg phenylmethanesulfonyl fluoride (PMSF), and 500 µg of lysozyme). The suspension was allowed to stand for 20 min before the cell membranes were disrupted using 3 rounds of sonication (35 pulses of probe sonication, 1 sec/pulse at 75 W with 1 sec rest/pulse) and the debris pelleted by centrifugation at 11,000 g for 30 min. The supernatant was incubated with 100 µL of Ni-NTA agarose beads and gently rotated for 4 h. The beads were pelleted using a bench top centrifuge operating at 5,000 g for 2 min. The supernatant was discarded and the pellet was washed with PBS buffer containing imidazole (50 mM NaH_2PO_4, 100 mM NaCl, 10 mM imidazole, pH = 8.0). The same spin and wash sequence was repeated with 15 mM, 20 mM, and 30 mM imidazole in PBS. The protein was eluted from the resin after a final spin, discarding of supernatant, and incubation with 500 mM imidazole in PBS for 4 h. The removal of imidazole was achieved by dialyzing the eluted protein against PBS (50 mM NaH_2PO_4, 100 mM NaCl, 10 mM imidazole, pH = 8.0) overnight using a 10,000 MWCO Slide-A-Lyzer. The protein was characterized using 12.5% acrylamide SDS-PAGE gel electrophoresis.

2.7.4 Purified Maltose Transporter Solubilized in Lipid Nanodisc

The methods used to purify and insert His_6-$MalFGK_2$ maltose transporter in lipid nanodiscs derived from membrane scaffolding proteins (MSP) followed those described in a previously reported protocol.[42]

2.7.5 TEM Grid Carbon Coating Procedure

A Formvar solution was prepared by dissolving 100 mg Formvar powder in 50 mL DCM. Copper grids (400 mesh) were purchased from Ted Pella and sonicated in acetone for 30 min before drying overnight in a dust free environment. Glass microscope slides were freshly cleaned with detergent, rinsed exhaustively with distilled water, dried overnight in a vacuum oven, and stored in a dust free environment until coated with Formvar solution for 30 seconds by partial immersion before drying for 5 min. The edges of the glass slides then were scrapped with a razor before floating the Formvar film on water by submersion of the glass slide into a darkly tinted Pyrex glass dish. The pre-cleaned copper grids were placed atop the floating Formvar film (15 - 20 grids, shiny side down) and picked up with a pre-cleaned glass slide before transfer to a Petri dish to dry overnight. Then, a carbon film was evaporated onto the glass slide with the TEM grids facing up before removal of the Formvar film by placement of the grids on top of filter paper soaked with $CHCl_3$ in a glass Petri dish for 30 min. Finally, the filter paper was removed and the grids dried overnight in a dust free environment before transfer to a standard TEM grid storage box.

2.7.6 Langmuir-Schaefer Film Deposition onto TEM Grids

Stock solutions of two lipid mixtures (1:99 Ni^{2+}:NTA-PEG2000-DTPE:mPEG350-DTPE and 5:95 Ni^{2+}:NTA-PEG2000-DTPE:mPEG350-DTPE) were prepared in $CHCl_3$ at 2.0 mg/mL and stored at -80 °C. Each of these were spread via 10 μL microsyringe at the air-water interface of a Kibron μTrough S and compressed to a final surface pressure of 30 mN/m (i.e., ~59 $Å^2$/molecule for 1:99 Ni^{2+}:NTA-PEG2000-DTPE:mPEG350-DTPE monolayers and ~66 $Å^2$/molecule for 5:95 Ni^{2+}:NTA-PEG2000-DTPE:mPEG350-DTPE monolayers). The compressed lipid monolayers were deposited onto TEM grids by Langmuir-Schaefer transfer using tabbed TEM grids (Ted Pella) to enable grid approach at 180° (and the transfer forceps at 90°) relative to the air-water interface and the LS film immediately blotted with filter paper. (n.b.: Standard TEM grids and forceps produced extensive disruption of the interface during the LS transfer step, making it impossible to determine accurate grid transfer ratios under these conditions.) The supported monolayer films were then polymerized for 10 min using a handheld 8W/m^2 254 nm lamp that was placed 6-8 cm above the grid surface before transfer to a standard TEM grid box for later use.

2.7.7 Fluorescence Microscopy

Sessile drops of His_8-GFPuv solution (3.5 μL, 2.0 mg GFP/mL in PBS) were deposited onto 1:99 Ni^{2+}:NTA-PEG2000-DTPE:mPEG350-DTPE, 5:95 Ni^{2+}:NTA-PEG2000-DTPE:mPEG350-DTPE, 100% mPEG350-DTPE, or bare carbon coated grid surfaces for 2 min, followed by removal of excess sample using a microsyringe. Grids

were then washed 3 times with 20 μL drops of Tris buffer before removal of the excess solution via microsyringe. For elution of Ni^{2+}:NTA-bound T7 bacteriophage from the surface of the grid, 500 mM imidazole was deposited on the grid surface for 5 min before washing twice with 20.0 μL of PBS. After preparation, the TEM grid was sandwiched between a microscope slide and coverslip and sealed with nail polish before recording the fluorescence images.

2.7.8 Negative Staining Procedure

T7 bacteriophage and RplL cell lysate samples were prepared by incubating a 5.0 μL drop of cell lysate on the grid surface for 2.0 min before gentle removal by microsyringe. The grids were then washed 6 times with 20 μL drops of Tris buffer followed by a final wash with 20 μL of distilled water. A 5 μL drop of 2% uranyl acetate was placed on the grid for 1 min before removal of the excess solution with a wedge of filter paper. Ni^{2+}:NTA-immobilized samples were eluted from the grids by adding 5 μL of 500 mM imidazole in Tris buffer immediately after sample deposition (i.e., instead of 6 Tris buffer washes). Nanodisc solubilized His_6-$MalFGK_2$ and purified his_6-T7 bacteriophage samples were prepared in the same manner as the cell lysate samples, except that the incubation time of the samples on DLPC and mPEG350-DTPE modified grids was increased to 3 min. Negatively stained samples were imaged using a Tecnai TF20 transmission electron microscope operating at 200 kV.

2.7.9 Preparation of Frozen Hydrated Samples for Cryo-EM

TEM grids modified with stabilized 5:95 Ni^{2+}:NTA-PEG2000-DTPE:mPEG350-DTPE monolayers were treated with His-tag protein samples as described above for negative-staining. After application of the protein solution, the excess sample was removed by blotting the grids twice for 3 secoonds with an offset of -1 at 80 % humidity using a Vitrobot (FEI Company). The grids were then cryo-fixed by plunging into liquid ethane and imaged at 200 kV on an FEI CM200 transmission electron microscope using low-dose techniques. Images were recorded using a Gatan Ultrascan CCD.

2.8 Acknowledgements

His_8-GFPuv expressing *E. coli* cells were a gift provided by Professor Dinesh Yernool at Purdue University. The financial support of NIH Grant #R41GM098017 is gratefully acknowledged.

2.9 References

1. Bartesaghi, A., 2.2 A Resolution Cryo-EM Structure of β-Galactosidase in Complex with a Cell-Permeant Inhibitor. *Science* **2015,** *348*, 1147-1151.

2. Uzgiris, E. E.; Kornberg, R. D., Two-Dimensional Crystallization Technique for Imaging Macromolecules, With Application to Antigen-Antibody Complement Complexes. *Nature* **1983,** *301*, 125-129.

3. Thompson, D. H.; Zhou, M. K.; Grey, J.; Kim, H. K., Design, Synthesis, and Performance of NTA-Modified Lipids as Templates for Histidine-Tagged Protein Crystallization. *Chem Lett* **2007,** *36* (8), 956-975.

4. (a) Schmitt, L.; Dietrich, C.; Tampe, R., Synthesis and Characterization of Chelator-lipids for Reversible Immobilization of Engineered Proteins at Self-assembled Lipid Interfaces. *J. Am. Chem. Soc.* **1994,** *116*, 8485-8491; (b) Kubalek, E. W.; Le Grice, S. F. J.; Brown, P. O., Two-Dimensional Crystallization of Histidine-Tagged, HIV-1 Reverse Transcriptase Promoted by a Novel Nickel-chelating Lipid. *J. Struct. Biol.* **1994,** *113*, 117-123; (c) Dietrich, C.; Schmitt, L.; Tampe, R., Molecular Organization of Histidine-Tagged Biomolecules at Self-assembled Lipid Interfaces Using a Novel Class of Chelator Lipids. *Proc. Nat'l. Acad. Sci. U.S.A.* **1995,** *92*, 9014-9018; (d) Dietrich, C.; Boscheinen, O.; Scharf, K. D.; Schmitt, L.; Tampe, R., Functional Immobilization of a DNA-Binding Protein at a Membrane Interface via Histidine Tag and Synthetic Chelator Lipids. *Biochemistry* **1996,** *35*, 1100-1105; (e) Barklis, E.; McDermott, J.; Wilkens, S.; Schabtach, E.; Schmid, M.; Fuller, S.; Karanjia, S.; Love, Z.; Jones, R.; Zhao, X.; Rui, Y.; Thompson, D. H., Structural Analysis of Membrane-Bound Retrovirus Capsid Proteins. *EMBO J.* **1997,** *16*, 1199-1213; (f) Barklis, E.; McDermott, J.; Wilkens, S.; Fuller, S.; Thompson, D. H., Organization of HIV-1 Capsid Proteins on a Lipid Monolayer. *J. Biol. Chem.* **1998,** *273*, 7177-7180.

5. Kelly, D. F.; Abeyrathne, P. D.; Dukovski, D.; Walz, T., The Affinity Grid: A Pre-fabricated EM grid for Monolayer Purification. *J. Mol. Biol.* **2008,** *382*, 423-433.

6. (a) Kelly, D. F.; Dukovski, D.; Walz, T., Monolayer Purification: A Rapid Method for Isolating Protein Complexes for Single-Particle Electron Microscopy. *Proc. Nat'l. Acad. Sci. U.S.A.* **2008,** *105*, 4703-4708; (b) Dukovski, D.; Li, Z.; Kelly, D. F.; Mack, E.; Walz, T., Structural and Functional Studies on the Stalk of the Transferrin Receptor. *Biochem. Biophys. Res. Comm.* **2009,** *381*, 712-716.

7. Kelly, D. F.; Dukovski, D.; Walz, T., Strategy for the Use of Affinity Grids to Prepare Non-His-Tagged Macromolecular Complexes for Single-Particle Electron Microscopy. *J. Mol. Biol.* **2010,** *400*, 675-681.

8. Sharma, G.; Pallesen, J.; Das, S.; Grassucci, R.; Langlois, R.; Hampton, C. M.; Kelly, D. F.; des Georges, A.; Frank, J., Affinity Grid-based Cryo-EM of PKC Binding to RACK1 on the Ribosome. *J. Struct. Biol.* **2013,** *181*, 190-194.

9. (a) Boomer, J. A.; Inerowicz, H. D.; Zhang, Z.-Y.; Bergstrand, N.; Edwards, K.; Kim, J.-M.; Thompson, D. H., Acid-Triggered Release from Sterically-Stabilized Fusogenic Vesicles: A Novel DePEGylation Strategy. *Langmuir* **2003,** *19*, 6408-6415; (b) Longo, G.; Thompson, D. H.; Szleifer, I., Ligand-Receptor Interactions Between Surfaces: The Role of Binary Polymer Spacers. *Langmuir* **2008,** *24*, 10324-10333; (c) Shin, J.; Shum, P.; Grey, J.; Malhotra, G. S.; Fujiwara, S.; González-Bonet, A. M.; Moase, E.; Allen, T. M.; Thompson, D. H., Acid-Labile PEG-Vinyl Ether-Lipids with Tunable pH Sensitivity: Synthesis and Structural Effects on Hydrolysis Rates, Calcein Release Performance and Biodistribution of Their DOPE Dispersions. *Mol. Pharm.* **2012,** *9*, 3266-3276.

10. (a) Zhou, M.; Haldar, S.; Franses, J.; Kim, J.-M.; Thompson, D. H., Synthesis and Self-Assembly Properties of Acylated Cyclodextrins and Nitrilotriacetic Acid (NTA)-Modified Inclusion Ligands for Interfacial Protein Crystallization. *Supramolecular Chem.* **2005,** *17*, 101-111; (b) Kang, E.; Park, J. W.; McClellan, S.; Kim, J.-M.; Holland, D. P.; Lee, G. U.; Franses, E.; Park, K.; Thompson, D. H., Specific Adsorption of Histidine-Tagged Proteins on Silica Surfaces Modified with Ni2+:NTA-Derivatized Poly(ethylene glycol). *Langmuir* **2007,** *23*, 6281-6288.

11. Yu, G.; Vago, F.; Zhang, D.; Snyder, J. E.; Yan, R.; Zhang, C.; Benjamin, C.; Jiang, X.; Kuhn, R. J.; Serwer, P.; Thompson, D. H.; Jiang, W., Single-Step Antibody-Based Affinity Cryo-Electron Microscopy for Imaging and Structural Analysis of Macromolecular Assemblies. *J. Struct. Biol.* **2014,** *187*, 1-9.

12. (a) Lee, J. H.; Kopecek, J.; Andrade, J. D., Protein-Resistant Surfaces Prepared by PEO-containing Block Copolymer Surfactants. *J. Biomed. Mater. Res.* **1989,** *23*, 351-368; (b) Jeon, S. I.; Andrade, J. D., Protein-Surface Interactions in the Presence of Polyethylene Oxide. *J. Coll. Interfac. Sci.* **1991,** *142*, 159-166; (c) Malmsten, M.; Emoto, K.; Van Alstine, J. M., Effect of Chain Density on Inhibition of Protein Adsorption by Poly(ethylene glycol) Based Coatings. *J. Coll. Interfac. Sci.* **1998,** *202*, 507-517.

13. Wegner, G., Topochemical Polymerization of Monomers with Conjugated Triple Bonds. *Angew Chem Int Edit* **1971,** *10* (5), 355-&.

14. Kelly, D. F.; Dukovski, D.; Walz, T., Monolayer Purification: a Rapid Method for Isolating Protein Complexes for Single-Particle Electron Microscopy. *Proc Natl Acad Sci U S A* **2008,** *105* (12), 4703-8.

15. (a) Jonas, U.; Shah, K.; Norvez, S.; Charych, D. H., Reversible Color Switching and Unusual Solution Polymerization of Hydrazide-Modified Diacetylene Lipids. *J Am Chem Soc* **1999,** *121* (19), 4580-4588; (b) Li, F.; Shishkin, E.; Mastro, M. A.; Hite, J. K.; Eddy, C. R., Jr.; Edgar, J. H.; Ito, T., Photopolymerization of Self-Assembled Monolayers of Diacetylenic Alkylphosphonic Acids on Group-III Nitride Substrates. *Langmuir* **2010,** *26* (13), 10725-30.

16. Frank, J., Single-Particle Imaging of Macromolecules by Cryo-Electron Microscopy. *Annu Rev Biophys Biomol Struct* **2002,** *31*, 303-19.

17. Schmitt, J.; Hess, H.; Stunnenberg, H. G., Affinity Purification of Histidine-Tagged Proteins. *Mol Biol Rep* **1993,** *18* (3), 223-30.

18. Iwanczyk, J.; Sadre-Bazzaz, K.; Ferrell, K.; Kondrashkina, E.; Formosa, T.; Hill, C. P.; Ortega, J., Structure of the Blm10-20 S Proteasome Complex by Cryo-Electron Microscopy. Insights Into the Mechanism of Activation of Mature Yeast Proteasomes. *J Mol Biol* **2006,** *363* (3), 648-59.

19. (a) Dang, T. X.; Farah, S. J.; Gast, A.; Robertson, C.; Carragher, B.; Egelman, E.; Wilson-Kubalek, E. M., Helical Crystallization on Lipid Nanotubes: Streptavidin as a Model Protein. *J Struct Biol* **2005,** *150* (1), 90-9; (b) Han, B. G.; Walton, R. W.; Song, A.; Hwu, P.; Stubbs, M. T.; Yannone, S. M.; Arbelaez, P.; Dong, M.; Glaeser, R. M., Electron Microscopy of Biotinylated Protein Complexes Bound to Streptavidin Monolayer Crystals. *J Struct Biol* **2012,** *180* (1), 249-53.

20. (a) Jiang, Q. X.; Chester, D. W.; Sigworth, F. J., Spherical Reconstruction: a Method for Structure Determination of Membrane Proteins from Cryo-EM Images. *J Struct Biol* **2001,** *133* (2-3), 119-31; (b) Wang, L.; Sigworth, F. J., Structure of the BK Potassium Channel in a Lipid Membrane from Electron Cryomicroscopy. *Nature* **2009,** *461* (7261), 292-5.

21. (a) Bell, J. M.; Chen, M.; Baldwin, P. R.; Ludtke, S. J., High Resolution Single Particle Refinement in EMAN2.1. *Methods* **2016,** *100*, 25-34; (b) Zhu, Y.; Carragher, B.; Glaeser, R. M.; Fellmann, D.; Bajaj, C.; Bern, M.; Mouche, F.; de Haas, F.; Hall, R. J.; Kriegman, D. J.; Ludtke, S. J.; Mallick, S. P.; Penczek, P. A.; Roseman, A. M.; Sigworth, F. J.; Volkmann, N.; Potter, C. S., Automatic Particle Selection: Results of a Comparative Study. *J Struct Biol* **2004,** *145* (1-2), 3-14.

22. (a) Jiang, Z. Y.; Xu, S. W.; Wang, Y. Q., Chemistry for Pegylation of Protein and Peptide Molecules. *Chinese J Org Chem* **2003,** *23* (12), 1340-1347; (b) Li, J.; Kao, W. J., Synthesis of Polyethylene Glycol (PEG) Derivatives and PEGylated-Peptide Biopolymer Conjugates. *Biomacromolecules* **2003,** *4* (4), 1055-1067; (c) Mahou, R.; Wandrey, C., Versatile Route to Synthesize Heterobifunctional Poly(ethylene glycol) of Variable Functionality for Subsequent Pegylation. *Polymers-Basel* **2012,** *4* (1), 561-589.

23. (a) Lata, S.; Piehler, J., Stable and Functional Immobilization of Histidine-Tagged Proteins via Multivalent Chelator Headgroups on a Molecular Poly(ethylene glycol) Brush. *Anal Chem* **2005,** *77* (4), 1096-105; (b) Lata, S.; Reichel, A.; Brock, R.; Tampe, R.; Piehler, J., High-Affinity Adaptors for Switchable Recognition of Histidine-Tagged Proteins. *J Am Chem Soc* **2005,** *127* (29), 10205-15; (c) Hyun, S. H.; Kim, H. K.; Kim, J. M.; Thompson, D. H., Oriented Insertion of phi29 N-Hexahistidine-Tagged gp10 Connector Protein Assemblies into C(20)BAS Bolalipid Membrane Vesicles. *J Am Chem Soc* **2010,** *132* (48), 17053-17055.

24. Tinazli, A.; Tang, J.; Valiokas, R.; Picuric, S.; Lata, S.; Piehler, J.; Liedberg, B.; Tampe, R., High-Affinity Chelator Thiols for Switchable and Oriented Immobilization of Histidine-Tagged Proteins: a Generic Platform for Protein Chip Technologies. *Chemistry* **2005,** *11* (18), 5249-59.

25. Sanchez, A.; Pedroso, E.; Grandas, A., Maleimide-Dimethylfuran Exo Adducts: Effective Maleimide Protection in the Synthesis of Oligonucleotide Conjugates. *Org Lett* **2011,** *13* (16), 4364-7.

26. Scheich, C.; Sievert, V.; Bussow, K., An Automated Method for High-Throughput Protein Purification Applied to a Comparison of His-tag and GST-tag Affinity Chromatography. *BMC Biotechnology* **2003,** *3*, 12.

27. Boomer, J. A.; Qualls, M. M.; Inerowicz, H. D.; Haynes, R. H.; Patri, V. S.; Kim, J.-M.; Thompson, D. H., Cytoplasmic Delivery of Liposomal Contents Mediated by an Acid-labile Cholesterol-Vinyl Ether-PEG Conjugate. *Bioconjugate Chem.* **2009,** *20*, 47-59.

28. (a) Hansen, P. L.; Cohen, J. A.; Podgornik, R.; Parsegian, V. A., Osmotic Properties of Poly(Ethylene Glycols): Quantitative Features. *Biophys. J.* **2003,** *84*, 350-355; (b) Ham, A. S. W.; Klibanov, A. L.; Lawrence, M. B., Action at a Distance: Lengthening Adhesion Bonds with Poly(ethylene glycol) Spacers Enhances Mechanically Stressed Affinity for Improved Vascular Targeting of Microparticles. *Langmuir* **2009,** *25*, 10038-10044.

29. (a) Nguyen, T. D. H.; Perrin, F.-X.; Dinh, L. N., New Hybrid Materials Based on Poly(etheleneoxide)-Grafted Polysilazane by Hydrosilylation and Their Anti-Fouling Activities. *Beilstein J.* **2013,** *4*, 671-677; (b) Banerjee, I.; Pangule, R. C.; Kane, R. S., Antifouling Coatings: Recent Developments in the Design of Surfaces That Prevent Fouling by Proteins, Bacteria, and Marine Organisms. *Adv. Mater.* **2011,** *23*, 690-718.

30. Agirrezabala, X.; Martin-Benito, J.; Caston, J. R.; Miranda, R.; Valpuesta, M.; Carrascosa, J. L., Maturation of Phage T7 Involves Structural Modification of Both Shell and Inner Core Components. *EMBO J* **2005,** *24* (21), 3820-3829.

31. Ackermann, H. W.; Jolicoeur, P.; Berthiaume, L.; Advantages and Inconveniences of Uranyl Acetate in Comparative Virology: Study of 4 Tailed Bacteriophages. *Can J Microbiol* **1974,** *20* (8), 1093-9.

32. Kastner, B.; Fischer, N.; Golas, M. M.; Sander, B.; Dube, P.; Boehringer, D.; Hartmuth, K.; Deckert, J.; Hauer, F.; Wolf, E.; Uchtenhagen, H.; Urlaub, H.; Herzog, F.; Peters, J. M.; Poerschke, D.; Luhrmann, R.; Stark, H., Grafix: Sample Preparation for Single-Particle Electron Microscopy. *Nature Methods* **2008,** *5*, 53-55.

33. Wittmann, H. G., Architecture of Prokaryotic Ribosomes. *Annu. Rev. Biochem.* **1983,** *52*, 35-65.

34. (a) Frank, J.; Zhu; Penczek, P.; Li, Y.; Srivastava, S.; Verschoor, A.; Radermacher, M.; Grassucci, R.; Lata, R. K.; Agrawal, R. K., A Model of Protein Synthesis Based on Cryo-Electron Microscopy of the E. coli Ribosome. *Nature* **1995,** *376*, 441-444; (b) Stark, H.; Mueller, F.; Orlova, E. V.; Schatz, M.; Dube, P.; Erdemir, T.; Zemlin, F.; Brimacombe, R.; van Heel, M., The 70S Escherichia coli Ribosome at 23Å Resolution: Fitting the Ribosomal RNA. *Structure* **1995,** *3*, 815-821.

35. Baas, B. J.; Denisov, I. G.; Sligar, S. G., Homotropic Cooperativity of Monomeric Cytochrome P450 3A4 in a Nanoscale Native Bilayer Environment. *Arch. Biochem. Biophys.* **2004,** *430*, 218-228.

36. (a) Frauenfeld, J.; Gumbart, J.; van der Sluis, E. O.; Funes, S.; Gartmann, M.; Beatrix, B.; Mielke, T.; Berninghausen, O.; Becker, T.; Schulten, K.; Beckman, R., Cryo-EM Structure of the Ribosome-SecYE Complex in the Membrane Environment. *Nature Struct. Mol. Biol.* **2011,** *5*, 614-621; (b) Pandit, A.; Shirzad-Wasei, N.; Wlodarczyk, L. M.; van Roon, H.; Boekema, E. J.; Dekker, J. P.; de Grip, W. J., Assembly of the Major Light-harvesting Complex II in Lipid Nanodiscs. *Biophys. J.* **2011,** *101*, 2507-2515.

37. Leitz, A. J.; Bayburt, T. H.; Barnakov, A. N.; Springer, B. A.; Sligar, S. G., Functional Reconstitution of Beta-2-Adrenergic Receptors Utilizing Self-assembling Nanodisc Technology. *BioTechniques* **2006,** *40*, 601-612.

38. Wang, Z.; Raines, L. L.; Hooy, R. M.; Roberson, H.; Leahy, D. J.; Cole, P. A., Tyrosine Phosphorylation of Mig6 Reduces its Inhibition of the Epidermal Growth Factor Receptor. *ACS Chem. Biol.* **2013,** *8*, 2372-2376.

39. Shen, H.-H.; Lithgow, T.; Martin, L. L., Reconstitution of Membrane Proteins into Model Membranes: Seeking Better Ways to Retain Protein Activities. *Int. J. Mol. Sci.* **2013,** *14*, 1589-1607.

40. Ly, S.; Bourguet, F.; Fischer, N. O.; Lau, E. Y.; Coleman, M. A.; Laurence, T. A., Quantifying Interactions of a Membrane Protein Embedded in a Lipid Nanodisc Using Fluorescence Correlation Spectroscopy. *Biophys. J.* **2014,** *106*, L5-L8.

41. (a) Ngassam, V. N.; Howland, M. C.; Sapuri-Butti, A.; Rosidic, N.; Parikh, A. N., A Comparison of Detergent Action on Supported Lipid Monolayers and Bilayers. *Soft Matter* **2012,** *8*, 3734-3738; (b) Kragh-Hansen, U.; le Maire, M.; Moller, J. V., The Mechanism of Detergent Solubilization of Liposomes and Protein-Containing Membranes. *Biophys. J.* **1998,** *75*, 2932–2946.

42. Alvarez, F. J. D.; Orelle, C.; Davidson, A. L., Functional Reconstruction of an ABC Transporter in Nanodisc for Use in Electron Paramagnetic Resonance Spectroscopy. *J. Am. Chem. Soc.* **2010,** *132*, 9513-9515.

CHAPTER THREE:
DEVELOPMENT OF GRAPHENE-OXIDE-BASED AFFINITY GRIDS FOR SINGLE-PARTICLE CRYO-EM

3.1 Introduction

Single particle cryo-EM analysis (SPA) is a rapidly growing method for elucidating structure of biological materials at near atomic resolution[1] due to recent advances in instrumentation and computational algorithms[2]. One aspect of the SPA process that is not well optimized, however, is sample preparation. Furthermore, materials approaches to modification of traditional TEM grid surfaces can dramatically increase the relative scope of the technique[3]. Traditionally, proteins targeted for structural analysis must be overexpressed and subjected to time-consuming purification and concentration steps, sometimes under harsh conditions that disrupt protein-protein interactions of interest. Recently, there have been efforts reported that seek to address these limitations, either by improving grid rigidity to reduce beam-induced motion[4] or by effecting on-grid purification with 'affinity grids'[3c, 5] that employ metal chelating lipids that were originally developed for two-dimensional protein crystallization at the lipid-water interface[6]. The latter approach seeks to selectively capture biological target molecules from complex mixtures such as cell lysates as an integral part of the TEM sample preparation process[3c, 7].

Although lipid monolayer affinity grids have shown some success in producing samples for cryo-EM reconstruction at 20 Å resolution[5a], robust performance of the reported grid coatings may be limited by film instability and non-uniformity under the evaporative casting methods that have been reported. Additionally, these lipid films require a thin polymer layer or a holey carbon substrate layer to provide mechanical support of the deposited film. The electrical conductivity of monolayer graphene is six orders of magnitude higher than amorphous carbon, and although the level of conductivity in graphene decreases with the extent of oxidation, it has been shown to recover much of this conductivity upon reduction with H_2 plasma[9]. Additionally, unlike unsupported lipid monolayers, the elasticity of graphene makes it ideal to resist permanent deformation due to mechanical transfer techniques from the material-water interface. Our interest in utilizing graphene-based affinity substrates is focused on exploiting the superior mechanical strength and conductivity it offers. By conferring better target specificity to this substrate, affinity graphenic substrates have the potential to offer both improved stability and resistance to non-specific adsorption such that direct capture from cell lysates may be feasible.

3.2 Design of Graphene-Oxide-NTA-Based Affinity Grids

We sought to address the limitations of lipid monolayer coated affinity grids by employing a GO derivative that minimizes background signal due to the single atom thickness and improved conductivity as a way to combat sample charging and instability during image capture[8]. Here we demonstrate the utility of affinity grids using Langmuir-Schaefer (LS) transfer of GO monolayer sheets that have been functionalized with

covalently linked N^{α}, N^{α}-dicarboxymethyllysine (GO-NTA). Using these affinity grids, we were able to selectively capture both His_6-T7 bacteriophage and His_6-GroEL. When the prepared grids were further modified with bovine serum albumin (BSA), a common antifouling agent that limits non-specific adsorption of non-targeted cellular debris, we were able to selectively capture these proteins directly from bacterial lysate while avoiding deposition of non-target proteins (Figure 3.1).

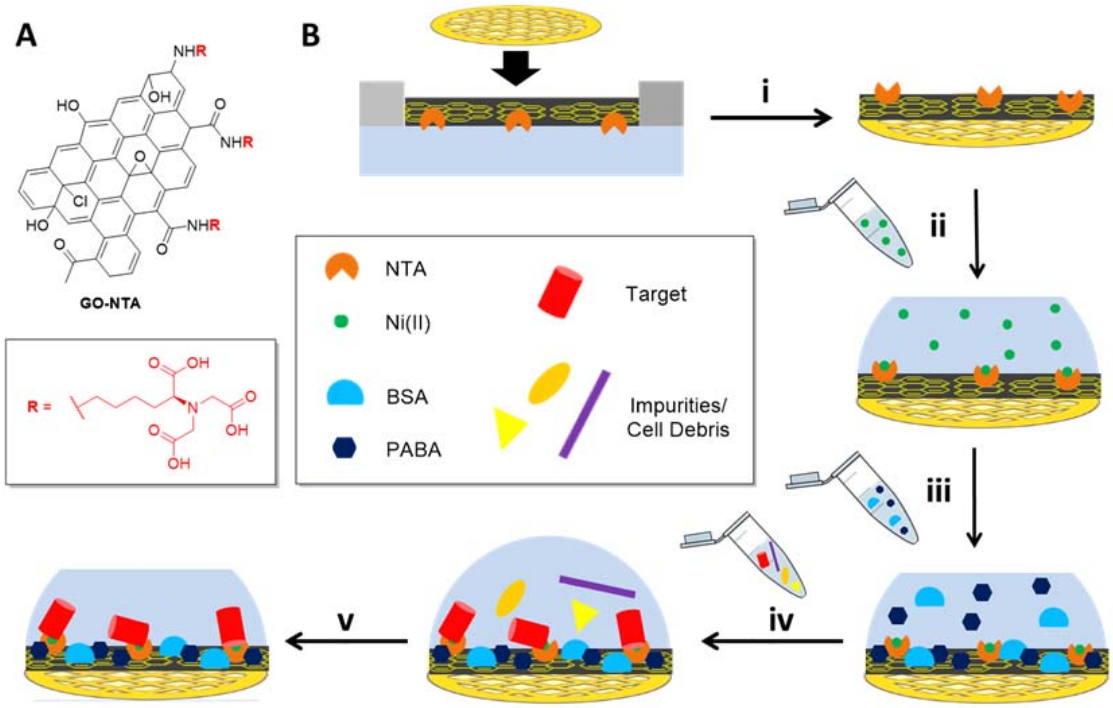

Figure 3.1 Conceptual Diagram of Sample Preparation Using a GO-NTA-Modified TEM Grid. (i) GO-NTA monolayer deposition onto TEM grid via L-S transfer; (ii) activation of NTA with Ni^{2+}; (iii) blocking of non-specific reaction and/or adsorption sites with 4-aminobenzoic acid (PABA) and bovine serum albumin (BSA); (iv) incubation of clarified lysate with blocked grid; (v) washing of non-target molecules from grid, followed by cryo-fixation or staining.

3.3 Synthesis and Characterization of GO-NTA

GO was produced from graphene using Hummer's method[8]. Activation of the GO carboxylic acid groups with $SOCl_2$ prior to reaction with the tris-*t*-butyl ester of lysine NTA (**15**) gave GO-NTA-(O-*t*-Bu)$_3$. TFA deprotection of this intermediate gave GO-NTA (**51**) (Scheme 3.1). Fourier transfer infrared spectroscopy was used to monitor these reactions as shown in Figure 3.2[9]. The spectra of GO displayed a broad absorption at 3236 cm^{-1} (O-H stretch) and a sharper absorption at 1648 cm^{-1} (C=O stretch)[16]. The NTA-GO tris-*t*-butyl ester displayed an additional absorption at 2933 cm^{-1} (C-H stretch) due to the incorporation of the lysine and *t*-butyl moieties. Following treatment of NTA-GO tris-*t*-butyl ester with TFA, the presence of the aliphatic C-H stretching was greatly reduced, indicating successful deprotection of the NTA chelator substituents[10].

3.3.1 Synthesis of Graphene-Oxide-NTA

GO was synthesized using an improved Hummers' method[8] that is easier to execute, is higher yielding, and does not evolve toxic gases (Scheme 3.1). This method involves oxidation of bulk graphite powder by potassium permanganate in the presence of sulfuric acid and phosphoric acid. It has been reported that there is no decrease in conductivity in the final product between the original and improved method, making it an attractive route for large scale production of GO.

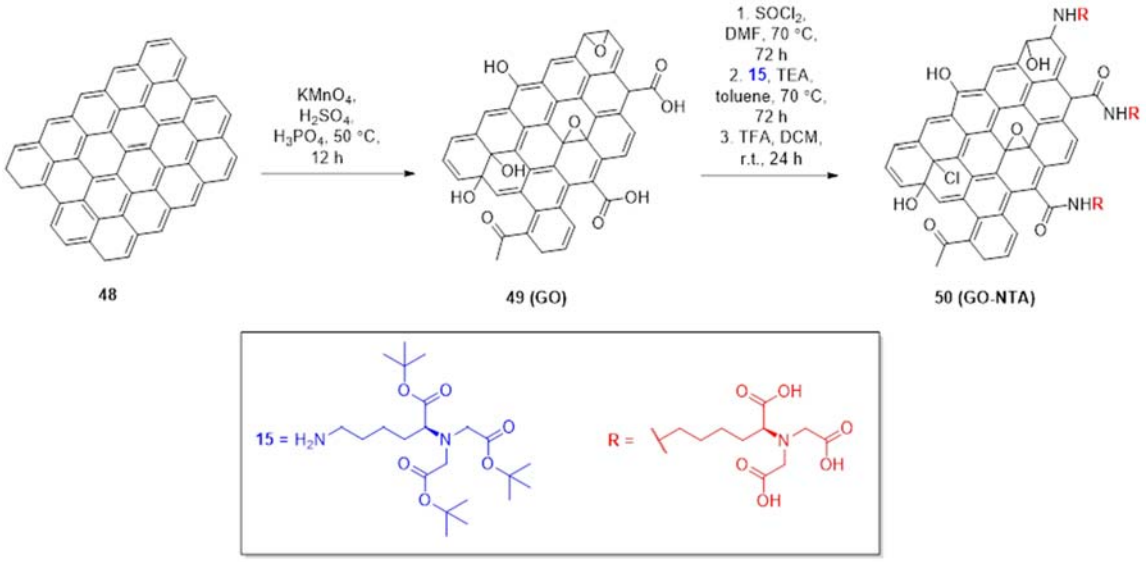

Scheme 3.1 Synthesis of GO-NTA.

Activation of the GO carboxylic acid groups with $SOCl_2$ prior to reaction with the tris-*t*-butyl ester of lysine NTA (**15**) gave GO-NTA-(O-*t*-Bu)$_3$. TFA deprotection of this intermediate gave GO-NTA (Scheme 3.1).

3.3.2 FT-IR Analysis of GO Derivatives

Fourier transfer infrared spectroscopy was used to monitor these reactions as shown in Figure 3.2[9]. The spectra of GO displayed a broad absorption at 3236 cm^{-1} (O-H stretch) and a sharper absorption at 1648 cm^{-1} (C=O stretch)[8]. The NTA-GO tris-*t*-butyl ester displayed an additional absorption at 2933 cm^{-1} (C-H stretch) due to the incorporation of the lysine and *t*-butyl moieties.

Previous work has shown that the typical GO sheet absorption band at ~240 nm is shifted to ~270 nm when the GO sheets are dispersed in aqueous solution. The origin of

this hypsochromic shift is due to n-π* electronic transitions arising from the C=O bonds introduced by oxidation[11]. GO-NTA samples prepared in this manner exhibited a major absorption peak at ~280 nm, in good agreement with these reports.

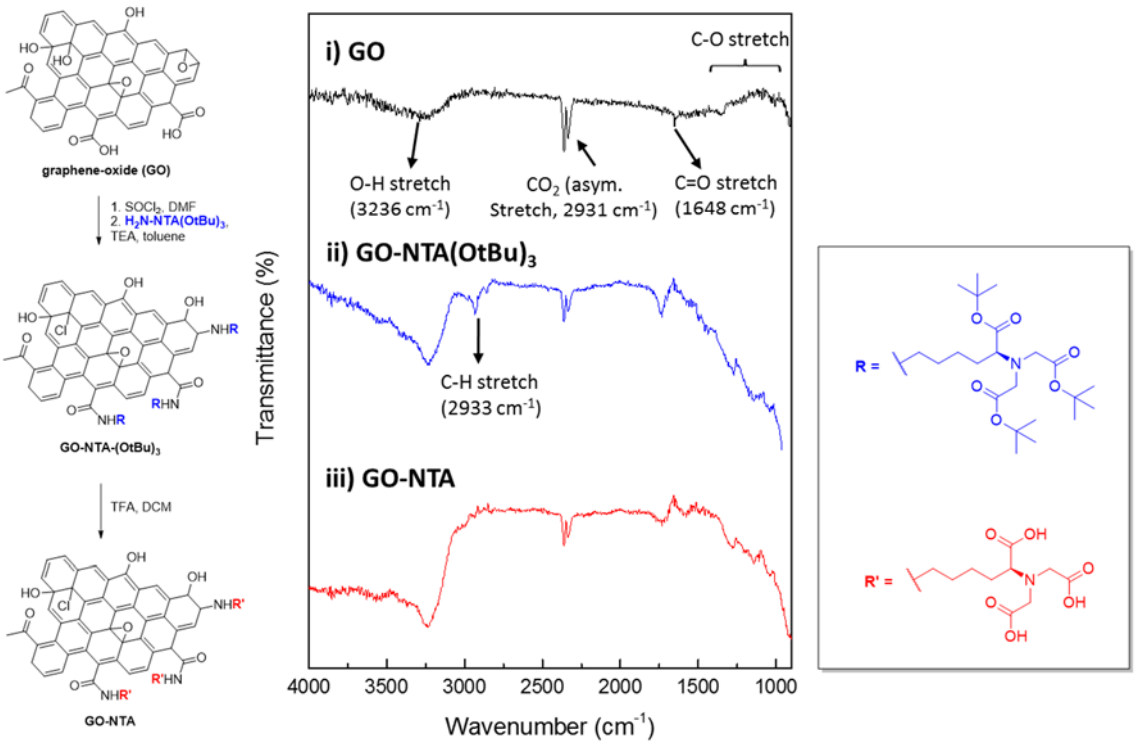

Figure 3.2 FTIR Analysis of GO, GO-NTA-tris-t-butyl Ester and GO-NTA

Following treatment of NTA-GO tris-*t*-butyl ester with TFA, the presence of the aliphatic C-H stretching was greatly reduced, indicating successful deprotection of the NTA chelator substituents[10].

3.3.3 Synthesis of Pyrene-NTA

In a similar approach, we sought to use hydrophobic interactions between pyrene-NTA conjugate and graphene-coated TEM grids to generate a novel affinity grid surface. We were interested in taking advantage of existing commercial graphene-functionalized TEM grid technologies, as well as novel exfoliated graphene-coated grids, to utilize affinity interactions for monolayer purification. To this end, a pyrene-functionalized NTA derivative **53** was synthesized via two step sequence (Scheme 3.2).

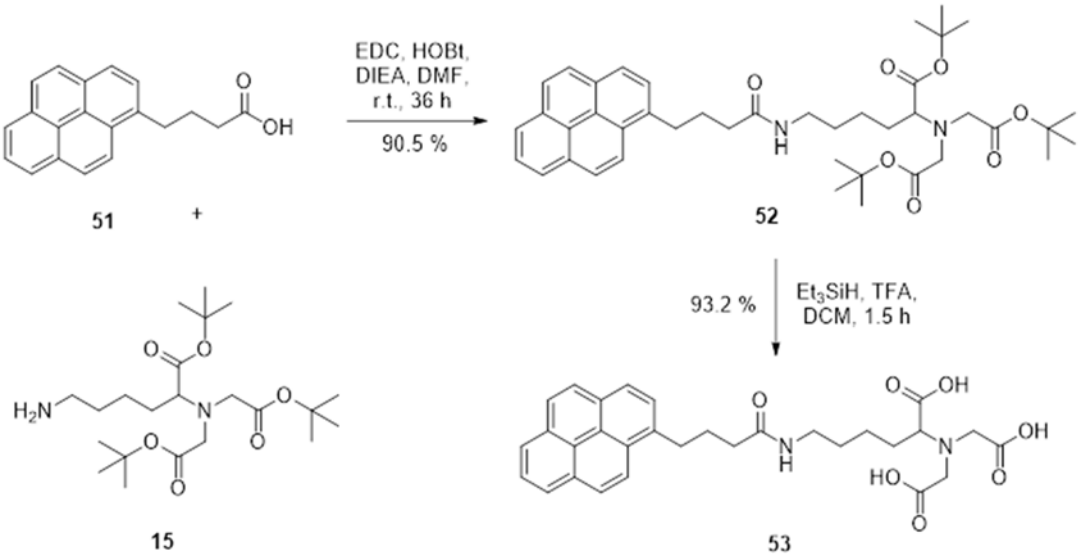

Scheme 3.2 Synthesis of Pyrene-NTA.

Pyrene-NTA was synthesized via EDC-mediated coupling reaction between **15** and 4-pyrenebutyric acid (**51**) to yield **52** in 90.5 % yield after chromatographic purification. Deprotection using TFA was used to give Compound **53** in 93.2 % yield.

3.3.4 Synthesis of Triethoxysilyl-NTA

To enable affinity modification of glass surfaces with NTA ligand for affinity purification, a triethoxysilyl-NTA derivative was designed and synthesized. This material is designed to be used for modification of glass surfaces followed by treatment of the modified surface with TFA to deprotect the t-butyl ester protecting groups.

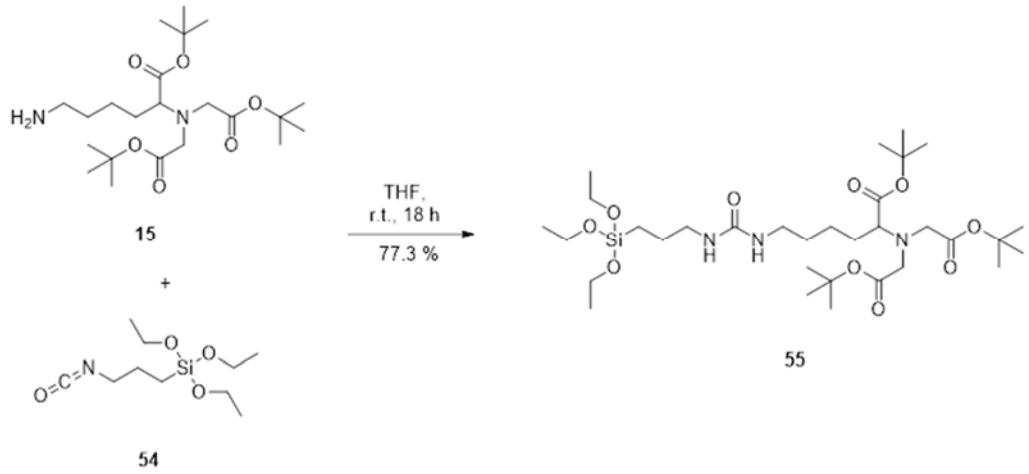

Scheme 3.3 Synthesis of Triethoxysilyl-NTA.

To this end, Compound **15** was coupled to 3-(triethyxysilyl)propyl isocyanate (**54**) in THF to give the target Compound **55** in 77.3 % yield after chromatographic purification (Scheme 3.3).

3.4 Fabrication and Evaluation of GO-NTA-Based Affinity Grids

Most reports of Langmuir dispersions of GO at the air-water interface focus on surfactant-assisted dispersion methods to stabilize GO sheets dispersed in water[12]. Treatment of GO with surfactants in these cases; however, biases the interfacial activity towards water-surfactant activity rather than GO-NTA activity due to their high relative abundance. The planar structure and functional group distribution on GO-NTA confers edge amphiphilicity due to the distribution of hydrophilic carboxyl, ketone, aldehyde, amide, and alcohol groups around the periphery of the hydrophobic aryl GO-NTA core (Figure 3.2)[13]. Since GO-NTA becomes increasingly hydrophobic as displacement toward the core from the GO-NTA edge increases, larger sheets will tend to be more hydrophobic and migrate to the air-water interface, whereas smaller more hydrophilic GO-NTA sheets are displaced into the aqueous subphase by the larger GO-NTA sheets[14].

3.4.1 GO-NTA Monolayer Formation

Previously, it was thought that the use of surface-active agents was needed to disperse GO sheets. More recent work; however, has shown that GO layers form at the air-water interface in the absence of surfactant molecules[15]. Brewster angle microscopy studies have shown that the interfacial refractive index of GO solutions change after a few hours of stirring pure GO dispersions in water[16]. This suggests a time-dependent mechanism for GO absorption at the air-water interface, with slower interfacial adsorption rates attributable to slower diffusion rates of large graphene sheets relative to typical surfactant molecules used for studies of the air-water interfaces. To increase the amount of surface-

active graphene sheets present at the air-water interface while circumventing hours of stirring, studies using rising gas bubbles of CO_2 and N_2 as a way of transporting these sheets to the surface have proven successful[14]. These studies show that GO can migrate to the air-water interface, while other work suggests that the surface activity of GO sheets in water can be increased using volatile, polar protic solvents to enable their manipulation using Langmuir compression[15].

3.4.2 Characterization of GO-NTA Affinity Monolayers

Compression of the GO-NTA material at the interface gave a characteristic surface pressure-area isotherm (Figure 3.3), suggesting a progression from isolated GO-NTA sheets to close edge-to-edge packing of GO-NTA sheets, followed by folding, wrinkling, and sliding of the nearest neighbor GO-NTA sheets atop one another upon further compression[17], in a manner analogous to pressure-induced collapse of Langmuir phospholipid monolayer films[15]. Repulsive electrostatic interactions and attractive van der Waals forces compete as GO-NTA sheets come into close contact.

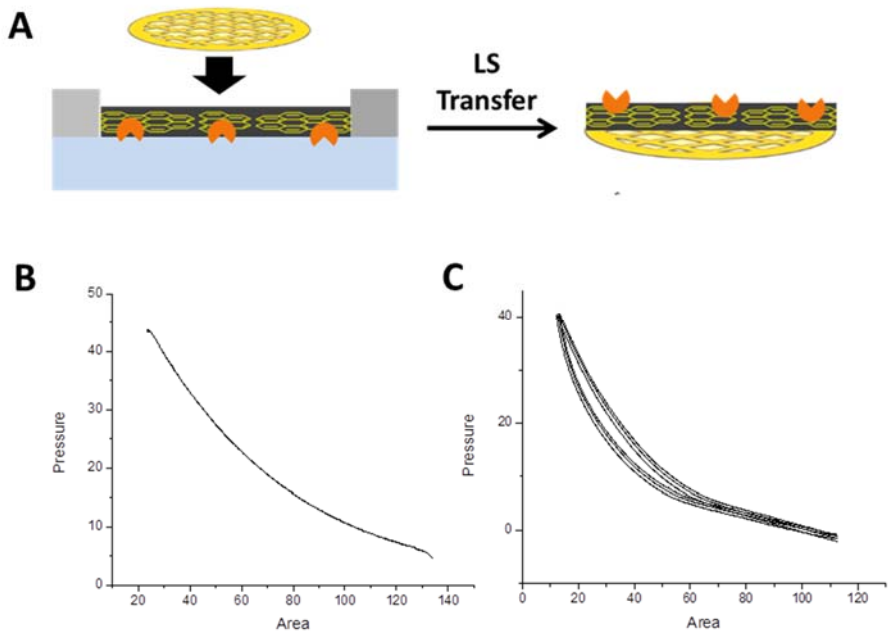

Figure 3.3 Spreading Behavior of GO-NTA Using a Langmuir Trough. A) Cartoon depicting LS-transfer of GO-NTA surfaces onto TEM grids. B) Typical surface pressure-area isotherm for GO-NTA. C) GO-NTA monolayer subjected to several compression-decompression cycles on the Langmuir trough.

Previous work with GO monolayers has suggested that over-compression of GO causes irreversible coagulation above ~15 mN/m[15] due to the increasing participation of attractive van der Waals interactions once the repulsive electrostatic interactions between sheet edges has been overcome by lateral compression. Transfer of these films onto silicon substrates at multiple surface pressures enabled the transfer of single layer GO sheets at surface pressures above 15 mN/m.

3.4.2.1 Fluorescence Microscopy Analysis of GO-NTA

Epifluorescence microscopy, AFM, and SEM was employed to determine the thickness and lateral distribution of GO-NTA sheets deposited onto solid substrates by L-S transfer from the air-water interface[18]. In particular, epifluorescence microscopy of Fluorescein-modified-PABA-GO-NTA (F-PABA-GO-NTA) monolayers proved useful because opacity of the graphene-based sheet is directly related to its thickness as revealed by analysis of monolayer-coated grid and negative control bare Cu TEM grid samples that showed significantly greater fluorescence intensity for grids coated with F-PABA-GO-NTA (Figure 3.4).

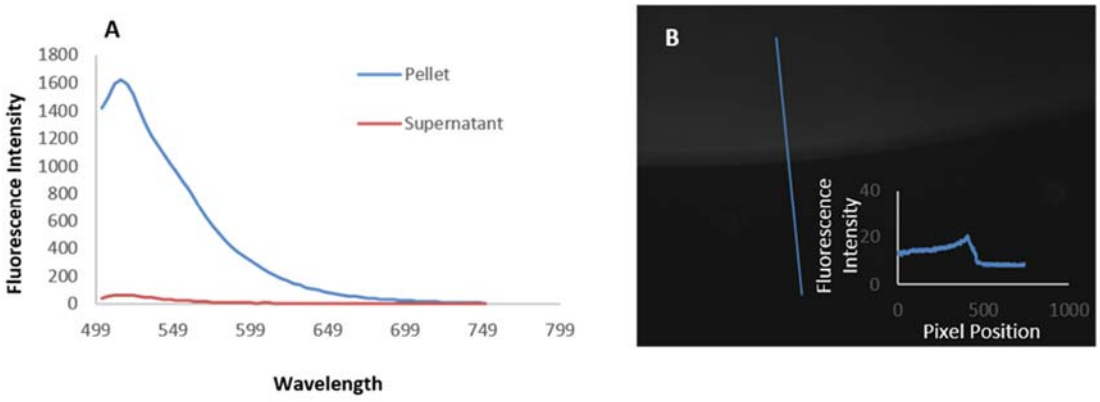

Figure 3.4 Analysis of F-PABA-GO-NTA Films by (A) Fluorescence Spectroscopy and (B) Epifluorescence Microscopy. Fluorescence spectra were measured for the supernatant (A, red spectrum) and the pellet (A, blue spectrum) after reaction of PABA-GO with aminofluorescein. (B) Epifluorescence image of F-PABA-GO-NTA film on TEM grid across the region indicated by the line in the epifluorescence image.

We then evaluated drop casting and L-S transfer deposition methods for the production of the thinnest films possible, while yielding films with the highest density of

NTA capture ligands. Drop casting[18-19], followed by slow evaporation of solvent, resulted in a fluorescence signal that completely spanned the holes of Formvar-coated 400 mesh Cu grids (data not shown). Slow solvent evaporation enables GO sheets to settle on top of one another to form a multi-layered film covering the TEM grid holes. Although successful, our findings suggest that drop casting typically yields sheets that are too thick and heterogeneous for protein structure elucidation applications by cryoEM. L-S transfer in the presence of 2-propanol (IPA) proved successful for depositions onto 1500 mesh grids, both with and without Formvar coating; however, L-S transfers with pure water resulted in thicker heterogeneous coatings over a limited area of the holes. L-S transfer onto Si wafers under identical conditions confirmed the presence of multilayered films (Figure 3B & D). We were not able to fabricate functional coatings with 400 mesh grids using L-S transfer, a finding we attribute to the mismatch between the average GO-NTA sheet size of ~16 μm x 16 μm and the 37 μm x 37 μm grid holes of these grids. It is worth noting that the GO-NTA sheet size can vary as a function of oxidation reaction duration and sonication time employed during GO synthesis[20].

3.4.2.2 AFM Analysis of GO-NTA

To gain further insight into the structure of these GO-NTA films, SEM and AFM analyses were performed after compression to 15 mN/m and L-S transfer of GO-NTA monolayer sheets onto Si wafers. To prepare Si wafers for L-S transfer, ~2.25 cm^2 wafers were cut and glued (bottom side) onto a transfer tube. The surface pressure was maintained until the Si wafer contacted the monolayer; the film was then recompressed to

15 mN/m after the L-S transfer step. The area difference before and after L-S transfer indicated transfer efficiencies of 75 – 85%.

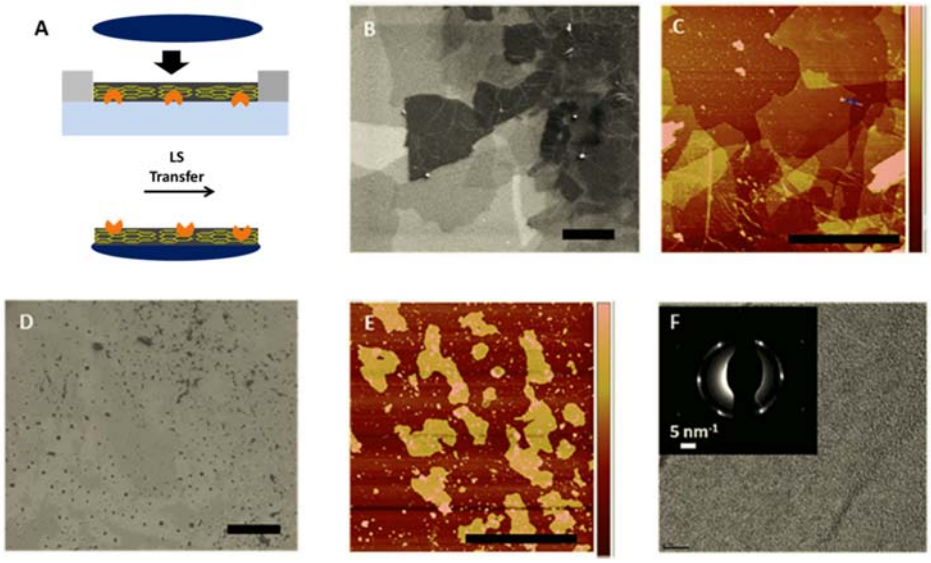

Figure 3.5 Characterization of GO-NTA Surfaces. (A) Pressure-area isotherm for GO-NTA sheets at the air:water interface, dispersed at 67 ng/mL in water at 20 °C. GO-NTA sheets compressed at a rate of 500 mm^2/min. (B) SEM images taken 1.0 keV, with 5 µm scale bar and (C) AFM images of GO-NTA after LS-transfer onto Si wafers from a subphase of pure H_2O (5 µm scale bar). (D) SEM images taken at 0.5 keV (5 µm scale bar) and (E) AFM of GO-NTA after LS-transfer onto Si wafers from a subphase of IPA/H_2O (5 µm scale bar). (F) TEM image of GO-NTA monolayers after LS transfer from a subphase of IPA/H_2O onto TEM grids; Inset: Selected area electron diffraction analysis of GO-NTA monolayer.

Image analysis of the coated Si wafers revealed the presence of GO-NTA monolayer sheets transferred from IPA-containing subphases with ~1.3 nm thicknesses that were relatively uniform (Figure 3D & E), in good agreement with previously reported values for single layer GO[21]. In the absence of IPA; however, data from SEM

and AFM experiments revealed GO-NTA films comprised of overlapping sheets and undesirable layer thickness variations (Figure 3.5 B & C).

3.4.2.3 SEM and SAED Analysis of GO-NTA

Selected area electron diffraction analysis of GO-NTA L-S films deposited onto bare 2000 mesh grids from the air-IPA/H_2O interface revealed a hexagonal diffraction pattern, indicative of a single layer of graphenic material (Figure 3.5 F). The measured intensity of the inner and outer peaks confirms the presence of a single GO-NTA layer (Figure 3.6)[19].

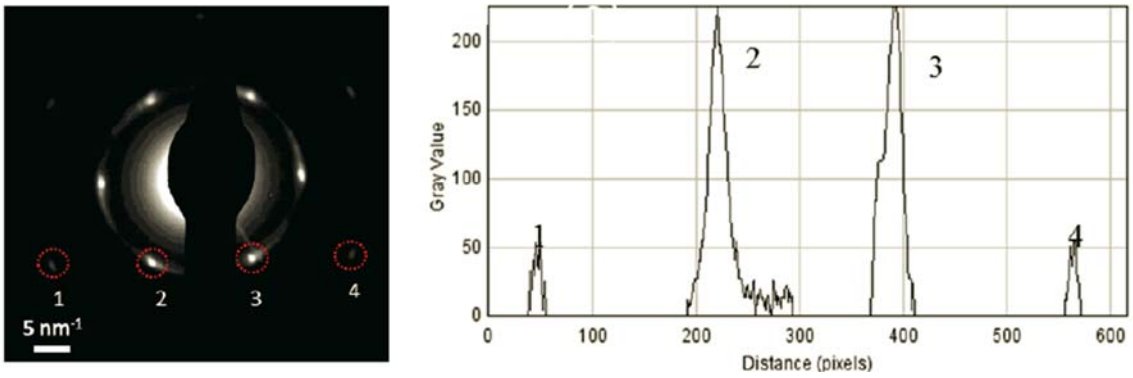

Figure 3.6 SAED of GO-NTA L-S Films on Bare 2000 Mesh TEM Grids.

3.4.3 Affinity Capture of His_6-T7 Phage Using BSA and PABA as Antifouling Agents

The capacity of GO-NTA coated grids to capture his_6-T7 bacteriophage (his_6-T7) by affinity interaction was examined first by negative-stain TEM. After a 2 min exposure of purified his_6-T7 on GO-NTA modified 1500 mesh grids, dense clusters of phage particles were found on the GO-NTA surface in the absence of Ni^{2+} (Figure 3.7 A). Paradoxically, we observed fewer phage particles after charging the GO-NTA grids with Ni^{2+} (Figure 3.7 B). We attribute these findings to non-specific and random covalent coupling of lysine residues with epoxide and aldehyde residues on the GO sheets that are inactivated upon exposure to the metal ion[22]. To obviate this problem, we chemically deactivated these functional groups by treatment of GO-NTA with 4-aminobenzoic acid (PABA) after L-S transfer. The resulting PABA-GO-NTA grids showed a reduction in, but incomplete abrogation of, non-specific His_6-T7 binding under the same incubation conditions (Figure 3.7 C). When activated with Ni^{2+}, PABA-GO-NTA grids revealed a higher density of phage particles due to engagement of the NTA:Ni^{2+}:his_6 affinity interaction (Figure 3.7 D).

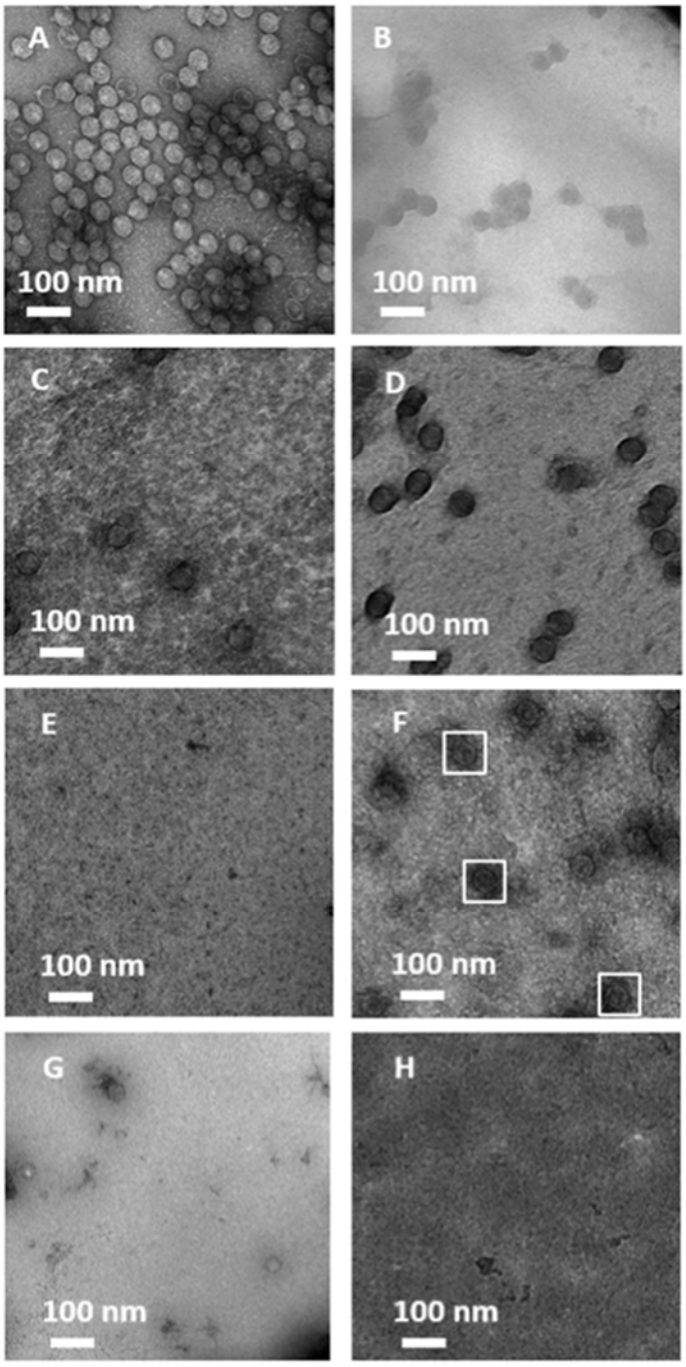

Figure 3.7 Micrographs of Negatively Stained His_6-T7 Bacteriophage Using Various TEM Grid Coatings: (A, B) GO-NTA; (C, D) PABA-GO-NTA; and (E–H) BSA-PABA-GO-NTA. Negative controls (A, C, E) demonstrate no capture of purified phage when Ni^{2+} is absent, whereas coatings treated with Ni^{2+} (B, D, F) show capture of purified phage. Affinity capture of phage from lysate (G) can be reversed by incubation of (G) with 500 mM imidazole (H) that removes the Ni^{2+} from the coating and abrogates the affinity interaction between the phage and the grid surface.

To further enhance the anti-fouling properties of this material, we incubated the PABA-GO-NTA grids with BSA immediately before the affinity capture step. Under these conditions, BSA appears to complete the blockade of non-specific viral particle adsorption (Figure 3.7 E), suggesting that BSA inhibits non-specific binding more effectively than PABA modification. After Ni^{2+} activation of the BSA-blocked PABA-GO-NTA surfaces, we observed a recovery in his_6-T7 binding to the grids (Figure 3.7 F). To further demonstrate the Ni^{2+} dependence of this interaction, we treated the grid with 500 mM imidazole, leading to the elution of his_6-T7 from the grid (data not shown). Taken together, these findings demonstrate the importance of deactivating highly reactive chemical functionalities on the surface of GO prior to use in affinity capture experiments.

Next, we sought to capture his_6-T7 directly from clarified *E. coli* lysate. The engineered His-tag does not interfere with his_6-T7 infectivity, thereby enabling the infection of BL21 cells and viral replication *in vitro*. A negative control experiment demonstrated that Ni^{2+}-free BSA-PABA-GO-NTA grids resulted in little or no capture of phage and minimal background adsorption from non-targeted cellular material (Figure S4); however, Ni^{2+} activation prompted selective his_6-mediated binding of bacteriophage to the grid surface (Figure 3.7 G). As an additional control, the grid was washed with 500 mM imidazole after Ni^{2+}, but prior to incubation with lysate, to demonstrate that imidazole stripping of the metal ion results in the abrogation of his_6-T7 binding (Figure 3.6 H). These results indicate that BSA-PABA-GO-NTA coated grids are able to effectively purify his_6-T7 directly from clarified lysate on the grid using the reversible NTA:Ni^{2+}:his_6 affinity interaction.

3.4.4 Affinity Capture of His_6-GroEL from Lysate Using BSA-PABA-GO-NTA Affinity Grids

The performance of antifouling BSA-PABA-GO-NTA coatings for high-resolution single particle reconstruction analysis was then evaluated by performing on-grid affinity capture of his_6-GroEL from *E. coli* lysates. As observed for His_6-T7 capture, specific binding of his_6-GroEL occurred only with Ni^{2+}-activated (Figure 3.8 B), but not Ni^{2+}-free (Figure 3.8 A) or 500 mM imidazole treated grids (Figure 3.8 C).

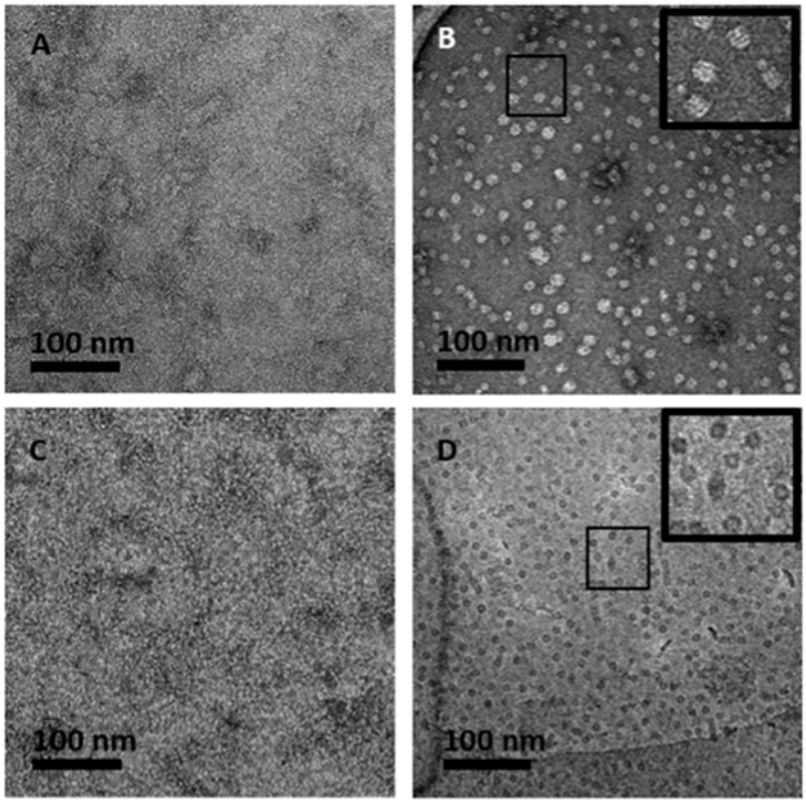

Figure 3.8 Micrographs of His_6-GroEL Lysate Affinity Capture Using BSA-PABA-GO-NTA TEM Grid Coating. Micrographs (A–C) are negatively stained. (A) Negative control showing no capture of his_6-GroEL when Ni^{2+} is absent. (B) Affinity coating activated with Ni^{2+} displays specific capture of his_6-GroEL from lysate. Treatment of the grid in (B) with 500 mM imidazole (C) leads to Ni^{2+} stripping from the coating and abrogation of his_6-GroEL capture. (D) Representative cryo-EM image of affinity captured his6-GroEL from lysate.

Next, we obtained cryo-EM images of his_6-GroEL deposited onto BSA-PABA-GO-NTA coated grids (Figure 3.8 D). Initial attempts at his_6-GroEL capture and cryofixation on 1500 mesh grids coated with BSA-PABA-GO-NTA generated unacceptably thick sample vitrification; however, high quality samples of his_6-GroEL captured from lysate were afforded by BSA-PABA-GO-NTA films deposited by L-S transfer onto lacey carbon-supported 400 mesh copper grids.

3.4.5 Single-Particle Analysis of His_6-GroEL

EMAN 2.1[23] was used for single particle analysis of his_6-GroEL deposited onto BSA-PABA-GO-NTA coated grids since this protein target is often used for gauging workflow performance and data processing robustness[24]. The reconstruction effort followed the usual steps from within the application, except that the particles were manually picked. Background signal contributions by the BSA blocking layer may also have contributed to the difficulties encountered during attempts at automated particle picking. Nonetheless, 5363 particles were hand-picked from 217 micrographs and the particles rapidly converged into coherent classes displaying high contrast (Figure 3.9 A).

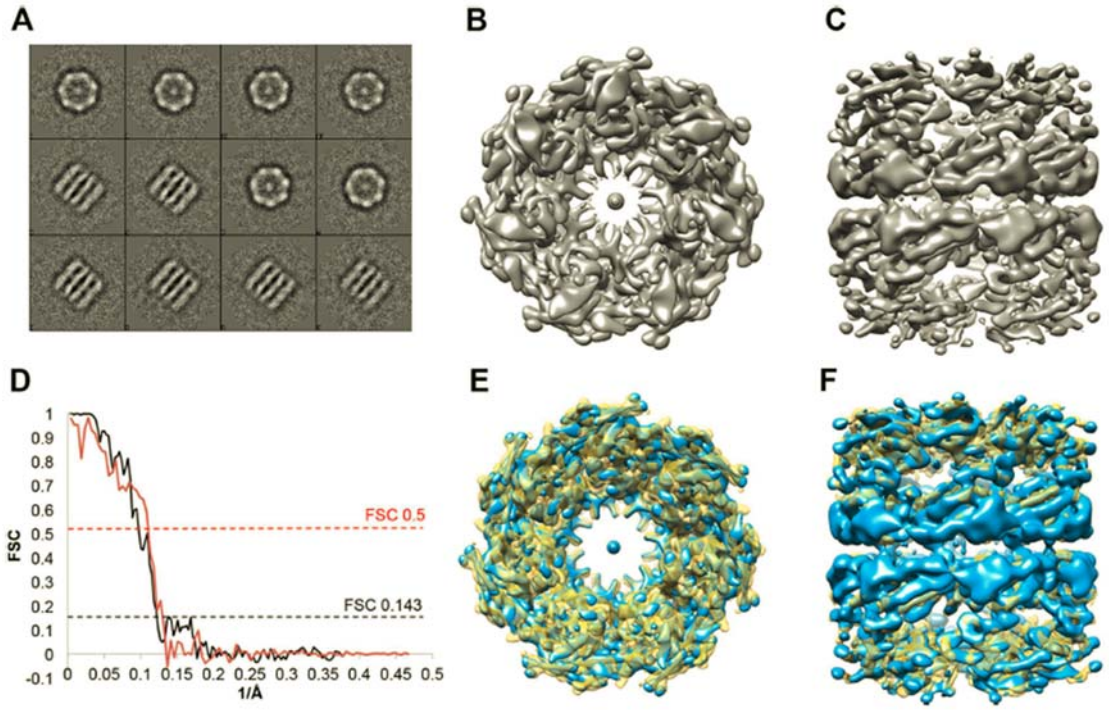

Figure 3.9 Single-Particle Analysis of his_6-GroEL Captured from Lysate. (A) Class averages of his_6-GroEL images captured from BSA-PABA-GO-NTA coated grids that were used to build the initial model; (B) Top and (C) side views of refined his_6-GroEL EM map at 8.1 Å resolution (gold standard, 0.143 criteria); (D) Fourier Shell Correlations: gold standard using conservative masking (black), and cross-validation between published GroEL map EMD-5001 and our map (red); (E) Top and (F) side views of overlay with our his_6-GroEL EM map (blue) and EMD-5001 (yellow).

Of 50 total class averages, 12 were chosen to produce an initial model with imposed D7 symmetry (Figure 3.9 A). After 12 refinement iterations with an angular sampling of 1.76 degrees, we were able to produce a gold standard (0.143 criteria) density map having 8.1 Å resolution using conservative masking (Figures 3.9 B-D). There were visible nodes in the FSC curve at regular intervals that resulted from an uneven distribution of micrograph defocuses.

To verify the accuracy of our model, we performed a comparison with published 4.2 Å resolution cryo-EM map EMD-5001[24c] that was also produced by EMAN using D7 symmetry. Chimera[25] was used to fit the volumes before calculating the FSC, yielding a 9 Å resolution using 0.5 criteria (Figure 3.9 D-F).

A substantial difference between our map and the published structure was observed, wherein additional electron density within the inner pore of the protein was found in the case of our his_6-GroEL map. We attribute this finding to the extended amino acid sequences at the N- and C-termini (i.e., MRGSHHHHHHTDPALRA and GLCGR, respectively) of our his_6-GroEL construct derived from the ASKA Library.

Wild type N- and C-termini of the protomers are located at the surface of the inner pore lining the assembled tetradecameric complex. Thus, the 14 engineered subunits comprising our His_6-GroEL complex yield an additional 308 residues that occupy the pore, of which 84 are histidines. Given the large number of potential metal chelation regioisomers and topoisomers, as well as the high potential for conformational flexibility in the N- and C-terminal sequences, we believe that this density is unlikely to adopt a defined structure and instead appears as a filled "droplet" within each ring. Also, there is a noticeable decrease in density in the flexible apical region that suggests less structural coherency. We infer from these findings that the additional pore residues, along with NTA chelation, may create dynamic distortions to the structure of GroEL that could vary for each particle, reducing coherency and map density at the apical ends. Further experiments that vary the length and number of his-tag linkers per particle may allow for a better model convergence with improved resolution, and potentially improved resemblance to wild type GroEL.

3.5 Conclusions

Our findings show that a new functionalized GO-NTA monolayer sheet can be used as a coating to facilitate on-grid affinity purification from clarified cell lysates for negative stain TEM and cryo-EM single particle reconstruction analysis. GO sheets were successfully functionalized with lysine-NTA affinity ligands and compressed monolayer films at the air-water interface were prepared by employing an IPA/H_2O mixture to lower surface tension before L-S transfer onto EM grids. SEM, AFM, fluorescence spectroscopy, and TEM analysis of these films suggests that single monolayer sheets of GO-NTA can be transferred onto Si wafers, bare copper grids, and holey carbon grids using this method. Since GO films are thinner than amorphous carbon substrates and offer better electron dissipation than lipid-based affinity grids, we believe these two benefits will yield improved contrast for cryo-EM image acquisition of biological molecules.

Two blocking techniques, PABA coupling and BSA adsorption, were needed to deactivate the reactive GO surface towards non-specific adsorption of occult impurities present in complex samples such as cell lysates. Our data shows that further investigations into blocking agents that minimize background noise and improve cryofixation reliability are needed. Nonetheless, this grid coating approach showed good specificity for capture of His-tagged T7 bacteriophage and GroEL from highly complex cell lysates, while limiting background adsorption of non-targeted cellular material.

The utility of these grids for on-grid purification from cell lysates and single particle reconstruction was demonstrated using His_6-GroEL. Capture of this target onto the surface of GO-NTA affinity grids from clarified cell lysates was then used as the key

step to enable selection of 5363 particles for reconstruction analysis, yielding a map with a gold standard resolution of 8.1 Å. The presence of additional His-tag and linker amino acids in our engineered GroEL was distinctly visible in our density map, but our final map could still be fit to a published high-resolution EM map to 9 Å resolution using 0.5 criteria. We conclude based on these findings that affinity capture-based graphenic materials offer great potential for simplified and accelerated cryo-EM sample preparation for high-resolution structure elucidation. These coatings possess many advantages over NTA-lipid-modified grids[5a, 5b] or other grid coatings that lack protection from non-specific binding[4], thereby offering substantial improvements in sample preparation time and reduced sample volumes needed to acquire high resolution structural information of a given protein target and, potentially, its interaction partners.

3.6 Experimental Methods

All reactions were carried out under a blanket of N_2 gas. Reaction progress was monitored by thin-layer chromatography (TLC) analysis. TLC spots were visualized either by UV light (254nm), exposure by ninhydrin staining (100 mL n-BuOH, 3 mL Accor, 0.3 g ninhydrin), or by staining with I_2. Flash column chromatography was carried out using 230-400 mesh silica gel and analytical grade solvents. ^{1}H and ^{13}C nuclear magnetic resonance (NMR) spectra were recorded on either a Bruker AV500HD (500MHz) or a Bruker ARX400 spectrometer (400 MHz). Chemical shifts are reported in ppm relative to the residual solvent peaks as internal standard. Flake graphite (F516, 200-300 mesh) was obtained from Asbury Carbons Inc. EDC, HOBt, and DIEA were purchased from Advanced Chemtech. DCM, toluene, and acetonitrile (ACN) were

distilled from CaH_2. Tetrahydrofuran (THF) was distilled from sodium benzophenone ketyl. All other reagents were purchased from Sigma Aldrich and used without further purification.

3.6.1 GO-NTA Synthesis

GO (**49**). A 9:1 mixture of H_2SO_4 and H_3PO_4 (130 mL total volume) was stirred with 1 g of graphite flakes (**48**, F516 flake graphite, 200-300 mesh, Asbury Carbons, Inc.) and $KMnO_4$ (6.0 g, 6.0 wt. equiv.). The reaction began with heating to ~40 °C and proceeded with further heating and stirring at 50 °C for 12 hours before cooling to 20 °C and pouring the reaction mixture into 120 mL of ice cold-water with 1 mL 30% H_2O_2. Next, this suspension was passed through a metal U.S. Standard testing sieve (W.S. Tyler, 300 μm) and then passed through a glass wool plug to filter larger particulates. The filtrate was then centrifuged at 4,000 rpm for 4 h, the supernatant discarded, and the pellet washed twice with a 1:1:1 volumetric ratio of H_2O, 30% HCl, and EtOH before passing the material through the testing sieve and centrifuging the filtrate at 4,000 rpm for 4 h to pellet the aggregated material. The supernatant was precipitated with Et_2O (200 mL) and filtered through a 0.45 μm PTFE membrane to gather the solid. The final material was dried under a 15 μm vacuum for 12 h, yielding **49** (1.8 g).

GO-NTA (**50**). **GO** (**49**, 335 mg) was stirred in a mixture of $SOCl_2$ (60 mL) and DMF (1.5 mL) at 70 °C for 72 hours before evaporating the $SOCl_2$ and DMF and washing the residue with dry DCM (3 x 50 mL). Toluene (50 mL) and Et_3N (3 mL) were then added and the mixture stirred for 30 min. Tris(O-*t*-butyl)-N^{α},N^{α}-

dicarboxymethyllysine ester (**15**, 533 mg) was then added and the mixture stirred at 70 ˚C for 72 hours before washing with THF and H_2O (9,000 rpm for 15 min, 3 times for each solvent), then vacuum drying at 60 ˚C for 24 h. TFA (10 mL) in DCM (30 mL) was added to the dried *t*-butyl-NTA ester intermediate (180 mg) and stirred at 60 ˚C for 5 h before washing with THF and H_2O (11,000 rpm x 15 min, 3 times for each solvent)[11, 26].

3.6.2 Synthesis of Pyrene-NTA

Di-tert-butyl 2,2'-((1-(tert-butoxy)-1-oxo-6-(4-(pyren-1-yl)butanamido)hexan-2-yl)azanediyl)diacetate (52). 1-Pyrenebutyric acid (**51**, 0.198 g, 0.69 mmol) Compound **15** (0.296 g, 0.69 mmol) and HOBt were combined in an oven-dried 50 mL round bottom flask equipped with a magnetic stir bar. DMF (5 mL) was added followed by EDC (0.145 g, 0.76 mmol). The contents were swirled to dissolve the solids and the flask sealed with a rubber septum and filled with argon gas. The reaction was stirred at ambient temperature for 30 minutes. DIEA (0.444 g, 3.43 mmol) was added via syringe and the reaction was stirred for an additional 36 hours at ambient temperature. Volatiles were evaporated and the residue was purified by flash chromatography using 2:3 EtOAc:hexane as eluent. Compound **52** was obtained as a slightly yellow oil. (0.447 g, 90.5 %). R_f 2:3 EtOAc:hexane 0.29. ^{1}H-NMR (500 MHz, $CDCl_3$) δ 8.25 (d, J = 9.2 Hz, 1H), 8.15 – 8.06 (m, 2H), 8.06 – 7.99 (m, 2H), 7.99 – 7.86 (m, 3H), 7.80 (d, J = 7.8 Hz, 1H), 6.19 (s, 1H), 3.56 – 3.39 (m, 4H), 3.37 – 3.23 (m, 4H), 3.18 (s, 1H), 2.28 (t, J = 7.3 Hz, 2H), 2.23 – 2.10 (m, 2H), 1.63 (s, 2H), 1.53 (s, 3H), 1.43 (s, 11H), 1.40 (s, 17H). ^{13}C NMR (126 MHz, CDCl3) δ 172.84, 172.43, 170.78, 136.15, 131.36, 130.89, 129.82,

128.73, 127.46, 127.28, 126.57, 125.76, 125.02, 124.76, 123.47, 81.12, 80.73, 77.48, 77.23, 76.97, 64.90, 53.98, 39.19, 35.98, 32.92, 29.81, 28.42, 27.57, 22.90.

2,2'-((1-Carboxy-5-(4-(pyren-1-yl)butanamido)pentyl)azanediyl)diacetic acid (53). Compound **52** (0.447 g, 0.638 mmol) was dissolved in DCM (20 mL) and triethylsilane (0.371 g, 3.191 mmol) was added. TFA (20 mL) was added and the solution turned a slight clear black color. The solution was stirred at ambient temperature for 1.5 hours under a slight argon flow. After about 40 minutes, the reaction turned a slight beige/yellow color. After 1.5 hours, the solution was concentrated *in vacuo*. The residue was combined with DCM (80 mL) and evaporated twice to remove left over TFA. The residue was dissolved in deionized water and lyophilized to give Compound **53** as a yellow powder. (0.317 g, 93.2 %). ^{1}H NMR (500 MHz, DMSO-d6) δ 12.54 (s, 2H), 8.36 (d, J = 8.9 Hz, 1H), 8.26 (d, J = 7.1 Hz, 2H), 8.20 (d, J = 6.1 Hz, 2H), 8.10 (d, J = 9.2 Hz, 2H), 8.04 (t, J = 7.1 Hz, 1H), 7.92 (d, J = 7.4 Hz, 1H), 7.78 (s, 1H), 3.60 (s, 4H), 3.48 (d, J = 13.4 Hz, 5H), 3.29 (s, 4H), 3.02 (s, 2H), 2.48 (s, 4H), 2.20 (s, 2H), 1.99 (s, 2H), 1.56 (d, J = 49.6 Hz, 2H), 1.36 (d, J = 23.3 Hz, 6H), 1.12 (d, J = 26.8 Hz, 1H), 0.88 (s, 1H). ^{13}C NMR (126 MHz, DMSO) δ 174.32, 173.53, 172.10, 137.06, 131.34, 130.89, 129.75, 128.61, 128.00, 127.91, 127.66, 126.94, 126.58, 125.38, 125.24, 124.69, 124.61, 123.98, 64.70, 53.72, 40.31, 39.97, 39.64, 38.80, 35.44, 32.74, 29.73, 29.38, 28.15, 23.62.

3.6.3 Synthesis of Triethpxysilyl-NTA

tert-Butyl 16-(2-(tert-butoxy)-2-oxoethyl)-15-(tert-butoxycarbonyl)-4,4-diethoxy-9-oxo-3-oxa-8,10,16-triaza-4-silaoctadecan-18-oate (55). Compound **15** (0.102 g, 0.237 mmol) was dissolved in THF (2 mL) in an oven-dried 25 mL round bottom flask equipped with a rubber septum and magnetic stir bar. The solution was evacuated and purged with argon before cooling to 0 °C in an ice bath and addition of 3-(triethoxysilyl)propyl isocyanate (**54**) via syringe dropwise over 3 minutes. The solution was allowed to warm to ambient temperature and stirred for an additional 18 hours. The volatiles were evaporated *in vacuo* and the residue was purified by flash chromatography using 95:5 DCM:MeOH as eluent to give Compound **55** as a colorless oil. (0.142 g, 77.3 %). ^{1}H NMR (500 MHz, Chloroform-*d*) δ 3.74 (q, *J* = 7.0 Hz, 6H), 3.47 – 3.32 (m, 4H), 3.29 – 3.21 (m, 1H), 3.21 – 3.13 (m, 1H), 3.09 (d, *J* = 3.7 Hz, 3H), 1.59 (d, *J* = 6.4 Hz, 3H), 1.55 – 1.47 (m, 3H), 1.39 (d, *J* = 4.3 Hz, 27H), 1.15 (t, *J* = 7.0 Hz, 10H). ^{13}C NMR (126 MHz, $CDCl_3$) δ 172.48, 170.85, 158.61, 81.08, 80.83, 76.83, 64.89, 58.29, 54.00, 42.88, 39.68, 29.57, 28.58, 28.16, 23.79, 22.51, 18.26, 7.63.

3.6.4 GO-NTA Exfoliation

The GO-NTA **50** sheets were ultrasonically exfoliated at 1 mg/mL by suspension of the powder in 5:1 MeOH:H_2O using probe sonication at 150 watts for five cycles (45 s sonication followed by 45 s of rest in each cycle). The product was centrifuged at 1200 g for 10 min, after which the supernatant of exfoliated GO-NTA sheets was removed from the sediment of aggregated sheets and subjected to another 5 rounds of sonication. A final

centrifugation at 1200 g for 10 min was performed prior to removal of the supernatant to yield a GO-NTA solution that was stored for subsequent grid coating experiments.

3.6.5 Langmuir Trough Setup

Exfoliated GO-NTA was deposited at the air-water interface of a Kibron μTrough via a syringe pump fitted with a 20 mL syringe. The GO-NTA dispersion was loaded into the syringe and slowly introduced at the air-water interface at a rate of 100 μL/min until the surface pressure reached 15 mN/m. The film was then allowed to relax for 5 min, followed by slow compression of the film to 15 mN/m. IPA was then added to the subphase and the film transferred to either Si wafers, bare 1500 mesh TEM grids, or holey carbon grids by Langmuir-Schaefer (L-S) transfer.

3.6.6 4-Aminobenzoic Acid (PABA) Modification of GO-NTA

GO-NTA (1 mg/mL) was partially deactivated by adding PABA (30 mg) to a 10 mL GO-NTA dispersion. This mixture was probe sonicated at 150 W for 30 sec of continuous sonication, followed by shaking for 24 h on a rotary mixer. The PABA-GO-NTA was then exfoliated and washed as described above for GO-NTA exfoliation.

3.6.7 Fluorescein Modification of GO-NTA

Fluorescein modification of GO-NTA was performed by adding 2 mg of aminofluorescein to an aqueous solution of PABA-GO-NTA (10 mL at 1 mg/mL). This mixture was probe sonicated for 30 s at 150 W of continuous sonication and then placed

on a rotary mixer in the dark for another 24 h. The material was then centrifuged to pellet the GO species before re-suspending in water, addition of 5:1 MeOH:H_2O, re-pelleted, and decanted a total of 10 times before exfoliation of the Fluorescein-PABA-GO-NTA (F-PABA-GO-NTA) product as described above for GO-NTA.

3.6.8 Bovine Serum Albumin (BSA) Modification of GO-NTA

Following L-S transfer of GO-NTA or PABA-GO-NTA onto EM grids and overnight drying in a desiccator, the grids were placed on a strip of Teflon before addition of BSA (10 µL of 0.1 mg/mL) and incubation for 5 min, followed by 3 x 20 µL double deionized H_2O washes. The modified grids were then stored in a desiccator until use.

3.6.9 Fluorescence Microscopy Sample Preparation

F-PABA-GO-NTA was deposited onto 1500 mesh grids in the dark by L-S transfer as described above. After transfer, the grids were allowed to dry in the dark for 1 d before sandwiching them between a glass and cover slip with 5 µL of double deionized H_2O and the sandwich sealed with nail polish. The glass slide was then mounted on a light microscope for epifluorescence imaging.

3.6.10 GO Concentration Measurements

The concentrations of the GO-NTA dispersions were measured at different steps of the synthesis by monitoring the UV-vis spectra of the products. The extinction coefficient data used for one batch of GO-NTA is shown (Figure S1A). Since each batch of GO-NTA has minor differences in concentration, each preparation was evaluated for its own experimentally determined extinction coefficient for subsequent concentration measurements. Standard solutions used to determine the extinction coefficients were prepared by dispersing a weighed amount of dry GO-NTA into known volumes of 5:1 MeOH:H_2O and measuring the absorbance at 280 nm across a series of dilutions with 5:1 MeOH:H_2O. The extinction coefficient was derived from the slope of these concentration-dependent absorption plots.

3.6.11 GO-NTA Grid Treatment with Purified His_6-T7 Phage

Purified C-terminal gp10 His_6-T7 bacteriophage was initially prepared at a concentration of 10^{12} particles/mL, with dilution to 10^{10} particles/mL in HEPES buffer (pH = 7.4) before application to the affinity grid surface. GO-NTA modified grids were placed on a Teflon strip, 1 mM $NiSO_4$ (10 μL) added and the grids incubated for 5 min before washing with double deionized H_2O (2 x 20 μL) and HEPES buffer (1 x 20 μL). Purified phage (3.5 μL) was then applied to the surface and incubated for 2 min before washing with HEPES (2 x 20 μL), double deionized H_2O (1 x 20 μL), and staining with 2% uranyl acetate (5 μL).

3.6.12 GO-NTA Grid Treatment with His_6-T7 Phage Lysate

BL21 bacterial cells in 1 mL of LB media were grown to an OD of 0.8 before adding 1.0 µL of His_6-T7 bacteriophage (1×10^{12} particles/mL) to the media and shaking the culture for 1 h. After bench top centrifugation of the cells, the supernatant was withdrawn for use in His_6-T7 bacteriophage particle capture studies. The grids were Ni^{2+}-activated as described above, except that His_6-T7 lysate (5 µL) was applied to the surface before incubation for 2 min. The grids were then washed with HEPES (2 x 20 µL), double deionized H_2O (1 x 20 µL), and then stained with 2% uranyl acetate (5 µL).

3.6.13 GO-NTA Grid Treatment with His_6-GroEL Lysate

The ASKA Library was used to express N-terminal His_6-GroEL. Cells containing N-His_6-GroEL gene overexpression vector were grown to OD = 0.6 (in 100 mL of LB broth using a 37 ˚C shaker/incubator) and induced with a final concentration of 1.0 mM IPTG, before allowing the cells to grow for an additional 4 h. After centrifugation and removal of the supernatant, the cell pellet was re-suspended in lysis buffer (20 mM HEPES, 100 mM NaCl, pH = 7.4, 100 µg aprotinin, 174 µg phenylmethanesulfonyl fluoride (PMSF), and 500 µg of lysozyme) and allowed to sit for 20 min. Further disruption of the cell membranes was effected by 110 W probe sonication (35 pulses at 1 second/pulse), followed by centrifugation at 11,000 g for 10 min. The supernatant containing His_6-GroEL was diluted 10-fold and assayed for affinity binding using the Ni^{2+}-activation procedure described above, except that N-His_6-GroEL lysate (5 µL) was applied to the surface and incubated for 2 min. The grids were then washed and stained with 2% uranyl acetate as described above.

3.6.14 Affinity Capture of His_6-GroEL from Lysate onto BSA-PABA-GO-NTA Affinity Grids for Cryo-EM Imaging

Samples were prepared as described above for negative stain TEM imaging, except that BSA-PABA-GO-NTA modified grids were exposed to His_6-GroEL lysate, after which the excess solution was removed by blotting twice for 6 s per blot using an offset setting of -1 at 80% humidity using a Vitrobot device (FEI Company). The grids were then plunged into liquid ethane for cryofixation and imaged at 300 kV on an FEI Titan Krios equipped with a Gatan K2 Summit direct electron detection camera using low-dose techniques. Integrated microscope automation software Leginon[27] was used to acquire a large set of micrographs at 11,000x magnification with an exposure time of 7.6 sec.

3.6.15 Single-Particle Analysis of His_6-GroEL

Direct electron detector movie frames were processed in Appion[28] to produce a set of averaged, motion-compensated micrographs to be used in subsequent steps. The micrographs had a 1.32 $Å^2$/pixel resolution across a 4096 Å x 4096 Å array. EMAN 2.1 software[31] was used for reconstruction of 5363 particles that were manually picked from 217 micrographs using a box size of 256. Automatic contrast transfer function (CTF) estimation and structure factor were determined from the incoherent sum of particles using e2ctf and phase-flipped to generate high-pass CTF-corrected particle stacks. Defocus was estimated to range between 0.4 μm – 4 μm, but 55% of the particles were defocused between 2 μm – 3 μm which resulted in a somewhat jagged CTF slope. Particles were binned 2X for class averaging and 12 classes were chosen to create an

initial model with imposed D7 symmetry. The classes contained a mix of top and side views. In the refinement steps, the input set of particles was divided into even/odd halves, each containing 2682 particles. Two independent refinements were generated, producing a gold standard of 8.1 Å (using 0.143 criteria) after 12 iterations over two refinements with an angular sampling of 1.76 degrees. Additionally, we performed Fourier shell correlation against an existing high-resolution cryo-EM map, EMD-5001[34]. The maps were rotated and translated using Chimera[35] to fit the volumes together. The correlation of our model against EMD-5001 (4.2 Å) gave an approximate resolution of 9 Å.

3.7 Acknowledgements

Asbury Carbons Inc. is acknowledged for its generous donation of flake graphite for basic research. Christopher J. Benjamin performed the Fluorescence microscopy, TEM, and cryo-EM. Scott Bolton did the reconstruction of His-GroEL. Dr. Seok-Hee Hyun performed the AFM, SEM, and SAED measurements.

3.8 References

1. (a) Bartesaghi, A. M.; Banerjee, S.; Matthies, D.; Wu, X.; Milne, J. L. S.; Subramaniam, S., 2.2 Å Resolution Cryo-EM Structure of β-Galactosidase in Complex with a Cell-Permeant Inhibitor. *Science* **2015,** *348* (6239); (b) Banerjee, S.; Bartesaghi, A.; Merk, A.; Rao, P.; Bulfer, S. L.; Yan, Y.; Green, N.; Mroczkowski, B.; Neitz, R. J.; Wipf, P.; Falconieri, V.; Deshaies, R. J.; Milne, J. L.; Huryn, D.; Arkin, M.; Subramaniam, S., 2.3 A Resolution Cryo-EM Structure of Human p97 and Mechanism of Allosteric Inhibition. *Science* **2016,** *351* (6275), 871-5.

2. Cheng, Y.; Grigorieff, N.; Penczek, P. A.; Walz, T., A Primer to Single-Particle Cryo-Electron Microscopy. *Cell* **2015,** *161* (3), 438-49.

3. (a) Jiang, Q. X.; Chester, D. W.; Sigworth, F. J., Spherical Reconstruction: a Method for Structure Determination of Membrane Proteins from Cryo-EM Images. *J Struct Biol* **2001,** *133* (2-3), 119-31; (b) Wang, L.; Sigworth, F. J., Structure of the BK Potassium Channel in a Lipid Membrane from Electron Cryomicroscopy. *Nature* **2009,** *461* (7261), 292-5; (c) Kelly, D. F.; Abeyrathne, P. D.; Dukovski, D.; Walz, T., The Affinity Grid: a Pre-Fabricated EM Grid for Monolayer Purification. *J. Mol. Biol.* **2008,** *382* (2), 423-33.

4. (a) Russo, C. J.; Passmore, L. A., Controlling Protein Adsorption on Graphene for Cryo-EM Using Low-Energy Hydrogen Plasmas. *Nature Methods* **2014,** *11* (6), 649-52; (b) Meyerson, J. R.; Rao, P.; Kumar, J.; Chittori, S.; Banerjee, S.; Pierson, J.; Mayer, M. L.; Subramaniam, S., Self-Assembled Monolayers Improve Protein Distribution on Holey Carbon Cryo-EM Supports. *Sci Rep* **2014,** *4*, 7084; (c) Russo, C. J.; Passmore, L. A., Ultrastable Gold Substrates: Properties of a Support for High-Resolution Electron Cryomicroscopy of Biological Specimens. *J Struct Biol* **2016,** *193* (1), 33-44.

5. (a) Kelly, D. F.; Dukovski, D.; Walz, T., Monolayer Purification: a Rapid Method for Isolating Protein Complexes for Single-Particle Electron Microscopy. *Proc Natl Acad Sci U S A* **2008,** *105* (12), 4703-8; (b) Kelly, D. F.; Dukovski, D.; Walz, T., Strategy for the Use of Affinity Grids to Prepare Non-His-Tagged Macromolecular Complexes for Single-Particle Electron Microscopy. *J. Mol. Biol.* **2010,** *400* (4), 675-81; (c) O. Kutsay, O. L., A. Gontar, V. Perevertailo, O. Zanevskyy, A. Katrusha, S. Ivakhnenko, V. Gorokhov, S. Starik, V. Tkach, and N. Novikov, Surface Properties of Amorphous Carbon Films. *Diamond Relat Mater* **2008,** *17* (7-10), 1689-1691.

6. (a) Kubalek, E. W.; Le Grice, S. F.; Brown, P. O., Two-Dimensional Crystallization of Histidine-Tagged, HIV-1 Reverse Transcriptase Promoted by a Novel Nickel-Chelating Lipid. *J Struct Biol* **1994,** *113* (2), 117-23; (b) Lutz Schmitt, C. D., Robert Tampe, Synthesis and Characterization of Chelator-Lipids for Reversible Immobilization of Engineered Proteins at Self-Assembled Lipid Interfaces. *J Am Chem Soc* **1994,** *116* (19), 8485-8491; (c) Barklis, E.; McDermott, J.; Wilkens, S.; Schabtach, E.; Schmid, M. F.; Fuller, S.; Karanjia, S.; Love, Z.; Jones, R.; Rui, Y.; Zhao, X.; Thompson, D., Structural Analysis of Membrane-Bound Retrovirus Capsid Proteins. *EMBO J* **1997,** *16* (6), 1199-213; (d) Thompson, D. H.; Zhou, M. K.; Grey, J.; Kim, H. K., Design, Synthesis, and Performance of NTA-Modified Lipids as Templates for Histidine-Tagged Protein Crystallization. *Chem Lett* **2007,** *36* (8), 956-975.

7. Benjamin, C. J.; Wright, K. J.; Hyun, S. H.; Krynski, K.; Yu, G.; Bajaj, R.; Guo, F.; Stauffacher, C. V.; Jiang, W.; Thompson, D. H., Nonfouling NTA-PEG-Based TEM Grid Coatings for Selective Capture of Histidine-Tagged Protein Targets from Cell Lysates. *Langmuir* **2016,** *32* (2), 551-9.

8. Marcano, D. C.; Kosynkin, D. V.; Berlin, J. M.; Sinitskii, A.; Sun, Z. Z.; Slesarev, A.; Alemany, L. B.; Lu, W.; Tour, J. M., Improved Synthesis of Graphene Oxide. *ACS Nano* **2010,** *4* (8), 4806-4814.

9. Zhang, J.; Yu, J.; Jaroniec, M.; Gong, J. R., Noble Metal-Free Reduced Graphene Oxide-ZnxCd(1)-xS Nanocomposite with Enhanced Solar Photocatalytic H(2)-Production Performance. *Nano Lett* **2012,** *12* (9), 4584-9.

10. Guoxiu Wang, B. W., Jinsoo Park, Juan Yang, Xiaoping Shen, Jane Yao, Synthesis of Enhanced Hydrophilic and Hydrophobic Graphene Oxide Nanosheets by a Solvothermal Method. *Carbon* **2009,** *47* (1), 68-72.

11. Paredes, J. I.; Villar-Rodil, S.; Martinez-Alonso, A.; Tascon, J. M., Graphene Oxide Dispersions in Organic Solvents. *Langmuir* **2008,** *24* (19), 10560-4.

12. Gengler, R. Y.; Veligura, A.; Enotiadis, A.; Diamanti, E. K.; Gournis, D.; Jozsa, C.; van Wees, B. J.; Rudolf, P., Large-Yield Preparation of High-Electronic-Quality Graphene by a Langmuir-Schaefer Approach. *Small* **2010,** *6* (1), 35-9.

13. Jaemyung Kim, L. J. C., Franklin Kim, Wa Yuan, Kenneth R. Shull, and Jiaxing Huang, Graphene Oxide Sheets at Interfaces. *J Am Chem Soc* **2010,** *132*, 8180-8186.

14. Ed. by Burrows, H. W., Ron / Stohner, Jürgen, Graphene Oxide as Surfactant Sheets. *Pure Appl Chem* **2010,** *83* (1), 95-110.

15. Cote, L. J.; Kim, F.; Huang, J. X., Langmuir-Blodgett Assembly of Graphite Oxide Single Layers. *J Am Chem Soc* **2009,** *131* (3), 1043-1049.

16. Kim, J.; Cote, L. J.; Huang, J., Two Dimensional Soft Material: New Faces of Graphene Oxide. *AccChem Res* **2012,** *45* (8), 1356-64.

17. Qingbin Zheng, L. S., Peng-Cheng Ma, Qingzhong Xue, Jing Li, Zhihong Tanga and Junhe Yang, Structure Control of Ultra-Large Graphene Oxide Sheets by the Langmuir-Blodgett Method. *RSC Advances* **2013,** *3*, 4680-4691.

18. Z. H. Ni, H. M. W., J. Kasim, H. M. Fan, T. Yu, Y. H. Wu, Y. P. Feng, and Z. X. Shen, Graphene Thickness Determination Using Reflection and Contrast Spectroscopy. *Nano Lett* **2007,** *7* (9), 2758-2763.

19. Wilson, N. R.; Pandey, P. A.; Beanland, R.; Young, R. J.; Kinloch, I. A.; Gong, L.; Liu, Z.; Suenaga, K.; Rourke, J. P.; York, S. J.; Sloan, J., Graphene Oxide: Structural Analysis and Application as a Highly Transparent Support for Electron Microscopy. *ACS Nano* **2009,** *3* (9), 2547-56.

20. Pan, S.; Aksay, I. A., Factors Controlling the Size of Graphene Oxide Sheets Produced via the Graphite Oxide Route. *ACS Nano* **2011,** *5* (5), 4073-83.

21. Jinping Song, J. Q., Shaomin Shuang, Yujing Guo and Chuan Dong, Synthesis of Neutral Red Covalently Functionalized Graphene Nanocomposite and the Electrocatalytic Properties Toward Uric Acid. *J Mater Chem* **2012,** *22*, 602-608.

22. Ema, T.; Miyazaki, Y.; Koyama, S.; Yano, Y.; Sakai, T., A Bifunctional Catalyst for Carbon Dioxide Fixation: Cooperative Double Activation of Epoxides for the Synthesis of Cyclic Carbonates. *Chem Comm* **2012,** *48* (37), 4489-91.

23. Tang, G.; Peng, L.; Baldwin, P. R.; Mann, D. S.; Jiang, W.; Rees, I.; Ludtke, S. J., EMAN2: an Extensible Image Processing Suite for Electron Microscopy. *J Struct Biol* **2007,** *157* (1), 38-46.

24. (a) Ludtke, S. J.; Jakana, J.; Song, J. L.; Chuang, D. T.; Chiu, W., A 11.5 A Single Particle Reconstruction of GroEL Using EMAN. *J Mol Biol* **2001,** *314* (2), 253-62; (b) Ludtke, S. J.; Chen, D. H.; Song, J. L.; Chuang, D. T.; Chiu, W., Seeing GroEL at 6 Å Resolution by Single Particle Electron Cryomicroscopy. *Structure* **2004,** *12* (7), 1129-36; (c) Ludtke, S. J.; Baker, M. L.; Chen, D. H.; Song, J. L.; Chuang, D. T.; Chiu, W., De Novo Backbone Trace of GroEL from Single Particle Electron Cryomicroscopy. *Structure* **2008,** *16* (3), 441-8.

25. Pettersen, E. F.; Goddard, T. D.; Huang, C. C.; Couch, G. S.; Greenblatt, D. M.; Meng, E. C.; Ferrin, T. E., UCSF Chimera--a Visualization System for Exploratory Research and Analysis. *J Comput Chem* **2004,** *25* (13), 1605-12.

26. Laura J. Cote, J. K., Zhen Zhang, Cheng Sun, and Jiaxing Huang Tunable Assembly of Graphene Oxide Surfactant Sheets: Wrinkles, Overlaps and Impacts on Thin Film Properties. *Soft Matter* **2010,** *6*, 6096-6101.

27. Suloway, C.; Pulokas, J.; Fellmann, D.; Cheng, A.; Guerra, F.; Quispe, J.; Stagg, S.; Potter, C. S.; Carragher, B., Automated Molecular Microscopy: the New Leginon System. *J Struct Biol* **2005,** *151* (1), 41-60.

28. Lander, G. C.; Stagg, S. M.; Voss, N. R.; Cheng, A.; Fellmann, D.; Pulokas, J.; Yoshioka, C.; Irving, C.; Mulder, A.; Lau, P. W.; Lyumkis, D.; Potter, C. S.; Carragher, B., Appion: an Integrated, Database-Driven Pipeline to Facilitate EM Image Processing. *J Struct Biol* **2009,** *166* (1), 95-102.

CHAPTER FOUR:
DEVELOPMENT OF AFFINITY POLYROTAXANE CONSTRUCTS FOR SINGLE PARTICLE CRYO-EM

4.1 Introduction

There are great opportunities for the design of new organic materials as tools for the elucidation of protein structure[1], particularly in cases where traditional structure determination methods are ineffective or impractical. A host of different materials and approaches for interfacial templating have been developed including affinity lipids[2], facial amphiphiles[3], conformationally-restricted amphiphiles[4], nanodiscs[5], lysolipid-guided cubic phase formation[6], symmetry-guided chelation[7], and polymer nucleants[8]. Some of these agents are directed toward the accelerated production of protein crystals for x-ray diffraction (XRD) analysis, while others are intended to facilitate single particle analysis (SPA) by cryoelectron microscopy (cryo-EM).

XRD and NMR based methods account for the vast majority of high-resolution protein structures to date[9], however, these methods are exceptionally challenging for the analysis of integral membrane protein (IMP), multiprotein complex structures, and other biomacromolecular assemblies, such as viral particles. Cryo-EM has become an increasingly powerful method for determining the three-dimensional structures of proteins and their assemblies via SPA[10]. Recently, the technique has been used to determine protein structural information at 2.2 Å resolution[11]. Cryo-EM, unlike other

electron microscopy techniques, does not require staining or embedding in non-physiological media. A key challenge for structure determination via cryo-EM is that the method requires the collection of more than 30,000 images of the target structure to enable image reconstruction at near atomic resolution. Since protein concentrations used for SPA are typically in the μg-mg/mL range, data collection is a laborious and time-consuming process under these conditions because there are typically a limited number of particles in the field of view at the magnification (18,000-24,000x) required to image the nano-scale targets. Thus, accelerated SPA by cryo-EM requires the development of materials and methods that increase the probability of finding the target particles in the vitrified sample.

One method of overcoming this challenge is through the use of automated methods[12]. Alternative strategies seek to concentrate proteins at material interfaces for structural analysis. The first effort of this type was reported by Kornberg[13] and coworkers who used antibody-based affinity interactions to concentrate protein targets on affinity lipid monolayer surfaces.

The desire for more general methods to promote specific monolayer-protein interactions eventually led to the development of NTA-modified lipids that are capable of binding recombinant proteins bearing six or more repeating histidine residues (i.e. his-tag). Thompson and coworkers first demonstrated the ability of NTA-lipids to facilitate the two-dimensional crystallization and structural determination of his-tagged Moloney leukemia virus capsid (his_6-MoCA) at the air-water interface[14]. Negative-stain TEM was used to determine the his_6-MoCA structure at 9.5 Å resolution. More recently, this

method has been adapted and used by Walz[15] and coworkers for the elucidation of the-transferrin receptor complex and the human rp13 ribosomal complex.

A disadvantage of the lipid-monolayer approach, however, is that two-dimensional crystals or adsorbates can only be used to produce projection maps of the target structure unless a tilt series of images is collected to produce a three-dimensional structure with a "missing cone" due to sample tilting limitations beyond ~60˚. The lipid-tubule method[16] was developed to overcome these difficulties by using liquid-phase galactosylceramide lipid tubule templates that have been doped with low molar ratios of affinity lipids to promote specific interactions with the lipid template surface. These materials enable specific adsorption of proteins such that a single TEM image reveals all orientations of the adsorbed molecules, thereby eliminating the need for tilt-series imaging or multiple constructs of the protein with the affinity tag placed at different protein loci. This approach enabled the rapid elucidation of perfringolysin 0 at ~25 Å resolution[17]. The major limitation of this approach is that a highly consistent tubule diameter is required for high-resolution re-construction.

4.2 Design of Novel NTA-Modified Polyrotaxanes for Cryo-EM

These challenges led us to develop a family of polyrotaxane (PR) materials, a class of supramolecular structures where one or more macrocycles are threaded onto a linear polymer that has been subsequently end-capped with bulky substituents to prevent dethreading of the macrocycle(s)[18]. The term rotaxane is derived from Latin for wheel and axle. The supramolecular materials consist of three main components: the macrocycle or "wheel" which is usually a cyclic molecule (e.g. cyclodextrin, crown-

ether, etc.), the axle, which is usually a linear polymer bearing an affinity for the macrocycle interior, and the endcap which is a bulky molecule (larger than the diameter of the macrocycle) which can be conjugated to the axle termini. If the endcap is smaller than the diameter of the macrocycle, the material is referred to as a pseudorotaxane or pseudopolyrotaxane. The kinetic and thermodynamic properties of the rotaxanation process are determined by the non-covalent interactions between the macrocycle and linear polymer and interactions between macrocycles of adjacent rotaxanes[19].

Table 4.1 Physical Properties of Cyclodextrins.

Cyclodextrin	Mass	Outer diameter (nm)	Cavity diameter (nm)		Cavity volume (mL/g)	Solubility (g/kg H_2O)	Hydrate H_2O	
			inner rim	outer rim			cavity	external
α, $(glucose)_6$	972	1.52	0.45	0.53	0.10	129.5	2.0	4.4
β, $(glucose)_7$	1134	1.66	0.60	0.65	0.14	18.4	6.0	3.6
γ, $(glucose)_8$	1296	1.77	0.75	0.85	0.20	249.2	8.0	5.4

Cyclodextrins are commercially-available, water-soluble[20], well-defined, biocompatible, easily-modified and available in different cavity diameters (Table 4.1). CD's also may protect their threaded axle from degradation after threading[21]. Cyclodextrins (CD) have been utilized for polyrotaxanes synthesis and applications extensively[22]. Cyclodextrins (Figure 4.1) are cyclic oligosaccharides of glucose referred to as α-cyclodextrin (α-CD, 6 units), β-cyclodextrin (β-CD, 7 units) and γ-cyclodextrin (γ-CD, 8 units). α-CD and γ-CD exhibit very high water solubility with β-CD only having moderate solubility. CD-based polyrotaxanes are capable of producing a wide variety of molecular architectures.

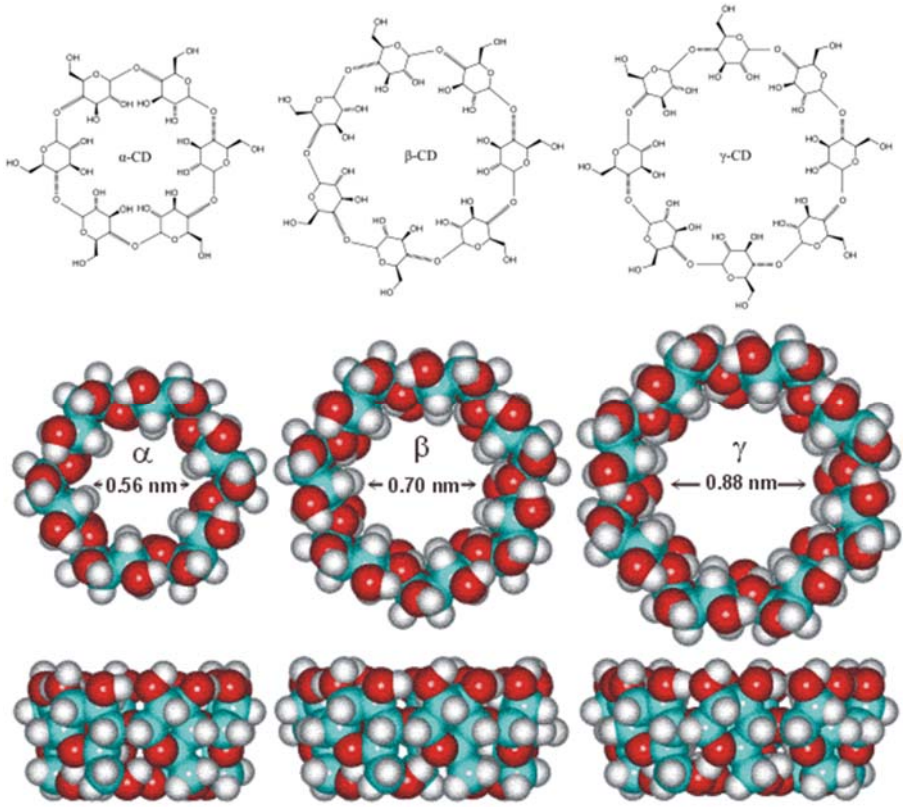

Figure 4.1 Molecular Structures of Cyclodextrins.

Similarly, many different axle components have been utilized for rotaxane synthesis. These materials are generally polymeric in nature with linear polymers being the most heavily utilized. The axle may be any component with a cross-section smaller than the macrocycle cavity and a length greater than that of the macrocycle.

Polyrotaxanes are generally synthesized by either threading, followed by endcapping, clipping, or slippage. Of these, threading, followed by endcapping is the most common (Figure 4.2). The endcapping process is formally referred to as rotaxanation. Cyclodextrin-based polyrotaxanes are the most widely-studied PR derivatives for biomedical and life science applications. They have been used as

transfection reagents[22c, 23], as therapeutic agents[22a], for modulation of ligand-protein interactions[24], etc.[21, 25].

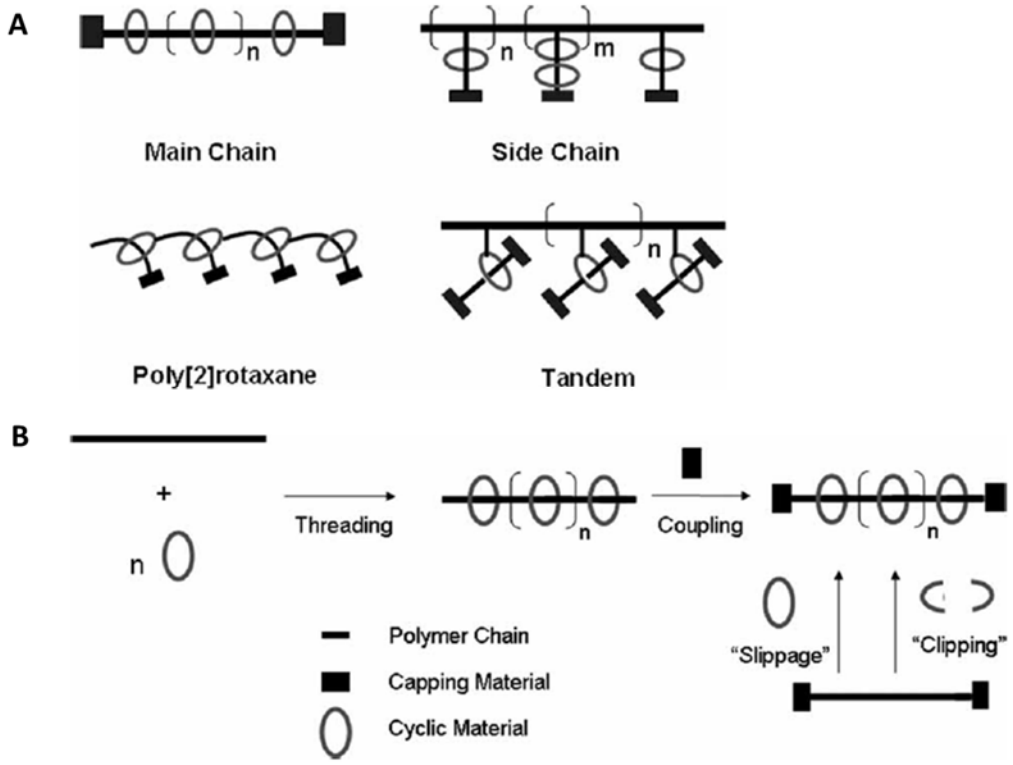

Figure 4.2 Summary of Polyrotaxane Architectures and Syntheses[19]. (A) Different CD-based polyrotaxane architectures (B) Methods of forming main-chain type polyrotaxanes.

These structures possess several uniquely advantageous properties resulting from the non-covalent interactions between polymer axle and macrocycle, such as free lateral and rotational mobility of the threaded macrocycles so that they can adapt to the steric demands of the adsorbate, facile preparation from inexpensive precursors, and uniform diameters that are defined by the macrocycle. The great structural diversity possible with

these materials[26] has led to a number of proposed applications, including their use as carriers for drug and gene delivery[27]. There are few reports in the literature, however, of polyrotaxanes that have been used specifically for studying protein-binding or protein-protein interactions[28].

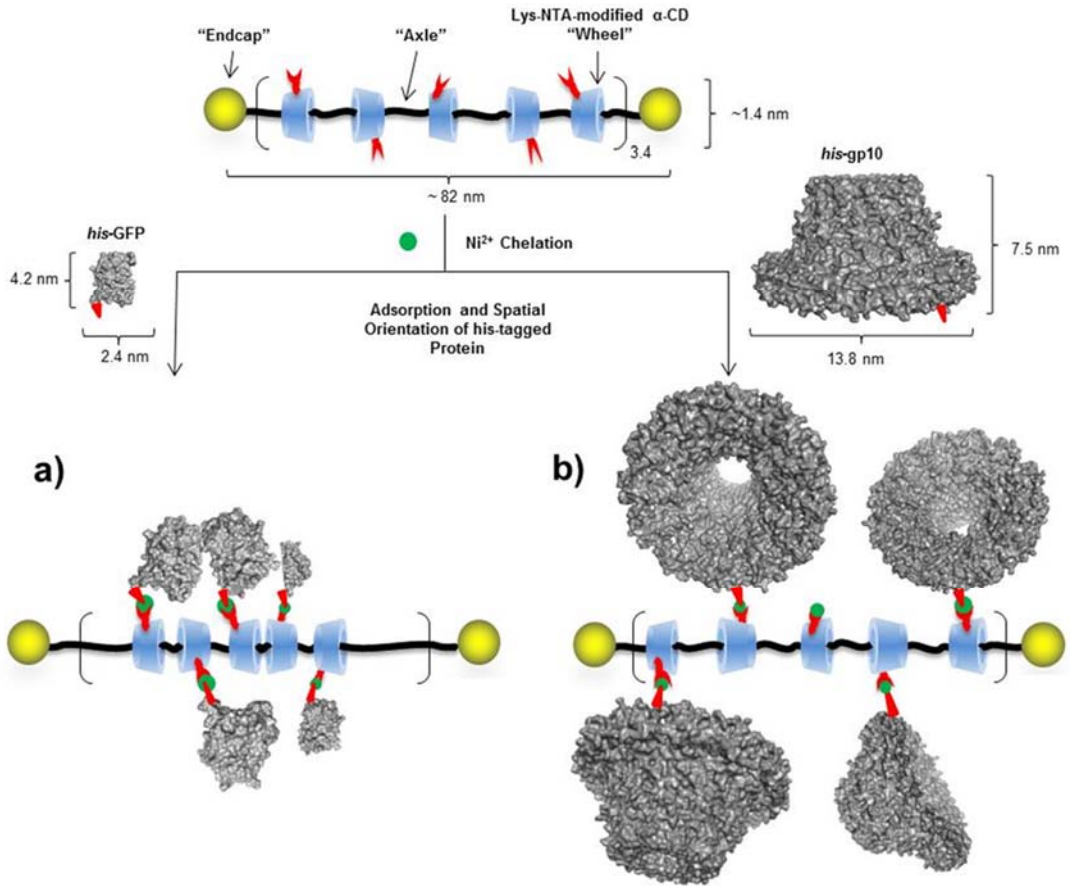

Figure 4.3 Conceptual Diagram of His-Tagged Protein Adsorption onto NTA-Modified-Polyrotaxane Scaffolds. Polyrotaxanes bearing multiple laterally-and rotationally-mobile-Lys-NTA-α-CD's facilitate adsorption of his-tagged proteins. The relatively small protein, his_6-GFP, (31 kD) yields a complex with a high degree of α-CD mobility, enabling favorable CD-CD and GFP-GFP interactions. Comparatively large protein assemblies (e.g. his_6-gp10 connector polypeptide, 440 kD) lead to complexes with more constrained α-CD mobility due to molecular crowding of the bound proteins. In both cases, adsorbed proteins are presented in all possible orientations due to the dynamic mobility of the threaded Lys-NTA-α-CD to which they are chelated.

In the present study, the development of an approach that is conceptually similar to the NTA-lipid tubule template method that would retain the specific recognition and lateral diffusion properties of the lipid-tubule approach in a more chemically robust format is described. This strategy utilizes the principle of NTA:Ni^{2+}:polyhistidine recognition on a polyrotaxane template that bears multiple laterally- and rotationally-mobile lysine-N_{α},N_{α}-di(carboxylmethyl)-α-cyclodextrins (LysNTA-α-CD) to concentrate his-tagged proteins on a spatially well-defined scaffold for single particle analysis by cryo-EM.

These materials are designed to have good solubility in biological buffers and facilitate SPA of his-tagged proteins since: (1) like the lipid tubule approach, each TEM image reveals all 3D orientations of the adsorbed protein; (2) data collection is expedited by protein concentration at the polyrotaxane surface rather than being randomly distributed in solution; (3) polyrotaxanes offer a constant diameter template at the threaded cyclodextrin core; and (4) the rod-like polyrotaxane morphology should suppress information loss due to protein-protein overlap and secondary scattering events in projection EM images that is much more likely using a conventional polymer modification approach (Figure 4.3).

4.3 Synthesis and Characterization of NTA-Modified Polyrotaxanes

4.3.1 Synthesis of Homobifunctional PEG Derivatives

In a similar fashion described in Chapter 1 for mPEG derivatives, a small library of homobifunctional PEG derivatives was synthesized (Scheme 4.1) following modified protocols previously reported for end group modification of PEG[29]. PEG of various molecular weight (~2000-35,000 Da) **56a-e** was converted to the mesylate (**57a-e**) via treatment with methansulfonyl chloride in dichloromethane (DCM) in the presence of triethylamine with average yield of 89-95 %. The mesylates were converted to *bis*-azide-terminal-PEG (**58a-e**) via S_N2 displacement by sodium azide in N,N-dimethylformamide (DMF) in 90-98 % average yield. Reduction using hydrogen gas (1 atm) and 10 mol % palladium on carbon (Pd/C) support in ethyl acetate (EtOAc) gave the terminal amine (**59a-e**) in 88-96 % average yield.

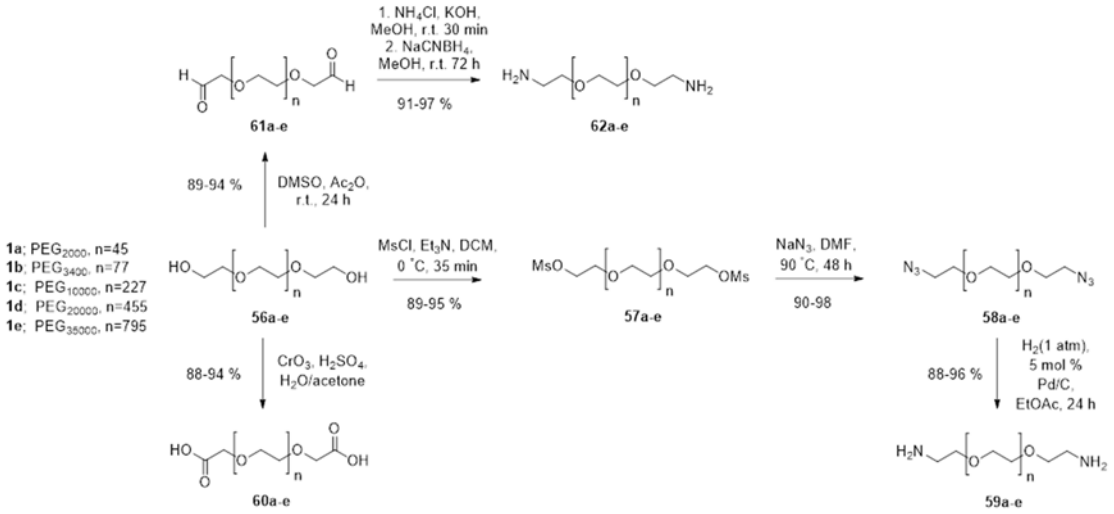

Scheme 4.1 Synthesis of Homobifunctional PEG Derivatives.

Carboxyl-terminal PEG were obtained via Jones oxidation of **56a-e** giving **60a-e** in 88-94 % average yield. Conversion was determined via TLC analysis combined with staining with bromocresol green to verify oxidation. An alternative route to amine terminal PEG through an aldehyde-terminal intermediate was also utilized. The aldehyde-terminal PEG derivatives were obtained via Albright-Goldman oxidation of **56a-e** to give **61a-e** in 89-94 % average yield. The aldehyde-terminal PEG were then converted to the amine **62a-e** via reductive amination mediated by sodium cyanoborohydride and ammonia in methanol in 91-97 % overall yield. Reported yields are given as percent recovery. Polymers were purified via extractions and precipitation into diethyl ether. The efficiency of conversion for Jones oxidation is near complete[29b]. Conversions reported for the Albright-Goldman and reductive amination protocols are 78-86 %[29b].

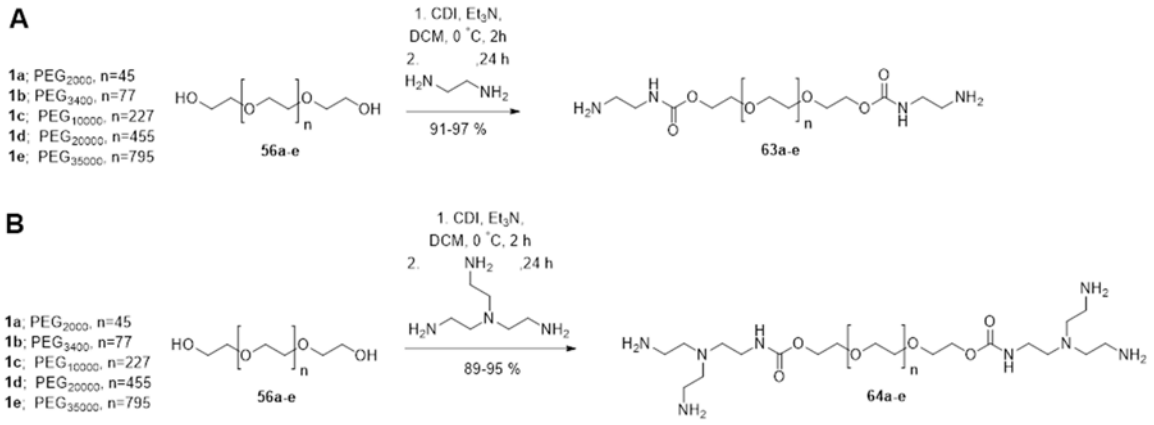

Scheme 4.2 Synthesis of Amine-Terminal PEG via CDI-Coupling.

Additionally, in order to generate a third PEG-bis-amine with a different synthetic methodology, Compounds **63a-e** were synthesized via coupling of ethylenediamine to the terminal hydroxyl groups of PEG via CDI-mediated coupling, in the presence of triethylamine, forming an N'-2-aminoethylcarbamate terminus. Compounds **63a-e** were obtained in 91-97 % average yield). Similarly, in order to generate a tetrafunctional PEG-amine capable of accommodating two endcaps per terminus, tris(2-aminoethyl)amine was coupled to terminal hydroxyl groups of PEG via CDI-coupling in the presence of triethylamine. Compounds **64a-e** were obtained in 89-95 % average yield.

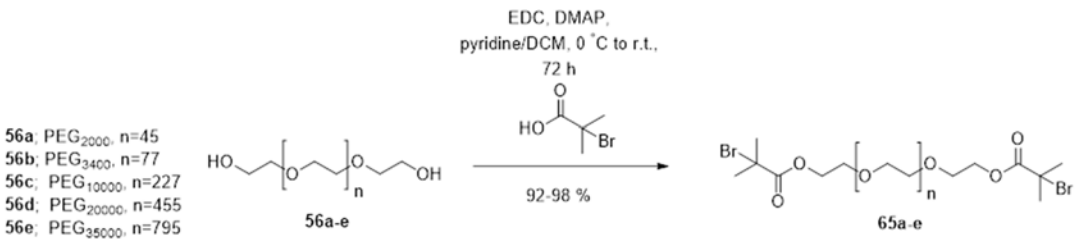

Scheme 4.3 Synthesis PEG-bis-MBPA.

Additionally, bis-tertiary bromide terminal PEG was synthesized by direct esterification of PEG (**56a-e**) with 2-methyl-2-bromopropionic acid (Scheme 4 .3) mediated by EDC and DMAP in a solution of DCM and pyridine. Compounds **65a-e** were obtained in 92-98 % yield.

4.3.2 Synthesis of TNB-Capped Polyrotaxanes

A small library of TNBS-capped polyrotaxanes composed of PEG and α-CD as the axle and macrocycle, respectively, was synthesized by threading α-CD and PEG in aqueous solution followed by rotaxanation via reaction of 2,4,6-trinitrobenzenesulfonic acid (TNBS) with PEG-bis-amine (**59a-d**). The polyrotaxanes (**66a-d**) were isolated by exploiting the poor aqueous solubility of the polyrotaxanes compared to the high solubility of both PEG and α-CD by a centrifugal purification process followed by dialysis (Scheme 4.4).

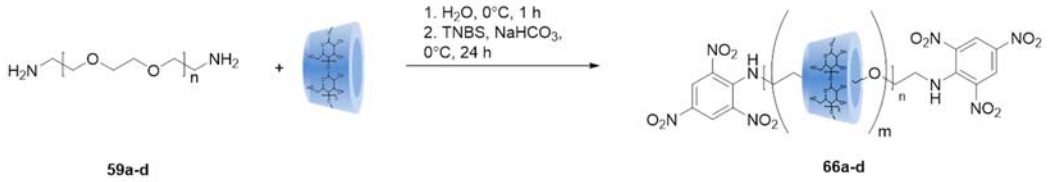

Scheme 4.4 Synthesis of TNB-Capped Polyrotaxanes from **59**.

The polyrotaxanes were characterized via ^{1}H-NMR to determine the number of CD's, threading efficiency and estimated molecular weight (Table 4.2). The yields were highest for the PEG of low molecular weight. Threading efficiency was also generally higher for polyrotaxanes synthesized from lower molecular weight PEG.

Table 4.2 Characterization of TNB-Capped Polyrotaxanes from **59**.

Entry	Yield	PEG MW	CD	# CD's (NMR)	Threading Eff.	M_n (NMR)
66a	5.068 g	2.0 kDa	α	8.8	38.6 %	10.9 kDa
66b	1.605 g	3.4 kDa	α	19.3	50.0 %	22.6 kDa
66c	1.029 g	10.0 kDa	α	45.2	39.8 %	54.4 kDa
66d	0.653 g	20.0 kDa	α	52.4	23.0 %	71.4 kDa

Similarly, polyrotaxanes were synthesized from Compounds **63a**, **63c**, **63e** via threading of the PEG and α-CD in water followed by rotaxanation via substitution reaction of TNBS with terminal amino functionalities of PEG. The compounds were purified by centrifugal washing and dialysis.

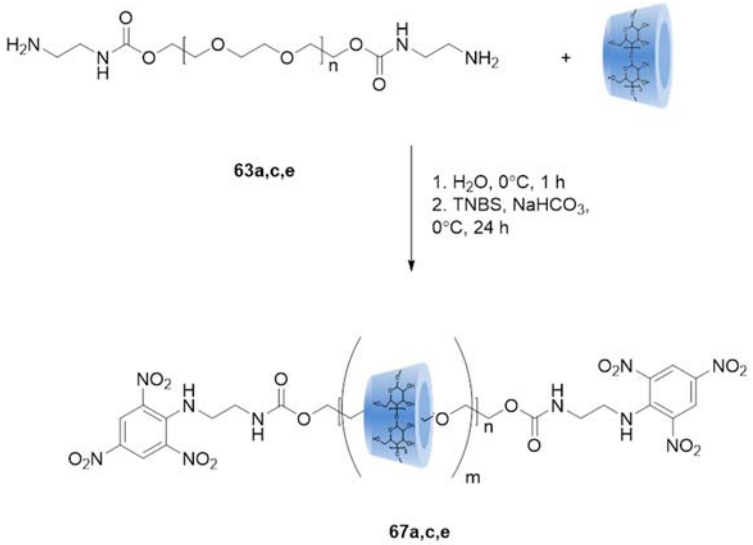

Scheme 4.5 Synthesis of TNB-Capped Polyrotaxanes from **63**.

The polyrotaxanes were characterized via ^{1}H-NMR to determine the number of CD's, threading efficiency and estimated molecular weight (Table 4.3). Yields were generally high and relatively consisted for the different molecular weights of PEG. This suggests that rotaxanation efficiency may be better for Compounds **67a**, **67c**, and **67e** relative to Compounds **66a-d** due to greater end group fidelity in Compound **63** relative to Compound **59**. This further suggests that generating PEG-bis-amine by direct coupling mediated by CDI with ethylenediamine is a better strategy relative to the three step synthesis used to generate **59**.

Table 4.3 Characterization of TNB-Capped Polyrotaxanes from **63**.

Entry	Yield	PEG MW	CD	# CD's (NMR)	Threading Eff.	M_n (NMR)
67a	3.017 g	2.0 kDa	α	7.7	34.0 %	10.0 kDa
67c	4.434 g	10.0 kDa	α	33.8	29.7 %	43.5 kDa
67e	4.687 g	35.0 kDa	α	89.7	22.5 %	122.8 kDa

In order to generate test if a larger endcap may lead to less dethreading from slipping Compounds **64b** and **64c** were similarly threaded with α-CD in aqueous solution followed by endcapping via reaction of the terminal amines with TNBS. In this case, since two TNBS molecules may be present on each of the two polyrotaxane termini, it should be less likely to dethread during post-modification in organic solution (Scheme 4.6).

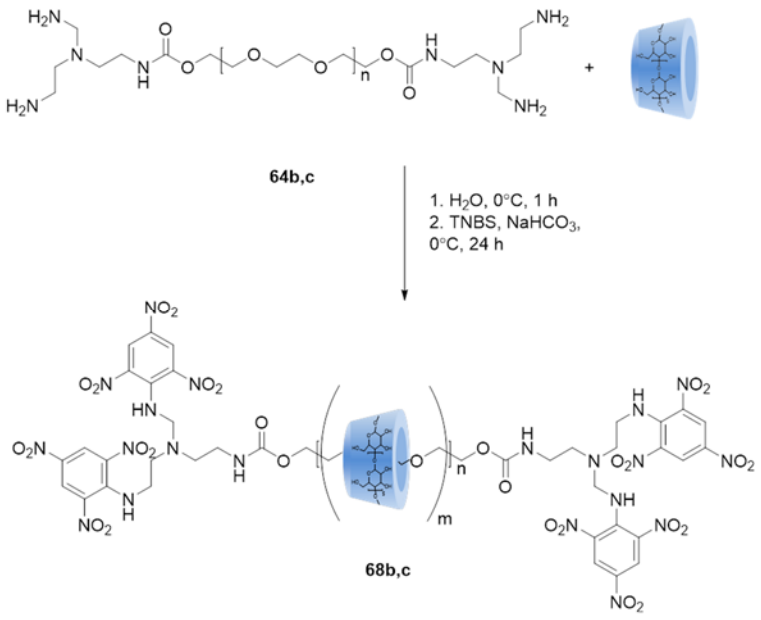

Scheme 4.6 Synthesis of TNB-capped polyrotaxanes from **64**.

The polyrotaxanes were characterized via ^{1}H-NMR to determine the number of CD's, threading efficiency and estimated molecular weight (Table 4.2). Yields were relatively low. It was also observed that during threading of PEG and α-CD precipitation of pseudopolyrotaxanes usually happens relatively quickly (less than 30 min) and generally happens quicker for lower PEG molecular weight. This suggests that lower weight PEG effectively presents more polymer termini present in solution on which a CD may become threaded. During threading of Compounds **63** and **64** pseudorotaxane formation was slow and the overall viscosity of the solution remained relatively low indicating that termini of Compounds **63** may be too bulky to be suitable for threading of α-CD. Threading efficiency for Compound **63b** was extremely high while Compound **63c** was comparable to other polyrotaxanes based on PEG of molecular weight of 10.0 kDa (Table 4.4).

Table 4.4 Characterization of TNB-Capped Polyrotaxanes from **63**.

Entry	Yield	PEG MW	CD	# CD's (NMR)	Threading Eff.	M_n (NMR)
68b	0.266 g	3.4 kDa	α	31.3	81.0 %	35.0 kDa
68c	0.170 g	10.0 kDa	α	27.5	24.2 %	37.8 kDa

Overall, TNBS-capped polyrotaxanes were synthesized from three different PEG-bis-amine constructs accessed through different synthetic methodologies. All three strategies successfully generated polyrotaxanes with PEG-bis-ethylenediamine showing the best yield likely due to greater overall amine-conversion in the PEG starting material.

4.3.3 Modification of TNB-Capped Polyrotaxanes with NTA

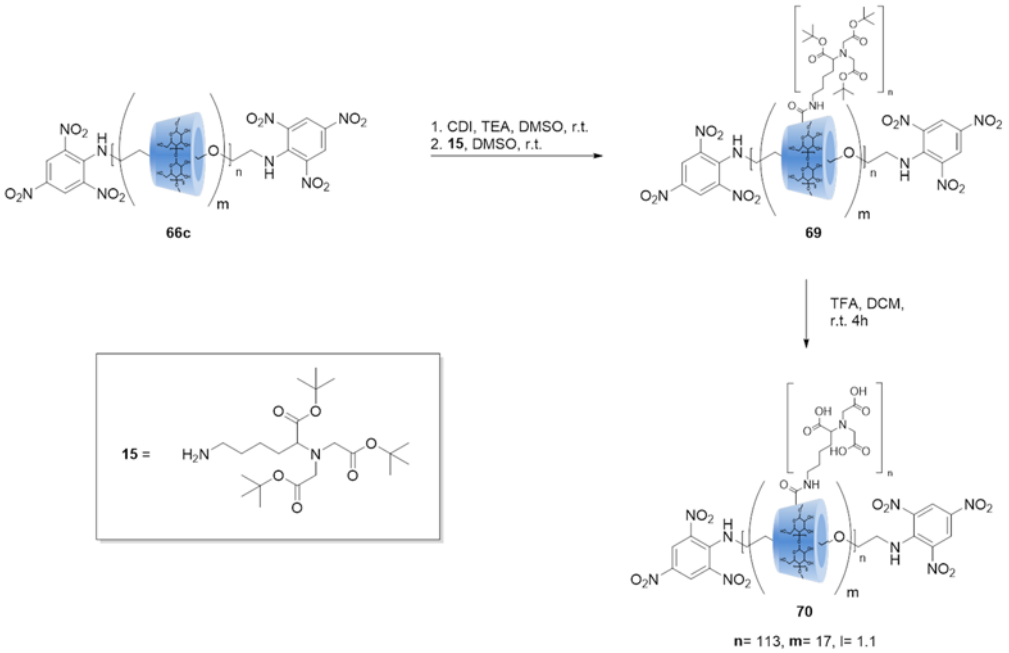

Scheme 4.7 Modification of TNB-Capped Polyrotaxane with NTA.

Compound **66c** was randomly conjugated modified with NTA via CDI-mediated coupling between the hydroxyl moieties of α-CD and Compound **15**. This methodology yields a carbamate linkage which is expected to exhibit high stability for TFA-mediated deprotection and aqueous applications of the material (Scheme 4.7). Compound **69** was deprotected to yield the free acid groups of NT via treatment with TFA. Compound **70** was purified via dialysis and size exclusion chromatography to remove small molecular contaminants and occult impurities. NMR and GPC revealed that Compound **70** was composed of approximately 17 CD's with an average of 1.1 NTA/CD after the two step post-modification approach. One downside of this approach is that even after successive treatments with TFA, some t-butyl moieties were present in the NMR spectra. This observation is proposed to be due to O-alkylation by the reactive species (t-butyl cation) generated during deprotection. This side reaction could not be effectively avoided even via addition of scavengers commonly used in peptide synthesis (triethylsilane, phenol, etc.).

In an effort to avoid the associated side-reactions of deprotection of t-butyl-protected-NTA-modified polyrotaxanes, a small library of NTA and tris-NTA derivatives was synthesized with (2-trimethylsilyl)ethyl ester protecting groups. These esters employ mild fluoride-mediated ester deprotection, generating the carboxylic acid, ethene, and trimethylsilyl fluoride. Any O-silylation of hydroxyl groups of polyrotaxanes modified with these derivatives during deprotection should be hydrolysable during the subsequent aqueous dialytic purification.

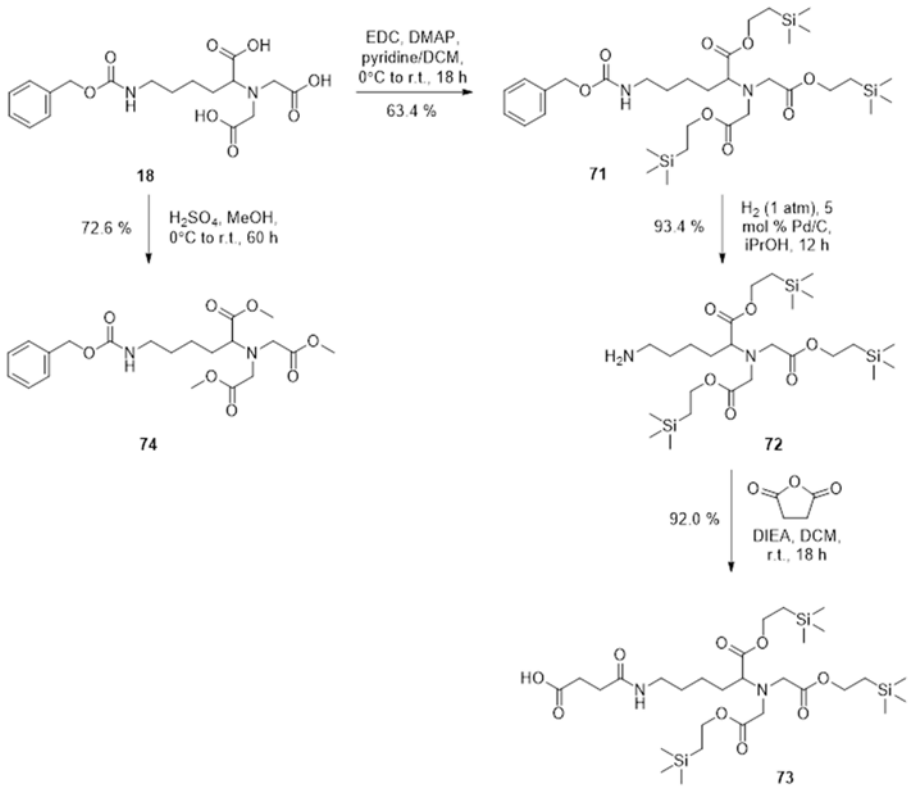

Scheme 4.8 Synthesis of (2-trimethylsilyl)ethyl-Protected NTA.

Starting from Compound **18**, EDC and DMAP were utilized to esterify the free carboxyl groups of Compound **18** with (2-trimethylsilyl)ethanol in a mixture of pyridine and DCM to give Compound **71** in 63.4 % yield. Hydrogenation on 10 Pd/C in isopropyl alcohol under 1 atm. hydrogen gave Compound **72** in 93.4 % yield. Compound **72** was further succinylated to give carboxylate derivative **73** in 92.0 % yield. Methyl ester NTA-derivative **74** was also synthesized via acid-catalyzed esterification in MeOH. Sulfuric acid was found to be superior to p-toluenesulfonic acid (PTSA) for this purpose as the PTSA salt was difficult to remove.

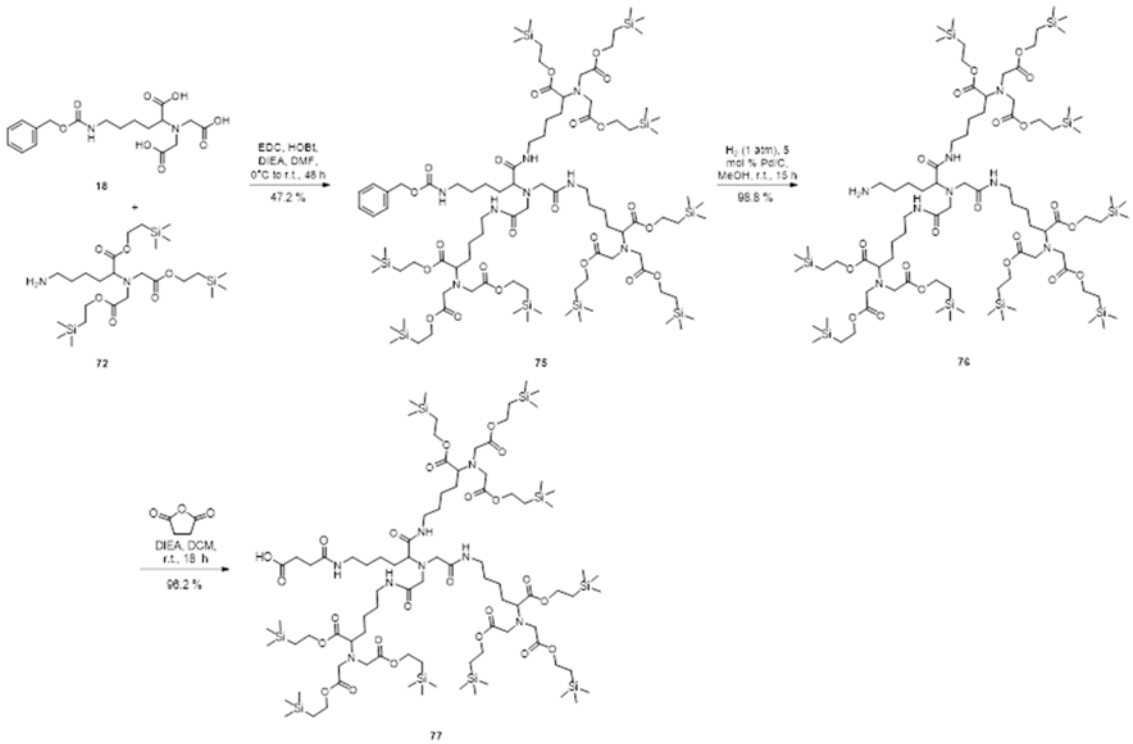

Scheme 4.9 Synthesis of (2-trimethylsilyl)ethyl-Protected tris-NTA.

A (2-trimethylsilyl)ethyl derivative of tris-NTA was also synthesized. Compounds **18** and **72** were coupled to give Compound **75** in 47.2 % yield. Compound **75** was hydrogenated to remove the Z-protecting group to give Compound **76** in 98.8 % yield. Compound **76** was further succinylated to give carboxylic acid derivative **77** in 98.2 % yield (Scheme 4.9).

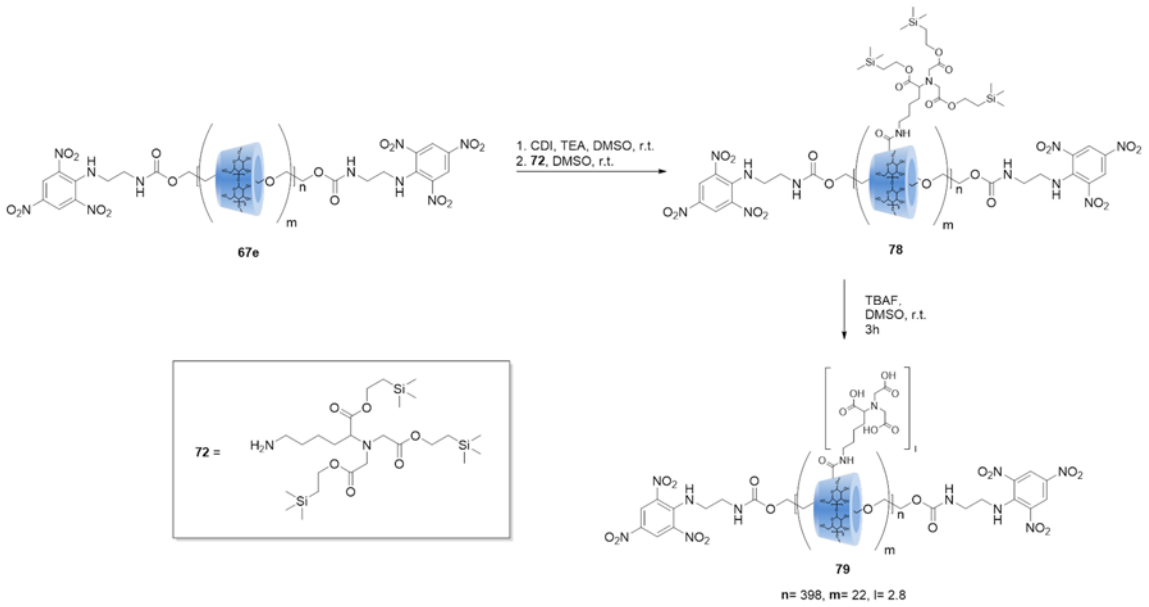

Scheme 4.10 Synthesis of NTA-Modified Polyrotaxanes Using (2-trimethylsilyl)ethyl Ester-Protected NTA.

Next, an attempt to synthesize NTA-modified polyrotaxanes using the post-modification and fluoride-mediated deprotection was made. Polyrotaxane **67e** was post-modified with Compound **72** mediated by CDI in DMSO. The NTA-modified polyrotaxane **78** was isolated via dialysis. ^{1}H-NMR indicated the presence of 29 CD's, with approximately 6.2 NTA/CD and an associated estimated molecular weight of 110.0 kDa. Compound **78** was then subjected to treatment with tetrabutylammonium fluoride (TBAF) in DMSO to effect deprotection of the (2-trimethylsilyl)ethyl ester groups of NTA. This strategy proved successful. After purification by dialysis and size-exclusion chromatography, ^{1}H-NMR indicated the presence of NTA-modified polyrotaxane with approximately 24 CD's and 2.8 NTA/CD after the two step post-modification sequence. The NMR spectra also indicated the presence of butyl groups, which could be from

tetrabutylammonium cation or possibly due to N-alkylation by TBAF, which has been reported.

4.3.4 Screening of Aqueous Endcapping Methods

Due to the moderate success using the post-modification-deprotection strategy for synthesis of NTA-modified polyrotaxanes, a small screening study was performed to identify possible aqueous endcapping methodologies, which might be used to install bulkier endcaps than TNBS due to the observation of loss of CD (possibly from slippage) during previous strategies.

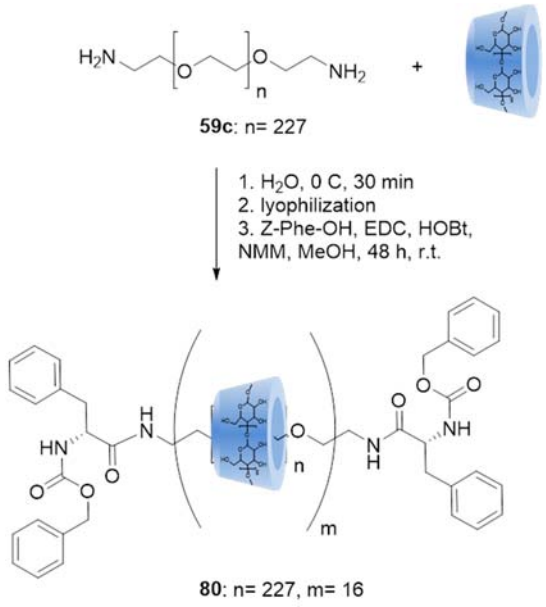

Scheme 4.11 Synthesis of Z-Phenylalanine-Capped Polyrotaxanes.

Compound **80** was synthesized from the pseudopolyrotaxane composed of PEG-bis-amine (**59c**) and α-CD via amide-coupling between the terminal amino groups of the lyophilized pseudopolyrotaxane and free carboxylate of Z-phenylalanine mediated by EDC, HOBt, and N-methylmorpholine (NMM) in MeOH. The reaction was unsuccessful when the same process was repeated using ethanol in place of methanol. The polyrotaxane was purified via centrifugation and dialysis ^{1}H-NMR indicated the presence of 16 CD's.

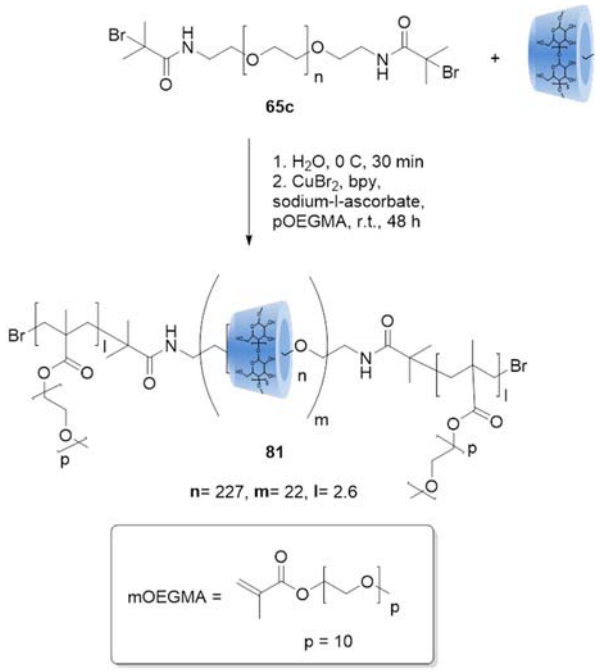

Scheme 4.12 Synthesis of POEGMA-Capped Polyrotaxanes.

An ATRP strategy[30] was also utilized to grow a short poly(oligoethylene glycol) methacrylate (POEGMA) from tertiary-bromide terminal PEG **65c**. This polyrotaxane was synthesized via threading of Compound **65c** by α-CD in water followed by aqueous

ATRP as the rotaxanation reaction. The polyrotaxanes were isolated via centrifugation and dialysis. ^{1}H-NMR revealed that the POEGMA polymer did not undergo a high degree of polymerization with only about 2.6 monomers incorporated on each terminus and approximately 22 CD's threaded. In fact, the process was completely unsuccessful several times, which is attributed to no polymerization in those cases.

4.3.5 Synthesis of Fluorescein-Capped Polyrotaxanes via CuAAC

Next, we sought to design a small library of polyrotaxanes incorporating a larger endcap that could also impart fluorescence properties for imaging studies. Fluorescein is a water soluble heterocyclic compound commonly used as a dye[31]. Many derivatives have previously been synthesized.

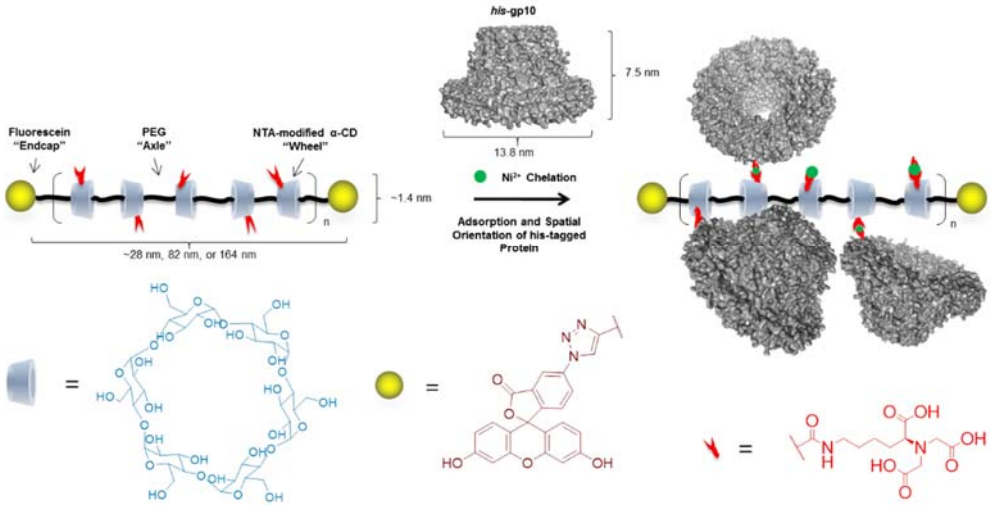

Figure 4.4 Design of Fluorescein-Capped Polyrotaxanes.

The copper-catalyzed azide-alkyne cycloaddition[32] (CuAAC) was chosen as an endcapping method since it is a very high efficiency reaction that is compatible with aqueous conditions and conjugation of large macromolecules. During the previous screening study, this strategy had been identified as a high-yielding strategy for aqueous polyrotaxane synthesis (data not shown). We sought to use bis-alkynyl-terminal PEG and an azido-derivative of fluorescein to synthesize these materials

To utilize this strategy, a small library of bis-alkynyl-PEG derivatives was synthesized (Scheme 4.13) via direct coupling of propargylamine with Compounds **68a-e**. Since the Jones oxidation effectively oxidizes PEG termini in high efficiency, this two-step protocol (also utilizing EDC coupling, another high-yielding reaction) is expected to yield polymers with high end group fidelity.

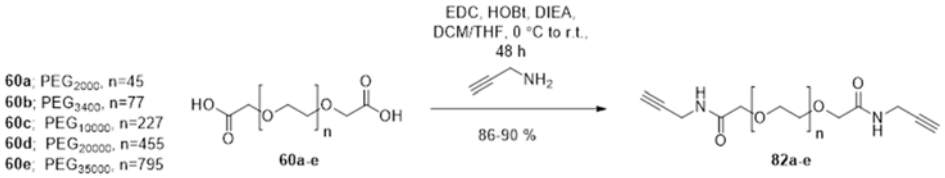

Scheme 4.13 Synthesis of PEG-bis-alkyne.

Next, we sought to synthesize an azide derivative of fluorescein. Compound **84** has previously been reported[33] in 66.5 % yield via diazotization followed by substitution using sodium nitrite and sodium azide in methanol. However, this protocol suffers from poor yield and lack of purity. The product was also never characterized.

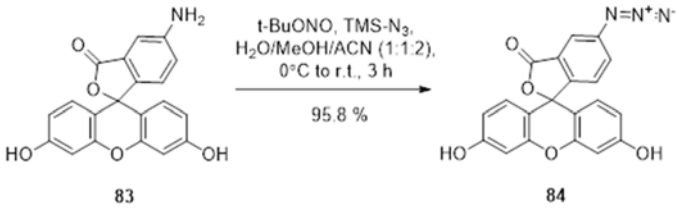

Scheme 4.14 Synthesis of 5-Azidofluorescein.

An alternative synthetic protocol was designed (Scheme 4.14) utilizing organic nitrite and azide derivatives whose by-product could be easily removed. The reaction was carried out with t-butyl nitrite and trimethylsilyl azide in a mixture of acetonitrile (ACN), methanol, and water. The product was purified chromatographically and isolated in 95.8 % yield.

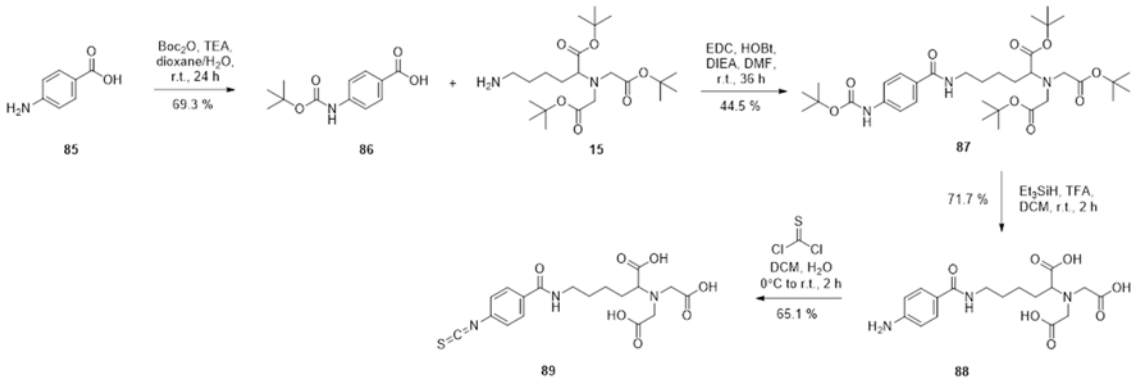

Scheme 4.15 Synthesis of Isothiocyanate-NTA Derivative.

Since previous experiences with post modification usually resulted in loss of CD's, which leads to a less rigid polyrotaxane, and harsh deprotection methodologies tended to lead to complications, a post modification strategy based around a two-step

protocol involving amine-functionalization of the polyrotaxane followed by direct conjugation of an isothiocyanate derivative of NTA was designed (Scheme 4.15).

4-Aminobenzoic acid (PABA, **85**) was Boc-protected in 69.3 % yield and coupled with Compound **15** via EDC-coupling in the presence of HOBt and DIEA in DMF to give Compound **87** in 44.5 % yield. A global TFA-mediated deprotection was used to give NTA-derivative **88** in 71.1 % yield. Compound **88** was converted to an isothiocyanate derivative via thiophosgene in a biphasic mixture of DCM and water to give Compound **89** in 65.1 % yield.

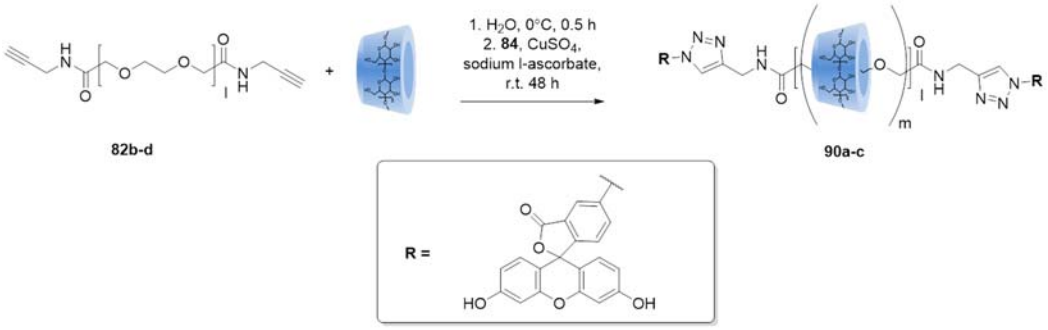

Scheme 4.16 Synthesis of Fluorescein-Capped Polyrotaxanes.

A small library of fluorescein-capped polyrotaxanes was synthesized from Compounds **82b-d**, α-CD and Compound **84** under aqueous conditions. Pseudorotaxane formation was carried out followed by aqueous CuAAC via addition of a DMSO solution of **84**, $CuSO_4$ and sodium-l-ascorbate. The heterogeneous rotaxanation reaction was allowed to proceed for 48 hours The polyrotaxanes were purified via centrifugation process utilizing water and aqueous solutions of EDTA to remove Cu(II) followed by dialysis against water to remove CD and unthreaded polymer.

Table 4.5 Characterization of Fluorescein-Capped Polyrotaxanes.

Entry	Yield	PEG MW	CD	# CD's (NMR)	Threading Eff.	M_n (NMR)	M_n (GPC)	M_w/M_n
90a	2.408 g	3.4K	α	20.0	52.0	23.6 kDa	21.6 kDa	1.039
90b	2.939 g	10K	α	67.3	59.3	76.3 kDa	58.2 kDa	1.169
90c	1.691 g	20K	α	98.1	43.2	116.2 kDa	93.1 kDa	1.110

Yields for Compounds **90a-**c were generally good, being superior in average yield and reproducibility than previous methods. Also, since fluorescein is a larger molecule than TNBS, it is anticipated that dethreading via slippage should be reduced in these materials. ^{1}H-NMR (Figure 4.5 C) indicated the threading were relatively high in comparison to previous methods.

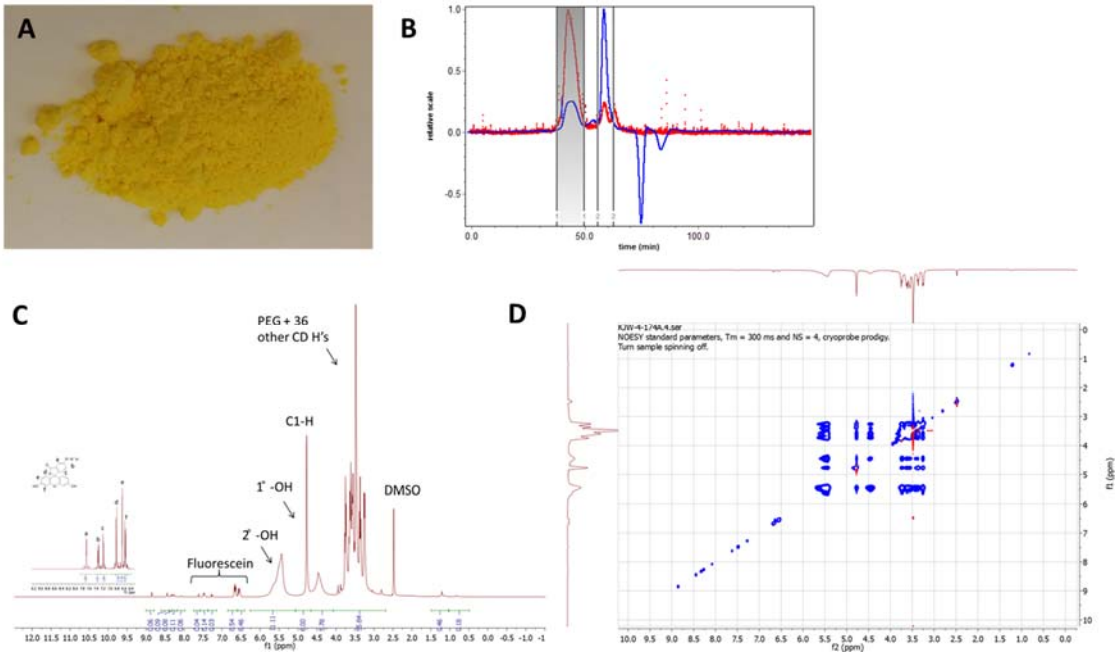

Figure 4.5 Characterization of Fluorescein-Capped Polyrotaxanes via NMR and GPC. (A) Physical appearance of **90a.** (B) GPC Chromatogram of **90a.** (C) ^{1}H-NMR spectral characterization of fluorescein-capped polyrotaxane **90a**. (D) 2D NOESY spectra of fluorescein-capped polyrotaxane **90a**.

Since the pseudorotaxane is kept under equilibrium conditions during the rotaxanation reaction, even though the rotaxanation reaction is slow, high yields and threading are still possible. 2D NMR showed the presence of proximal interactions between PEG and CD protons. GPC analysis (Figure 4.5B) of Compounds **90a-c** in DMSO yielded number average molecular weight data in relative agreement with NMR observation, but consistently lower, having greater difference with the higher weight PEG derivatives. This may be due to presence of dethreaded α-CD, which would not be differentiated from polyrotaxane-associated CD in NMR.

4.3.6 Modification of Fluorescein-Capped Polyrotaxanes with NTA

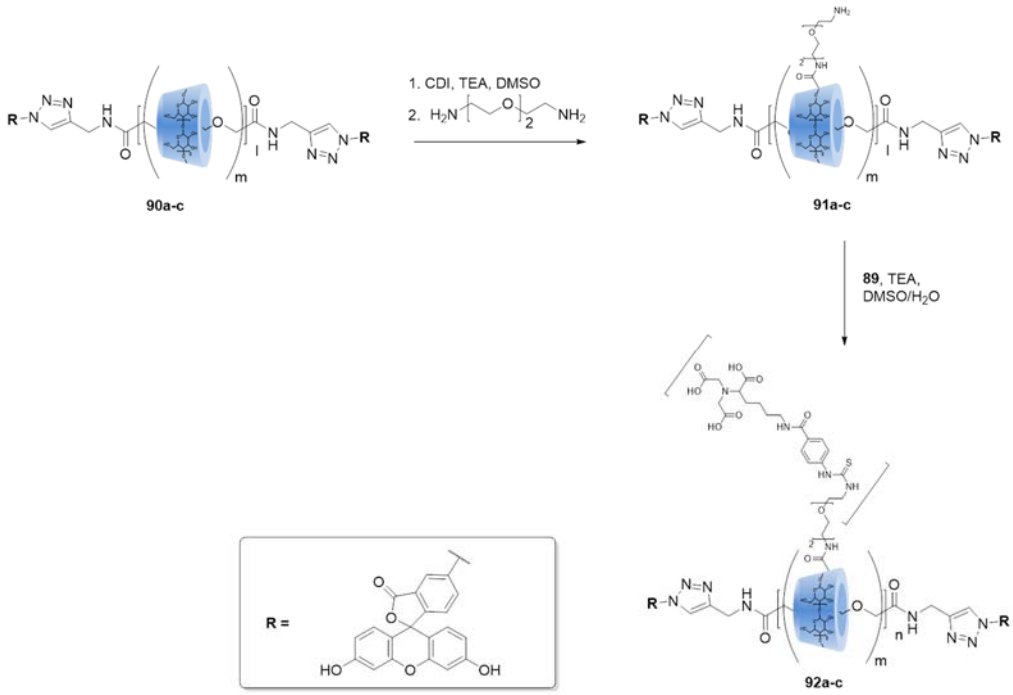

Scheme 4.17 Modification of Fluorescein-Capped Polyrotaxanes with Isothiocyanate-NTA Derivative.

Fluorescein-capped polyrotaxanes (**90a-c**) were modified with NTA via a two-step post-modification sequence. First, Compounds **9a-c** were modified with 2,2-(ethylenedioxy)bis(ethylamine) (EBE) via CDI-coupling in DMSO in the presence of triethylamine. Compounds **91a-c** were then conjugated with Compound **89** via thiourea formation in the presence of triethylamine in aqueous DMSO. The NTA-modified polyrotaxanes were purified between each step via dialysis against DMSO and water to remove unreacted starting materials, dethreaded CD's, etc.

Table 4.6 Characterization of NTA-Modified Fluorescein-Capped Polyrotaxanes.

Entry	Yield	PEG MW	# CD's (m)	Threading Eff.	# NTA (n, ICPMS)	M_n (NMR)	M_n (GPC)	M_w/M_n
92a	95 mg	3.4K	5.90	15.3	8.9	9.9 kDa	10.7 kDa	1.236
92b	92 mg	10K	17.8	15.7	12.0	28 kDa	30.4 kDa	1.452
92c	132 mg	20K	35.1	15.4	26.6	54.9 kDa	57.5 kDa	1.337

The NTA-modified polyrotaxanes **92a-c** were characterized via ^{1}H-NMR and GPC (Table 4.6). NMR revealed that the apparent number of threaded CD's and molecular weight had decreased considerable relative to the unmodified polyrotaxanes. This observation could be attributable to slippage, or hydrolysis of threaded CD's or removal of unthreaded CD's during purification. GPC showed good agreement with NMR for calculated molecular weight, although it was slightly higher than the calculated molecular weights from NMR. M_w/M_n was also observed to increase after post modification.

4.4 Evaluation of NTA-Modified Polyrotaxanes

To quantify the Ni^{2+} chelation capacity of **70**, the total Ni^{2+} content bound to NTA was analyzed by ICP-MS. A solution of 20 mM $NiSO_4$ was added to **70** and the metal bound PRTx isolated and purified by size exclusion chromatography using Sephadex G-25M. ICP-MS analysis of the purified material revealed a Ni^{2+} content corresponding to approximately 19 NTA units per polyrotaxane (assuming a 1:1 Ni^{2+}:NTA stoichiometry), a finding that is consistent with the ^{1}H-NMR data for this compound.

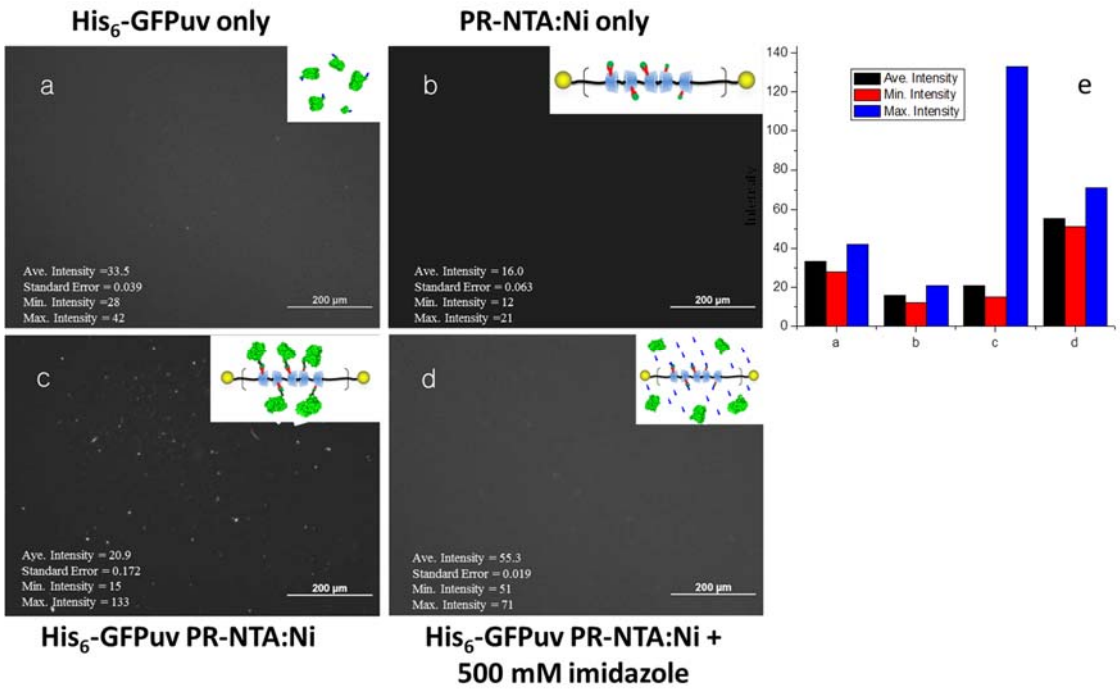

Figure 4.6. Fluorescence Microscopy Analysis of His_6-GFP Complexation with Ni^{2+}-Activated **70** (Olympus BX51, 10 X objective, DP71 CCD camera). (a) His_6-GFP (3.0 µM) in 10 mM HEPES buffer at pH 8.0. (b) Ni^{2+}:**70** complex (176 nM), (control). (c) Mixture of 3.0 µM his_6-GFP and 176 nM Ni^{2+}:**70** complex at a 1:1 his_6-GFP:α-CD stoichiometry. (d) Same as (c), except that 500 mM imidazole solution was added to (c) to strip the unbound Ni^{2+} from the **70:Ni** complex. (e) Fluorescence intensities of samples (a)-(d), with the average intensity (black bar), minimum intensity (striped bar) and maximum intensity (dotted bar) reported for the CCD counts collected over randomly selected 50 µm X 50 µm areas of the corresponding image.

Fluorescence microscopy was used to evaluate the protein adsorption properties of Ni^{2+}-activated **70** using his_6-green fluorescent protein (his_6-GFP). Figure 4.6A shows a 3.0 µM solution of his_6-GFP mounted between two glass slides and viewed by fluorescence microscopy. The appearance of a uniform fluorescence emission across the field of view indicates that GFP does not aggregate under these conditions. Figure 4.6B confirms that Ni^{2+}-activated **70** has no appreciable fluorescence emission under these

conditions. When 10 μL of a 176 nM Ni^{2+}-activated **70** solution was added to 3.0 μM his_6-GFP to produce a 1:1 GFP:α-CD ratio and imaged under identical conditions, many intensely fluorescent spots surrounded by zones of depleted fluorescence intensity were observed (Figure 4.6C). We infer from these observations that the regions of high emission intensity are due to locally high GFP concentrations that have been facilitated by the Ni^{2+}:**70** complex since GFP does not aggregate under the same conditions in the absence of the polyrotaxane additive. When a 500 mM imidazole solution was added to disrupt the Ni^{2+}:his_6-GFP complexation interaction, a rehomogenization of the fluorescence intensity was observed. This observation is consistent with the expectation that excess imidazole should outcompete the his-tags for Ni^{2+} binding, thereby disrupting the his_6-GFP:Ni^{2+}:**70** complex and re-dispersing his_6-GFP as a dilute solution of GFP monomer.

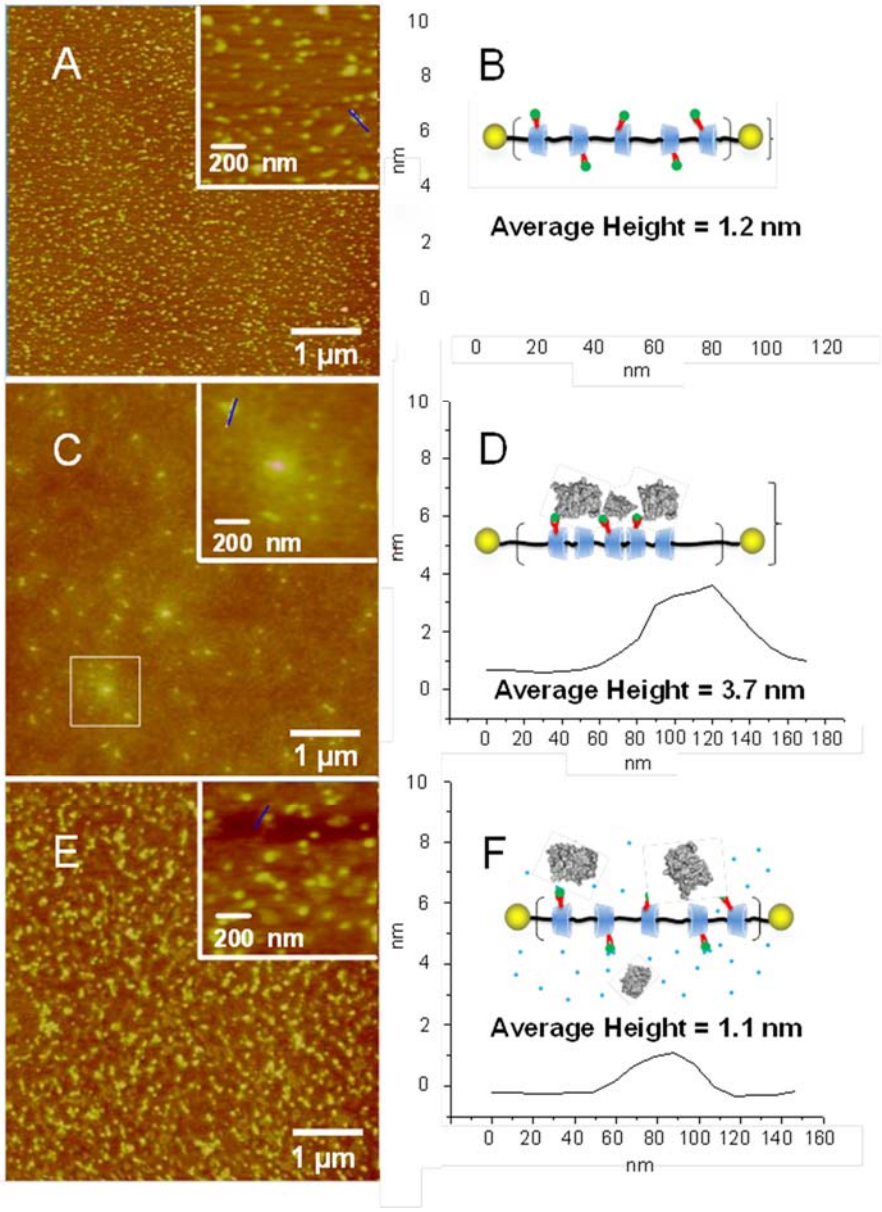

Figure 4.7 Tapping Mode AFM Analysis of His_6-GFP on NTA-Modified Polyrotaxane Scaffolds. Tapping mode AFM analysis of: (A, B) 176 nM Ni^{2+}:**70** complex; (C, D) his_6-GFP:Ni^{2+}:**70** complex, prepared by mixing 176 nM Ni^{2+}:**70** complex solution with a 3.0 µM his_6-GFP solution in 10 mM HEPES buffer at pH 8.0 to attain a 1:1 his_6-GFP:α-CD stoichiometry. (E, F) Sample C after addition of 500 mM imidazole solution. Samples were visualized on a Veeco Multimode AFM with a Nanoscope IIIa controller in air at 22 °C. The line scans in B, D & F correspond to the image areas shown in the insets of A, C, & E, respectively.

AFM studies were then performed to provide greater insight into the his_6-GFP aggregation phenomena in the presence of Ni^{2+}:**70** complex. AFM images of Ni^{2+}:**70** complexes deposited onto mica (Figure 4.7A) reveal the presence of features with an average long dimension of 60 nm and an average height of 1.2 nm. After addition of 3.0 μM his_6-GFP at a 1:1 GFP:α-CD molar ratio, these objects were transformed into rod-shaped structures with an average length of ~100 nm (Figure 4.7B) and an average height of 3.7 nm, consistent with the adsorption of his_6-GFP (GFP is a β-barrel structure that is approximately 4.2 nm high x 2.4 nm in diameter) onto the 1.4 nm diameter polyrotaxane scaffold. Addition of 500 mM imidazole to this solution, followed by incubation for 1 h prior to AFM imaging (Figure 4.7C), produced samples that had reverted back to the original morphology with an average diameter of ~40 nm and average height of 1.1 nm. These observations are consistent with our fluorescence microscopy observations and the expected reversible complexation of his_6-GFP with the Ni^{2+}:**70** complex.

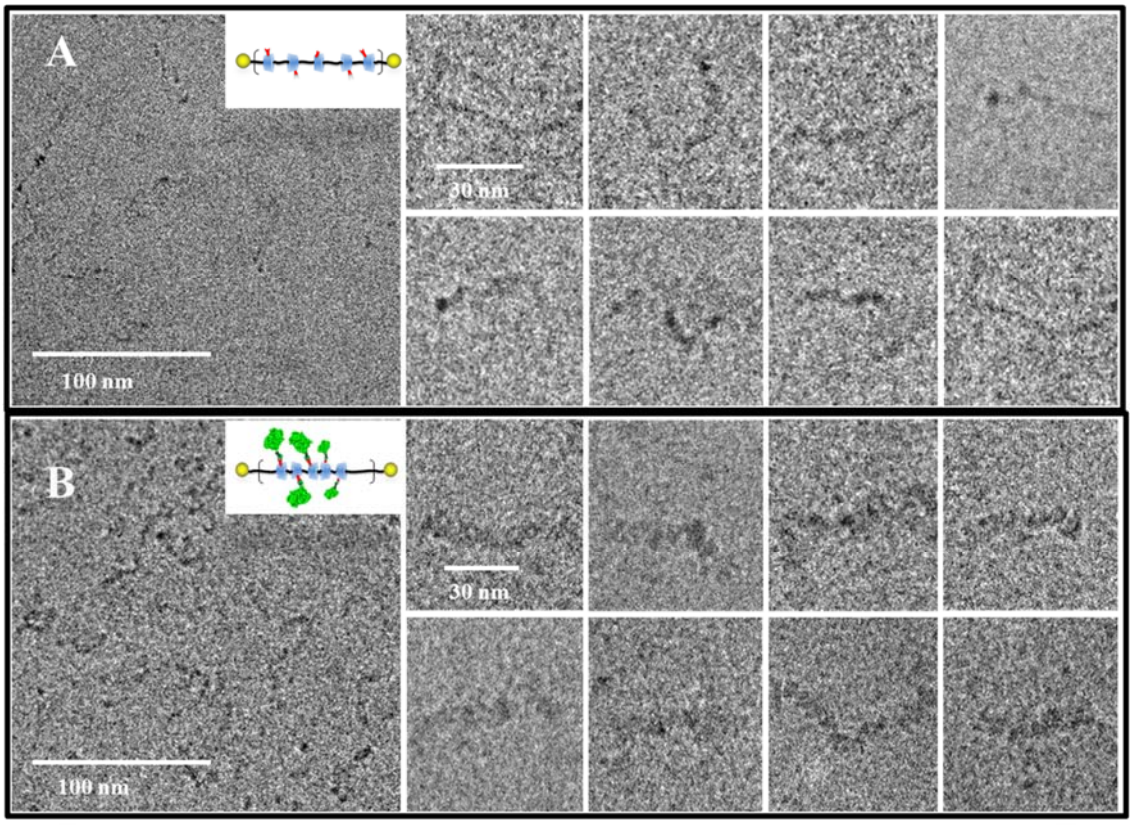

Figure 4.8 Cryo-EM Imaging of His_6-GFP adsorbed to NTA-Modified Polyrotaxane Scaffolds. Cryo-EM imaging of: (A) 1 mM Ni^{2+}:**70** complex; (B) 1 mM his_6-GFP:Ni^{2+}:**70** complex at a 1:1 his_6-GFP:α-CD stoichiometry. A gallery of Ni^{2+}:**70** complex features observed at higher magnification appear to the right for samples in the absence (A) and presence (B) of his_6-GFP. Samples were spread onto C-Flat™ grids and plunge-frozen in liquid ethane. Images were recorded using a Gatan 4k × 4k CCD camera on a Philips CM200 transmission electron microscope operating at 40 kV accelerating voltage.

In order to evaluate the potential of Ni^{2+}:**70** complexes for SPA applications, cryo-EM imaging was performed using a small protein target (his_6-GFP) that would otherwise be difficult to visualize with this technique due to the combined effects of low EM contrast and extensive protein dispersion. Cryo-EM imaging of his_6-GFP:Ni^{2+}:**70** complexes showed the presence of similar rod-like structures, however, these structures were noticeably larger in diameter and exhibited greater electron density than the protein-

free control. These observations are in agreement with our fluorescence microscopy and AFM data, providing further support for the hypothesis that his_6-GFP chelation to Ni^{2+}-activated **70** leads to protein concentration onto the polyrotaxane scaffold. Taking the AFM and cryo-EM imaging data together, our results suggest that a thin protein layer surrounding the polyrotaxane is formed, although the lateral and rotational organization of this adsorbate is still unclear.

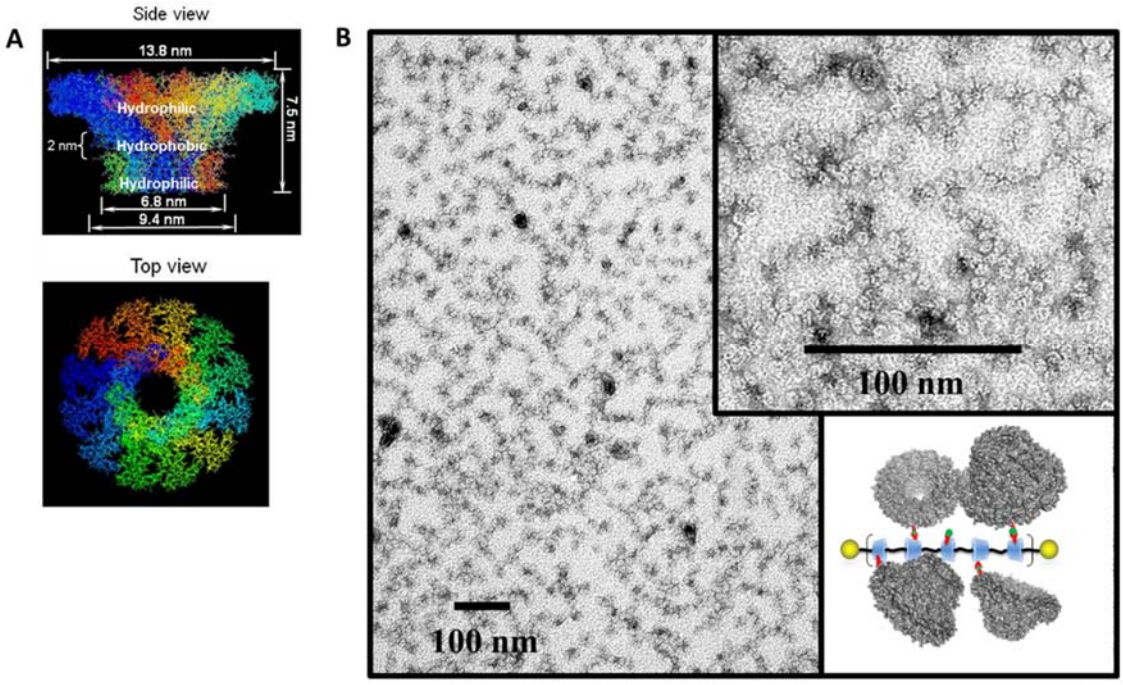

Figure 4.9. TEM Analysis of His_6-gp10 Adsorbed to NTA-Modified Polyrotaxane Scaffolds. (A) 3Dstructure of gp10 from the top and side. (B) Negative-stain TEM imaging of his_6-gp10:Ni^{2+}:**70** complexes**.** Images were taken with FEI/Philips CM-10 Bio-Twin instrument using glow discharged carbon-coated formvar copper 400 mesh grids (80 kV accelerating voltage) stained with a 2% $UO_2(OAc)_2$ solution.

In order to evaluate the ability of large protein assemblies to specifically adsorb to Ni^{2+}-activated NTA-polyrotaxanes, we performed negative stain TEM imaging of Ni^{2+}:**70** complexes treated with his-tagged bacteriophage phi29 connector protein assemblies (his_6-gp10) at a 1:1 his_6-gp10:α-CD ratio. This 440 kD protein dodecamer of gp10 connects the phage head to the ATP-driven motor that is responsible for DNA translocation and packaging during the formation of mature virion particles[34]. TEM images (Figure 4.9B) revealed the presence of many round pore-containing objects whose dimensions are consistent with phi29 connector protein assemblies; these features were presented in the same roughly linear arrangement seen for the Ni^{2+}-activated NTA-polyrotaxane control. We infer from these observations that his_6-gp10 is binding to the Ni^{2+}:**70** scaffold in a manner similar to his_6-GFP, except that the protein is not as densely packed along the polyrotaxane scaffold due to the spatial demands of the much larger phi29 connector array.

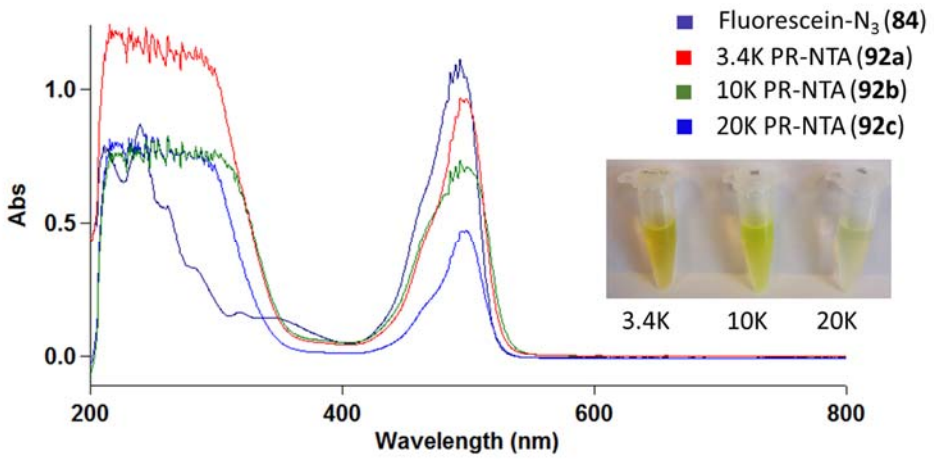

Figure 4.10. UV-Vis Analysis of Azidofluorescein (**84**) and Compounds **92a-c** in PBS. (Inset) Appearance of **92a-c** Solutions.

Ni^{2+} complexes of Compounds **92a-c** were prepared in a similar fashion to Compound **70**, Ni^{2+} complexes of **92a-c** were dialyzed to remove excess Ni^{2+} followed by lyophilization. Complexes were then analyzed by ICP-MS to determine the relative number of NTA's per polyrotaxane. UV-Vis spectra (Figure 4.10) were recorded for Compounds **92a-c** and Compound **84**, which is the endcap for the polyrotaxanes. All four solutions exhibited strong absorptions at 494 nm, which is characteristic of fluorescein[35]. All three polyrotaxanes **92a-c** exhibited absorption maxima characteristic of fluorescein and their color was also very similar to that of solutions of Compound **84**. This spectral evidence further illustrates the successful endcapping of polyrotaxanes by fluorescein and shows that the spectral properties of fluorescein can be utilized in experimentation with the fluorescein-capped polyrotaxane derivatives **92a-c**.

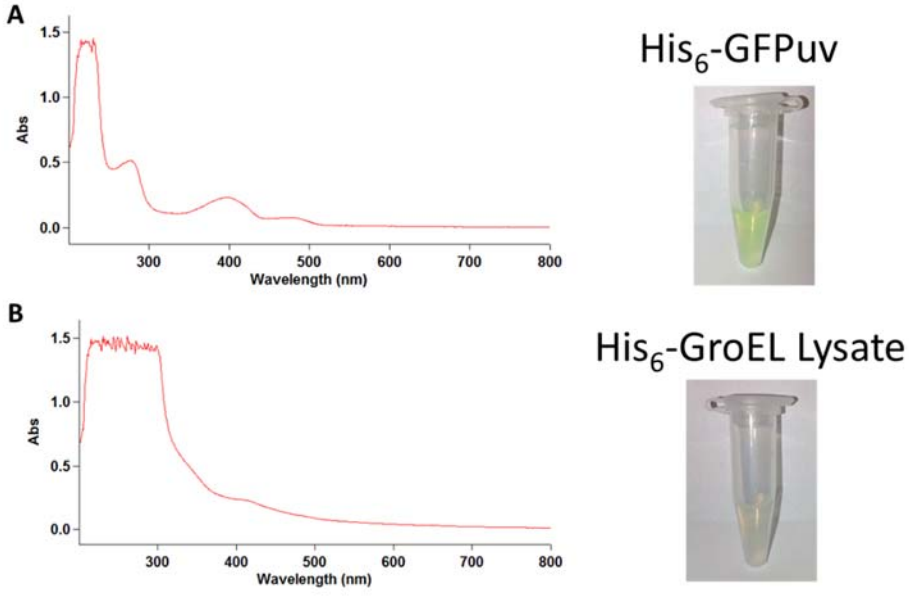

Figure 4.11. UV-Vis Spectra of (A) His_6-GroEL Lysate and (B) His_6-GFPuv Lysate.

Figure 4.11 shows the UV-Vis spectra of his_6-GroEL lysate and purified his_6-GFPuv. The GroEL lysate exhibits broad absorption from 200-400 nm characteristic of a crude lysate. The his_6-GFPuv exhibited spectral properties consistent with other GFP variants.

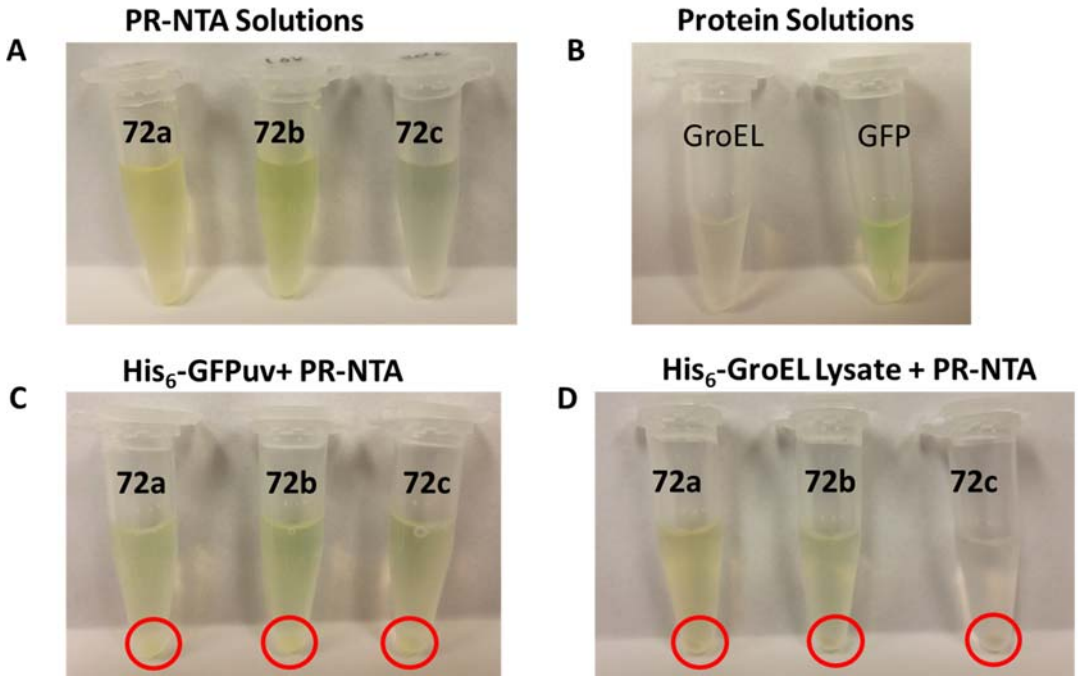

Figure 4.12. Centrifugal Isolation of **92a-c** Complexes with His_6-GFPuv and His_6-GroEL Lysate. (A) solutions of Compounds **92a-c**. (B) Appearance of his_6-GFP-uv and his_6-GroELlysate. (C) Appearance of sediments generated from **92a-c** and his_6-GFPuv. (D) Appearance of sediments generated from **92a-c** and his_6-GroEL.

From our previous fluorescence microscopy results, there was good evidence that the NTA-modified polyrotaxanes were forming complexes of very high molecular weight which were large enough to be visible by fluorescence microscopy. We developed a method to isolate these complexes via centrifugation of mixtures of **92a-c** with his-tagged

proteins. These complexes were isolated after 30 minute incubation via centrifugation at 12,000 g for 30 minutes. These pellets could then be resuspended and dispersed via sonication to generate samples suitable for imaging. This process is a variation on the monolayer purification approach[15, 36] that may be useful for cryo-EM sample preparation. Figure 4.12 visually shows the appearance of solutions of **92a-c**, his_6-Gro-EL, his_6-GFPuv and sediments generated via incubation of each PR and his-tagged protein, respectively.

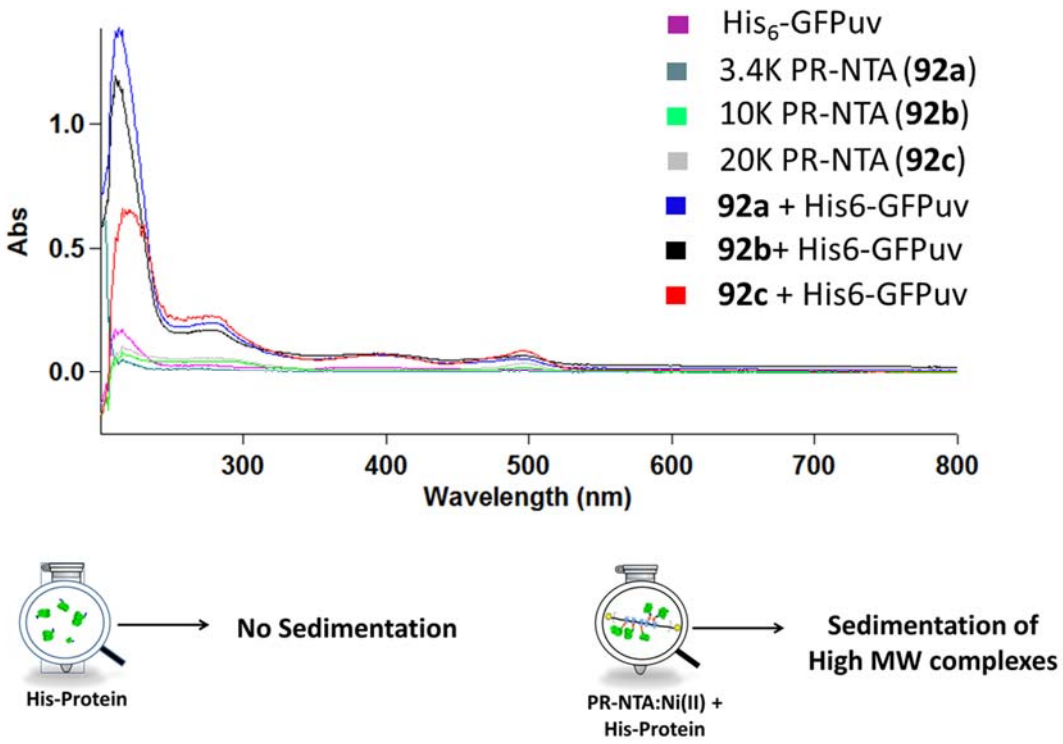

Figure 4.13. Centrifugal Isolation of His_6-GFPuv Complexed with **92a-c**.

In order to further demonstrate the capacity for isolation of his-tagged proteins from purified solution and crude cell lysate using NTA-modified polyrotaxanes, UV-Vis

spectra were recorded of various solutions subjected to the centrifugal isolation protocol used for isolation of his-tagged proteins (Figure 4.13). The controls where either protein only or polyrotaxane only showed relatively low fluorescence intensity because no sedimentation was observed. Residual spectra properties are attributed to some solution being left in the tube. However, UV-Vis spectra of the resuspended lysates all exhibited spectra similar to his$_6$-GFPuv with trace characteristics of **92a-c**.

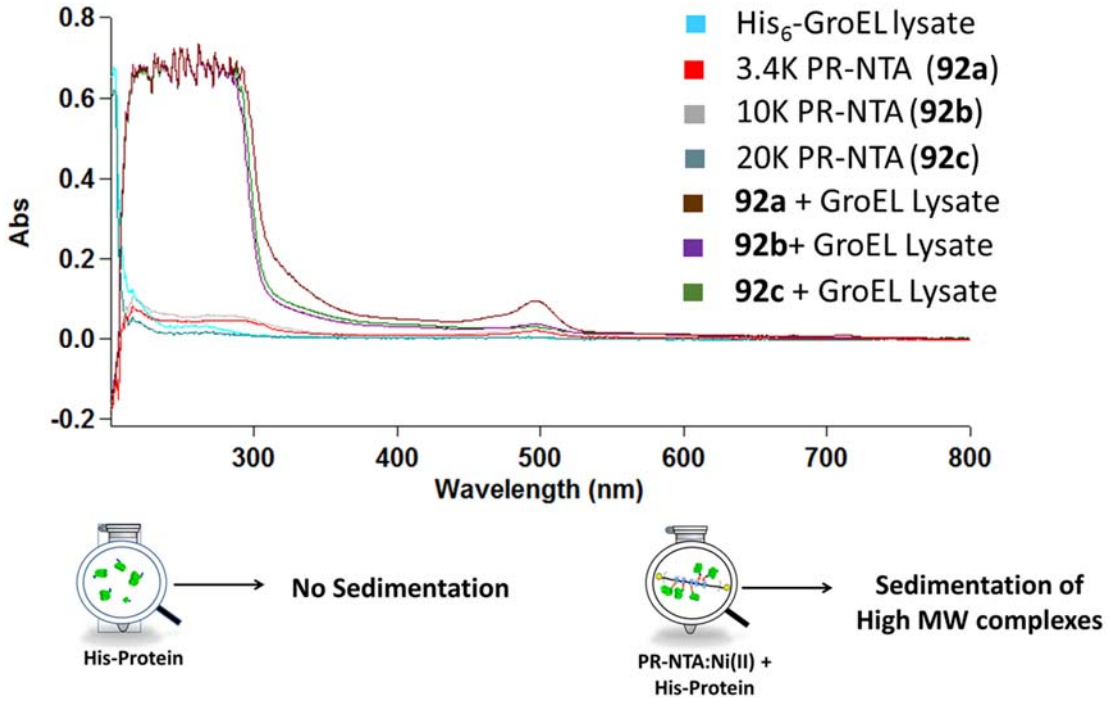

Figure 4.14. Centrifugal Isolation of His$_6$-GroEL Complexed with **92a-c**.

Similarly, UV-Vis spectra were recorded of various solutions subjected to the centrifugal isolation protocol used for isolation of his-tagged proteins (Figure 4.14) with his$_6$-GroEL lysate. The results are similar to those with his$_6$-GFP, the controls showed

low absorption and no visible sedimentation was observed. Residual absorption is attributed to solution left in the tube after decantation. All the Compounds **92a-c** with his_6-GroEL visible formed sediments and after resuspension, the UV-Vis spectra were similar to spectra of his_6-GroEL.

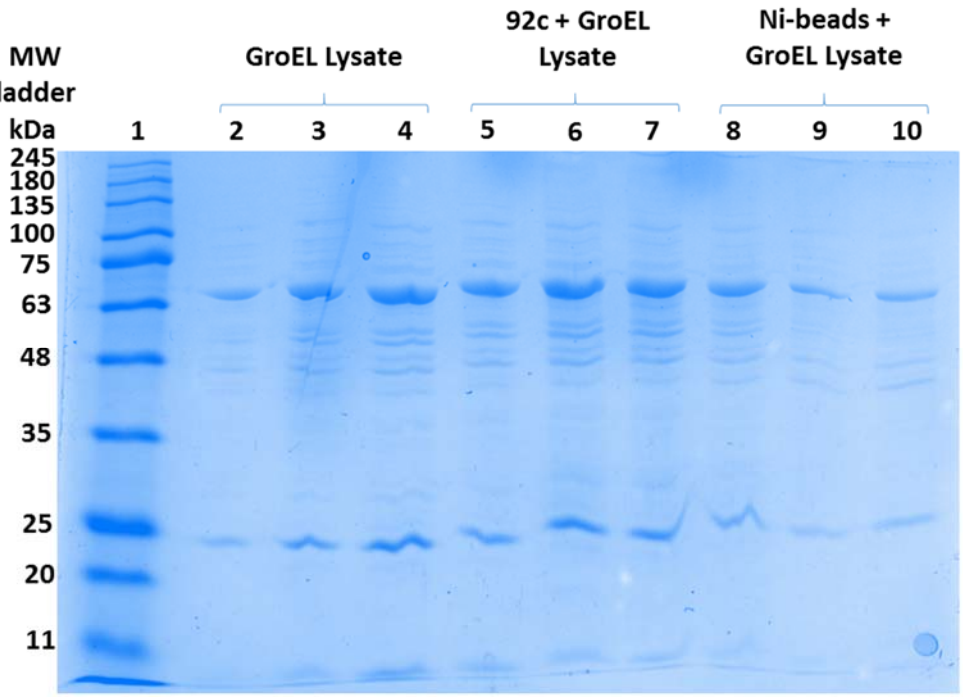

Figure 4.15. SDS-PAGE Analysis of Isolation of His_6-GroEL from Cell Lysate. Lane 1: Molecular weight ladder (BLUEStain). Lanes 2-4: his_6-GroEL lysate. Lanes 5-7: Compound **92c** + his_6-GroEL lysate. Lanes 8-10: Ni:NTA beads (Talon resin) + his_6-GroEL isolated via centrifugation protocol.

SDS-PAGE was used to evaluate the purity of pellets isolated via centrifugation and using a commercial Ni:NTA resin using the centrifugation protocol used to isolate his-tagged proteins with NTA-modified polyrotaxanes (Figure 4.15). Results indicate that the protein composition of the sediments resembles the lysate with a possible modest

degree of purification. The centrifugation process was modified slightly to use commercial Ni:NTA resin in place of Compounds **92a-c**. The protein composition of the material isolated also resembles the lysate. This shows that it may be possible to further modify the protocol to generate higher quality protein solutions via addition of washing steps or flow-based methods.

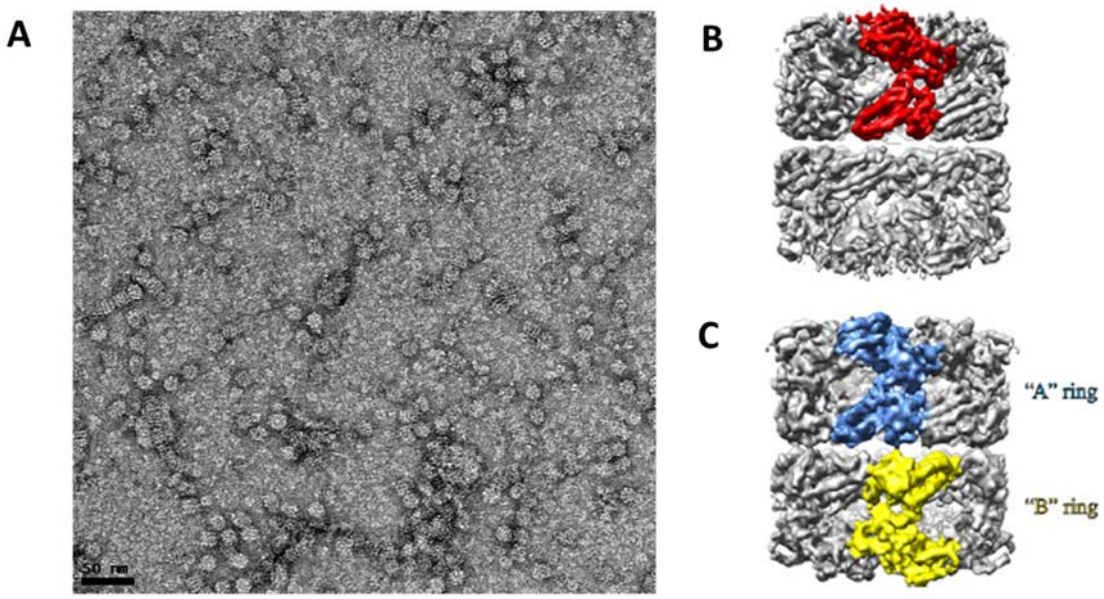

Figure 4.16. TEM Analysis of His_6-GroEL Isolated via Centrifugal Purification. (A) representative negatively-stained TEM image. (B) 4.2 Å reconstruction of native GroEL with D7 symmetry with a single subunit highlighted in red reported by Ludtke et al.[37] (C) 4.7 Å reconstruction of native GroEL with C7 symmetry reported by Ludtke et al.[37] A single subunit in the A ring is colored blue while a single subunit in the B ring is colored yellow.

In order to further evaluate the ability of Compounds **92a-c** for isolation and cryo-EM of his-tagged protein from cell lysate, GroEL cell lysate was subjected to the centrifugal isolation protocol detailed above and resuspended sediment was qualitatively evaluated by TEM. Figure 4.16 depicts a representative image from this dataset. The

image appears to show his_6-GroEL adsorbed to the tubular polyrotaxane scaffold. These particles are confirmed to be his_6-GroEL as reported in cryo-EM efforts previously by Ludtke[37]. The appearance of the adsorbed particles is concurrent with results from UV-Vis and SD-PAGE that his_6-GroEL is present in complex with Compounds **92a-c** via affinity interaction. Efforts are currently directed toward generation of 3D reconstruction from cryo-EM datasets generated using this isolation method.

4.5 Conclusions

A library of polyrotaxanes based on PEG, α-CD and various endcaps and rotaxanation methods was synthesized. Several of these compounds were further modified with NTA moieties to impart affinity interactions on the tubular polyrotaxane templates which might be used for isolation of proteins and assisted cryo-EM via homogenization of orientational distribution from lateral and rotational mobility of the CD's upon which the protein is adsorbed. The laterally- and rotationally-mobile NTA-CD ligating groups enabled the capture of two his-tagged proteins of substantially different size and facilitated their imaging via AFM, cryo-TEM, and TEM. This material may greatly facilitate the cryo-EM analysis of his-tagged proteins by concentrating them into large and readily detectable clusters that enables projection images of the protein structure in all possible 3D orientations. It is anticipated that these NTA-modified polyrotaxane materials may be an important new tool for facilitating SPA by reducing both the amount of purified protein necessary for SPA and the time required for acquisition of the large particle counts needed for high-resolution analysis.

4.6 Experimental Methods

All reactions were carried out under a blanket of N_2 or argon gas. Reaction progress was monitored by thin-layer chromatography (TLC) analysis. TLC spots were visualized either by UV light (254nm), exposure by ninhydrin staining, staining with phosphomolybdic acid (PMA), staining by bromocresol green, or by staining with I_2. Flash column chromatography was carried out using 230-400 mesh silica gel and analytical grade solvents. Solvents were purchased from Mallinckrodt/Baker and used without further purification unless noted. Toluene was purchased from Fisher. PEG polymers were from Sigma-Aldrich and were purified before use via precipitation from a solution in DCM into diethyl ether. 2,4,6-trinitrobenzenesulfonic acid (1.0 M in H_2O) was purchased from Aldrich. Sodium 2,4,6-Trinitrobenzenesulfonate (TNBS) was obtained by neutralization of 2,4,6-trinitrobenzenesulfonic acid solution with $NaHCO_3$. α-Cyclodextrin (α-CD) was purchased from Tokyo Kasei Inc. Dichloromethane (DCM), and toluene were distilled from CaH_2. Triethylamine (TEA) was distilled from CaH_2 and stored over BaO. Tetrahydrofuran (THF) was distilled from sodium-benzophenone ketyl. Dimethyl sulfoxide (DMSO) was distilled from CaH_2. N-(3-dimethylaminopropyl)-N'-ethylcarbodiimide hydrochloride (EDC) was purchased from Advanced Chemtech. All other chemicals were purchased from Sigma Aldrich and used without further purification.

^{1}H and ^{13}C nuclear magnetic resonance (NMR) spectra were recorded on either a Bruker AV500HD (500MHz) or a Bruker ARX400 spectrometer (400 MHz). Chemical shifts are reported in ppm relative to the residual solvent peaks as internal standard

4.6.1 Synthesis of Homobifunctional PEG Derivatives

PEG-bis-mesylate (57a-e). PEG was dried azeotropically with toluene several times and dried *in vacuo* for 18 hours. As a representative reaction, PEG (3.00 g) was dissolved in DCM (85 mL) and triethylamine (3.00 equiv.) was added. The solution was cooled to 0 °C in an ice bath and methansulfonyl chloride (MsCl, 2.2 equiv.) was added dropwise over 10 minutes. The reaction was stirred for an additional 30 minutes at 0 °C. The solution was transferred to a separatory funnel with an additional 50 mL DCM. The solution was washed with 100 mL ice water followed by 100 mL 5 % HCl solution. The organic solution was dried with anhydrous sodium sulfate and concentrated in vacuo. The oily residue was precipitated into cold diethyl ether (500-800 mL), filtered and dried *in vacuo* to give **57a-e** as white powders. Yield: (89-95 %).

PPEG-bis-azide (58a-e). PEG-bis-mesylate **57a-e** (3.00 g) was dissolved in DMF (150 mL) and sodium azide (20.0 equiv.) was added. The solution was stirred for 90 °C for 48 hours. DMF was evaporated *in vacuo*. The residue was dissolved in DCM (200 mL), filtered and washed with deionized water (150 mL) twice. The aqueous washes were extracted with DCM (100 mL) twice each and the organic extracts were combined with the original organic solution and concentrated *in vacuo*. The oily residue was precipitated into cold diethyl ether (500-800 mL), filtered and dried *in vacuo* to give **58a-e** as white powders. Yield: (90-98 %).

PEG-bis-amine (59a-e). PEG-bis-azide **58a-e** (3.00 g) was dissolved in ethyl acetate (50 mL) and 10% palladium on carbon (wet type) was added via spatula. The flask was

equipped with a three-way adapter and a hydrogen balloon. The flask was evacuated and purged with hydrogen three times and stirred vigorously under 1 atm hydrogen atmosphere for 24 hours at ambient temperature. The solution was gravity filtered through Celite and concentrated *in vacuo*. The oily residue was precipitated into cold diethyl ether (500-800 mL), filtered and dried *in vacuo* to give **59a-e** as white powders. Yield: (88-96 %).

PEG-bis-carboxylic acid (60a-e). Jones oxidation was used to produce carboxylic acid-terminal PEG**.** As a representative reaction, PEG (2.50 g) was dissolved in 280 mL acetone. Jones' Reagent (2.2 equiv) was added to a 500 mL round bottom flask and the mPEG solution was added to this flask dropwise over 1 hour via addition funnel. The resulting solution was stirred at 20 °C for 1 hour before quenching the excess Jones reagent with a few mL of iPrOH. The resulting green precipitate was removed by decantation of the liquid solution. The volatiles were removed under reduced pressure and the residue dissolved in 150 mL H_2O. The aqueous phase was extracted with DCM (4 x 120 mL). Depending of PEG molecular weight, it may be necessary to add MeOH (100-200 mL) to effect phase separation. The organic layers were combined and dried over anhydrous Na_2SO_4, filtered, and evaporated under reduced pressure. The oily residue was precipitated into cold diethyl ether (500-800-mL), filtered and dried *in vacuo* to give **60a-e** as white powders. TLC analysis was used to verify conversion using bromocresol green stain. Yield: (88-94 %).

PEG-bis-aldehyde (61a-e). Albright-Goldman oxidation was used to oxidize terminal hydroxyl-moieties of PEG to aldehyde groups. PEG **56a-e** was dissolved in a mixture of dimethyl sulfoxide (DMSO) and acetic anhydride (Ac_2O) (5 mL of 3:2 DMSO:Ac_2O for every 1 mmol of alcohol). This solution is prepared beforehand at least 24 hours before reaction. The solution was stirred for 24 hours at ambient temperature. The solution was concentrated *in vacuo*. The oily residue was precipitated into cold diethyl ether (500-800 mL) 2-3 times, filtered and dried *in vacuo* to give **61a-e** as white powders. Yield: (89-94 %).

PEG-bis-amine (62a-e). An alternative synthesis of amine-terminal PEG was developed utilizing reductive amination. PEG-aldehyde **61a-e** (3.00 g), ammonium chloride (10.0 equiv) and potassium hydroxide (3.3 equiv) were dissolved in anhydrous MeOH (25 mL). This solution was stirred for 30 min. A solution of sodium cyanoborohydride (10.0 equiv) in anhydrous MeOH (10 mL) was added. And the solution was stirred under argon at ambient temperature for 24 hours. The solution was poured into 100 mL of deionized water and extracted with DCM (100 mL) four times. The organic extracts were dried over anhydrous sodium sulfate and concentrated *in vacuo*. The oily residue was precipitated into cold diethyl ether (500-800 mL), filtered and dried *in vacuo* to give **62a-e** as white powders. Yield: (91-97 %).

PEG-bis-ethylenediamine (63a-e). An alternative synthesis of amine-terminal PEG was developed direct CDI coupling of ethylenediamine to PEG. PEG **56a-e** (2.00 g) was dissolved in DCM (100 mL), cooled down to 0 °C in an ice bath and triethylamine (10.00 equiv) was added followed by CDI (5.00 equiv). The solution was stirred for 2 hours

warming to room temperature and ethylenediamine (20.0 equiv) was added via syringe. The solution was stirred for an additional 24 hours at ambient temperature. The solution was transferred to a separatory funnel and washed with 100 mL 5 % HCl twice followed by deionized water. The organic phase was dried over sodium sulfate, concentrated and precipitated into diethyl ether (600-800 mL), filtered and dried *in vacuo* to give **63a-e** as a white powders. Yield: (91-97 %).

PEG-bis-(tris-2-aminoethyl)amine) (64a-e). An alternative synthesis of amine-terminal PEG was developed direct CDI coupling of tris-(2-aminoethyl)amine to PEG**.** PEG **56a-e** (2.00 g) was dissolved in DCM (100 mL), cooled down to 0 °C in an ice bath and triethylamine (10.00 equiv) was added followed by CDI (5.00 equiv). The solution was stirred for 2 hours warming to room temperature and tris-(2-aminoethyl)amine (20.0 equiv) was added via syringe. The solution was stirred for an additional 24 hours at ambient temperature. The solution was transferred to a separatory funnel and washed with 100 mL 5 % HCl twice followed by deionized water. The organic phase was dried over sodium sulfate, concentrated and precipitated into diethyl ether (600-800 mL), filtered and dried *in vacuo* to give **63a-e** as a white powders. Yield: (89-95 %).

PEG-bis-(2-methyl-2-bromopropionamide) (65a-e). PEG-bis-amine **(59a-e)** (2.00 g), 2-methyl-2-bromopropionic acid (20.0 equiv), and HOBt (16.0 equiv) were dissolved in 20 mL DCM. DIEA (30.0 equiv) was added via syringe and the solution was cooled to 0 °C in an ice bath. EDC was added and the solution was stirred for 48 hours warming to room temperature. The solution was diluted with 50 mL DCM and washed with % % HCl (50 mL) twice then deionized water (50 mL). The organic solution was dried over

anhydrous sodium sulfate, filtered and precipitated into diethyl ether (600-800 mL), filtered and dried *in vacuo* to give **65a-e** as white solids. Yield: (92-88 %).

4.6.2 Synthesis of TNBS-Capped Polyrotaxanes

TNBS-capped-PEG-bis-amine-α-CD polyrotaxanes (66a-d). α-CD (10.0 g, 10.28 mmol) was fully dissolved in 120 mL of deionized H_2O before addition of PEG-bis-amine (1.50 g). The mixture was sonicated for 30 min at 20 °C and the resulting white gel-like substance stored at 20 °C for 12 h. TNBS was neutralized to pH of 9.0 via addition of solid $NaHCO_3$ to generate sodium 2,4,6-trinitrobenznesulfonate. Sodium 2,4,6-trinitrobenznesulfonate (4.00 equiv per mol polymer) was then added as an aqueous slurry and stirred at 20 °C for 12 hours. The reaction mixture was washed via centrifugation sequentially with water 8 times before dialyzing the product (molecular weight cut-off 6,000-8,000) against DMSO for 3 d, then water for 3 d. The retained dialysate was then lyophilized to give polyrotaxane **66a-d** as yellow powders. Yield: (92-88 %). Yield: **a**: 5.068 g, **b**: 1.605 g, **c**: 1.029 g, **d**: 0.653 g; ^{1}H NMR (400 MHz, DMSO-d_6) δ 8.73-8.97 (s, TNB-C-H), δ 5.51 (d, α-CD-OH), 5.43 (s, α-CD-OH), 4.79 (s, α-CD-OH), 4.47 (t, α-CD-C_1-H), 3.87 – 3.06 (m, α-CD and PEG).

TNBS-capped-PEG-bis-ethylenediamine α-CD polyrotaxanes (67a,c,e). α-CD (10.0 g, 10.28 mmol) was fully dissolved in 120 mL of deionized H_2O before addition of PEG-bis-ethylenediamine (1.50 g). The mixture was sonicated for 30 min at 20 °C and the resulting white gel-like substance stored at 20 °C for 12 h. TNBS was neutralized to pH of 9.0 via addition of solid $NaHCO_3$ to generate sodium 2,4,6-trinitrobenznesulfonate.

Sodium 2,4,6-trinitrobenzenesulfonate (4.00 equiv per mol polymer) was then added as an aqueous slurry and stirred at 20 °C for 12 hours. The reaction mixture was washed via centrifugation sequentially with water 8 times before dialyzing the product (molecular weight cut-off 6,000-8,000) against DMSO for 3 d, then water for 3 d. The retained dialysate was then lyophilized to give polyrotaxanes **67a,c,e** as yellow powders. Yield: (92-88 %). Yield: **a**: 3.017 g, **c**: 4.434 g, **e**: 4.687 g. ^{1}H NMR (400 MHz, DMSO-d_6) δ 8.73-8.97 (s, TNB-C-H), δ 5.51 (d, α-CD-OH), 5.43 (s, α-CD-OH), 4.79 (s, α-CD-OH), 4.47 (t, α-CD-C_1-H), 3.87 – 3.06 (m, α-CD and PEG).

TNBS-capped PEG- bis-(tris-2-aminoethyl)amine) α-CD polyrotaxanes (68b,c). α-CD (10.0 g, 10.28 mmol) was fully dissolved in 120 mL of deionized H_2O before addition of PEG- bis-(tris-2-aminoethyl)amine) (1.50 g). The mixture was sonicated for 30 min at 20 °C and the resulting white gel-like substance stored at 20 °C for 12 h. TNBS was neutralized to pH of 9.0 via addition of solid $NaHCO_3$ to generate sodium 2,4,6-trinitrobenzenesulfonate. Sodium 2,4,6-trinitrobenzenesulfonate (8.00 equiv per mol polymer) was then added as an aqueous slurry and stirred at 20 °C for 12 hours. The reaction mixture was washed via centrifugation sequentially with water 8 times before dialyzing the product (molecular weight cut-off 6,000-8,000) against DMSO for 3 d, then water for 3 d. The retained dialysate was then lyophilized to give polyrotaxanes **68b,c** as yellow powders. Yield: (92-88 %). Yield: **b**: 0.266 g, **c**: 0.170; ^{1}H NMR (400 MHz, DMSO-d_6) δ 8.73-8.97 (s, TNB-C-H), δ 5.51 (d, α-CD-OH), 5.43 (s, α-CD-OH), 4.79 (s, α-CD-OH), 4.47 (t, α-CD-C_1-H), 3.87 – 3.06 (m, α-CD and PEG).

4.6.3 NTA-Modification of TNBS-Capped Polyrotaxanes

t-Butyl-NTA-Modified-TNBS-capped-PEG-bis-amine-α-CD polyrotaxane (69). Polyrotaxane **66c** (200 mg, 7.42 μmol) was dried in a 100 mL round bottom flask at 40 °C under vacuum for 48 h before adding dry DMSO (20 mL) and stirring until the material dissolved. *N*,*N*′-Carbonyldiimidazole (CDI, 1.328 g, 8.19 mmol) was added to the polyrotaxane solution and the reaction allowed to proceed for 24 h at 20 °C under a N_2 atmosphere. The reaction mixture was precipitated using a mixed ethereal solution (160 mL dry Et_2O and 50 mL dry THF). The precipitate was added to NTA intermediate **15** (0.485 g, 1.13 mmol) in 10 mL dry DMSO and triethylamine (0.181 mL, 1.30 mmol) and the reaction stirred for 24 h at 20 °C under N_2. The product was dialyzed (molecular weight cut-off 6.0-8.0 kDa) against DMSO for 48 hours then deionized water for 48 hours. The retained material was lyophilized to give t-butyl-NTA-modified polyrotaxane **69** as a yellow powder. Yield: 0.150 g.

NTA-Modified-TNBS-capped-PEG-bis-amine-α-CD polyrotaxane (70). Compound **69** (0.276 g) was dissolved in DMSO (20 mL). TFA (20 mL) was added with stirring for 6 hours to deprotect the NTA *t*-butyl esters. The solution was concentrated *in vacuo* to remove TFA. The residue was dialyzed (molecular weight cut-off 6.0-8.0 kDa) against DMSO for 72 hours followed by deionized water for 72 hours. The material was further purified by Sephadex G-25 gel filtration chromatography using water as eluent. Polyrotaxane **70** was recovered by lyophilization. Yield: 0.103 g.

Bis(2-(trimethylsilyl)ethyl) 2,2'-((14,14-dimethyl-3,10-dioxo-1-phenyl-2,11-dioxa-4-aza-14-silapentadecan-9-yl)azanediyl)diacetate (71). Compound **18** (10.62 g, 26.8 mmol), 2-(trimethylsilyl)ethanol (19.01 g, 160.8 mmol) and DMAP (2.45 g, 20.1 mmol) were added to an oven dried 250 mL round bottom flask equipped with a magnetic stir bar and a rubber septum. The contents were dissolved in a 3:1 DMF: pyridine solution (250 mL) and cooled down to 0 °C in an ice bath. EDC (16.22 g, 84.6 mmol) was added. The solution was stirred for 18 hours warming to room temperature. The solution was concentrated and redissolved in Et_2O (300 mL) and filtered. The filtrate was transferred to a separatory funnel and washed with 5 % HCl (100 mL) twice then deionized water (100 mL). The organic phase was dried over anhydrous sodium sulfate, concentrated and purified by flask chromatography using 4:1 hexane: EtOAc as eluent. The pure fractions were combined, concentrated and dried *in vacuo* to give **71** as a clear oil. Yield: 11.726 g (62.8 %).; TLC: R_f= 0.33 (4:1 Hex: EtOAc); ^{1}H NMR (400 MHz, $CDCl_3$) δ 7.47 – 7.29 (m, 4H), 5.08 (s, 2H), 4.93 (s, 1H), 4.33 – 3.96 (m, 6H), 3.60 (s, 4H), 3.39 (t, J = 7.5 Hz, 1H), 3.26 – 2.99 (m, 2H), 1.80 – 1.60 (m, 2H), 1.60 – 1.43 (m, 4H), 1.43 – 1.33 (m, 1H), 1.33 – 1.04 (m, 1H), 0.98 (q, J = 8.4 Hz, 6H), 0.03 (d, J = 6.1 Hz, 28H).

Bis(2-(trimethylsilyl)ethyl) 2,2'-((6-amino-1-oxo-1-(2-(trimethylsilyl)ethoxy)hexan-2-yl)azanediyl)diacetate (72). Compound **71** (12.136 g, 17.4 mmol) was dissolved in MeOH (80 mL) in a 250 mL round bottom flask equipped with a stir bar and a three-way adapter with 90° stopcock equipped with a balloon. A spatula tip of 10 % palladium on carbon (wet type) was added and the flask was evacuated and purged with hydrogen 5 times. The heterogeneous mixture was stirred for 12 hours at ambient temperature. The

solution was gravity filtered through a pad of Celite and activated carbon and the filtrate was concentrated *in vacuo* to give Compound **72** as a clear oil. Yield: 9.156 g (93.4 %).; TLC: R_f= 0.01 (4:1 Hex: EtOAc); ^{1}H NMR (400 MHz, $CDCl_3$) δ 4.47 (s, 3H), 4.21 – 3.99 (m, 6H), 3.53 (s, 4H), 3.33 (t, J = 7.5 Hz, 1H), 2.74 (t, J = 7.0 Hz, 2H), 1.63 (dd, J = 14.6, 7.9 Hz, 2H), 1.52 (tt, J = 17.2, 9.3 Hz, 3H), 1.37 – 1.27 (m, 1H), 1.06 – 0.70 (m, 5H), -0.03 (d, J = 4.2 Hz, 25H).

2,2-Dimethyl-6,15-dioxo-8-(2-oxo-2-(2-(trimethylsilyl)ethoxy)ethyl)-9-((2-(trimethylsilyl)ethoxy)carbonyl)-5-oxa-8,14-diaza-2-silaoctadecan-18-oic acid (73). Compound **72** (0.743 g, 1.31 mmol) was dissolved in DCM (30 mL). DIEA was added via syringe (0.171 g, 1.32 mmol) followed by succinic anhydride (0.198 g, 1.98 mmol). The solution as stirred for 18 hours under nitrogen at ambient temperature. The solution was concentrated and redissolved in Et_2O (150 mL). The solution was transferred to a separatory funnel and washed with 0.1 M HCl (50 mL) twice. The organic phase was dried over anhydrous sodium sulfate, concentrated and purified using a gradient of 10 % MeOH/DCM to 15 % MeOH/DCM. The pure fractions were combined, concentrated and dried *in vacuo* to give Compound **73** as a clear oil. Yield: 0.805 g (92.0 %).; TLC: R_f= 0.58 (15 % MeOH/DCM); ^{1}H NMR (400 MHz, $CDCl_3$) δ 9.22 (s, 1H), 6.70 (s, 1H), 4.13 (dd, J = 11.1, 5.6 Hz, 6H), 3.73 – 3.62 (m, 1H), 3.56 (d, J = 12.5 Hz, 3H), 3.38 (t, J = 7.5 Hz, 1H), 3.21 (dd, J = 12.0, 5.5 Hz, 2H), 2.61 (dd, J = 13.9, 7.0 Hz, 3H), 2.52 (d, J = 6.3 Hz, 2H), 1.79 – 1.60 (m, 2H), 1.58 – 1.34 (m, 4H), 1.32 – 1.10 (m, 1H), 0.95 (q, J = 8.1 Hz, 6H), -0.00 (d, J = 4.7 Hz, 25H).

Dimethyl 2,2'-((6-(((benzyloxy)carbonyl)amino)-1-methoxy-1-oxohexan-2-yl)azanediyl)diacetate (74). Compound **18** (8.353 g, 21.1 mmol) was dissolved in anhydrous MeOH in an oven-dried 500 mL round bottom flask equipped with a magnetic stir bar and rubber septum. The solution was cooled to 0 °C in an ice bath and sulfuric acid (4.28 mL) was added dropwise via Pasteur pipette. A reflux condenser was attached and the solution was heated to reflux and stirred for 60 hours. The solution was concentrated *in vacuo* and redissolved in Et_2O (250 mL). The solution was washed with 5 % $NaHCO_3$ solution (80 mL) twice followed by deionized water (80 mL) and brine (80 mL). The organic phase was dried over anhydrous sodium sulfate, concentrated and purified via flash chromatography using a gradient of 4:1 hexane: EtOAc to 1:1 hexane: EtOAc. The pure fractions were combined, concentrated and dried *in vacuo* to give Compound **74** as a clear oil. Yield: 6.711 g (72.6 %).; TLC: R_f= 0.37 (1:1 hexane: EtOAc); ^{1}H NMR (400 MHz, $CDCl_3$) δ 7.09 (s, 5H), 5.52 (s, 1H), 4.85 (s, 2H), 3.42 (s, 13H), 3.19 (s, 1H), 2.93 (s, 2H), 1.45 (s, 2H), 1.27 (s, 3H), 1.14 (s, 1H). ^{13}C NMR (101 MHz, $CDCl_3$) δ 172.64, 171.42, 156.28, 136.73, 128.11, 127.66, 77.81, 77.49, 77.17, 65.89, 64.19, 52.01, 51.16, 50.97, 40.44, 32.72, 29.60, 29.05, 22.64.

Z-Lys-tris-NTA-(Otmse) (75). Compound **18** (1.61 g, 4.06 mmol) and Compound **72** (9.156 g, 16.3 mmol) and HOBt (1.98 g, 14.7 mmol) were added to an oven-dried 500 mL round bottom flask equipped with a magnetic stir bar and rubber septum. The contents were dissolved in DMF (90 mL) and cooled to 0 °C in an ice bath. EDC (3.00 g, 14.7 mmol) was added and the solution was stirred for 48 hours warming to room temperature. The solution was concentrated *in vacuo* and redissolved into EtOAc (200

mL). the solution was washed with 5% HCl (80 mL) three times. The organic solution was dried over anhydrous sodium sulfate, concentrated and purified via flash chromatography using a gradient of 1:1 hexane:EtOAc to 100 % EtOAc. The pure fractions were combined, concentrated and dried *in vacuo* to give Compound **75** as a clear viscous oil. Yield: 3.894 g (47.2 %).; TLC: R_f= 0.77 (100 % EtOAc); ^{1}H NMR (400 MHz, $CDCl_3$) δ 7.45 (s, 1H), 7.33 (s, 4H), 5.13 (s, 1H), 5.07 (s, 2H), 4.37 – 3.90 (m, 19H), 3.58 (s, 11H), 3.37 (q, J = 10.2, 7.2 Hz, 6H), 3.28 – 2.89 (m, 10H), 1.84 – 1.61 (m, 7H), 1.50 (s, 12H), 1.35 (dp, J = 21.8, 6.9 Hz, 5H), 0.98 (q, J = 8.8 Hz, 18H), 0.03 (d, J = 5.1 Hz, 76H).

H_2N-Lys-tris-NTA-(Otmse) (76). Compound **75** (1.00 g, 0.49 mmol) was dissolved in MeOH (50 mL) in a 250 mL round bottom flask equipped with a magnetic stir bar and a three-way adapter equipped with a balloon and a 90°stopcock. A spatula tip of 10 % palladium on carbon was added and the flask was evacuated and purged with hydrogen three times and the heterogeneous mixture was stirred at ambient temperature under 1 atm hydrogen for 18 hours. The mixture was gravity filtered through a pad of Celite and activated carbon. The filtrate was concentrated and dried *in vacuo* to give Compound **76** as a clear oil. Yield: 0.922 g (98.8 %).; TLC: R_f= 0.02 (100 % EtOAc); ^{1}H NMR (400 MHz, $CDCl_3$) δ 7.90 (s, 1H), 6.28 (s, 1H), 4.37 – 3.88 (m, 18H), 3.67 – 3.43 (m, 12H), 3.39 (s, 3H), 3.32 (s, 3H), 3.26 – 3.02 (m, 9H), 2.95 (s, 1H), 1.62 (s, 9H), 1.37 – 1.13 (m, 4H), 0.94 (q, J = 8.4 Hz, 17H), -0.02 (d, J = 4.7 Hz, 74H).

HO_2C-Lys-tris-NTA-(Otmse) (77). Compound **76** (0.488 g, 0.26 mmol) was dissolved in DCM (50 mL) in an oven-dried 250 mL round bottom flask equipped with a stir bar and rubber septum. DIEA (183 μL, 1.03 mmol mmol) was added followed by succinic anhydride (0.155 g, 1.55 mmol). The solution was stirred for 18 hours at ambient temperature. The solution was concentrated *in vacuo* and redissolved in 120 mL Et_2O. The solution was transferred to a separatory funnel and washed with 0.1 M HCl (50 mL) twice then deionized water (50 mL). The organic phase was dried over anhydrous sodium sulfate, concentrated and purified via flash chromatography using 10 % MeOH/DCM as eluent. The pure fractions were combined, concentrated and dried *in vacuo* to give Compound **77** as a clear viscous soil. Yield: 0.492 g (97.4 %).; TLC: R_f= 0.29 (10 % MeOH/DCM); ^{1}H NMR (400 MHz, $CDCl_3$) δ 7.65 (s, 1H), 4.26 – 3.94 (m, 18H), 3.61 (d, J = 30.5 Hz, 11H), 3.50 – 3.40 (m, 3H), 3.34 (s, 4H), 3.23 (d, J = 22.1 Hz, 10H), 2.98 (s, 1H), 2.62 (d, J = 10.1 Hz, 6H), 1.83 (d, J = 11.7 Hz, 1H), 1.75 – 1.58 (m, 6H), 1.58 – 1.36 (m, 12H), 1.36 – 1.27 (m, 4H), 1.25 – 1.14 (m, 5H), 1.11 (d, J = 6.4 Hz, 1H), 0.96 (q, J = 8.0 Hz, 17H), 0.00 (d, J = 4.9 Hz, 72H).

Tmse-NTA-Modified-TNBS-capped-PEG-bis-ethylenediamine-α-CD polyrotaxane (78). Polyrotaxane **67e** (400 mg) was dried in a 100 mL round bottom flask at 40 °C under vacuum for 48 h before adding dry DMSO (25 mL) and stirring until the material dissolved. *N,N'*-Carbonyldiimidazole (CDI, 1.909 g) was added to the polyrotaxane solution and the reaction allowed to proceed for 24 h at 20 °C under a N_2 atmosphere. The reaction mixture was precipitated using a mixed ether solution (160 mL dry Et_2O and 50 mL dry THF). The precipitate was added to NTA intermediate **72** (0.633 g, 1.12

mmol) in 10 mL dry DMSO and triethylamine (0.476 μL) and the reaction stirred for 24 h at 20 °C under N_2. The product was dialyzed (molecular weight cut-off 6.0-8.0 kDa) against DMSO for 48 hours then deionized water for 48 hours. The retained material was lyophilized to give t-butyl-NTA-modified polyrotaxane **69** as a yellow powder. Yield: 0.600 g.

NTA-Modified-TNBS-capped-PEG-bis-ethylenediamine-α-CD polyrotaxane (79). 1.0 M TBAF in THF (6.6. mL) was added to 15 mL DMSO and THF was stripped *in vacuo*. Compound **78** (0.400 g) was dissolved in this solution. The solution was stirred at ambient temperature for 3 hours. The solution was dialyzed (molecular weight cut-off 6.0-8.0 kDa) against DMSO for 72 hours followed by deionized water for 72 hours. Polyrotaxane **79** was recovered by lyophilization. Yield: 0.267 g.

4.6.4 Screening of Aqueous Endcapping Methods

N^{α}-Cbz-l-Phenylalanine-capped-PEG-bis-carboxylate-α-CD polyrotaxane (80). α-CD (8.0 g, 10.28 mmol) was fully dissolved in 60 mL of deionized H_2O before addition of PEG-bis-carboxylate **52c** (0.750 g). The mixture was sonicated for 30 min at 20 °C and the resulting white gel-like substance stored at 20 °C for 12 h. The slurry was transferred to two 50 mL centrifuge tubes and pelleted. The water supernatant was decanted and the pseudorotaxane was lyophilized. A solution of N^{α}-Z-l-phenylalanine (0.434 g, 1.50 mmol), NMM (0.379 g, 3.75 mmol) and HOBt (36.5 mg, 0.27 mmol) in MeOH (30 mL). This solution was added to the lyophilized pseudorotaxane and EDC (0.288 g, 1.50 mmol) was added. The heterogeneous slurry was stirred for 48 hours at

ambient temperature. The reaction mixture was washed via centrifugation sequentially with water 8 times before dialyzing the product (molecular weight cut-off 6,000-8,000) against DMSO for 3 d, then water for 3 d. The retained dialysate was then lyophilized to give polyrotaxane **80** as a white powder. Yield: 0.285 g.

Poly(oligoethyene glycol) methacrylate-capped-PEG-bis-(2-methyl-2-bromopropionamide)-α-CD polyrotaxane (81). All deionized water was degassed via sonication followed by bubbling nitrogen for 30 min. α-CD (8.00 g) was dissolved in deionized water (60 mL). PEG-bis-(2-methyl-2-bromopropionamide) **65c** (0.750 g) was dissolved in 10 mL deionized water. The two aqueous solutions were combined in a 125 mL flask. The mixture was sonicated for 30 min at 20 °C and the resulting white gel-like substance stored at 20 °C for 12 hours under nitrogen. mPEG-methacrylate (avg. M_n = 500 Da, 7.652 mL, 16.5 mmol) was added via syringe. Copper(II) bromide solution (1.45 mL, 1.0 M in deionized water, 1.46 mmol) and 2,2-bypyridine solution (bpy, 2.0 mL, 125 mg/mL in DMSO, 1.60 mmol) were combined and added to the pseudorotaxane solution via syringe. Sodium-l-ascorbate solution (145.6 µL, 0.1 M in deionized water, 14.6 µmol) was added via syringe and the slurry was stirred for 48 hours at ambient temperature. The reaction mixture was washed via centrifugation sequentially with water 8 times before dialyzing the product (molecular weight cut-off 6,000-8,000) against DMSO for 3 d, then water for 3 d. The retained dialysate was then lyophilized to give polyrotaxane **81** as a white powder. Yield: 0.878 g.

4.6.5 Synthesis of Fluorescein-Capped Polyrotaxanes

PEG-bis-alkyne (82a-e). mPEG-bis-carboxylate **60a-e** (2.50 g) were dissolved in DCM (20 mL) in an oven dried 100 mL round bottom flask equipped with a magnetic stir bar and rubber septum. HOBt (5.00 equiv), DIEA (10.00 equiv) and propargylamine (20.0 equiv) were added. The solution was cooled to 0 °C in an ice bath. EDC (10.0 equiv) was added and the solution was stirred warming to ambient temperature for 48 hours. The solution was diluted with 60 mL DCM. The solution was transferred to a separatory funnel and washed with 5 % HCl (70 mL) twice then deionized water (70 mL) twice. The aqueous washes were combined and extracted with DCM (50 mL) three times. The organic extract was combined with the original DCM solution and dried over anhydrous sodium sulfate. The solution was filtered, concentrated and precipitated into 400 mL diethyl ether twice, filtered and dried *in vacuo* to give Compounds **82a-e** as white powders. Yield: (86-90 %).

5-Azido-3',6'-dihydroxy-3H-spiro[isobenzofuran-1,9'-xanthen]-3-one (84). 5-aminofluorescein (.100 g, 0.29 mmol) was dissolved in a mixture of 1:1:2 (water:MeOH: acetonitrile) (8 mL) in a 50 mL round bottom flask. The flask was filled with nitrogen and stirred at 0 °C for 10 min. tert-Butyl nitrite (51.3 µL, 0.40 mmol) was added by syringe, followed by trimethylsilyl azide (47.8 µL, 0.36 mmol) over 5 min. The flask was covered with foil and stirred for 3 hours at ambient temperature. The solution was concentrated *in vacuo* and purified by flash chromatography on silica with 85:15 (DCM:MeOH). Yield: 0.206 g (95.8 %).; TLC: R_f= 0.53 (15 % MeOH/DCM); ^{1}H NMR (400 MHz, Methanol-d_4) δ 7.79 – 7.57 (m, 1H), 7.44 – 7.26 (m, 1H), 7.26 – 7.04 (m, 1H),

6.95 – 6.73 (m, 2H), 6.72 – 6.62 (m, 2H), 6.59 (dd, J = 12.1, 2.3 Hz, 1H), 6.56 – 6.50 (m, 1H). ^{13}C NMR (101 MHz, DMSO) δ 171.40, 167.83, 156.22, 143.49, 131.14, 129.19, 124.88, 117.83, 117.15, 113.30, 103.75, 49.64, 49.43, 49.22, 49.00, 48.79, 48.58, 48.37. ESI^{+}: expected 373.32, found 374.2 (M+H).

4-((tert-Butoxycarbonyl)amino)benzoic acid (86). 4-Aminobenzoic acid (4.00 g, 29.17 mmol) was dissolved in dioxane (100 mL) and deionized water (50 mL) in an oven-dried 250 mL round bottom flask equipped with a magnetic stir bar and rubber septum. Di-tert-butyl-dicarbonate (12.720 g, 58.28 mmol) was added followed by triethylamine (8.16 mL, 58.28 mmol). The solution was stirred for 24 hours at ambient temperature. The solution was concentrated *in vacuo* and the crude product was precipitated via addition of 3.0 M HCl (15 mL). The crude product was filtered and recrystallized from MeOH/deionized water to give Compound **86** as an off white crystalline solid. Yield: 4.799 g (69.3 %); ^{1}H NMR (400 MHz, DMSO-d$_6$) δ 12.59 (s, 1H), 9.72 (s, 1H), 7.82 (d, J = 8.6 Hz, 2H), 7.54 (d, J = 8.5 Hz, 2H), 1.46 (s, 9H). ^{13}C NMR (101 MHz, DMSO) δ 189.46, 167.90, 153.41, 144.66, 131.91, 124.82, 121.23, 118.80, 117.71, 117.37, 117.34, 80.53, 76.15, 41.00, 40.80, 40.59, 40.38, 40.17, 39.96, 39.75.

Di-tert-butyl 2,2'-((1-(tert-butoxy)-6-(4-((tert-butoxycarbonyl)amino)benzamido)-1-oxohexan-2-yl)azanediyl)diacetate (87). Compound **86** (0.896 g, 3.78 mmol), Compound **15** (1.626 g, 3.78 mmol) and HOBt (0.567 g, 4.34mmol) were combined in an oven dried 250 mL round bottom flask equipped with a stir bar and rubber septum. The contents were dissolved in DMF (38 mL). The solution was cooled to 0 °C in an ice bath and EDC (0.833 g, 4.34 mmol) was added. The solution was stirred for 48 hours warming

to ambient temperature. The solution was concentrated *in vacuo* and the residue was dissolved in DCM (120 mL). The solution was transferred to a separatory funnel and washed with 0.1 M HCl (80 mL) twice and deionized water (80mL). The organic solution was dried over anhydrous sodium sulfate, filtered, concentrated and purified via flash chromatography using 5 % MeOH/DCM as eluent. The pure fractions were combined, concentrated and dried *in vacuo* to give Compound **87** as a clear oil. Yield: 1.090 g (44.5 %).; TLC: R_f= 0.35 (5 % MeOH/DCM); ^{1}H NMR (500 MHz, $CDCl_3$) δ 7.74 (d, J = 8.7 Hz, 2H), 7.39 (d, J = 8.6 Hz, 2H), 7.18 (s, 1H), 6.74 (t, J = 5.2 Hz, 1H), 3.69 (t, J = 6.6 Hz, 2H), 3.53 – 3.32 (m, 7H), 3.32 – 3.17 (m, 1H), 1.90 – 1.52 (m, 11H), 1.43 (d, J = 26.5 Hz, 25H), 1.37 (s, 15H). ^{13}C NMR (126 MHz, CDCl3) δ 172.41, 170.75, 167.11, 152.50, 141.41, 128.78, 128.12, 117.57, 81.10, 80.71, 77.35, 77.10, 76.84, 67.89, 64.97, 53.95, 39.68, 29.94, 28.57, 28.28, 28.18, 28.07, 25.57, 23.03.

2,2'-((5-(4-Aminobenzamido)-1-carboxypentyl)azanediyl)diacetic acid (88). Compound **87** (1.090 g, 1.68 mmol) was dissolved in DCM (15 mL) in an oven-dried 100 mL round bottom flask equipped with a magnetic stir bar and rubber septum. Triethylsilane (0.195 g, 1.68 mmol) was added via syringe and the solution was cooled to 0 °C in an ice bath. TFA (15 mL) was added slowly and the solution was stirred for 2 hours warming to room temperature. The solution was concentrated and rotovapped together with DCM (60 mL) three times. The residue was recrystallized twice from Et_2O/MeOH, filtered and dried *in vacuo* to give Compound **88** as a white crystalline solid. Yield: 1.090 g (44.5 %); ^{1}H NMR (500 MHz, Methanol-d_4) δ 7.72 (d, J = 8.0 Hz, 2H), 6.93 (d, J = 7.9 Hz, 2H), 3.82 – 3.59 (m, 5H), 3.55 – 3.44 (m, 2H), 3.36 (t, J = 6.5

Hz, 2H), 3.30 (s, 2H), 1.83 (d, J = 13.5 Hz, 1H), 1.64 (d, J = 13.2 Hz, 3H), 1.57 – 1.38 (m, 4H). ^{13}C NMR (126 MHz, MeOD) δ 174.04, 168.46, 145.48, 128.63, 126.51, 116.58, 65.35, 53.87, 48.11, 47.94, 47.77, 47.60, 47.43, 47.26, 47.09, 39.22, 29.18, 28.73, 26.96, 23.45, 14.04.

2,2'-((1-carboxy-5-(4-isothiocyanatobenzamido)pentyl)azanediyl)diacetic acid (89). Compound **88** (0.786 g, 2.06 mmol) was dissolved in deionized water (46.2 mL). The slightly cloudy solution was cooled to 0 °C in an ice bath. Thiophosgene (355 mg, 3.09 mmol) was dissolved in DCM (12.73 mL) in an oven-dried 20 mL scintillation vial. The thiophosgene solution was added to the aqueous solution of Compound **88** slowly. The biphasic solution was stirred vigorously for 2 hours warming to ambient temperature. The solution was stirred for an additional 30 min at 45 °C. The solution was concentrated to remove DCM and the remaining aqueous solution was lyophilized to give Compound **89** as a white solid. Yield: 0.568 g (65.1 %); ^{1}H NMR (500 MHz, DMSO-d_6) δ 8.52 (t, J = 5.4 Hz, 1H), 7.87 (d, J = 8.7 Hz, 2H), 7.48 (d, J = 8.6 Hz, 2H), 3.62 – 3.42 (m, 5H), 3.38 (t, J = 7.3 Hz, 1H), 3.21 (q, J = 6.8 Hz, 2H), 1.70 – 1.59 (m, 1H), 1.56 (d, J = 10.2 Hz, 1H), 1.53 – 1.44 (m, 2H), 1.45 – 1.20 (m, 5H). ^{13}C NMR (126 MHz, DMSO) δ 174.14, 173.32, 165.26, 135.20, 134.12, 132.74, 129.23, 126.29, 64.78, 53.74, 40.47, 40.31, 40.14, 39.97, 39.80, 39.64, 39.47, 29.62, 29.19, 28.18, 23.64.

Fluorescein-capped-PEG-bis-alkyne α-CD polyrotaxanes (90a-c). Alpha-cyclodextrin (α-CD) (5.33 g) was dissolved in 35 mL water. PEG-bis alkyne (**82b-d**, **a** = 0.500 g, 0.15 mmol; **b** = 0.500 g, 0.05 mmol; **c** = 0.500 g, 0.025 mmol) was dissolved in 11.66 mL water. The solutions were combined flushed with nitrogen and sonicated for 1 hour. After

several minutes the materials formed a white gel. The solutions were stirred at ambient temperature for 12 hours. 5-Azidofluorescein **84** (**a** = 219 mg, 0.587 mmol; **b** = 75 mg, 0.200 mmol; **c** = 38 mg, 0.102 mmol) was added as a solution in 2 mL DMSO and the solutions were stirred for 10 min. 1.0 M $CuSO_4$ solution (**a** = 148 μL, 0.148 mmol; **b** = 50 μL, 0.052 mmol; **c** = 25 μL, 0.025 mmol) and 1.0 M sodium-l-ascorbate solution (**a** = 294 μL, 0.293 mmol; **b** = 100 μL, 0.010 mmol 0.100 mmol, **c** = 50 μL, 0.050 mmol) were added via syringe and the heterogeneous solution was stirred for 48 hours at ambient temperature. The material was centrifuged, the supernatant was decanted, and the centrifugate resuspended in 5% EDTA solution and centrifuged. This process was repeated twice more to remove the remaining copper(II) and copper(I). The material was dialyzed against DMSO (MWCO = 6-8 kDa, Fisher) to remove unreacted materials for 3 days and deionized water for 3 days with regeneration of the dialysate 2-3 times/day. The material remaining was lyophilized to obtain the unmodified Fluorescein-capped polyrotaxanes **90a-**c as yellow powders. Yield: a = 2.408 g, b = 2.939 g, c = 1.691 g.

4.6.6 NTA-Modification of Fluorescein-Capped Polyrotaxanes

EBE-modified-fluorescein-capped-PEG-bis-alkyne α-CD polyrotaxanes (91a-c). Compounds **90a,b,c** (0.500 g) were dissolved in DMSO (15 mL). The solutions were sonicated to obtain complete dissolution. TEA (**a**,**b**,**c** = 414 μL, 0.003 mmol) was added followed by CDI (**a** = 0.196 g, 1.21 mmol; **b** = 0.204 g, 1.26 mmol, **c** = 0.192 g, 1.18 mmol). The solutions were flushed with nitrogen and stirred for 24 hours at ambient temperature. 2,2'-(Ethylenedioxy)bis(ethylamine) (EBE, **a** = 4.33 mL, 29.70 mmol, **b** = 4.58 g, 30.23 mmol; **c** = 4.38 g, 29.55 mmol) was added by syringe and the solutions

were stirred for an additional 24 hours. The material was dialyzed against DMSO (MWCO = 6-8 kDa, Fisher) to remove unreacted materials for 3 days and deionized water for 3 days with regeneration of the dialysate 2-3 times/day. The material remaining was lyophilized to obtain the EBE-modified-fluorescein-capped polyrotaxanes **91a-**c as yellow powders. Yield: a = 0.259 g, b = 0.215 g, c = 0.302 g.

NTA-modified-fluorescein-capped-PEG-bis-alkyne α-CD polyrotaxanes (92a-c). EBE-modified-fluorescein-capped-PEG-bis-alkyne α-CD polyrotaxanes (91a-c: **a**: 0.125 g, **b**: 0.103 g, **c**; 0.156 g) were dissolved in DMSO (4 mL) and deionized water (3 mL) in oven-dried 100 mL round bottom flasks equipped with magnetic stir bars and rubber septa. Compound **89** (**a-c**: 70 mg) was added followed by DIEA (**a-c**: 100 µL). The solutions were stirred for 18 hours at ambient temperature. The material was dialyzed against deionized water (MWCO = 6-8 kDa, Fisher) to remove unreacted materials for 8 days with regeneration of the dialysate 2-3 times/day. The material remaining was lyophilized to obtain the EBE-modified-fluorescein-capped polyrotaxanes **91a-**c as yellow powders. Yield: a = 0.095 g, b = 0.092 g, c = 0.132 g.

4.6.7 Ni-Activation of NTA-Modified Polyrotaxanes

NTA-modified polyrotaxane **70** (100 mg) was dissolved in 1 mL of 20 mM Ni^{2+} solution and the excess Ni^{2+} removed by gel filtration using Sephadex G-25M. After lyophilization, the Ni^{2+}:**70** complex was obtained as a solid (60 mg).

NTA-modified polyrotaxanes **92a-c** (50 mg) were dissolved in 1mL of 20 mM Ni^{2+} solution and the excess Ni^{2+} was removed via dialysis against deionized water

(MWCO = 2.0 kDa) to remove free Ni^{2+}. After the dialysate contained to Ni^{2+}, the solutions were flash frozen and lyophilized.

4.6.8 Gel-Permeation Chromatography (GPC)

GPC was performed using an Agilent 1200 Series GPC equipped with a Wyatt Dawn Heleos-II multi-angle light scattering (MALS) detector, Wyatt Optilab rEX refractive index (RI) detector and Wyatt quasi-elastic light scattering (QELS) detector using a single Shodex OHpakSB-803 HQ (8.0x3000 mm, 6 μm) column preceded by a Shodex OHpak SB807G (8.0x50.0 mm, 35 μm) guard column using DMSO as eluent. dn/dc was determined for each sample using a five-point calibration curve (0.5-2.5 mg/mL) generated using Optilab rEX detector in flow mode in combination with ASTRA software. Samples were dissolved at 1.8 mg/mL in DMSO and run at 0.2 mL/min. M_n and M_w/M_n were calculated using ASTRA software.

4.6.9 Preparation of ICP-MS Samples

Ni^{2+}:**70** or Ni^{2+}:**92a-c** complex (2.6 mg) was digested in 1 mL 70% HNO_3 (Aristar Ultra, VWR, West Chester, PA) solution for 3 days. The solution was diluted with double deionized water until reaching a concentration of 2% HNO_3 (35 mL, 2.25 μM) and then further diluted 10^3-fold with 2% HNO_3 solution. Standard solutions of Ni^{2+} were prepared by diluting a $NiSO_4$ standard solution (Exaxol, Clearwater, FL) with 2% HNO_3 solution until reaching a final concentration of 10 ppb. Blank 2% HNO_3 solutions were prepared by diluting 70% HNO_3 (Aristar Ultra) with double deionized water.

4.6.10 Fluorescence Microscopy

A 3.0 μM his_6-GFP solution in 10 mM HEPES buffer at pH 8.0 was prepared and a 10 μL aliquot transferred to a glass slide, covered with a cover slip and examined by fluorescence microscopy (Figure 2A). In order to visualize the Ni^{2+}:**70** complex, a solution of Ni^{2+}:**70** complex without protein (control) was prepared by mixing a 20 mM $NiSO_4$ solution and NTA-polyrotaxane in a 1:1 Ni^{2+}:NTA ratio to yield a 176 nM solution which was then transferred to a glass slide, covered with a cover slip and examined by fluorescence microscopy (Figure 2B). In order to visualize the his_6-GFP:Ni^{2+}:**70** complex, a his_6-GFP:Ni^{2+}:**70** solution was prepared by adding an aliquot of 3.0 μM his_6-GFP in 10 mM HEPES buffer at pH 8.0 to a 176 nM Ni^{2+}:**70** solution to attain 1:1 his_6-GFP:α-CD stoichiometry. A 10 μL sample of this solution was transferred to a glass slide, covered with a cover slip and examined by fluorescence microscopy (Figure 2C). A 10 μL aliquot of 500 mM imidazole was added to the solution in Figure 2C and a 10 μL sample of this mixture sealed with a cover slip and evaluated by fluorescence microscopy (Figure 2D). All measurements were made using a Olympus BX51 microscope with a 10 X objective and a DP71 CCD camera; the raw data were analyzed using Metavue Processing Software. Final images were converted to grayscale and the brightness and contrast adjusted equally in all images to enhance visualization.

4.6.11 Atomic Force Microscopy

AFM samples were prepared to further visualize the adsorption properties of the his_6-GFP: Ni^{2+}:**70** complex (Figure 3A). A 176 nM solution of Ni^{2+}:**70** complex without protein (control) was prepared by mixing a 20 mM $NiSO_4$ solution and NTA-

polyrotaxane in a 1:1 Ni^{2+}:NTA ratio to yield a 176 nM solution (Figure 3B). A 176 nM Ni^{2+}:4 complex solution and a 3.0 μM his_6-GFP solution in 10 mM HEPES buffer at pH 8.0 were mixed to attain a 1:1 his_6-GFP:α-CD stoichiometry on the mica surface (Figure 3C). A third sample was prepared as described for Figure 3B, except that a 10μL aliquot of a 500 mM imidazole solution was added to a 10μL sample of the solution in Figure 3B to strip GFP from the polyrotaxane scaffold. The samples were visualized by tapping-mode AFM using a Multimode AFM with a Nanoscope IIIa controller (Veeco) in air at 22 °C. The AFM tips (NSC15/AlBS, MikroMasch, USA) used had a typical uncoated probe tip radius of 10 nm or less; the cantilevers had a spring constant of 40 N/m.

4.6.12 Transmission Electron Microscopy

TEM was performed using a FEI/Philips CM-10 Bio-Twin instrument and captured on Kodak electron image film (type so-163). Copper 400 mesh grids stabilized with formvar and carbon (Ted Pella INC. product No. 01814-F) were glow discharged under a plasma for 30 seconds prior to specimen loading. The imaging conditions were: spot size 3, accelerating voltage = 80kV, and apertures of 50 μm (AuF objective) and 200 μm (condenser). All specimens were stained with an aqueous 2% uranyl acetate solution as described below.

A 7.0 μL drop of the specimen was loaded onto the grid and left for 10 sec. Filter paper was used to wick away most of the 7.0 μL drop (leaving just enough to cover the surface of the grid) followed by 3 washing steps with 7.0 μL of double de-ionized water (wicking with filter paper after each wash). After the last washing step with water, 7.0 μL

of staining solution was applied to the grid, wicked away with filter paper, and repeated a second time. The specimen was then allowed to dry before imaging.

4.6.13 Cryogenic Electron Microscopy

For cryo-EM imaging using Compound **70.** A 176 nM Ni^{2+}:**70** solution (Figures 4A & S2A) and a mixed solution of 176 nM Ni^{2+}:**70** complex + 3.0 μM his_6-GFP (1:1 his_6-GFP:α-CD stoichiometry) in 10 mM HEPES buffer, pH 8.0 (Figures 4B & S2B) were concentrated to ~1 mM, spread onto C-Flat™ grids then plunge-frozen in liquid ethane. Images were recorded using a Gatan 4k × 4k charge-coupled device camera on a Philips CM-200 TEM.

For cryo-EM imaging using Compound **92c**. Samples were prepared as detailed in SDS-PAGE and resuspended into 50 μL PBS, spread onto C-flat™ grids then plunge-frozen in liquid ethane. Images were recorded using a Gatan 4k × 4k charge-coupled device camera on a Philips CM-200 TEM.

4.6.14 Expression of His_6-GroEL and His_6-GFP

The ASKA Library was used to express N-terminal His_6-GroEL. Cells containing N-His_6-GroEL gene overexpression vector were grown to OD = 0.6 (in 100 mL of LB broth using a 37 ˚C shaker/incubator) and induced with a final concentration of 1.0 mM IPTG, before allowing the cells to grow for an additional 4 h. After centrifugation and removal of the supernatant, the cell pellets were stored at -80 °C and split among 5 different 50 mL tubes (200 mL broth equivalent). Each cell pellet was re-suspended in

lysis buffer (6.0 mL 50 mM PBS, 500 mM NaCl, pH = 7.4, 100 µg aprotinin, 174 µg phenylmethanesulfonyl fluoride (PMSF), and 500 µg of lysozyme) and allowed to sit for 1.5 h (stirring every 30 min). Further disruption of the cell membranes was effected by 110 W probe sonication (35 pulses at 1 second/pulse), followed by centrifugation at 11,000 g for 30 min. The supernatant was removed and filtered through a 0.1 µm PVDF membrane and used for experiments immediately.

His_6-GFP was expressed from BL21 (DE3, MW 27.950.3 g/mol, ε_{280} = 22015, pI= 6.30)) *E. coli* containing the his_6-GFPuv pT7-7plasmid with C-terminal his-tag. His_6-GFP gene overexpression vector were grown to OD = 0.6 (in 100 mL of LB broth using a 37 °C shaker/incubator) and induced with a final concentration of 1.0 mM IPTG, before allowing the cells to grow for an additional 3 h. Cells were centrifuged at 4,000 g for 10 minutes at 4 °C. The cell pellets were stored at -80 ^{o}C. The pellet was resuspended in 25.0 mL PBS containing 1mM PMSF. The cell suspension was vortexed and sonicated and a spatula tip of lysozyme was added. The suspension was incubated for 1.5 h (mixing every 30 min.). The suspension was probe sonicated and for 15 minutes using microtip (pulsed, 30 % duty cycle) and centrifuged at 11,000 rpm for 30 min at 4 °C. The supernatant was removed and filtered through a 0.1 µm PVDF membrane and further purified by FPLC.

4.6.15 SDS-PAGE

A solution of **92** (450 µg/mL) in PBS 20 mM, 500 mM NaCl) was made and any undissolved material was removed by centrifugation followed by filtration of the supernatant through a 0.1 µm PVDF membrane. **92**:his_6-GroEL solution was made by

mixing different volumes of GroEL lysate with **92** solution. The solution was allowed to sit for 30 min at 4 °C and was centrifuged at 12,000 g for 30 min. The supernatant was decanted and the pellet was resuspended in 50 µL PBS.

4.6.16 UV-Vis Analysis of PR-NTA Interaction with His_6-GroEL and His_6-GFP

A solution of Compound **84** was made at 15 µg/mL in PBS (20 mM, 500 mM NaCl). Solutions of **92a-c** were made at 350 µg/mL in PBS (20 mM, 500 mM NaCl). Any undissolved material was removed via centrifugation and filtration of the supernatant through a 0.1 µm PVDF membrane. Mixtures of **92** and his_6-Gro-EL lysate and his_6-GFP were made by mixing 1.0 mL of the protein solution with 100 µL of **92** solution. Samples were centrifuged at 12,000 g for 30 min at 4 °C and samples were resuspended in 50 µL PBS (20mM, 500 mM NaCl) and analyzed via UV Vis spectroscopy. This process was scaled up to generate larger samples for UV-Vis analysis and visual analysis (e.g. the photos of the complex pellets).

4.7 Acknowledgements

The authors would like to acknowledge the financial support of NIH GM079058 and the technical assistance provided by Valorie Bowman of the Biological Electron Microscope Facility at Purdue University. The support of the Purdue University NMR Facility, Mass Spectrometry Facility, Life Science Microscopy Facility, and the Purdue University Center for Cancer Research are gratefully acknowledged.

4.8 References

1. (a) Thompson, D. H.; Zhou, M. K.; Grey, J.; Kim, H. K., Design, Synthesis, and Performance of NTA-Modified lipids as Templates for Histidine-Tagged Protein Crystallization. *Chem Lett* **2007**, 36 (8), 956-975; (b) Grey, J. L. Thompson, D. H., Challenges and Opportunities for New Protein Crystallization Strategies in Structure-Based Drug Design. *Expert Opin Drug Disc* **2010**, 5 (11), 1039-1045.

2. (a) Schmitt, L.; Dietrich, C.; Tampe, R., Synthesis and Characterization of Chelator-Lipids for Reversible Immobilization of Engineered Proteins at Self-Assembled Lipid Interfaces. *J Am Chem Soc* **1994**, 116, 8485-8491; (b) Dietrich, C.; Schmitt, L.; Tampe, R., Molecular-Organization of Histidine-Tagged Biomolecules at Self-Assembled Lipid Interfaces Using a Novel Class of Chelator Lipids. *P Natl Acad Sci USA* **1995**, 92 (20), 9014-9018; (c) Barklis, E.; McDermott, J.; Wilkens, S.; Fuller, S.; Thompson, D., Organization of HIV-1 Capsid Proteins on a Lipid Monolayer. *J Biol Chem* **1998**, 273, 7177-7180; (d) Venien-Bryan, C.; Lenne, P. F.; Zakri, C.; Renault, A.; Brisson, A.; Legrand, J. F.; Berge, B., Characterization of the Growth of 2D Protein Crystals on a Lipid Monolayer by Ellipsometry and Rigidity Measurements Coupled to Electron Microscopy. *Biophys J* **1998**, 74, 2649-2657; (e) Lebeau, L.; Nuss, S.; Schultz, P.; Oudet, P.; Mioskowski, C., Self-Assembly of Soluble Proteins on Functionalized Lipid Layers: A Tentative Correlation Between the Fluidity Properties of the Lipid Film and Protein Ordering. Chem Phys Lipids 1999, 103, 37-46; (f) Zhou, M. K.; Haldar, S.; Franses, J.; Kim, J. M.; Thompson, D. H., Synthesis and Self-assembly Properties of Acylated Cyclodextrins and Nitrilotriacetic Acid (NTA)-Modified Inclusion Ligands for Interfacial Protein Crystallization. *Supramol Chem* **2005**, 17, 101-111.

3. (a) Chae, P. S.; Gotfryd, K.; Pacyna, J.; Miercke, L. J. W.; Rasmussen, S. G. F.; Robbins, R. A.; Rana, R. R.; Loland, C. J.; Kobilka, B.; Stroud, R.; Byrne, B.; Gether, U.; Gellman, S. H., Tandem Facial Amphiphiles for Membrane Protein Stabilization. *J Am Chem Soc* **2010**, 132, 16750-16752; (b) Zhang, Q.; Ma, X.; Ward, A.; Hong, W.-X.; Jaakola, V.-P.; Stevens, R. C.; Finn, M. G.; Chang, G., Designing Facial Amphiphiles for the Stabilization of Integral Membrane Proteins. *Angew Chem Int Edit* **2007**, 46, 7023-7025.

4. (a) Chae, P. S.; Rasmussen, S. G. F.; Rana, R. R.; Gotfryd, K.; Chandra, R.; Goren, M. A.; Kruse, A. C.; Nurva, S.; Loland, C. J.; Pierre, Y.; Drew, D.; Popot, J.-L.; Picot, D.; Fox, B. G.; Guan, L.; Gether, U.; Byrne, B.; Kobilka, B.; Gellman, S. H., Maltose-Neopentyl glycol (MNG) Amphiphiles for Solubilization, Stabilization and Crystallization of Membrane Proteins. *Nature Meth* **2010**, 7, 1003-1008; (b) Rasmussen, S. G. F.; Choi, H.-J.; Fung, J. J.; Pardon, E.; Casarosa, P.; Chae, P. S.; DeVree, B. T.; Rosenbaum, D. M.; Thian, F. S.; Kobilka, T. S.; Schnapp, A.; Konetzki, I.; Sunahara, R. K.; Gellman, S. H.; Pautsch, A.; Steyaert, J.; Weis, W. I.; Kobilka, B. K., Structure of a Nanobody-Stabilized Active State of the b2 Adrenoceptor. *Nature* **2011**, 469, 175-180.

5. (a) Nath, A.; Atkins, W. M.; Sligar, S. G., Applications of Phospholipid Bilayer Nanodiscs in the Study of Membranes and Membrane Proteins. *Biochemistry* **2007**, 46, 2059-2069; (b) Popot, J.-L., Amphipols, Nanodiscs, and Fluorinated Surfactants: Three Nonconventional Approaches to Studying Membrane Proteins in Aqueous Solutions. *Ann. Rev. Biochem*. **2010**, 79, 737-775.

6. Caffrey, M.; Cherezov, V., Crystallizing Membrane Proteins Using Lipidic Mesophases. *Nature Protocols* **2009**, 4, 706-731.

7. Grey, J. L.; Kim, H.-k.; Paul, L. N.; Gonzalez-Bonet, A.; Peng, L.; Benjamin, C.; Ridilla, M.; Schilling, B.; Marholz, L.; Hyun, S.-H.; Burgner, J.; Das, C.; Yernool, D.; Thompson, D. H., Controlled Speciation and Nucleation of His-Protein Assemblies Using Rigid, Symmetrical Multivalent Nitrilotriacetic Acid Ligand Scaffolds. *In Preparation*.

8. Saridakis, E.; Chayen, N. E., Towards a "Universal" Nucleant for Protein Crystallization. *Trends Biotechnol* **2009**, 27, 99-106.

9. Grey, J.; Thompson, D. H., Challenges and Opportunities for New Protein Crystallization Strategies in Structure-Based Drug Design. *Curr. Op. Drug Disc*. **2010**, 5, 1039-1045.

10. Cheng, Y.; Walz, T., The Advent of Near-atomic Resolution in Single Particle Electron Microscopy. *Ann. Rev. Biochem*. **2009**, 78, 723-742.

11. (a) Bartesaghi, A.; Banerjee, S.; Matthies, D.;Wu, X.; Milne, J. L. S.; Subramaniam, S., 2.2 Å Resolution Cryo-EM Structure of β-Galactosidase in Complex with a Cell-Permeant Inhibitor. *Science* **2015**, 348 (6239); (b) Banerjee, S.; Bartesaghi, A.; Merk, A.; Rao, P.; Bulfer, S. L.; Yan, Y.; Green, N.; Mroczkowski, B.; Neitz, R. J.; Wipf, P.; Falconieri, V.; Deshaies, R. J.; Milne, J. L.; Huryn, D.; Arkin, M.; Subramaniam, S., 2.3 A Resolution Cryo-EM Structure of Human p97 and Mechanism of Allosteric Inhibition. *Science* **2016**, 351 (6275), 871-5.

12. (a) Stagg, S. M.; Lander, G. C.; Pulokas, J.; Fellmann, D.; Cheng, A. C.; Quispe, J. D.; Mallick, S. P.; Avila, R. M.; Carragher, B.; Potter, C. S., Automated CryoEM Data Acquisition and Analysis of 284,742 Particles of GroEL. *J Struct Biol* **2006**, 155, 470-481; (b) Nicholson, W. V.; White, H.; Trinick, J., An Approach to Automated Acquisition of CryoEM Images From Lacey Carbon Grids. *J Struct Biol* **2010**, 172, 395-399.

13. Uzgiris, E. E.; Kornberg, R. D., Two-Dimensional Crystallization Technique for Imaging Macromolecules, with Application to Antigen-Antibody Complement Complexes. *Nature* **1983**, 301 (5896), 125-129.

14. Barklis, E.; McDermott, J.; Wilkens, S.; Schabtach, E.; Schmid, M. F.; Fuller, S.; Karanjia, S.; Love, Z.; Jones, R.; Rui, Y. J.; Zhao, X. M.; Thompson, D., Structural Analysis of Membrane-bound Retrovirus Capsid Proteins. *EMBO J* **1997**, 16, 1199-1213.

15. Walz, T.; Kelly, D. F.; Dukovski, D., Monolayer Purification: A Rapid Method for Isolating Protein Complexes for Single-Particle Electron Microscopy. *P Natl Acad Sci USA* **2008**, 105, 4703-4708.

16. Milligan, R. A.; Wilson-Kubalek, E. M.; Brown, R. E.; Celia, H., Lipid Nanotubes as Substrates for Helical Crystallization of Macromolecules. *P Natl Acad Sci USA* **1998**, 95 (14), 8040-8045.

17. Wilson-Kubalek, E. M.; Dang, T. X.; Farah, S. J.; Gast, A.; Robertson, C.; Carragher, B.; Egelman, E., Helical Crystallization on Lipid Nanotubes: Streptavidin as a Model Protein. *J Struct Biol* **2005**, 150, 90-99.

18. (a) Harada, A.; Kamachi, M., Complex-Formation Between Poly(ethylene Glycol) and Alpha-Cyclodextrin. *Macromolecules* **1990**, 23 (10), 2821-2823; (b) Stoddart, J. F.; Belowich, M. E.; Valente, C., Template-Directed Syntheses of Rigid Oligorotaxanes under Thermodynamic Control. *Angew Chem Int Edit* **2010**, 49, 7208-7212; (c) Ooya, T.; Yui, N., Polyrotaxanes: Synthesis, Structure, and Potential in Drug Delivery. *Crit Rev Ther Drug* **1999**, 16, 289-330; (d) Miyake, K.; Yasuda, S.; Harada, A.; Sumaoka, J.; Komiyama, M.; Shigekawa, H., Formation Process of Cyclodextrin Necklace - Analysis of Hydrogen Bonding on a Molecular Level. *J Am Chem Soc* **2003**, 125, 5080-5085; (e) Yui, N.; Ooya, T., Synthesis of theophylline-polyrotaxane conjugates and their drug release via supramolecular dissociation. *J Control Release* **1999**, 58 (3), 251-269.

19. Loethen, S.; Kim, J. M.; Thompson, D. H., Biomedical Applications of Cyclodextrin Based Polyrotaxanes. *Polym Rev* **2007**, 47 (3), 383-418.

20. Loftsson, T.; Duchene, D., Cyclodextrins and Their Pharmaceutical Applications. *Int J Pharm* **2007**, 329 (1-2), 1-11.

21. Li, J. J.; Zhao, F.; Li, J., Polyrotaxanes for Applications in Life Science and Biotechnology. *Appl Microbiol Biotechnol* **2011**, 90 (2), 427-43.

22. (a) Collins, C. J.; McCauliff, L. A.; Hyun, S. H.; Zhang, Z.; Paul, L. N.; Kulkarni, A.; Wirth, M. J.; Storch, J.; Zick, K.; Thompson, D. H., Synthesis, Characterization, and Evaluation of Pluronic-based β-Cyclodextrin Polyrotaxanes for Mobilization of Accumulated Cholesterol from Niemann-Pick Type C Fibroblasts. *Biochemistry* **2013**; (b) Fujita, H.; Ooya, T.; Yui, N., Thermally-Responsive Properties of a Polyrotaxane Consisting of β-cyclodextrins and a Poly(ethylene glycol)-poly(propylene glycol) Triblock-Copolymer. *Polym J* **1999**, 31 (11), 1099-1104; (c) Kulkarni, A.; Defrees, K.; Schuldt, R. A.; Hyun, S. H.; Wright, K. J.; Yerneni, C. K.; Verheul, R.; Thompson, D. H., Cationic alpha-Cyclodextrin:Poly(ethylene glycol) Polyrotaxanes for siRNA Delivery. *Mol Pharm* **2013**, 10 (4), 1299-305; (d) Loethen, S.; Ooya, T.; Choi, H. S.; Yui, N.; Thompson, D. H., Synthesis, Characterization, and pH-Triggered Dethreading of alpha-Cyclodextrin-poly(ethylene glycol) Polyrotaxanes Bearing Cleavable Endcaps. *Biomacromolecules* **2006**, 7 (9), 2501-6.

23. (a) Garcia-Rio, L.; Otero-Espinar, F. J.; Luzardo-Alvarez, A.; Blanco-Mendez, J., Cyclodextrin Based Rotaxanes, Polyrotaxanes and Polypseudorotaxanes and Their Biomedical Applications. *Curr Top Med Chem* **2014**, 14 (4), 478-93; (b) Kulkarni, A.; DeFrees, K.; Schuldt, R. A.; Vlahu, A.; VerHeul, R.; Hyun, S. H.; Deng, W.; Thompson, D. H., Multi-Armed Cationic Cyclodextrin:Poly(ethylene glycol) Polyrotaxanes as Efficient Gene Silencing Vectors. *Integr Biol (Cambr)* **2013**, 5 (1), 115-21; (c) Li, J.; Loh, X. J., Cyclodextrin-Based Supramolecular Architectures: Syntheses, Structures, and Applications for Drug and Gene Delivery. *Adv Drug Deliv Rev* **2008**, 60 (9), 1000-17.

24. Hyun, H.; Yui, N., Ligand Accessibility to Receptor Binding Sites Enhanced by Movable Polyrotaxanes. *Macromol Biosci* **2011**, 11 (6), 765-71.

25. Li, J. J.; Zhao, F.; Li, J., Supramolecular Polymers Based on Cyclodextrins for Drug and Gene Delivery. *Adv Biochem Eng Biotechnol* **2011**, 125, 207-49.

26. Thompson, D. H.; Loethen, S.; Kim, J. M., Biomedical Applications of Cyclodextrin Based Polyrotaxanes. *Polym Rev* **2007**, 47, 383-418.

27. (a) Harashima, H.; Shaheen, S. M.; Akita, H.; Yamashita, A.; Katoono, R.; Yui, N.; Biju, V.; Ishikawa, M., Quantitative Analysis of Condensation/Decondensation Status of pDNA in the Nuclear Sub-domains by QD-FRET. *Nucleic Acids Res* **2011**, 39, E48-U108; (b) Nelson, A.; Belitsky, J. M.; Vidal, S.; Joiner, C. S.; Baum, L. G.; Stoddart, J. F., A Self-Assembled Multivalent Pseudopolyrotaxane for Binding Galectin-1. *J Am Chem Soc* **2004**, 126, 11914-11922.

28. (a) Ooya, T.; Yui, N., Multivalent Interactions Between Biotin-Polyrotaxane Conjugates and Streptavidin as a Model of New Targeting for Transporters. *J Control Release* **2002**, 80, 219-228; (b) Hyun, H.; Yui, N., Ligand Accessibility to Receptor Binding Sites Enhanced by Movable Polyrotaxanes. *Macromol. Biosci*. **2011**, 11, 765-771.

29. (a) Jiang, Z. Y.; Xu, S. W.; Wang, Y. Q., Chemistry for Pegylation of Protein and Peptide Molecules. *Chinese J Org Chem* **2003**, 23 (12), 1340-1347; (b) Li, J.; Kao, W. J., Synthesis of Polyethylene Glycol (PEG) Derivatives and PEGylated-Peptide Biopolymer Conjugates. *Biomacromolecules* **2003**, 4 (4), 1055-1067; (c) Mahou, R.; Wandrey, C., Versatile Route to Synthesize Heterobifunctional Poly(ethylene glycol) of Variable Functionality for Subsequent Pegylation. *Polymers-Basel* **2012**, 4 (1), 561-589.

30. Averick, S.; Simakova, A.; Park, S.; Konkolewicz, D.; Magenau, A. J. D.; Mehl, R. A.; Matyjaszewski, K., ATRP under Biologically Relevant Conditions: Grafting from a Protein. *ACS Macro Lett* **2012**, 1 (1), 6-10.

31. Hoffman, M. T.; Sheung, J.; Selvin, P. R., Fluorescence Imaging with One Nanometer Accuracy: In Vitro and In Vivo Studies of Molecular Motors. Single Molecule Enzymology: *Methods and Protocols* **2011**, 778, 33-56.

32. (a) Lutz, J. F.; Zarafshani, Z., Efficient Construction of Therapeutics, Bioconjugates, Biomaterials and Bioactive Surfaces Using Azide-Alkyne "Click" Chemistry. *Adv Drug Deliv Rev* **2008**, 60 (9), 958-70; (b) Shin, J. A.; Lim, Y. G.; Lee, K. H., Copper-Catalyzed Azide-Alkyne Cycloaddition Reaction in Water Using Cyclodextrin as a Phase Transfer Catalyst. *J Org Chem* **2012**, 77 (8), 4117-22.

33. (a) Jao, C. Y.; Salic, A., Exploring RNA Transcription and Turnover in vivo by Using Click Chemistry. *Proc Natl Acad Sci USA* **2008**, 105 (41), 15779-84; (b) Salic, A.; Mitchison, T. J., A Chemical Method for Fast and Sensitive Detection of DNA Synthesis In Vivo. *Proc Natl Acad Sci USA* **2008**, 105 (7), 2415-20.

34. Hyun, S. H.; Kim, H. K.; Kim, J. M.; Thompson, D. H., Oriented Insertion of phi29 N-Hexahistidine-Tagged gp10 Connector Protein Assemblies into C(20)BAS Bolalipid Membrane Vesicles. *J Am Chem Soc* **2010**, 132 (48), 17053-17055.

35. Zhang, X. F.; Zhang, J.; Liu, L., Fluorescence Properties of Twenty Fluorescein Derivatives: Lifetime, Quantum Yield, Absorption and Emission Spectra. *J Fluoresc* **2014**, 24 (3), 819-26.

36. Kelly, D. F.; Abeyrathne, P. D.; Dukovski, D.; Walz, T., The Affinity Grid: a Pre-Fabricated EM Grid for Monolayer Purification. *J. Mol. Biol*. **2008**, 382 (2), 423-33.

37. Ludtke, S. J.; Baker, M. L.; Chen, D. H.; Song, J. L.; Chuang, D. T.; Chiu, W., De Novo Backbone Trace of GroEL from Single Particle Electron Cryomicroscopy. *Structure* **2008**, 16 (3), 441-8.

CHAPTER FIVE:
DEVELOPMENT OF NOVEL BLOCK COPOLYMERS FROM ORGANOCATALYTIC RING-OPENING POLYMERIZATION FOR DRUG AND GENE DELIVERY

5.1 Introduction

There has been considerably increased interest in the use of nanoparticle-based drug delivery systems in recent decades[1]. Nanoparticles[2] are defined as colloidal-sized particles having diameters between 1 and 1000 nm. These materials may have drugs or other therapeutic agents dispersed passively or via chemical ligation to alter the pharmacokinetic and pharmacodynamics properties of the therapeutic agent[3].

A wide variety of nanoparticles composed of a vast array of materials including lipids, polymers, biomolecules and inorganic materials have been investigated, resulting in diverse delivery systems that vary in their physicochemical properties and are suited to address a variety of challenges. Thus far, many different nanoparticle-based drug delivery systems have been developed including, but not limited to, liposomes[4], micelles[5], nanospheres[6], niosomes[7], nanocapsules[8], solid lipid nanoparticles[9], microemulsions, polymersomes[10] and carbon nanotubes[11] (Figure 5.1).

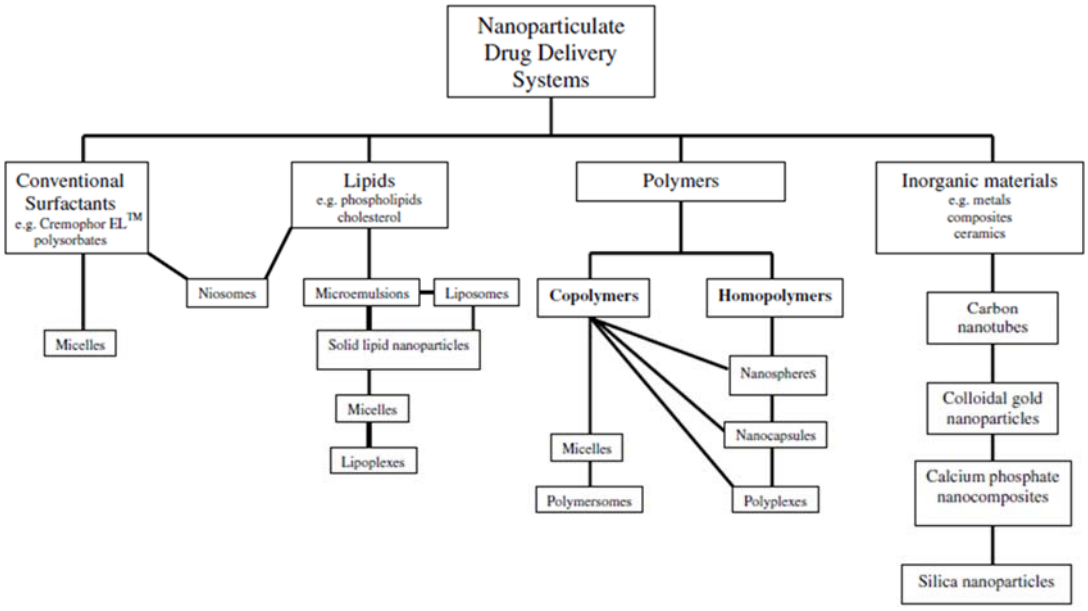

Figure 5.1 Classification of Nanoparticulate-Based Drug-Delivery Systems[8b].

5.1.1 Diblock Copolymers in Drug and Gene Delivery

Amphiphilic block copolymers have been one of the most extensively studied delivery platforms owing to their synthetic accessibility, modular properties, and the variety of nanoparticle types which may be formulated using these materials. The interest in amphiphilic polymer-based nanoparticles owes in part to several advantages they provide for delivering their payload. The nano-scale size of these materials allows for direct administration of the therapeutic agent to the bloodstream via intravenous injection. Nanoparticles under ~200 nm show increased circulation times, which may be attributed to increased radius of curvature, which smaller particles possess compared to larger particles and may prevent efficient binding of opsinins[12]. They also show decreased renal excretion if the particles are sufficiently large enough to avoid glomerular filtration. Furthermore, the extended circulation times of nanoparticle-based drug

delivery systems has also been shown to lead to increased accumulation of nanoparticle-associated therapeutic agents in tissues with increased vascular permeability and impaired lymphatic drainage[13]. This principle, known as the enhanced permeability and retention (EPR) effect[1b], has been proposed to allow for passive targeting of the therapeutic agent to its site of action while reducing accumulation in healthy tissue. This may allow for enhanced therapeutic efficacy in comparison to the therapeutic agent in the absence of the drug delivery system. Nanoparticles have also been used to increase the aqueous solubility of hydrophobic drugs via solubilization within the hydrophobic cores of the delivery system[14].

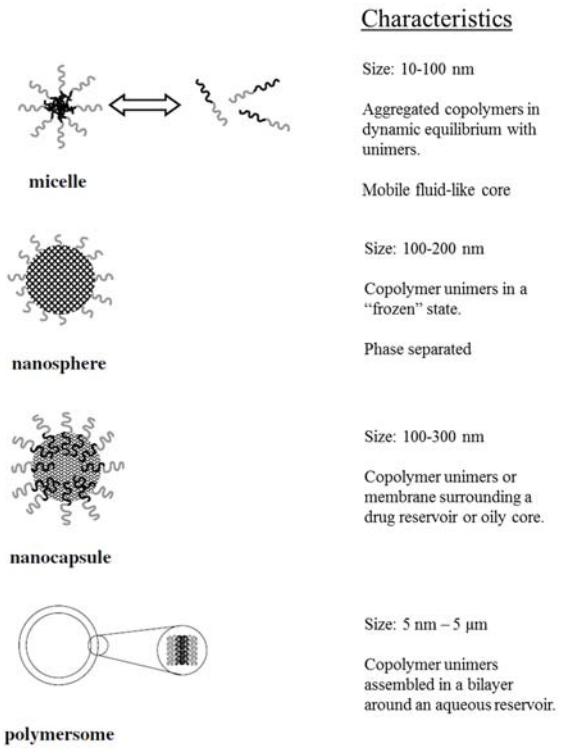

Figure 5.2 Amphiphilic Copolymer-Based Drug Delivery Platforms and Their General Characteristics[8b].

Amphiphilic block copolymers have attracted a great deal of attention in terms of their ability to form many different types of nanoparticles (Figure 5.2). These compounds are typically prepared via polymerization of multiple monomers or the macroinitiation of a polymerization by an existing polymer. Amphiphilic copolymers typically consist of a hydrophilic block and a hydrophobic block. The amphiphilic detergent-like nature of the resulting copolymer enables access to many different nanoparticle structures.

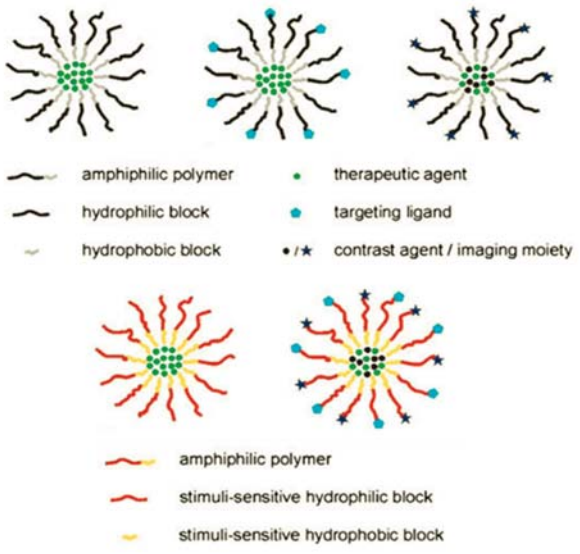

Figure 5.3 Architectures of Various Therapeutic Strategies Utilizing Amphiphilic Block Copolymers.

Amphiphilic copolymers often consist of biocompatible, biodegradable hydrophobic blocks like polyesters[15], poly(amino acids)[16], polycarbonates[17], polyphosphoesters[18] and polysiloxanes[19] conjugated to biocompatible hydrophilic blocks. Common hydrophobic blocks include poly(lactic acid) (PLA)[20], polycaprolactone (PCL)[15a, 21], polyvalerolactone (PVL), poly(lactide-co-glycolide) (PLGA)[6, 15b, 22] among

many others. Amphiphilic copolymer-based systems often incorporate poly(ethylene glycol) (PEG) to act as a hydrophilic component and barrier to adhesion[12a, 23]. However, other hydrophilic polymers blocks like poly(N-vinyl-2-pyrrolidone), poly(2-ethyl-2-oxazoline)[19a] and poly(acrylic acid)[24] have also been used. Amphiphilic copolymers enable the design of complex multifunctional drug delivery platforms via the facile incorporation of targeting ligands, imaging agents, therapeutic agents and other cargo (Figure 5.3). These constructs may also be designed to undergo stimuli-sensitive degradation to achieve controlled release of their cargo.

To date, many different block copolymers have been synthesized composed of varying block compositions and relative block lengths. By precisely controlling the composition and relative molecular weights of block copolymers, various nanoparticle structures such as micelles, nanospheres, core-shell nanoparticles, nanocapsules, and polymersomes may be obtained. Many different methods of formulation have been utilized for production of these materials including, but not limited to, emulsification[25], nanoprecipitation, emulsion polymerization, or microfluidic strategies[26].

5.1.2 Organocatalytic ROP

In recent years, organic catalysis has become an increasingly attractive method for the synthesis of functional amphiphilic copolymers and has become a powerful alternative to traditional metal-based catalysis[27]. Since the first report of living polymerization of lactide using 4-dimethylamino-pyridine (DMAP) reported by Nederberg et al[28], organocatalysis has progressed to the point that organic catalysts can

now offer many tangible advantages in comparison with their organometallic counterparts. Most organic catalysts are relatively inexpensive commercially-available chemicals, which are generally easily purified, have long shelf lives, and are well-suited for a range of reaction conditions, solvents and monomers. Generally, they are organic acids or bases, which simply require drying to allow for good control of molecular weight and end group fidelity. This is because water can typically act as an initiator, leading to altered end groups and decreased polymer molecular weight relative to the targeted molecular weight.

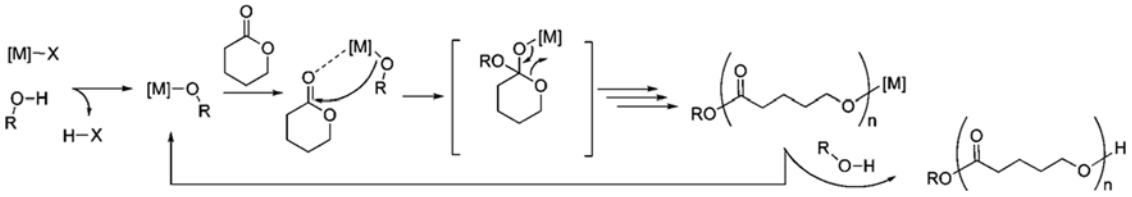

Figure 5.4 Coordination-Insertion Mechanism for Metal-Catalyzed ROP.

Ring-opening polymerization (ROP) is the most common method for synthesis of well-defined biodegradable block copolymers. ROP may be used to generate many different polymers including polyesters, polycarbonates, etc., which are attractive for therapeutic applications. Traditional metal-based catalysts generally function via the coordination-insertion mechanism (Figure 5.4) as in the case of the polymerization of l-lactide by tin(II) 2-ethylhexanoate. These catalysts have generated concerns related to trace contamination of the polymer with catalyst, which may lead to significant toxicity.

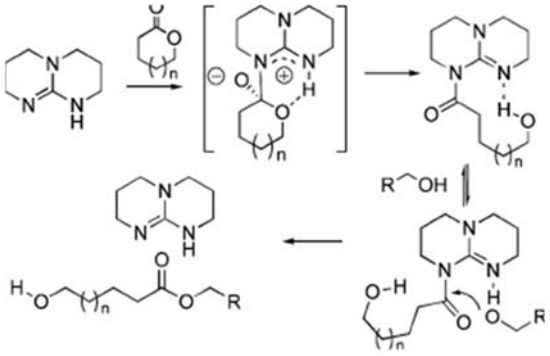

Figure 5.5 Dual Activation Mechanism of Monomer and Initiator in ROP of δ-Valerolactone by TBD.

Common orgnanocatalysts for ROP include N-heterocyclic carbenes, organic "super base" catalysts[29] and bifunctional catalysts. (-)-Sparteine has been used as an organocatalyst, but due to its low availability as a natural product, it has not been extensively studied. Tris[2-(dimethylamino)ethyl]amine (Me_6TREN) has been shown to exhibit similar activity to (-)-sparteine. Bifunctional thiourea-amine catalysts were first applied to the polymerization of lactide[30]. These systems involve simultaneous activation of monomer by the thiourea (a Lewis acid) and the initiator (an alcohol) by the amine-component. This strategy was applied to two-component systems of thiourea and organic base and bifunctional thiourea-amine (TU/A) catalysts[30]. However, these systems show relative sluggish polymerization kinetics for other monomers (caprolactones, carbonates, etc.).

The most common super-base catalysts include 1,8-diazabicyclo[5.4.0]undec-7-ene (DBU), 1,4,5-triazabicyclo[4.4.0]dec-5-ene (TBD), 7-methyl-3,5,7-triazabicyclo[4.4.0]dec-5-ene (MTBD), and other phosphazene-based compounds[27]. These catalysts are more active than the TU/A system, display different activities (TBD >

MTBD > DBU) and have been applied for the polymerization of many different cyclic monomers[31]. TBD, in particular has been shown to exhibit very high reactivity for monomers with low ring strain or which exhibit low conversion with other catalysts. TBD functions via dual activation of the monomer and initiator in an analogous fashion to the TU/A-based catalysts (Figure 5.5). Alternatively, TBD has been shown to polymerize L-lactide via an H-bonding mechanism which does not involve acyl transfer[32].

5.1.3 Pendant Polymer-Based Gene Delivery

Gene delivery involves the treatment of human disease via the transfer of genetic material into specific cells of the patient[33]. Advances in biotechnology, along with the completion of the human genome project, have led to the identification of numerous disease-causing genes. Gene therapy may offer potential therapeutic benefit for genetic diseases that are currently untreatable or involve challenging treatment regimens.

Various approaches to gene delivery have been proposed, but gene delivery vectors are classified as being either viral or non-viral. Viruses like retrovirus, adenovirus, lentivirus, herpes simplex virus and pox virus may all be transformed into gene delivery vehicles by replacement of part of the viral genome with the therapeutic gene of interest. Viral vectors account for the majority of gene delivery studies in the literature and ongoing clinical trials. However, safety concerns associated with immunogenicity of viral vectors have been the primary bottleneck to progress on viral

gene delivery. There are also concerns associated with large scale production of viral-based gene therapies.

Non-viral gene therapy[34] offers the potential for improved safety, greater flexibility, and more facile and robust design and production strategies. Non-viral gene delivery vectors function to electrostatically bind the nucleic acid cargo, condense the cargo into particles, protect the cargo from degradation and mediate cellular entry. Many different material strategies have been proposed as non-viral gene-delivery vectors[11, 35].

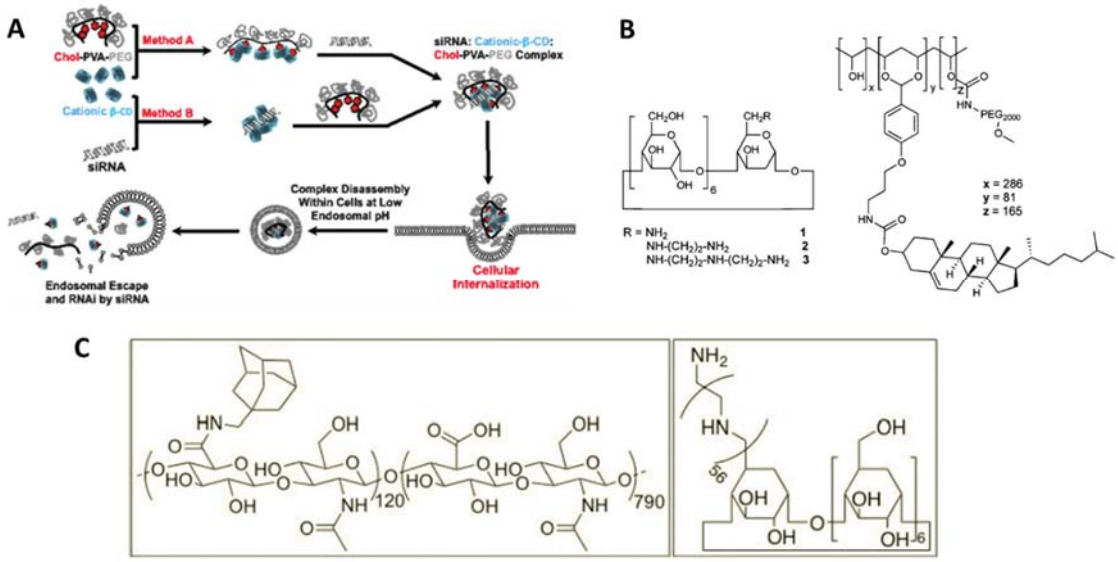

Figure 5.6 Pendant Polymer-Based Gene Delivery Strategies. (A) Fabrication of Chol-PVA-PEG pendant polymer-based transfection complexes and transfection. (B) Chemical structures of Chol-PVA-PEG and cationic β-CD derivatives[36]. (C) Structures of hyaluronic acid (HA)-based pendant polymers and β-CD -PEI.

Kulkarni et al.[36-37] first introduced the concept of pendant-polymer-based gene delivery with the system composed of poly(vinyl alcohol) (PVA) grafted with PEG and also grafted with cholesterol via acid-sensitive benzylidene acetal linkages, amine-

modified-β-cyclodextrin and siRNA as a therapeutic agent (Figure 5.6A,B). These materials effectively formed transfection complexes in the 120-170 nm range via electrostatic interaction of siRNA and the cationic cyclodextrins, which are further held together via non-covalent interactions of cholesterol with the CD-cavities. β-CD has been shown to possess host-guest interactions with a wide variety of compounds with binding constants in the $10^{0.5}$-10^{5} M^{-1} in aqueous media[38]. Another approach, based on cyclodextrin-containing oligomers, has also been introduced by Davis[3, 35b, 39]. The pendant polymer concept was further applied to microfluidic assembly of transfection complexes composed of hyaluronic acid (HA)-modified with adamantine, β-CD-PEI conjugate and siRNA[26a].

Although these materials showed good performance, several issues related to the reproducibility of the PVA and HA-based material synthesis, and the limitations associated with working from pre-formed commercial materials, prompted the design of a second generation of pendant polymers. We sought to improve on the pendant polymer concept by utilizing organocatalytic ROP to synthesize a library of well-defined block-copolymers, which could allow for tunable synthesis, the incorporation of targeting moieties and biodegradability.

5.2 Organocatalytic ROP Synthesis of PEG-b-Polycarbonate Pendant Polymers

The oligocarbonate-based non-viral gene delivery introduced by Cooley et al[31b] prompted the design of pendant polymers based on PEG-polycarbonate diblock copolymers (Figure 5.7). These materials are designed for tunable synthesis via organocatalytic ROP mediated by various organic catalysts. Specifically, TBD and the

DBU/thiourea-based system[30] were utilized due to their respective activities and abilities to generate well-defined copolymers with low polydispersity[29a]. Polycarbonate diblocks are also expected to show controlled and sustained degradation rates and degrade into non-acidic and non-toxic by-products, which are suitable for biomedical applications. In addition to homopolymerization of cyclic carbonate monomers initiated by mPEG (Figure 5.7A), copolymers where the cyclic carbonate monomer is blended with trimethylene carbonate (TMC) are also included in the library to evaluate the effect of pendant group density on nanoparticle formation and efficacy of transfection complexes derived from mPEG-b-polycarbonate materials (Figure 5.7B).

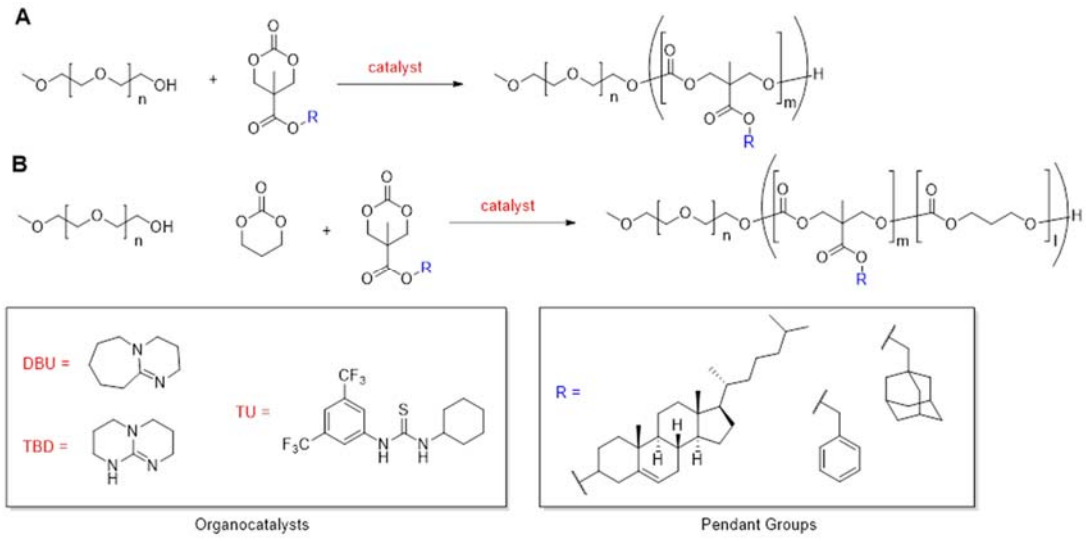

Figure 5.7 Chemical Structures of Targeted mPEG-b-Polycarbonate Pendant Polymer Library. (A) Homopolymerization of carbonate monomers. (B) Copolymerization of carbonate monomers blended with trimethylene carbonate (TMC).

We sought to synthesize a library of mPEG-b-polycarbonate diblock copolymers bearing various moieties, which exhibit affinity for the β-CD cavity, various overall

molecular weight and relative block length, and various densities of pendant group along the linear polycarbonate backbone. These materials were designed to form transfection complexes together with the β-CD-PEI conjugate introduced previously[26a] and the nucleic acid cargo to effect gene delivery (Figure 5.8).

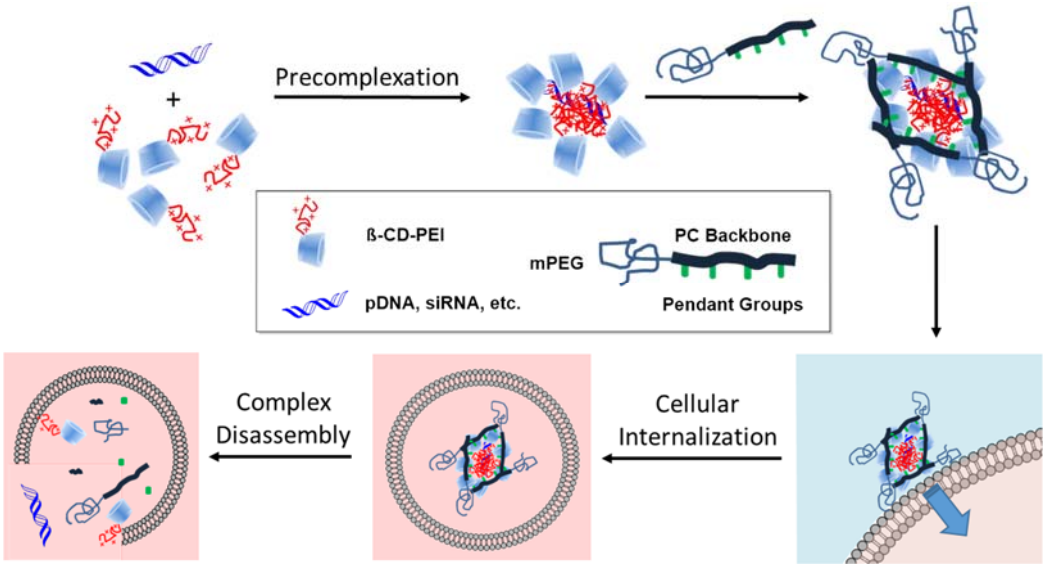

Figure 5.8 Schematic of Gene Delivery Using the mPEG-b-Polycarbonate:β-CD-PEI-Based Gene Delivery Strategy.

5.2.1 Synthesis of Cyclic Carbonate Monomers

In order to generate a library of mPEG-b-polycarbonate pendant polymers, a small library of cyclic carbonate monomers bearing ethyl, benzyl, cholesteryl, and adamantyl esters were synthesized following a modified method previously reported for synthesis of cyclic carbonates with various functionalities[40]. These pendant groups were chosen due to their known host:guest interaction with β-CD.

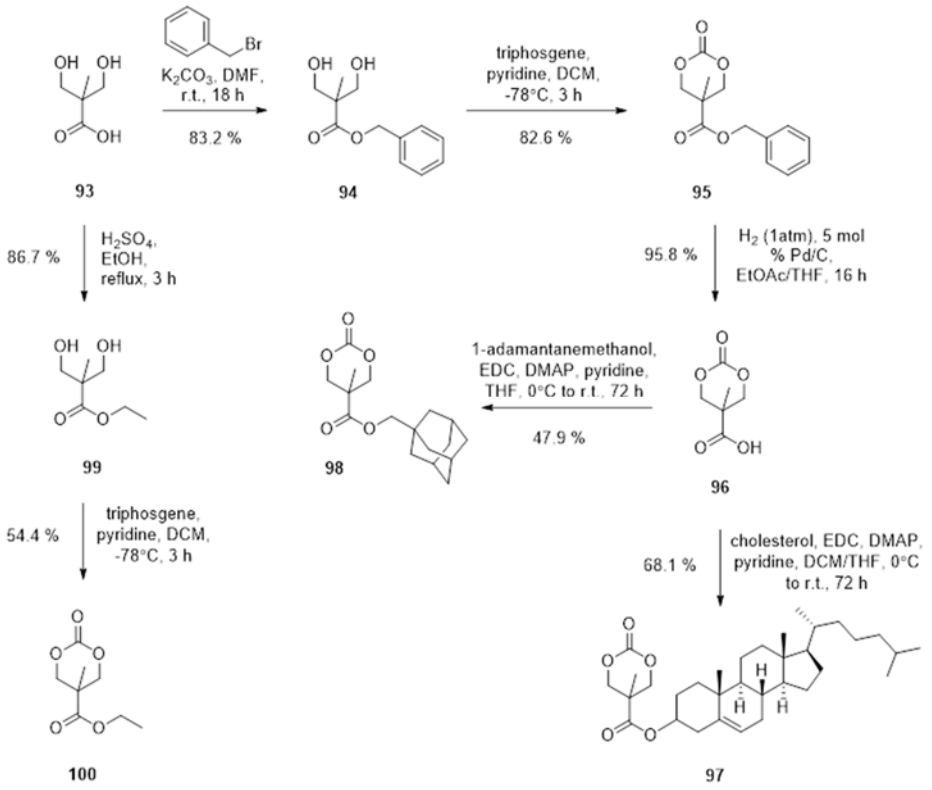

Scheme 5.1 Synthesis of Cyclic Carbonate Monomers.

2,2-Bis(hydroxymethyl)propionic acid (BHMPA, **93**) was chosen as the commercial feedstock for synthesis of cyclic carbonate pendant monomers. BHMPA is a cheap, commercially available common building block for synthesis of six-membered cyclic carbonates. Treatment of BHMPA with benzyl bromide in DMF after formation of the potassium salt of BHMPA gave Compound **94** in 83.2 % yield after recrystallization. Compound **94** was treated with triphosgene in a solution of DCM and pyridine at -78 °C to yield the benzyl carbonate monomer **95** in 82.6 % yield after chromatographic purification. Carboxylate derivative **96** was obtained via benzyl ester hydrogenolysis with

10 % palladium on carbon to give **96** in 95.8% yield. Cholesteryl ester derivative **97** was synthesized via esterification of Compound **96** and cholesterol mediated by EDC and DMAP in a solution of DCM and THF in 68.1% yield after chromatographic purification and recrystallization. Adamantyl ester derivative **98** was synthesized via esterification of Compound **96** and 1-adamantanemethanol mediated by EDC and DMAP in THF in 47.9% yield after chromatographic purification and recrystallization.

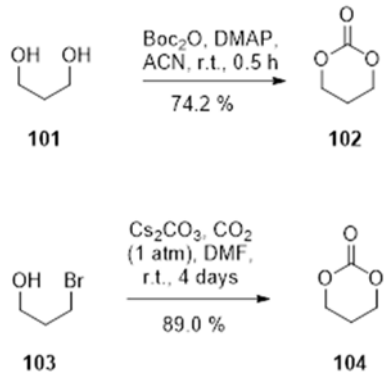

Scheme 5.2 Syntheses of Trimethylene Carbonate.

Trimethylene carbonate (TMC) was synthesized as a spacing monomer in order to vary pendant group density along the linear polycarbonate backbone. TMC was initially synthesized using di-tert-butyl dicarbonate (Boc_2O) and DMAP in acetonitrile to give **102** in 74.2% yield after chromatographic purification and recrystallization. This method is very fast, but suffers from the use of large quantities of reagents and necessitates chromatographic purification. An alternative synthesis of TMC utilizing 3-bromo-1-propanol under 1 atm of carbon dioxide in the presence of cesium carbonate in DMF was

used to give **104** in 89.0% yield after recrystallization. This method gives TMC in overall higher yield and only requires crystallization to yield monomer suitable for polymerization. However, this method requires extended reaction times to generate TMC in respectable yield.

5.2.2 Homopolymerization of Carbonate Monomers by TBD

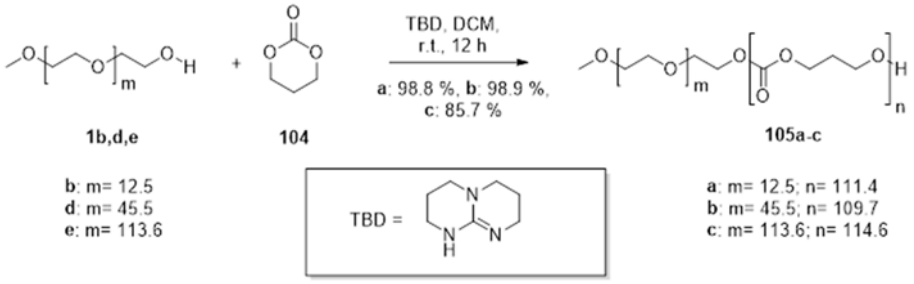

Scheme 5.3 Synthesis of mPEG-b-PTMC Diblock Copolymers.

Initial polymerization studies focused on synthesis of mPEG-b-PTMC via organocatalytic ROP of TMC initiated by mPEG of various molecular weights catalyzed by TBD (Scheme 5.3). PEG and TMC were purified by precipitation and recrystallization, respectively, before polymerization. A molecular weight of 12.0 kDa was targeted for the PTMC blocks of the three diblock copolymers **105a-c**. Polymerizations were carried out under nitrogen at 1.0 M initial TMC concentration in DCM with 5 mol % TBD as catalyst. Polymerizations were quenched after 12 hours with benzoic acid and purified via precipitation into diethyl ether.

Table 5.1 Characterization of mPEG-b-PTMC.

Entry	Initiator	TBD (mol %)	n (targeted)	PTMC-M_n (NMR)	n (NMR)	M_n (GPC)	% Conversion	M_w/M_n (GPC)	% Yield
105a	$mPEG_{550}$	5	117.5	11.4 kDa	111.4	12.8 kDa	94.8	1.22	98.8
105b	$mPEG_{2000}$	5	117.5	11.2 kDa	109.7	13.9 kDa	93.3	1.19	98.9
105c	$mPEG_{5000}$	5	117.5	11.7 kDa	114.6	18.2 kDa	97.5	1.23	85.7

Compounds **105a-c** were characterized via ^{1}H-NMR and GPC. The results are summarized in Table 5.1. M_n was determined based on ^{1}H-NMR and GPC. % Conversion was calculated based off of M_n from ^{1}H-NMR. Overall, % conversions were high ranging from 94.8 % - 97.5 %, suggesting near complete conversion of monomer. M_n calculated from ^{1}H-NMR all fall just below 12.0 kDa, while the average M_n calculated from GPC of the diblock copolymers in THF were consistently higher. M_w/M_n determined from GPC all fall around 1.2, suggesting that the diblock copolymers are relatively monodisperse.

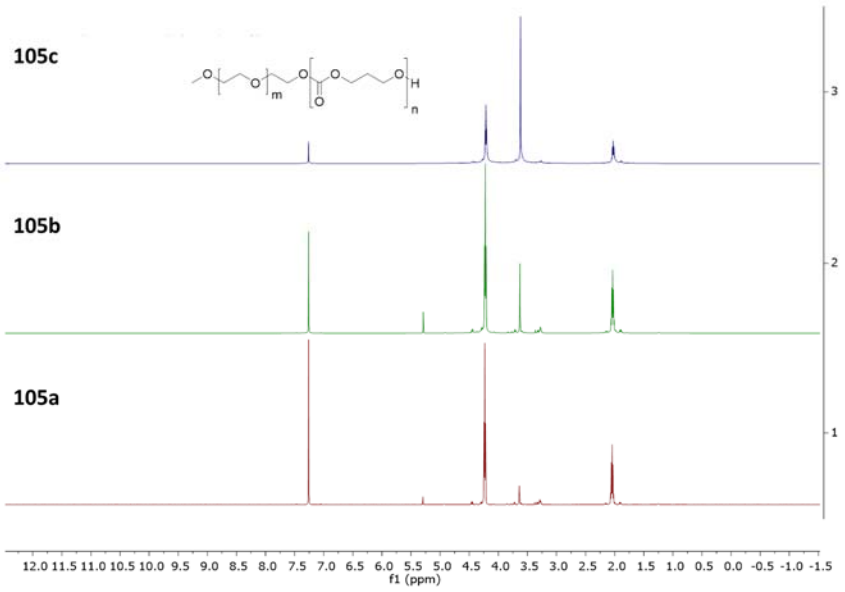

Figure 5.9 ^{1}H-NMR Spectra of mPEG-b-PTMC Diblock Copolymers.

^{1}H-NMR-spectra were used to determine M_n by integrating the PEG methylene regions according to the number of protons present for a monodisperse polymer of the reported average molecular weight of the commercial mPEG **1a-e**. The sum of integrals of the TMC protons were used to calculate M_n and % conversion. NMR spectra also reveal that the isolated materials show no evidence of unreacted monomer or catalyst.

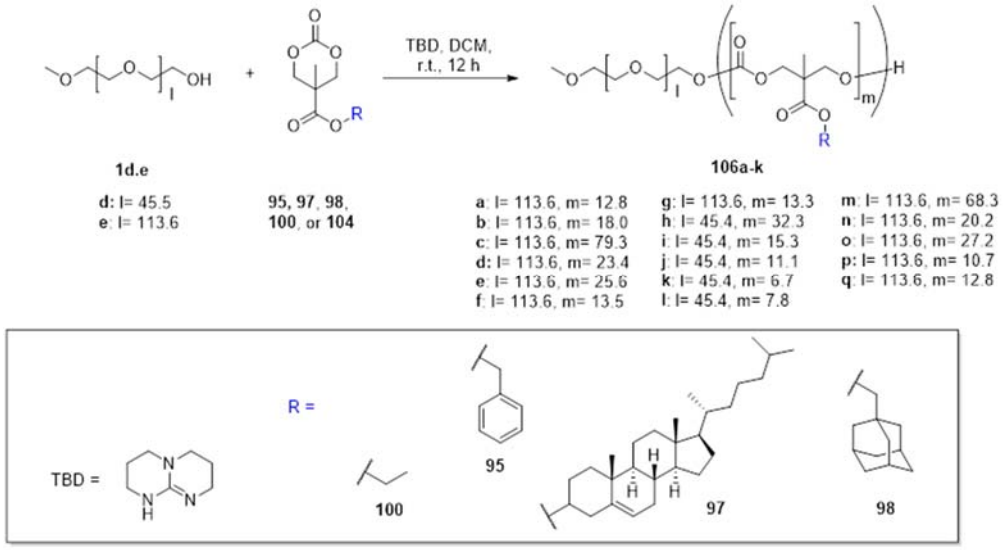

Scheme 5.4 Homopolymerization of Carbonate Monomers by TBD.

Next, efforts were made to generate a small library of mPEG-b-polycarbonate homopolymers using ROP of Compounds **95**, **97**, **98**, **100** and **104**. Polymerizations were carried out under nitrogen for 12 hours in DCM solution. Monomers and PEG were purified immediately beforehand via recrystallization and precipitation into diethyl ether, respectively. Polymerizations were carried out at [M] of 1.0 M using either 5 or 10 mol % TBD as catalyst. A molecular weight of 10.0 kDa was targeted for the polycarbonate

block when **1e** (mPEG5K) was used as an initiator and a molecular weight of 5.0 kDa was targeted for the polycarbonate block when **1d** (mPEG2K) was used an initiator. Polymerizations were quenched via addition of benzoic acid and purified via precipitation into diethyl ether.

Table 5.2 Characterization of TBD-catalyzed mPEG-b-Polycarbonate Homopolymers.

Entry	R	Initiator	TDB (mol%)	m (targeted)	m (NMR)	% Conversion	PC-M_n (NMR)	M_n (GPC)	M_w/M_n (GPC)	Time (h)	Yield (%)
106a	Et	**1e**	10	53.1	12.8	24.1	2.4 kDa	12.0 kDa	1.86	12	46.2
106b	Chol	**1e**	10	18.9	18.0	95.2	9.5 kDa	20.7 kDa	1.11	12	95.3
106c	TMC	**1e**	10	98.0	79.3	80.9	8.1 kDa	11.4 kDa	1.45	12	85.3
106d	Et	**1e**	10	53.1	23.4	44.1	4.4 kDa	17.1 kDa	1.32	12	79.3
106e	Bn	**1e**	10	40.0	25.6	64.0	6.4 kDa	15.3 kDa	1.34	12	87.7
106f	Chol	**1e**	10	19.0	13.5	71.1	7.1 kDa	16.2 kDa	1.39	12	80.7
106g	Ad	**1e**	10	32.4	14.3	44.1	4.4 kDa	12.1 kDa	1.28	12	70.7
106h	TMC	**1d**	10	49.0	32.3	65.9	3.3 kDa	8.1 kDa	1.08	12	86.8
106i	Et	**1d**	10	26.6	15.3	57.5	2.9 kDa	7.7 kDa	1.20	12	58.5
106j	Bn	**1d**	10	20.0	11.1	55.5	2.8 kDa	7.5 kDa	1.38	12	74.5
106k	Chol	**1d**	10	9.5	6.7	70.5	3.5 kDa	6.4 kDa	1.38	12	84.0
106l	Ad	**1d**	10	16.2	7.8	48.1	2.4 kDa	5.5 kDa	1.26	12	65.5
106m	TMC	**1e**	5	98.0	68.3	69.7	7.0 kDa	14.2 kDa	1.26	12	86.7
106n	Et	**1e**	5	53.1	20.2	38.0	3.8 kDa	9.6 kDa	1.34	12	75.5
106o	Bn	**1e**	5	40.0	27.2	68.0	6.8 kDa	14.6 kDa	1.24	12	80.0
106p	Chol	**1e**	5	18.9	10.7	56.6	5.7 kDa	12.9 kDa	1.28	12	62.7
106q	Ad	**1e**	5	32.4	12.8	39.5	4.0 kDa	15.8 kDa	1.36	12	70.7

^{1}H-NMR and GPC in THF were used to characterize the mPEG-b-polycarbonate homopolymers synthesized via TBD-catalyzed ROP of cyclic carbonate monomers. % Conversion and M_n calculated from ^{1}H-NMR showed that there was a high degree of variability for homopolymers generated using TBD. % Conversions varied from very low (24.1%) to high (95.2%). M_n calculated from NMR roughly agreed with M_n calculated from GPC after taking into account the additional molecular weight due to mPEG. M_w/M_n varied greatly from 1.08-1.86 with most centered from 1.2-1.4. This indicates a relatively high degree of polydispersity which could be due to transesterification at extended reaction times, although no evidence was obtained from ^{13}C-NMR.

5.2.3 Copolymerization of Carbonate Monomers by TBD

Next, a small library of copolymers was synthesized where carbonate monomers **95**, **97**, or **98** were copolymerized with Compound **100 (**Figure 5.5). Molecular weights of 12.0 kDa and n:m of 1:3 were targeted. Polymerizations were carried out in DCM solution at [M] = 1.0 M using 10 mol % TBD relative to [M]. Monomers and PEG were purified beforehand and polymerizations were run for 12 hours at ambient temperature. Polymerizations were quenched via addition of benzoic acid and purified via precipitation into diethyl ether.

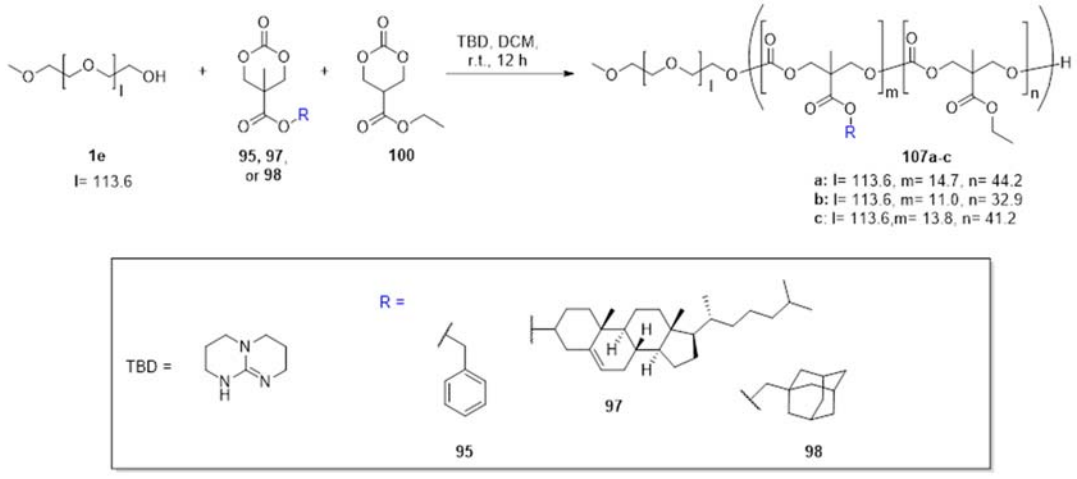

Scheme 5.5 Copolymerization of Carbonate Monomers by TDB.

^{1}H-NMR and GPC in THF were used to characterize the copolymers generated via TBD catalyzed ROP. Total % conversions were moderate, indicating that the polymerizations only proceeded moderately efficiently. Calculated values for relative number of monomers incorporated into the polycarbonate polymers agreed with the

targeted ratio of 1:3, indicating that the different monomers did not likely differ greatly in their activities toward ROP. M_n from ^{1}H-NMR agreed relatively well with GPC values, with a slightly higher value from GPC consistent with previous data. M_w/M_n ranged from 1.35-1.42, which is comparable to values obtained from homopolymerizations (table 5.3).

Table 5.3 Characterization of TBD-catalyzed mPEG-b-Polycarbonate Copolymers.

Entry	R	Initiator	TDB (mol%)	m:n (targeted)	m:n (NMR)	% Conversion	PC-M_n (NMR)	M_n (GPC)	M_w/M_n (GPC)	Time (h)	Yield (%)
107a	Et:Bn	**1e**	10	14.7: 44.2	8.7:25.2	57.6	8.0 kDa	16.2 kDa	1.42	12	77.3
107b	Et:Chol	**1e**	10	11.0: 32.9	6.4: 17.8	66.1	6.7 kDa	14.3 kDa	1.35	12	72.0
107c	Et:Ad	**1e**	10	13.8: 41.2	6.1: 19.3	46.2	5.5 kDa	13.1 kDa	1.39	12	69.2

5.2.4 Homopolymerization of Carbonate Monomers by DBU/TU

Having obtained modest results for homopolymerizations and copolymerizations of carbonate monomers using TBD as catalyst, we sought to move to a milder ROP catalyst. We chose to go with the combination of DBU and thiourea Compound **110**. This co-catalyst combination has been previously used to generate oligomers of similar monomers using various alcohols as catalysts[31b, 41]. This catalyst functions via activation of the monomer by the thiourea and activation of the initiator or propagating polymer terminus by the base (DBU). Interestingly, other thioureas have shown little or no activity. This observation has been attributed to the specific N-H acidity imparted on the thiourea by the 3,3-ditrifluoromethyl substituents[30].

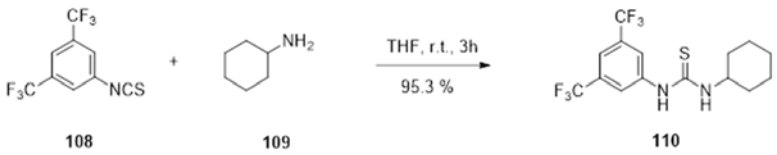

Scheme 5.6 Synthesis of Thiourea (TU) Co-Catalyst.

Compound **110** was synthesized via reaction between cyclohexylamine (**108**) and 3,5-ditrifluoromethyl-phenyl isothiocyanate (**109**) in THF. A yield of 95.3 % was obtained after chromatographic purification.

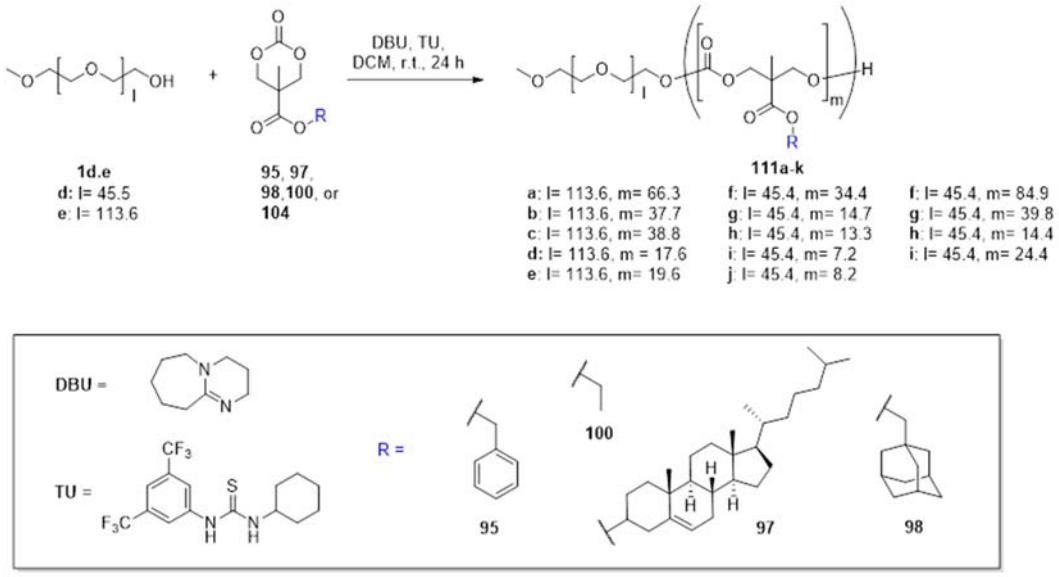

Scheme 5.7 Homopolymerization of Carbonate Monomers by DBU/TU.

With Compound **110** in hand, a small library of mPEG-b-polycarbonate homopolymers was synthesized via organocatalytic ROP of cyclic carbonate monomers **95**, **97**, **98**, **100** and **104**. All monomers and PEG were purified immediately beforehand by recrystallization and precipitation, respectively. Polymerizations were carried out under nitrogen at ambient temperature using 5 mol % each of DBU and TU (**110**) in DCM at a concentration where initial [M] = 1.0 M. Polymerizations were run for 24 or 48 hours and quenched with benzoic acid before precipitation into diethyl ether to remove catalysts and unreacted monomers.

Table 5.4 Characterization of DBU/TU-Catalyzed mPEG-b-Polycarbonate Homopolymers.

Entry	R	Initiator	TDB (mol%)	m (targeted)	m (NMR)	% Conversion	PC-M_n (NMR)	M_n (GPC)	M_w/M_n (GPC)	Time	Yield (%)
111a	TMC	**1e**	5	98.0	66.3	67.7	6.8 kDa	13.9 kDa	1.18	48 h	83.7
111b	Et	**1e**	5	53.1	37.7	71.0	7.1 kDa	14.5 kDa	1.23	48 h	85.3
111c	Bn	**1e**	5	40.0	38.8	97.0	9.7 kDa	15.9 kDa	1.12	48 h	87.7
111d	Chol	**1e**	5	19.0	17.6	92.6	9.3 kDa	16.6 kDa	1.19	48 h	92.4
111e	Ad	**1e**	5	32.4	19.6	60.5	6.0 kDa	13.2 kDa	1.23	48 h	71.3
111f	TMC	**1d**	5	49.0	34.4	70.2	3.5 kDa	5.9 kDa	1.20	48 h	92.7
111g	Et	**1d**	5	26.6	14.7	55.3	2.7 kDa	3.8 kDa	1.09	48 h	80.0
111h	Bn	**1d**	5	20.0	13.3	66.5	3.3 kDa	5.8 kDa	1.14	48 h	90.3
111j	Chol	**1d**	5	9.5	7.2	75.8	3.8 kDa	6.2 kDa	1.18	48 h	89.0
111k	Ad	**1d**	5	16.2	8.2	50.6	2.5 kDa	5.0 kDa	1.22	48 h	81.3
111l	TMC	**1e**	5	98.0	84.9	86.6	8.7 kDa	14.9 kDa	1.16	24 h	87.0
111m	Bn	**1e**	5	40.0	39.8	99.5	10.0 kDa	16.1 kDa	1.16	24 h	94.7
111n	Chol	**1e**	5	19.0	14.4	75.8	7.6 kDa	14.8 kDa	1.15	24 h	81.0
111o	Ad	**1e**	5	32.4	24.4	75.3	7.5 kDa	14.1 kDa	1.11	24 h	71.3

^{1}H-NMR and GPC in THF were used to characterize mPEG-b-polycarbonate homopolymers (**111a-o**). % Conversion indicated that the DBU/TU co-catalyst system allowed for synthesis of higher molecular weight polycarbonate polymers and provided much better control and subsequent polydispersity. Interestingly, little difference between 24- and 48-hour reaction times was observed, indicating that all monomers were

consumer by 24 hours. M_n as measured by NMR and GPC were in relative agreement with a slight bias for increased molecular weight for GPC measurements similar to the trend observed for previous compounds. M_w/M_n were significantly improved for DBU/TU relative to TBD ranging from 1.11-1.23. These observations are consistent with other materials synthesized using this co-catalyst system.

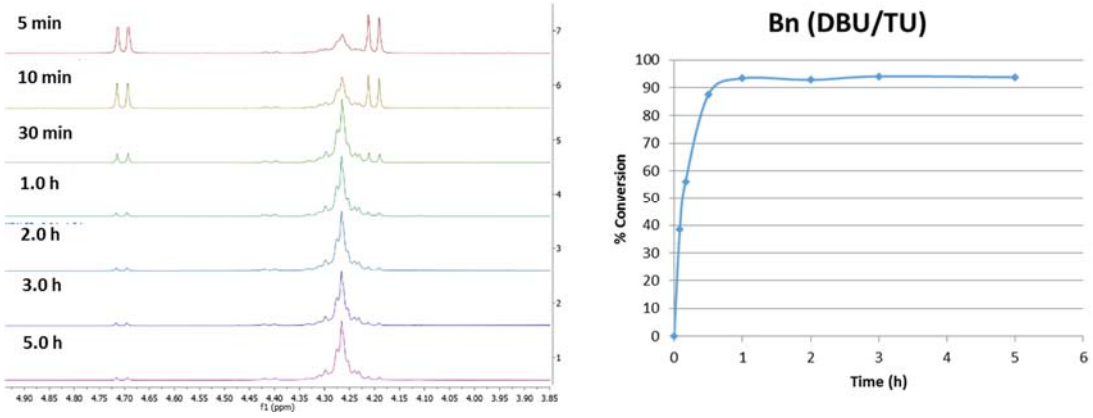

Figure 5.10 Monitoring of **95** Polymerization using DBU/TU by ^{1}H-NMR.

A brief kinetic experiment was used to monitor monomer consumption via ^{1}H-NMR in order to determine optimal reaction times for polymerization of the carbonate monomers using DBU/TU and the conditions outlined above for homopolymerization of carbonate monomers (Figure 5.10). Conditions used for synthesis of **111c** were used and aliquots were removed at pre-determined time points, quench with benzoic acid and analyzed via ^{1}H-NMR after drying. During polymerization, the carbonate monomers become decyclized, leading to a homogenization of the methylene protons on either side

of the carbonate functional group. In the monomer, these protons give two distinct doublets at 4.2 and 4.7 ppm. This is due to interaction of these methylene protons with the carbonyl of the ester moiety through space. Upon polymerization, these proton signals become homogenized in NMR due to the flexibility of the carbonate backbone. The ratios of integrals of these two sets of protons were used to determine the relative % monomer consumption at various time points. Results indicated that polymerizations reached a maximum of ~94 % monomer conversion by approximately 1 hour after initiation of polymerization. These results indicate that extended reaction times are not necessary for polymerization of cyclic carbonate monomers using the DBU/TU system. This also suggests that low % conversion, and high polydispersity of diblock copolymers generated using TBD as catalyst, may be due to side reactions associated with extended reaction times and possible transesterification of the pendant ester moieties, although no evidence of this was observed via ^{13}C-NMR.

5.2.5 Copolymerization of Carbonate Monomers by DBU/TU

Having obtained positive results for homopolymerization of carbonate monomers using the DBU/TU system, we synthesized a small library of diblock copolymers where the polycarbonate block consisted of the pendant carbonate monomers blended with TMC. The purpose of these materials was to evaluate the effect of pendant group density along the linear polycarbonate backbone on material performance. Since the monomers are expected to show similar activities for ROP using DBU/TU, we can expect relatively homogenous distributions of pendant moieties in the resultant polymer. If one monomer

has increased reactivity, it will be present in greater proportion towards beginning of the polycarbonate block.

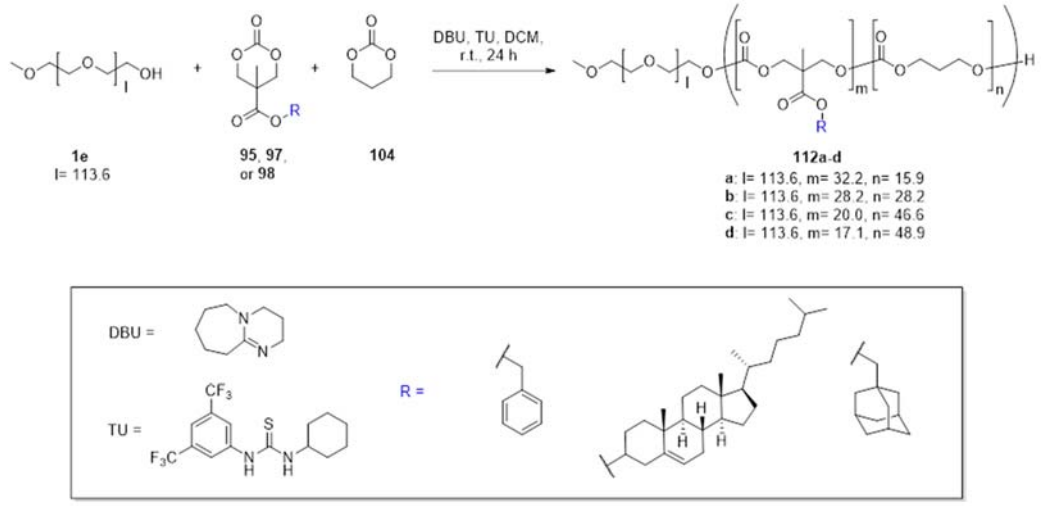

Scheme 5.8 Copolymerization of Carbonate Monomers by DBU/TU.

Copolymerizations were carried out under nitrogen using 10 mol % DBU/TU in DCM such that the total [M] was 1.0 M, initially. Reactions were allowed to proceed for 24 hours before quenching with benzoic acid followed by precipitation into diethyl ether to remove catalysts and unreacted monomers. Total polycarbonate molecular weights of 10.0 kDa were targeted with various ratios of **95** to TMC (2:1, 1:1, 1:2, 1:4).

Table 5.5 Characterization of DBU/TU-Catalyzed mPEG-b-Polycarbonate Copolymers.

Entry	R	Initiator	TDB (mol%)	m:n (feed ratio)		m:n (NMR)		% Conversion	PC-M_n (NMR)	M_n (GPC)	M_w/M_n (GPC)	Time	Yield (%)
				m	n	m	n						
112a	TMC:Bn	**1e**	10	2	1	32.2	15.9	96.6	9.7 kDa	16.2 kDa	1.22	24 h	92.9
112b	TMC:Bn	**1e**	10	1	1	28.2	28.2	99.3	10.0 kDa	15.6 kda	1.14	24 h	92.7
112c	TMC:Bn	**1e**	10	1	2	20.0	46.6	99.1	9.7 kDa	15.9 kDa	1.2	24 h	91.3
112d	TMC:Bn	**1e**	10	1	4	17.1	48.9	86.9	9.3 kDa	14.8 kda	1.18	24 h	82.9

^{1}H-NMR and GPC were used to characterize copolymers generated via DBU/TU-catalyzed ROP of cyclic monomers, **95** and TMC initiated by **1e**. ^{1}H-NMR indicated high % conversion of monomers and good control of monomer incorporation ratios via control of monomer feed ratios. M_n calculated from ^{1}H-NMR and GPC were in good agreement. M_w/M_n as determined from GPC measurements ranged from 1.14-1.22, indicating relatively monodisperse copolymer formation.

5.3 Performance of mPEG-b-Polycarbonate Pendant Polymers

Next, some of the homopolymers generated via TBD-catalyzed ROP were tested for their abilities to effectively form nanoparticles in combination with β-cyclodextrin-poly(ethyleneimine) (β-CD-PEI) conjugate (as described by Kulkarni, et al.[26a]) and pDNA.

5.3.1 Formulation of mPEG-b-Polycarbonate Pendant Polymer-Based Transfection Complexes

Transfection complexes composed of various mPEG-b-polycarbonate diblock copolymers, β-CD-PEI and pDNA were prepared via precomplexation of β-CD-PEI and the pDNA before addition of the diblock copolymer, which acts as a polymeric coating via host:guest interaction of the pendant groups with cyclodextrin cavities and hydrophobic interactions. This method was first referred to as "Method B" by Kulkarni et al[42].

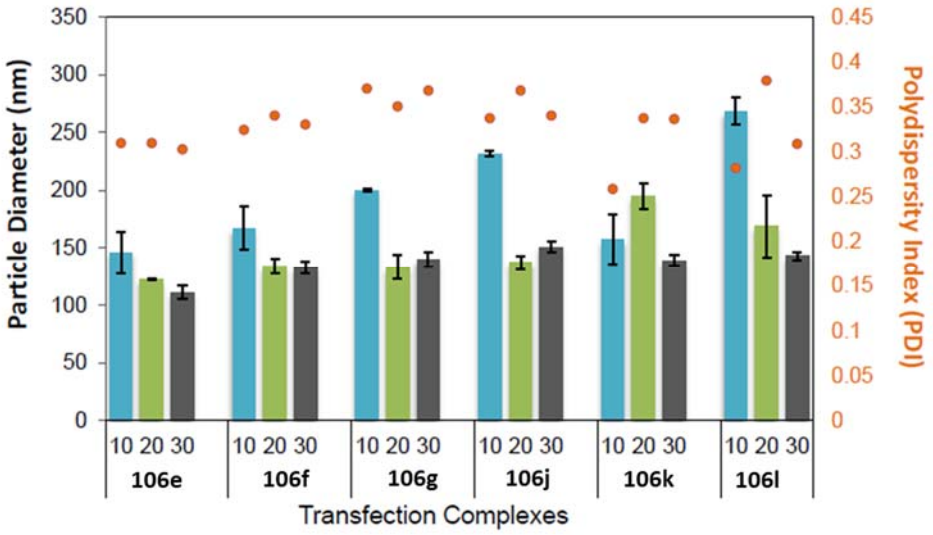

Figure 5.11 Size Analysis of Transfection Complexes at Various N/P Ratios by DLS.

Dynamic light scattering (DLS) was used to determine size and polydispersity of transfection complexes generated using Compounds **106e-g** and **106j-l** (Figure 5.11). Transfection complexes ranged in size from approximately 100-250 nm in size. This size regime is highly amenable to gene delivery applications. Transfection complexes formed from lower weight diblock copolymers showed relatively larger sizes compared to those of higher weight polymers. Particle sizes generally decreased with increasing N/P and little correlation in particle size and pendant group was observed. Polydispersity indices ranged from 0.25-0.4.

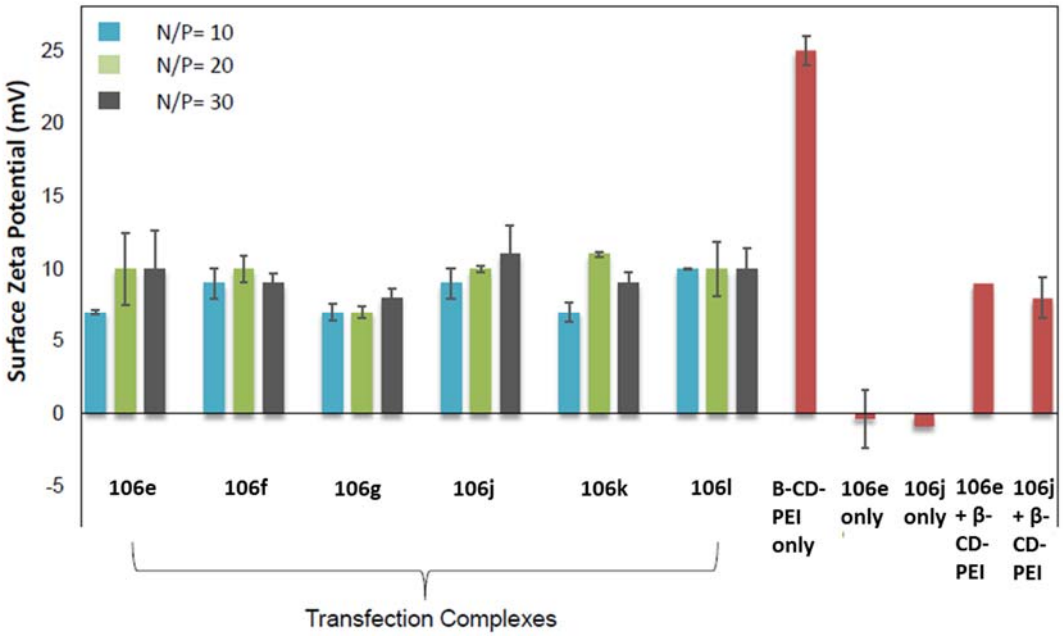

Figure 5.12 Surface Zeta (ζ) Potential Analysis of Transfection Complexes at Various N/P Ratios.

Zeta potential analysis revealed slightly positive zeta potentials in the range of 5-10 mV. This slightly positive surface charge is generally preferred in order to promote internalization via electrostatic interaction of the positively-charged nanoparticle surface and the negatively-charged cellular surface. N/P of 10, 20, and 30 resulted in similar surface charges. β-CD-PEI alone exhibited an elevated positive surface charge. Copolymers **106e** and **106j** both exhibited neutral charge in solution while mixtures of the copolymer with β-CD-PEI resulted in positive surface charges that were lower in magnitude than β-CD-PEI alone, indicating that the diblock copolymers effectively screen the positive surface charge of β-CD-PEI. Furthermore, β-CD-PEI in combination with the diblock copolymers showed similar zeta potential to the transfection complexes.

This suggests that siRNA is likely not surface exposed and, thus, protected from degradation.

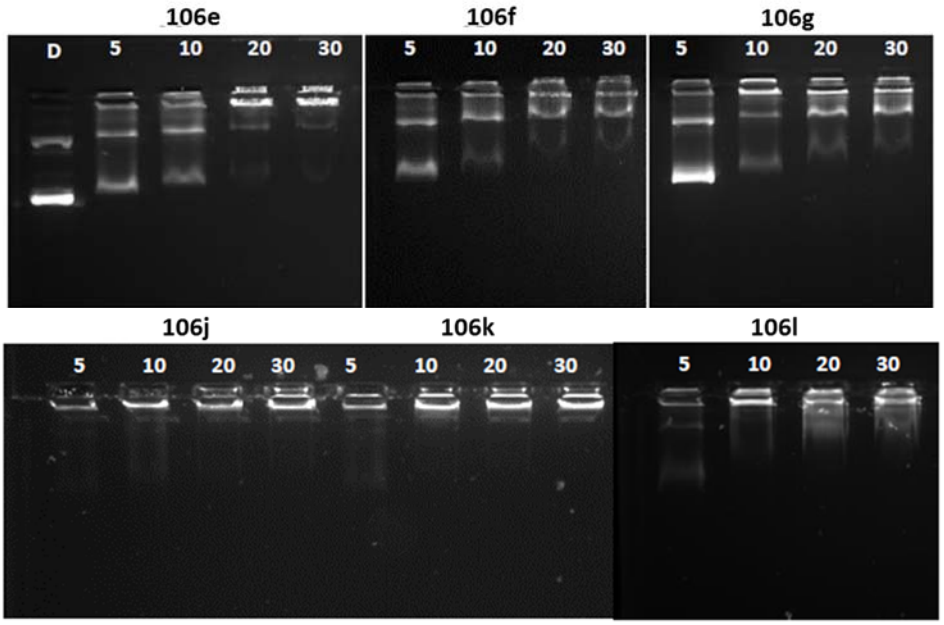

Figure 5.13 Gel Retardation Analysis of Transfection Complexes at Various N/P Ratios.

Next, a gel retardation assay was performed to determine the ability of the mPEG-b-polycarbonate:β-CD-PEI-based materials to condense pDNA at various N/P ratios. Higher molecular weight diblock copolymers resulted in the need for high N/P ratios (e.g. >20) to effectively condense pDNA, while lower molecular weight diblock copolymers effectively condensed pDNA at N/P =5 in two of three cases with the other effectively condensing pDNA at N/P = 10.

5.3.2 Transfection Efficiency in HeLa Cells

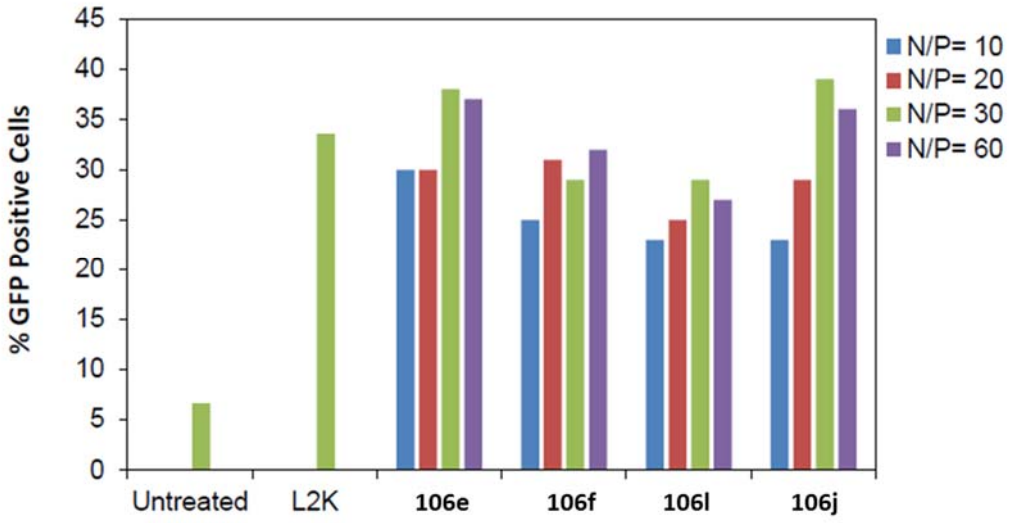

Figure 5.14 % GFP Positive HeLa Cells Treated with Transfection Complexes Containing AcGFP pDNA.

Transfection complexes prepared from mPEG-b-polycarbonates **106e**, **106f**, **106j**, or **106l** in combination with β-CD-PEI and AcGFP pDNA were evaluated for their transfection efficiencies in HeLa cells (Figure 5.14). Transfection complexes showed similar efficiency in terms of positive cells to Lipofectamine (L2K). Overall, transfection complexes prepared from mPEG-b-polycarbonates with different pendant groups showed similar transfection efficiencies. Polymer molecular weight also seemed to have little correlation to transfection efficiency. Higher N/P tended to give higher transfection efficiency. This observation may be due to higher overall surface charge for particles at N/P = 60, for instance.

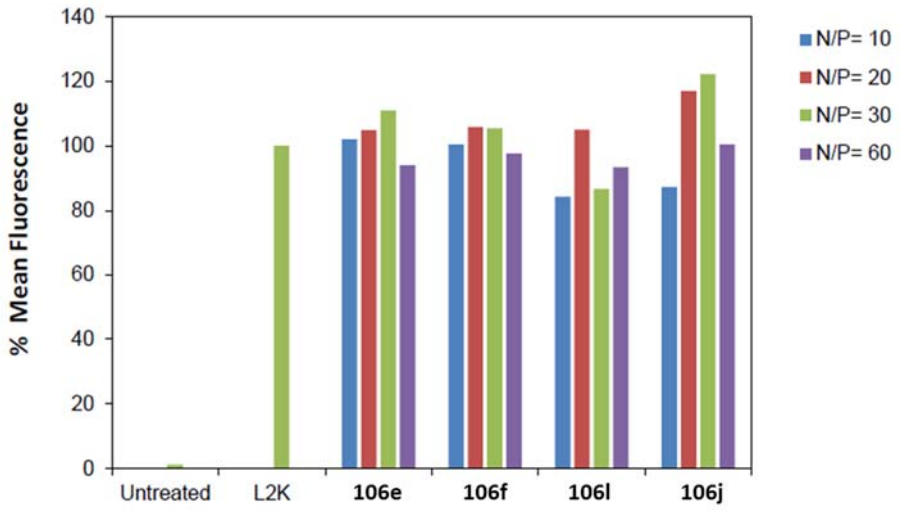

Figure 5.15 % Mean Fluorescence of HeLa Cells Treated with Transfection Complexes Containing AcGFP pDNA.

When transfection efficiency is evaluated in terms of % mean fluorescence (Figure 5.15), similar trends are revealed. All the transfection complexes performed with similar efficiency to L2K. Transfection efficiencies were consistent for different transfection complexes with no clear correlation between transfection efficiency and polymer molecular weight, or pendant group. N/P ratios of 20-30 tended to show highest transfection efficiency.

5.4 Organocatalytic ROP Synthesis of mPEG-b-PCL and SILY-PEG-b-PCL

In an effort to design and evaluate a novel microparticle-based drug delivery system for delivery of hydrophobic anti-inflammatory compounds to the GI tract, and utilizing a novel collagen-binding peptide (SILY) pioneered by Paderi and Panitch[43] for specific targeting of exposed collagen, a small library of mPEG-b-PCL diblock copolymers were synthesized via organocatalytic ROP mediated by TBD (Scheme 5.9).

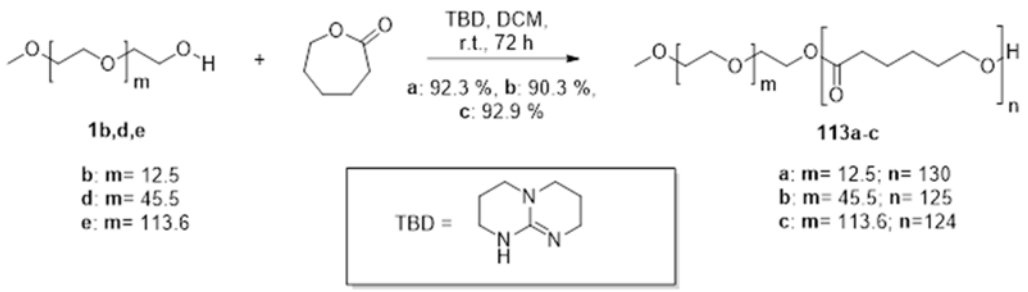

Scheme 5.9 ROP of ε-Caprolactone by TBD Using mPEG as Macroinitiator.

Polymerizations were performed under nitrogen in DCM, yielding [M] of 2.0 M and 5 mol % TBD relative to [M]. Molecular weights of 15.0 kDa were targeted for each polymer so as to yield diblock copolymers possessing similar PCL blocks (~15.0 kDa) and PEG blocks of various molecular weight (550 Da, 2.0 kDa, 5.0 kDa). Polymerization reactions were allowed to run for 72 hours before quenching with benzoic acid to yield the catalyst inactive and precipitation into ether to remove catalyst and unreacted monomer.

Table 5.6 Characterization of mPEG-b-PCL Copolymers.

Entry	Initiator	TBD (mol %)	n (targeted)	PCL-M_n (NMR)	n (NMR)	M_n (GPC)	% Conversion	M_w/M_n (GPC)	% Yield
113a	$mPEG5_{550}$	5	131.4	14.8 kDa	129.7	15.8 kDa	98.7	1.13	92.3
113b	$mPEG_{2000}$	5	131.4	14.3 kDa	125.5	17.2 kDa	95.5	1.16	90.3
113c	$mPEG_{5000}$	5	131.4	14.2 kDa	124.5	20.4 kDa	94.8	1.12	92.9

^{1}H-NMR and GPC in THF were used to characterize the small family of mPEG-b-PCL diblock copolymers synthesized via organocatalytic ROP mediated by TBD in DCM. Relative % conversion and M_n calculated from ^{1}H-NMR indicated that nearly all

of the monomer was incorporated into polymer for all three cases with % conversions upwards of 95 %. M_n calculated by ^{1}H-NMR was just below 15.0 kDa for all three polymers, while M_n calculated from GPC was very consistent with the expected molecular weights after taking into account the molecular weight of the macroinitiator in addition to the PCL block. M_w/M_n calculated from GPC were surprisingly low, indicating well-controlled living polymerization of ε-caprolactone under these conditions.

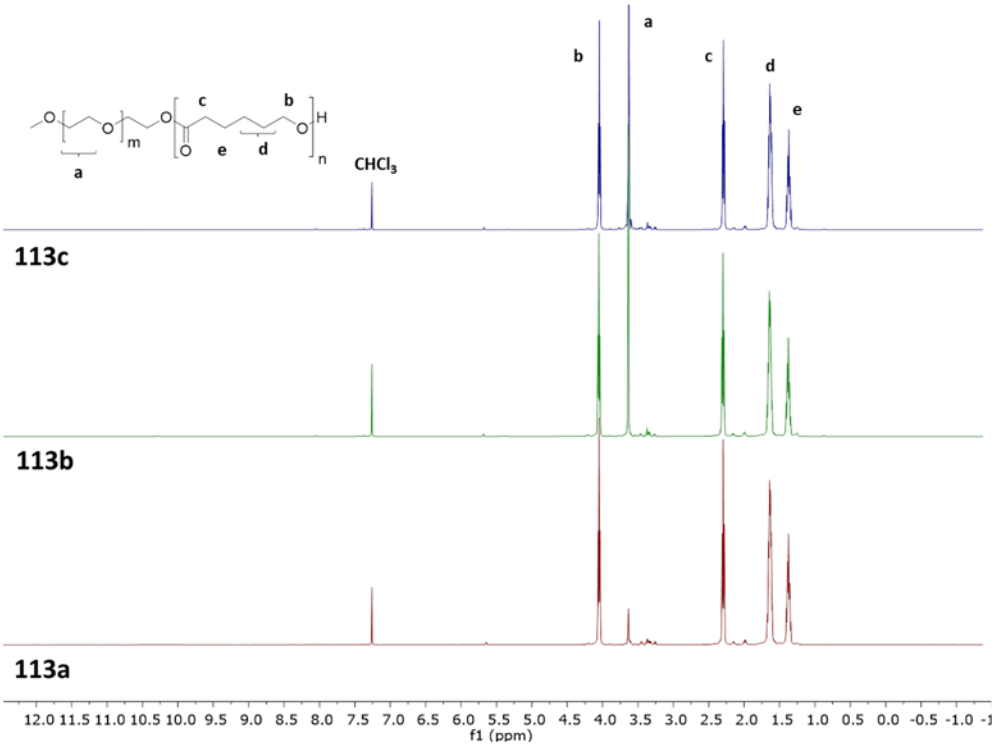

Figure 5.16 ^{1}H-NMR Spectra of mPEG-b-PCL Diblock Copolymers.

^{1}H-NMR spectra of Compounds **113a-c** revealed that the compounds were isolated in high purity with no traces of catalyst, unreacted monomers or other occult impurities (Figure 5.16).

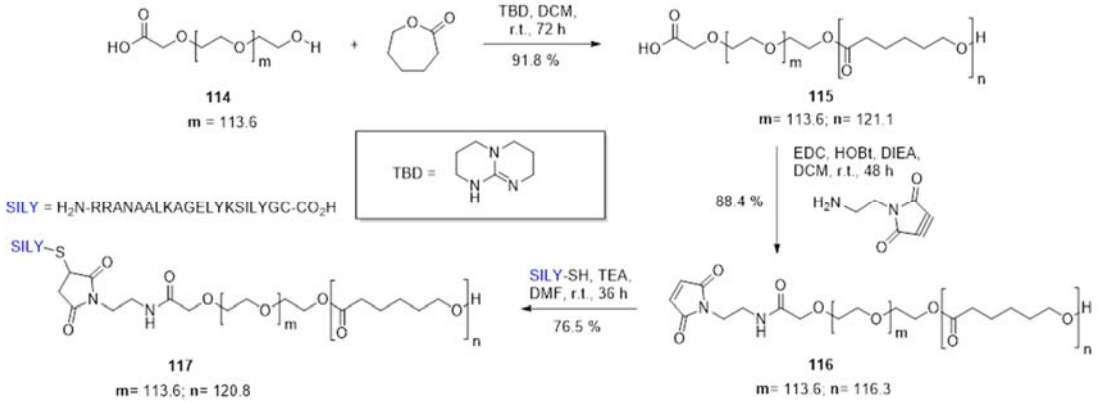

Scheme 5.10 Synthesis of Collagen-Binding SILY-PEG-b-PCL Conjugate.

A novel strategy for synthesis of conjugates between thiol-containing peptides and PEG-b-PCL diblock copolymers was used to generate the SILY-PEG-b-PCL conjugate **117** via a two-step post-modification process after organocatalytic ROP of ε-caprolactone by heterobifunctional PEG derivative **114** (Scheme 5.10).

SILY peptide (H_2N-RRANAALKAGELYKSILYGC-CO_2H) was first developed as a synthetic peptide used to synthesize a dermatan sulfate-containing peptidoglycan based on decorin, a natural collagen-binding peptideglycan. The SILY peptide functions as a collagen binding motif. This synthetic peptidoglycan was shown to specifically bind collagen, delay fibrillogenesis and increase collagen gel stiffness in the same way decorin does.

Polymerization of ε-caprolactone catalyzed by TBD using heterobifunctional α-carboxyl-ω-hydroxyl-PEG derivative **114** was performed using 5 mol % TBD relative to [M] with an additional 1.0 equivalent to account for deprotonation of the terminal

carboxyl group in DCM at ambient temperature. PCL block molecular weight of 15.0 kDa was targeted. The reaction was allowed to proceed for 72 hours, then quenched with benzoic acid before precipitation into diethyl ether to remove catalysts and unreacted monomer to give Compound **115**. Compound **115** was then coupled to N-(2-aminoethyl)maleimide via EDC-mediated coupling in the presence of HOBt and DIEA in DCM to give maleimide-PEG-b-PCL (**116**). Compound **116** was then conjugated to SILY via Michael addition of the thiol group of the lone cysteine residue of SILY and the maleimide terminus of Compound **116** to give peptide-polymer conjugate **117**.

Table 5.7 Characterization of SILY-PEG-b-PCL and Precursors.

Entry	TDB (mol %)	n (targeted)	PCL M_n (NMR)	n (NMR)	M_n (GPC)	% Conversion	M_w/M_n (GPC)	% Yield
115	5	131.4	13.8 kDa	121.1	19.8 kDa	0.92	1.14	91.9
116	n/a	n/a	13.3 kDa	116.3	19.2 kDa	n/a	1.20	88.4
117	n/a	n/a	13.8 kDa	120.8	20.8 kDa	n/a	1.24	76.5

SILY-PEG-b-PCL and precursors were characterized via ^{1}H-NMR and GPC in THF (Table 5.7). Compound **115** showed high monomer conversion and M_n from ^{1}H-NMR and GPC were consistent and suggested (note that n from NMR represents molecular weight of the PCL block, while M_n from GPC represents the molecular weight of the entire construct). M_w/M_n for Compound **115** was 1.14, suggesting a relatively monodisperse diblock copolymer. After coupling to N-(2-aminoethyl)maleimide, Compound **116** showed consistent M_n in comparison to Compound **115** indicating that the PCL block was retained with minimal degradation. After coupling to SILY, Compound **117** showed consisted M_n for the PCL block from and NMR and GPC

reflected the additional molecular weight of the peptide. Mw/Mn increased slightly after each post-modification reaction. This may be due to some hydrolysis of PCL during the reaction sequence.

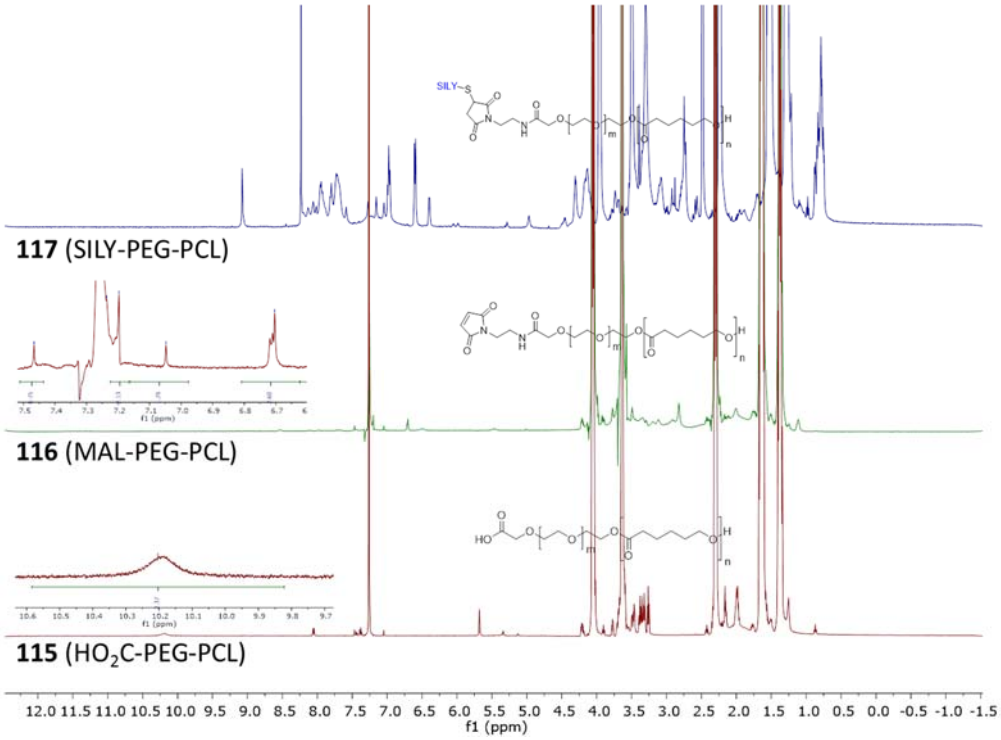

Figure 5.17 ^{1}H-NMR Analysis of SILY-PEG-b-PCL and Precursors.

^{1}H-NMR analysis of SILY-PEG-b-PCL in combination with GPC was used to verify successful reaction efficiency for each step in the sequence (Figure 5.17). The terminal carboxyl group of Compound **115** is apparent as a broad singlet at approximately 10.2 ppm. Peaks consistent with maleimide protons were observed in the ^{1}H-NMR of Compound **116**. SILY-PEG-b-PCL (**117**) displayed numerous alkyl and aromatic signals corresponding to various moieties of the peptide. This data, along with

the increased M_n observed from GPC verify that SILY-PEG-b-PCL conjugate was synthesized successfully.

5.5 Organocatalytic ROP Synthesis of mPEG-b-PLGA

A small library of mPEG-b-PLGA diblock copolymers was synthesized via organocatalytic ROP mediated by DBU using a method pioneered by Qian et al.[44] involves controlled addition of glycolide, the more reactive monomer, to generate random copolymers of PLGA grown from macroinitiators via organocatalytic ROP. PLGA is a biodegradable hydrophobic polyester commonly used in a wide variety of biomedical applications, which is typically synthesized in bulk using tin-based organometallic catalysts. However, this method results in high polydispersities. The method of Qian et al allows for fast and efficient synthesis of random well-defined PLGA polymers.

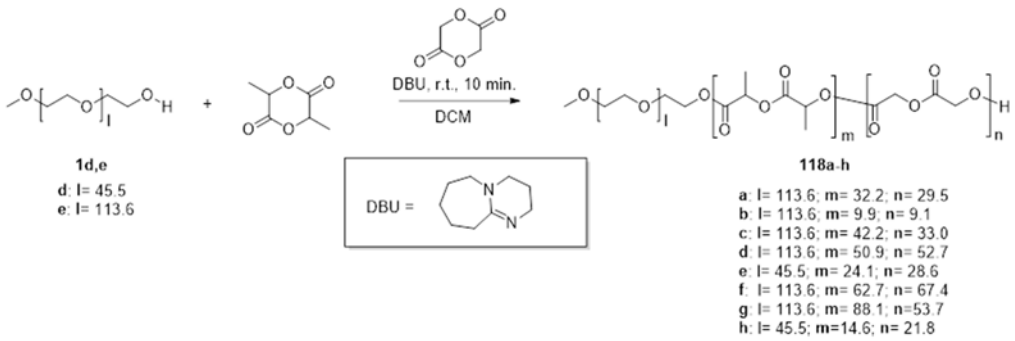

Scheme 5.11 Organocatalytic ROP Synthesis of mPEG-b-PLGA Catalyzed by DBU.

Lactide and glycolide were each recrystallized immediately beforehand allowed to dry until constant mass was observed and used for polymerization. Polymerizations were run in DCM using 1.0 equivalent of DBU relative to the macroinitiator. Polymerizations were carried out by constant addition of glycolide solution to the polymerization vessel containing PEG, lactide, and the catalyst. Polymerizations were run for 10 min before quenching with benzoic acid to cease catalyst activity. This strategy functions to effectively maintain a low concentration of glycolide relative to lactide to maintain random incorporation of either monomer into the growing polyester. This is necessary because glycolide is much more active toward ROP than lactide. This method allows for control of the relative ratios of lactide to glycolide (LA:GA) in the product copolymer. In this study, LA:GA of 1:1 were targeted.

Table 5.8 Characterization of mPEG-b-PLGA Diblock Copolymers.

Entry	Initiator	m ^{1}H-MR)	n (^{1}H-NMR)	PLGA M_n (^{1}H-NMR)	LA M_n (^{1}H-NMR)	GA M_n (^{1}H-NMR)	LA:GA	Yield
118a	**1e**	32.2	29.5	8.0 kDa	4.6 kDa	3.4 kDa	1.00: 0.92	1.116 g
118b	**1e**	9.9	9.1	2.5 kDa	1.4 kDa	1.1 kDa	1.00: 0.92	0.809 g
118c	**1e**	42.4	33	9.9 kDa	6.1 kDa	3.8 kDa	1.00: 0.78	1.489 g
118d	**1e**	50.9	52.7	13.4 kDa	7.3 kDa	6.1 kDa	0.97: 1.00	1.675 g
118e	**1d**	24.1	28.6	6.8 kDa	3.5 kda	3.3 kDa	0.84: 1.00	1.633 g
118f	**1e**	62.7	67.4	16.9 kDa	9.0 kDa	7.8 kDa	0.93: 1.00	1.755 g
118g	**1e**	88.1	53.7	18.9 kDa	12.7 kDa	6.2 kDa	1.00: 0.61	1.131 g
118h	**1d**	14.6	21.8	4.6 kDa	2.1 kDa	2.5 kDa	0.67: 1.00	1.298 g

^{1}H-NMR was used to determine the molecular weight of mPEG-b-PLGA diblock copolymers and relative lactide:glycolide ratios of monomer conversion (Table 5.8). Overall, obtained PLGA M_n from ^{1}H-NMR was variable. M_n of 10.0 kDa was targeted for polymerizations using **1e** as macroinitiator and 5.0 kDa was targeted when **1d** was used. Variability between targeted and obtained molecular weights is attributable to slight differences in polymerization kinetics over the very short reaction period, which makes optimal quenching times difficult to predict in the absence of real-time monitoring of the polymerization. However, ratios of lactide to glycolide calculated from ^{1}H-NMR suggested nearly 1:1 stoichiometry with some variability for the polymers, which also showed decreased control of molecular weight.

5.6 Synthesis of Cyclic Amino-Acid N-Carboxyanhydride Monomers

There has been significant interest in the chemical synthesis of polypeptides. Most polypeptides are synthesized via solid-phase peptide synthesis (SPPS) protocols [45]. Solid-phase peptide synthesis methodologies allow fast, efficient synthesis of short peptides of an exact determinable sequence. However, this method has several weaknesses including,

cost per amino acid, limitation of the maximum attainable molecular weight, and scalability. Today, medium sized peptides (30-50 residues) can be routinely synthesized via SPPS protocols using uronium-based coupling reagents and the standard orthogonal Fmoc-Boc methodology[45a]. The advantages of SPPS lie in its sequence specificity and relative standardization. Recently, the drug glatarimer acetate (Copaxone), which is a random synthetic copolymer of glutamic acid, lysine, alanine, and tyrosine with average M_n of 6.4 kDa, was approved for the treatment of multiple sclerosis. The drug is a myelin-basic protein biomimetic. Thus, glatarimer acetate may act as a decoy, averting an autoimmune response against myelin.

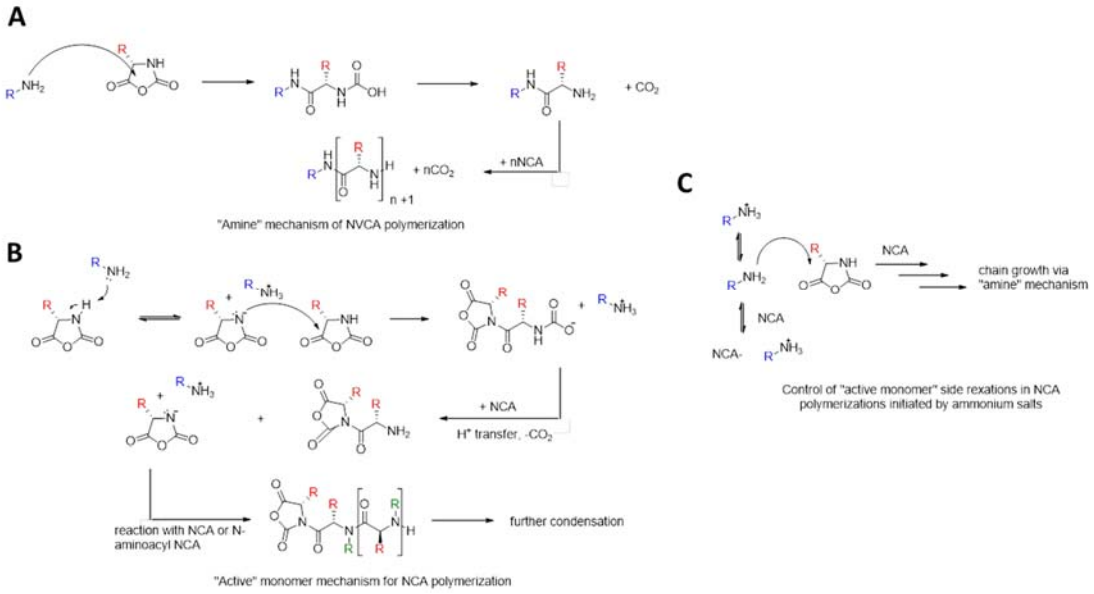

Figure 5.18 Polymerization of Amino Acid N-Carboxyanhydride Monomers. (A) The "amine" mechanism of NCA polymerization. (B) "Active Monomer" mechanism of NCA polymerization. (C) NCA polymerization using ammonium salts.

An alternative strategy for the synthesis of polypeptides involves the ring opening polymerization of amino acid N-carboxyanhydrides (NCA). The NCA approach is the most commonly used approach for producing high molecular weight peptide homo- and copolymers on a gram or greater scale. NCA polymerization is the method of choice for synthesizing peptides like glatarimer acetate, where the exact sequence specificity is not required. By employing amine-terminal macroinitiators one can obtain block copolymers with a synthetic block and a polypeptide block or blocks. These so called "hybrid block copolymers" or "molecular chimeras" may be of particular utility in the fields of drug and gene delivery due to their inherent biocompatibility and programmable properties.

NCA polymerization should preferentially proceed via the amine mechanism (Figure 5.18A). That is, nucleophillic attach of the NCA by an initiating primary amino group. This reaction is commonly run in dimethylformamide (DMF) at room temperature. However, using the amine mechanism, broad polydispersity indices in excess of 1.4-1.6 are commonly observed. This is due to side reactions involving deprotonation of weakly acidic N-H protons from an NCA monomer or an amide of the growing polypeptide chain (Figure 5.18B). This can lead to branching and contributes to an overall broadening of the polydispersity of the polymer[46].

Alternative strategies have sought to avoid the amine mechanism and thereby the active monomer side reaction by using catalytic systems. Deming, et al. used transition metal catalysts based on nickel (II) complexes[47]. Since amines can act as effective nucleophiles and bases, an effective switching between the amine mechanism and active monomer mechanism will always occur in NCA polymerization. There is also evidence that these side reactions may depend heavily on the purity of the NCA monomers.. High

vacuum technique has also been utilized to speed the amine mechanism by fast degradation of the carbamic acid byproduct.

Dimitrov and Schlaad[48] found that by simply adding protons or using a hydrochloride salt to initiate the polymerization, polymers were obtained with PDIs near unity (Figure 5.18C). They used amine-hydrochloride-terminal polystyrene to initiate a polymerization of an NCA derivative of N_{ε}-benzyloxycarbonyl-l-lysine (Z-L-Lys). The underlying hypothesis assumes that by keeping the propagating amine protonated when the active monomer is formed, it will be much more likely to be reprotonated rather than initiating acyl transfer. Polymer growth proceeds via the "amine" mechanism. These reactions were slow, taking several hours to complete due to decreased effective concentration of the propagating amine. The desirability of this mode of NCA polymerization comes from the accessibility of primary amine hydrochlorides and the simplicity of the reaction conditions.

Several different amino acid-based N-carboxyanhydride monomer synthesis methods have been previously described. Initially NCA's were synthesized via suspension of the amino acid in a dry solvent (dioxane, EtOAc) at elevated temperature before passing phosgene through the mixture until a homogeneous solution is obtained[49]. The resulting solution must then be evaporated or purged for extended periods to remove excess phosgene before purification by recrystallization. This procedure is potentially unsafe due to the use of phosgene. N^{α}-Cbz-protected amino acids may also be converted to the corresponding NCA via treatment with phosphorus pentachloride.

Later, the Fuchs-Farthing method[50] was developed utilizing triphosgene as carbonylation reagent in place of phosgene using ethyl acetate (EtOAc) as solvent. This

method generally involved sequential crystallization to remove impurities. A method employing flash chromatographic purification of NCA's was also introduced. Numerous NCA's have been reported via this method including NCA's derived from γ-benzyl-L-glutamate, L-alanine, N^{ε}-benzyloxycarbonyl-L-lysine, O-benzyl-L-threonine, O-benzyl-L-serine, β-benzyl-L-aspartate, L-leucine, L-tyrosine, and glycine.

During the course of experimentation into applying the pendant polymer concept to peptide copolymers derived from NCA's, we attempted to use the Fuchs-Farthing method to numerous amino-acid NCA's but found that it was not applicable to many amino acids due to their inability to become dissolved in ethyl acetate as solvent even at elevated temperatures in excess of 80 °C. In particular, L-alanine proved non-amenable to NCA synthesis. Thus, several solvents were screened to determine a solvent for triphosgene-based NCA synthesis with broad applicability for a wide variety of amino acid starting materials.

Tetrahydrofuran (THF) was found to be a suitable solvent for every amino acid that we attempted to convert to the corresponding NCA at relatively mild temperatures. Since THF is easily dried, readily evaporated after NCA synthesis and miscible with water, it is especially amenable to previous purification strategies applied to NCA's. In order to test the utility of the modified Fuchs-Farthing method in THF, we synthesized a small library of NCA monomers, including some previously reported NCA's and some novel NCA's. The lowest temperature required to effect solubilization of the starting materials was used to avoid side reactions. The results of this study are reported in Scheme 5.12.

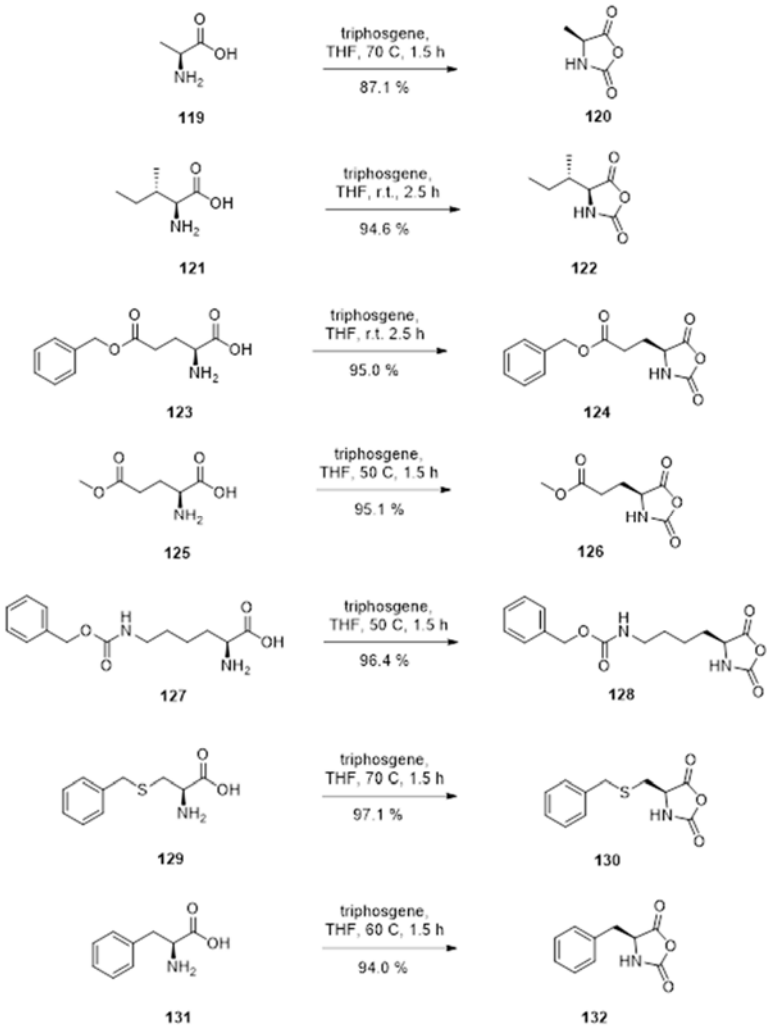

Scheme 5.12 Synthesis of Amino Acid-NCA Monomers.

NCA's were obtained in high yield (87.1% - 97.1%) and in high purity based on NMR. Relatively hydrophilic amino acids (L-alanine, S-benzyl-L-cysteine) required the highest temperature (70 °C) to effect conversion while L-phenylalanine was solubilized at 60 °C. N^{ε}-Cbz-L-lysine, and γ-methyl-L-glutamic acid were converted at 50 °C. Relatively lipophilic amino acids (γ-benzyl-L-glutamate, L-isoleucine) were converted to the corresponding NCA's at ambient temperature in THF. This modified synthetic

approach to NCA synthesis using THF as universal solvent for carbonylation of amino acids using triphosgene is expected to be applicable to a wide range of natural and synthetic amino acid derivatives. Since THF is a good solvent able to solubilize a wide variety of compounds, is easily evaporated and miscible with water, this synthetic procedure may extend the range of accessible NCA's and the corresponding molecular architectures of polypeptides derived from NCA polymerization.

5.7 Conclusions

The pendant polymer-based gene delivery concept has shown potential as a novel non-viral gene delivery strategy. However, we sought to address material-specific limitations of previously reported pendant polymer materials by using modern synthetic strategies to design and synthesize a more well-defined new generation of pendant polymers based on diblock copolymers derived from organocatalytic ROP. A family of mPEG-b-polycarbonate diblock pendant polymers was successfully synthesized from several novel and previously reported cyclic carbonate monomers via organocatalytic ROP using TBD and the bifunctional DBU/TU system. Several copolymerizations of the cyclic carbonate monomers were performed to generate materials having tunable pendant group density alone the polymer backbone. These materials were characterized by NMR and GPC. The diblock copolymers showed the ability to form nanoparticles, typically 100-250 nm in size, with slightly positive surface zeta-potentials, effectively condensed pDNA at N/P ratios above 10, and showed comparable transfection efficiencies to Lipofectamine-2000 (L2K) in HeLa Cells.

A small library of mPEG-b-PCL diblock copolymers was successfully synthesized via organocatalytic ROP of ε-caprolactone catalyzed by TBD using mPEG as a macroinitiator. A collagen binding peptide (SILY) conjugate (SILY-PEG-b-PCL) was also synthesized via organocatalytic ROP of ε-caprolactone catalyzed by TBD using α-carboxyl-ω-hydroxyl-heterobifunctional PEG as a macroinitiator. DBU was used to synthesize a small library of mPEG-b-PLGA diblock copolymers having controlled random incorporation of lactide and glycolide into the PLGA backbone. These materials were characterized via ^{1}H-NMR and GPC.

A new synthetic method for preparation of amino acid N-carboxyanhydrides (NCA's) was developed based on a modified method which was previously reported where THF was substituted as solvent for the reaction. This protocol showed broad applicability for synthesis of several NCA's from amino acids having highly varied solubility properties, including L-alanine. This method may provide for synthesis of a wide variety of novel NCA's in the future.

5.8 Future Directions

Future efforts for the polycarbonate-based pendant polymers will focus on evaluation of the complete library for performance and investigation of the pendant group density on performance. Furthermore, a similar strategy to that used to synthesize SILY-PEG-b-PCL may be applied to the polycarbonate system to generate targeted-PEG-b-polycarbonate pendant polymers. This strategy could prove to be a powerful modular approach to actively-targeted gene delivery systems. The amino-acid-NCA's may also be

used to generate a similar library of polypeptide-based pendant polymers, which may exhibit unique properties relative to other pendant polymer materials.

5.9 Experimental Methods

All reactions were carried out under a blanket of N_2 or argon gas. Reaction progress was monitored by thin-layer chromatography (TLC) analysis. TLC spots were visualized either by UV light (254nm), exposure by ninhydrin staining, staining with phosphomolybdic acid (PMA), staining with p-anisaldehyde or by staining with I_2. Flash column chromatography was carried out using 230-400 mesh silica gel and analytical grade solvents. Solvents were purchased from Mallinckrodt/Baker and used without further purification unless noted. Toluene was purchased from Fisher. α-Methoxy-poly(ethylene glycol) (mPEG, **1a-e**) having average molecular weights of 350 Da, 550 Da, 750 da, 2.0 kDa, and 5.0 kDa were purchased from Sigma Aldrich and purified prior to polymerization by precipitation of a dichloromethane (DCM) solution into an excess of diethyl ether (Et_2O) three times each followed by vacuum filtration and drying *in vacuo* for 24 hours. 1,8-Diazabicyclo[5.4.0]undec-7-ene (DBU) was purchased from Sigma Aldrich and stirred together with CaH_2 for 48 hours, followed by distillation *in vacuo*. 1,5,7-Triazabicyclo [4.4.0]dec-5-ene (TBD) was purchased from Sigma Aldrich and purified by stirring a DCM solution in the presence of CaH_2 for 48 hours, followed by filtration and recrystallization from DCM/pentane. ε-Caprolactone was purchased from Sigma and purified via stirring with CaH_2 for 48 hours, followed by vacuum distillation. Lactide was purchased from Sigma Aldrich and purified via recrystallization from toluene. Glycolide was purchased from Sigma Aldrich and purified via recrystallization

from toluene/THF. 2-Maleimidoethylamine hydrochloride was purchased from Santa Cruz Biotechnology and used without further purification. Benzoic acid was purchased from Sigma Aldrich and purified by recrystallization from aqueous ethanol. N-(3-Dimethylaminopropyl)-N'-ethylcarbodiimide hydrochloride (EDC) and N-hydroxybenzotriazole hydrate (HOBt) were purchased from Advanced Chemtech and used without purification. Dichloromethane (DCM) and toluene were purified by distillation from CaH_2. Tetrahydrofuran (THF) was purified by distillation from sodium benzophenone ketyl. HPLC grade THF used for GPC was purchased from Fisher Scientific and used without further purification. Dialysis tubing (regenerated cellulose) was purchased from Spectrum Labs. NMR solvents were purchased from Cambridge Isotope Laboratories and used without further purification. Other reagents were purchased from Sigma Aldrich and used without further purification. Other solvents were purchased from Fisher Scientific and used without further purification.

^{1}H-NMR and ^{13}C-NMR samples were prepared by dissolving ~10 mg of sample in $CDCl_3$ and spectra were acquired using a Bruker AV-III-500-HD NMR spectrometer at 500 mHz for ^{1}H and 125 mHz for ^{13}C or a Bruker ARX-400 NMR spectrometer at 400 mHz for ^{1}H and 100 mHz for ^{13}C using residual solvent as an internal standard. Monomer % conversion and number average molecular weight (M_n) were calculated relative to the theoretical number of protons associated with the initiator with respect to the average of polymer-associated protons.

Gel permeation chromatography (GPC) was performed using an Agilent 1200 Series GPC equipped with a Wyatt Dawn Heleos-II multi-angle light scattering (MALS) detector, Wyatt Optilab rEX refractive index (RI) detector and Wyatt quasi-elastic light

scattering (QELS) detector using a single Waters Styragel HR-3 5 μm 7.8x300 mm column preceded by a Waters Styragel 20 μm 4.6x30 mm guard column using THF as eluent. Flow rates of 0.2-0.5 mL/min were used and 100 μL injections of 1.8 mg/mL samples were used. dn/dc was determined for each sample using a five-point calibration curve (samples from 0.5-2.5 mg/mL, 2.0 mL total) generated using Optilab rEX detector in flow mode in combination with ASTRA software. M_n and M_w/M_n were calculated using ASTRA software.

PEI (2.5kD) was purchased from Polysciences, Inc. Dialysis membranes (MWCO: 6000-8000) were purchased from Fisher Scientific. AcGFP1 plasmid vector and MTS reagent were purchased from Promega®. pDNA was amplified in *E. coli* and purified according to the supplier's protocol (Qiagen, Hilden, Germany). The concentration and purity of the pDNA was determined by absorption at 260 and 280 nm and by agarose gel electrophoresis, respectively. The purified pDNA was re-suspended in TE bu□er (10 mM Tris-Cl, pH 7.5, 1 mM EDTA) and kept frozen in aliquots at a concentration of 0.5 mg/mL. Lipofectamine®2000 (L2K) transfection reagent was purchased from Invitrogen. Cell culture reagents such as DMEM and RPMI media, FBS, sodium pyruvate, trypsin, and PBS were obtained from Atlanta Biologicals.

5.9.1 Synthesis of Cyclic Carbonate Monomers

Benzyl 3-hydroxy-2-(hydroxymethyl)-2-methylpropanoate (94). Benzyl bromide was purified beforehand via shaking with conc. H_2SO_4, water, sat. $NaHCO_3$, then water, followed by drying over anhydrous sodium sulfate and vacuum distillation. 2,2-Dihydroxymethylpropionic acid (36.00 g, 268.4 mmol) was added to an oven dried 1L round bottom flask equipped with a magnetic stir bar and rubber septum. DMF (500 mL) was added and the solid was dissolved with stirring. Anhydrous potassium carbonate (55.64 g, 402.6 mmol) was added and the mixture was stirred for 30 min under ambient conditions to generate the potassium carboxylate salt. Benzyl bromide (68.86 g, 402.6 mmol) was added via addition funnel dropwise over 30 min at ambient temperature. The mixture was stirred for an additional 18 hours at ambient temperature under nitrogen. The reaction mixture was poured into 1L deionized water and this solution was divided into three equal parts. Each part was extracted with EtOAc (170 mL) four times each. The combined extracts were dried over anhydrous sodium sulfate, concentrated *in* vacuo and the residue was crystallized from benzene to give Compound **94** as a white crystalline solid. Yield: 50.06 g (83.2 %); ^{1}H NMR (500 MHz, $CDCl_3$) δ 7.45 – 7.28 (m, 5H), 5.21 (s, 2H), 3.93 (dd, J = 11.2, 6.0 Hz, 2H), 3.73 (dd, J = 11.3, 5.6 Hz, 2H), 2.89 (t, J = 6.1 Hz, 2H), 1.08 (s, 3H). ^{13}C NMR (126 MHz, CDCl3) δ 175.74, 135.66, 128.65, 128.33, 127.87, 77.30, 77.05, 76.79, 68.34, 66.71, 49.26, 17.13.

Benzyl 5-methyl-2-oxo-1,3-dioxane-5-carboxylate (95). Compound **94** (16.51 g, 73.6 mmol) was dissolved in DCM (280 mL) and pyridine (45 mL) in an oven-dried 500 mL round bottom flask equipped with a magnetic stir bar and an addition funnel. Triphosgene

(11.36 g, 38.3 mmol) dissolved in DCM (45 mL) was added to the addition funnel. The solution of **94** was cooled to -78 °C and the triphosgene solution was added dropwise over 1 hour at -78 °C. The dry ice/acetone bath was removed and the solution was allowed to stir for an additional 2 hours while warming to ambient temperature. The reaction was quenched via addition of 75 mL sat. NH_4Cl solution. The biphasic solution was transferred to a separatory funnel and the aqueous phase was removed. The organic phase was washed with 5% HCl (150 mL) three times, then deionized water (100 mL). The organic solution was dried over anhydrous sodium sulfate, concentrated and purified via flash chromatography using a gradient of 100 % DCM to 2.5 % MeOH/DCM. The pure fractions were combined, concentrated and recrystallized from toluene/hexane to give Compound **95** as a white crystalline solid. Yield: 15.22 g (82.6 %).; TLC: R_f= 0.47 (2.5 % MeOH/DCM); ^{1}H NMR (500 MHz, $CDCl_3$) δ 7.58 – 7.30 (m, 5H), 5.21 (s, 2H), 4.70 (d, J = 10.9 Hz, 2H), 4.20 (d, J = 10.9 Hz, 2H), 1.32 (s, 3H). ^{13}C NMR (126 MHz, $CDCl_3$) δ 170.93, 147.40, 134.77, 128.78, 128.75, 128.22, 77.31, 77.06, 76.81, 72.95, 67.92, 40.25, 17.59.

5-Methyl-2-oxo-1,3-dioxane-5-carboxylic acid (96). Compound **95** (5.00 g, 20.0 mmol) was added to an oven-dried 250 mL round bottom flask equipped with a magnetic stir bar and a rubber septum. The solid was dissolved in EtOAc (50 mL) and THF (70 mL) and a spatula tip of 10% palladium on carbon (wet type) was added. The flask was equipped with a three-way adapter attached to a balloon. The flask and balloon were evacuated and filled with hydrogen three times and stirred under 1 atm hydrogen for 16 hours. The catalyst was removed via gravity filtration through Celite, concentrated and recrystallized

from toluene/EtOAc to give Compound **96** as a white crystalline solid. The product is positive for staining with bromocresol green. Yield: 3.07 g (95.8 %).; TLC: R_f= 0.06 (5 % MeOH/DCM); ^{1}H NMR (400 MHz, DMSO-d6) δ 12.68 (s, 1H), 4.52 (d, J = 10.4 Hz, 2H), 4.29 (d, J = 10.4 Hz, 2H), 1.14 (s, 3H). ^{13}C NMR (101 MHz, CDCl3) δ 178.44, 152.46, 108.61, 77.79, 45.14, 44.93, 44.72, 44.51, 44.31, 44.10, 43.89, 21.50.

Cholesteryl 5-methyl-2-oxo-1,3-dioxane-5-carboxylate (97). Compound **96** (3.066 g, 19.1 mmol), cholesterol (8.144 g, 21.1 mmol) and DMAP (0.351 g, 2.9 mmol) were combined in an oven-dried 500 mL round bottom flask equipped with a stir bar and rubber septum. The contents were dissolved in DCM (50 mL), THF (50 mL) and pyridine (25 mL). The solution was cooled to 0 °C in an ice bath and EDC (4.405 g, 22.8 mmol) was added. The solution was stirred for 72 hours while warming to room temperature. The solution was concentrated *in vacuo* and the residue was dissolved in DCM (150 mL). The solution was washed with 5% HCl (150 mL) three times, saturated $NaHCO_3$ (120 mL) and brine (100 mL). The organic solution was dried over anhydrous sodium sulfate and purified via column chromatography using a gradient of 100 % DCM, 1.25 % MeOH/DCM and 2.5 % MeOH/DCM. The pure fractions were combined and recrystallized from toluene/MeOH to give Compound **97** as white crystalline flakes similar to cholesterol. Yield: 6.892 g (68.1 %).; TLC: R_f= 0.26 (100 % DCM); ^{1}H NMR (400 MHz, $CDCl_3$) δ 5.38 (d, J = 4.3 Hz, 1H), 4.70 (s, 1H), 4.67 (d, J = 10.6 Hz, 2H), 4.18 (d, J = 10.8 Hz, 2H), 2.32 (d, J = 6.9 Hz, 2H), 2.08 – 1.97 (m, 2H), 1.95 (s, 1H), 1.92 – 1.75 (m, 3H), 1.64 (s, 1H), 1.61 – 1.58 (m, 1H), 1.58 – 1.52 (m, 2H), 1.52 – 1.44 (m, 3H), 1.44 – 1.38 (m, 1H), 1.32 (d, J = 10.1 Hz, 6H), 1.25 (d, J = 11.8 Hz, 1H), 1.14 (dtd, J

= 22.4, 12.9, 11.1, 6.5 Hz, 7H), 1.06 – 0.95 (m, 6H), 0.92 (dd, J = 14.6, 6.1 Hz, 4H), 0.85 (d, J = 6.6 Hz, 6H), 0.67 (s, 3H). ^{13}C NMR (101 MHz, CDCl3) δ 170.37, 147.47, 138.82, 123.18, 108.59, 77.25, 76.94, 76.62, 75.96, 72.97, 56.55, 56.02, 49.86, 42.20, 40.04, 39.59, 39.41, 37.65, 36.71, 36.43, 36.07, 35.68, 31.79, 31.71, 28.11, 27.90, 27.41, 24.17, 23.72, 22.72, 22.46, 20.93, 19.20, 18.62, 17.47, 11.75.

((1s,3s)-Adamantan-1-yl)methyl 5-methyl-2-oxo-1,3-dioxane-5-carboxylate (98). Compound **96** (2.108 g, 13.2 mmol), 1-adamantanemethanol (2.19 g, 13.8 mmol) and DMAP (322 mg, 2.6 mmol) were added to an oven-dried 250 mL round bottom flask equipped with a magnetic stir bar and rubber septum. The contents were dissolved in THF (15 mL) and pyridine (10 mL) and cooled to 0 °C in an ice bath. EDC (3.280 g, 17.1 mmol) was added. The solution was stirred for 72 hours while warming to ambient temperature. The solution was concentrated *in vacuo* and poured into 100 mL deionized water. The mixture was extracted with DCM (80 mL) four times. The DCM extracts were combined, dried over anhydrous sodium sulfate and purified via column chromatography using a gradient of 4:1, 7:3, 3:2, and 1:1 (v/v) mixtures of hexane:EtOAc. The pure fractions were combined, concentrated and recrystallized from toluene/hexane to give Compound **98** as a white crystalline solid. Yield: 1.943 g (47.9 %).; TLC: R_f= 0.43 (1:1 Hex: EtOAc); ^{1}H NMR (400 MHz, $CDCl_3$) δ 4.75 – 4.57 (m, 2H), 4.28 – 4.10 (m, 2H), 3.76 (s, 2H), 1.96 (s, 3H), 1.70 (d, J = 12.3 Hz, 3H), 1.61 (d, J = 12.4 Hz, 3H), 1.49 (d, J = 2.5 Hz, 6H), 1.30 (s, 3H). ^{13}C NMR (101 MHz, CDCl3) δ 171.06, 147.35, 108.60, 77.33, 77.01, 76.69, 75.31, 72.94, 40.23, 39.01, 36.68, 33.28, 27.76, 17.57.

Ethyl 3-hydroxy-2-(hydroxymethyl)-2-methylpropanoate (99). Compound **93** (15.00 g, 111.8 mmol) was dissolved in 125 mL 200 proof ethanol in an oven-dried 250 mL round bottom flask equipped with a magnetic stir bar and a rubber septum. Conc. H_2SO_4 (5.00 mL) was added and the solution was stirred for 3 hours at reflux. Ethanol was evaporated *in vacuo* and the residue was redissolved into 200 mL EtOAc. The solution was washed with sat. $NaHCO_3$ (100 mL), then deionized water (100 mL) twice. The organic solution was dried over anhydrous sodium sulfate, and concentrated *in vacuo* to give Compound **99** as a clear viscous oil. Yield: 15.729 g (86.7 %).; TLC: R_f= 0.64 (15 % MeOH/DCM); ^{1}H NMR (400 MHz, $CDCl_3$) δ 4.04 (q, J = 7.1 Hz, 2H), 3.72 (d, J = 5.6 Hz, 2H), 3.66 (d, J = 6.1 Hz, 2H), 3.54 (dd, J = 10.4, 5.3 Hz, 2H), 1.14 (t, J = 7.1 Hz, 3H), 0.96 (s, 3H). ^{13}C NMR (101 MHz, CDCl3) δ 175.63, 77.42, 77.10, 76.78, 65.88, 60.70, 49.09, 16.95, 13.84.

Ethyl 5-methyl-2-oxo-1,3-dioxane-5-carboxylate (100). Compound **99** (5.564 g, 34.3 mmol) was dissolved in DCM (75 mL) and pyridine (15 mL) in an oven-dried 250 mL round bottom flask equipped with a magnetic stir bar and an addition funnel. In a separate 50 mL conical flask, triphosgene (5.294 g, 17.8 mmol) was dissolved in DCM (15 mL). The triphosgene solution was transferred to the addition funnel and the solution of Compound **99** was cooled to -78 °C in a dry ice/acetone bath. The triphosgene solution was added dropwise over 1 hour. The -78 °C bath was removed and the solution was stirred for an additional 3 hours while warming to ambient temperature. The reaction was quenched via addition of 100 mL sat. NH_4Cl solution. The biphasic solution was transferred to a separatory funnel and the aqueous layer was removed. The organic

solution was washed with 5% HCl (100 mL) twice, deionized water (100 mL) and brine (80 mL). The organic phase was dried over anhydrous sodium sulfate, concentrated *in vacuo*, and purified via flash chromatography using a gradient of 100 % DCM to 2.5 % MeOH/DCM to give Compound **100** as a clear waxy solid. Yield: 3.509 g (54.4 %).; TLC: R_f= 0.47 (2.5 % MeOH/DCM); ^{1}H NMR (400 MHz, $CDCl_3$) δ 4.54 (d, J = 10.8 Hz, 2H), 4.20 – 4.11 (m, 2H), 4.10 – 4.01 (m, 2H), 1.35 – 0.96 (m, 6H). ^{13}C NMR (101 MHz, CDCl3) δ 171.10, 147.51, 77.55, 77.23, 76.90, 72.82, 61.93, 39.91, 16.99, 13.75.

1,3-Dioxan-2-one (102). 1,3-Propanediol (0.930 g, 12.2 mmol) was added to an oven-dried 500 mL round bottom flask equipped with a stir bar and rubber septum. Di-tert-butyl dicarbonate (Boc_2O, 8.00 g, 36.7 mmol) was dissolved in 100 mL acetonitrile (ACN) in a separate 125 mL flask. The Boc_2O solution was added the 500 mL flask and DMAP (1.493 g, 12.2 mmol) immediately after. The solution was stirred at ambient temperature under nitrogen for 30 min. The solution was transferred to a separatory funnel together with 420 mL chloroform. The organic solution was washed with 1.0 M HCl (150 mL) twice, followed by deionized water (150 mL). The organic phase was dried over anhydrous sodium sulfate, concentrated and purified via flash chromatography using a gradient of 2.5 % MeOH/DCM to 5% MeOH/DCM. The pure fractions were combined and recrystallized from diethyl ether (Et_2O) to give Compound **102** as a white crystalline solid. Yield: 0.926 g (74.2 %).; TLC: R_f= 0.35 (5 % MeOH/DCM); ^{1}H NMR (400 MHz, $CDCl_3$) δ 4.76 – 3.98 (m, 4H), 2.12 (t, J = 8.4 Hz, 2H). ^{13}C NMR (101 MHz, $CDCl_3$) δ 148.42, 77.32, 77.00, 76.69, 67.89, 21.61.

1,3-Dioxan-2-one (104). 3-Bromo-1-propanol (5.00 g, 36.0 mmol) was added to an oven-dried 500 mL round bottom flask equipped with a magnetic stir bar. DMF was added (108 mL) followed by Cs_2CO_3 (12.893 g, 39.6 mmol). Carbon dioxide was bubbled through the solution vigorously for 5 min, then a three-way adapter equipped with a balloon was attached to the flask. The flask was evacuated and purged with carbon dioxide 5 times. The heterogeneous mixture was stirred vigorously under 1 atm carbon dioxide for 4 days. The mixture was filtered to remove Cs_2CO_3 and the cake was washed with DCM. The filtrate was concentrated *in vacuo* and redissolved in DCM (200 mL). The solution was washed with deionized water (80 mL) and the organic phase was dried over anhydrous sodium sulfate, concentrated and recrystallized from diethyl ether to give Compound **104** as a white crystalline solid. Yield: 3.259 g (89.0 %).; TLC: R_f= 0.34 (5 % MeOH/DCM; ^{1}H NMR (500 MHz, $CDCl_3$) δ 4.43 (d, J = 5.8 Hz, 4H), 2.13 (p, J = 5.8 Hz, 2H). ^{13}C NMR (126 MHz, $CDCl_3$) δ 148.49, 77.33, 77.08, 76.82, 67.96, 21.74.

5.9.2 Polymerizations of Carbonate Monomers Using TBD

mPEG-b-PTMC (105a-c). mPEG (**a**: 32.1 mg, **b**: 117mg, **c**: 292mg; 58.4μmmol) was added to an oven-dried 5.0 mL conical vial equipped with magnetic spin vane and PTFE septum. Trimethylene carbonate (**104**, 0.700 g, 6.86 mmol) was added and contents were dissolved in 5.5 mL DCM. TBD solution in DCM (35 mg/mL, 1.364 mL) was added via pipette and the vial was capped and filled with nitrogen. The solutions were stirred for 12 hours at ambient temperature. The polymerization was quenched via addition of 80 mg benzoic acid. The solution was precipitated twice into 250 mL diethyl ether from DCM, filtered and dried *in vacuo* to give **105a-c** as white powders. Yield: **a**: 723 mg, **b**: 808 mg,

c: 850 mg; ^{1}H NMR (500 MHz, $CDCl_3$) δ 4.63 – 3.90 (m, PTMC -C(=O)-O-CH_2-), 3.62 (PEG -CH_2-), 2.15 – 1.76 (m, PTMC).

TBD-catalyzed mPEG-b-polycarbonate diblock pendant copolymers (106a-q). 1d (mPEG2K) or **1e** (mPEG5K) (100 mg) was added to an oven-dried 5.0 mL conical vial equipped with magnetic spin vane and PTFE septum. Carbonate monomer (**95**, **97**, **98**, **100**, or **104**) (200 mg) was added and the contents were dissolved in DCM. TBD solution (35 mg/mL in DCM) was added (5 mol % relative to monomer). The amount of initial DCM used is equal to the volume required to give [M] = 1.0 M, taking into account the volume of the TBD solution. The vials were flushed with nitrogen and stirred for 12 hours at ambient temperature. The polymers were isolated via precipitation into 40 mL Et_2O plus 5 mL iPrOH in 50 mL centrifuge tubes. The precipitate was isolated via centrifugation and dried *in vacuo* to give Compounds **106a-q** as white solids. M_n was calculated by comparing PEG methylene proton integrals with characteristic integrals from the respective monomers. Yield: **a**: 139 mg, **b**: 286 mg, **c**: 256 mg, **d**: 238 mg, **e**: 263 mg, **f**: 242 mg, **g**: 212 mg, **h**: 261 mg, **i**: 176 mg, **j**: 224 mg, **k**: 252 mg, **l**: 197 mg, **m**: 260 mg, **n**: 227 mg, **o**: 240 mg, **p**: 188 mg, **q**: 212 mg.

TBD-catalyzed mPEG-b-polycarbonate diblock pendant polymers (107a-c). 1e (100 mg, 0.02 mmol), Compound **100** and one of either Compound **95**, **97**, or **98** were added to an oven-dried 5.0mL conical vial containing a magnetic spin vane and a PTFE septum. The total mass of monomers is equal to 200 mg. The relative amounts of monomers were determined by solving a system of equations targeting total polycarbonate molecular weight of 12.0 kDa and a 3:1 ratio of **100** to either **95**, **97**, or **98**. The DCM was added

and the solutions were stirred to dissolve mPEG and monomers. TBD solution was added next via syringe (35 mg/mL in DCM). The amounts of TBD solution and DCM were determined by targeting 10 mol % TBD relative to total [M]. The initial volume of DCM is equal to the total volume required to give [M] = 1.0 M minus the volume of the TBD solution. The vials were flushed with nitrogen and stirred at ambient temperature for 12 hours. The polymers were isolated via precipitation into 40 mL Et_2O plus 5 mL iPrOH in 50 mL centrifuge tubes. The precipitate was isolated via centrifugation and dried *in vacuo* to give Compounds **107a-c** as white solids. M_n was calculated by comparing PEG methylene proton integrals with characteristic integrals from the respective monomers. Yield: **a**: 232 mg, **b**: 216 mg, **c**: 208 mg.

5.9.3 Polymerization of Carbonate Monomers Using DBU/TU

1-(3,5-Bis(trifluoromethyl)phenyl)-3-cyclohexylthiourea (110). 3,5,-Bis-(trifluoromethyl)phenyl isothiocyanate (1.01 g, 3.72 mmol) was added to an oven-dried 25 mL round bottom flask equipped with a magnetic stir bar and a rubber septum. THF (5 mL) was added followed by cyclohexylamine (427 µL, 3.72 mmol). The flask was flushed with nitrogen and stirred for 3 hours at ambient temperature. The solution was filtered through a pad of Celite with DCM (20 mL). The filtrate was concentrated and purified via flash chromatography using a gradient of 2.5 % MeOH/DCM to 5 % MeOH/DCM. The pure fractions were combined, concentrated and recrystallized from DCM/pet. Ether to give Compound **110** as a white powder. Yield: 1.314 g (95.3 %).; TLC: R_f= 0.75 (5 % MeOH/DCM); ^{1}H NMR (500 MHz, $CDCl_3$ δ 8.40 (s, 1H), 7.75 (s, 2H), 7.70 (s, 1H), 6.08 (s, 1H), 4.20 (s, 1H), 2.06 (dd, J = 12.5, 3.4 Hz, 2H), 1.71 (d, J =

10.2 Hz, 2H), 1.63 (dd, J = 9.1, 4.1 Hz, 1H), 1.50 – 1.35 (m, 2H), 1.27 – 1.14 (m, 3H). ^{13}C NMR (126 MHz, $CDCl_3$) δ 179.12, 138.86, 133.51, 133.24, 132.97, 132.68, 125.99, 123.82, 121.65, 119.34, 77.28, 77.03, 76.77, 54.04, 32.36, 25.26, 24.56. ^{19}F NMR (471 MHz, DMSO-d_6) δ -62.75.

DBU/TU-catalyzed-mPEG-b-polycarbonate diblock pendant polymers (111a-n). 1d (mPEG2K) or **1e** (mPEG5K) (100 mg) was added to an oven-dried 5.0 mL conical vial equipped with magnetic spin vane and PTFE septum. Carbonate monomer (**95**, **97**, **98**, **100**, or **104**) (200 mg) was added and the contents were dissolved in DCM. TU (**110**) solution (0.125 M in DCM) was added via syringe, followed by DBU solution (1.0 M in DCM). The amounts of DBU and TU solution and DCM were determined by targeting 5 mol % DBU and TU relative to total [M]. The initial volume of DCM is equal to the total volume required to give [M] = 1.0 M, minus the volume of the DBU and TU solution volumes. The vials were flushed with nitrogen and stirred for 12 hours at ambient temperature. The polymers were isolated via precipitation into 40 mL Et_2O plus 5 mL iPrOH in 50 mL centrifuge tubes. The precipitate was isolated via centrifugation and dried *in vacuo* to give Compounds **111a-n** as white solids. M_n was calculated by comparing PEG methylene proton integrals with characteristic integrals from the respective monomers. Yield: **a**: 251 mg, **b**: 256 mg, **c**: 263 mg, **d**: 277 mg, **e**: 214 mg, **f**: 278 mg, **g**: 240 mg, **h**: 271 mg, **i**: 267 mg, **j**: 244 mg, **k**: 261 mg, **l**: 284 mg, **m**: 243 mg, **n**: 214 mg.

DBU/TU-catalyzed-mPEG-b-polycarbonate diblock pendant copolymers (112a-d). **1e** (150 mg, 0.03 mmol), Compound **104** and Compound **95**, were added to an oven-dried

5.0mL conical vial containing a magnetic spin vane and a PTFE septum. The total mass of monomers is equal to 300 mg. The relative amounts of monomers were determined by solving a system of equations targeting total polycarbonate molecular weight of 10.0 kDa and 1:2 (**a**), 1:1 (**b**), 2:1 (**c**), and 4:1 (**d**) ratios of **104:95**. DCM was added and the solutions were stirred to dissolve mPEG and monomers. TU (**110**) solution (0.125 M in DCM) was added via syringe, followed by DBU solution (1.0 M in DCM). The amounts of DBU and TU solution and DCM were determined by targeting 5 mol % DBU and TU relative to total [M]. The initial volume of DCM is equal to the total volume required to give [M] = 1.0 M, minus the volume of the DBU and TU solution volumes. The vials were flushed with nitrogen and stirred at ambient temperature for 24 hours. The polymers were isolated via precipitation into 40 mL Et_2O plus 5 mL iPrOH in 50 mL centrifuge tubes. The precipitate was isolated via centrifugation and dried *in vacuo* to give Compounds **112a-d** as white solids. M_n was calculated by comparing PEG methylene proton integrals with characteristic integrals from the respective monomers. Yield: **a**: 418 mg, **b**: 417 mg, **c**: 411 mg, **d**: 373 mg.

5.9.4 pDNA-Pendant Polymer Transfection Complex Formation

mPEG-b-polycarbonate pendant polymers solutions (1 mM equivalent of pendant groups) were vortex mixed with equal volumes of β-CD-PEI^+ (1mM equivalent of PEI) solution in water to form mPEG-b-polycarbonate:β-CD-PEI^+ complexes. Transfection complexes were formed by adding appropriate amount of mPEG-b-polycarbonate:β-CD-PEI^+ complexes to the 1 μg of pDNA (unmodified or FITC-labelled) dissolved in 30 μL of TE buffer in 1.5 mL centrifuge tubes. The amount of mPEG-b-polycarbonate:β-CD-

PEI^+ added to DNA varied from 1-3 μL so as to achieve final N/P ratios of 5, 10, 20 & 30. The above solution was incubated at 4 °C for 1 h before use in transfection experiments.

5.9.5 Particle Size and Zeta (ζ) Potential Measurements

The diameters, size distributions, and ζ-potentials of the materials were evaluated by dynamic light scattering (DLS) using a Zetasizer Nano S (Malvern Instruments Ltd.) at 20 °C with a scattering angle of 90°. At least 40 measurements were made and averaged for each sample. The particles were diluted to 1 mL with HEPES buffer prior to analysis.

5.9.6 Gel Retardation Assay

The complexation ability of mPEG-b-polycarbonate:CD-PEI^+ with pDNA was determined by low melting point 1% agarose gel electrophoresis. The agarose gels were precast in TBE buffer with GelRed® dye at 1:10,000 dilution. mPEG-b-polycarbonate:CD-PEI^+:pDNA complexes containing 0.2 μg of pDNA at different N/P ratios were loaded onto the gel before addition of loading dye (1:5 dilution) to each well and electrophoresis at a constant voltage of 55 V for 2 h in TBE buffer. The pDNA bands were then visualized under a UV transilluminator at λ = 365 nm.

5.9.7 *In Vitro* Transfection Assay in HeLa Cells

HeLa cells were cultured in complete DMEM medium with 10% FBS. All cells were incubated at 37 °C, 5% CO_2, and 95% relative humidity, respectively, at a cell density of 75,000 cells/well in 24-well plates. After 24 h, the culture media was replaced with serum free media, with addition of mPEG-b-polycarbonate:CD-PEI^+:pDNA complexes containing 1 μg of AcGFP, at N/P ratios of 5, 10, 20 and 30. The cells were incubated with the complexes for 4 h, after which the spent media was aspirated and fresh serum-supplemented media was added. After a total of 36 h incubation, the media was aspirated and the cells were washed with PBS, trypsinized, and analyzed by flow cytometry using a FC500. The % GFP mean fluorescence intensity was calculated relative to L2k controls, considered as 100%.

5.9.8 Synthesis of mPEG-b-PCL and SILY-PEG-b-PCL

mPEG-b-poly(ε-caprolactone) (113a-c). mPEG (**a**: 25.7 mg, **b**: 93.3 mg, **c**: 233.3 mg; 46.7 μmmol) was added to an oven-dried 5.0 mL conical vial equipped with magnetic spin vane and PTFE septum. ε-Caprolactone (0.700 g, 6.13 mmol) was added and contents were dissolved in 1.166 mL DCM. TBD solution in DCM (35 mg/mL, 1.22 mL) was added ([M] = 2.0 M) via pipette and the vial was capped and filled with nitrogen. The solutions were stirred for 72 hours at ambient temperature. The polymerization was quenched via addition of 80 mg benzoic acid. The solution was precipitated twice into 250 mL diethyl ether from DCM, filtered and dried *in vacuo* to give Compounds **113a-c** as white powders. Yield: **a**: 670 mg, **b**: 716 mg, **c**: 867 mg; ^{1}H NMR (500 MHz, $CDCl_3$)

δ 4.05 (t, PCL-CH_2), 3.64 (s, PEG-CH_2), 2.30 (t, PCL-CH_2), 1.64 (h, PCL-CH_2CH_2), 1.37 (p, PCL-CH_2). ^{13}C NMR (126 MHz, $CDCl_3$) δ 173.53, 77.29, 77.03, 76.78, 70.58, 64.15, 34.12, 28.35, 25.54, 24.58.

Carboxylate-PEG-b-poly(ε-caprolactone) (115). ε-Caprolactone (700 mg, 6.13 mmol) and HO_2C-PEG5K-OH (233.3 mg, 46.65 mmol) were added to an oven dried 5.0 mL conical vial equipped with a magnetic spin vane and PTFE septum. The vial was then evacuated and purged with argon three times. DCM (1.66 mL) was added via syringe and solid components were allowed to dissolve followed by 1.41 mL TBD solution (35 mg/mL in DCM) to produce [M] = 2.0 M. The solution was stirred for 72 hours and quenched with benzoic acid (1.2 equiv to TBD) at the end of the reaction period. Compound **115**) was purified by precipitation twice from DCM into 200 mL cold Et_2O, dried *in vacuo* for 24 hours and obtained as a white powder. Yield: 0.857 g (91.8 %).; ^{1}H NMR (500 MHz, $CDCl_3$) δ 10.13-10.27 (br, PEG-CO_2H), δ 4.05 (t, PCL-CH_2), 3.63 (s, PEG-CH_2), 2.30 (t, PCL-CH_2), 1.64 (dq, PCL-CH_2CH_2), 1.37 (p, PCL-CH_2).

Maleimide-PEG-b-poly(ε-caprolactone) (116). Compound **115** (250 mg, 12.6 μmol), 2-maleimidoethylamine hydrochloride (46.0 mg, 0.260 mmol) and HOBt (35.2 mg, 0.260 mmol) were added to an oven-dried 5.0 mL conical vial equipped with a magnetic spin vane and PTFE septum. DCM (3.0 mL) was added and solids were dissolved by stirring for 5 minutes and cooled to 4 °C in an ice bath. EDC (50.0 mg, 0.261 mmol) was added followed by diisopropylethylamine (DIEA, 116 μL, 0.651 mmol). The vial was evacuated and purged with argon three times and stirred for 48 hours warming to ambient temperature. At the end of the reaction period, the reaction mixture was combined with

50 mL DCM, 100 mL methanol (MeOH) and 50 mL deionized water in a 250 mL separatory funnel. The contents were shaken and allowed to separate. The lower organic phase was removed. The aqueous phase was extracted additionally with 50 mL DCM four times. Organic extracts were combined and dried with anhydrous sodium sulfate. The solution was concentrated to approximately 10 mL and the polymer was isolated via precipitation into 200 mL cold Et_2O followed by vacuum filtration. The precipitation process was repeated once more and the product was dried *in vacuo* for 24 hours and obtained as a white powder. Yield: 0.221 g (88.4 %).; ^{1}H NMR (500 MHz, $CDCl_3$) δ 6.79 (s, maleimide-CH_2), δ 4.05 (t, PCL-CH_2), 3.63 (s, PEG-CH_2), 2.30 (t, PCL-CH_2), 1.64 (dq, PCL-CH_2CH_2), 1.37 (p, PCL-CH_2).

SILY-PEG-b-Poly(ε-caprolactone) (117). Compound **116** (100 mg, 0.0052 mmol) and lyophilized SILY peptide (20.7 mg, 9.40 μmol) were added to an oven-dried 5.0 mL conical vial equipped with a magnetic spin vane and PTFE septum. The vial was evacuated and purged with argon three times. The contents were solubilized in 1.0 mL dimethylformamide (DMF) and stirred at ambient temperature for 24 hours. At the end of the reaction period, the reaction mixture was combined with 50 mL DCM, 100 mL MeOH and 50 mL deionized water in a 250 mL separatory funnel. The contents were shaken and allowed to separate. The lower organic phase was removed. The aqueous phase was extracted additionally with 50 mL DCM four times. Organic extracts were combined and dried with anhydrous sodium sulfate. The solution was concentrated and dialyzed against 500 mL DMSO (MWCO 5,000 Da) for 8 hours four times, followed by deionized water for 2 hours four times. After dialysis the aqueous turbid solution was

transferred to a 50 mL centrifuge tube, frozen and lyophilized. The lyophilized powder was dissolved in minimal DCM and precipitated into 50 mL cold Et_2O in a centrifuge tube, isolated via vacuum filtration and dried *in vacuo* for 24 hours to give Compound **117** as a white powder. Yield: 92.3 mg (76.5 %). ^{1}H NMR (500 MHz, DMSO-d_6) δ 9.08 (s, 9H), 8.12 (s, 9H), 8.04 (d, J = 23.1 Hz, 15H), 7.91 (d, J = 31.5 Hz, 30H), 7.85 – 7.62 (m, 58H), 7.58 (s, 8H), 7.28 (s, 12H), 7.16 (s, 11H), 7.05 (s, 5H), 6.98 (t, J = 8.8 Hz, 25H), 6.59 (s, 19H), 6.40 (s, 7H), 4.96 (d, J = 6.1 Hz, 3H), 4.47 (dd, J = 16.8, 9.8 Hz, 5H), 4.32 (s, 24H), 4.25 – 4.02 (m, 61H), 3.95 (d, J = 6.5 Hz, 225H), 3.80 – 3.58 (m, 41H), 3.50 (s, 454H), 3.39 (s, 14H), 3.30 (s, 126H), 3.08 (s, 36H), 2.92 (s, 15H), 2.74 (d, J = 11.6 Hz, 56H), 2.56 – 2.44 (m, 161H), 2.24 (t, J = 7.3 Hz, 241H), 1.62 – 1.40 (m, 542H), 1.29 (q, J = 8.0 Hz, 303H), 0.99 (d, J = 7.2 Hz, 4H), 0.92 – 0.68 (m, 110H).

5.9.9 Synthesis of mPEG-b-PLGA

mPEG-b-poly(lactide-co-glycolide) (118a-h). Lactide and glycolide were recrystallized from toluene and toluene/THF, respectively, before polymerizations. **1d** or **1e** (675 mg) was added together with lactide (1.350 g, 9.37 mmol) to an oven-dried 100 mL round bottom flask equipped with a magnetic stir bar and rubber septum. The contents were dissolved in DCM (33 mL). In a separate round bottom flask, glycolide (0.675 g, 5.82 mmol) was dissolved in THF (9 mL). The glycolide solution was added to the lactide/mPEG solution over 10 min via syringe pump. The polymerization was quenched via addition of 150 mg benzoic acid. The solution was concentrated and precipitated into 500 mL diethyl twice, filtered and dried *in vacuo* to give Compounds **118a-h** as white granular solids. Yield: **a**: 1.116 g, **b**: 0.809 g, **c**: 1.489 g, **d**: 1.675 g, **e**: 1.755 g, **f**: 1.131

g, **g**: 1.298 g; ^{1}H NMR (400 MHz, $CDCl_3$) δ 5.20 (m, PLA methine), 4.78 (m, PGA methylene), 4.43 – 4.22 (m, PEG), 3.62 (s, PEG methylene), 1.57 (m, PLA methyl). ^{13}C NMR (101 MHz, $CDCl_3$) δ 169.22, 166.25, 77.25, 76.94, 76.62, 70.46, 68.90, 60.72, 16.54.

5.9.10 Synthesis of Cyclic Amino Acid N-Carboxyanhydride Monomers

(S)-4-Methyloxazolidine-2,5-dione (120). A mortar and pestle was used to grind commercial L-alanine before drying *in vacuo* overnight at 50 °C in a vacuum oven. The ground and dried L-alanine (2.033 g, 22.8 mmol) was added to an oven-dried 2-necked round bottom flask equipped with a magnetic stir bar, rubber septum and inlet adapter attached to a nitrogen line containing a 10 % NaOH scrubber. TFF (60 mL) was added via syringe. The solution was heated to 70 °C and stirred for 5 min. In a separate 50 mL conical flask, triphosgene (3.047 g, 10.3 mmol) was dissolved in THF (20 mL). The trisphosgene solution was added to the heterogeneous suspension via syringe pump over 30 min. After the completion of the addition, the solution was nearly clear. The solution was stirred for an additional 1 hour at 70 °C. The solution was concentrated *in vacuo* and Compound **120** was recrystallized several times using THF/toluene/hexane, filtered and dried *in vacuo* at ambient temperature to give Compound **120** as a white crystalline solid. Yield: 2.288 g (87.1 %); ^{1}H NMR (400 MHz, DMSO-d_6) δ 9.00 (d, J = 20.1 Hz, 1H), 4.45 (hept, J = 7.2 Hz, 1H), 1.64 – 1.00 (m, 3H). ^{13}C NMR (101 MHz, DMSO) δ 221.66, 173.28, 152.57, 76.17, 53.71, 41.03, 40.82, 40.61, 40.40, 40.20, 39.99, 39.78, 17.66.

(S)-4-((S)-Sec-butyl)oxazolidine-2,5-dione (122). L-Isoleucine was dried beforehand in a vacuum over at 50 °C for 24 hours. L-Isoleucine (2.00 g, 15.2 mmol) was added to an oven-dried 2-necked round bottom flask equipped with a magnetic stir bar, rubber septum and inlet adapter attached to a nitrogen line containing a 10 % NaOH scrubber. THF (40 mL) was added via syringe. Triphosgene (1.719 g, 5.8 mmol) was dissolved in THF (8 mL) in a separate 20 mL conical round bottom flask. The triphosgene solution was added over 30 min via syringe pump. The solution was stirred for an additional 2 hours at ambient temperature. The solution became clear during the 2 hour stir. The solution was concentrated and purified via recrystallization from toluene/DCM/hexane to give **122** as a white crystalline solid. Yield: 2.268 g (94.8 %); ^{1}H NMR (400 MHz, $CDCl_3$) δ 7.10 (s, 1H), 4.28 (s, 1H), 2.26 – 1.76 (m, 1H), 1.74 – 1.44 (m, 1H), 1.37 (d, J = 6.5 Hz, 1H), 1.05 (d, J = 6.0 Hz, 3H), 0.95 (t, J = 7.1 Hz, 3H). ^{13}C NMR (101 MHz, $CDCl_3$) δ 168.79, 153.48, 77.27, 76.95, 76.64, 62.40, 37.24, 24.16, 14.72, 11.27.

Benzyl (S)-3-(2,5-dioxooxazolidin-4-yl)propanoate (124). L-Glutamic acid benzyl ester was dried beforehand in a vacuum over at 50 °C for 24 hours. L-glutamic acid benzyl ester (3.50 g, 14.8 mmol) was added to an oven-dried 2-necked round bottom flask equipped with a magnetic stir bar, rubber septum and inlet adapter attached to a nitrogen line containing a 10 % NaOH scrubber. THF (36 mL) was added via syringe and the solution became clear. Triphosgene (1.66 g, 5.6 mmol) was dissolved in THF (9 mL) in a separate 20 mL conical round bottom flask. The triphosgene solution was added over 30 min via syringe pump. The solution was stirred for an additional 2 hours at ambient temperature. The solution was concentrated and purified via recrystallization from

toluene/DCM/hexane to give **124** as a white crystalline solid. Yield: 3.689 g (95.0 %); ^{1}H NMR (400 MHz, DMSO-d_6) δ 12.37 (s, 2H), 7.59 (d, J = 8.1 Hz, 1H), 7.46 – 7.14 (m, 5H), 5.02 (s, 2H), 3.98 (td, J = 9.4, 4.9 Hz, 1H), 2.39 – 2.16 (m, 2H), 1.96 (tt, J = 13.0, 6.4 Hz, 1H), 1.83 – 1.60 (m, 1H). ^{13}C NMR (101 MHz, DMSO) δ 174.61, 174.47, 157.06, 137.87, 129.24, 128.60, 76.16, 66.31, 53.93, 41.04, 40.62, 40.41, 40.21, 39.79, 30.98, 26.97.

Methyl (S)-3-(2,5-dioxooxazolidin-4-yl)propanoate (126). L-Glutamic acid methyl ester was dried beforehand in a vacuum over at 50 °C for 24 hours. L-glutamic acid benzyl ester (3.00 g, 18.6 mmol) was added to an oven-dried 2-necked round bottom flask equipped with a magnetic stir bar, rubber septum and inlet adapter attached to a nitrogen line containing a 10 % NaOH scrubber. THF (50 mL) was added via syringe and the solution was heated to 50 °C and stirred for 5 min. Triphosgene (2.430 g, 8.2 mmol) was dissolved in THF (10 mL) in a separate 20 mL conical round bottom flask. The triphosgene solution was added over 30 min via syringe pump. The solution was stirred for an additional 2 hours at 50 °C during which the solution became clear. The solution was concentrated and purified via recrystallization from THF/hexane to give Compound **126** as a white crystalline solid. Yield: 3.312 g (95.1 %); ^{1}H NMR (400 MHz, DMSO-d_6) δ 9.08 (s, 1H), 4.57 – 4.35 (m, 1H), 3.59 (s, 3H), 2.48 – 2.31 (m, 2H), 2.11 – 1.97 (m, 1H), 1.89 (dq, J = 14.9, 7.4 Hz, 1H). ^{13}C NMR (101 MHz, DMSO) δ 173.15, 172.21, 152.74, 107.93, 57.07, 52.41, 41.05, 40.84, 40.63, 40.42, 40.21, 40.01, 39.80, 29.75, 27.29.

Benzyl (S)-(4-(2,5-dioxooxazolidin-4-yl)butyl)carbamate (128). H-Lys(Z)-OH was dried beforehand in a vacuum over at 50 °C for 24 hours. H-Lys(Z)-OH (4.00 g, 14.3 mmol) was added to an oven-dried 2-necked round bottom flask equipped with a magnetic stir bar, rubber septum and inlet adapter attached to a nitrogen line containing a 10 % NaOH scrubber. THF (50 mL) was added via syringe and the solution was heated to 50 °C and stirred for 5 min. Triphosgene (1.867 g, 6.3 mmol) was dissolved in THF (10 mL) in a separate 20 mL conical round bottom flask. The triphosgene solution was added over 30 min via syringe pump. The solution was stirred for an additional 2 hours at 50 °C during which the solution became clear. The solution was concentrated and purified via recrystallization from THF/hexane to give **128** as a white crystalline solid. Yield: 4.214 g (96.4 %); ^{1}H NMR (400 MHz, $CDCl_3$) δ 7.35 (d, J = 5.1 Hz, 5H), 7.15 (s, 1H), 5.09 (s, 2H), 5.01 (s, 1H), 4.25 (s, 1H), 3.18 (s, 2H), 2.05 – 1.87 (m, 1H), 1.86 – 1.71 (m, 1H), 1.53 (s, 3H), 1.34 (d, J = 63.9 Hz, 1H). ^{13}C NMR (101 MHz, $CDCl_3$) δ 169.85, 156.81, 152.47, 152.43, 136.26, 128.49, 128.13, 127.92, 77.25, 76.94, 76.62, 66.82, 57.40, 40.06, 30.75, 29.03, 21.25.

(R)-4-((Benzylthio)methyl)oxazolidine-2,5-dione (130). S-Benzyl-L-cysteine was dried beforehand in a vacuum over at 50 °C for 24 hours. S-benzyl-L-cysteine (3.00 g, 14.2 mmol) was added to an oven-dried 2-necked round bottom flask equipped with a magnetic stir bar, rubber septum and inlet adapter attached to a nitrogen line containing a 10 % NaOH scrubber. THF (45 mL) was added via syringe and the solution was heated to 70 °C and stirred for 5 min. Triphosgene (1.601 g, 5.4 mmol) was dissolved in THF (11 mL) in a separate 20 mL conical round bottom flask. The triphosgene solution was

added over 30 min via syringe pump. The solution was stirred for an additional 2 hours at 70 °C during which the solution became clear. The solution was concentrated and purified via recrystallization from THF/hexane to give Compound **130** as a white crystalline solid. Yield: 3.273 g (97.1 %); ^{1}H NMR (400 MHz, DMSO-d_6) δ 9.20 (s, 1H), 7.48 – 6.97 (m, 5H), 4.76 (t, J = 4.1 Hz, 1H), 3.93 – 3.62 (m, 2H), 3.05 – 2.63 (m, 2H). ^{13}C NMR (101 MHz, DMSO) δ 171.38, 152.90, 138.76, 129.83, 129.38, 127.98, 58.83, 41.04, 40.83, 40.62, 40.41, 40.21, 40.00, 39.79, 36.94, 32.58.

(S)-4-Benzyloxazolidine-2,5-dione (132). L-Phenylalanine was dried beforehand in a vacuum over at 50 °C for 24 hours. L-phenylalanine (3.50 g, 21.2 mmol) was added to an oven-dried 2-necked round bottom flask equipped with a magnetic stir bar, rubber septum and inlet adapter attached to a nitrogen line containing a 10 % NaOH scrubber. THF (70 mL) was added via syringe and the solution was heated to 60 °C and stirred for 5 min. Triphosgene (2.389 g, 8.1 mmol) was dissolved in THF (14 mL) in a separate 20 mL conical round bottom flask. The triphosgene solution was added over 30 min via syringe pump. The solution was stirred for an additional 2 hours at 60 °C during which the solution became clear. The solution was concentrated and purified via recrystallization from THF/hexane to give Compound **132** as a white crystalline solid. Yield: 3.809 g (94.0 %); ^{1}H NMR (400 MHz, DMSO-d_6) δ 9.09 (s, 1H), 7.29 (tt, J = 12.8, 6.2 Hz, 3H), 7.22 – 7.00 (m, 2H), 4.91 – 4.62 (m, 1H), 3.17 – 2.90 (m, 2H). ^{13}C NMR (101 MHz, DMSO) δ 171.69, 152.52, 135.65, 130.55, 129.29, 128.02, 59.11, 41.03, 40.82, 40.62, 40.41, 40.20, 39.99, 39.78, 37.16.

5.10 References

1. (a) Agemy, L.; Friedmann-Morvinski, D.; Kotamraju, V. R.; Roth, L.; Sugahara, K. N.; Girard, O. M.; Mattrey, R. F.; Verma, I. M.; Ruoslahti, E., Targeted Nanoparticle Enhanced Proapoptotic Peptide as Potential Therapy for Glioblastoma. *Proc Natl Acad Sci USA* **2011,** *108* (42), 17450-17455; (b) Bae, Y. H.; Park, K., Targeted Drug Delivery to Tumors: Myths, Reality and Possibility. *J Control Release* **2011,** *153* (3), 198-205.

2. Debbage, P., Targeted Drugs and Nanomedicine: Present and Future. *Curr Pharm Des* **2009,** *15* (2), 153-72.

3. Gaur, S.; Wang, Y.; Kretzner, L.; Chen, L.; Yen, T.; Wu, X.; Yuan, Y. C.; Davis, M.; Yen, Y., Pharmacodynamic and Pharmacogenomic Study of the Nanoparticle Conjugate of Camptothecin CRLX101 for the Treatment of Cancer. *Nanomedicine-UK* **2014,** *10* (7), 1477-86.

4. (a) Ahmad, I.; Longenecker, M.; Samuel, J.; Allen, T. M., Antibody-Targeted Delivery of Doxorubicin Entrapped in Sterically Stabilized Liposomes Can Eradicate Lung-Cancer in Mice. *Cancer Res* **1993,** *53* (7), 1484-1488; (b) Coon, B. G.; Crist, S.; Gonzalez-Bonet, A. M.; Kim, H. K.; Sowa, J.; Thompson, D. H.; Ratliff, T. L.; Aguilar, R. C., Fibronectin Attachment Protein from Bacillus Calmette-Guerin as Targeting Agent for Bladder Tumor Cells. *Int J Cancer* **2012,** *131* (3), 591-600; (c) Gerasimov, O. V.; Boomer, J. A.; Qualls, M. M.; Thompson, D. H., Cytosolic Drug Delivery Using pH- and Light-Sensitive Liposomes. *Adv Drug Deliver Rev* **1999,** *38* (3), 317-338; (d) Rui, Y. J.; Wang, S.; Low, P. S.; Thompson, D. H., Diplasmenylcholine-Folate Liposomes: An Efficient Vehicle for Intracellular Drug Delivery. *J Am Chem Soc* **1998,** *120* (44), 11213-11218.

5. (a) Becker, M. L.; Liu, J.; Wooley, K. L., Functionalized Micellar Assemblies Prepared via Block Copolymers Synthesized by Living Free Radical Polymerization Upon Peptide-Loaded Resins. *Biomacromolecules* **2005,** *6* (1), 220-8; (b) Cai, S.; Vijayan, K.; Cheng, D.; Lima, E. M.; Discher, D. E., Micelles of Different Morphologies-Advantages of Worm-like Filomicelles of PEO-PCL in Paclitaxel Delivery. *Pharm Res* **2007,** *24* (11), 2099-109; (c) Junjie Li, Z. G. a. S. L., PEG-Sheddable Polyplex Micelles as Smart Gene Carriers Based on MMP-Cleavable Peptide-Linked Block Copolymers. *Chem. Commun.* **2013,** *49*, 6974; (d) Kim, Y.; Dalhaimer, P.; Christian, D. A.; Discher, D. E., Polymeric Worm Micelles as Nano-Carriers for Drug Delivery. *Nanotechnology* **2005,** *16* (7), S484-S491.

6. Yamamoto, H.; Kuno, Y.; Sugimoto, S.; Takeuchi, H.; Kawashima, Y., Surface-Modified PLGA Nanosphere with Chitosan Improved Pulmonary Delivery of Calcitonin by Mucoadhesion and Opening of the Intercellular Tight Junctions. *J Control Release* **2005,** *102* (2), 373-81.

7. Dufes, C.; Muller, J. M.; Couet, W.; Olivier, J. C.; Uchegbu, I. F.; Schatzlein, A. G., Anticancer Drug Delivery with Transferrin Targeted Polymeric Chitosan Vesicles. *Pharm Res* **2004,** *21* (1), 101-107.

8. (a) Joshi, N.; Kaviratna, A.; Banerjee, R., Multi Trigger Responsive, Surface Active Lipid Nanovesicle Aerosols for Improved Efficacy of Paclitaxel in Lung Cancer. *Integr Biol* **2013,** *5* (1), 239-48; (b) Letchford, K.; Burt, H., A Review of the Formation and Classification of Amphiphilic Block Copolymer Nanoparticulate Structures: Micelles, Nanospheres, Nanocapsules and Polymersomes. *Eur J Pharm Biopharm* **2007,** *65* (3), 259-269.

9. (a) Freitas, C.; Mullera, R. H., Spray-Drying of Solid Lipid Nanoparticles (SLN TM). *Eur J Pharm Biopharm* **1998,** *46* (2), 145-51; (b) Gupta, Y.; Jain, A.; Jain, S. K., Transferrin-Conjugated Solid Lipid Nanoparticles for Enhanced Delivery of Quinine Dihydrochloride to the Brain. *J Pharm Biopharm* **2007,** *59* (7), 935-940.

10. (a) Christian, D. A.; Cai, S.; Bowen, D. M.; Kim, Y.; Pajerowski, J. D.; Discher, D. E., Polymersome Carriers: From Self-Assembly to siRNA and Protein Therapeutics. *Eur J Pharm Biopharm* **2009,** *71* (3), 463-74; (b) Discher, B. M.; Won, Y. Y.; Ege, D. S.; Lee, J. C. M.; Bates, F. S.; Discher, D. E.; Hammer, D. A., Polymersomes: Tough Vesicles Made from Diblock Copolymers. *Science* **1999,** *284* (5417), 1143-1146; (c) Jain, J. P.; Ayen, W. Y.; Kumar, N., Self Assembling Polymers as Polymersomes for Drug Delivery. *Curr Pharm Design* **2011,** *17* (1), 65-79.

11. Cho, K. J.; Wang, X.; Nie, S. M.; Chen, Z.; Shin, D. M., Therapeutic Nanoparticles for Drug Delivery in Cancer. *Clin Cancer Res* **2008,** *14* (5), 1310-1316.

12. (a) Bayard, F. J.; Thielemans, W.; Pritchard, D. I.; Paine, S. W.; Young, S. S.; Backman, P.; Ewing, P.; Bosquillon, C., Polyethylene Glycol-Drug Ester Conjugates for Prolonged Retention of Small Inhaled Drugs in the Lung. *J Control Release* **2013,** *171* (2), 234-240; (b) Jiang, Z. Y.; Xu, S. W.; Wang, Y. Q., Chemistry for Pegylation of Protein and Peptide Molecules. *Chinese J Org Chem* **2003,** *23* (12), 1340-1347.

13. (a) Beck-Broichsitter, M.; Merkel, O. M.; Kissel, T., Controlled Pulmonary Drug and Gene Delivery Using Polymeric Nano-Carriers. *J Control Release* **2012,** *161* (2), 214-24; (b) Maeda, H.; Bharate, G. Y.; Daruwalla, J., Polymeric Drugs for Efficient Tumor-Targeted Drug Delivery Based on EPR-Effect. *Eur J Pharm Biopharm* **2009,** *71* (3), 409-419.

14. (a) Alimohammadi, S.; Salehi, R.; Amini, N.; Davaran, S., Synthesis and Physicochemical Characterization of Biodegradable PLGA-Based Magnetic Nanoparticles Containing Amoxicilin. *B Korean Chem Soc* **2012,** *33* (10), 3225-3232; (b) Amoozgar, Z.; Park, J.; Lin, Q.; Weidle, J. H., 3rd; Yeo, Y., Development of Quinic Acid-Conjugated Nanoparticles as a Drug Carrier to Solid Tumors. *Biomacromolecules* **2013,** *14* (7), 2389-95; (c) Binauld, S.; Stenzel, M. H., Acid-Degradable Polymers for Drug Delivery: a Decade of Innovation. *Chem Comm* **2013,** *49* (21), 2082-102.

15. (a) Ahmed, F.; Discher, D. E., Self-Porating Polymersomes of PEG-PLA and PEG-PCL: Hydrolysis-Triggered Controlled Release Vesicles. *J Control Release* **2004,** *96* (1), 37-53; (b) Ghahremankhani, A. A.; Dorkoosh, F.; Dinarvand, R., PLGA-PEG-PLGA tri-Block Copolymers as In Situ Gel-Forming Peptide Delivery System: Effect of Formulation Properties on Peptide Release. *Pharm Dev Technol* **2008,** *13* (1), 49-55.

16. (a) Becker, M. L.; Liu, J.; Wooley, K. L., Peptide-Polymer Bioconjugates: Hybrid Block Copolymers Generated via Living Radical Polymerizations from Resin-Supported Peptides. *Chem Comm* **2003,** (2), 180-1; (b) Dmitrovic, V.; Habraken, G. J. M.; Hendrix, M. M. R. M.; Habraken, W. J. E. M.; Heise, A.; de With, G.; Sommerdijk, N. A. J. M., Random Poly(Amino Acid)s Synthesized by Ring Opening Polymerization as Additives in the Biomimetic Mineralization of $CaCO_3$. *Polymers-Basel* **2012,** *4* (2), 1195-1210; (c) Osada, K., Drug and Gene Delivery Based on Supramolecular Assembly of PEG-Peptide Hybrid Copolymers. *Peptide Hybrid Polymers* **2006,** *202*.

17. (a) Jiang, X.; Xin, H.; Gu, J.; Xu, X.; Xia, W.; Chen, S.; Xie, Y.; Chen, L.; Chen, Y.; Sha, X.; Fang, X., Solid Tumor Penetration by Integrin-Mediated Pegylated Poly(trimethylene carbonate) Nanoparticles Loaded with Paclitaxel. *Biomaterials* **2013,** *34* (6), 1739-46; (b) Zhang, Z.; Grijpma, D. W.; Feijen, J., Poly(trimethylene carbonate) and Monomethoxy Poly(ethylene glycol)-Block-Poly(trimethylene carbonate) Nanoparticles for the Controlled Release of Dexamethasone. *J Control Release* **2006,** *111* (3), 263-270; (c) Zhang, Z.; Kuijer, R.; Bulstra, S. K.; Grijpma, D. W.; Feijen, J., The In Vivo and In Vitro Degradation Behavior of Poly(trimethylene carbonate). *Biomaterials* **2006,** *27* (9), 1741-8.

18. (a) Dahiyat, B. I.; Richards, M.; Leong, K. W., Controlled-Release from Poly(Phosphoester) Matrices. *J Control Release* **1995,** *33* (1), 13-21; (b) Iwasaki, Y.; Yamaguchi, E., Synthesis of Well-Defined Thermoresponsive Polyphosphoester Macroinitiators Using Organocatalysts. *Macromolecules* **2010,** *43* (6), 2664-2666; (c) Zhang, S. Y.; Li, A.; Zou, J.; Lin, L. Y.; Wooley, K. L., Facile Synthesis of Clickable, Water-Soluble, and Degradable Polyphosphoesters. *ACS Macro Lett* **2012,** *1* (2), 328-333; (d) Zhao, Z.; Wang, J.; Mao, H. Q.; Leong, K. W., Polyphosphoesters in Drug and Gene Delivery. *Adv Drug Deliver Rev* **2003,** *55* (4), 483-499.

19. (a) Egli, S.; Nussbaumer, M. G.; Balasubramanian, V.; Chami, M.; Bruns, N.; Palivan, C.; Meier, W., Biocompatible Functionalization of Polymersome Surfaces: A New Approach to Surface Immobilization and Cell Targeting Using Polymersomes. *J Am Chem Soc* **2011,** *133* (12), 4476-4483; (b) Nilsson, R.; Sundelof, L. O., A Determination of the Concentration and Temperature Dependence of the Refractive Index Increment of Polydimethylsiloxane in Toluene. *Makromolekul Chem* **1963,** *66*, 11-18.

20. (a) Borchmann, D. E.; Brummelhuis, N. T.; Weck, M., GRGDS-Functionalized Poly(lactide)-Graft-Poly(ethylene glycol) Copolymers: Combining Thiol-Ene Chemistry with Staudinger Ligation. *Macromolecules* **2013,** *46* (11), 4426-4431; (b) Tsuji, H.; Miyauchi, S., Enzymatic Hydrolysis of Poly(lactide)s: Effects of Molecular Weight, L-Lactide Content, and Enantiomeric and Diastereoisomeric Polymer Blending. *Biomacromolecules* **2001,** *2* (2), 597-604.

21. Geng, Y.; Discher, D. E., Hydrolytic Degradation of Poly(ethylene oxide)-Block-Polycaprolactone Worm Micelles. *J Am Chem Soc* **2005,** *127* (37), 12780-1.

22. Patel, B.; Gupta, V.; Ahsan, F., PEG-PLGA Based Large Porous Particles for Pulmonary Delivery of a Highly Soluble Drug, Low Molecular Weight Heparin. *J Control Release* **2012,** *162* (2), 310-20.

23. (a) Du, J. Z.; Chen, D. P.; Wang, Y. C.; Xiao, C. S.; Lu, Y. J.; Wang, J.; Zhang, G. Z., Synthesis and Micellization of Amphiphilic Brush-Coil Block Copolymer Based on Poly(epsilon-caprolactone) and PEGylated Polyphosphoester. *Biomacromolecules* **2006,** *7* (6), 1898-903; (b) Li, S. D.; Huang, L., Stealth Nanoparticles: High Density but Sheddable PEG is a Key for Tumor Targeting. *J Control Release* **2010,** *145* (3), 178-81.

24. Teuchert, C.; Michel, C.; Hansen, F.; Park, D. Y.; Beckham, H. W.; Wenz, G., Cylindrical Polymer Brushes by Atom Transfer Radical Polymerization from Cyclodextrin-PEG Polyrotaxanes: Synthesis and Mechanical Stability. *Macromolecules* **2013,** *46* (1), 2-7.

25. (a) Alipour, S.; Montaseri, H.; Tafaghodi, M., Preparation and Characterization of Biodegradable Paclitaxel Loaded Alginate Microparticles for Pulmonary Delivery. *Colloids Surf., B* **2010,** *81* (2), 521-9; (b) Mundra, V.; Lu, Y.; Danquah, M.; Li, W.; Miller, D. D.; Mahato, R. I., Formulation and Characterization of Polyester/Polycarbonate Nanoparticles for Delivery of a Novel Microtubule Destabilizing Agent. *Pharm Res* **2012,** *29* (11), 3064-74.

26. (a) Kulkarni, A.; Verheul, R.; Defrees, K.; Collins, C. J.; Schuldt, R. A.; Vlahu, A.; Thompson, D. H., Microfluidic Assembly of Cationic-Beta-Cyclodextrin:Hyaluronic Acid-Adamantane Host:Guest pDNA Nanoparticles. *J Biomater Sci* **2013,** *1* (10); (b) Yang, S.; Guo, F.; Kiraly, B.; Mao, X.; Lu, M.; Leong, K. W.; Huang, T. J., Microfluidic Synthesis of Multifunctional Janus Particles for Biomedical Applications. *Lab Chip* **2012,** *12* (12), 2097-102.

27. Dove, A. P., Organic Catalysis for Ring-Opening Polymerization. *ACS Macro Lett* **2012,** *1* (12), 1409-1412.

28. Nederberg, F.; Connor, E. F.; Moller, M.; Glauser, T.; Hedrick, J. L., New Paradigms for Organic Catalysts: The First Organocatalytic Living Polymerization. *Angew Chem* **2001,** *40* (14), 2712-2715.

29. (a) Lohmeijer, B. G. G.; Pratt, R. C.; Leibfarth, F.; Logan, J. W.; Long, D. A.; Dove, A. P.; Nederberg, F.; Choi, J.; Wade, C.; Waymouth, R. M.; Hedrick, J. L., Guanidine and Amidine Organocatalysts for Ring-Opening Polymerization of Cyclic Esters. *Macromolecules* **2006,** *39* (25), 8574-8583; (b) Nederberg, F.; Lohmeijer, B. G. G.; Leibfarth, F.; Pratt, R. C.; Choi, J.; Dove, A. P.; Waymouth, R. M.; Hedrick, J. L., Organocatalytic Ring Opening Polymerization of Trimethylene Carbonate. *Biomacromolecules* **2007,** *8* (1), 153-160.

30. Dove, A. P.; Pratt, R. C.; Lohmeijer, B. G.; Waymouth, R. M.; Hedrick, J. L., Thiourea-Based Bifunctional Organocatalysis: Supramolecular Recognition for Living Polymerization. *J Am Chem Soc* **2005,** *127* (40), 13798-9.

31. (a) Pratt, R. C.; Lohmeijer, B. G. G.; Long, D. A.; Waymouth, R. M.; Hedrick, J. L., Triazabicyclodecene: A Simple Bifunctional Organocatalyst for Acyl Transfer and Ring-Opening Polymerization of Cyclic Esters. *J Am Chem Soc* **2006,** *128* (14), 4556-4557; (b) Cooley, C. B.; Trantow, B. M.; Nederberg, F.; Kiesewetter, M. K.; Hedrick, J. L.; Waymouth, R. M.; Wender, P. A., Oligocarbonate Molecular Transporters: Oligomerization-Based Syntheses and Cell-Penetrating Studies. *J Am Chem Soc* **2009,** *131* (45), 16401.

32. Chuma, A.; Horn, H. W.; Swope, W. C.; Pratt, R. C.; Zhang, L.; Lohmeijer, B. G. G.; Wade, C. G.; Waymouth, R. M.; Hedrick, J. L.; Rice, J. E., The Reaction Mechanism for the Organocatalytic Ring-Opening Polymerization of L-Lactide Using a Guanidine-Based Catalyst: Hydrogen-Bonded or Covalently Bound? *J Am Chem Soc* **2008,** *130* (21), 6749-6754.

33. Pack, D. W.; Hoffman, A. S.; Pun, S.; Stayton, P. S., Design and Development of Polymers for Gene Delivery. *Nat Rev Drug Discov* **2005,** *4* (7), 581-93.

34. (a) Beck-Broichsitter, M.; Merkel, O. M.; Kissel, T., Pulmonary Gene Delivery Using Polymeric Nonviral Vectors. *Bioconjugate Chem* **2012,** *23*, 3-20; (b) Huang, R. Q.; Qu, Y. H.; Ke, W. L.; Zhu, J. H.; Pei, Y. Y.; Jiang, C., Efficient Gene Delivery Targeted to the Brain Using a Transferrin-Conjugated Polyethyleneglycol-Modified Polyamidoamine Dendrimer. *FASEB J* **2007,** *21* (4), 1117-1125; (c) Takahashi, Y.; Nishikawa, M.; Takakura, Y., Development of Safe and Effective Nonviral Gene Therapy by Eliminating CpG Motifs from Plasmid DNA Vector. *Front Biosci (Schol Ed)* **2012,** *4*, 133-41.

35. (a) Andaloussi, S. E.; Lehto, T.; Mager, I.; Rosenthal-Aizman, K.; Oprea, II; Simonson, O. E.; Sork, H.; Ezzat, K.; Copolovici, D. M.; Kurrikoff, K.; Viola, J. R.; Zaghloul, E. M.; Sillard, R.; Johansson, H. J.; Said Hassane, F.; Guterstam, P.; Suhorutsenko, J.; Moreno, P. M.; Oskolkov, N.; Halldin, J.; Tedebark, U.; Metspalu, A.; Lebleu, B.; Lehtio, J.; Smith, C. I.; Langel, U., Design of a Peptide-Based Vector, PepFect6, for Efficient Delivery of siRNA in Cell Culture and Systemically In Vivo. *Nucleic Acids Res* **2011,** *39* (9), 3972-87; (b) Bellocq, N. C.; Pun, S. H.; Jensen, G. S.; Davis, M. E., Transferrin-Containing, Cyclodextrin Polymer-Based Particles for Tumor-Targeted Gene Delivery. *Bioconjugate Chem* **2003,** *14* (6), 1122-32; (c) Brannon-Peppas, L.; Blanchette, J. O., Nanoparticle and Targeted Systems for Cancer Therapy. *Adv Drug Deliv Rev* **2004,** *56* (11), 1649-59.

36. Kulkarni, A.; DeFrees, K.; Hyun, S. H.; Thompson, D. H., Pendant Polymer:Amino-beta-Cyclodextrin:siRNA Guest:Host Nanoparticles as Efficient Vectors for Gene Silencing. *J Am Chem Soc* **2012,** *134* (18), 7596-7599.

37. Kulkarni, A.; Badwaik, V.; DeFrees, K.; Schuldt, R. A.; Gunasekera, D. S.; Powers, C.; Vlahu, A.; VerHeul, R.; Thompson, D. H., Effect of Pendant Group on pDNA Delivery by Cationic-beta-Cyclodextrin:alkyl-PVA-PEG Pendant Polymer Complexes. *Biomacromolecules* **2014,** *15* (1), 12-9.

38. Popielarski, S. R.; Mishra, S.; Davis, M. E., Structural Effects of Carbohydrate-Containing Polycations on Gene Delivery Cyclodextrin Type and Functionalization. *Bioconjugate Chem* **2003,** *14* (3), 672-8.

39. (a) Bartlett, D. W.; Su, H.; Hildebrandt, I. J.; Weber, W. A.; Davis, M. E., Impact of Tumor-Specific Targeting on the Biodistribution and Efficacy of siRNA Nanoparticles Measured by Multimodality In Vivo Imaging. *Proc Natl Acad Sci USA* **2007,** *104* (39), 15549-54; (b) Gaur, S.; Chen, L.; Yen, T.; Wang, Y.; Zhou, B.; Davis, M.; Yen, Y., Preclinical Study of the Cyclodextrin-Polymer Conjugate of Camptothecin CRLX101 for the Treatment of Gastric Cancer. *Nanomedicine-UK* **2012,** *8* (5), 721-30.

40. Pratt, R. C.; Nederberg, F.; Waymouth, R. M.; Hedrick, J. L., Tagging Alcohols with Cyclic Carbonate: a Versatile Equivalent of Methacrylate for Ring-Opening Polymerization. *Chem Comm* **2008,** (1), 114-6.

41. Geihe, E. I.; Cooley, C. B.; Simon, J. R.; Kiesewetter, M. K.; Edward, J. A.; Hickerson, R. P.; Kaspar, R. L.; Hedrick, J. L.; Waymouth, R. M.; Wender, P. A., Designed Guanidinium-Rich Amphipathic Oligocarbonate Molecular Transporters Complex, Deliver and Release siRNA in Cells. *Proc Natl Acad Sci USA* **2012,** *109* (33), 13171-6.

42. Kulkarni, A.; Defrees, K.; Thompson, D., Pendant Polymer:Amino-beta-Cyclodextin Guest:Host Complexes as Safe and Efficient Vectors for Nucleic Acid Delivery. *Mol Ther* **2012,** *20*, S158-S158.

43. (a) Paderi, J. E.; Panitch, A., Design of a Synthetic Collagen-Binding Peptidoglycan that Modulates Collagen Fibrillogenesis. *Biomacromolecules* **2008,** *9* (9), 2562-6; (b) Paderi, J. E.; Sistiabudi, R.; Ivanisevic, A.; Panitch, A., Collagen-Binding Peptidoglycans: a Biomimetic Approach to Modulate Collagen Fibrillogenesis for Tissue Engineering Applications. *Tissue Eng Part A* **2009,** *15* (10), 2991-9.

44. Qian, H.; Wohl, A. R.; Crow, J. T.; Macosko, C. W.; Hoye, T. R., A Strategy for Control of "Random" Copolymerization of Lactide and Glycolide: Application to Synthesis of PEG-b-PLGA Block Polymers Having Narrow Dispersity. *Macromolecules* **2011,** *44* (18), 7132-7140.

45. (a) Coin, I.; Beyermann, M.; Bienert, M., Solid-Phase Peptide Synthesis: From Standard Procedures to the Synthesis of Difficult Sequences. *Nat Protoc* **2007,** *2* (12), 3247-3256; (b) Fields, G. B.; Noble, R. L., Solid-Phase Peptide-Synthesis Utilizing 9-Fluorenylmethoxycarbonyl Amino-Acids. *Int J Pept Prot Res* **1990,** *35* (3), 161-214.

46. Brzezinska, K. R.; Deming, T. J., Synthesis of AB Diblock Copolymers by Atom-Transfer Radical Polymerization (ATRP) and Living Polymerization of Alpha-Amino Acid-N-Carboxyanhydrides. *Macromol Biosci* **2004,** *4* (6), 566-9.

47. Cheng, J.; Deming, T. J., Synthesis of Polypeptides by Ring-Opening Polymerization of Alpha-Amino Acid N-Carboxyanhydrides. *Top Curr Chem* **2012,** *310*, 1-26.

48. Dimitrov, I.; Schlaad, H., Synthesis of Nearly Monodisperse Polystyrene-Polypeptide Block Copolymers via Polymerisation of N-Carboxyanhydrides. *Chem Comm* **2003,** (23), 2944-2945.

49. Fuller, W. D.; Verlander, M. S.; Goodman, M., A Procedure for the Facile Synthesis of Amino-Acid N-Carboxyanhydrides. *Biopolymers* **1976,** *15* (9), 1869-71.

50. Kramer, J. R.; Deming, T. J., General Method for Purification of Alpha-Amino Acid-N-Carboxyanhydrides Using Flash Chromatography. *Biomacromolecules* **2010,** *11* (12), 3668-72.

SYNTHESIS AND PERFORMANCE OF NOVEL SUPRAMOLECULAR TOOLS FOR SINGLE-PARTICLE CRYOGENIC ELECTRON MICROSCOPY AND DRUG AND GENE DELIVERY

VOLUME II

A Dissertation

Submitted to the Faculty

of

Purdue University

by

Kyle J. Wright

In Partial Fulfillment of the

Requirements for the Degree

of

Doctor of Philosophy

December 2016

Purdue University

West Lafayette, IndianaV

APPENDIX

APPENDIX

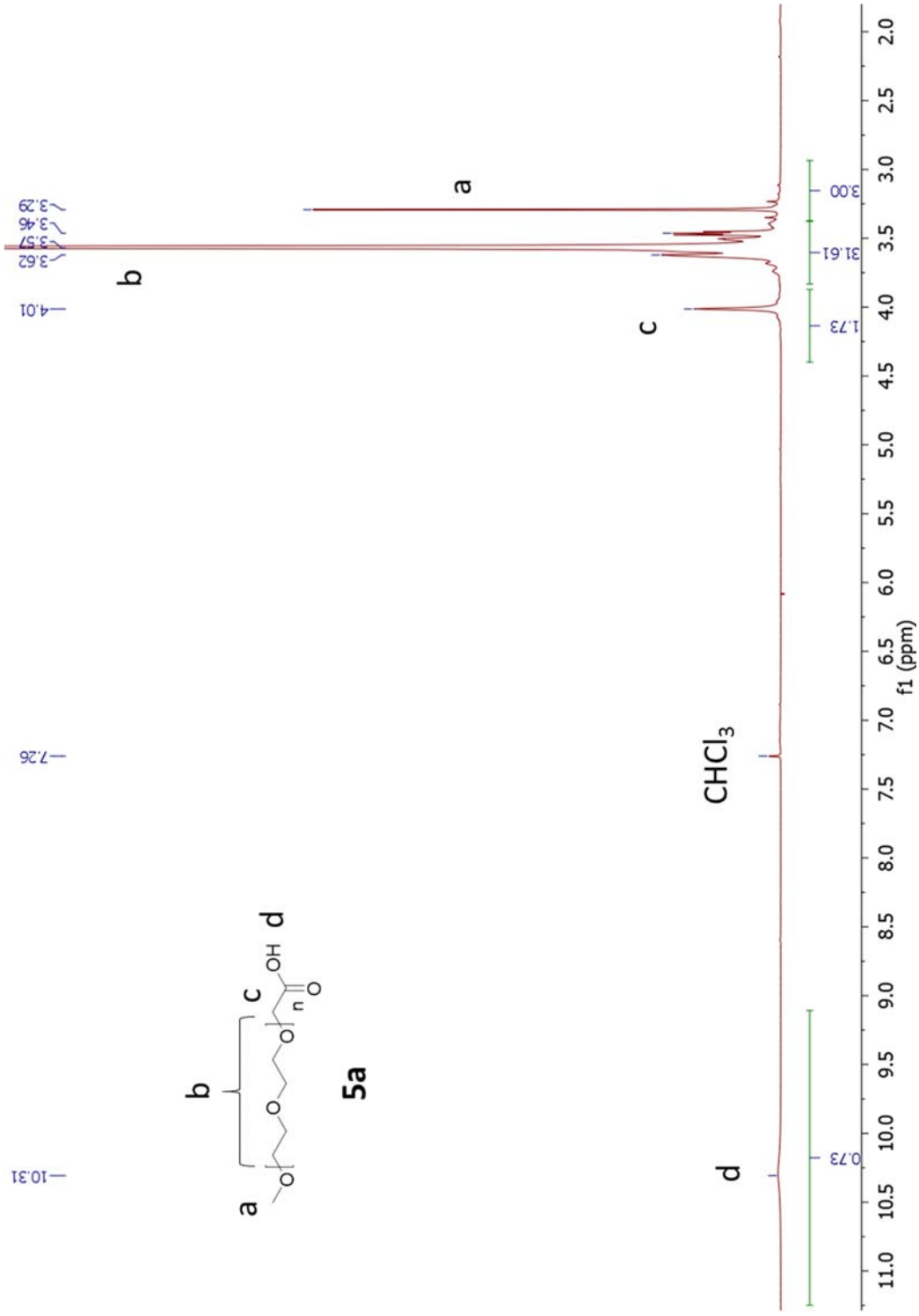

Figure A.1 ^{1}H-NMR of **5a**

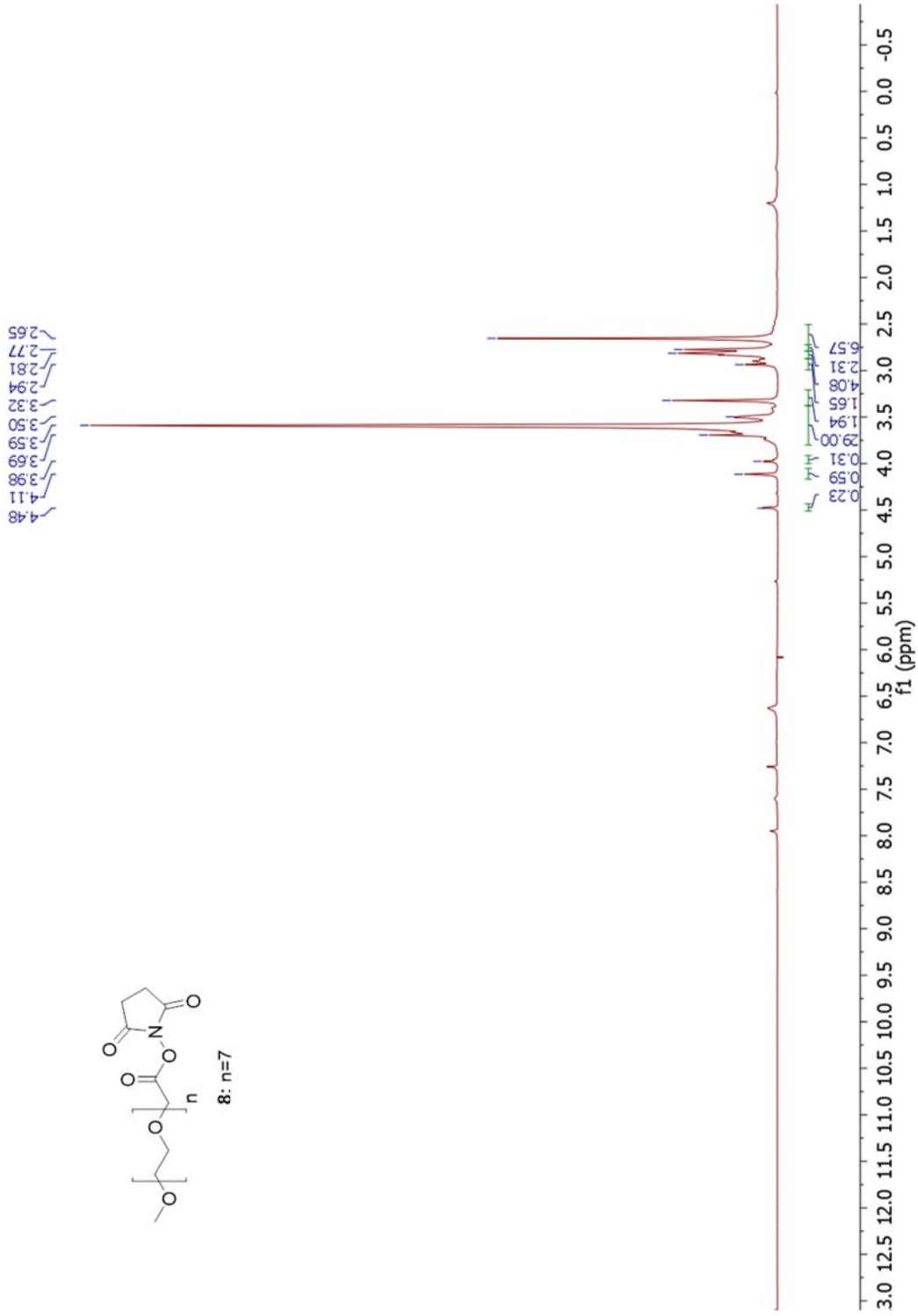

Figure A.2 ^{1}H-NMR of **8**

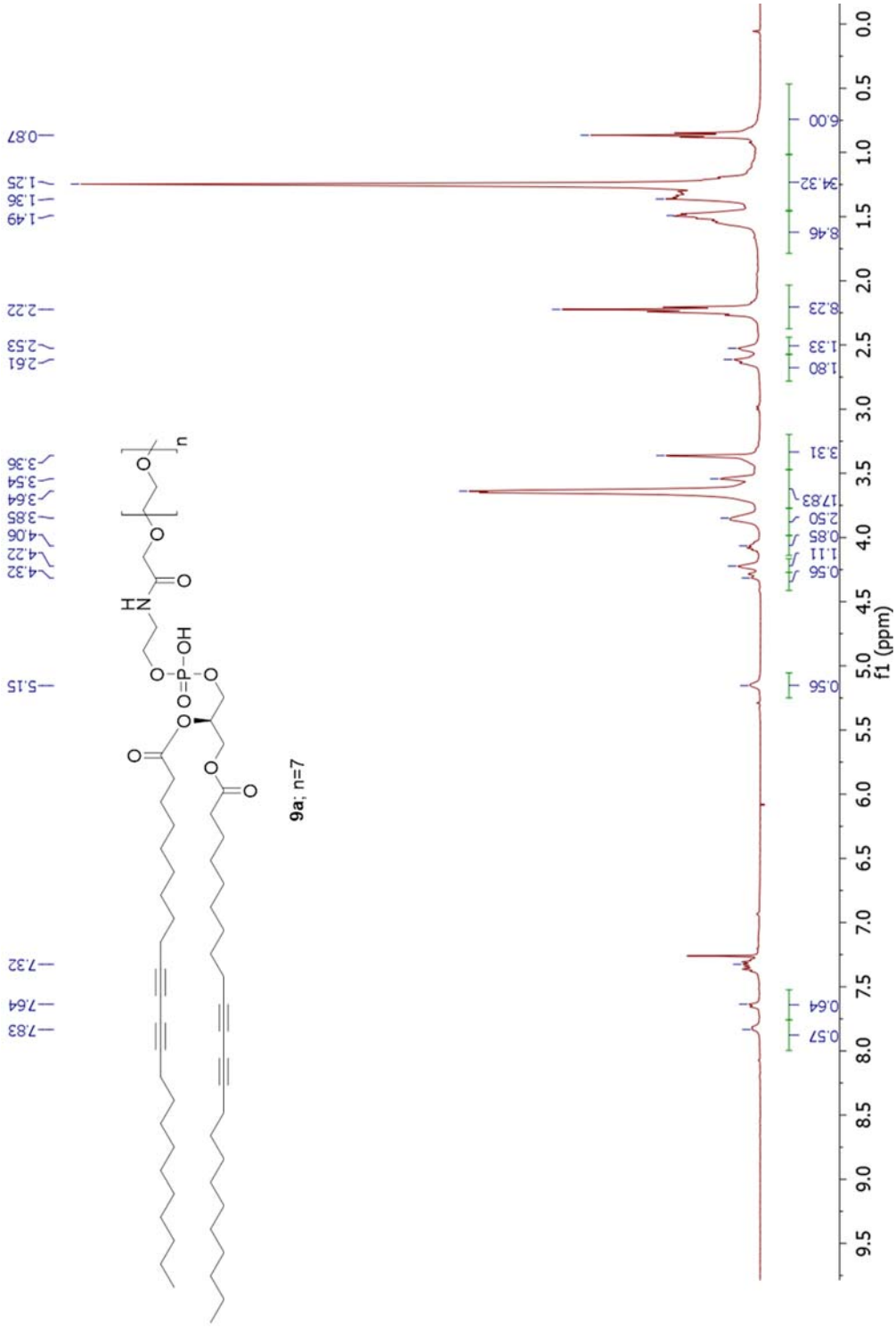

Figure A.3 ^{1}H-NMR of **9a**

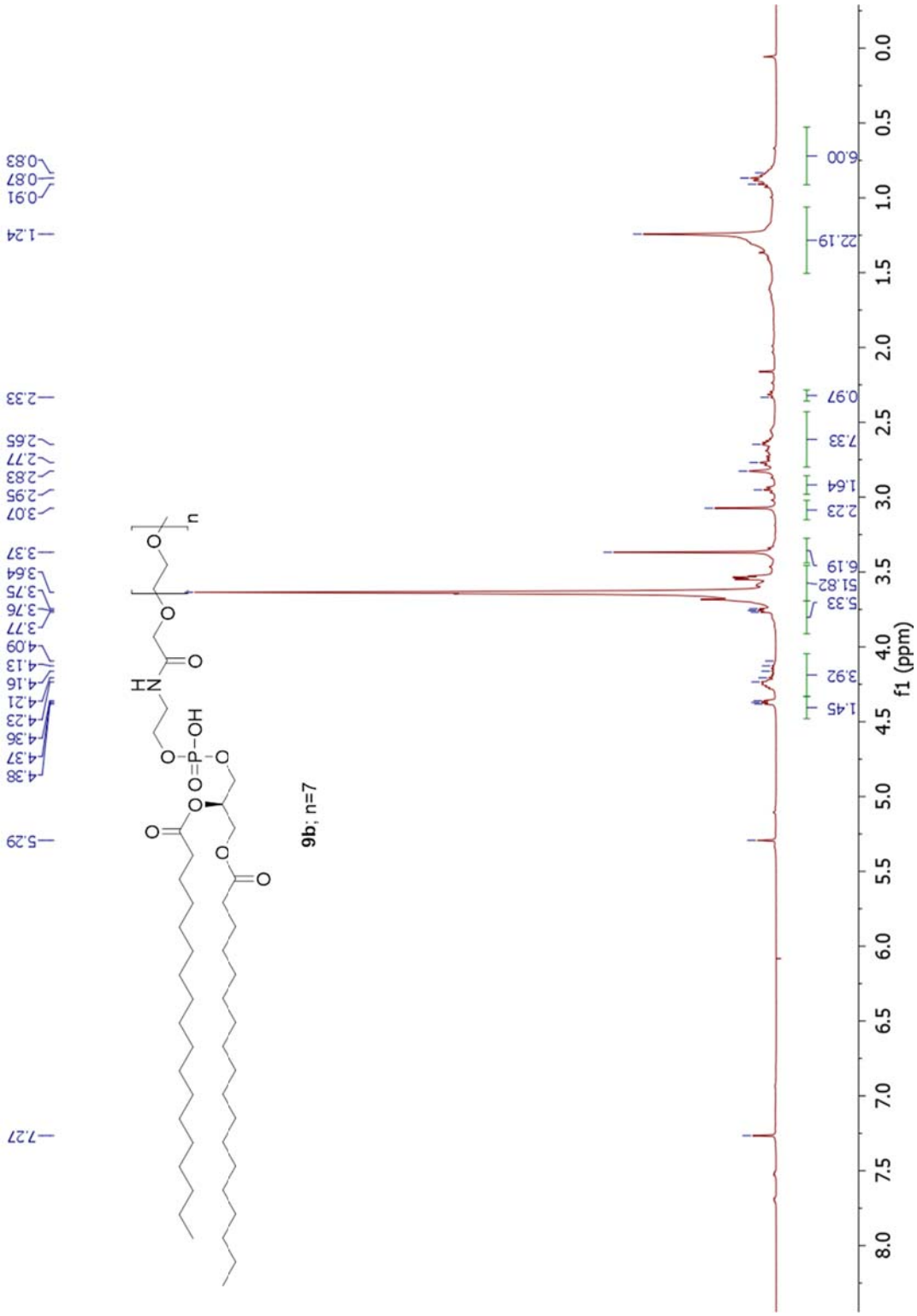

Figure A.4 ^{1}H-NMR of **9b**

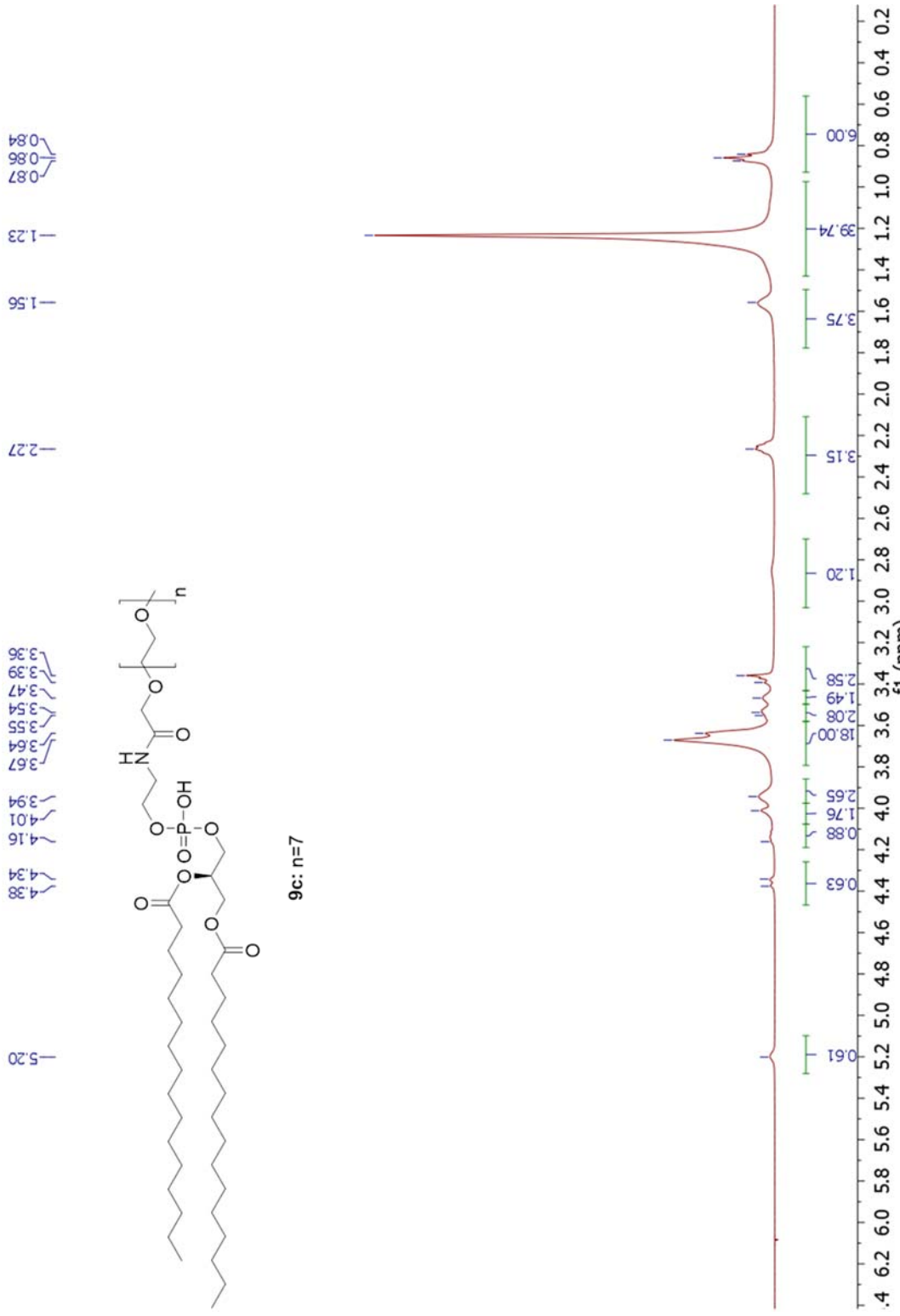

Figure A.5 ^{1}H-NMR of **9c**

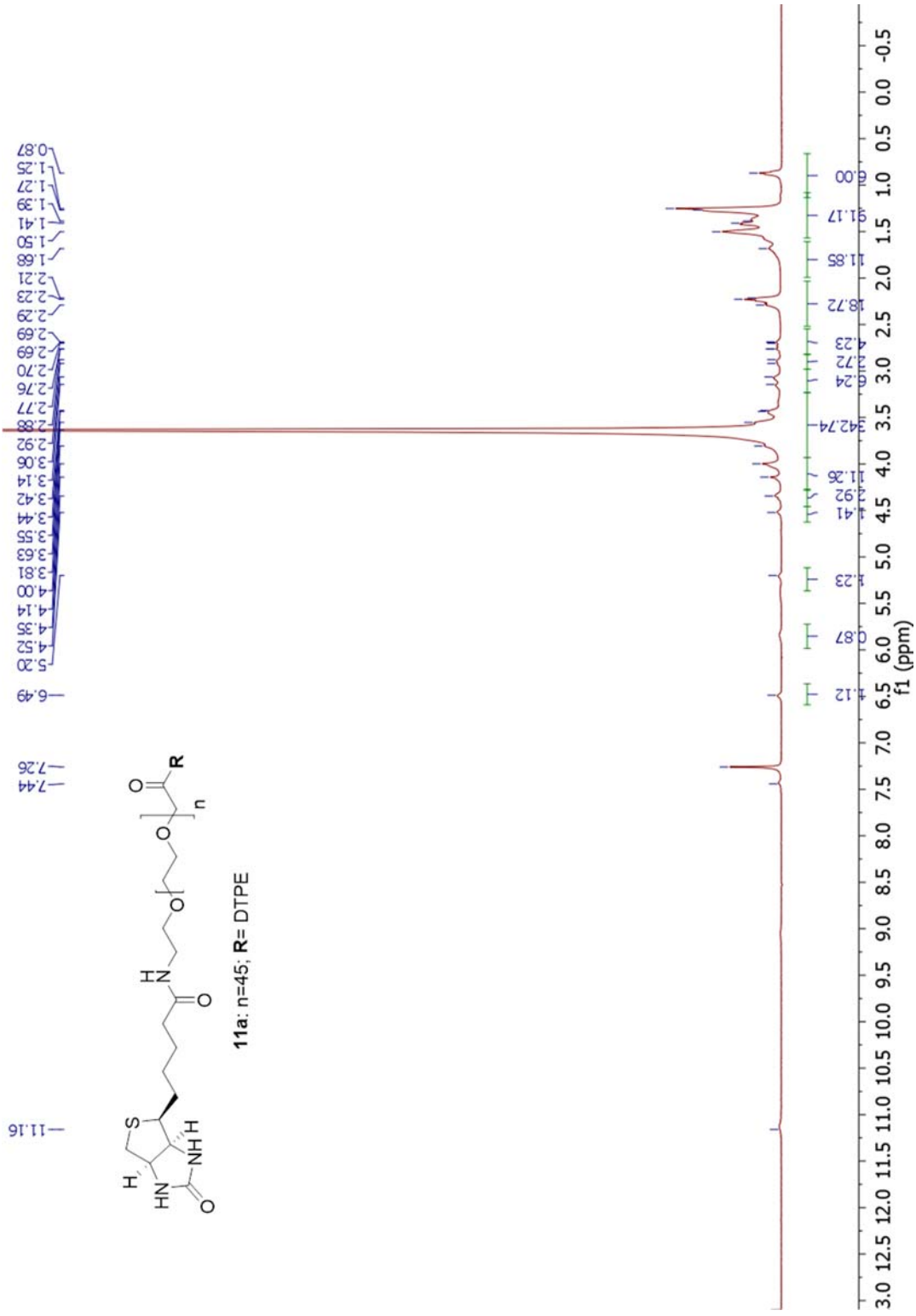

Figure A.6 ^{1}H-NMR of **11a**

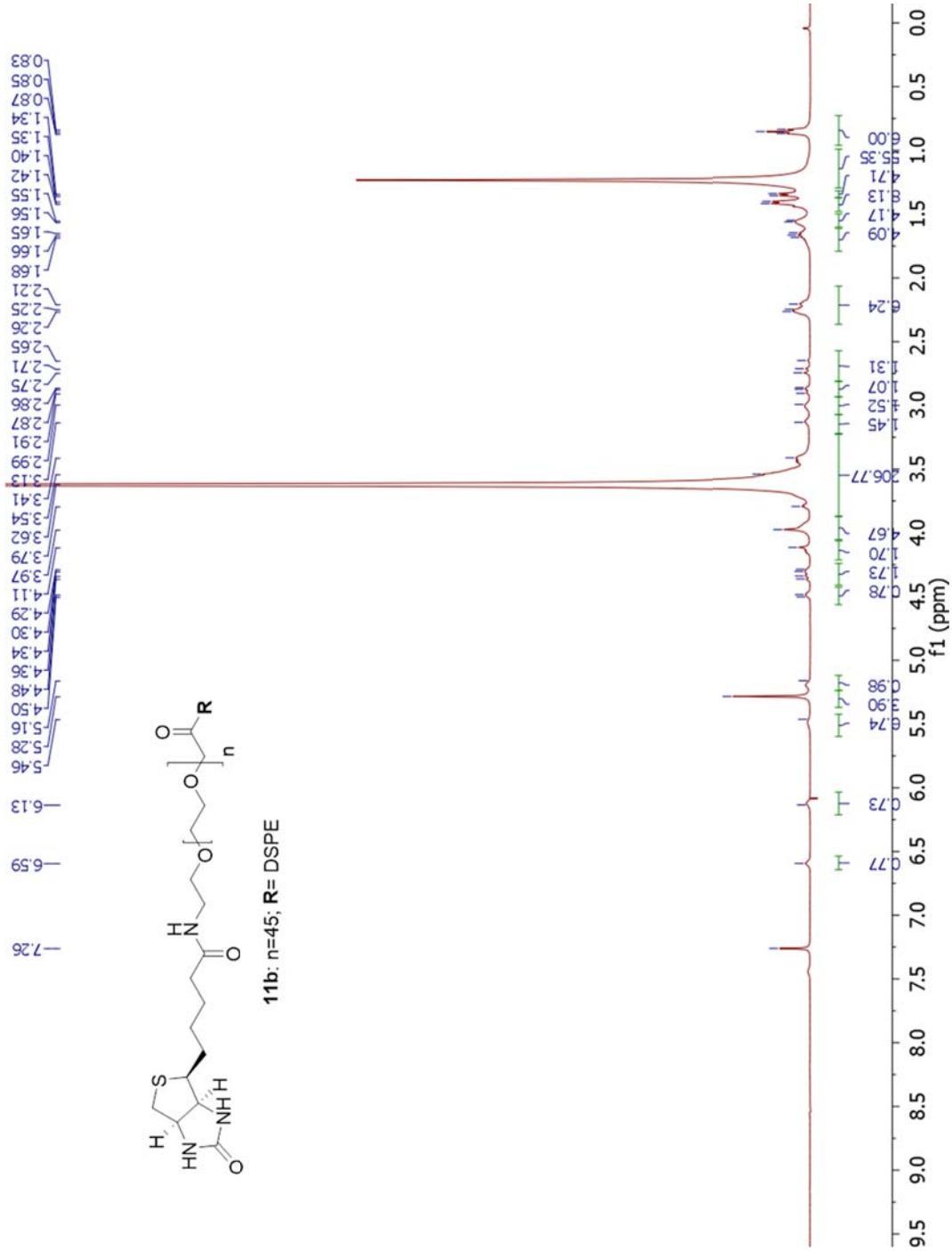

Figure A.7 ^{1}H-NMR of **11b**

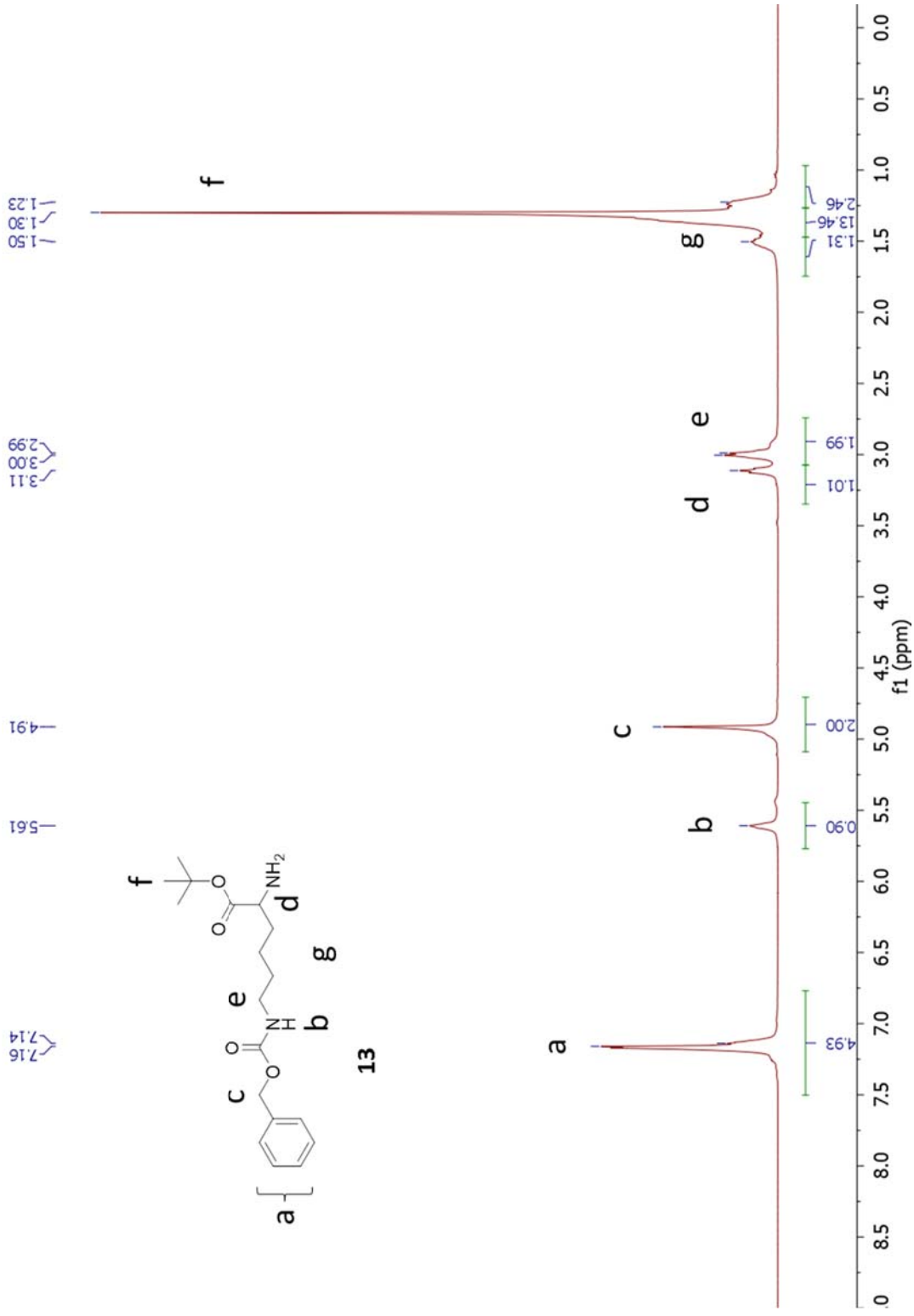

Figure A.8 ^{1}H-NMR of **13**

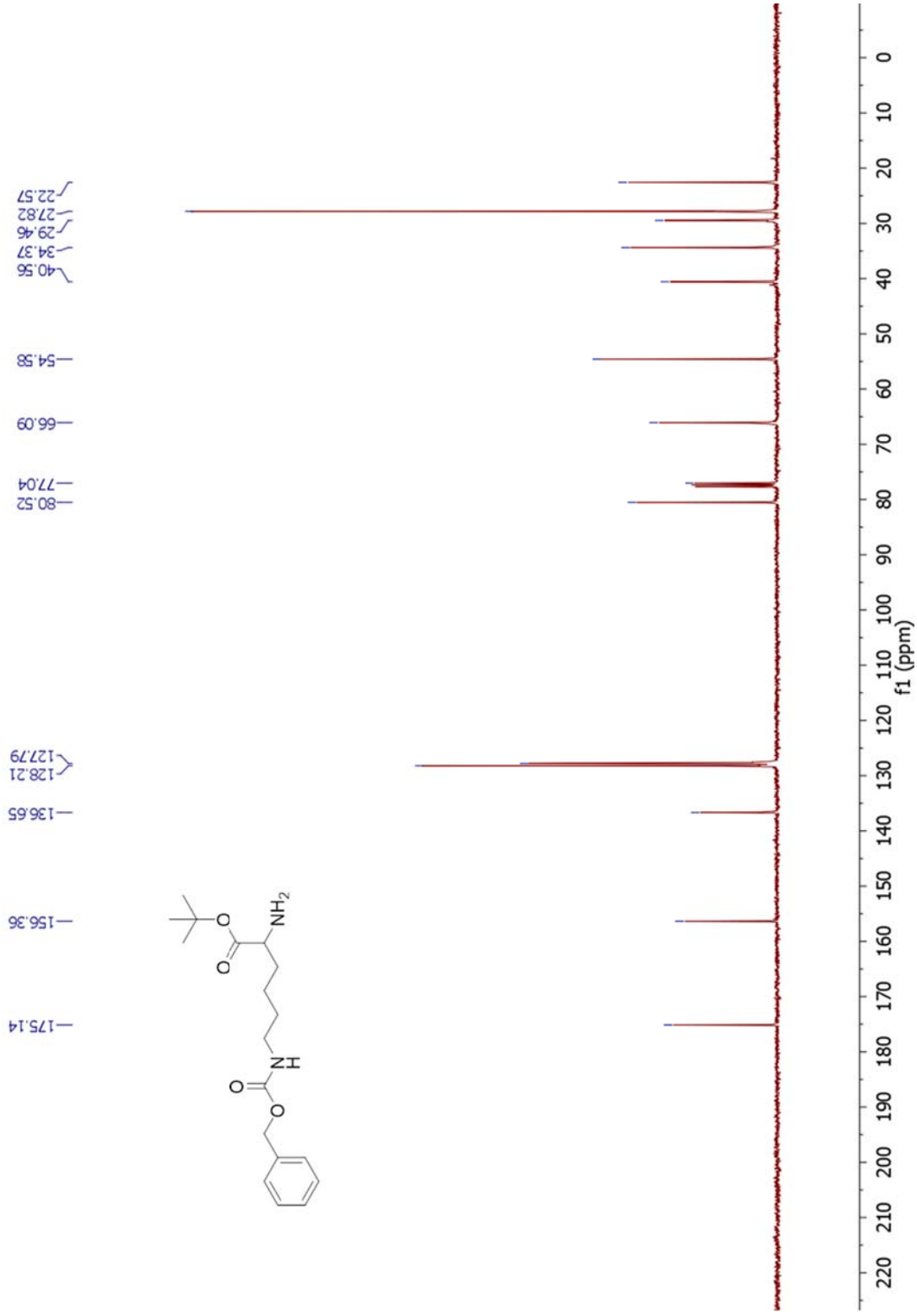

Figure A.9 ^{13}C-NMR of **13**

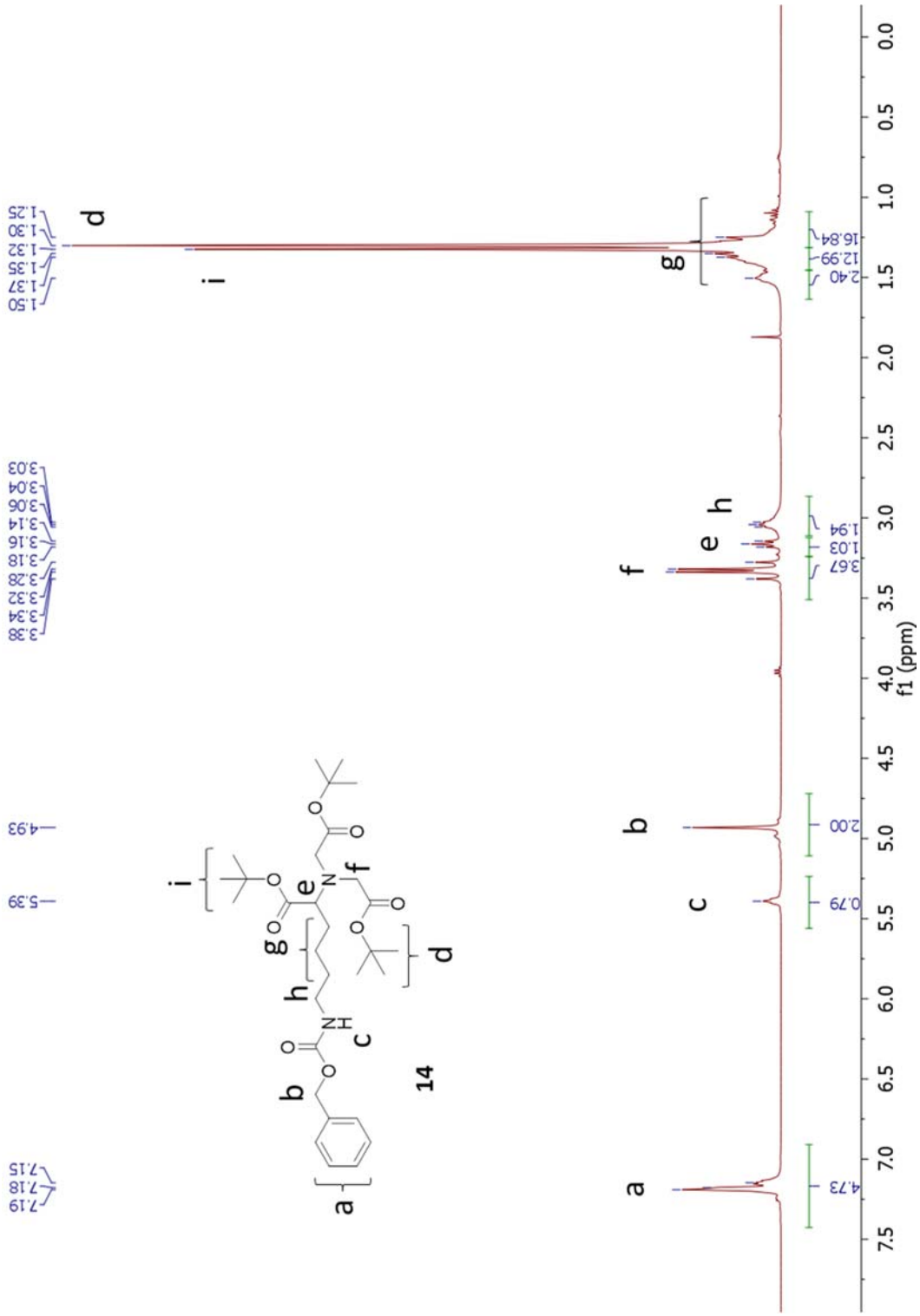

Figure A.10 ^{1}H-NMR of **14**

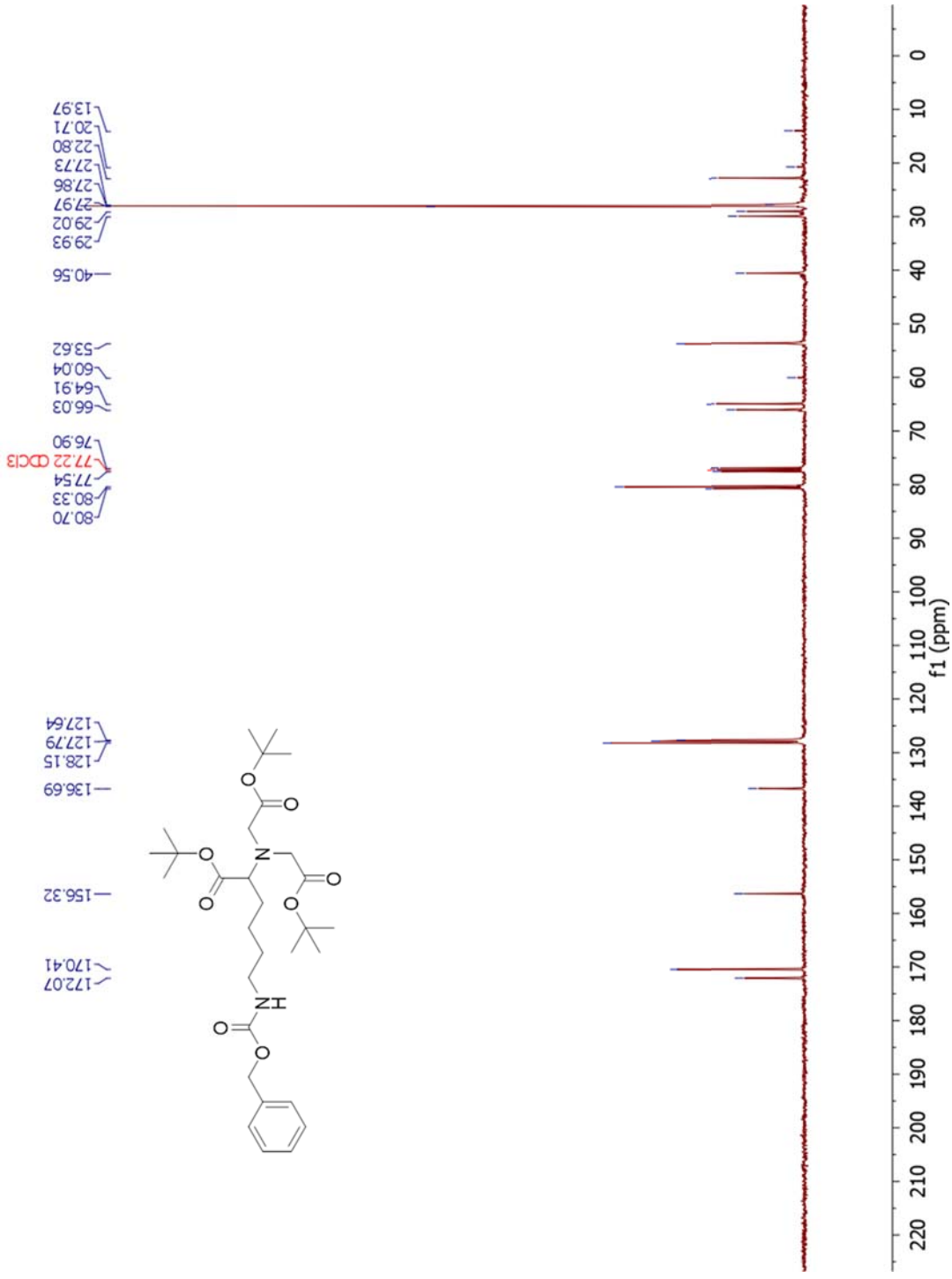

Figure A.11 ^{13}C-NMR of **14**

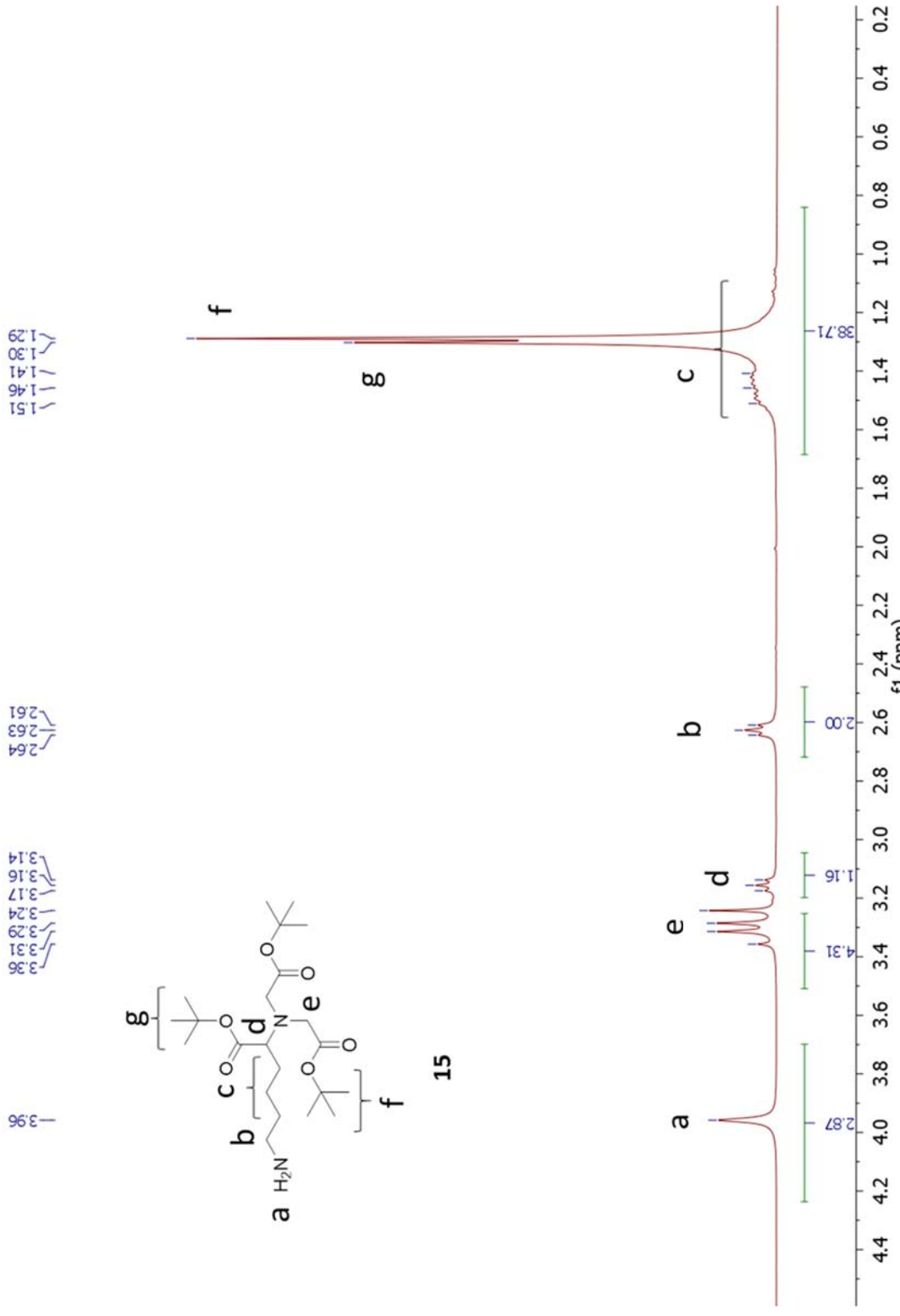

Figure A.12 ^{1}H-NMR of **15**

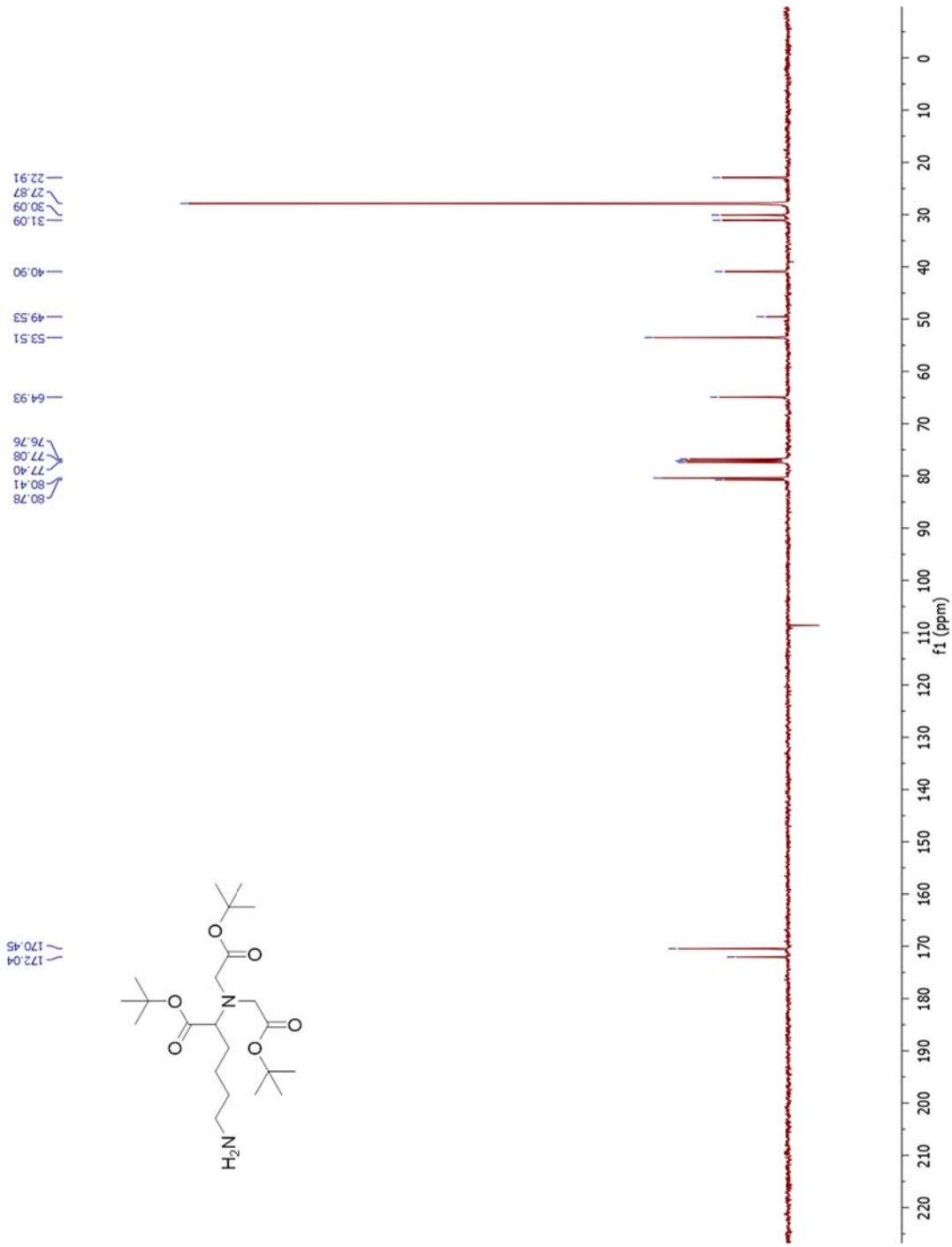

Figure A.13 ^{13}C-NMR of **15**

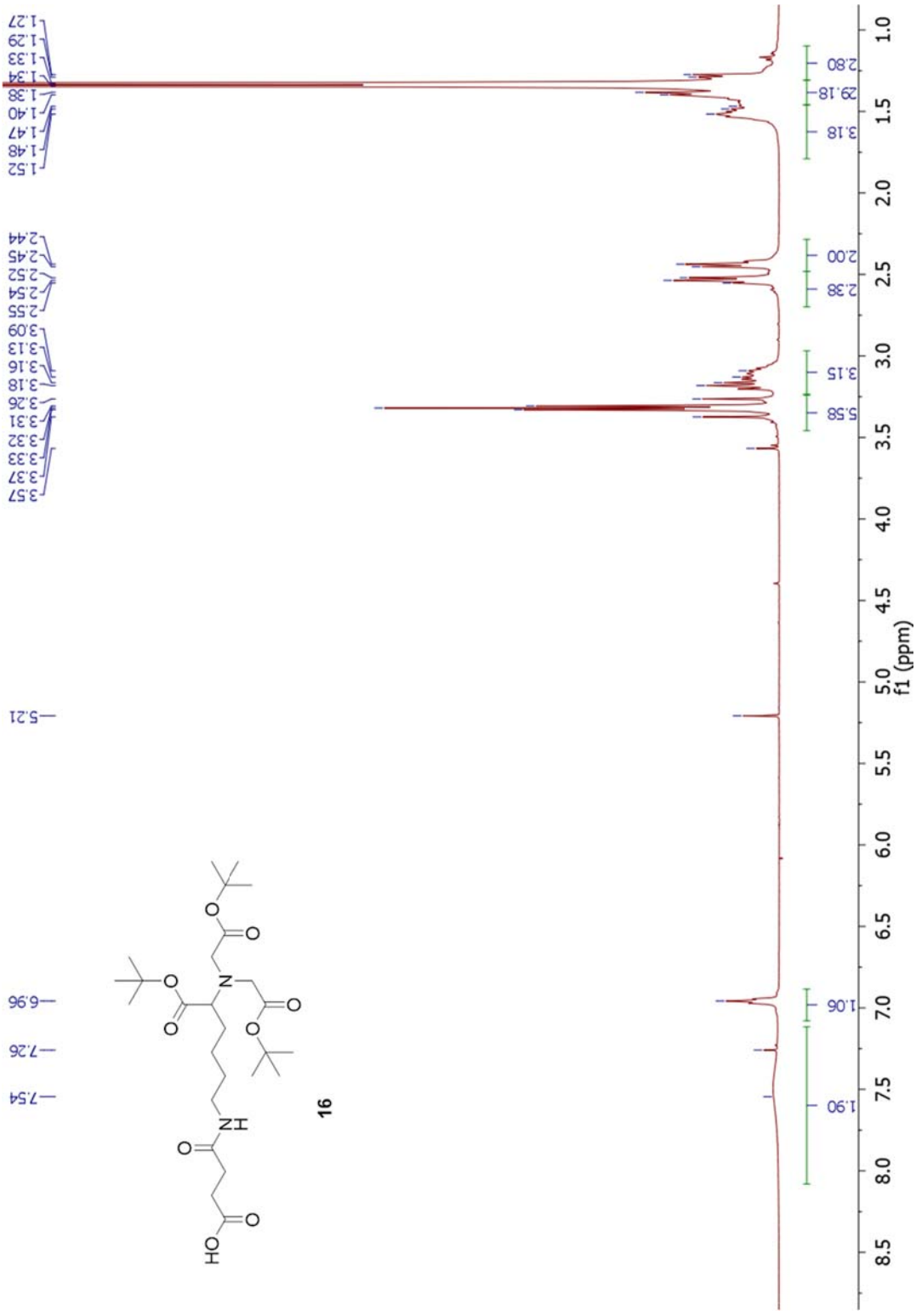

Figure A.14 ^{1}H-NMR of **16**

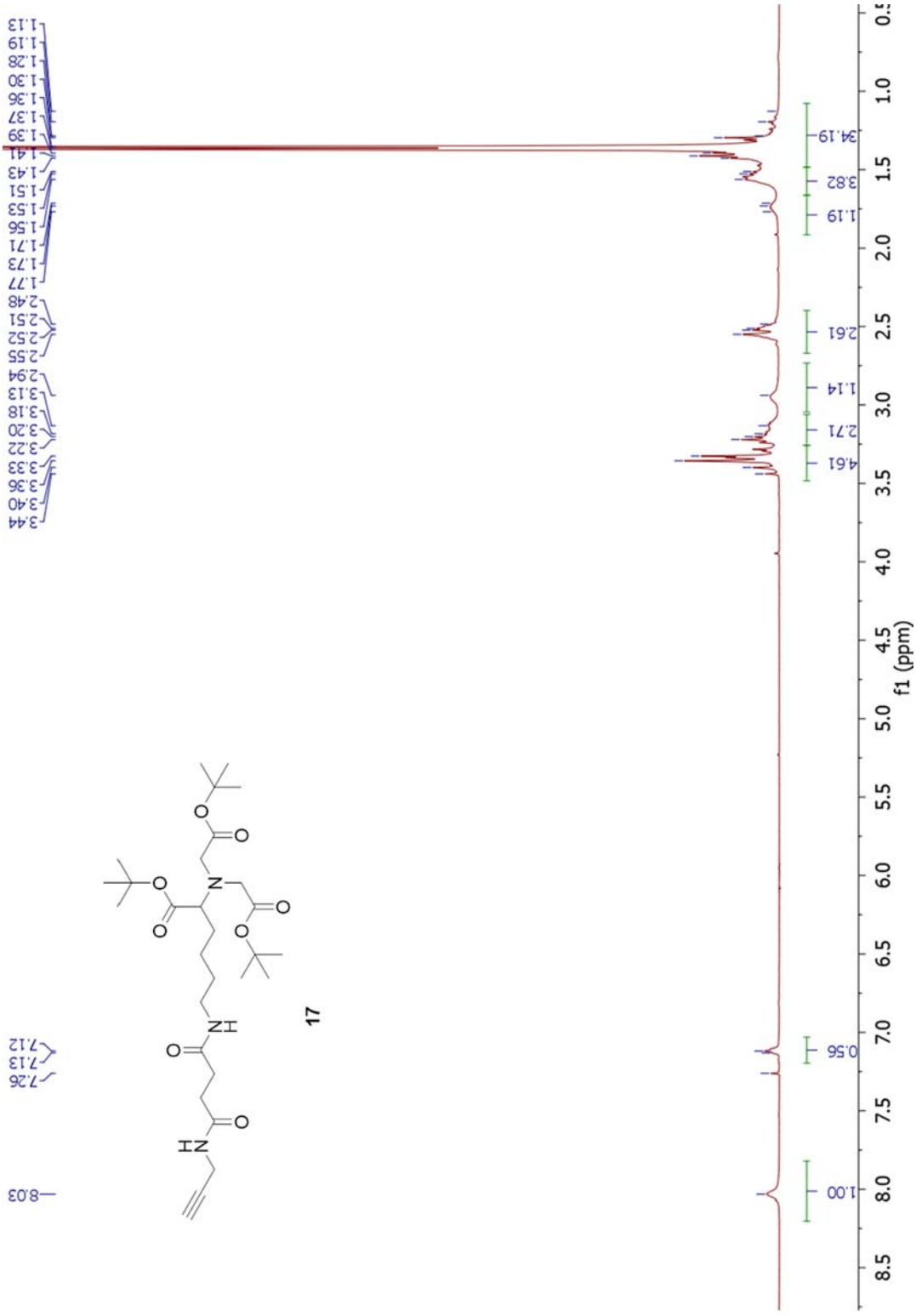

Figure A.15 ^{1}H-NMR of **17**

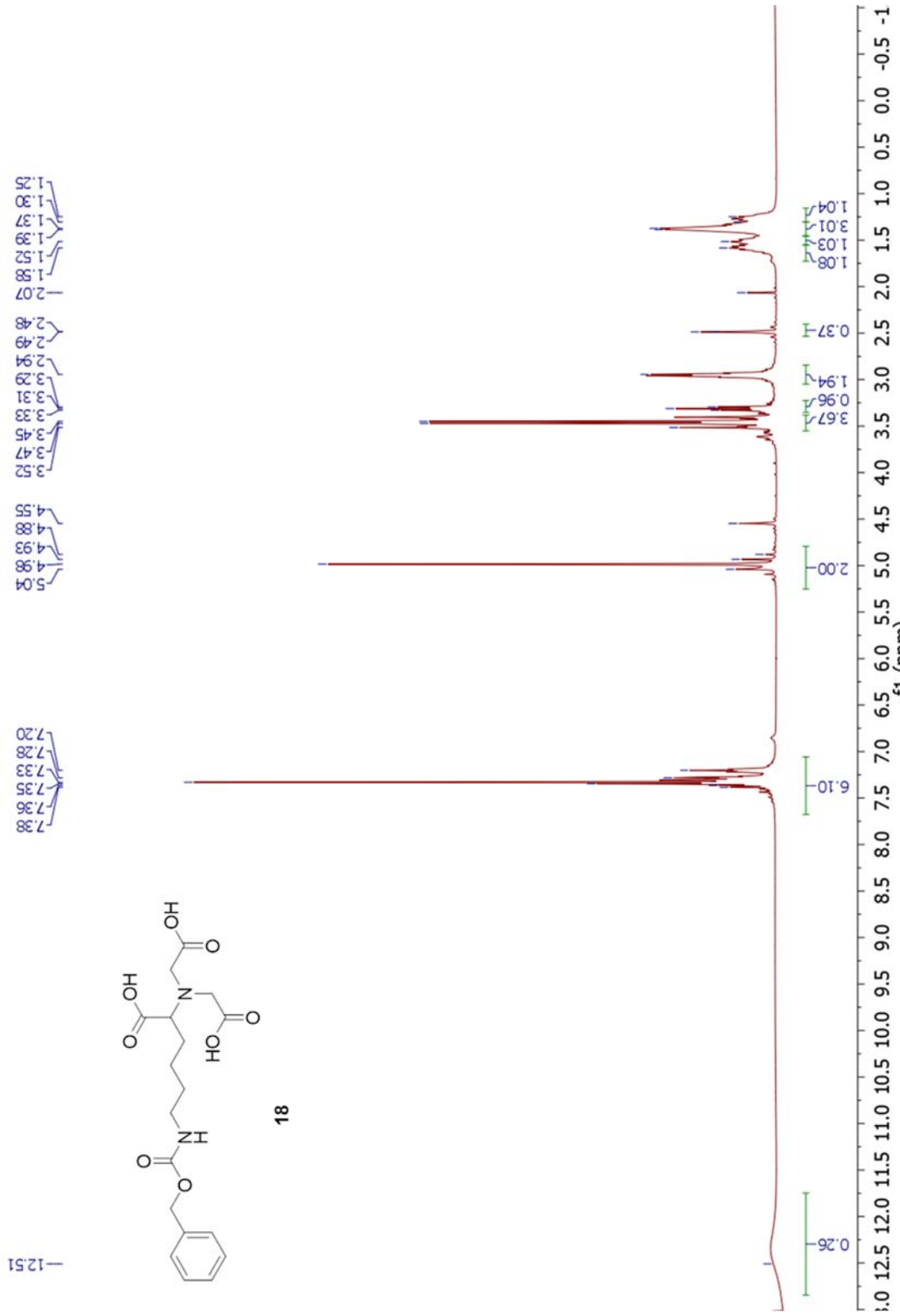

Figure A.16 ^{1}H-NMR of **18**

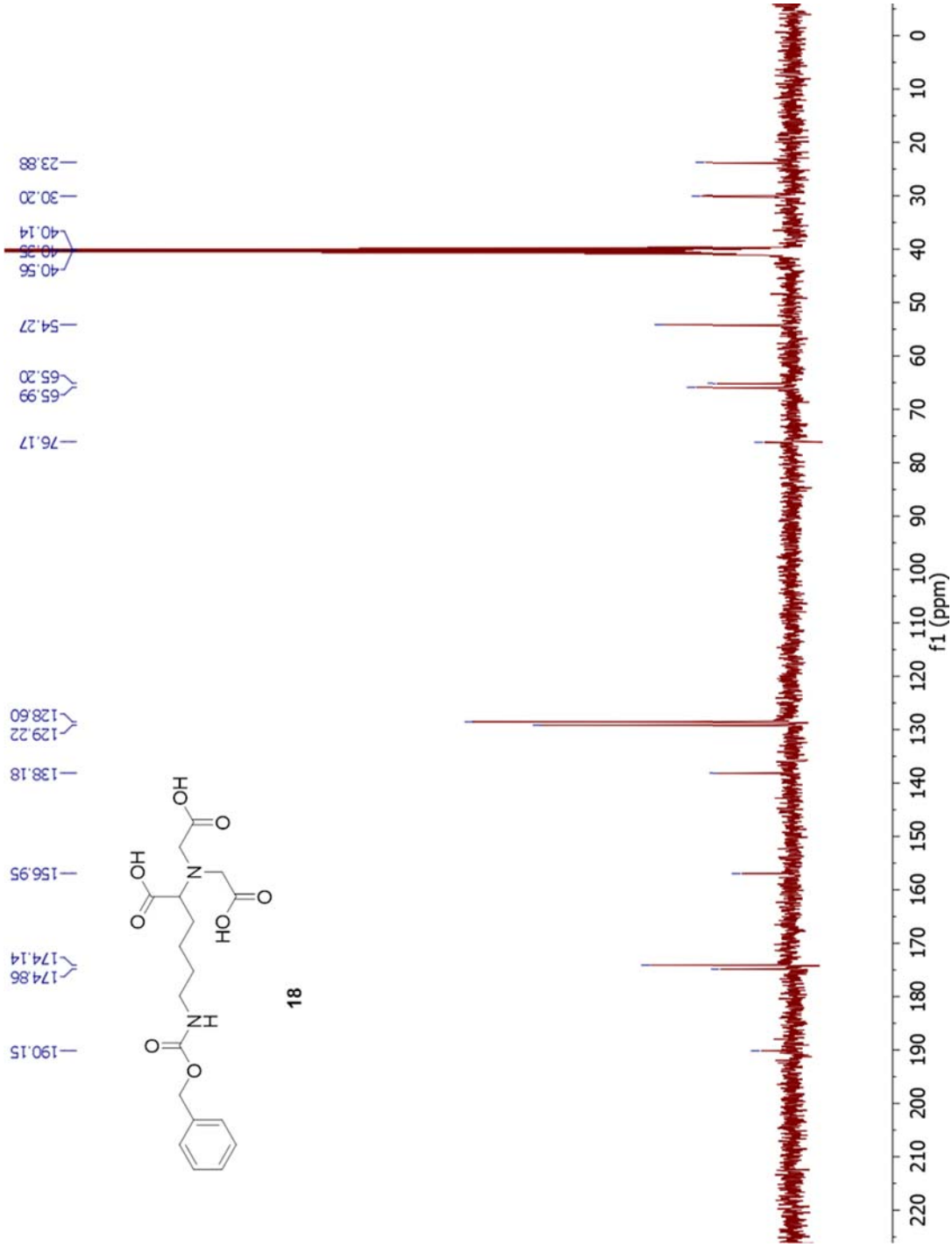

Figure A.17 ^{13}C-NMR of **18**

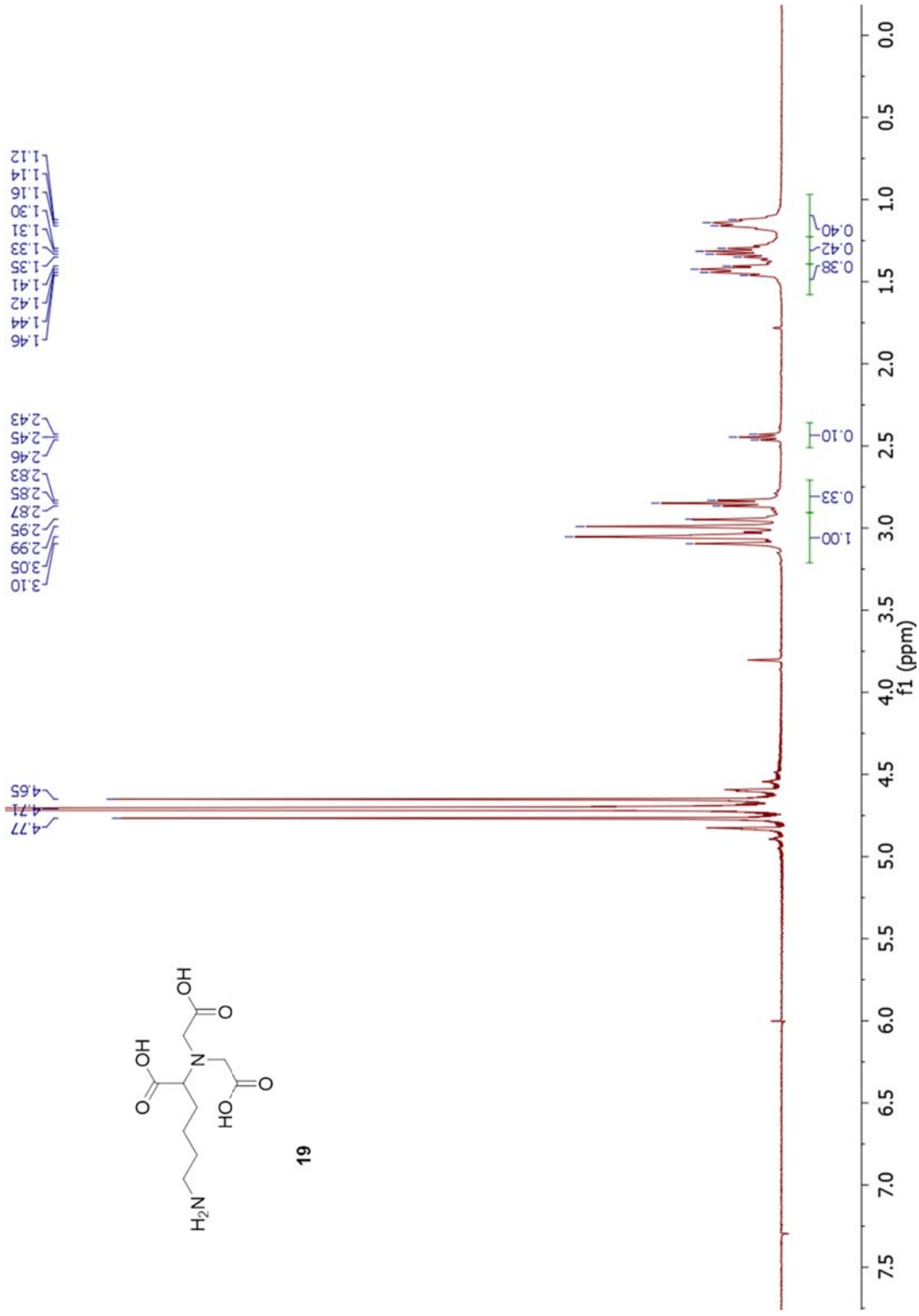

Figure A.18 ^{1}H-NMR of **19**

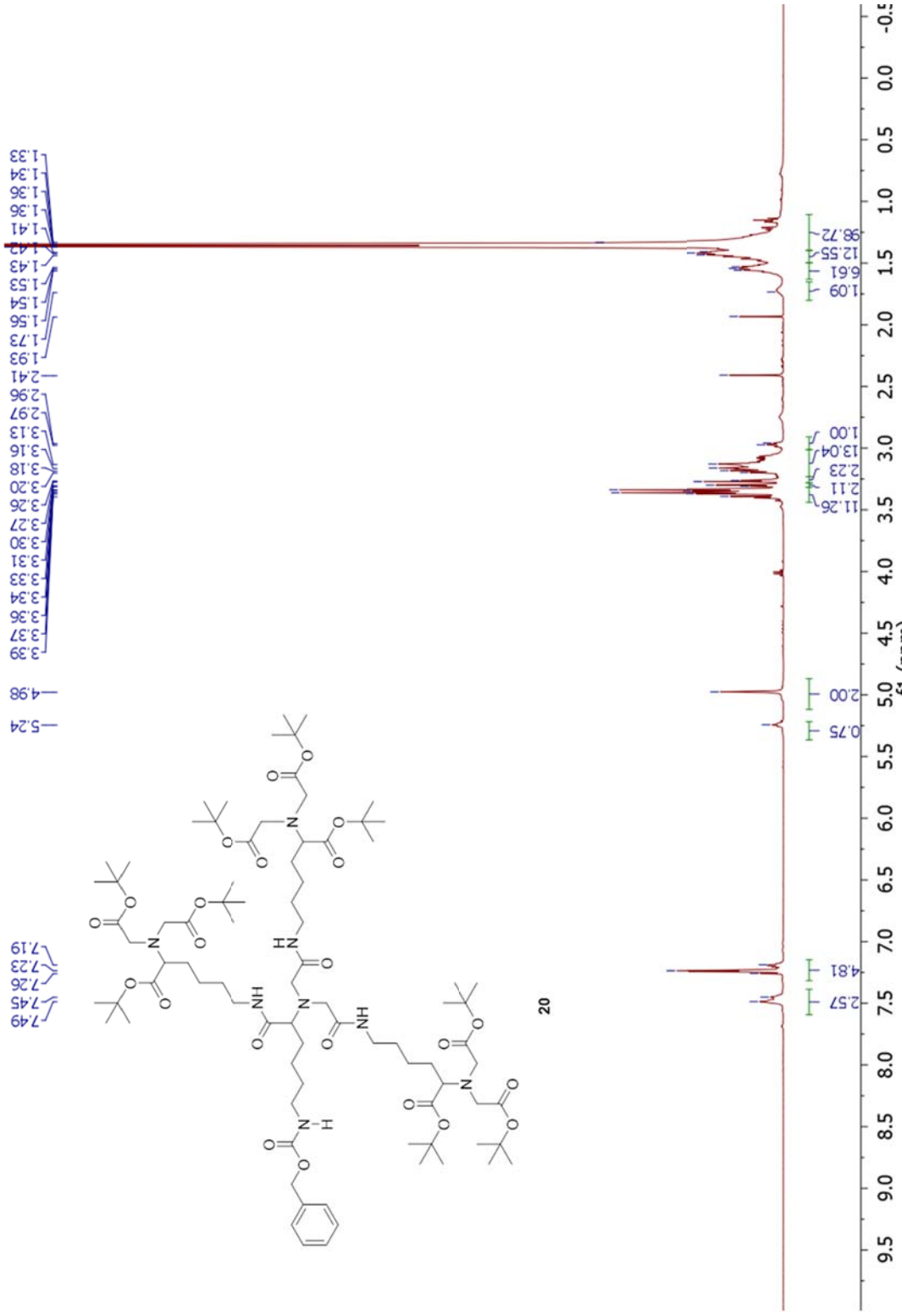

Figure A.19 ^{1}H-NMR of **20**

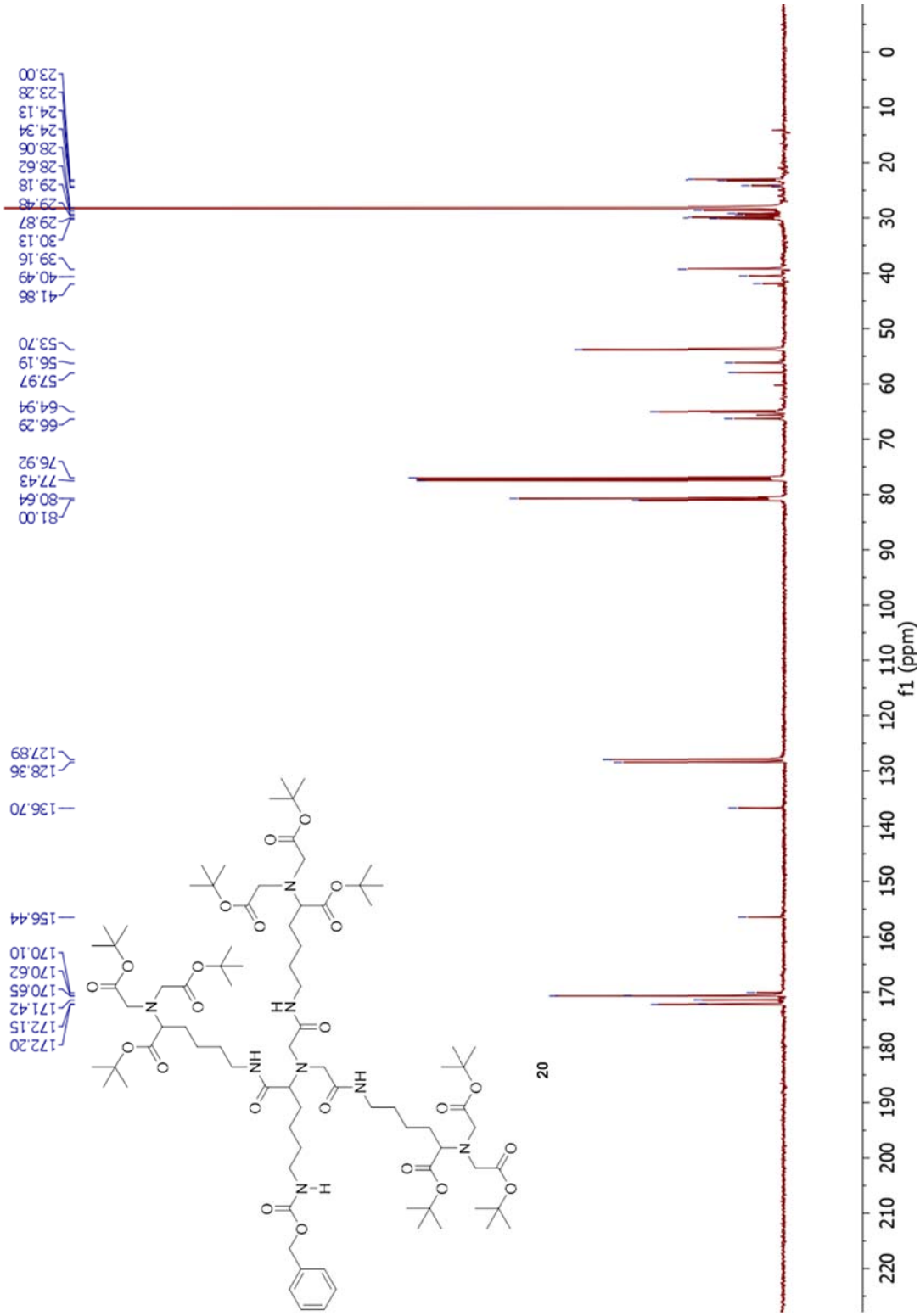

Figure A.20 ^{13}C-NMR of **20**

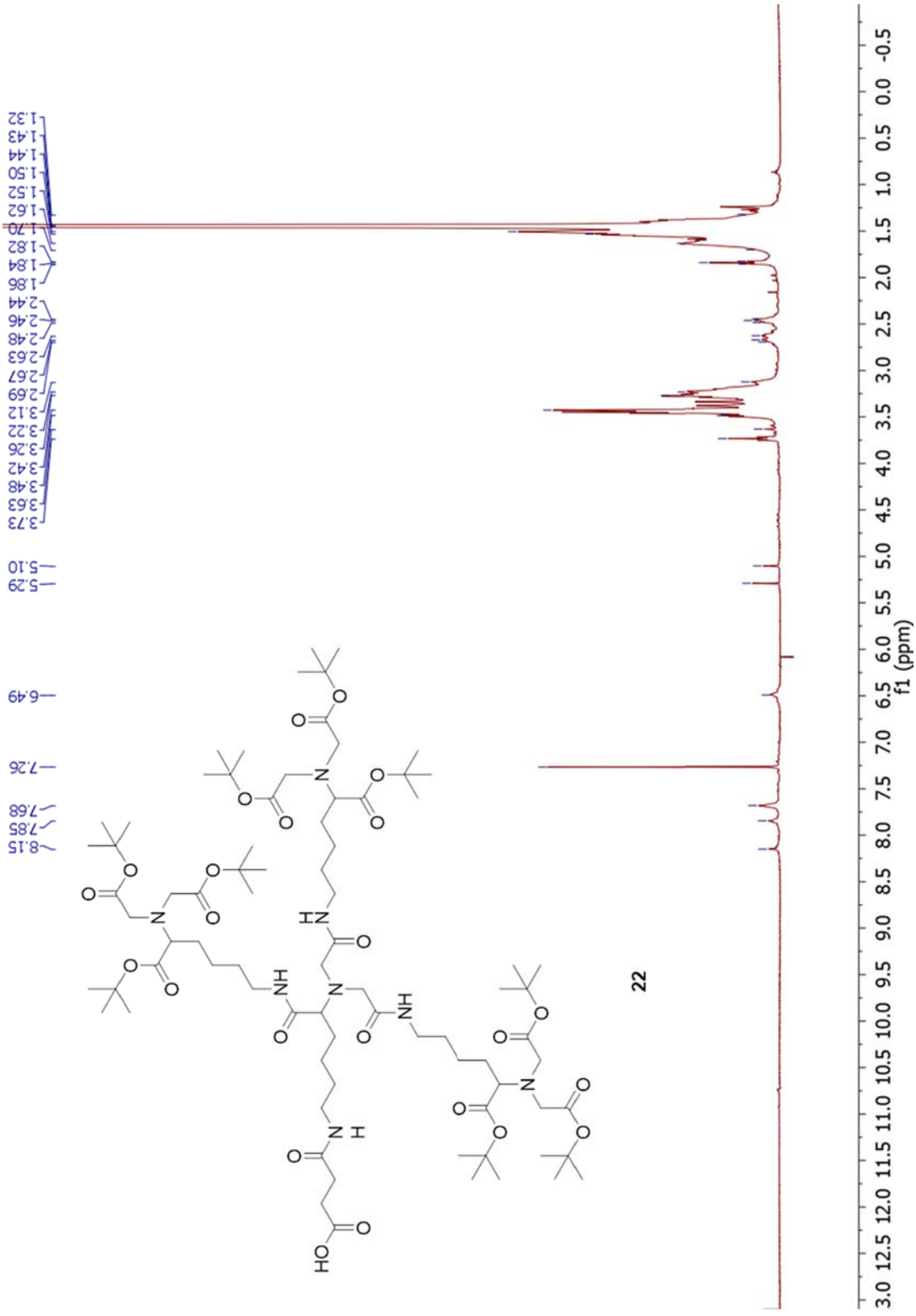

Figure A.21 ^{1}H-NMR of **22**

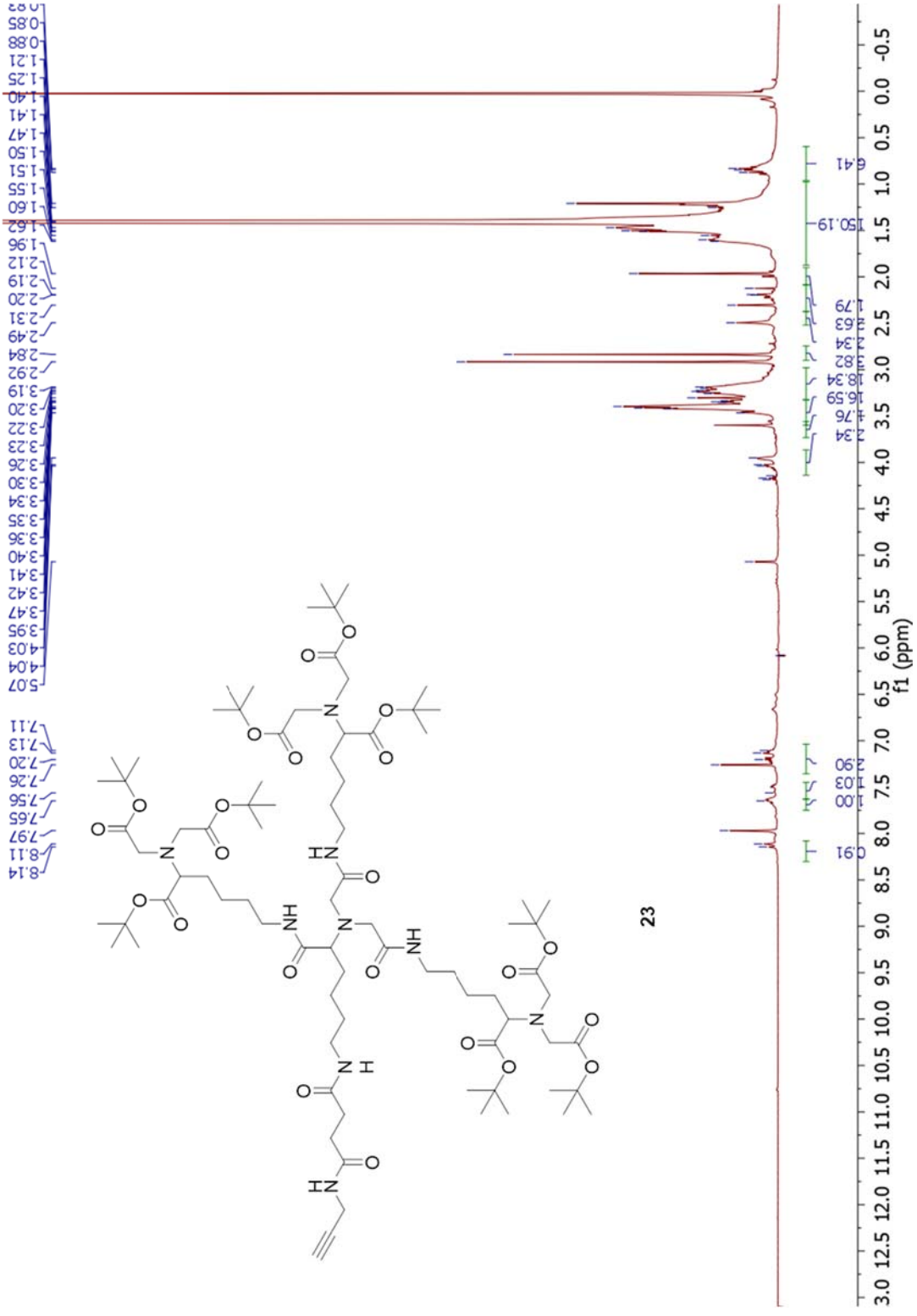

Figure A.22 ^{1}H-NMR of **23**

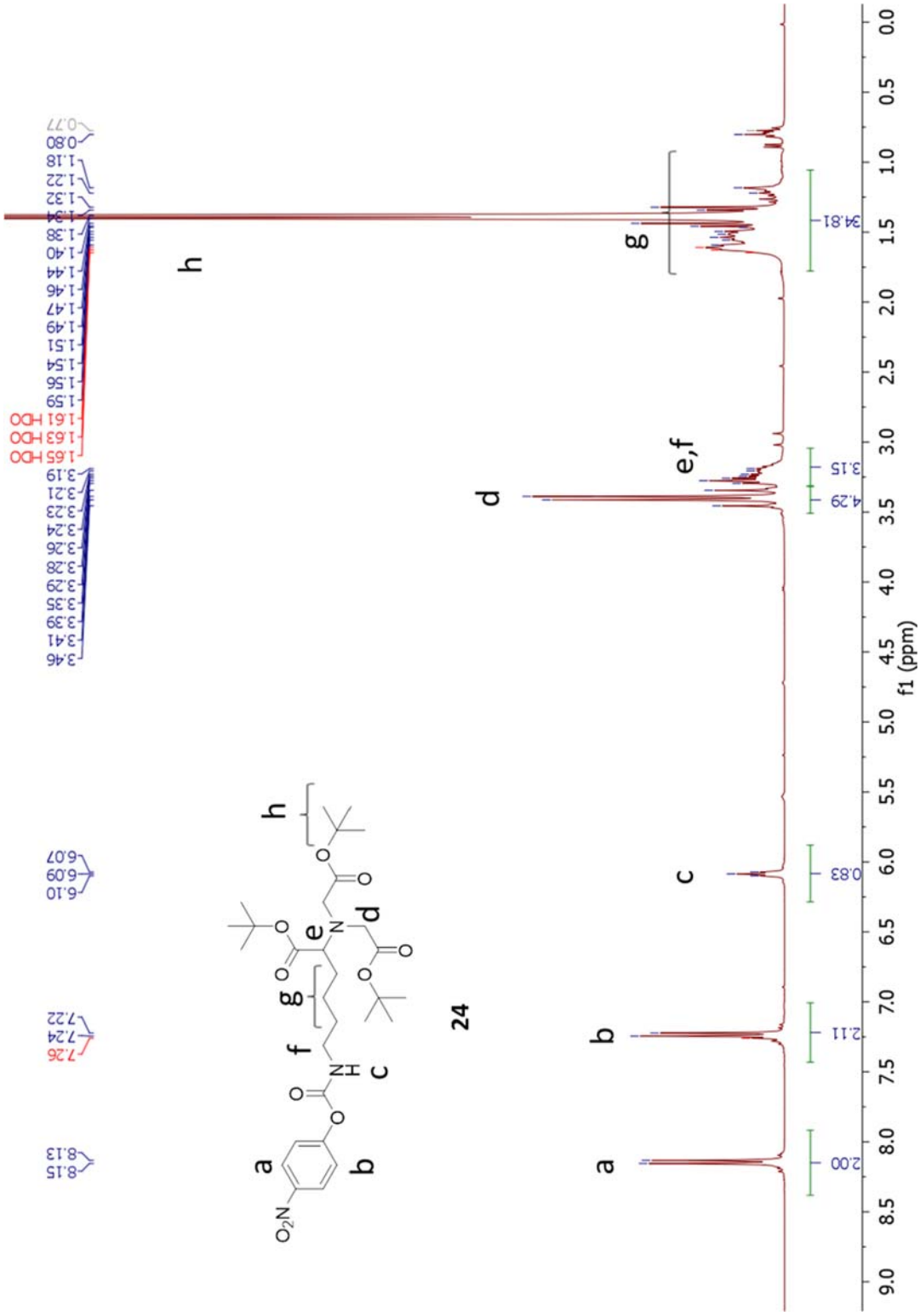

Figure A.23 ^{1}H-NMR of **24**

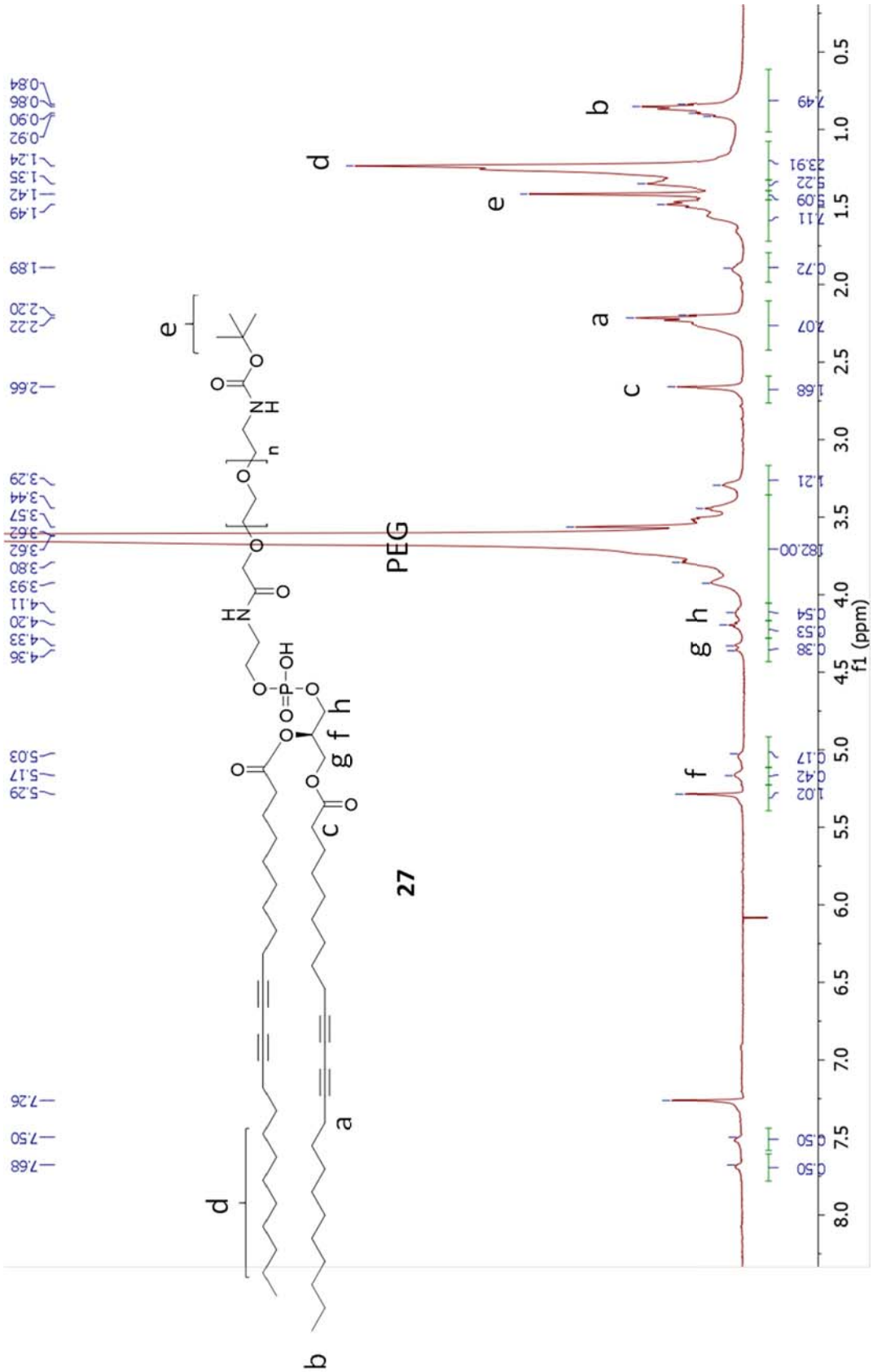

Figure A.24 ^{1}H-NMR of **27**

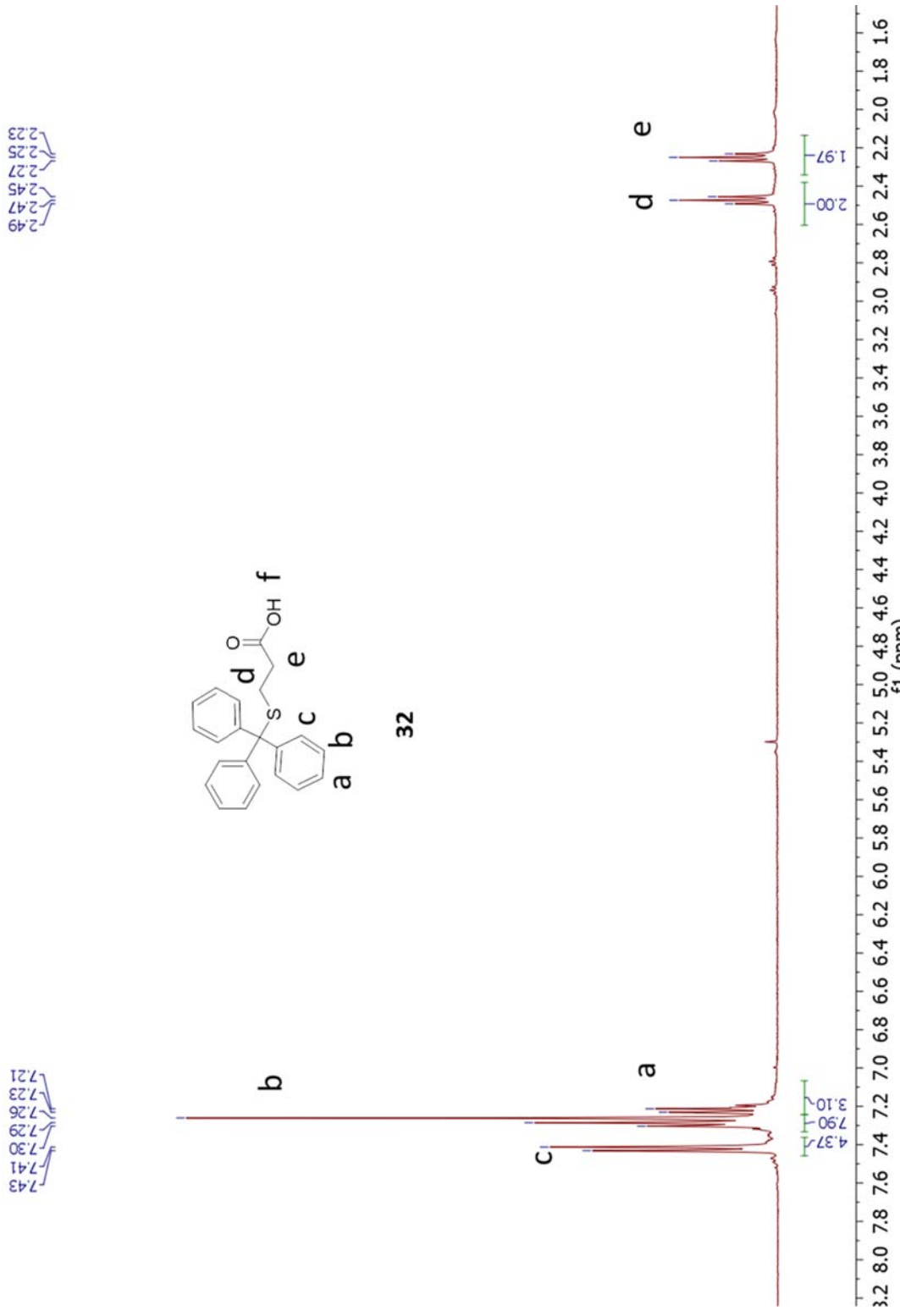

Figure A.25 ^{1}H-NMR of **32**

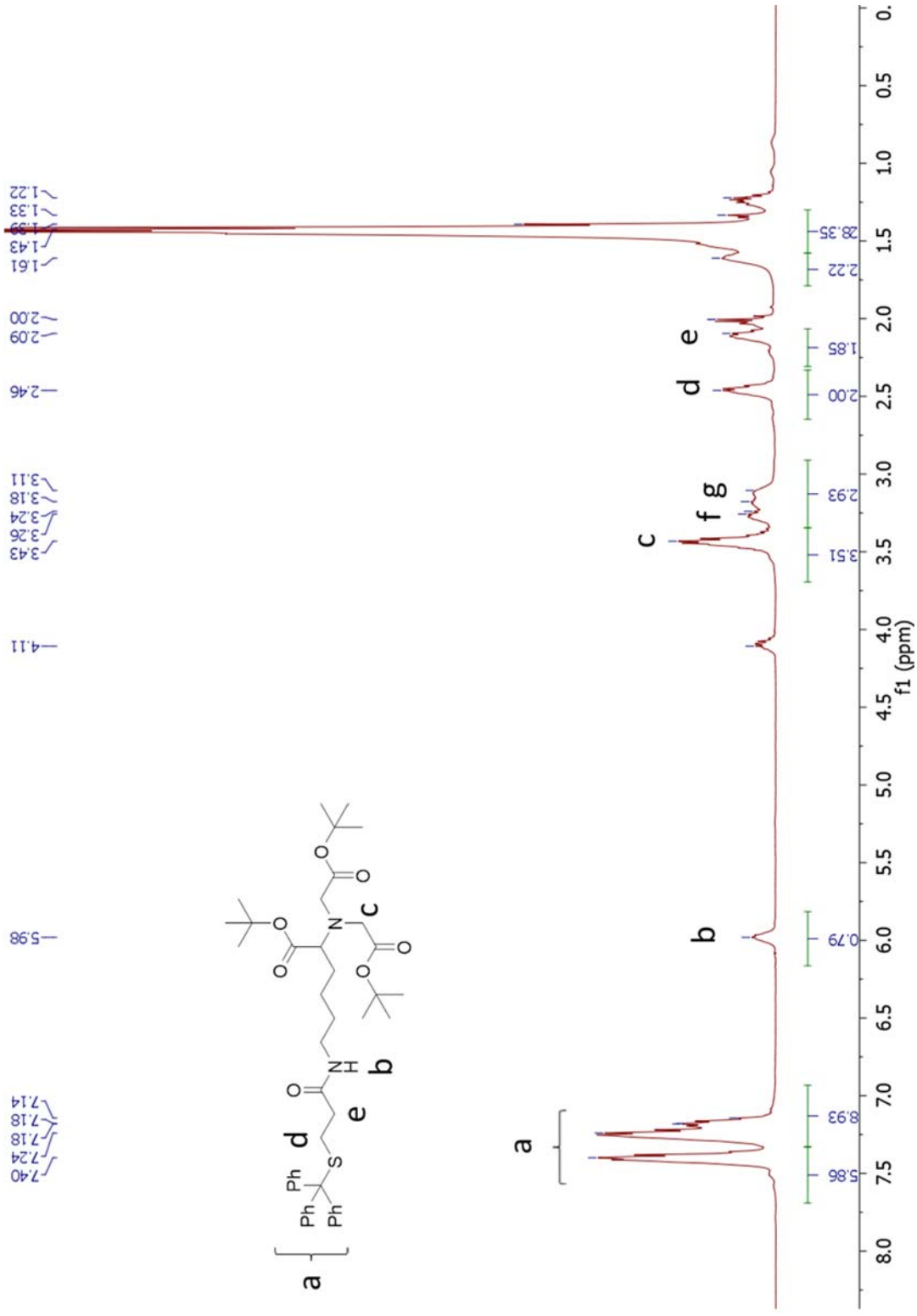

Figure A.26 ^{1}H-NMR of **33**

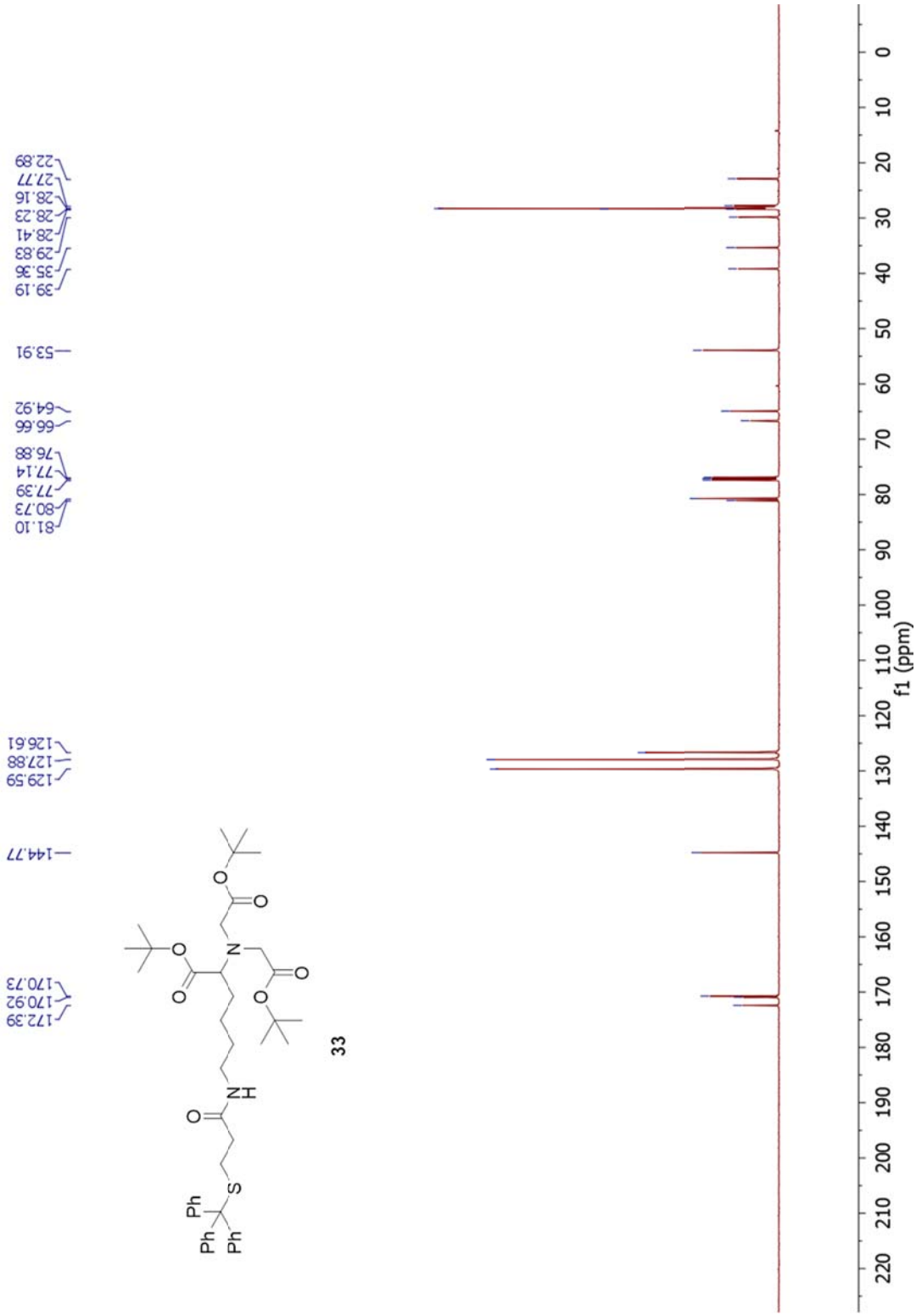

Figure A.27 ^{13}C-NMR of **33**

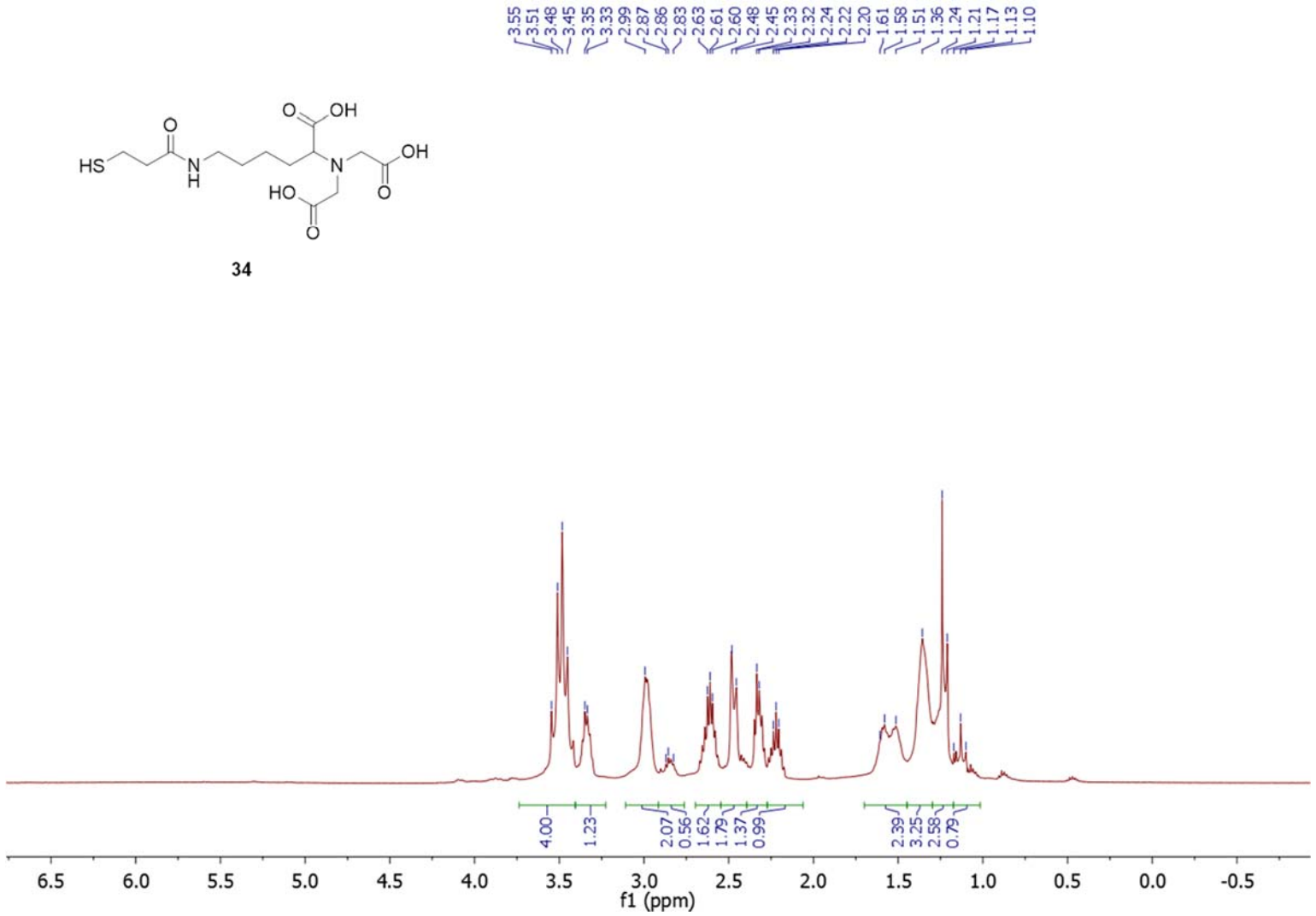

34

Figure A.28 ^{1}H-NMR of **34**

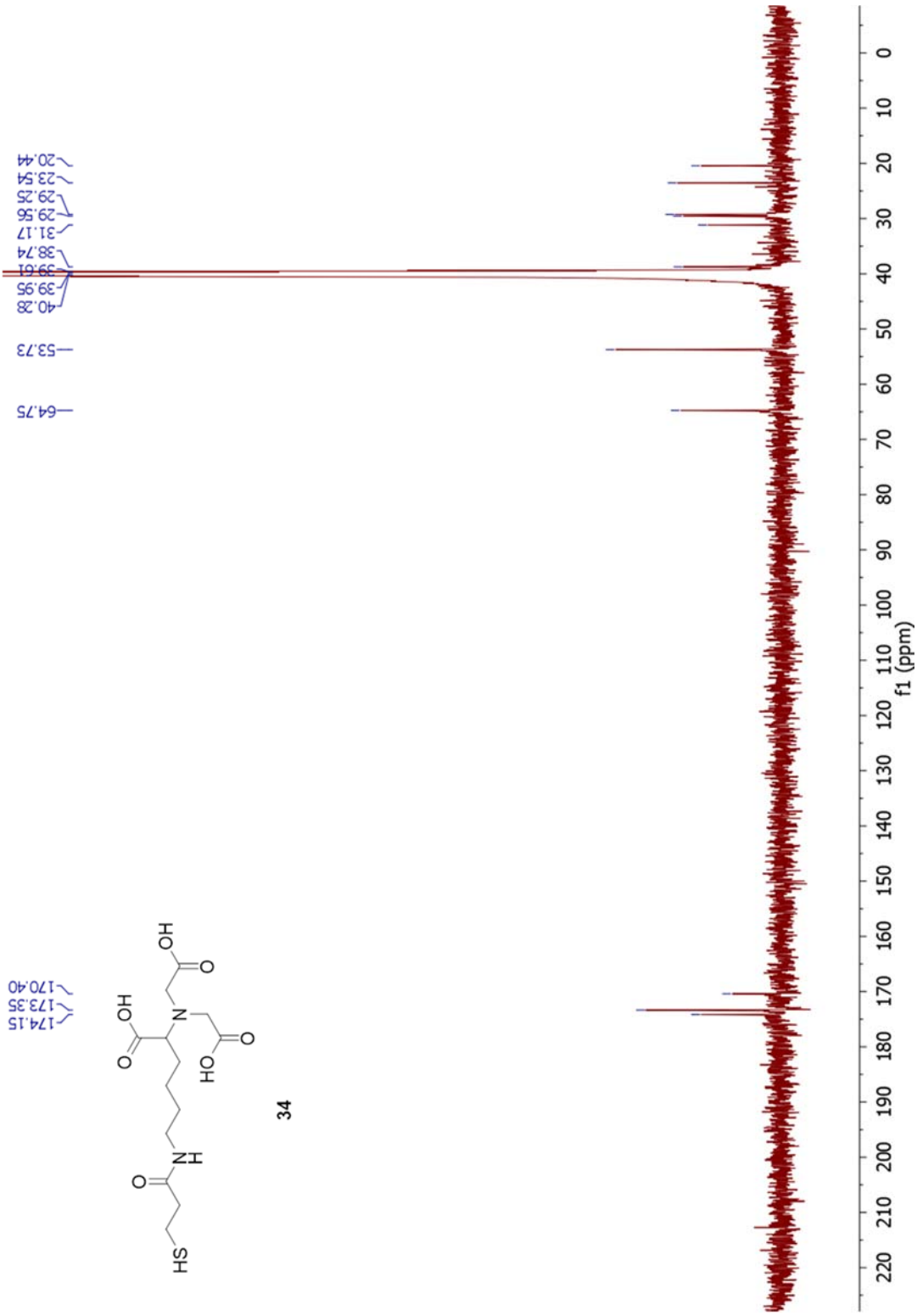

Figure A.29 ^{13}C-NMR of **34**

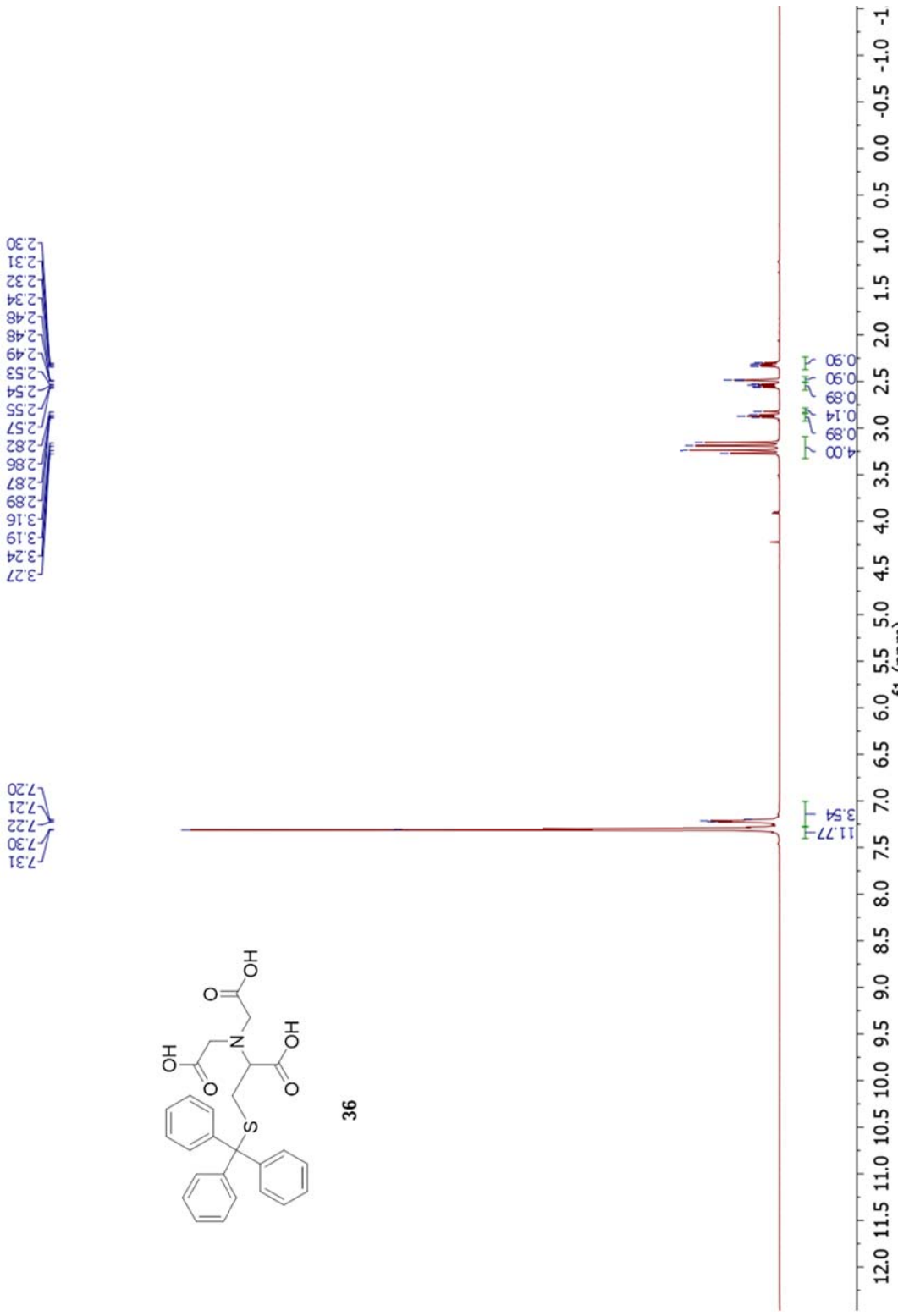

Figure A.30 ^{1}H-NMR of **36**

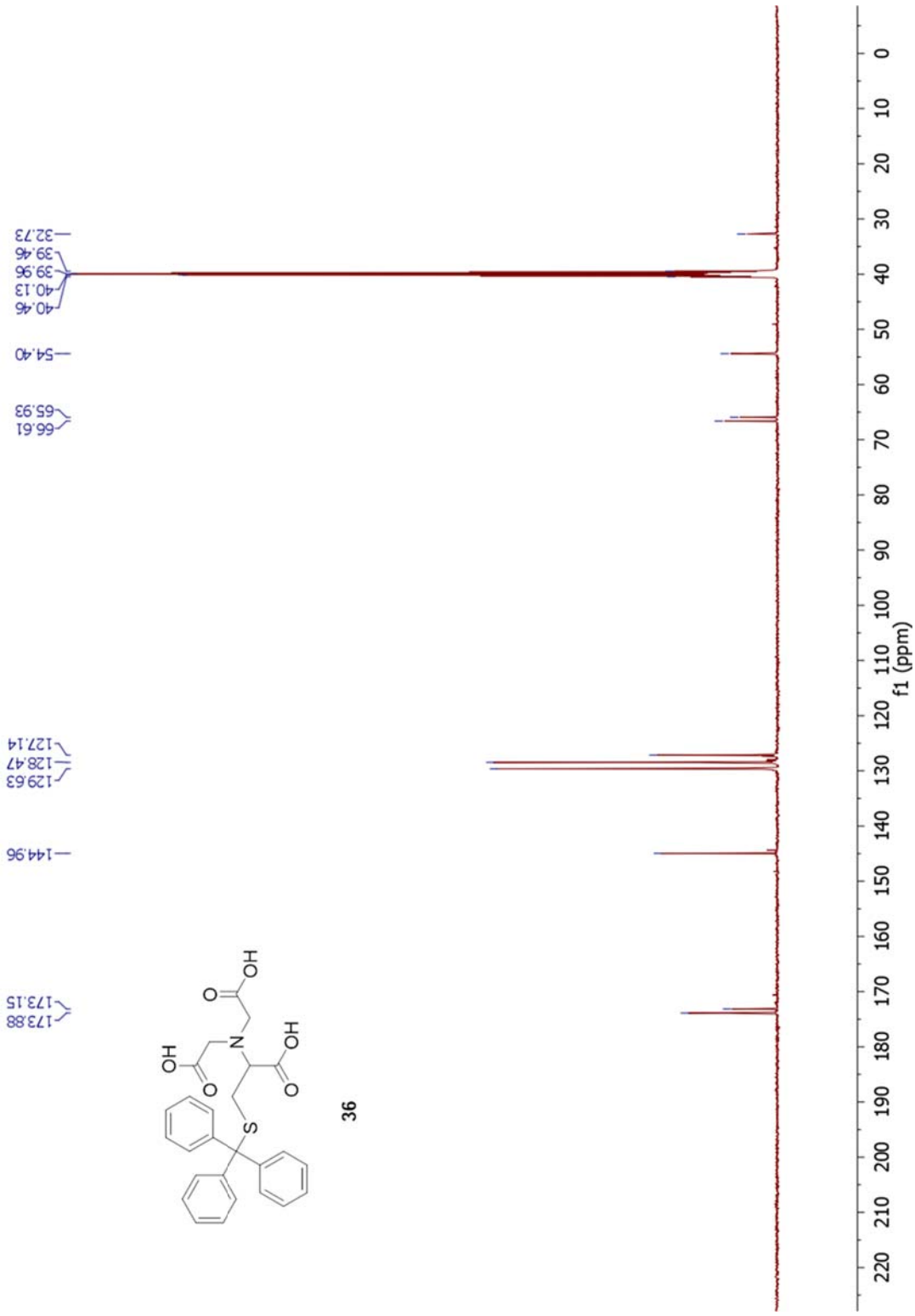

Figure A.31 ^{13}C-NMR of **36**

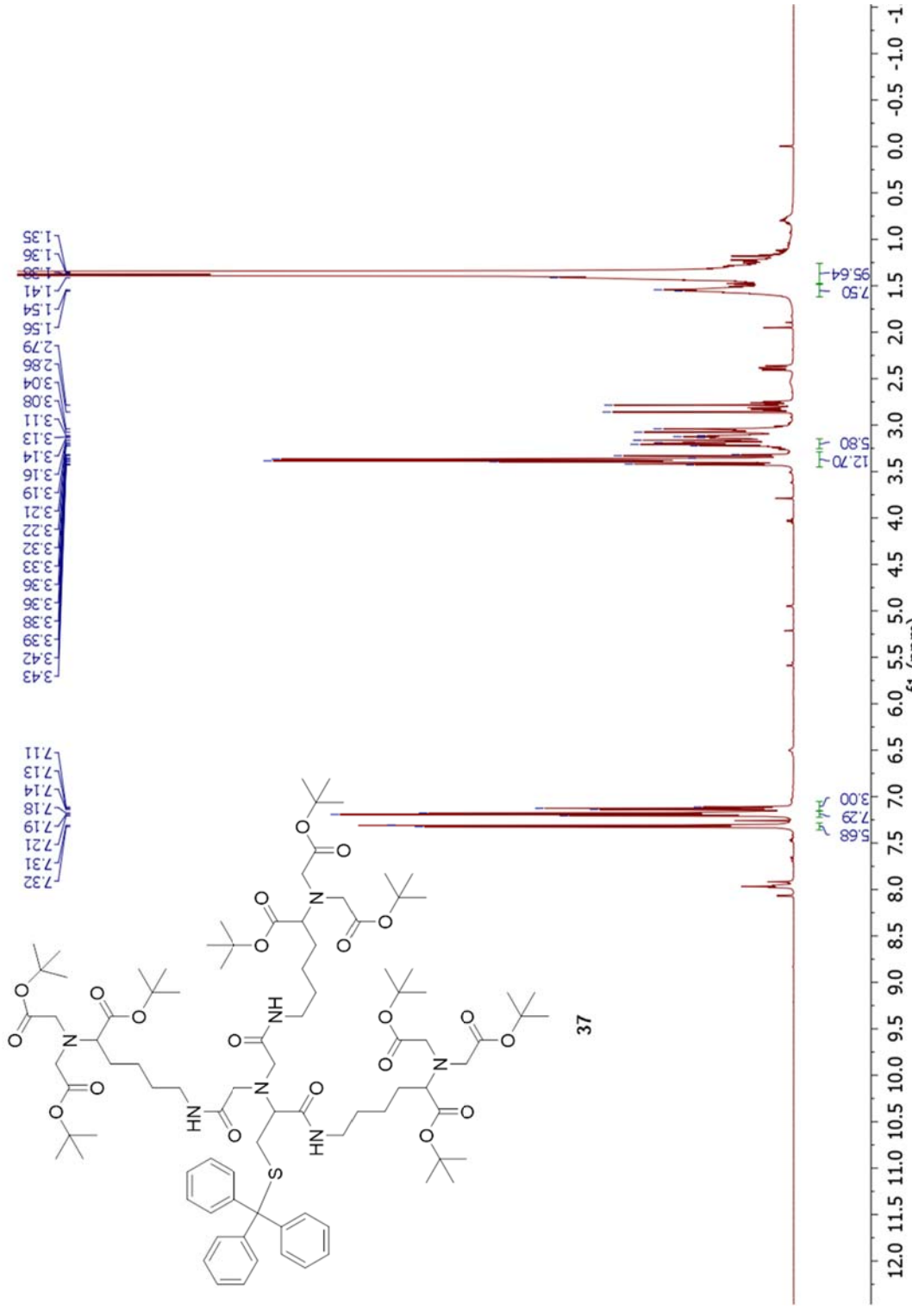

Figure A.32 ^{1}H-NMR of **37**

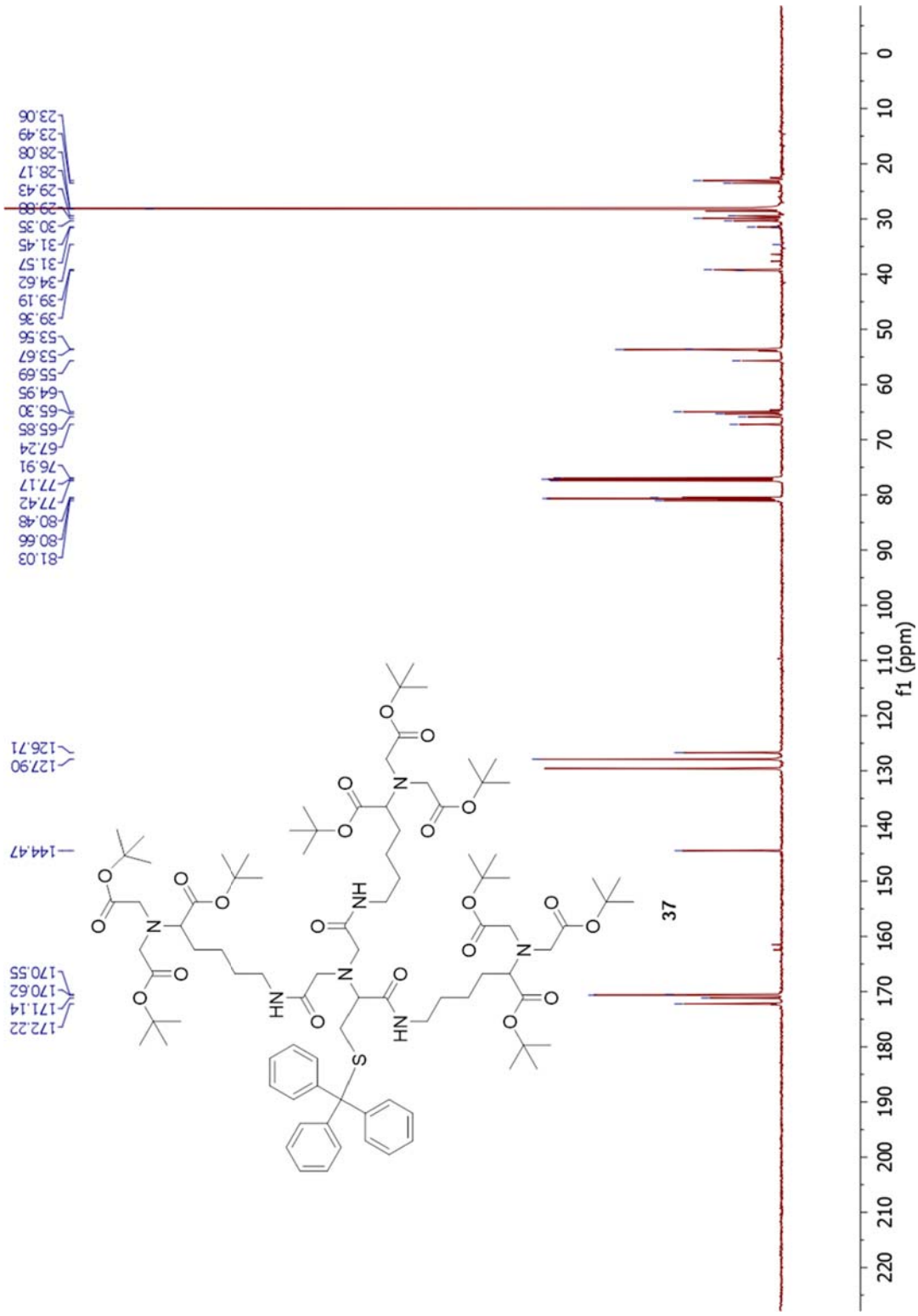

Figure A.33 ^{13}C-NMR of **37**

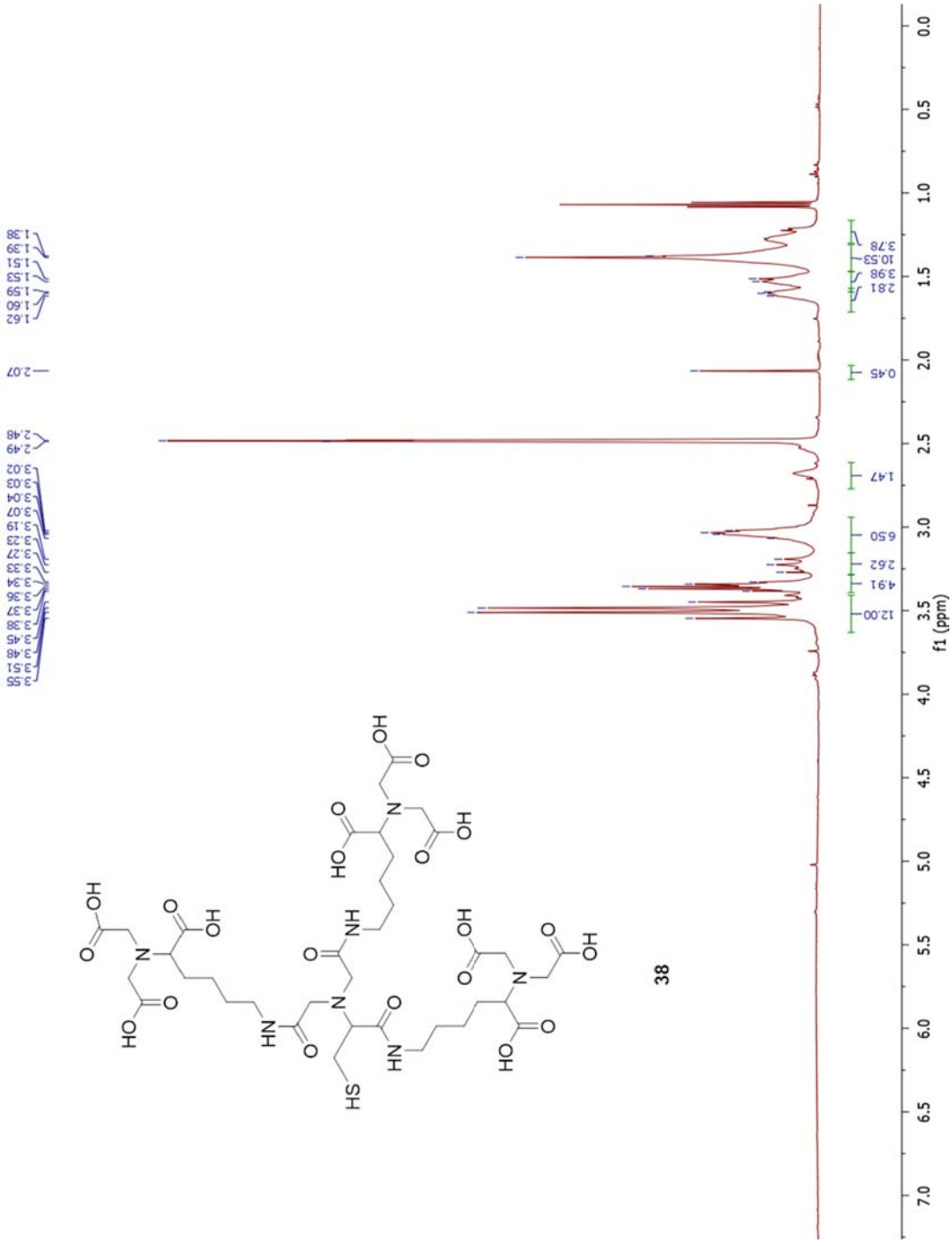

Figure A.34 ^{1}H-NMR of **38**

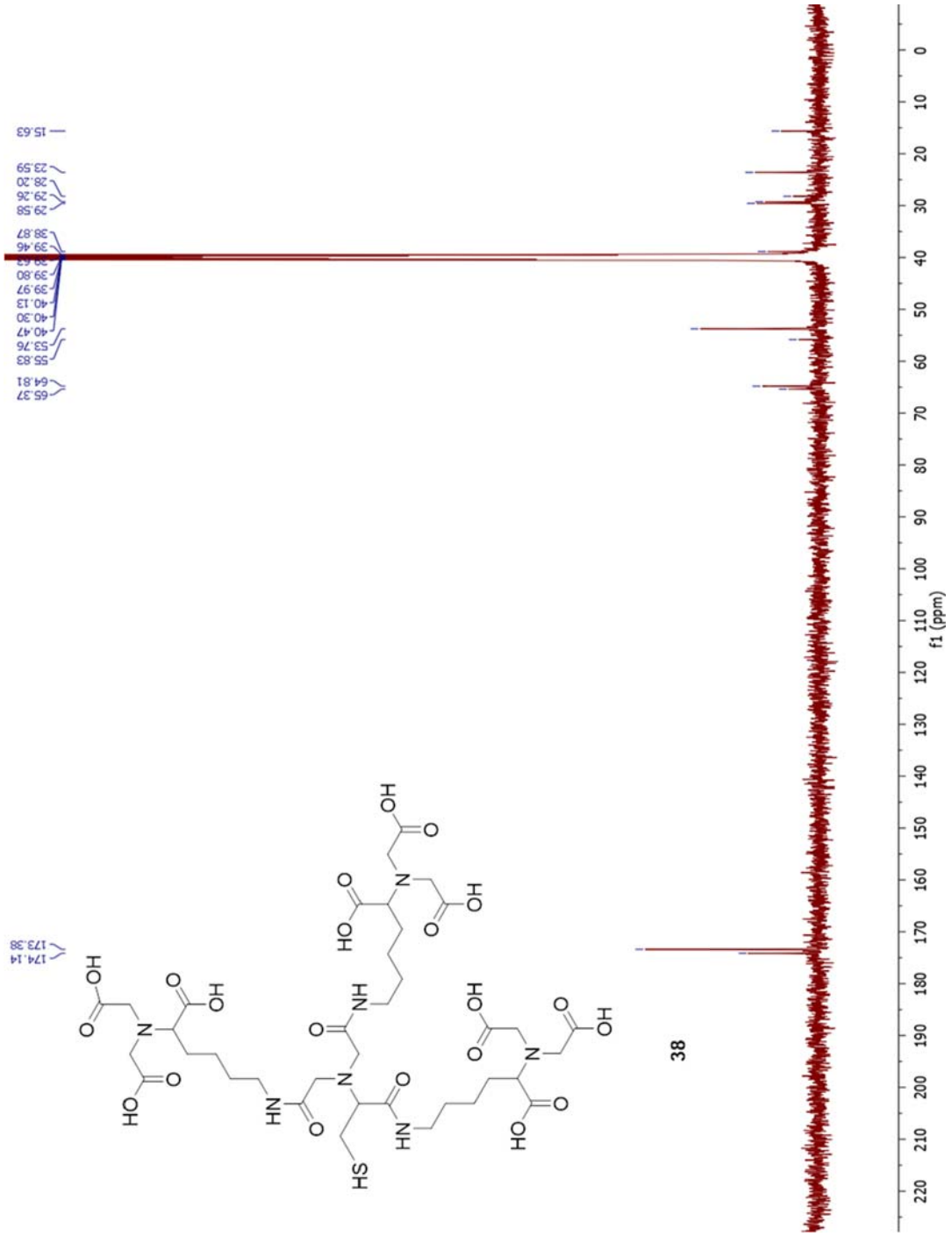

Figure A.35 ^{13}C-NMR of **38**

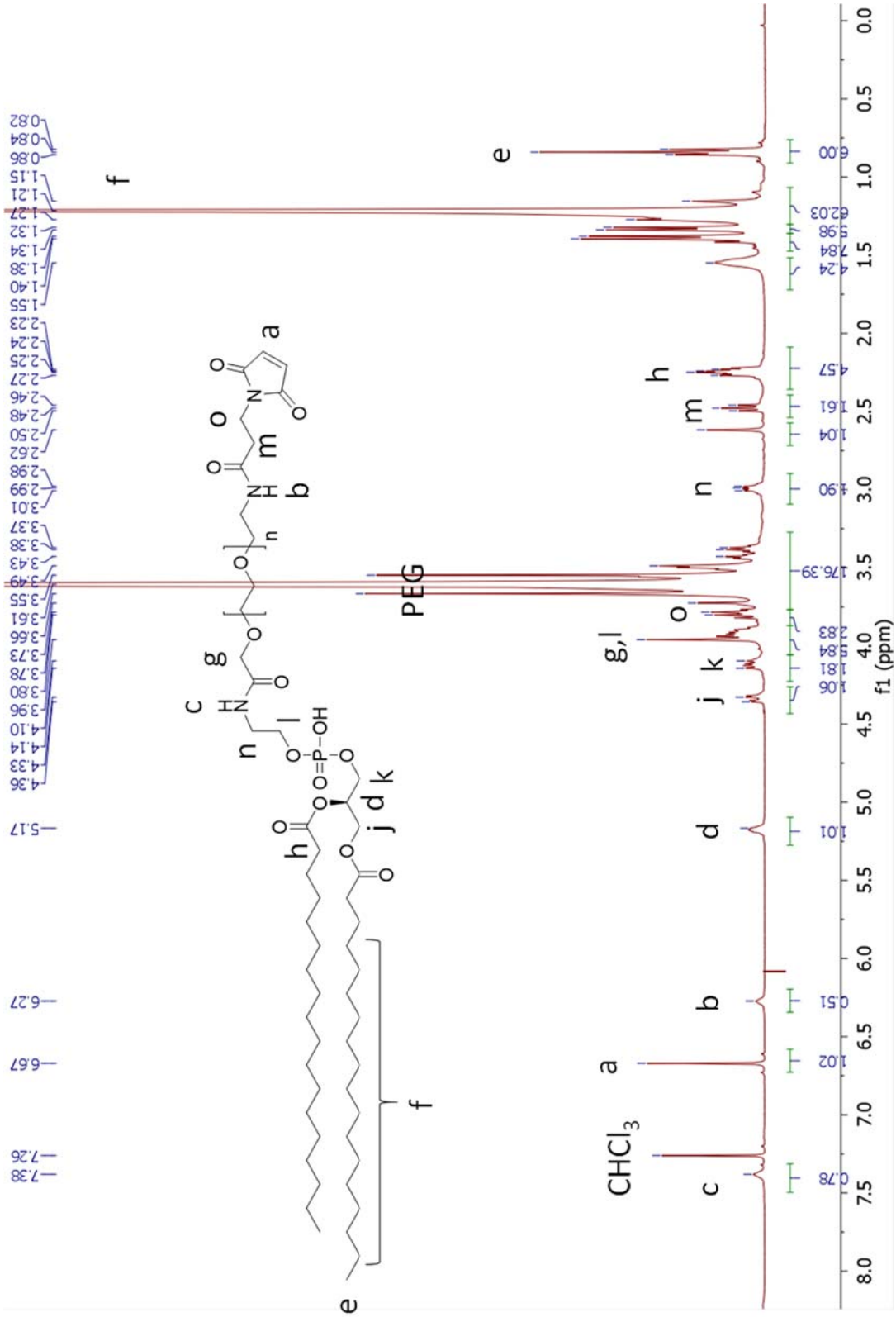

Figure A.36 ^{1}H-NMR of **40a**

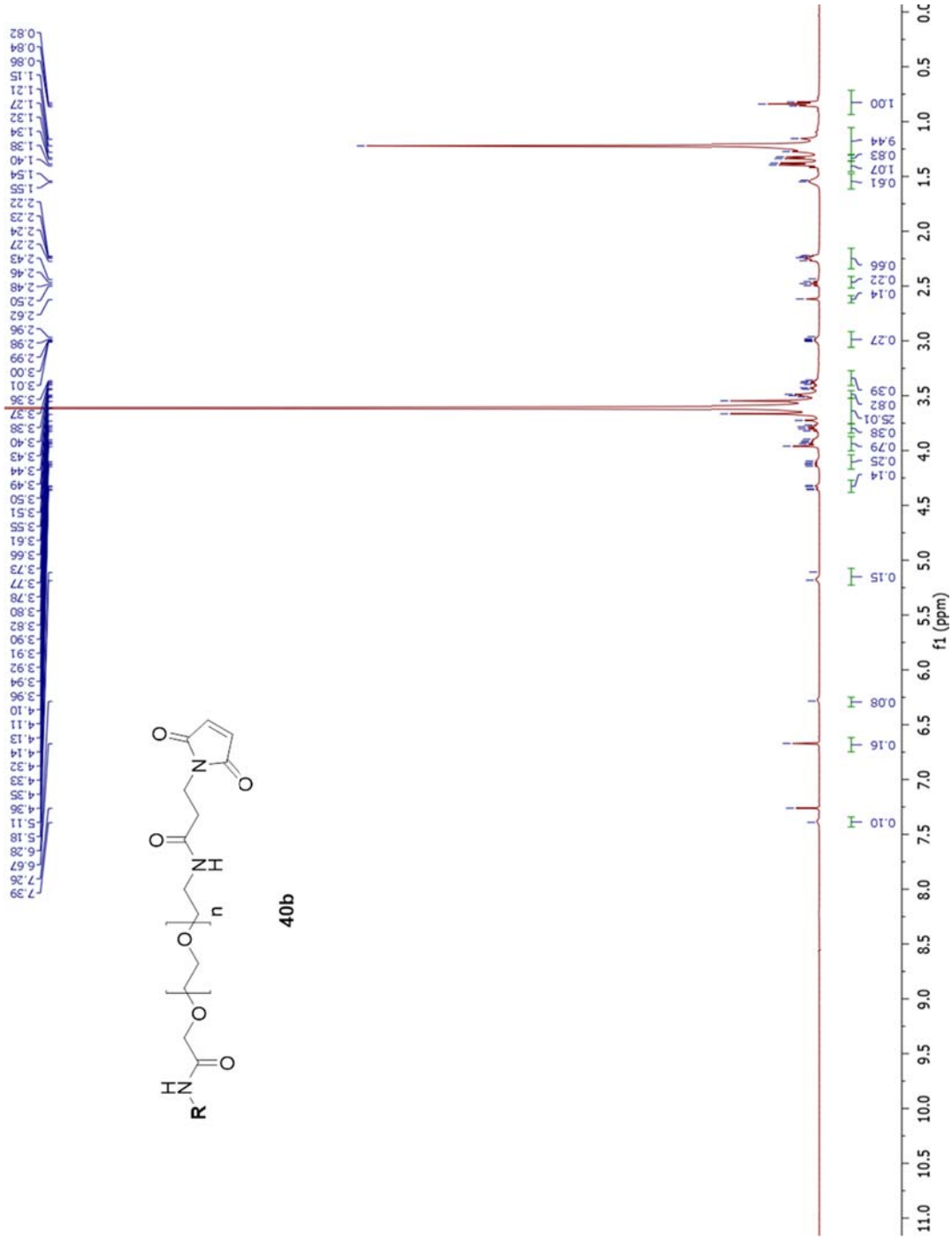

Figure A.37 ^{1}H-NMR of **40b**

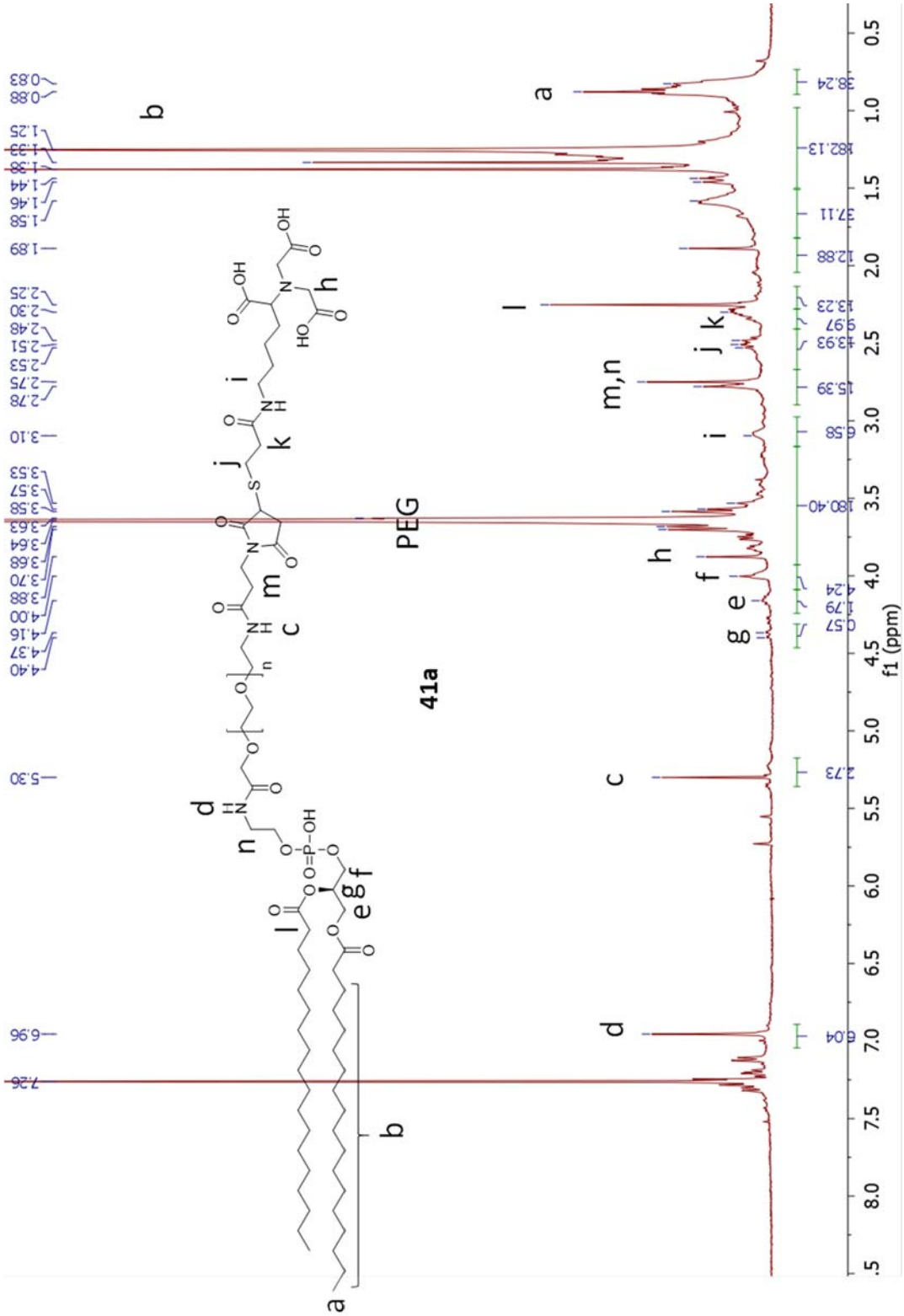

Figure A.38 ^{1}H-NMR of **41a**

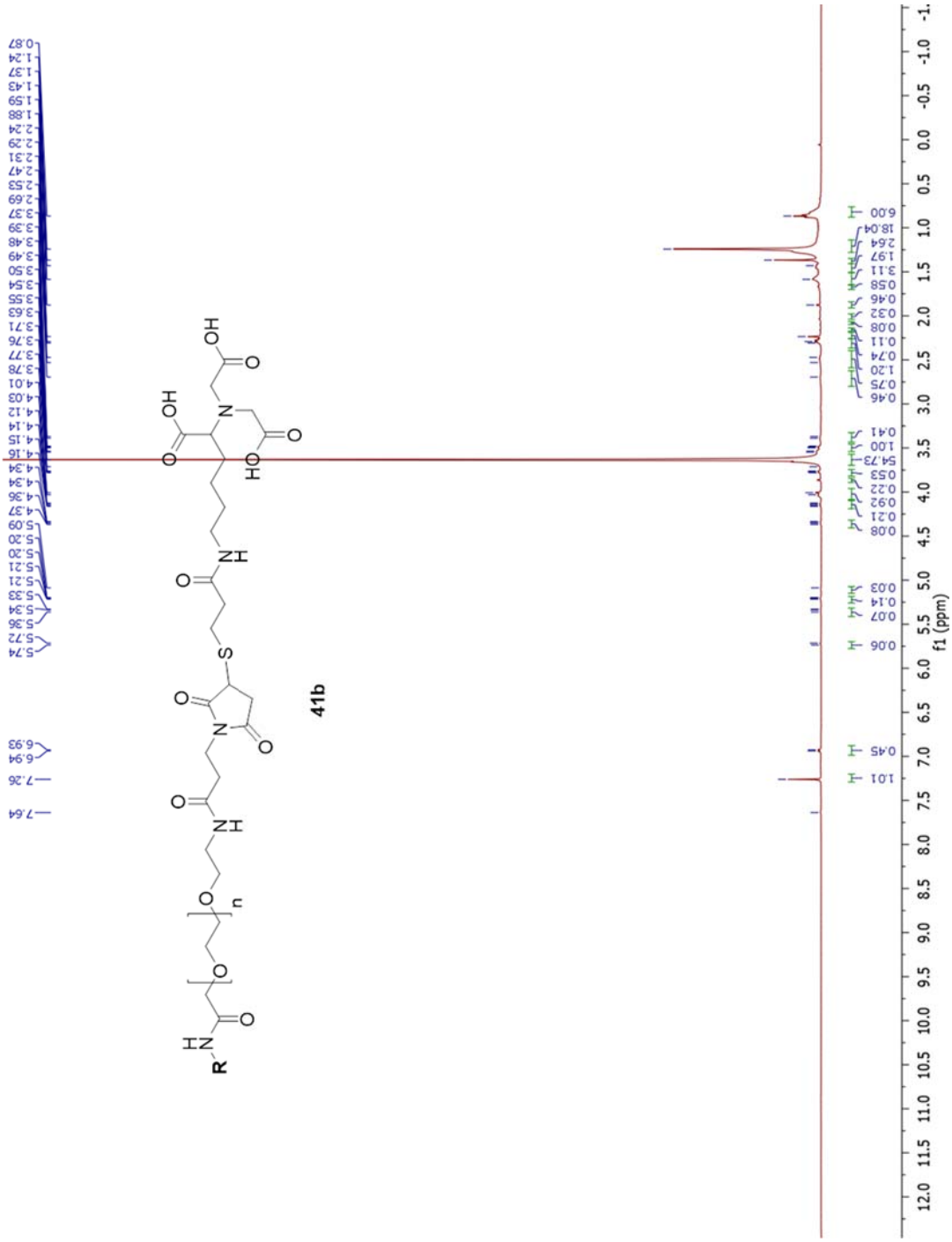

Figure A.39 ^{1}H-NMR of **41b**

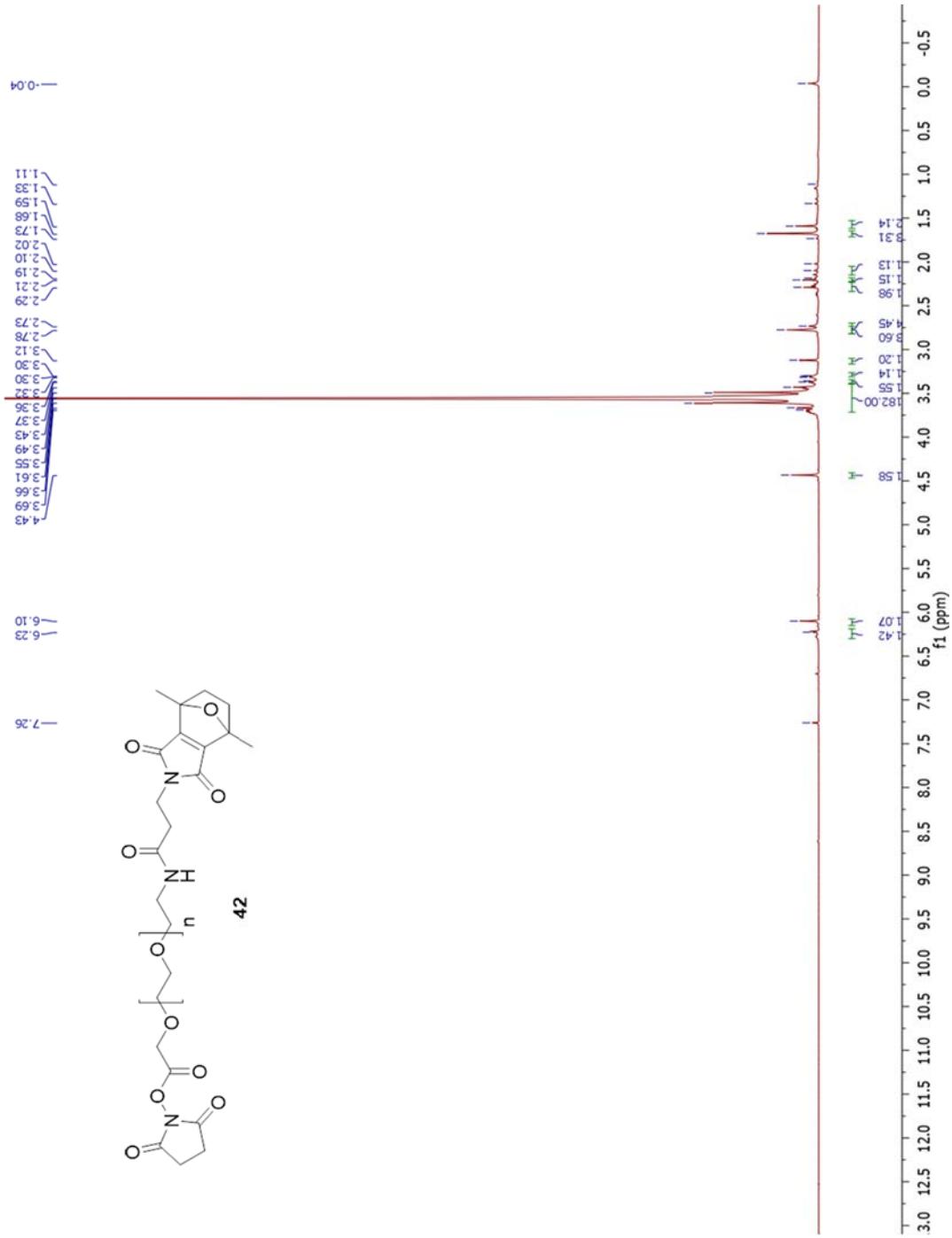

Figure A.40 ^{1}H-NMR of **42**

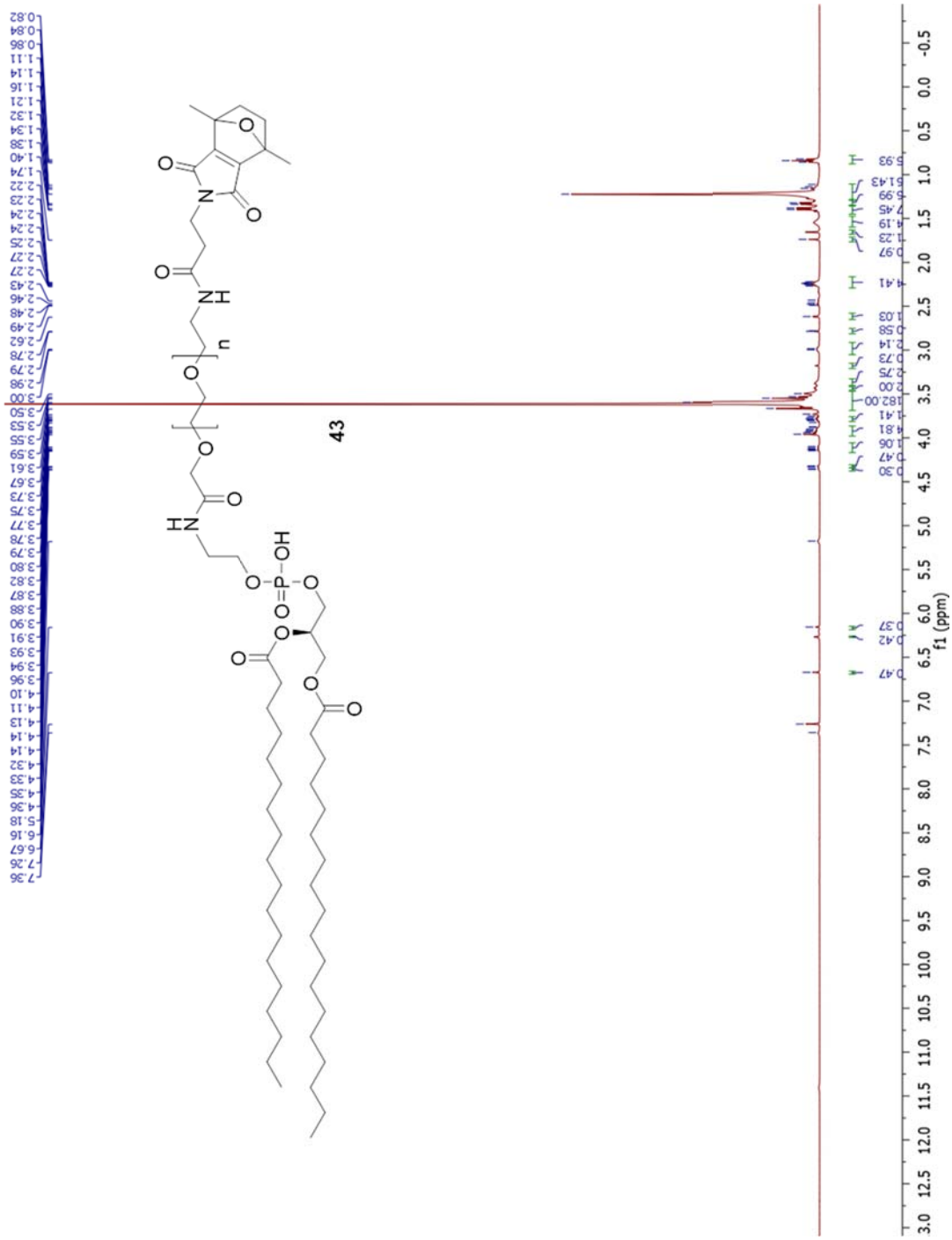

Figure A.41 ^{1}H-NMR of **43**

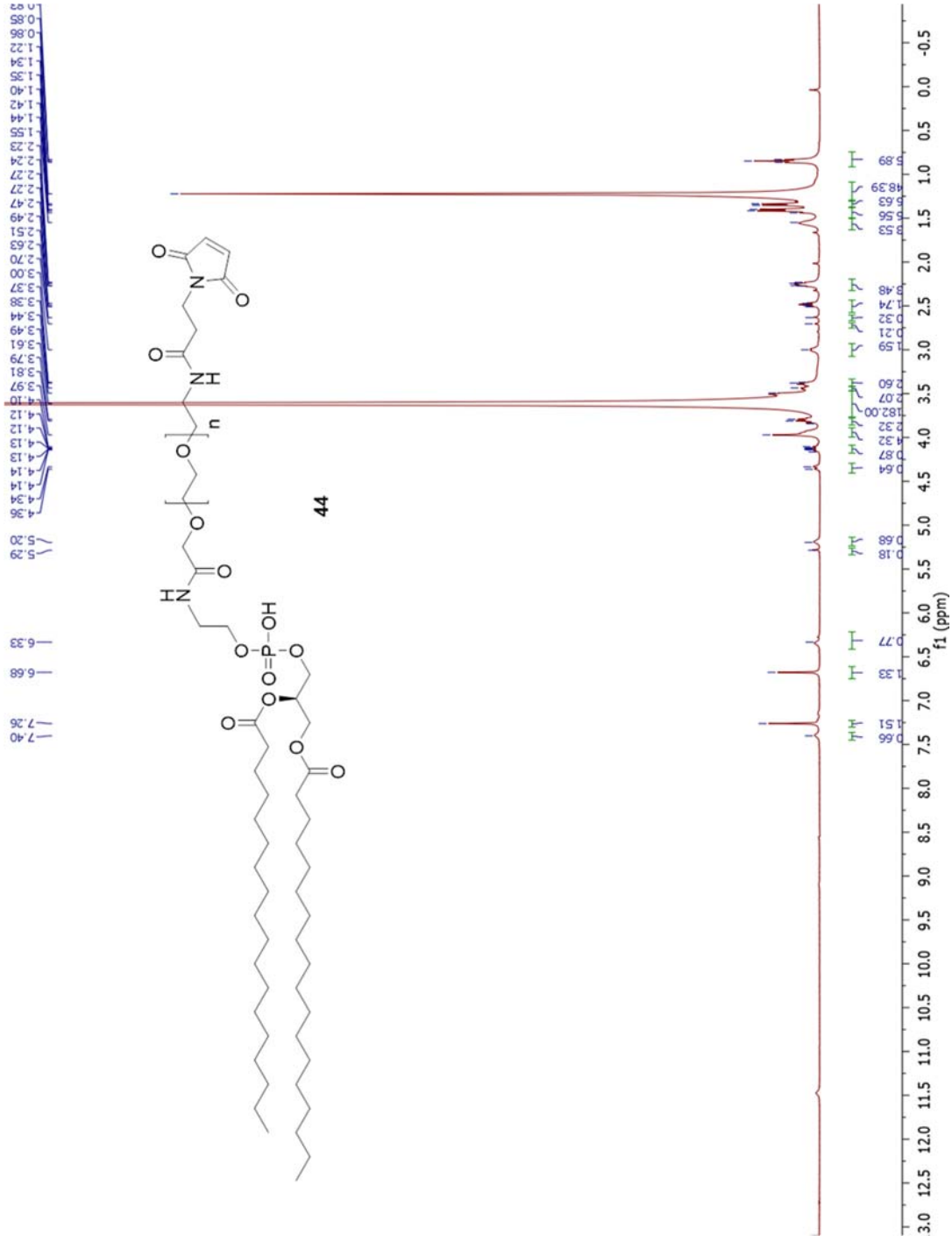

Figure A.42 ^{1}H-NMR of **44**

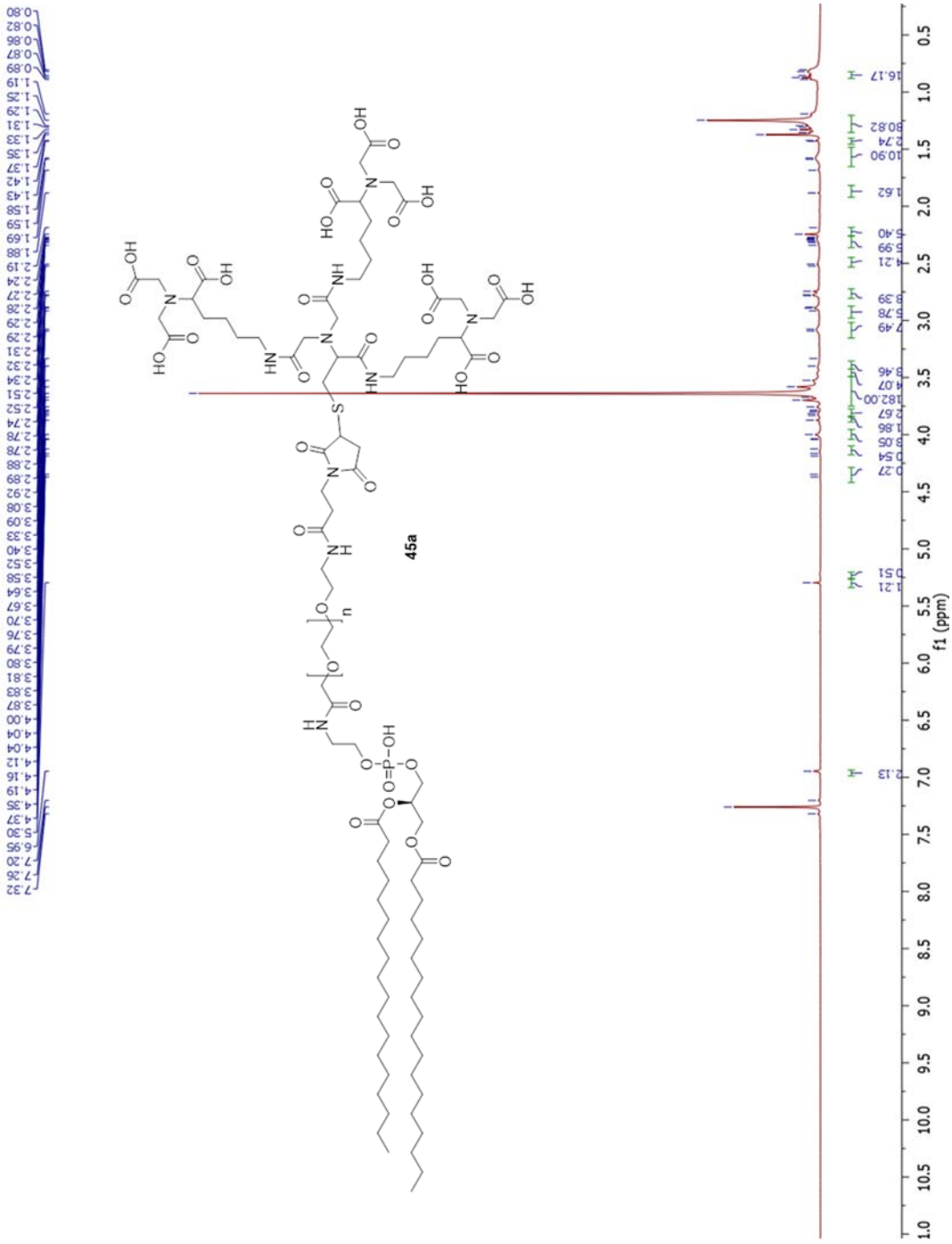

Figure A.43 ^{1}H-NMR of **45a**

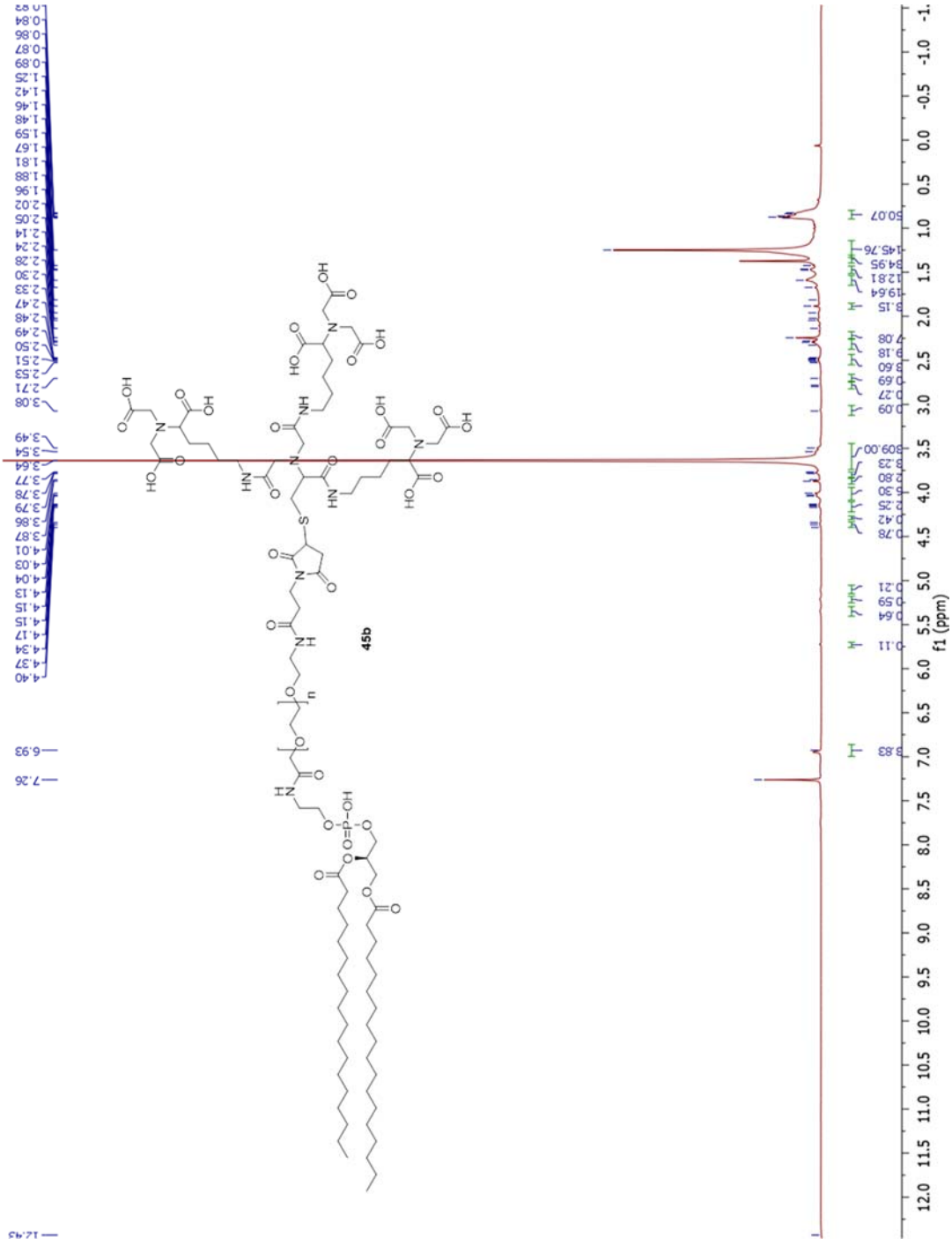

Figure A.44 ^{1}H-NMR of **45b**

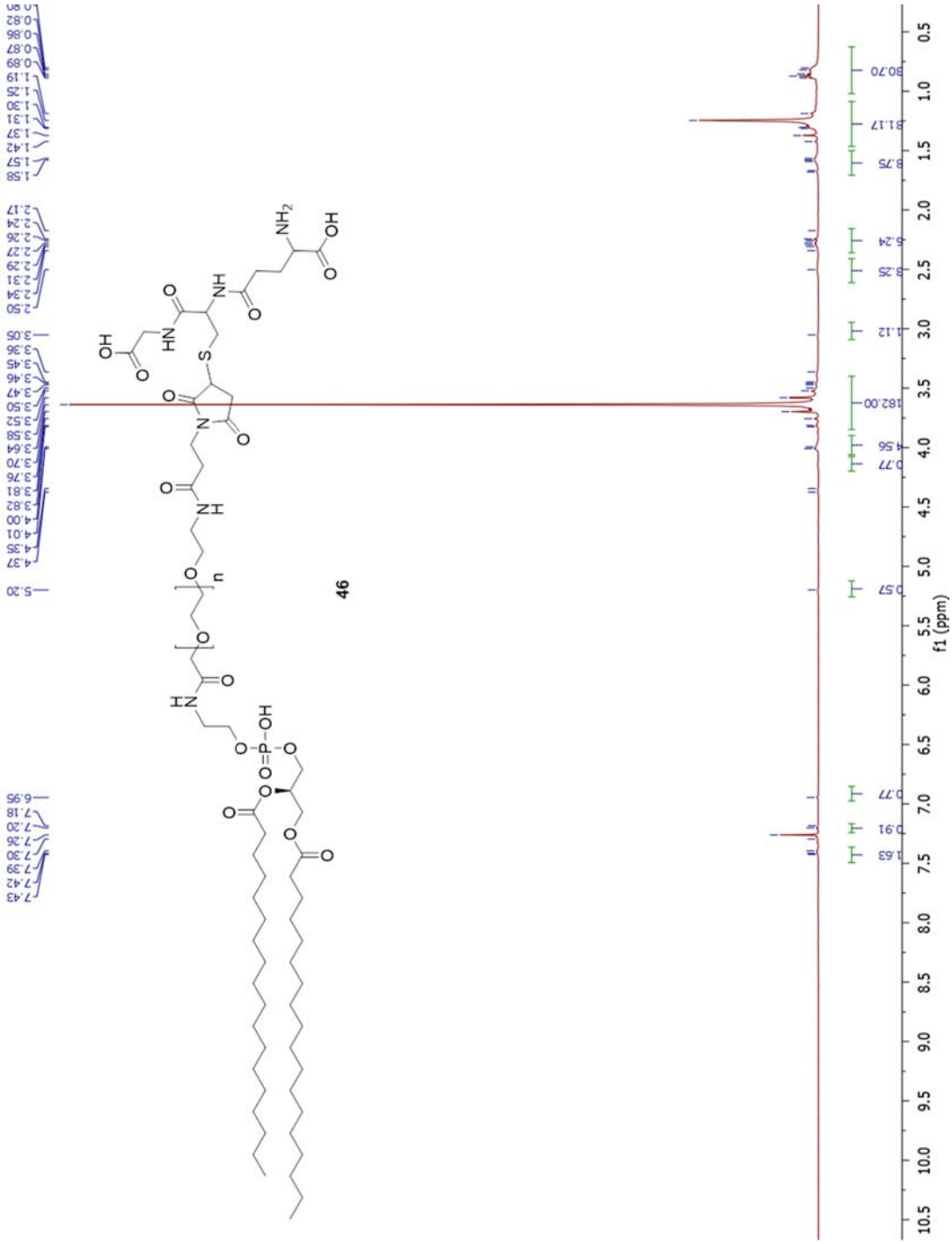

Figure A.45 ^{1}H-NMR of **46**

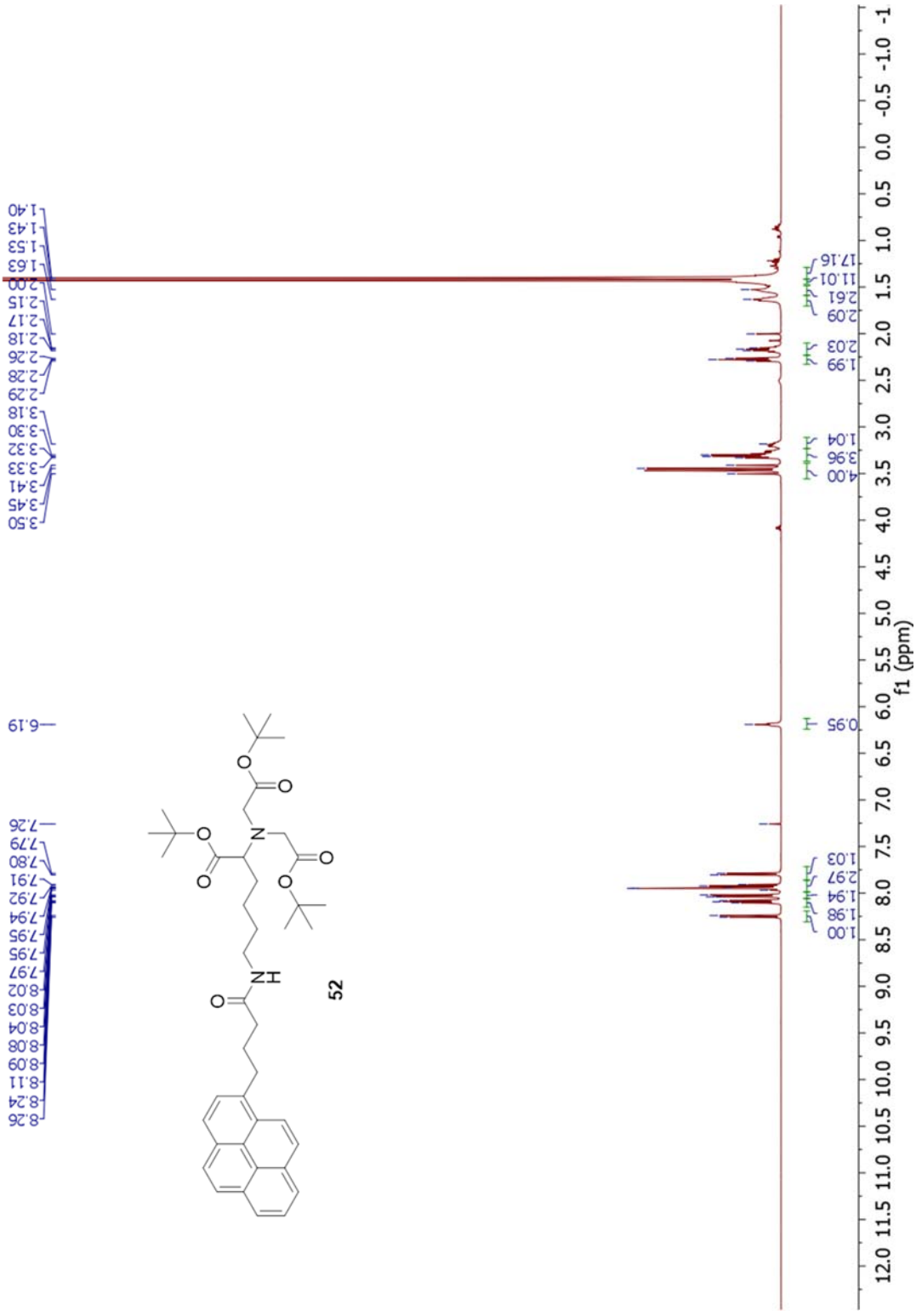

Figure A.46 ^{1}H-NMR of **52**

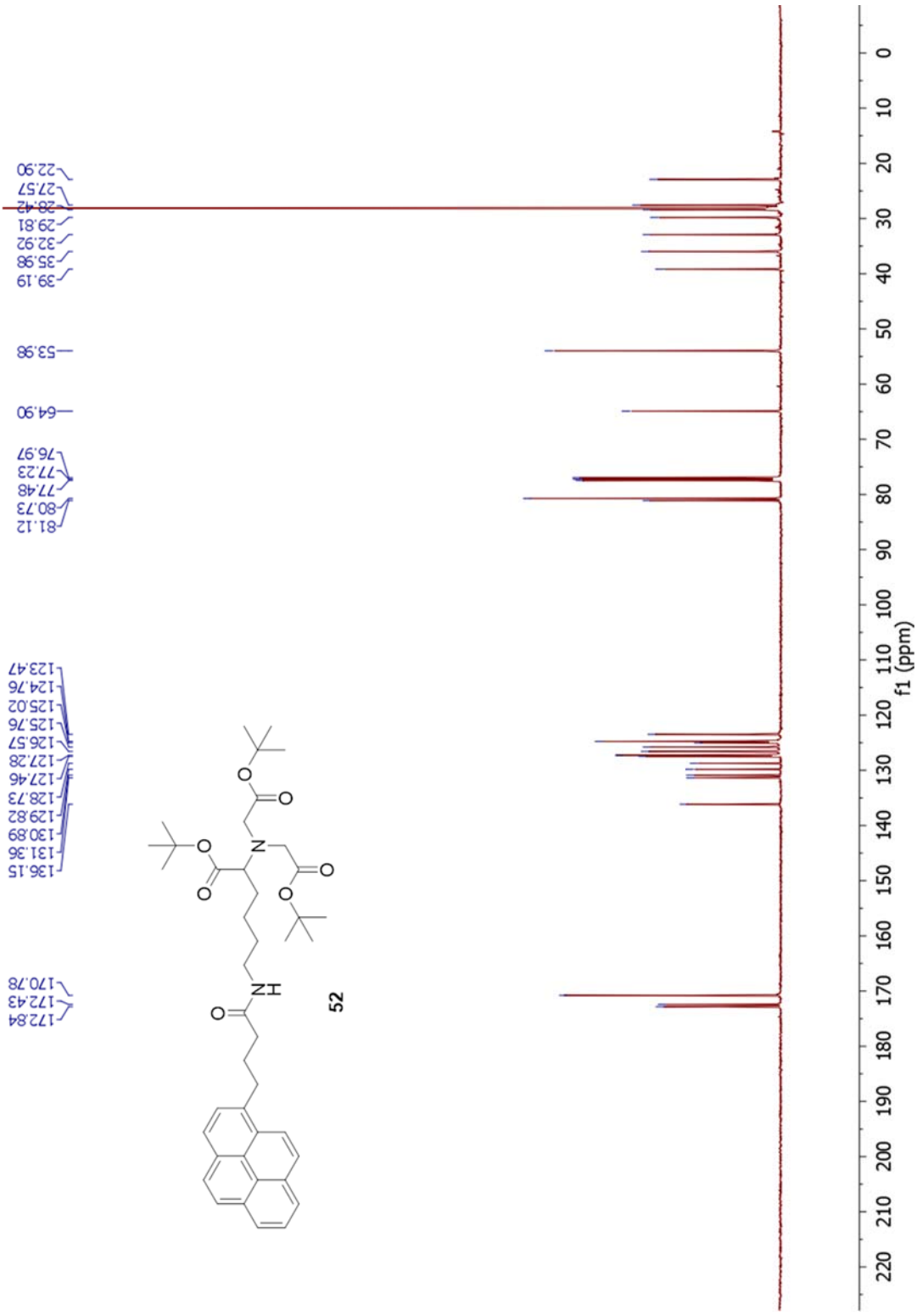

Figure A.47 ^{13}C-NMR of **52**

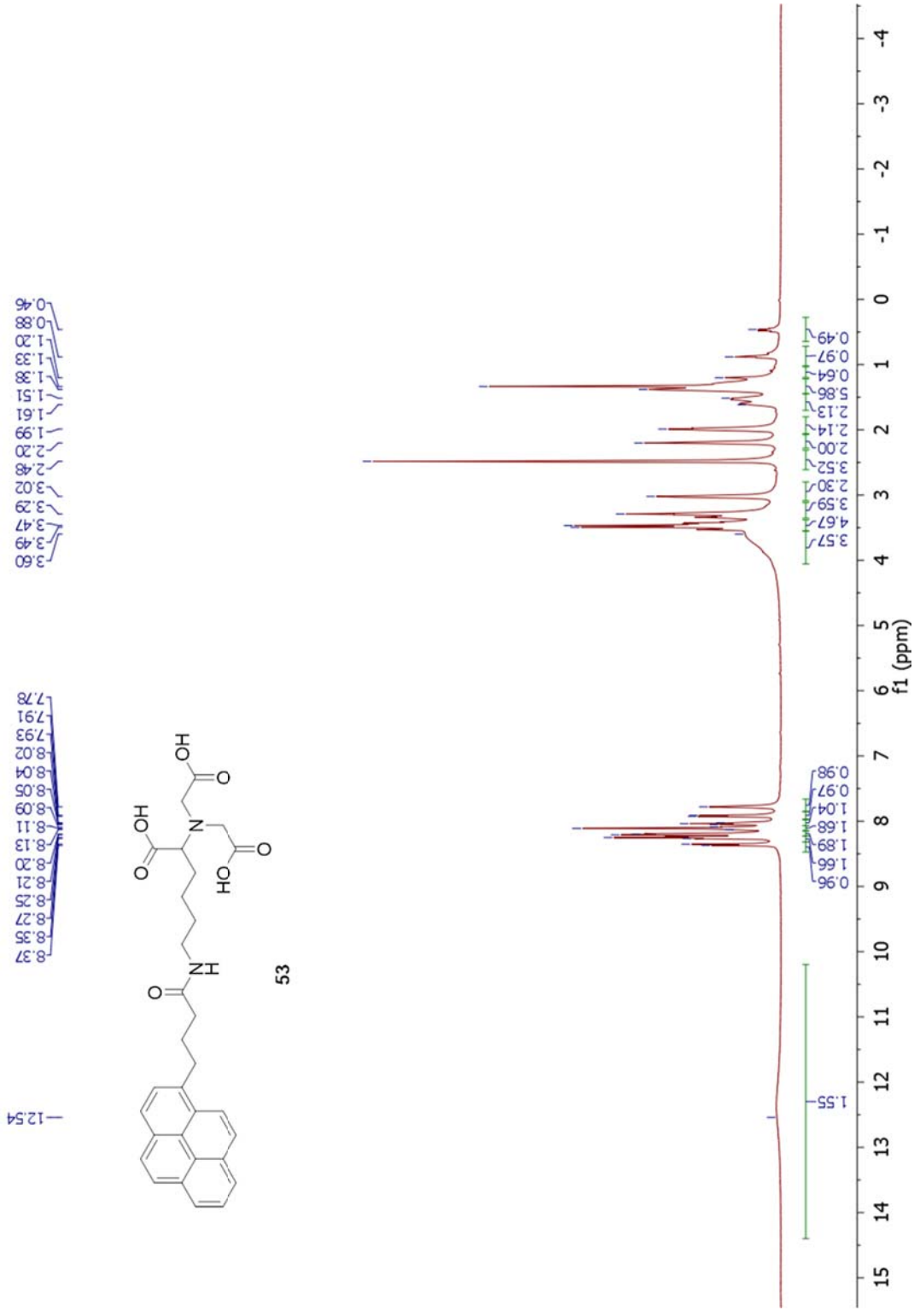

Figure A.48 ^{1}H-NMR of **53**

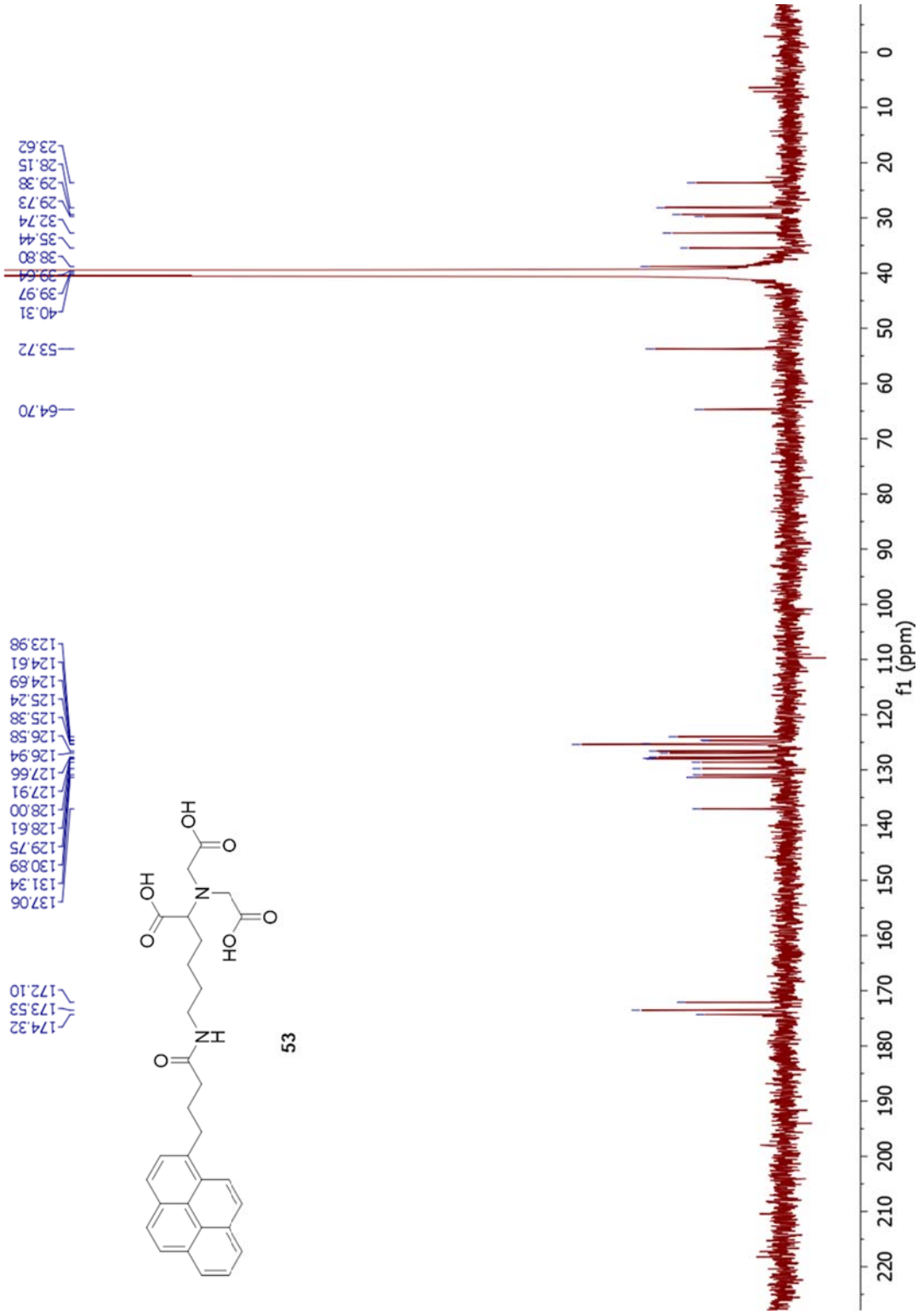

Figure A.49 ^{13}C-NMR of **53**

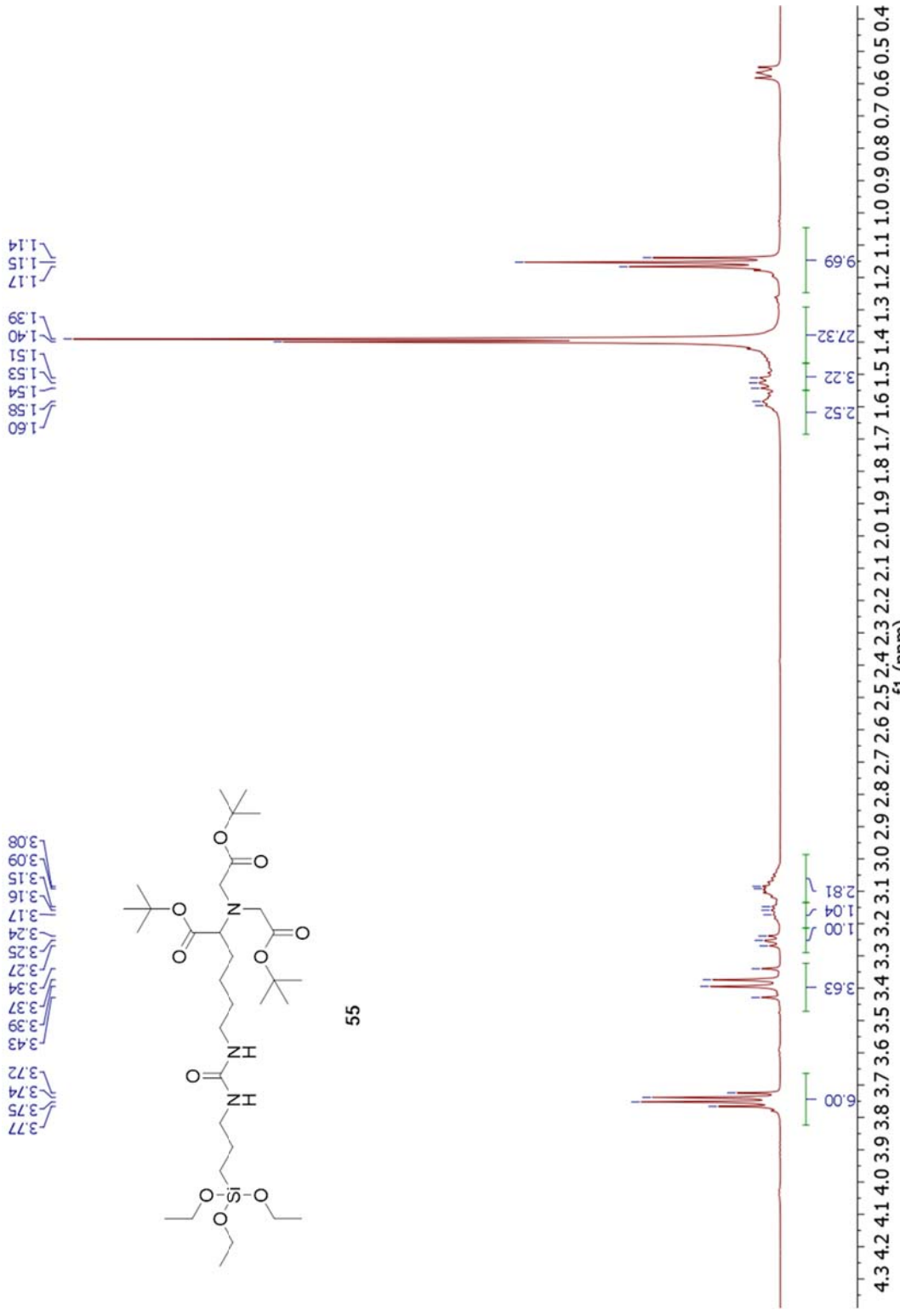

Figure A.50 ^{1}H-NMR of **55**

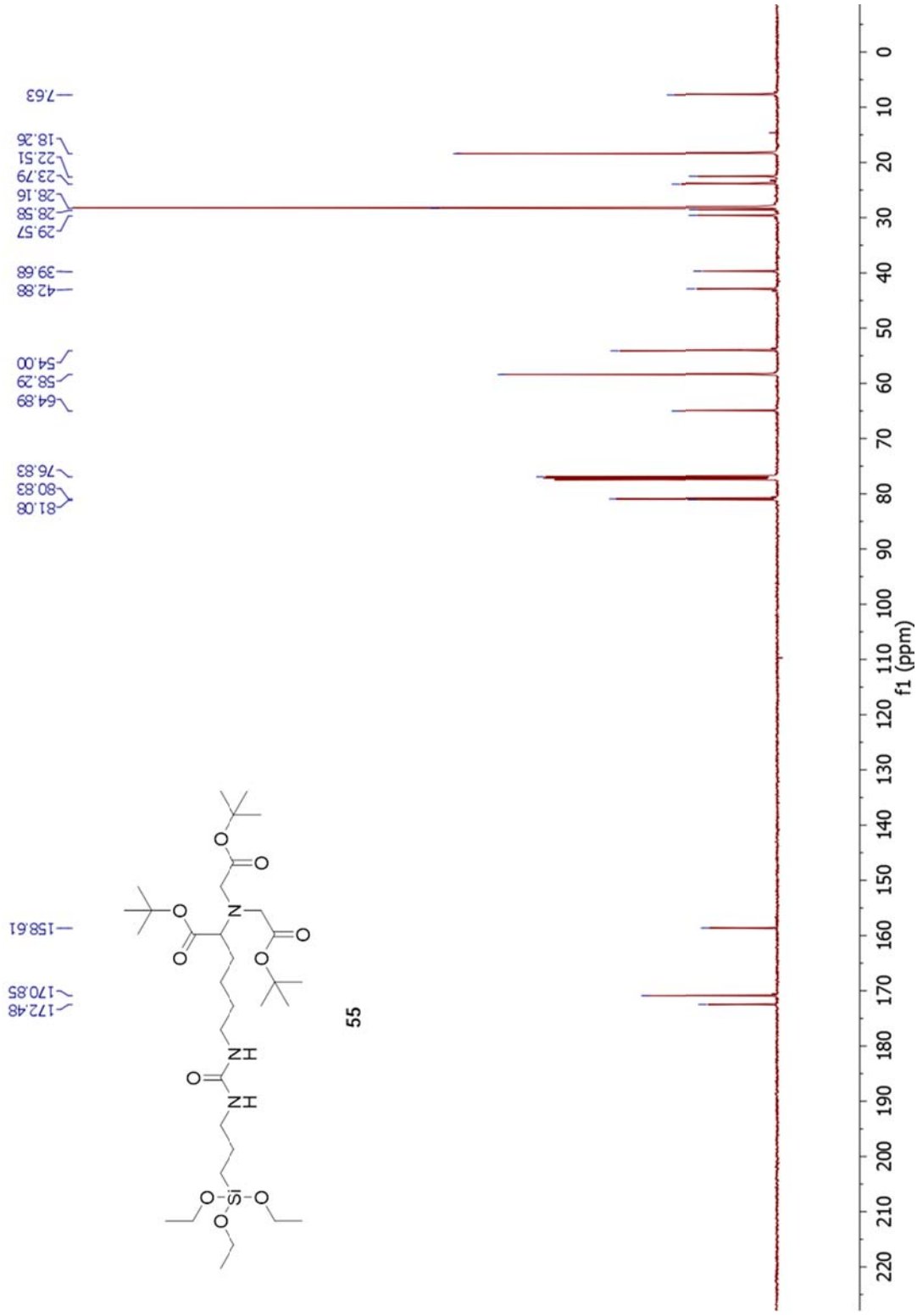

Figure A.51 ^{13}C-NMR of **55**

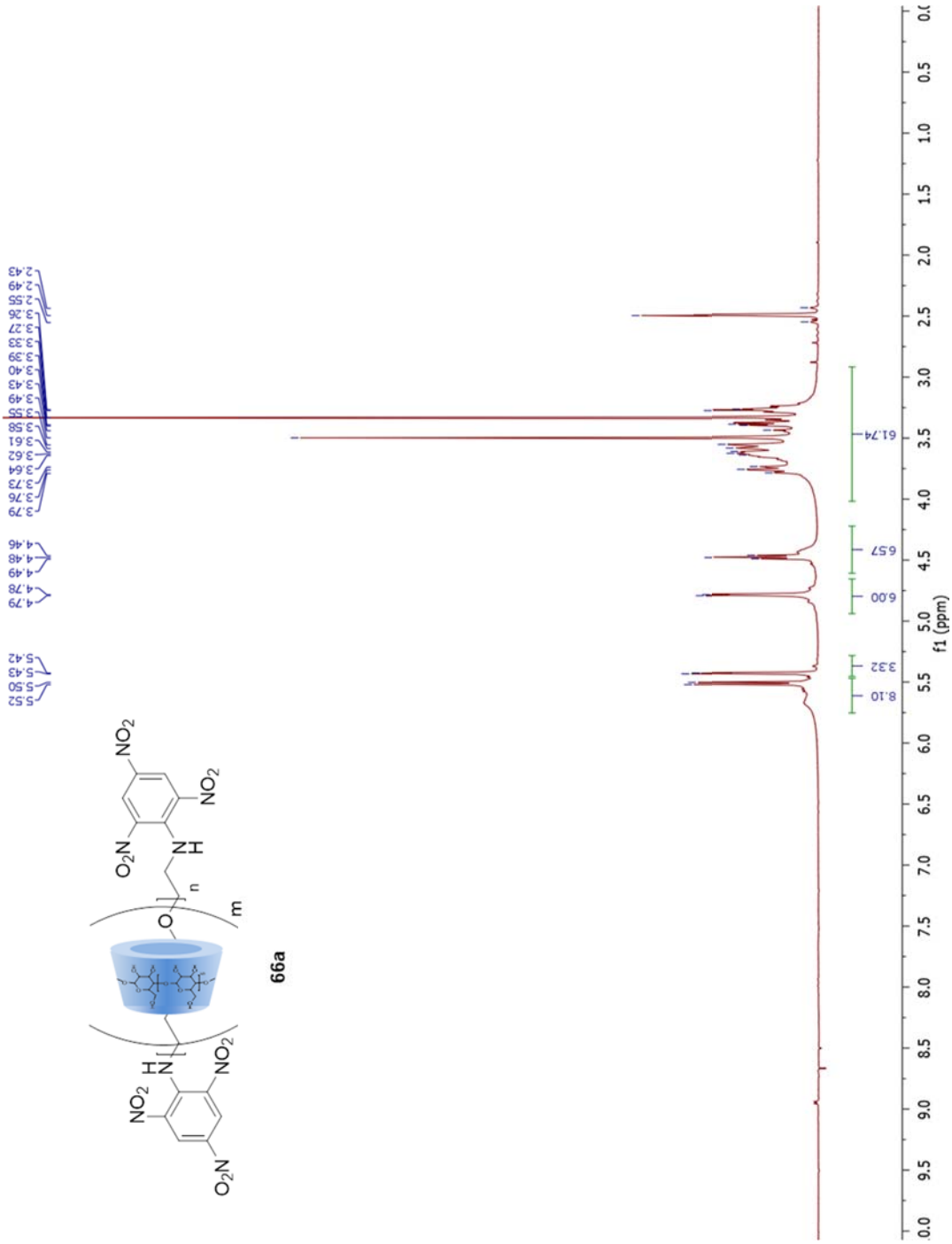

Figure A.52 ^{1}H-NMR of **66a**

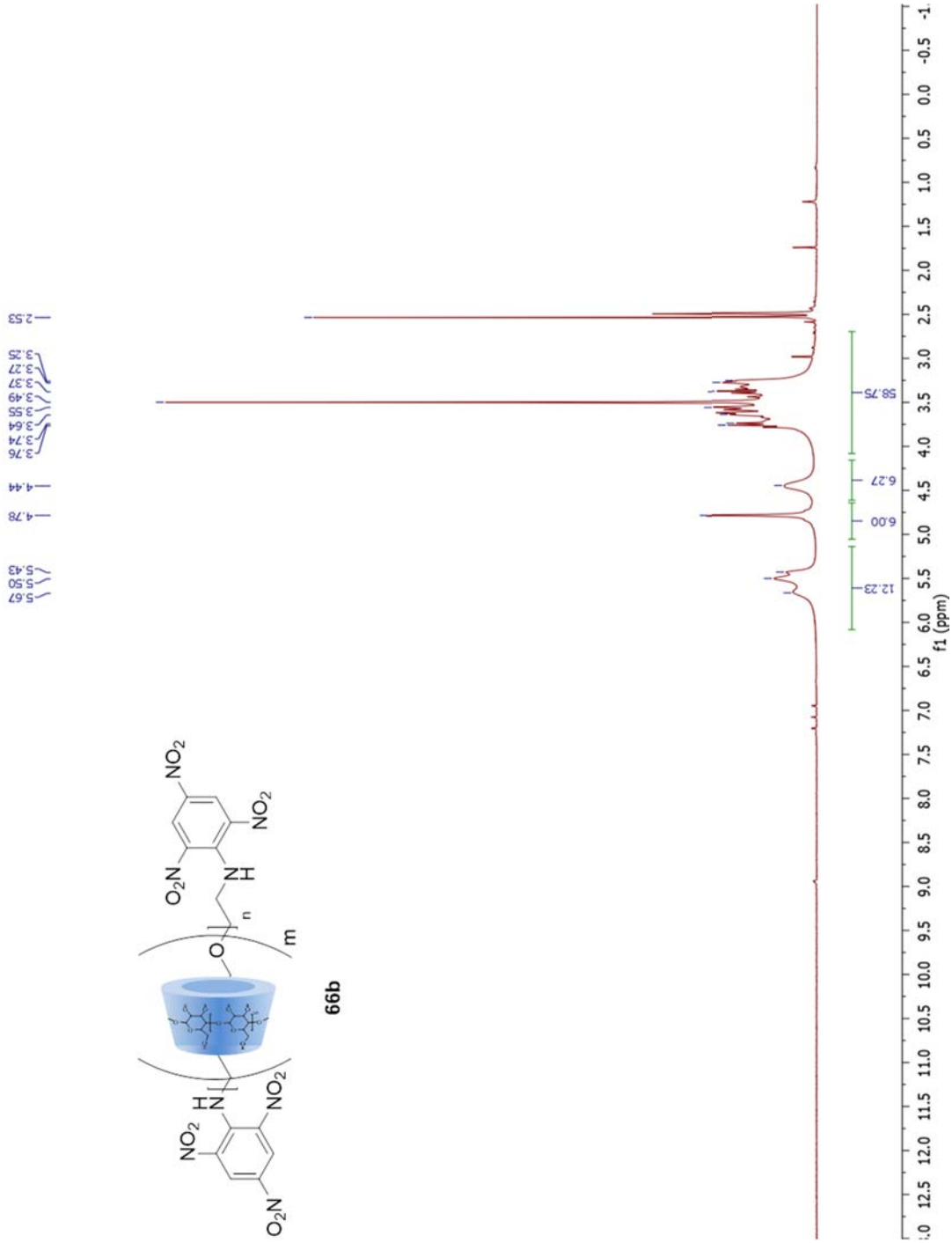

Figure A.53 ^{1}H-NMR of **66b**

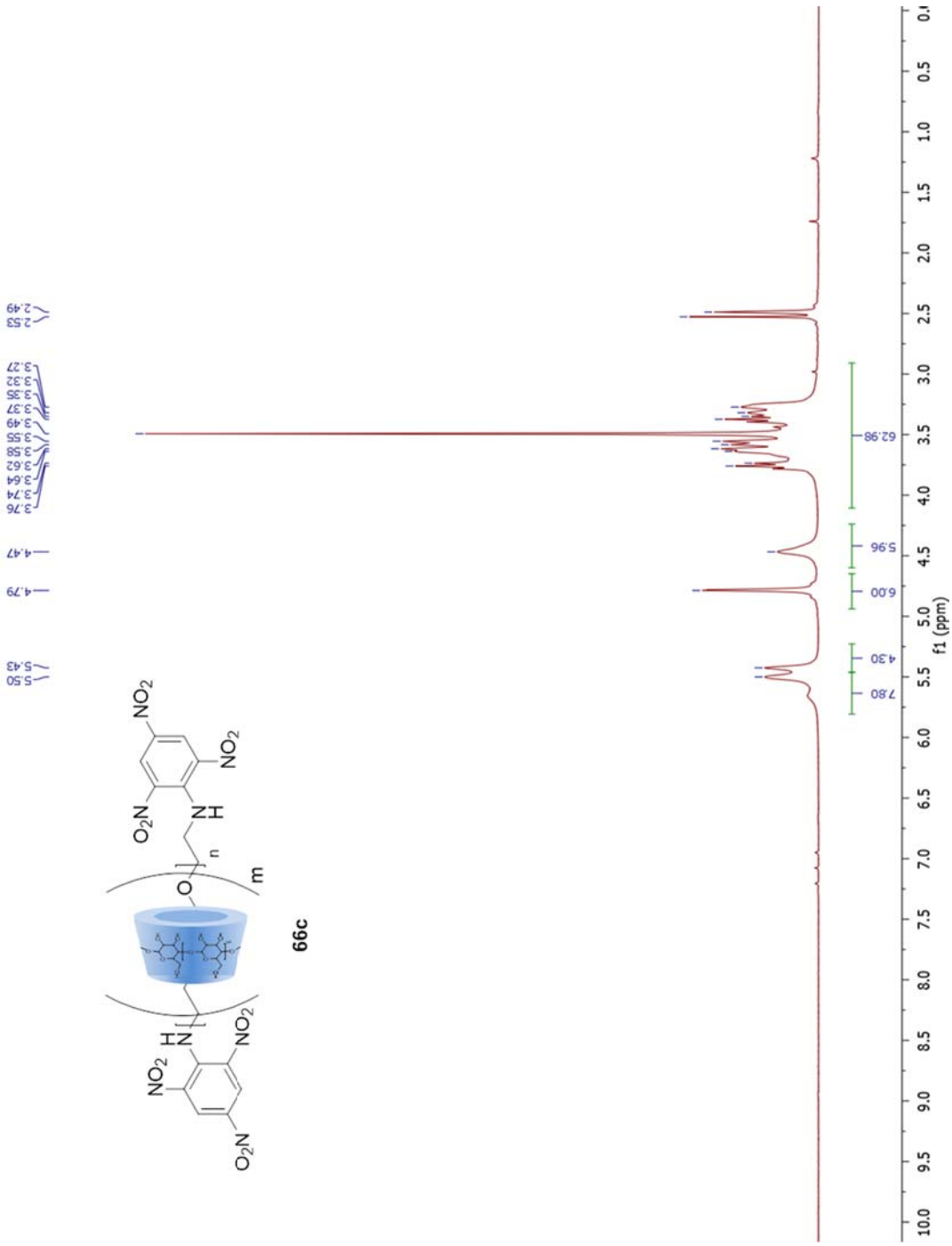

Figure A.54 ^{1}H-NMR of **66c**

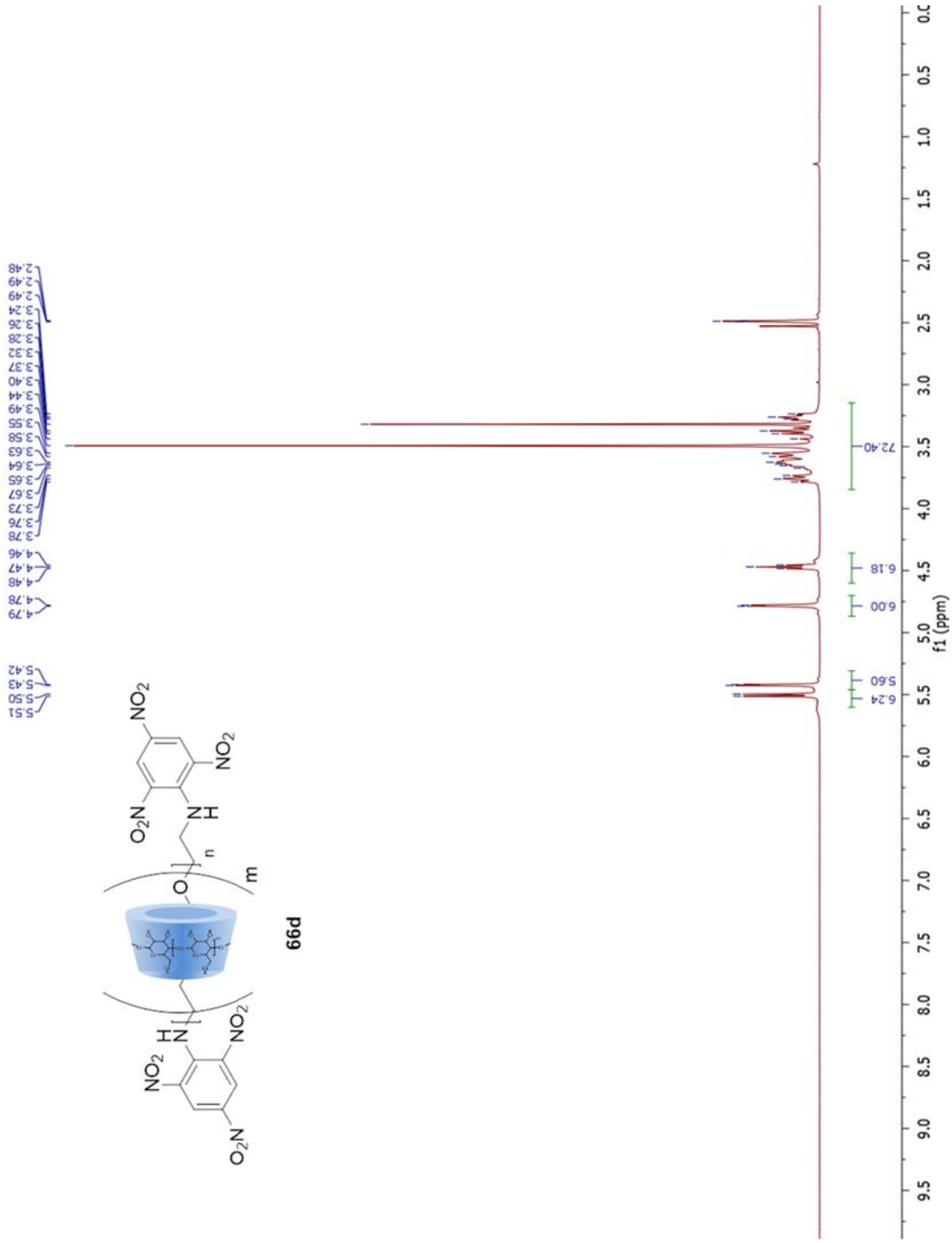

Figure A.55 ^{1}H-NMR of **66d**

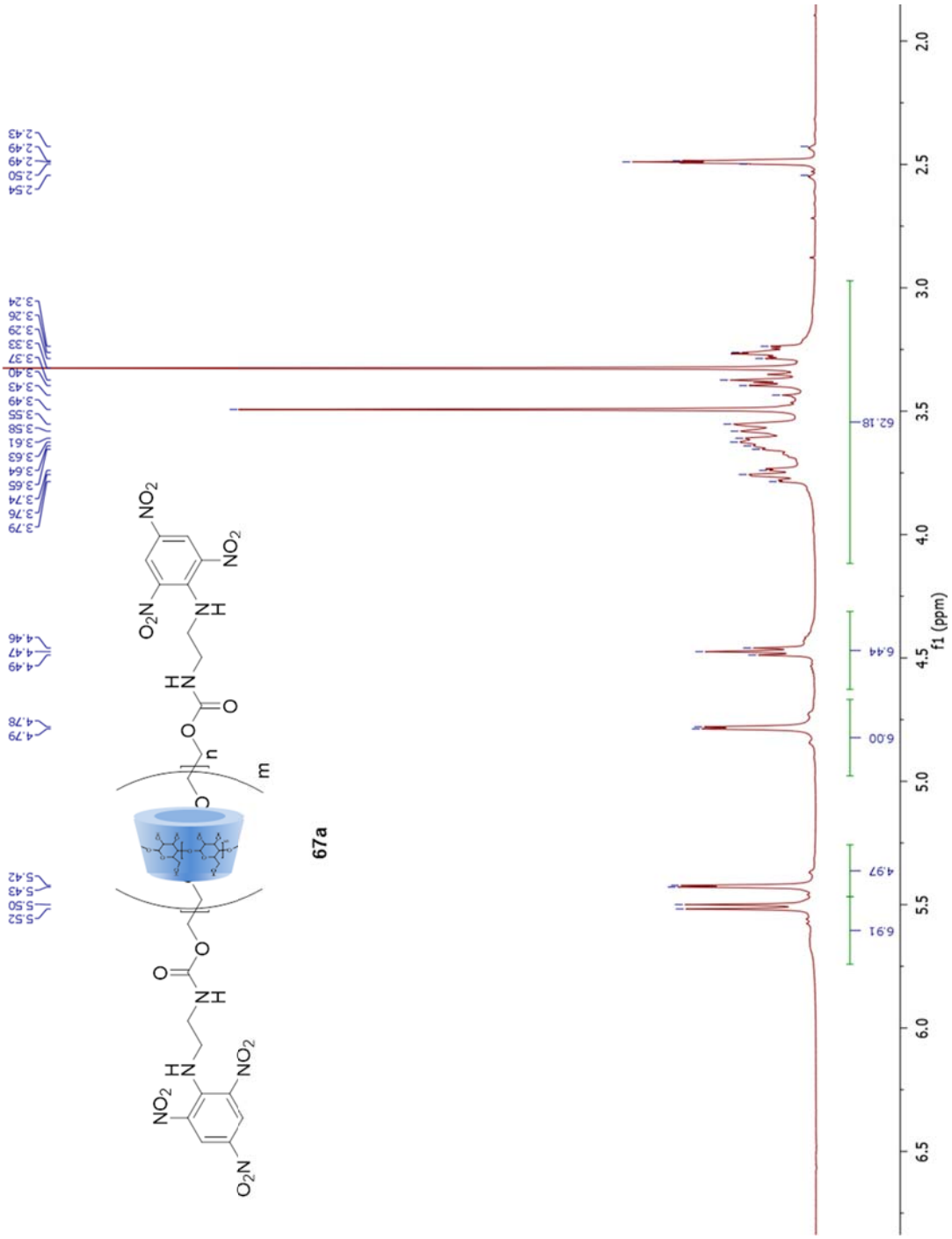

Figure A.56 ^{1}H-NMR of **67a**

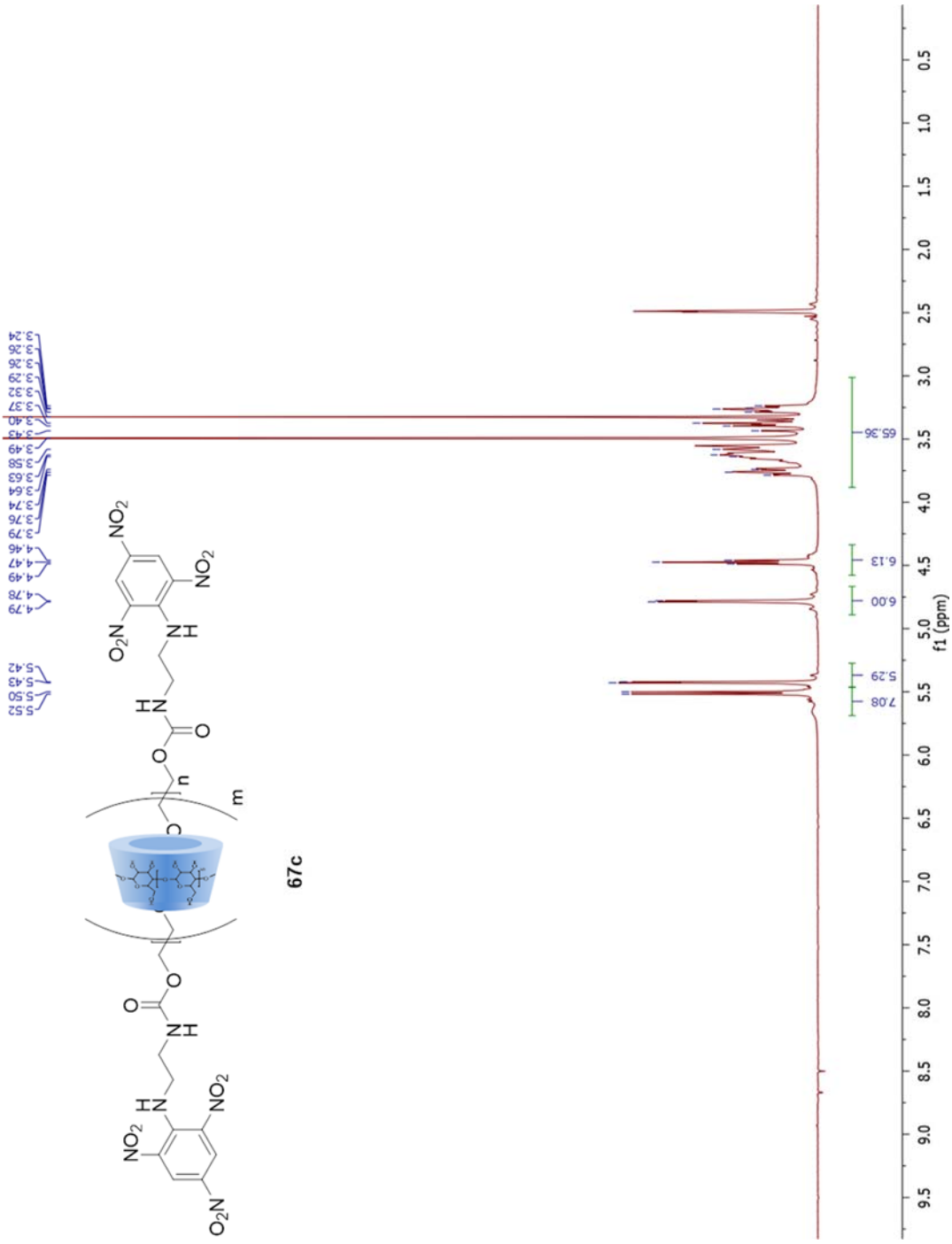

Figure A.57 ^{1}H-NMR of **67c**

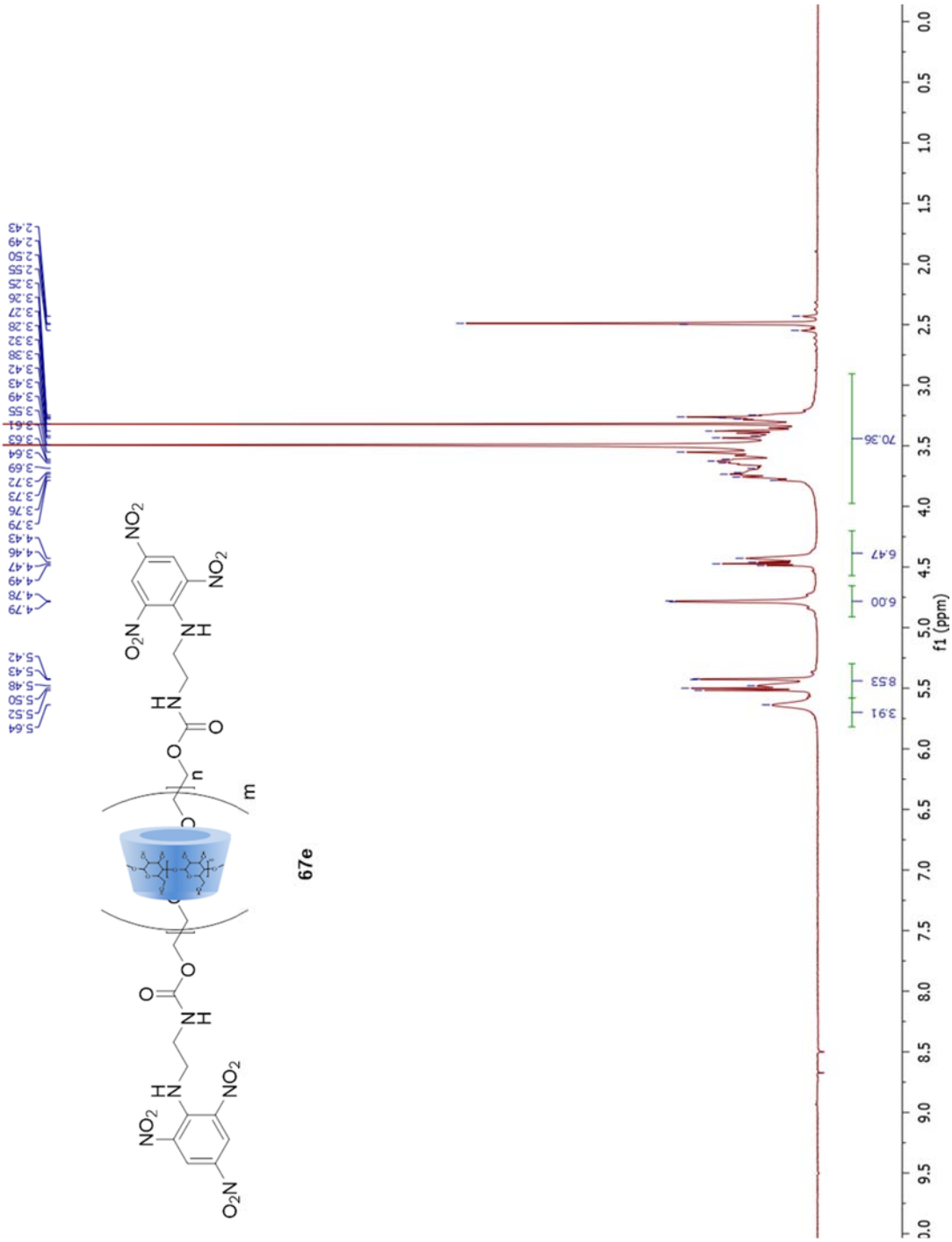

Figure A.58 ^{1}H-NMR of **67e**

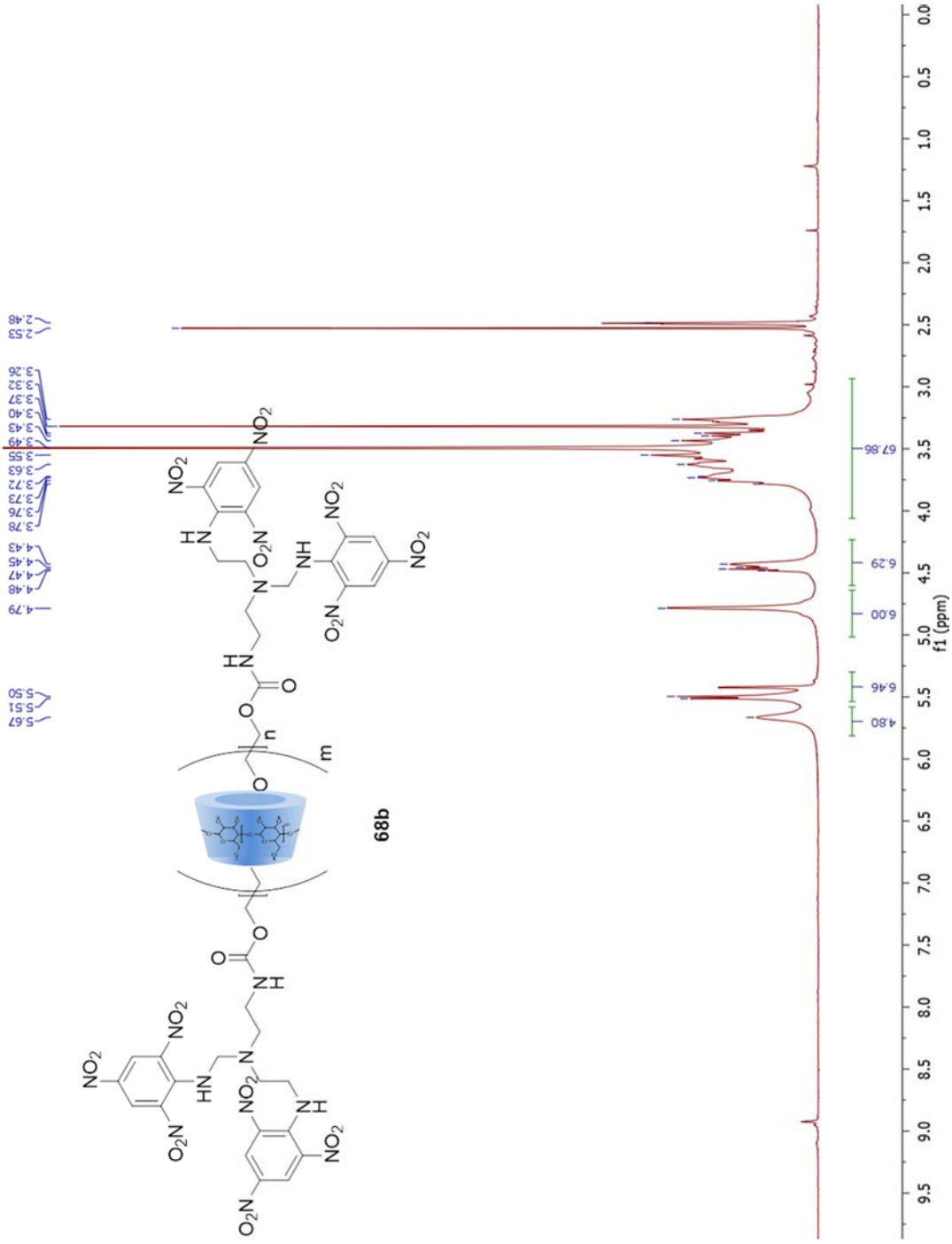

Figure A.59 ^{1}H-NMR of **68b**

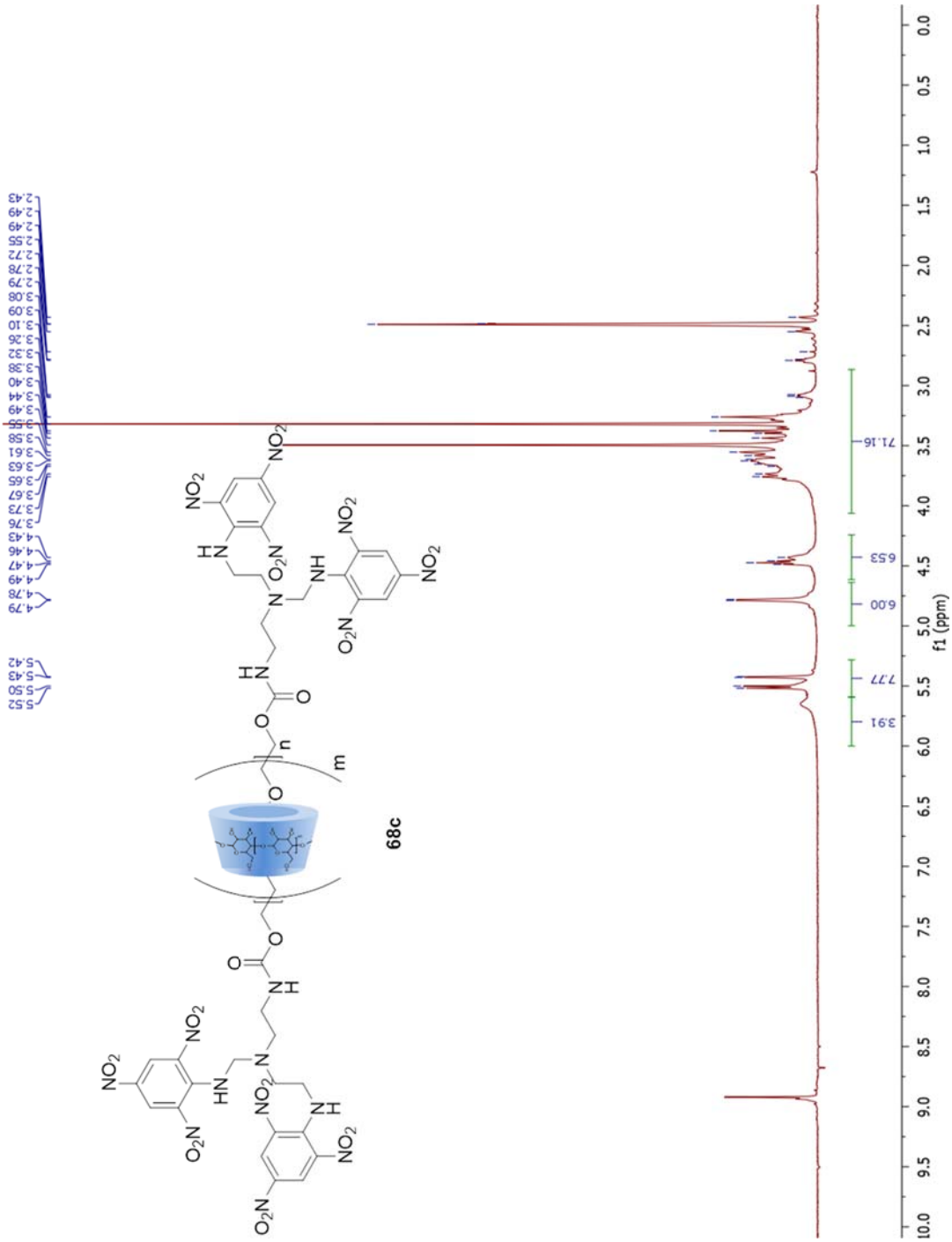

Figure A.60 ^{1}H-NMR of **68c**

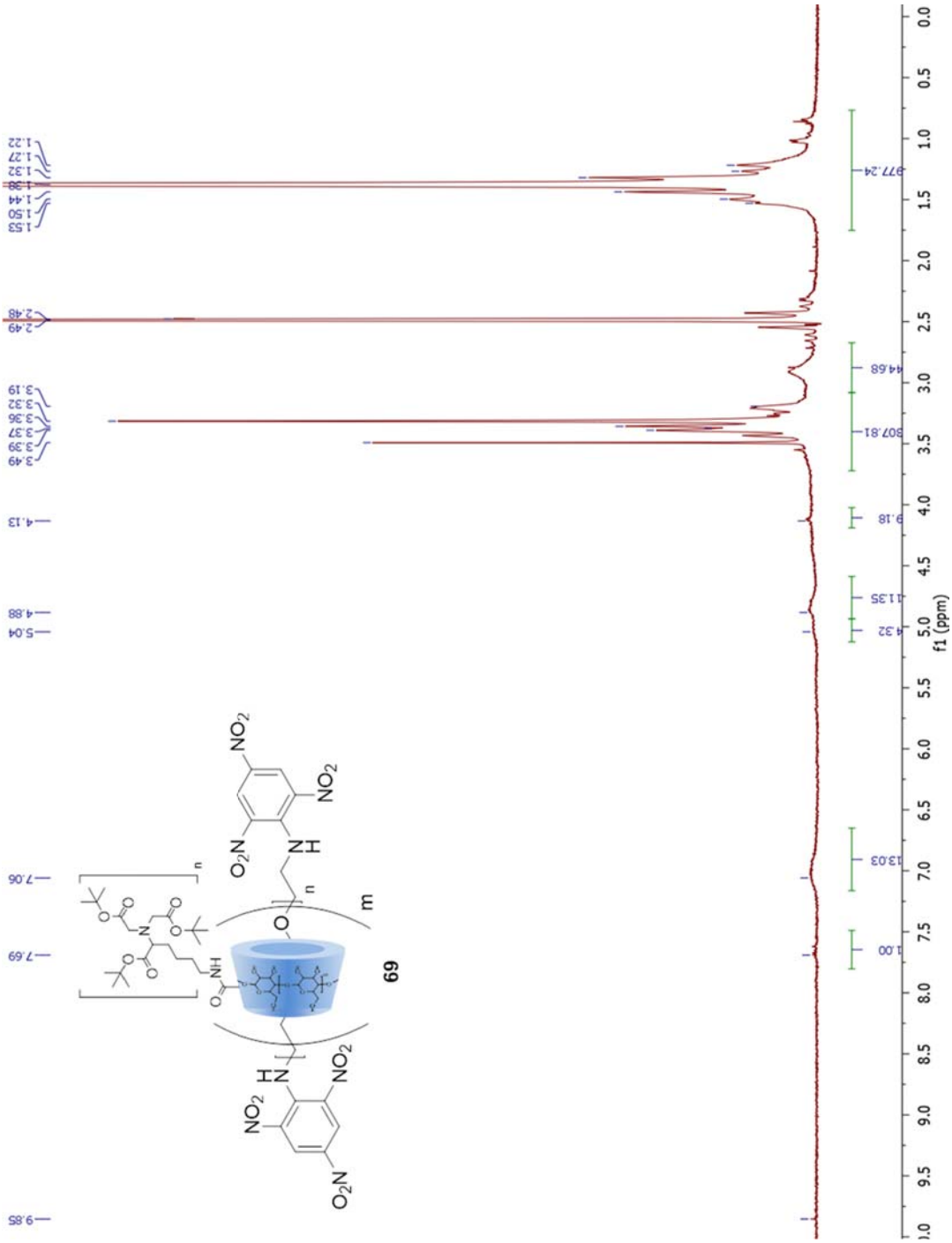

Figure A.61 ^{1}H-NMR of **69**

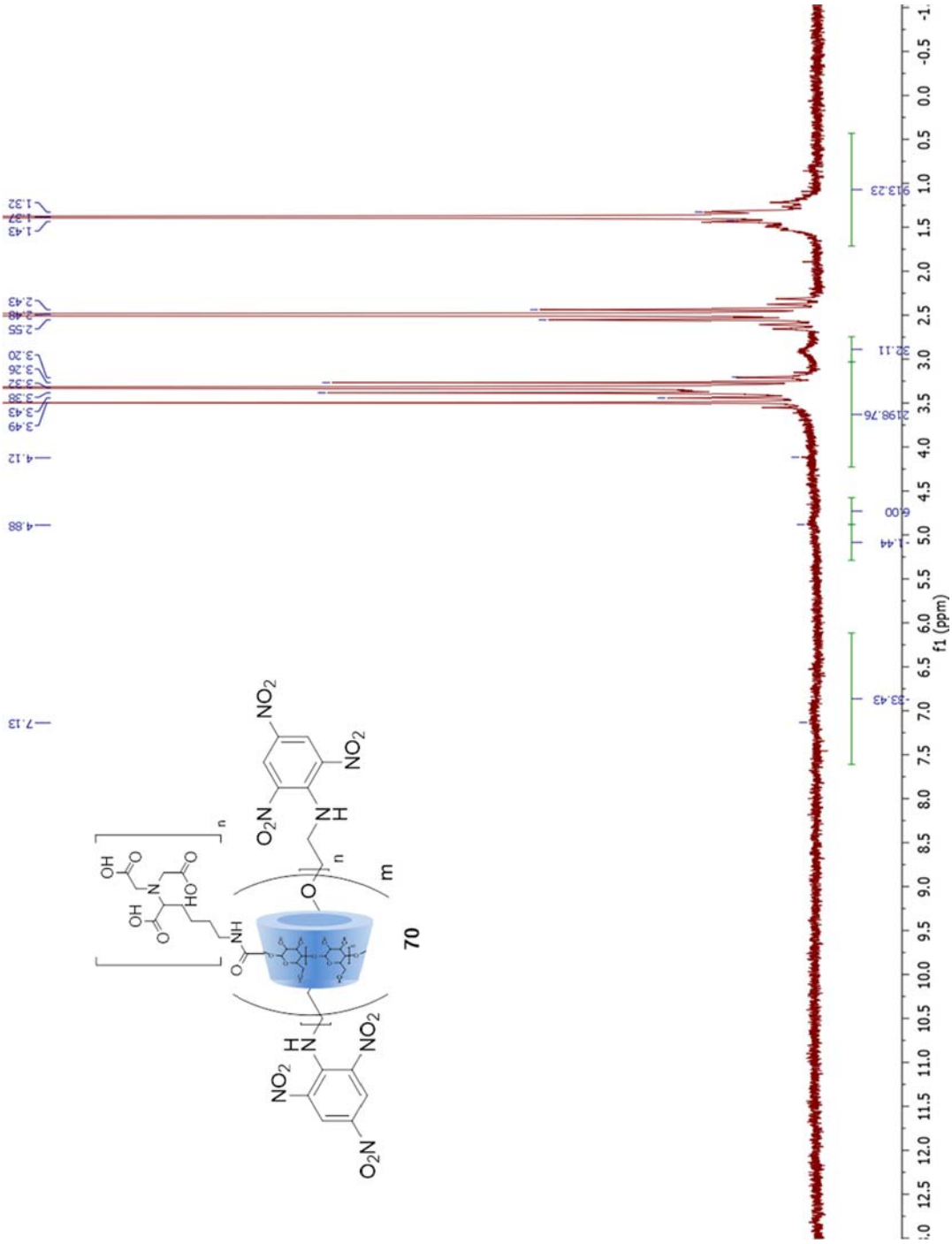

Figure A.62 ^{1}H-NMR of **70**

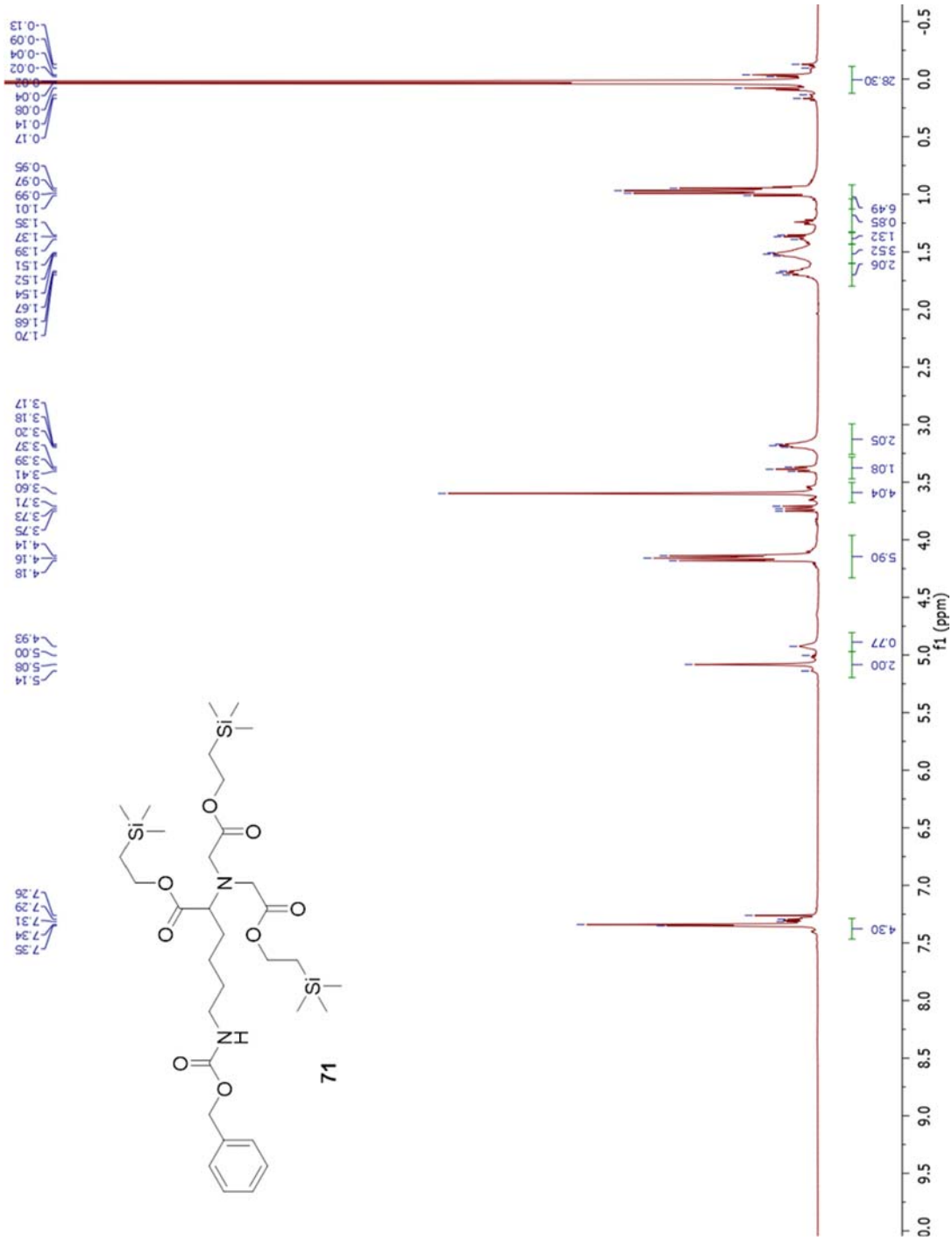

Figure A.63 ^{1}H-NMR of **71**

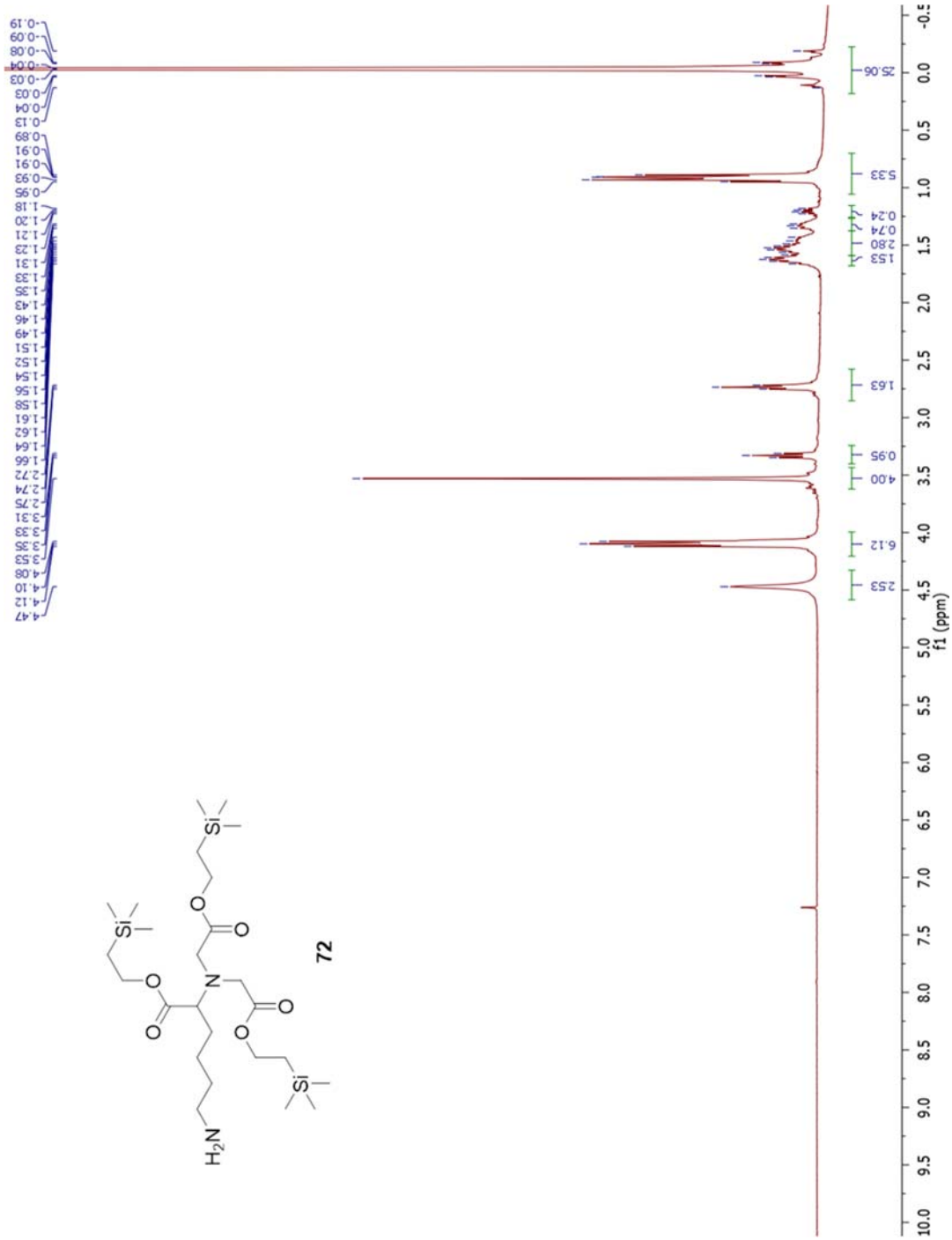

Figure A.64 ^{1}H-NMR of **72**

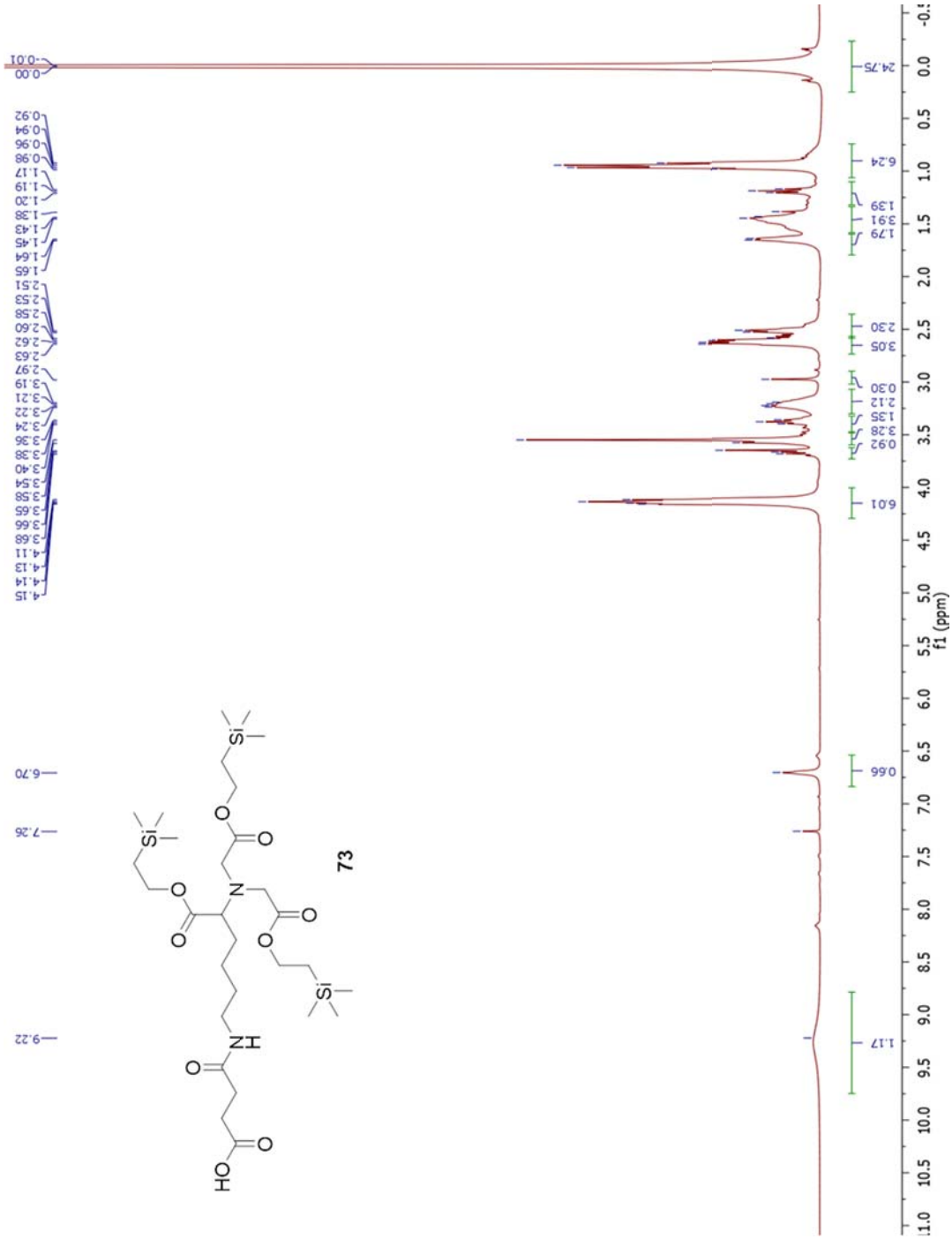

Figure A.65 ^{1}H-NMR of **73**

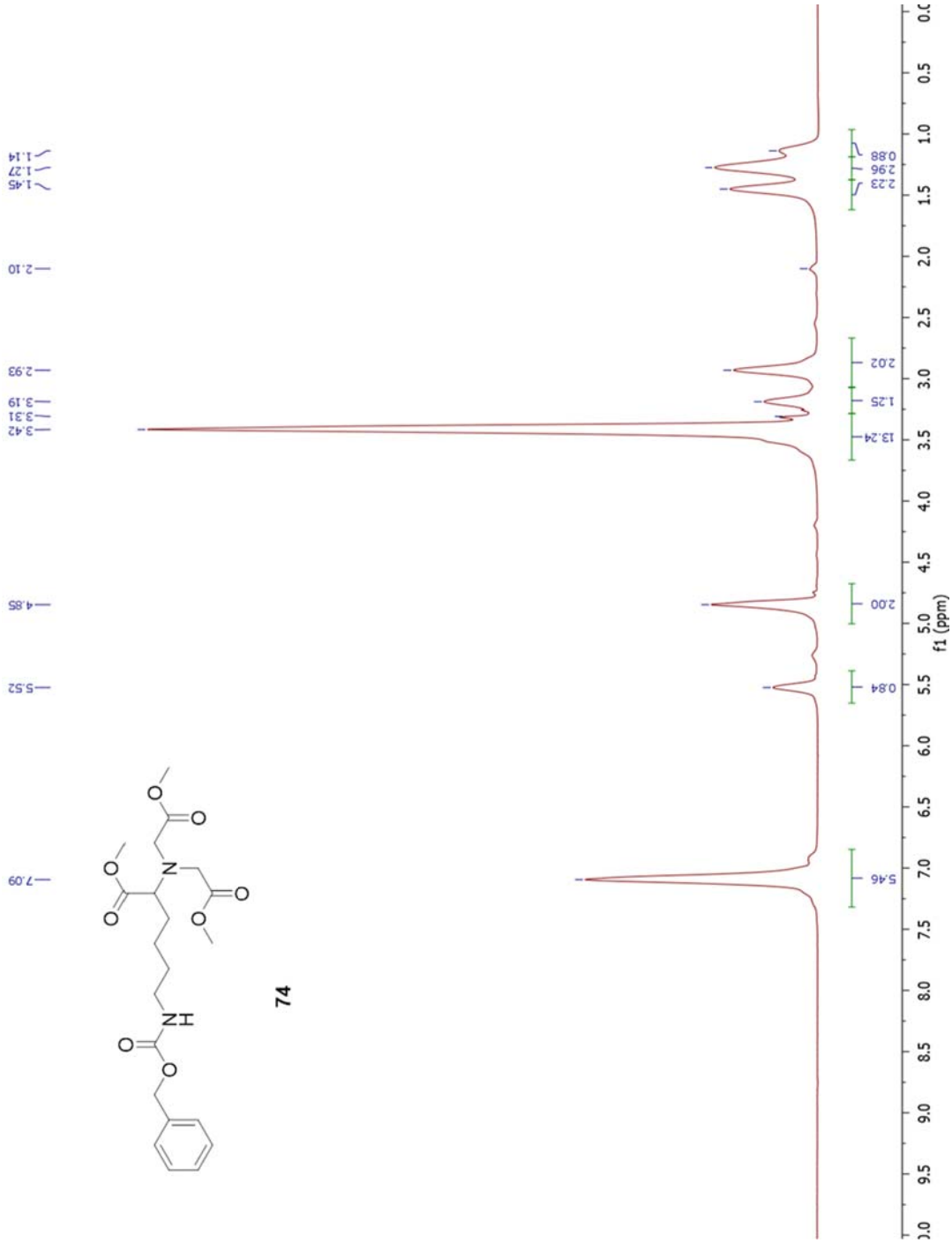

Figure A.66 ^{1}H-NMR of **74**

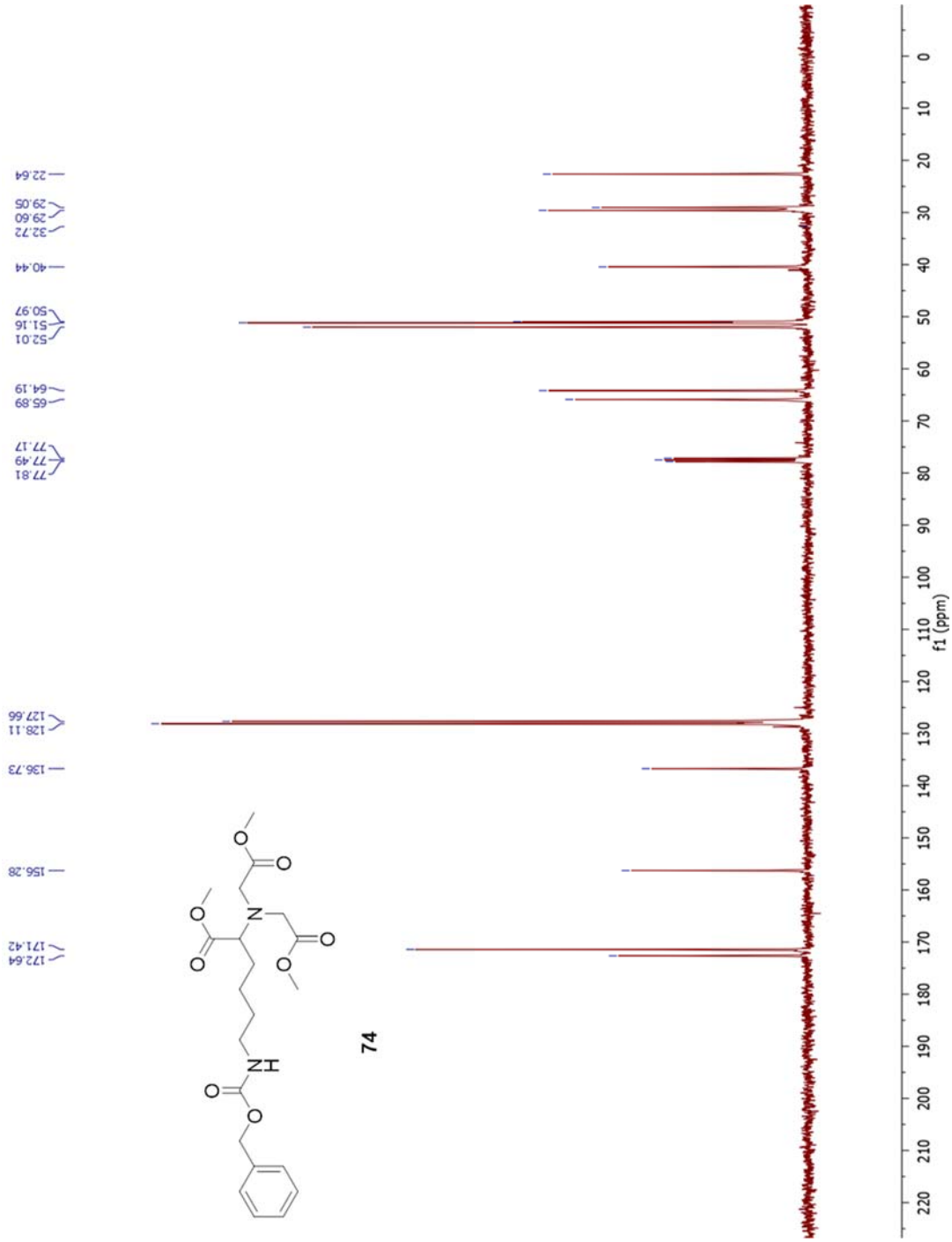

Figure A.67 ^{13}C-NMR of **74**

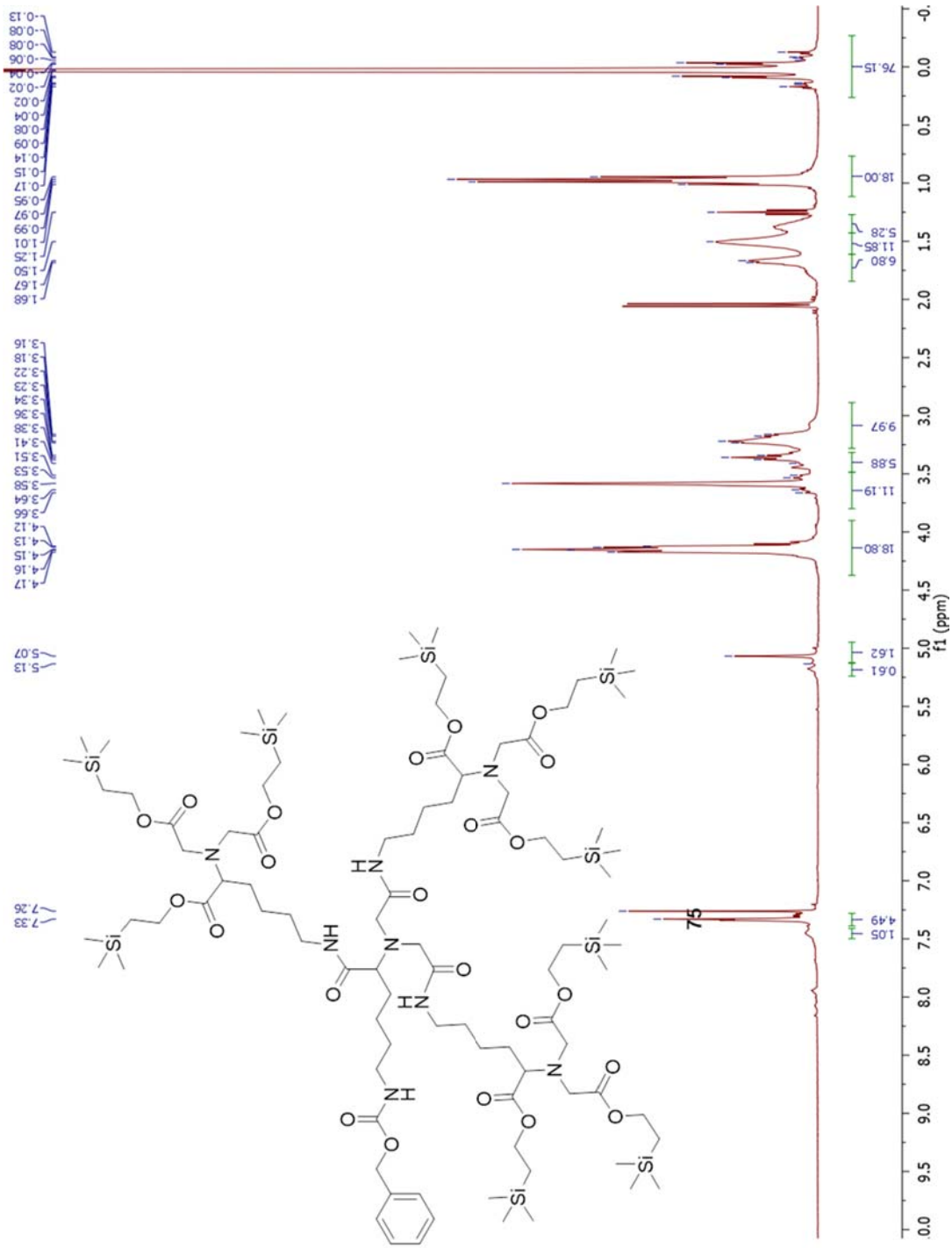

Figure A.68 ^{1}H-NMR of **75**

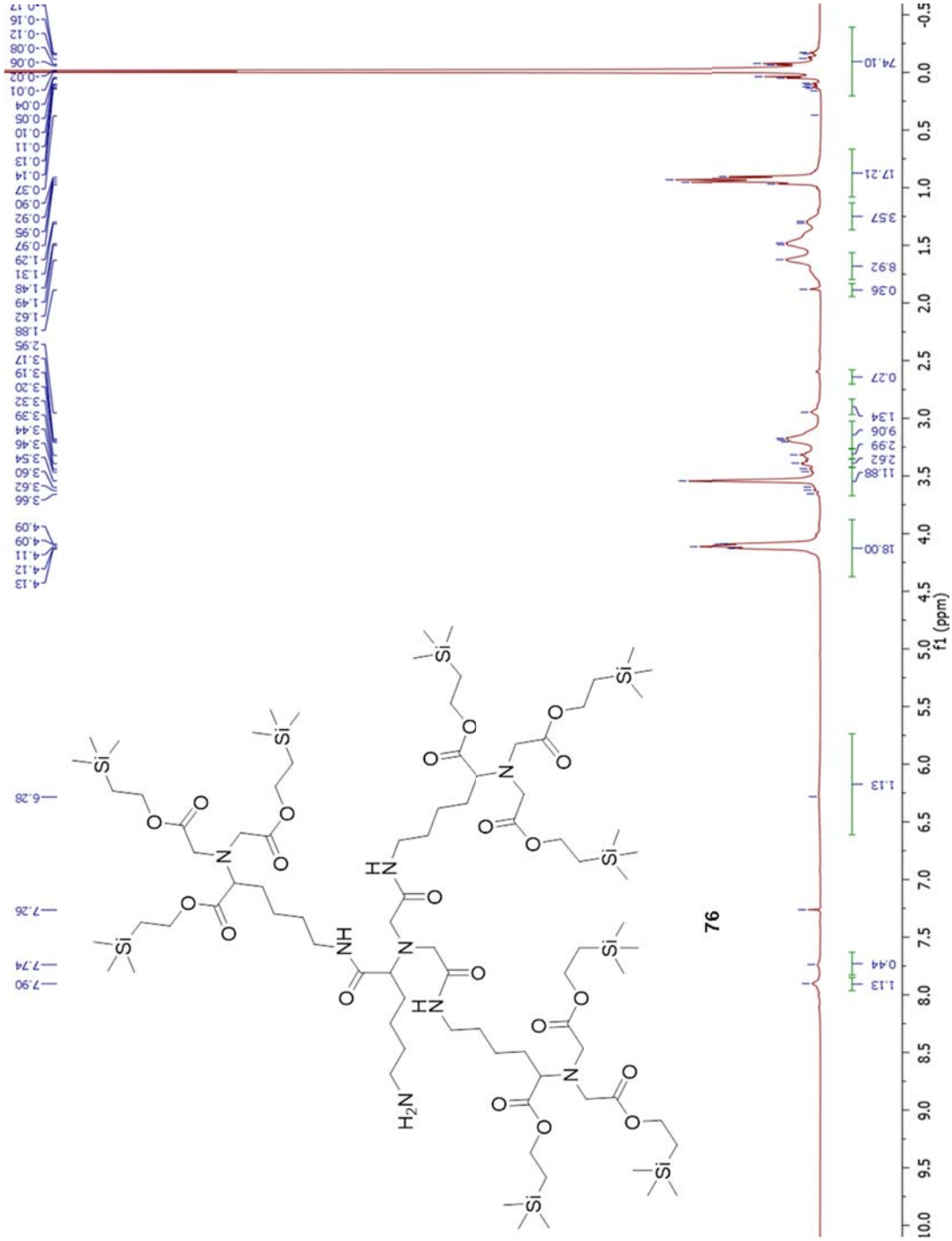

Figure A.69 ^{1}H-NMR of **76**

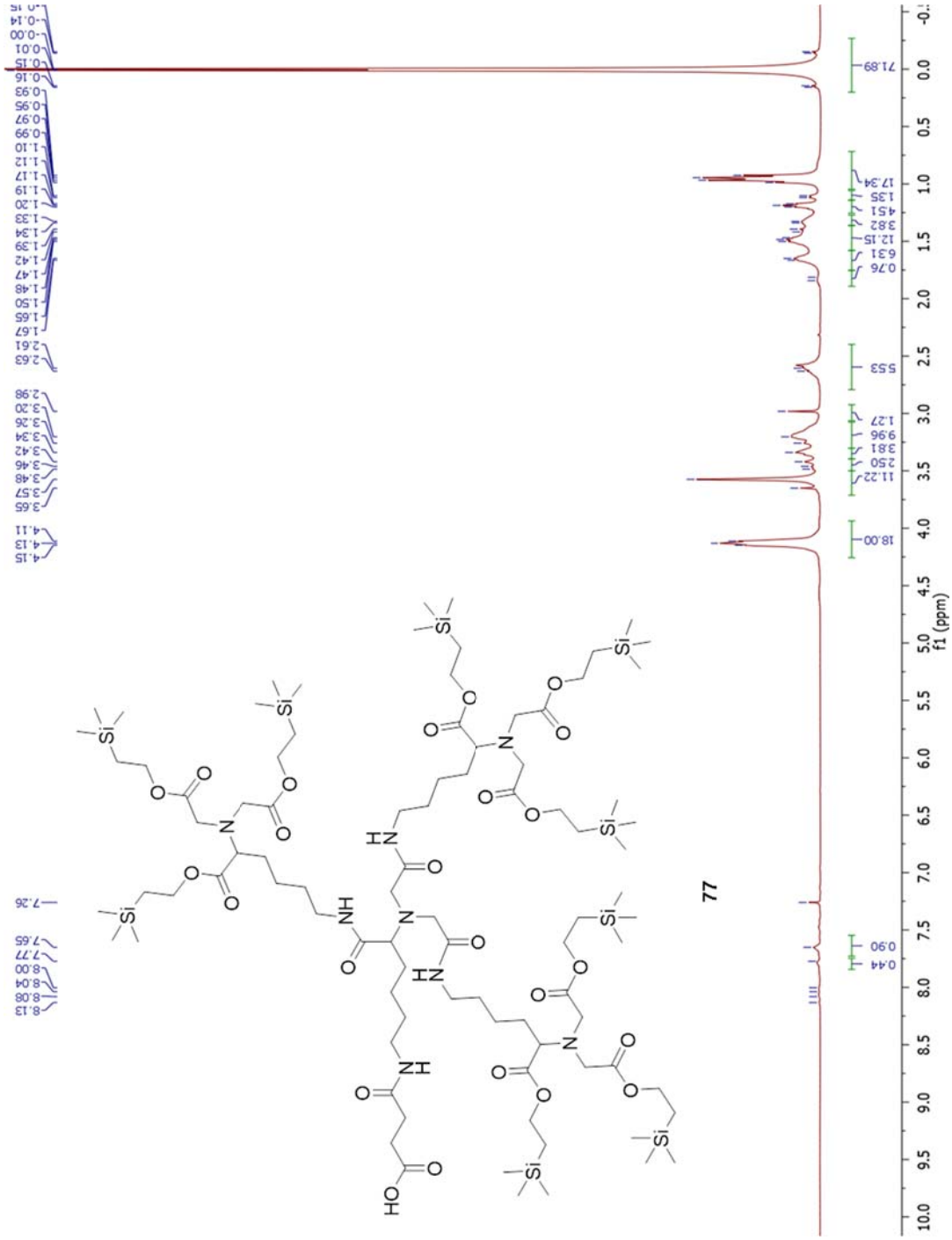

Figure A.70 ^{1}H-NMR of **77**

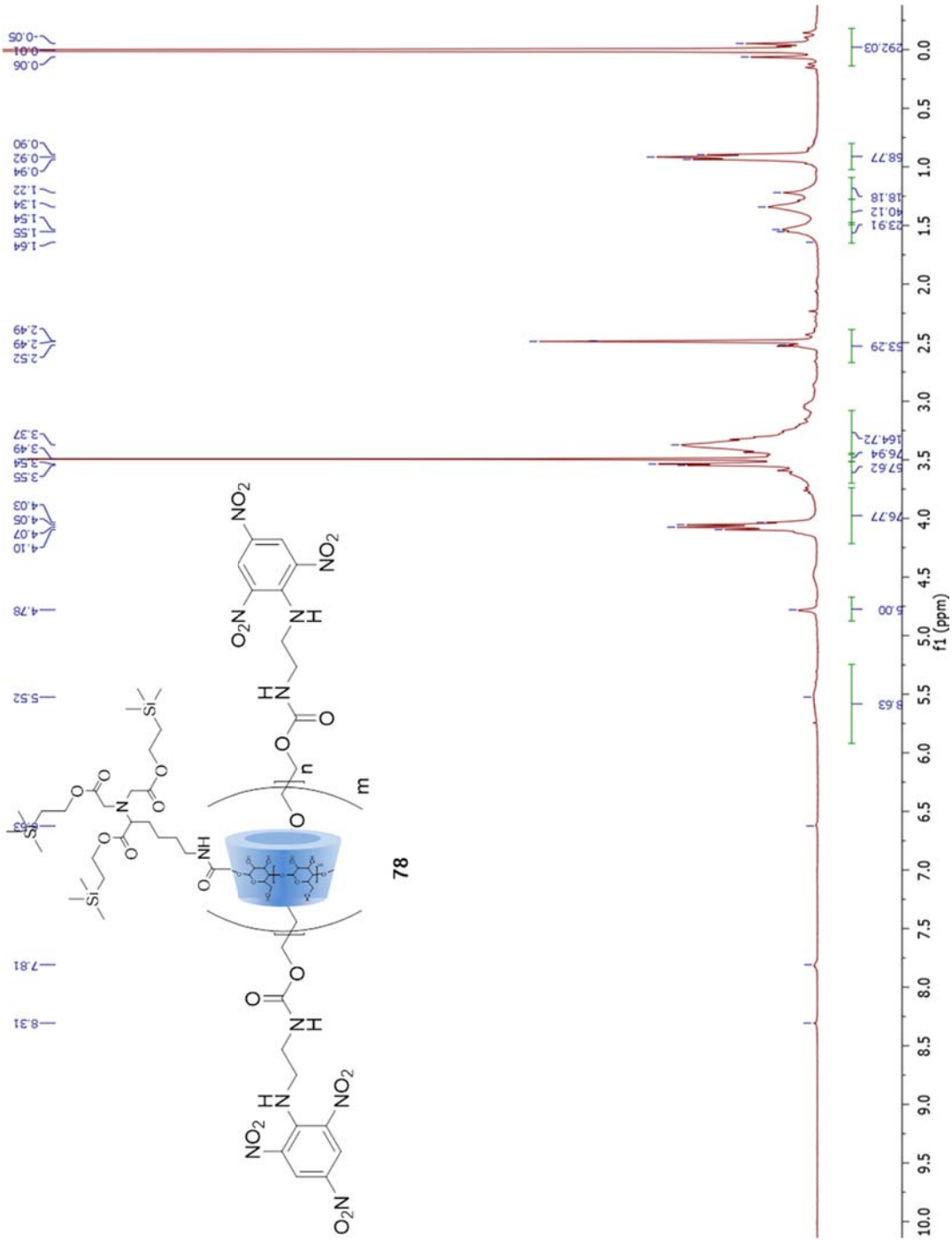

Figure A.71 ^{1}H-NMR of **78**

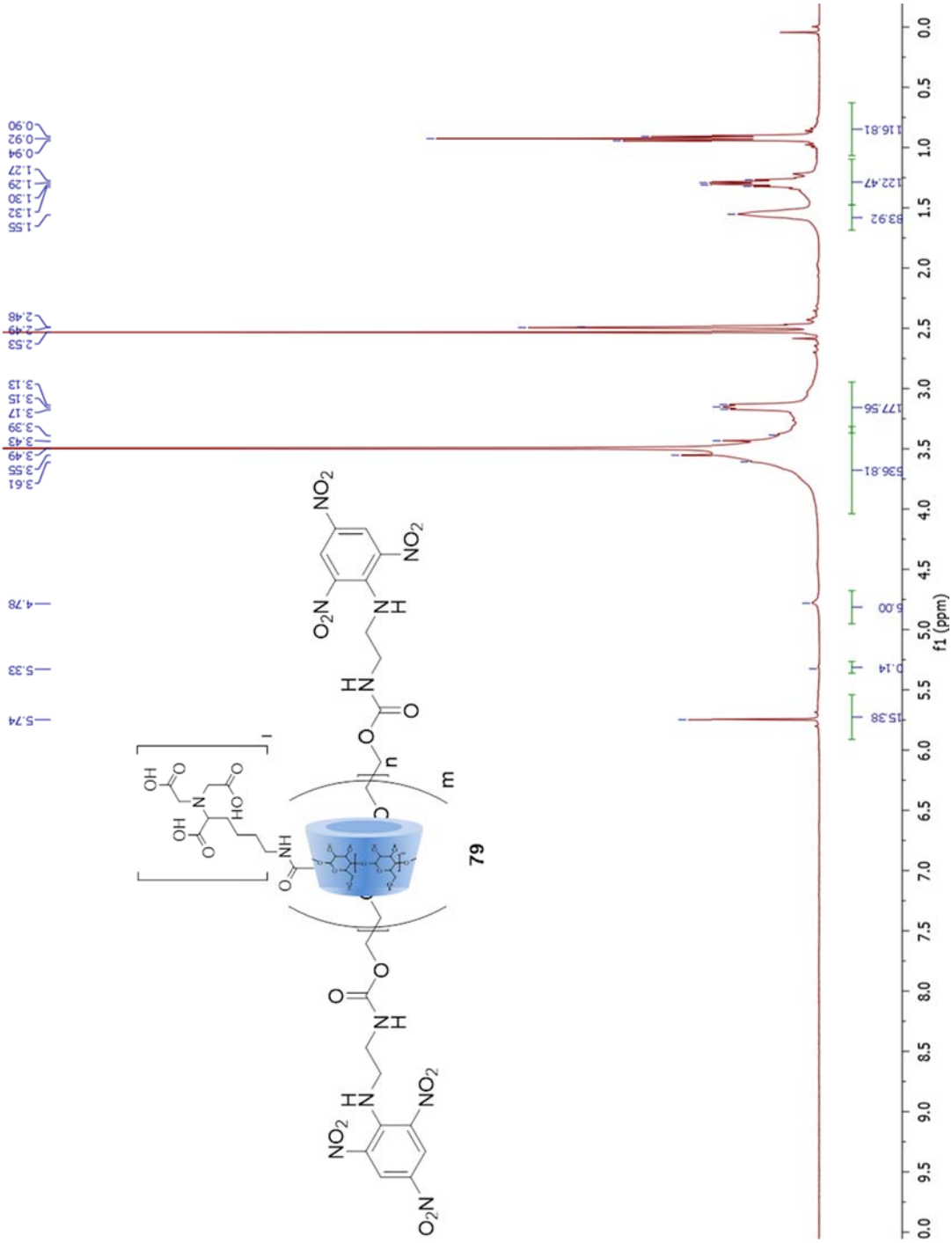

Figure A.72 ^{1}H-NMR of **79**

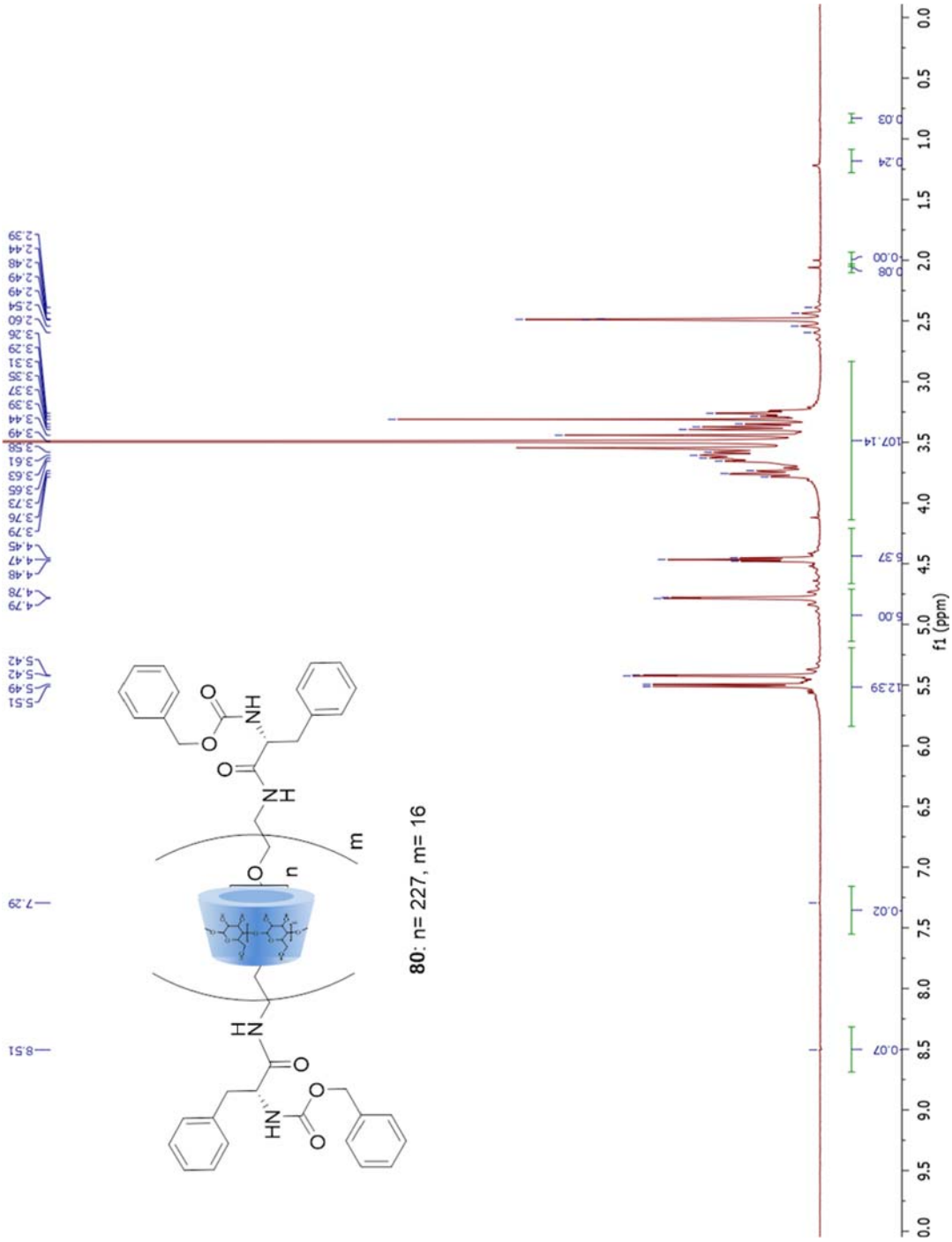

Figure A.73 ^{1}H-NMR of **80**

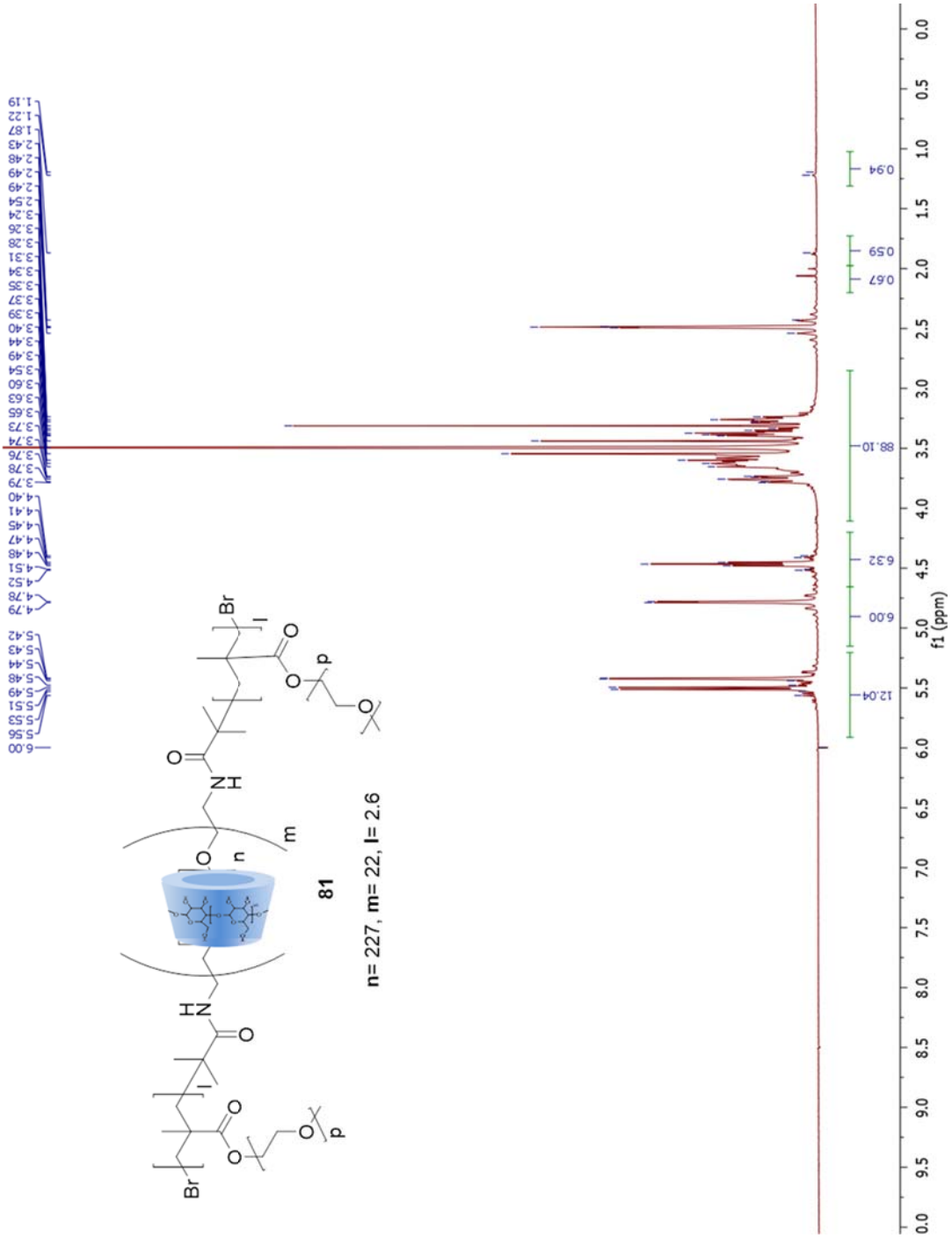

Figure A.74 ^{1}H-NMR of **81**

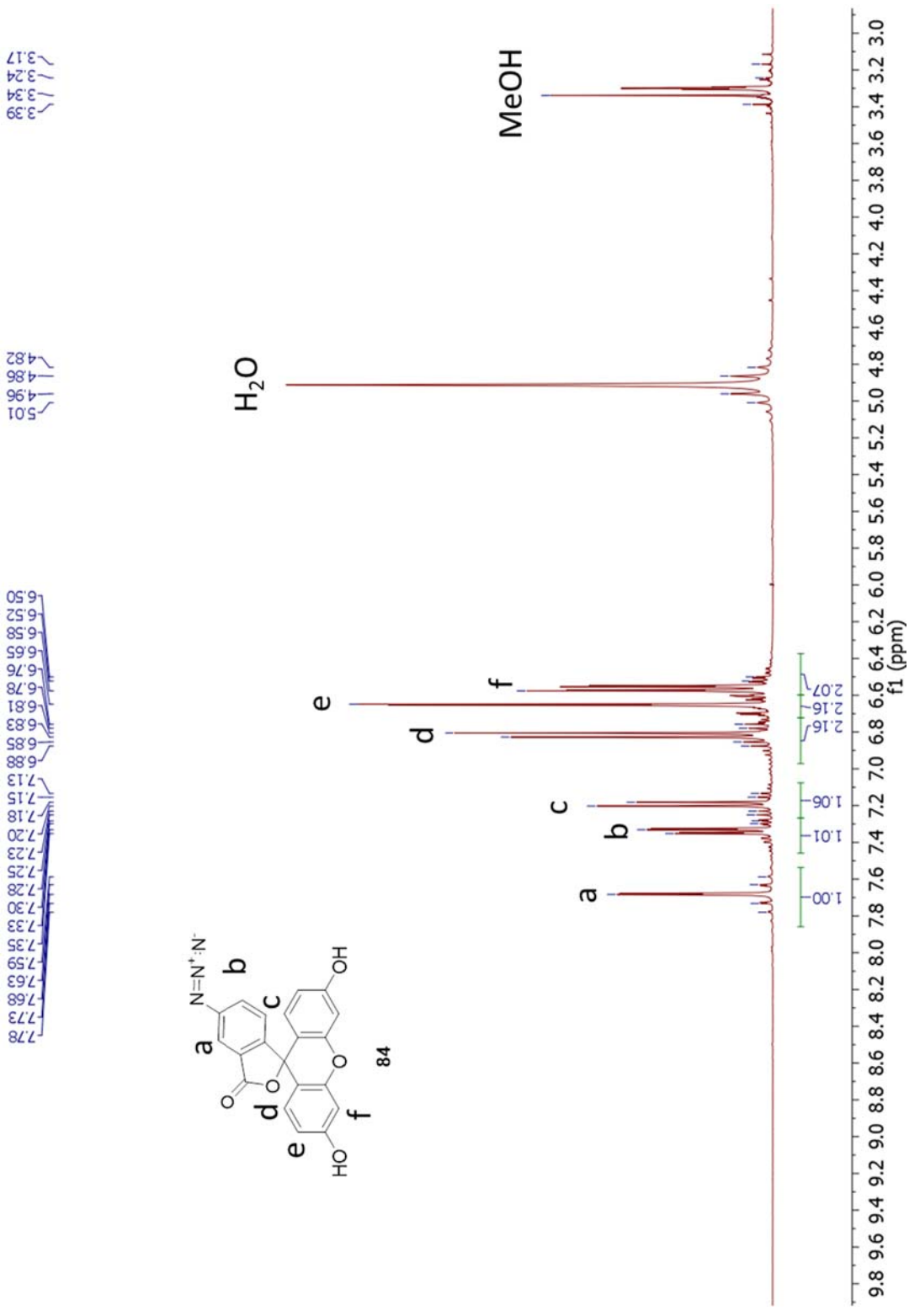

Figure A.75 ^{1}H-NMR of **84**

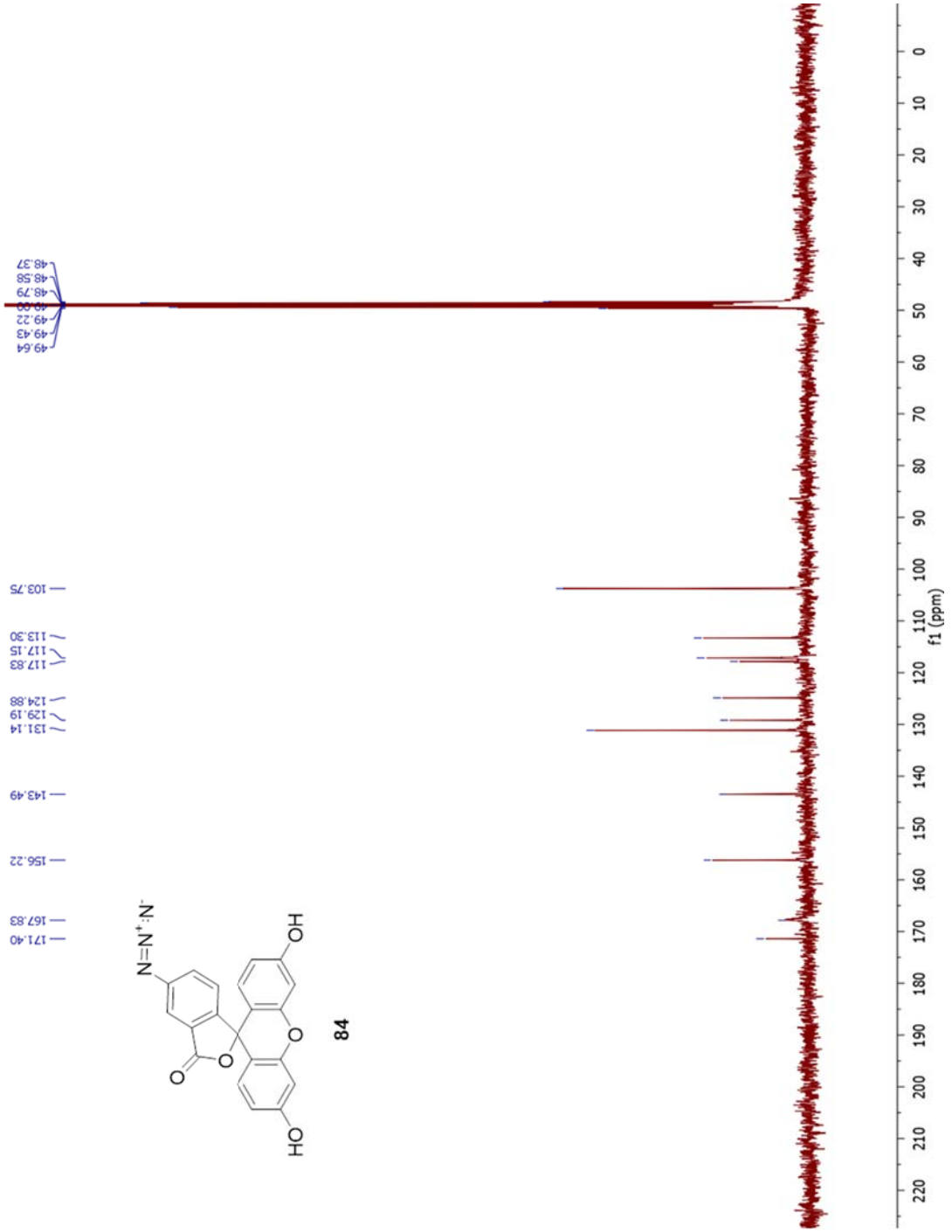

Figure A.76 ^{13}C-NMR of **84**

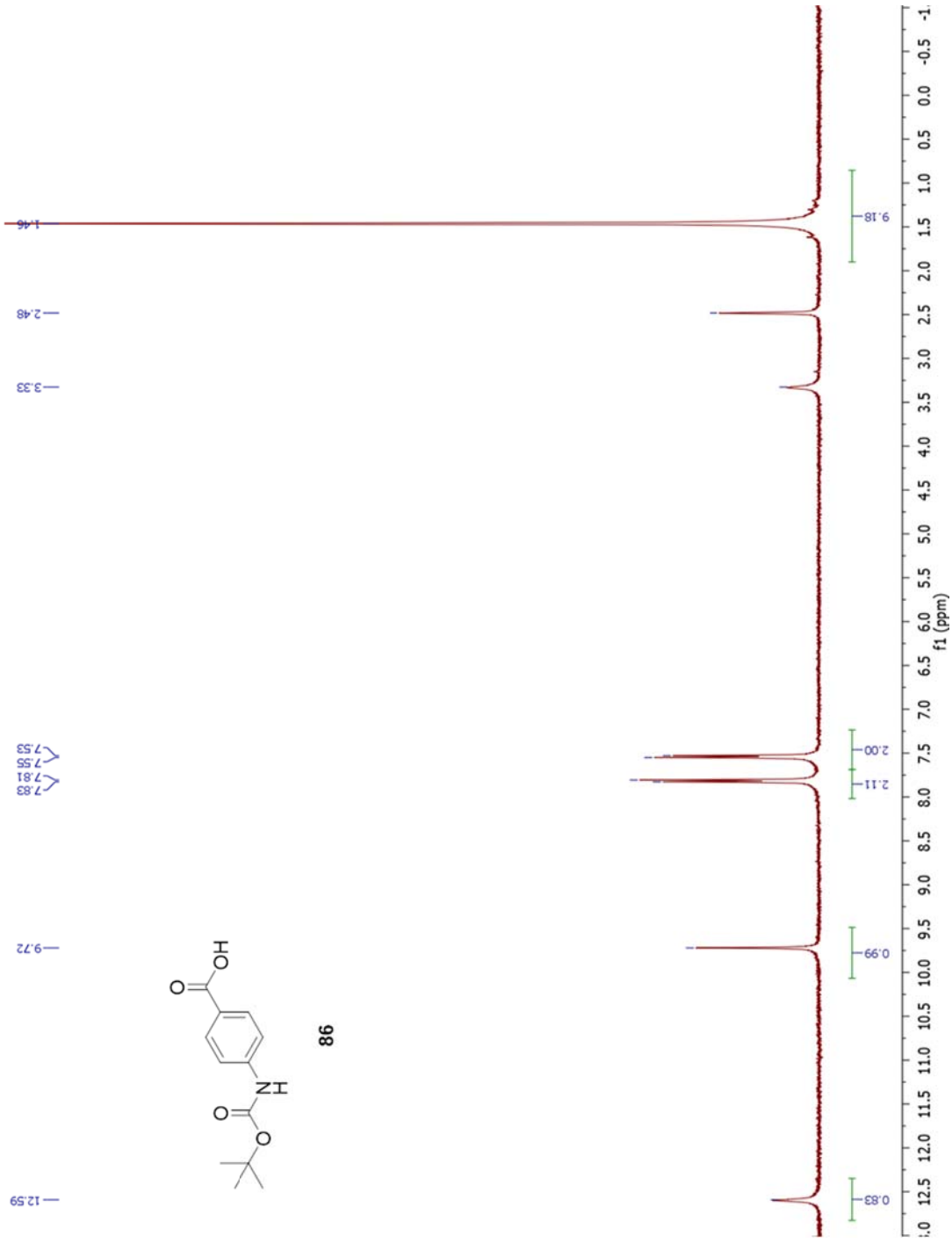

Figure A.77 ^{1}H-NMR of **86**

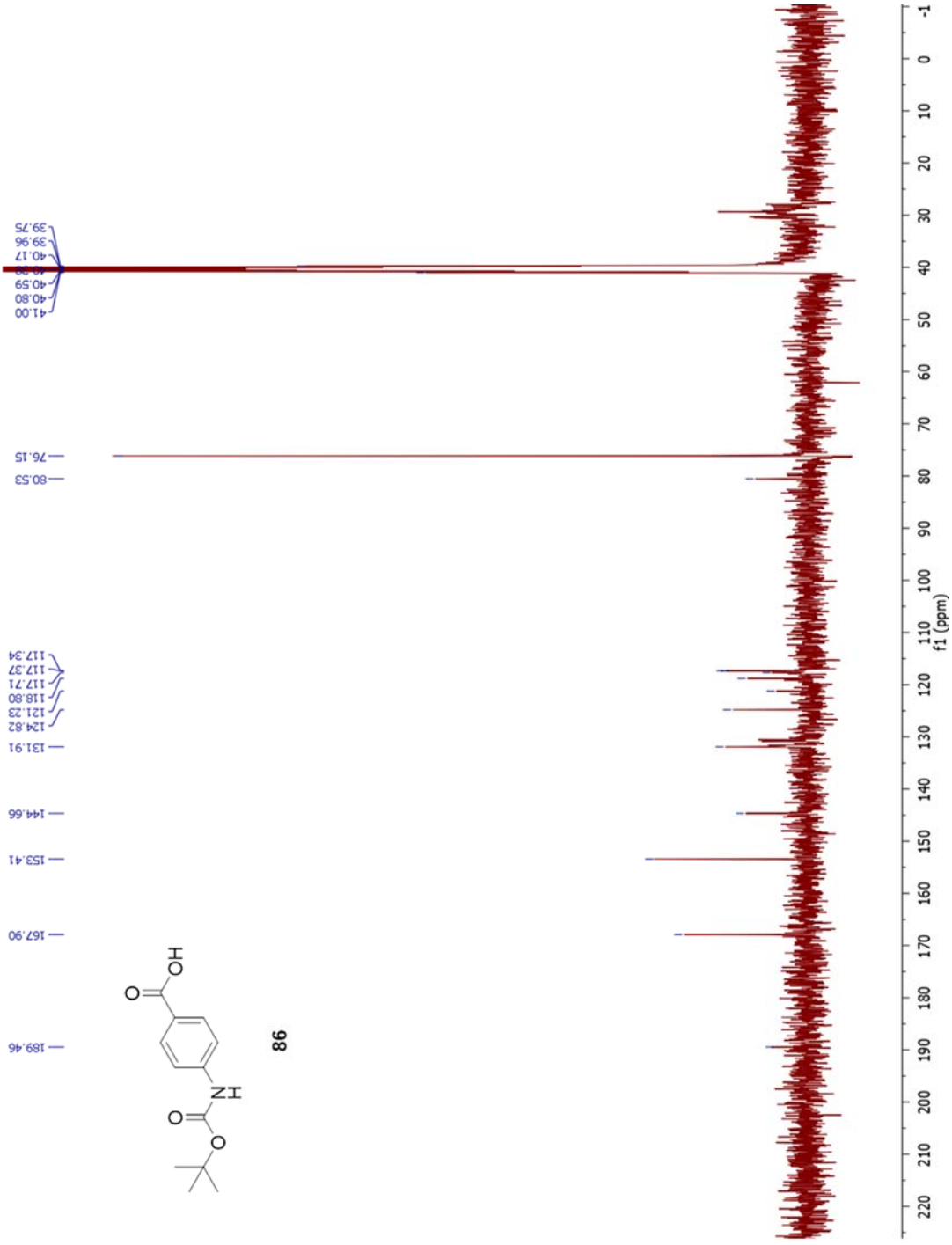

Figure A.78 ^{13}C-NMR of **86**

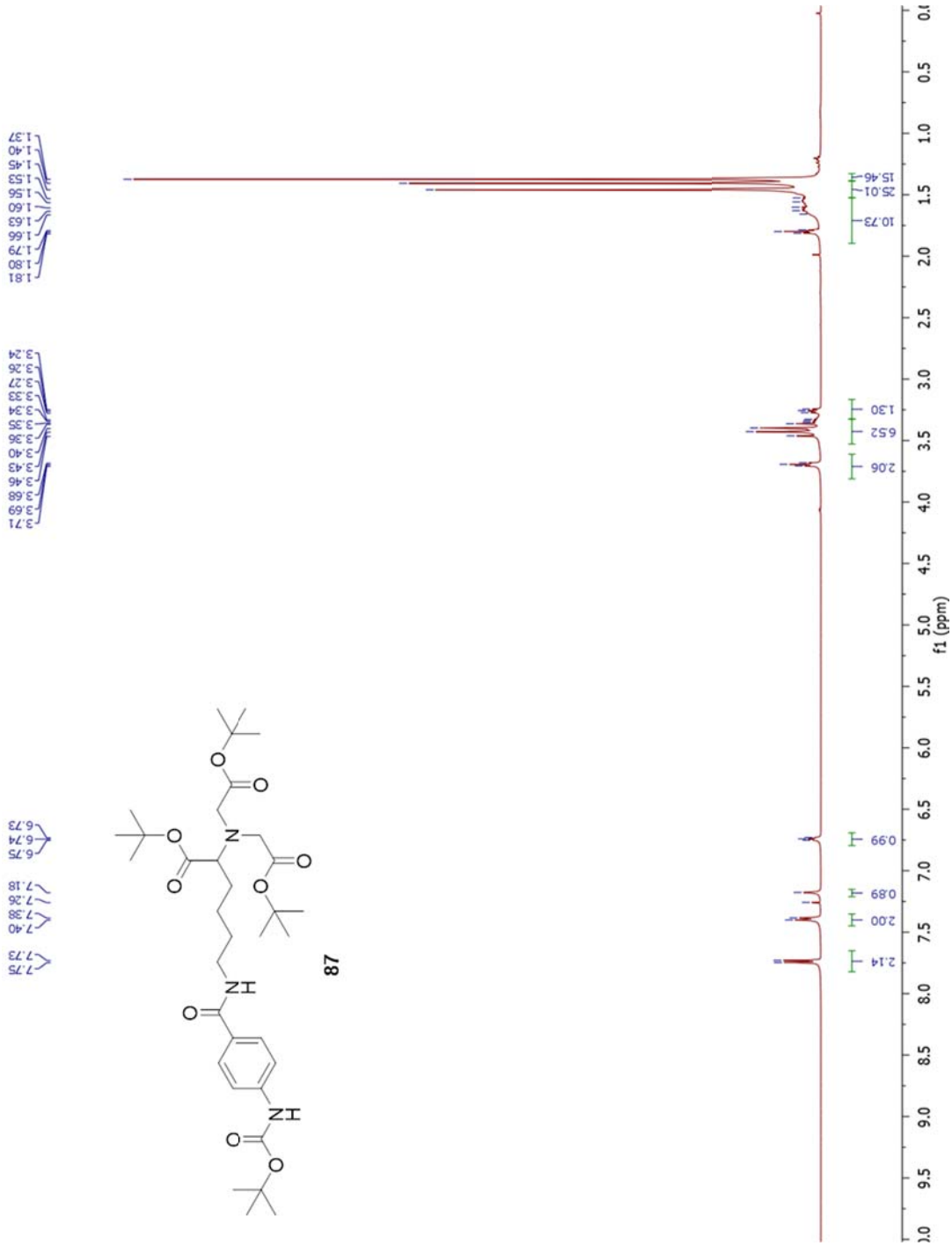

Figure A.79 ^{1}H-NMR of **87**

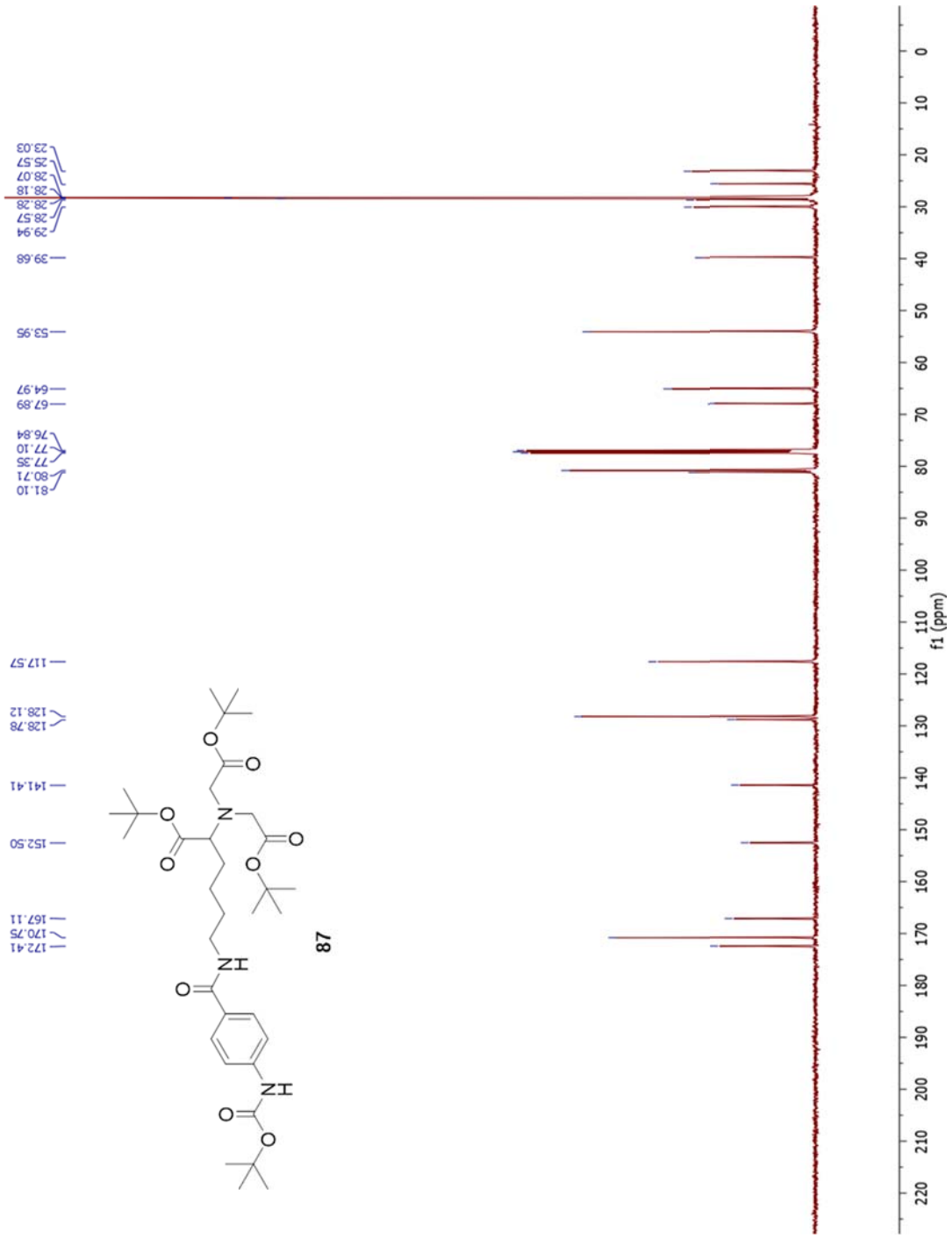

Figure A.80 ^{13}C-NMR of **87**

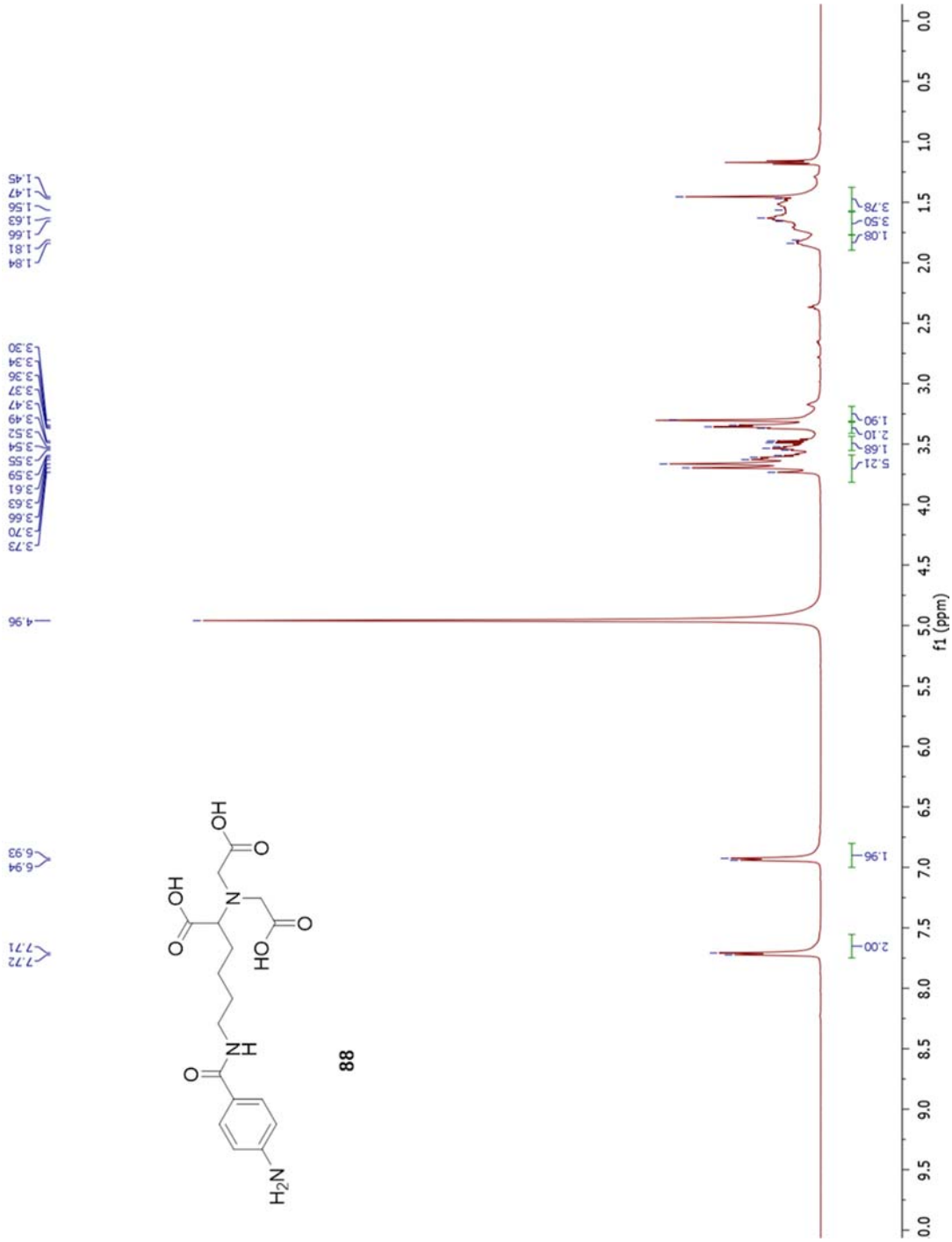

Figure A.81 ^{1}H-NMR of **88**

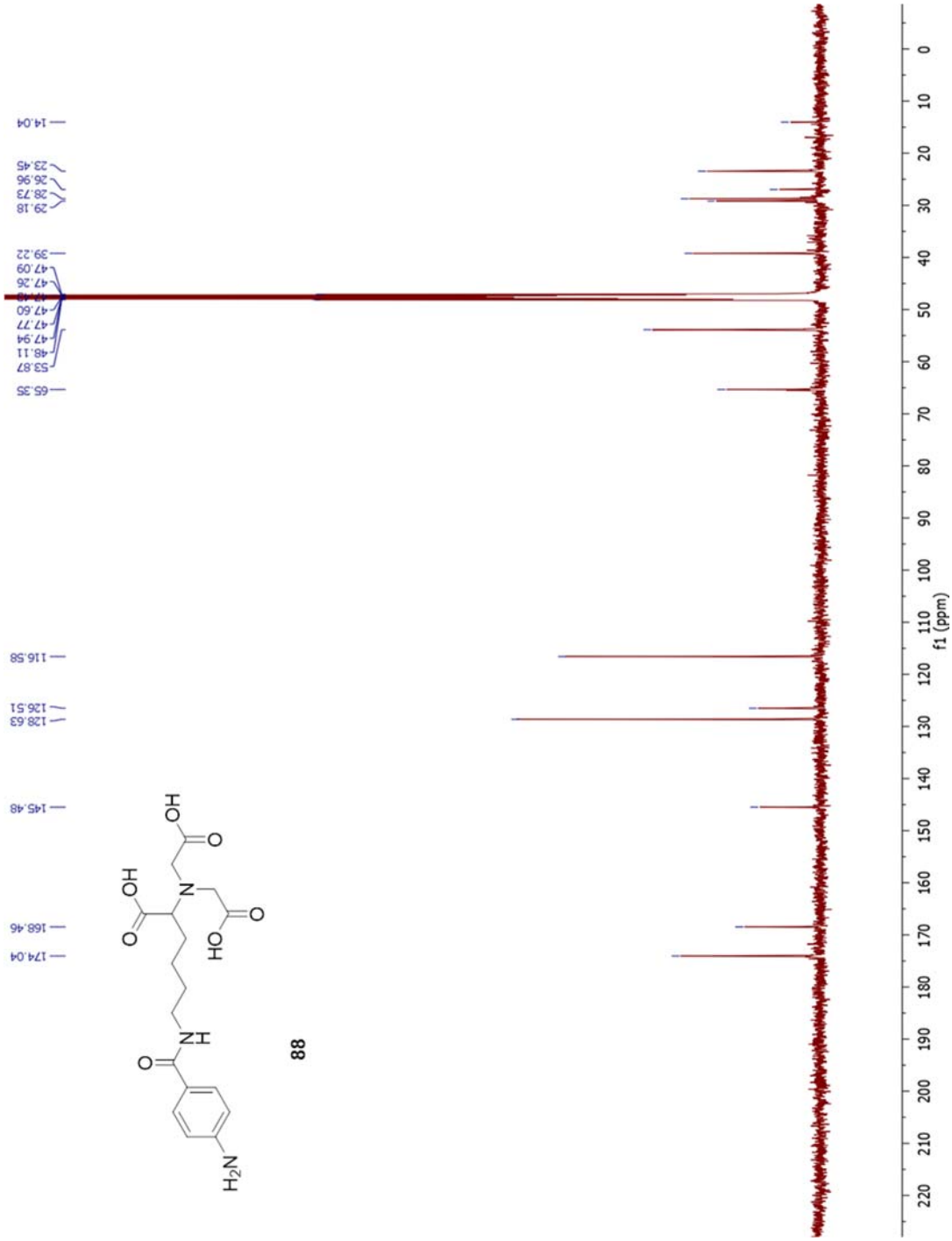

Figure A.82 ^{13}C-NMR of **88**

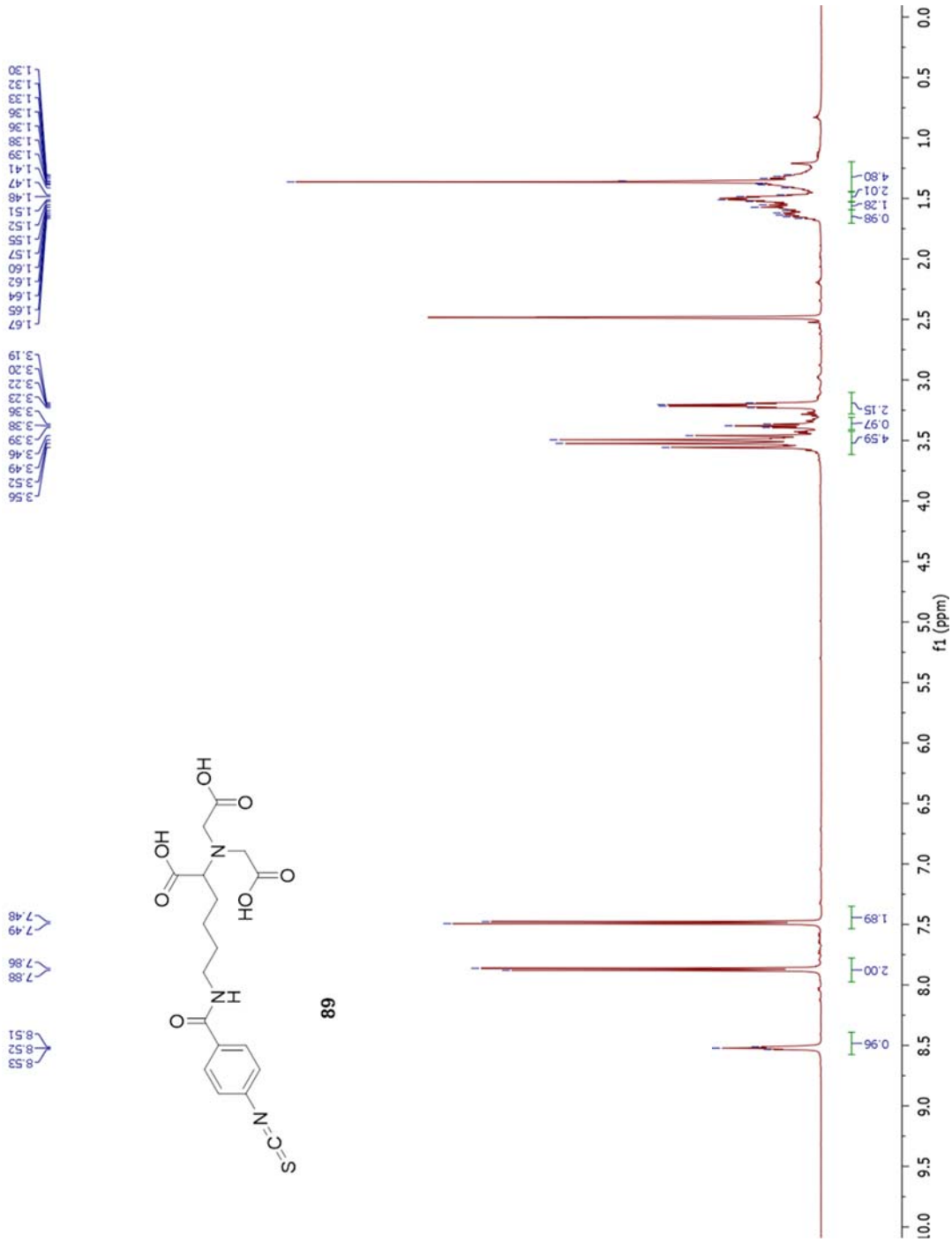

Figure A.83 ^{1}H-NMR of **89**

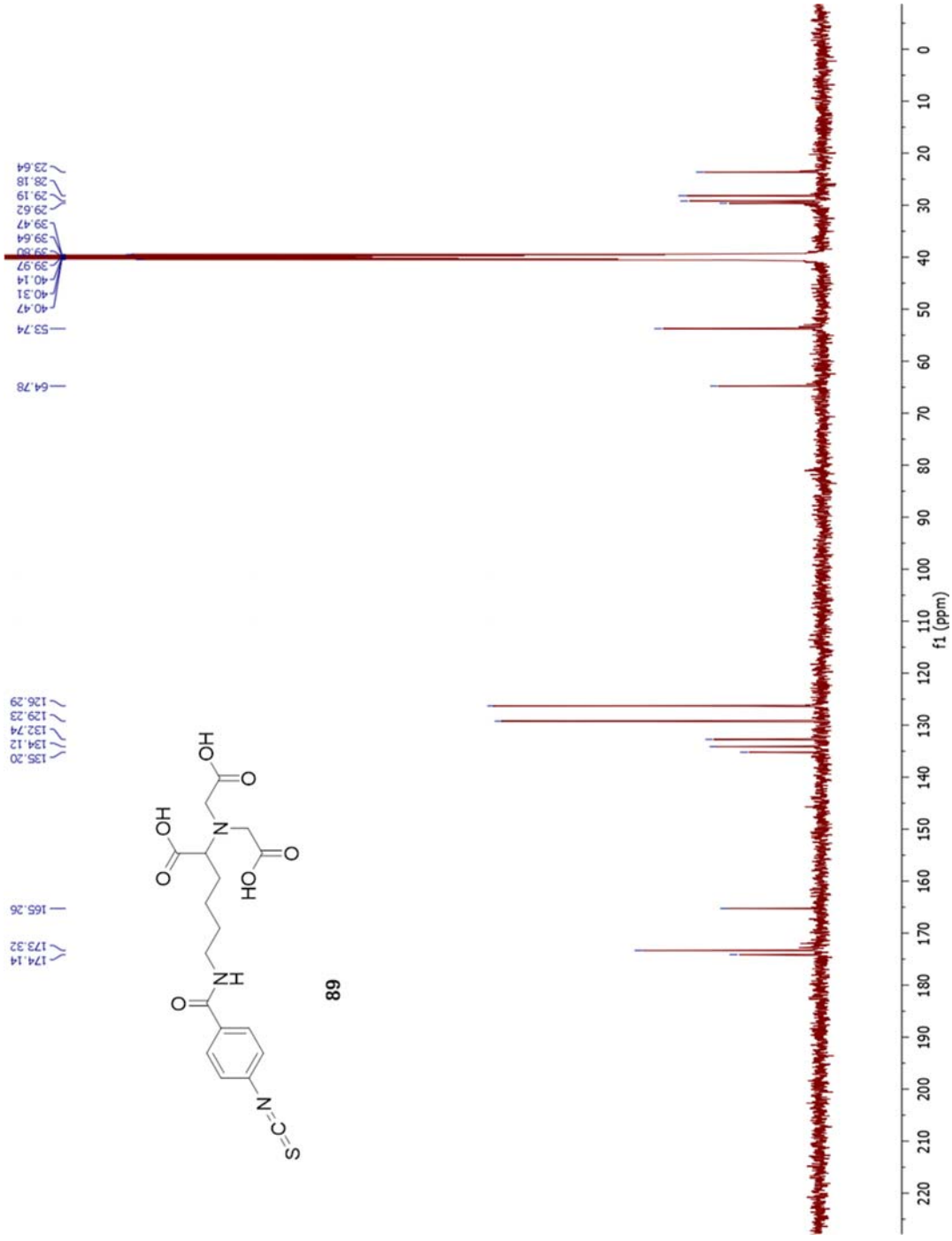

Figure A.84 ^{13}C-NMR of **89**

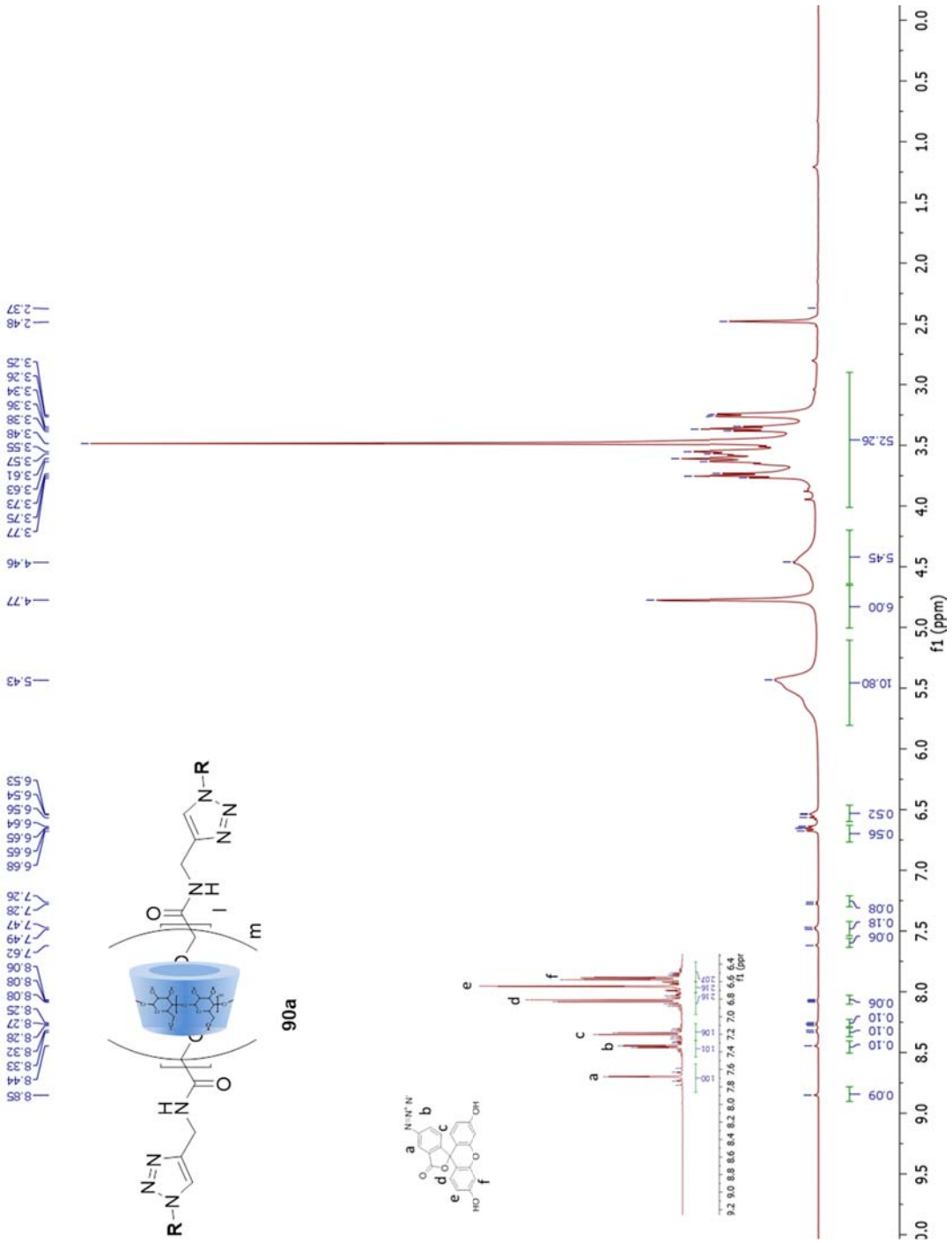

Figure A.85 ^{1}H-NMR of **90a**

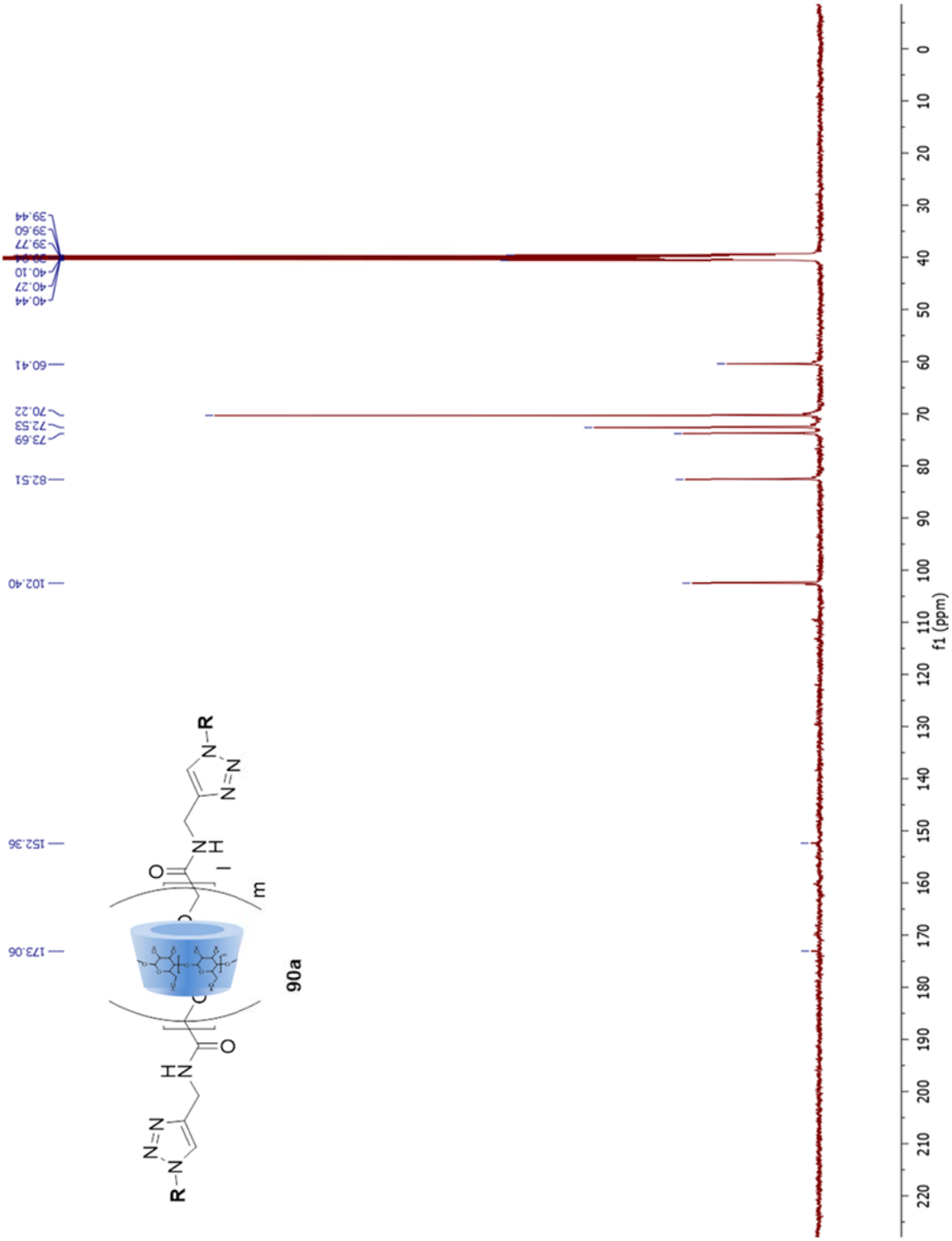

Figure A.86 ^{13}C-NMR of **90a**

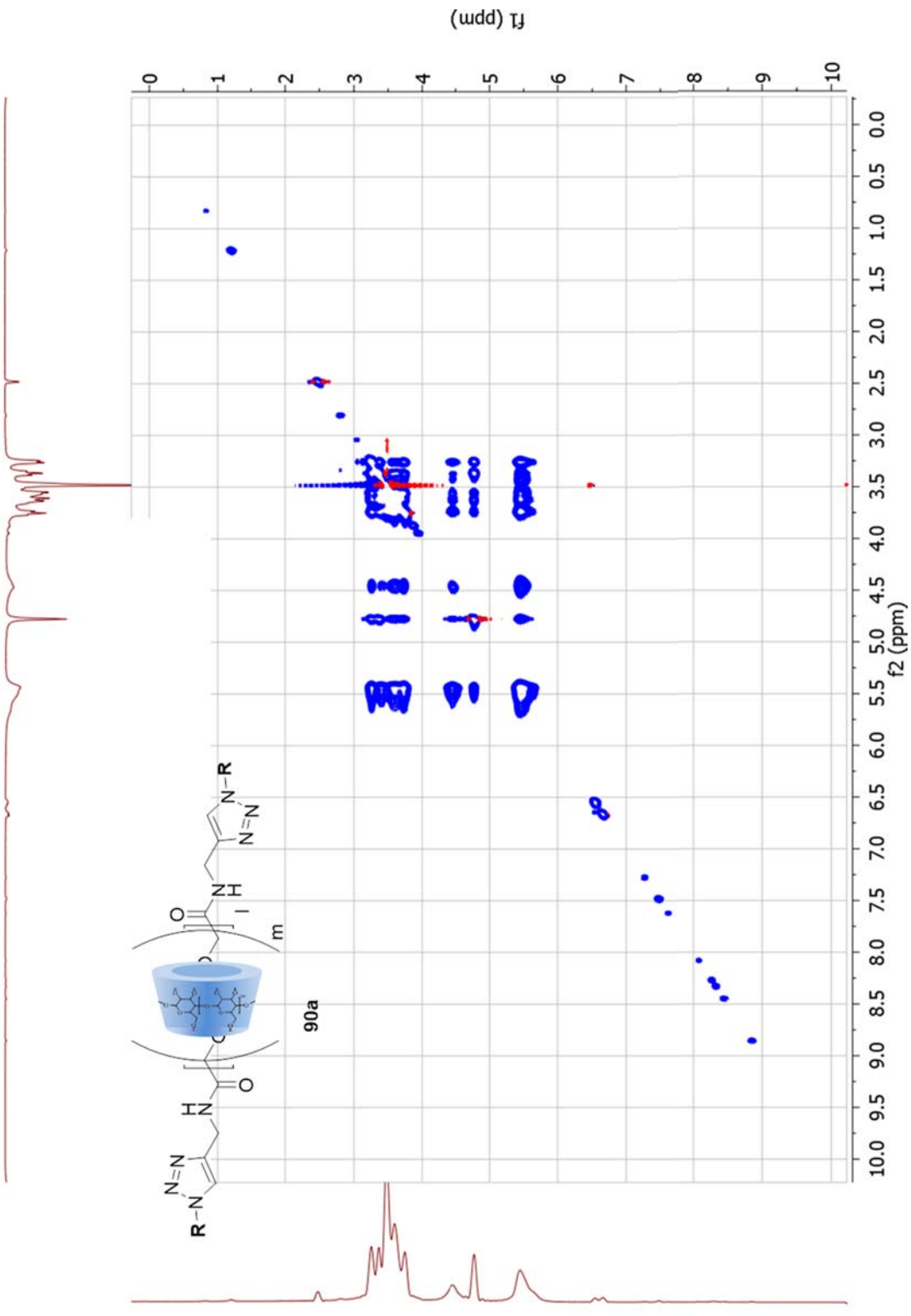

Figure A.87 2D NOESY Spectrum of **90a**

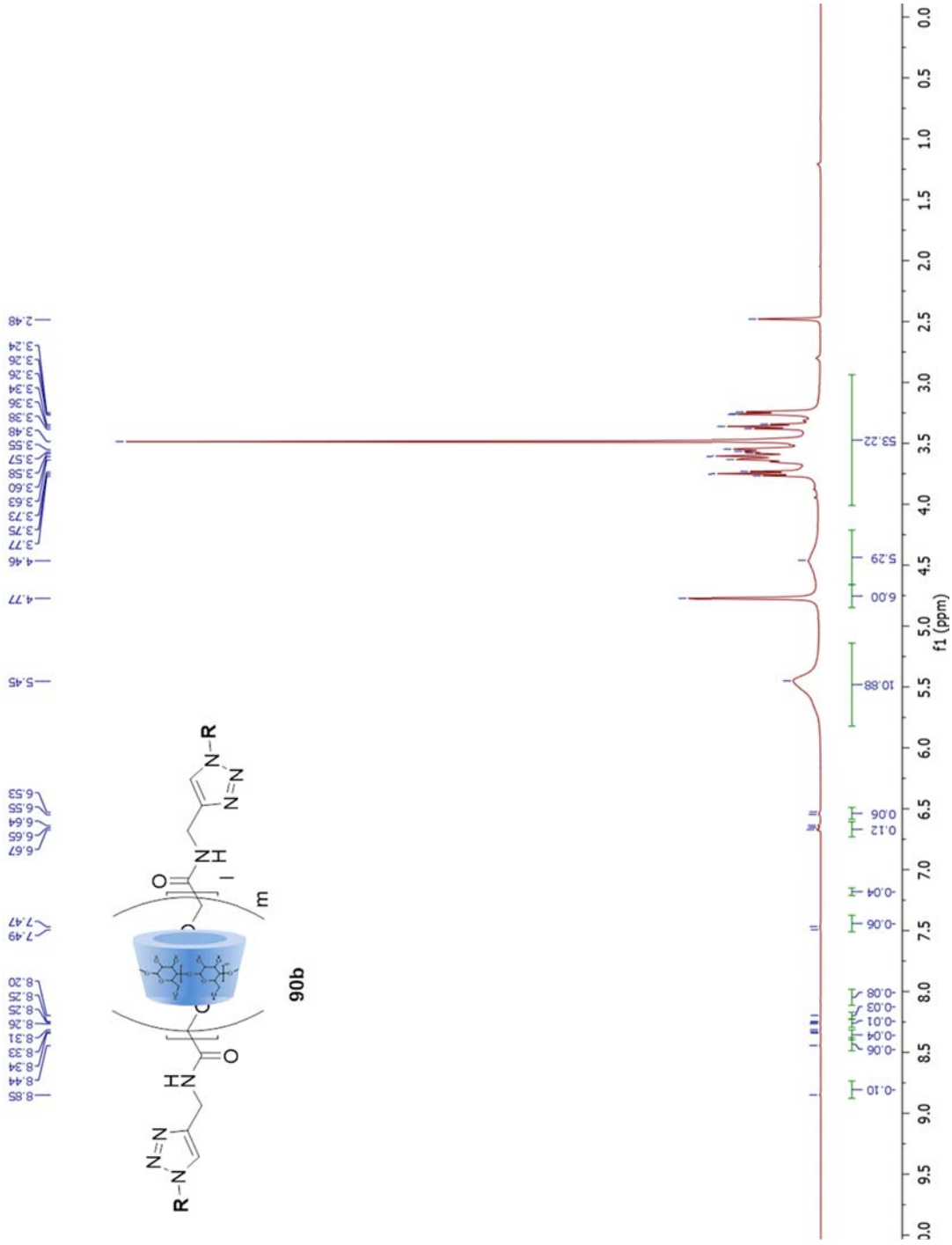

Figure A.88 ^{1}H-NMR of **90b**

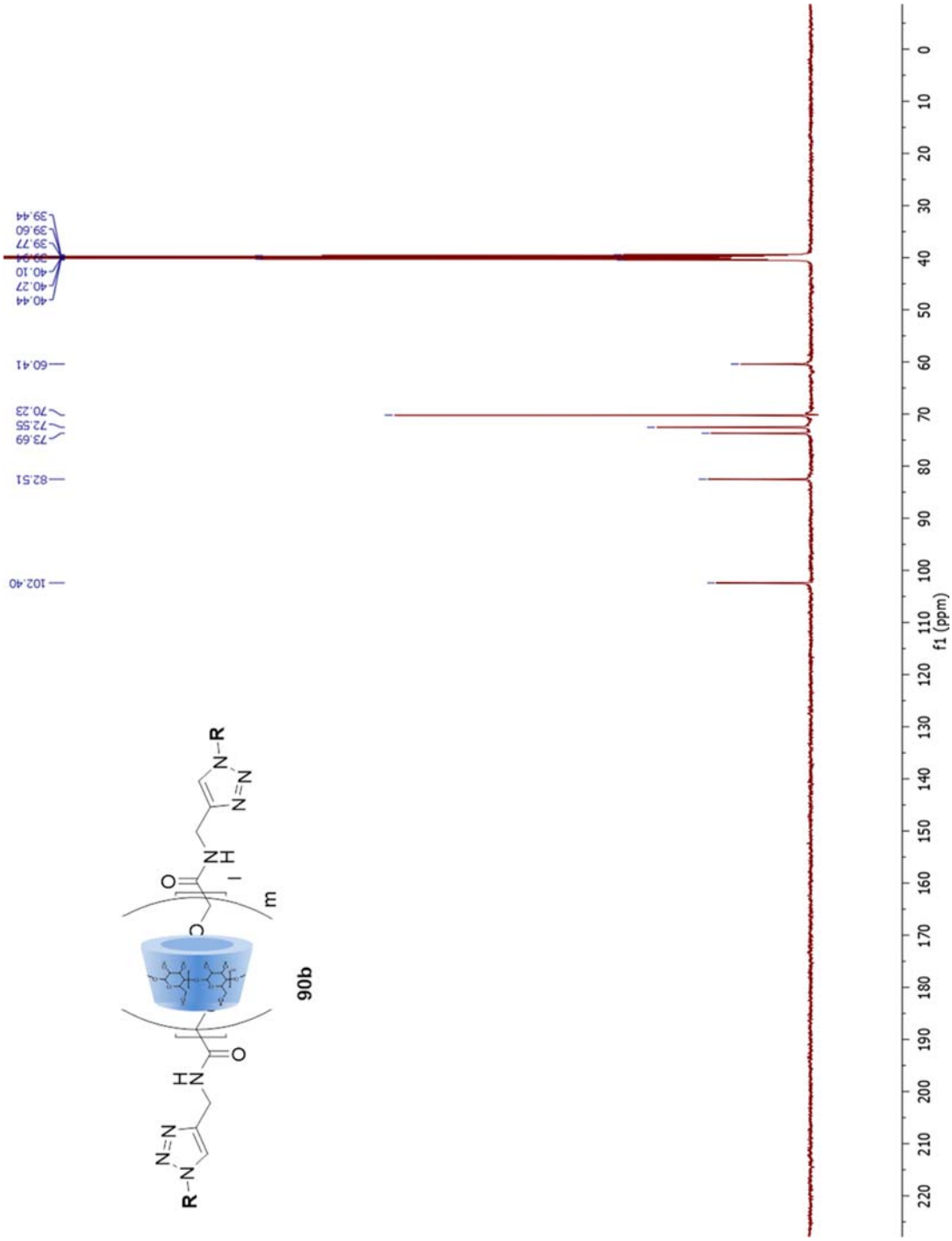

Figure A.89 ^{13}C-NMR of **90b**

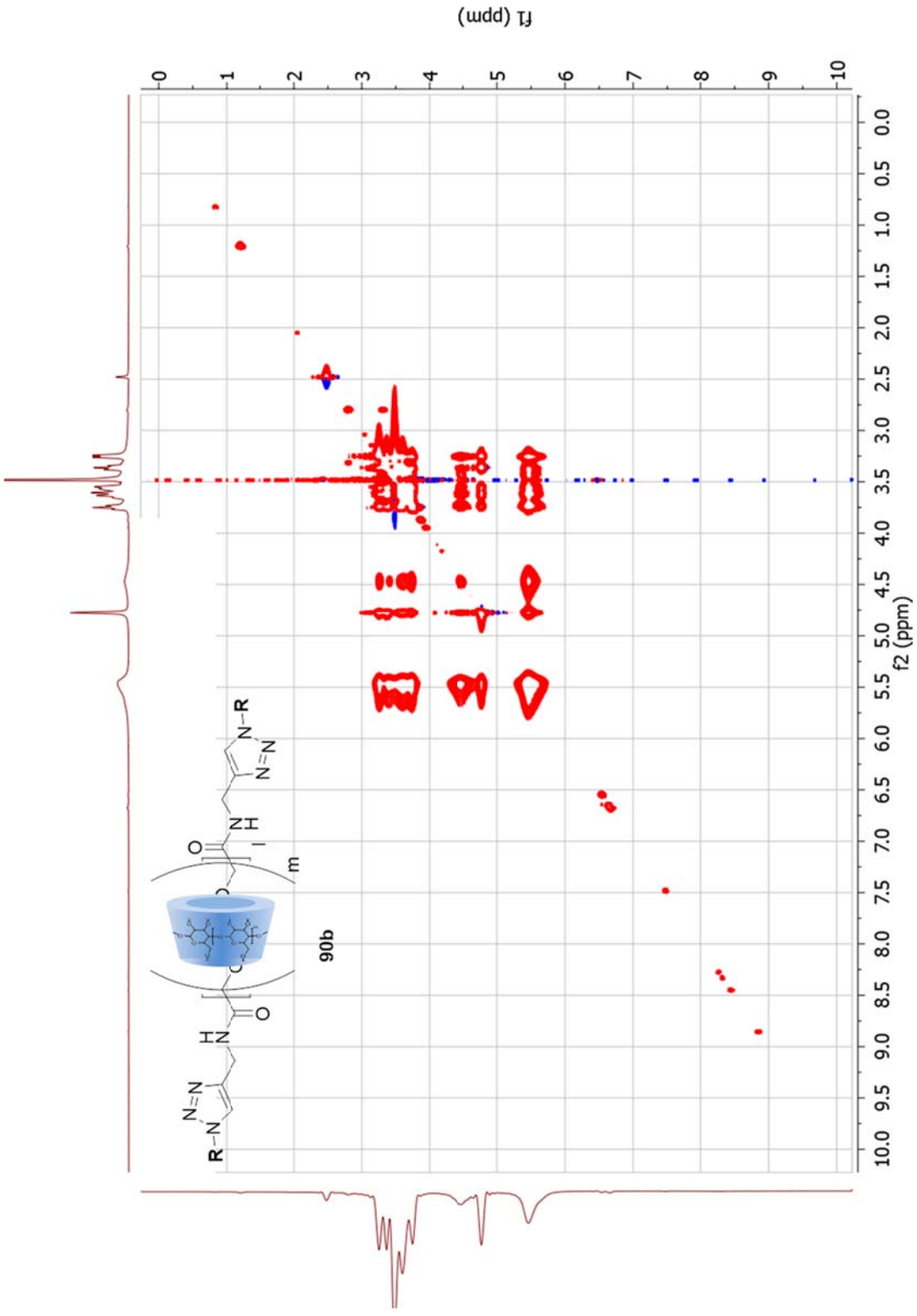

Figure A.90 2D NOESY Spectrum of **90b**

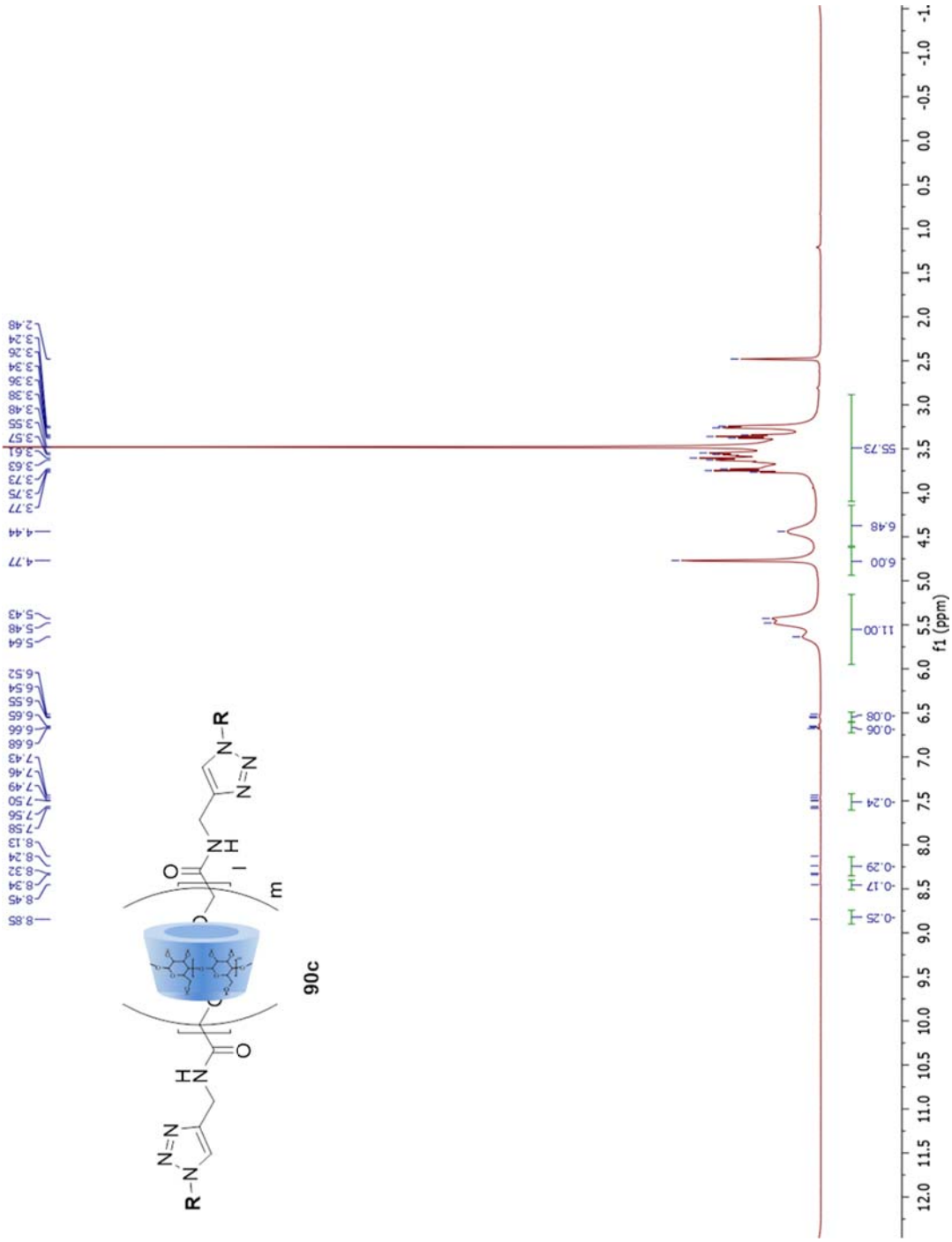

Figure A.91 ^{1}H-NMR of **90c**

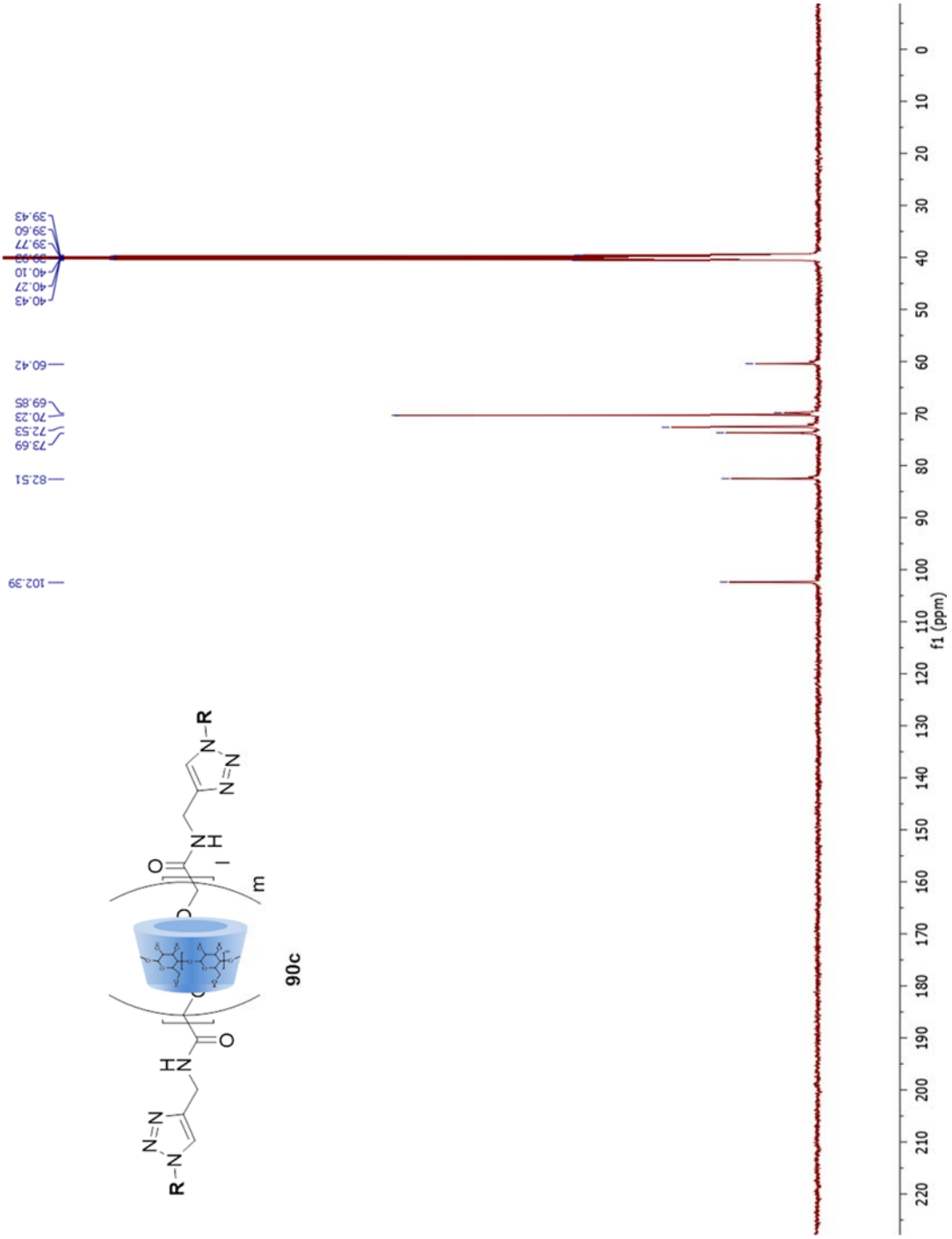

Figure A.92 ^{13}C-NMR of **90c**

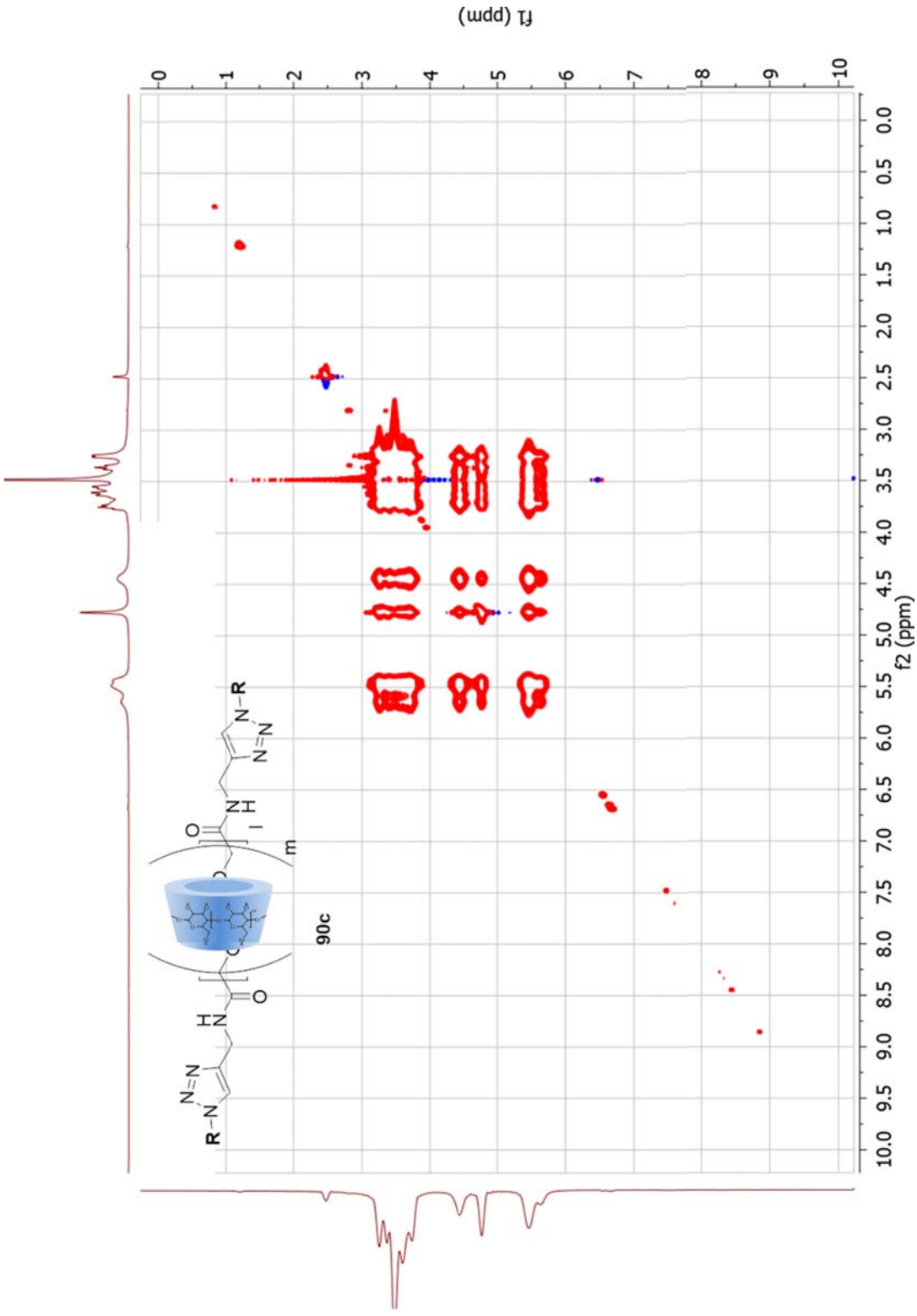

Figure A.93 2D NOESY Spectrum of **90c**

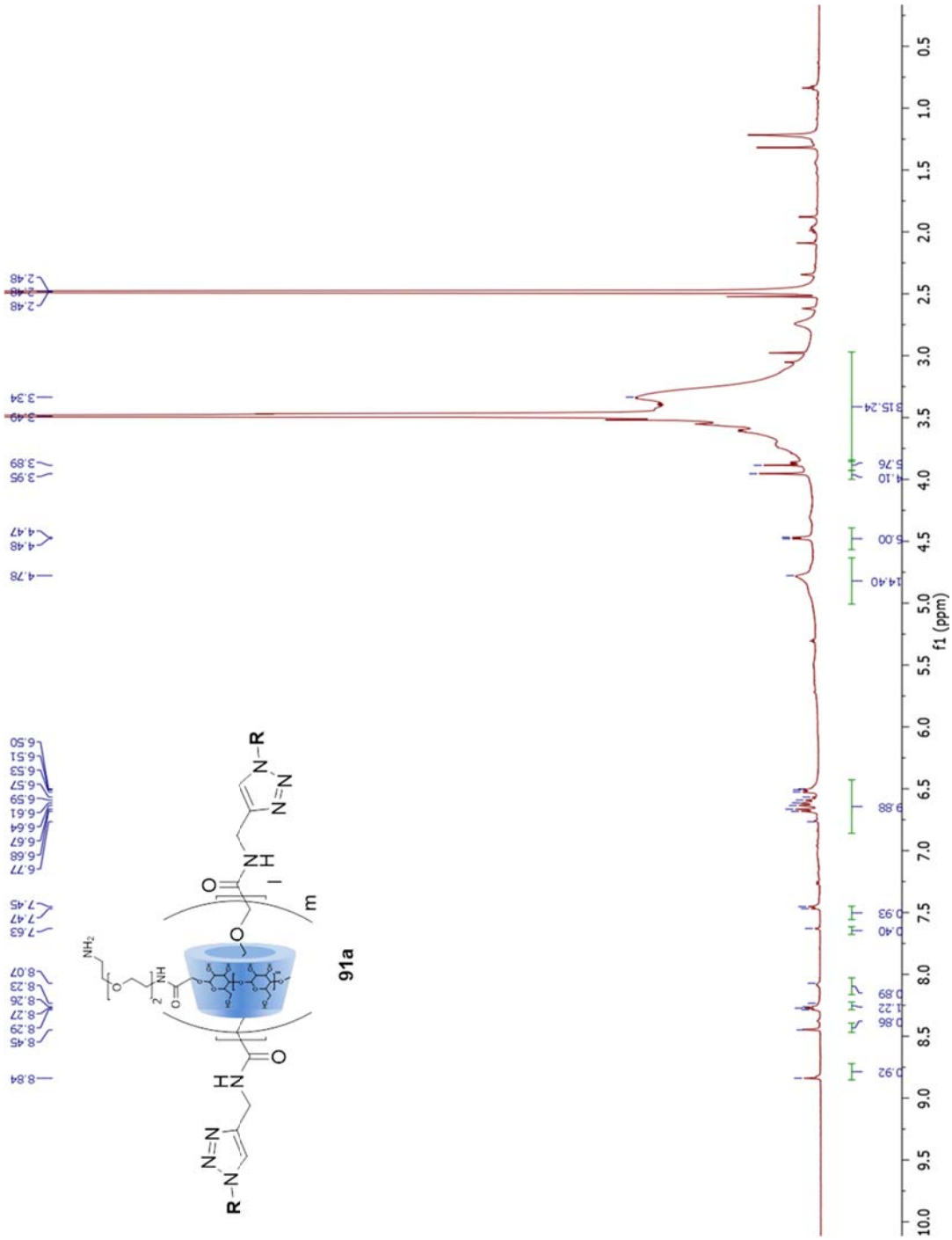

Figure A.94 ^{1}H-NMR of **91a**

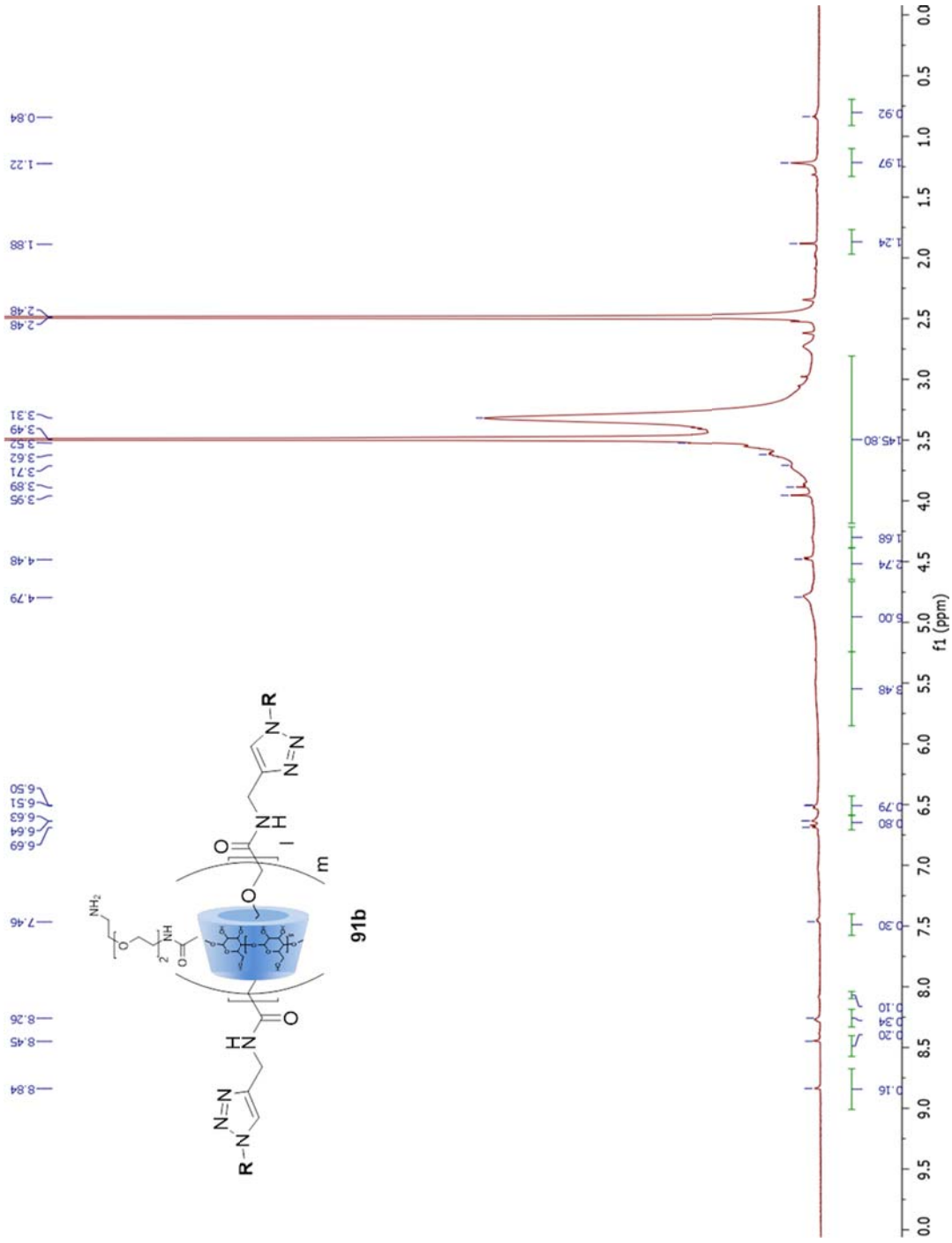

Figure A.95 ^{1}H-NMR of **91b**

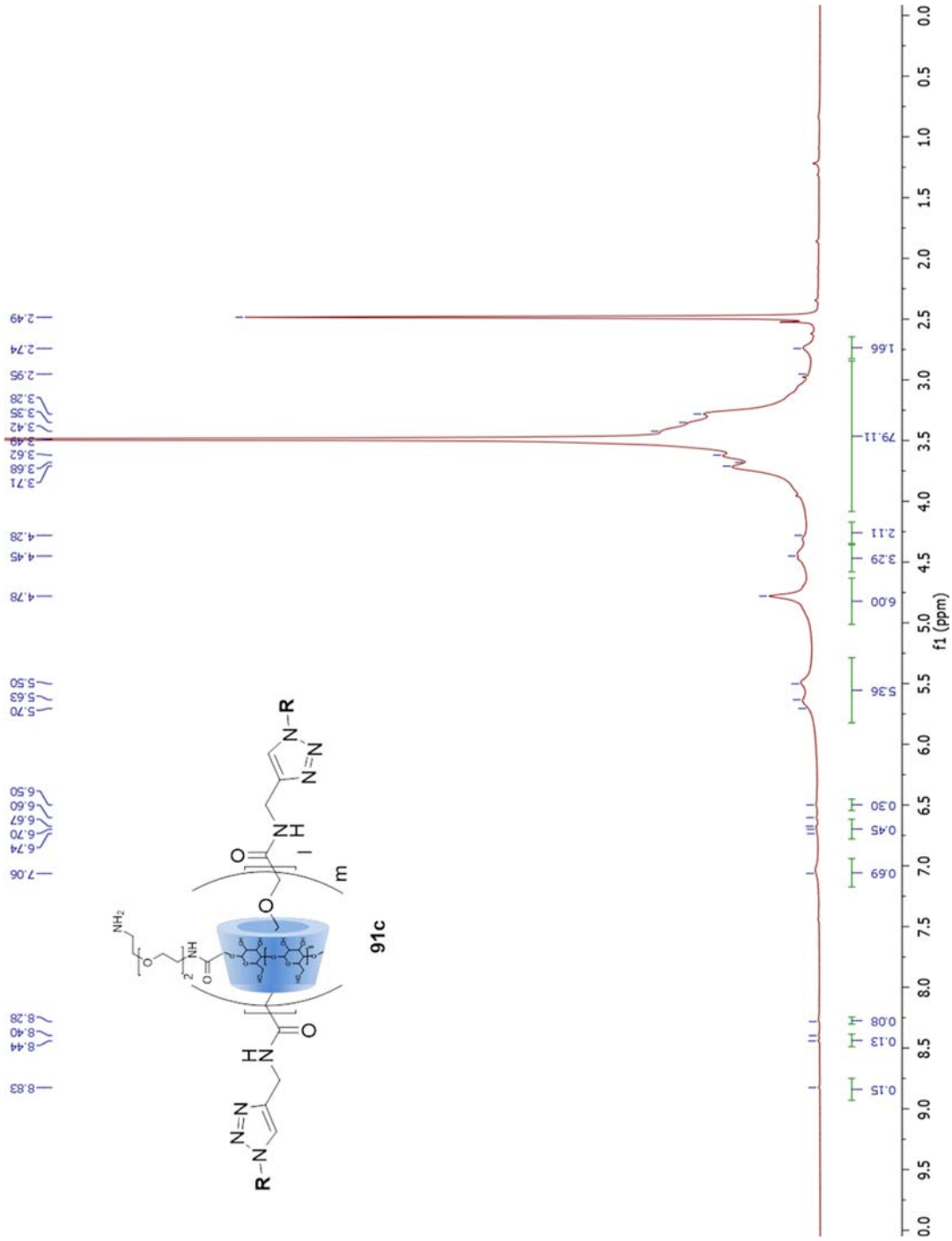

Figure A.96 ^{1}H-NMR of **91c**

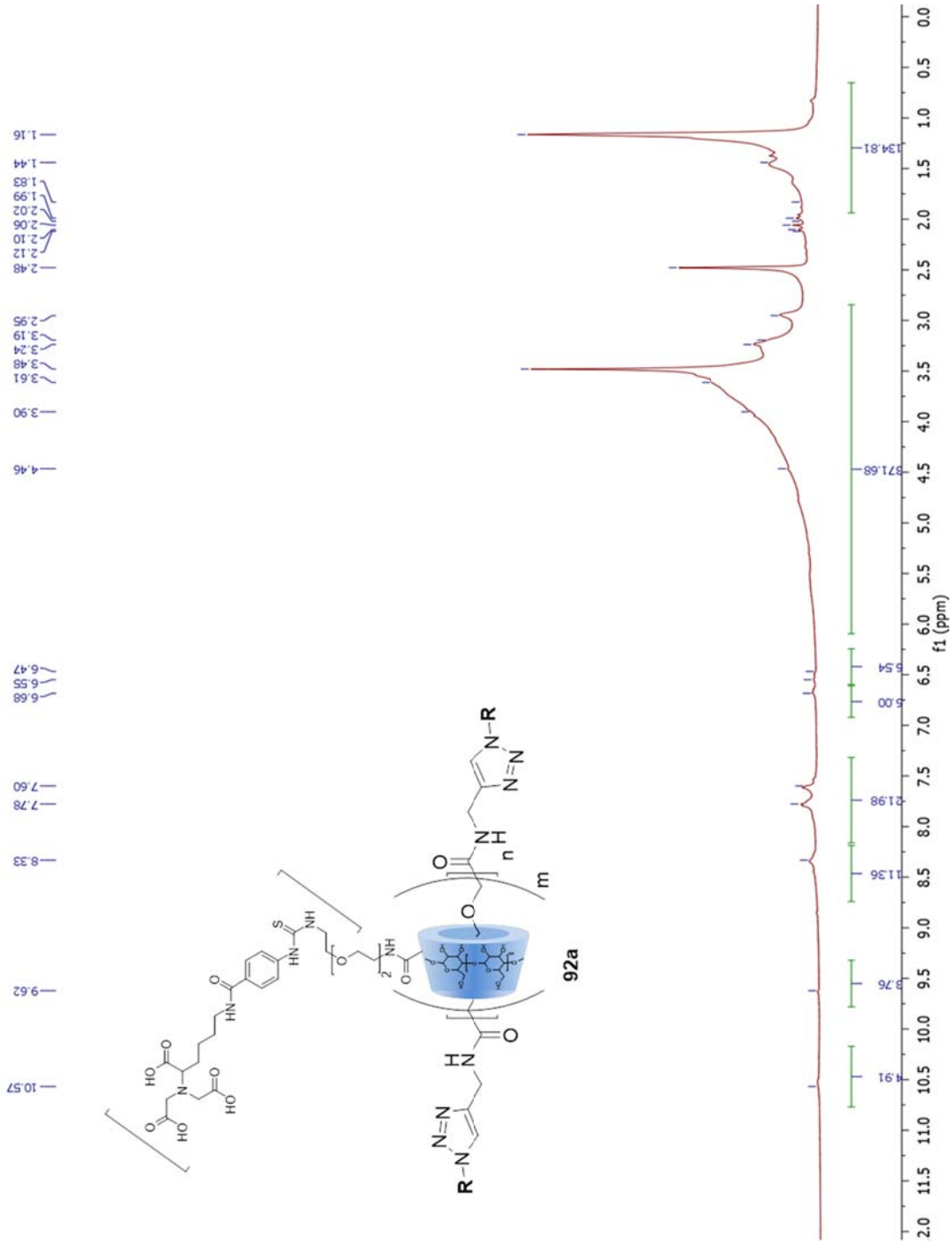

Figure A.97 ^{1}H-NMR of **92a**

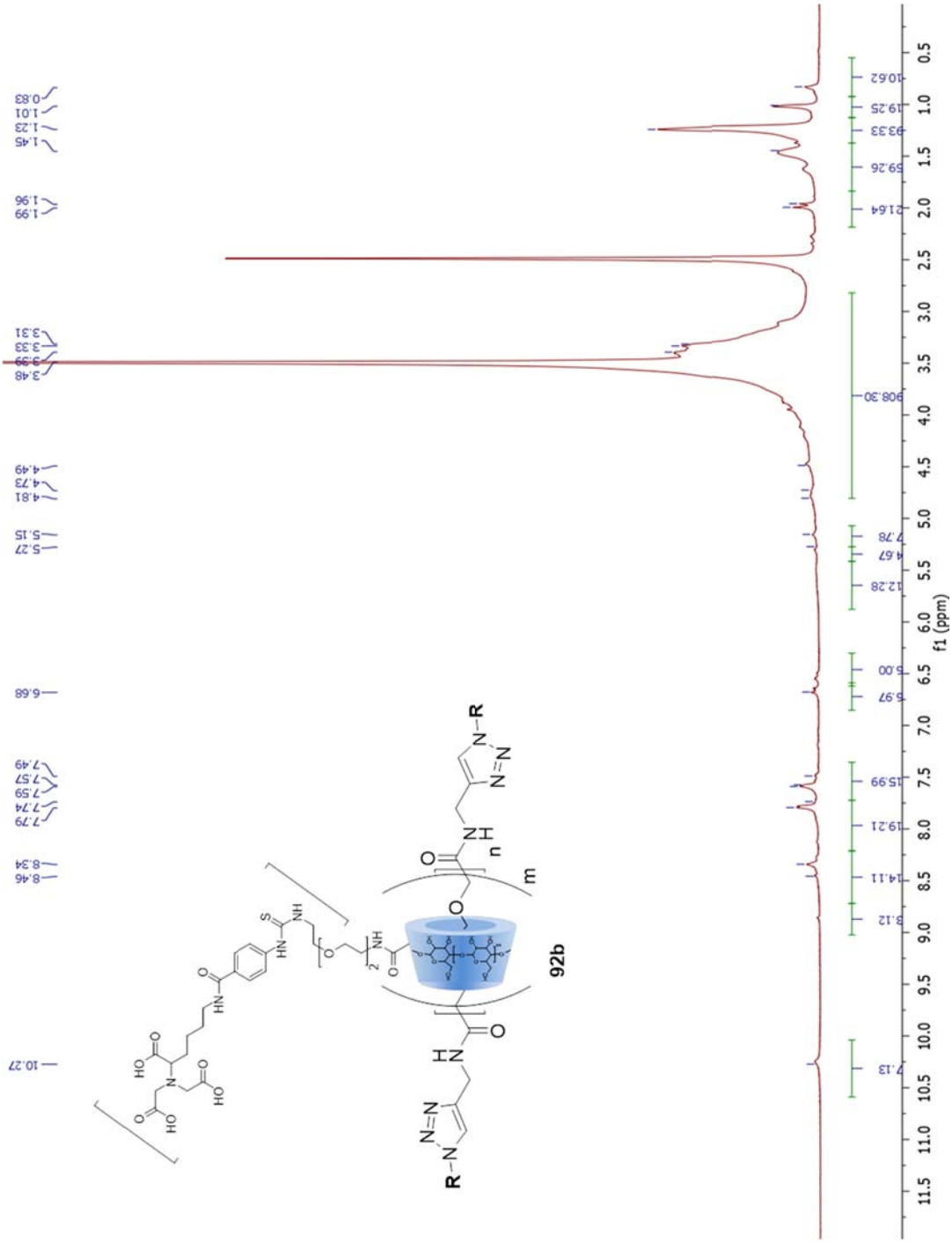

Figure A.98 ^{1}H-NMR of **92b**

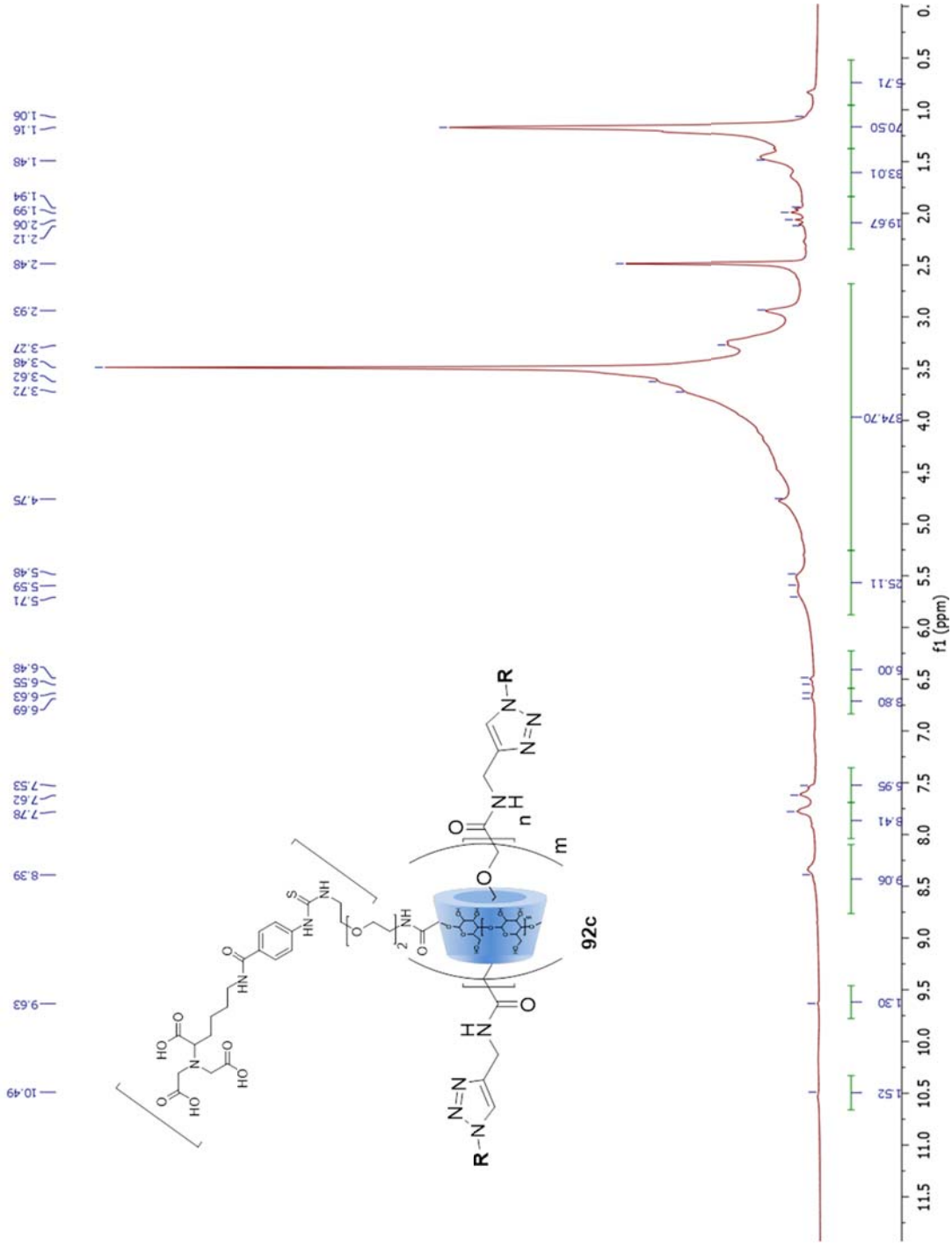

Figure A.99 ^{1}H-NMR of **92c**

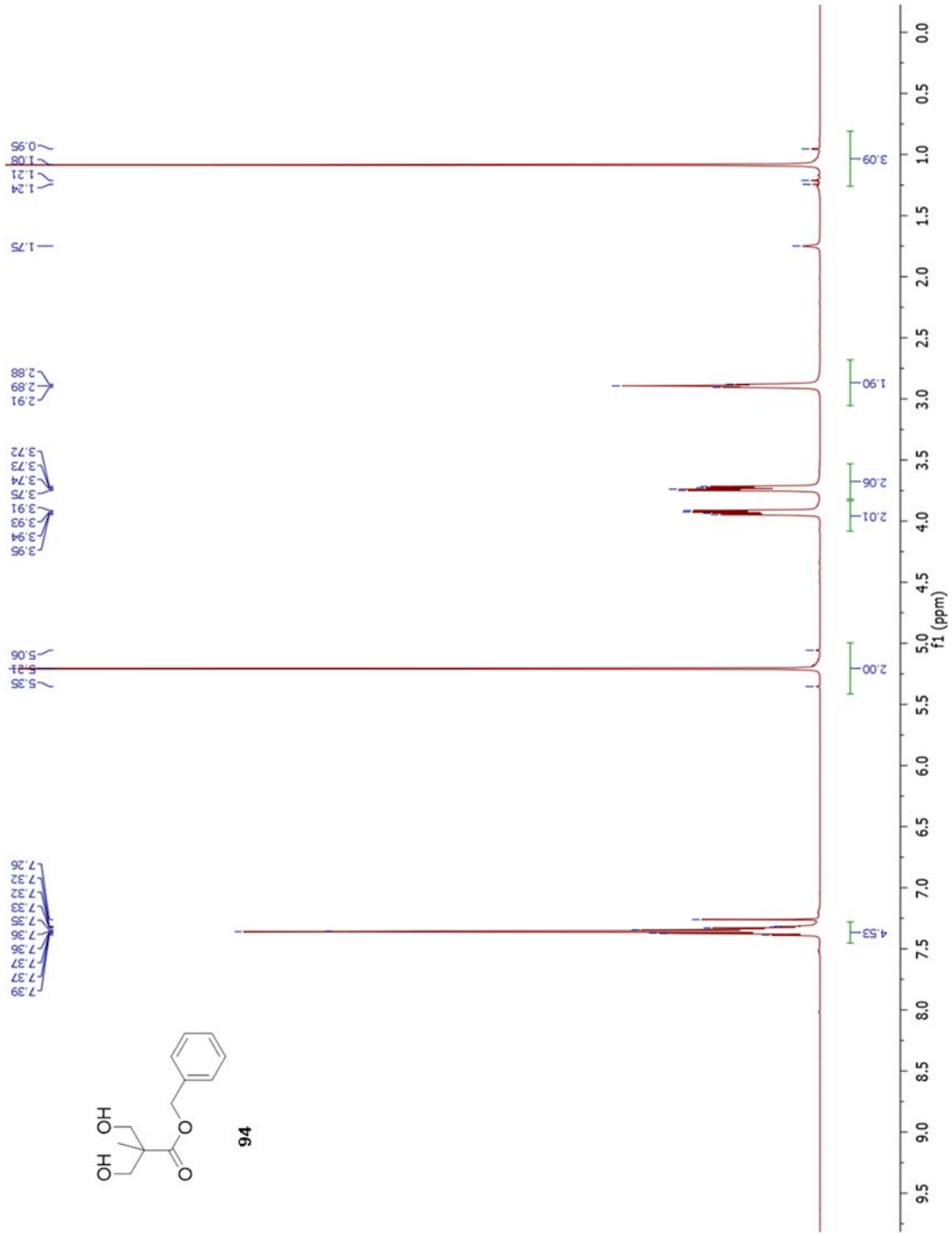

Figure A.100 ^{1}H-NMR of **94**

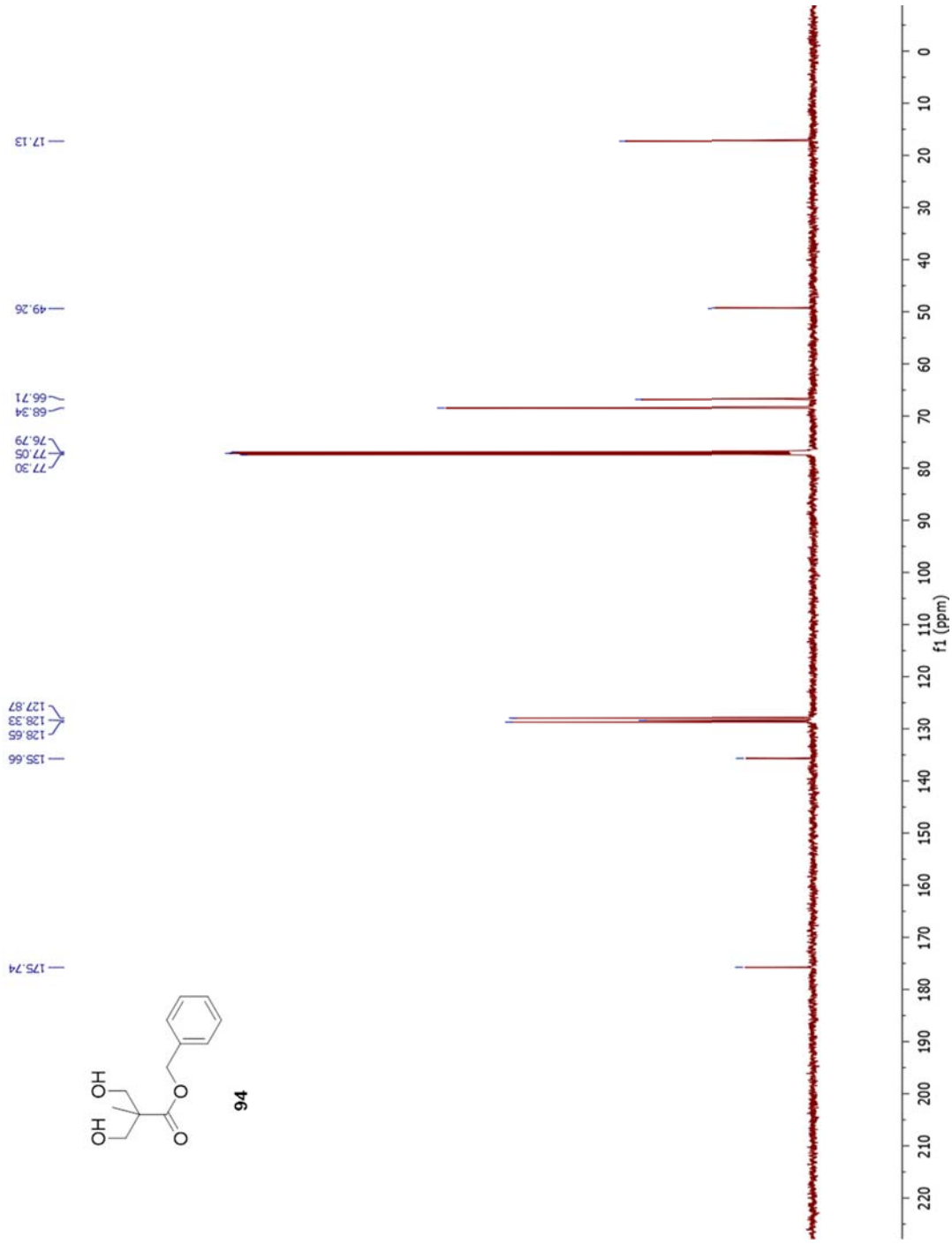

Figure A.101 ^{13}C-NMR of **94**

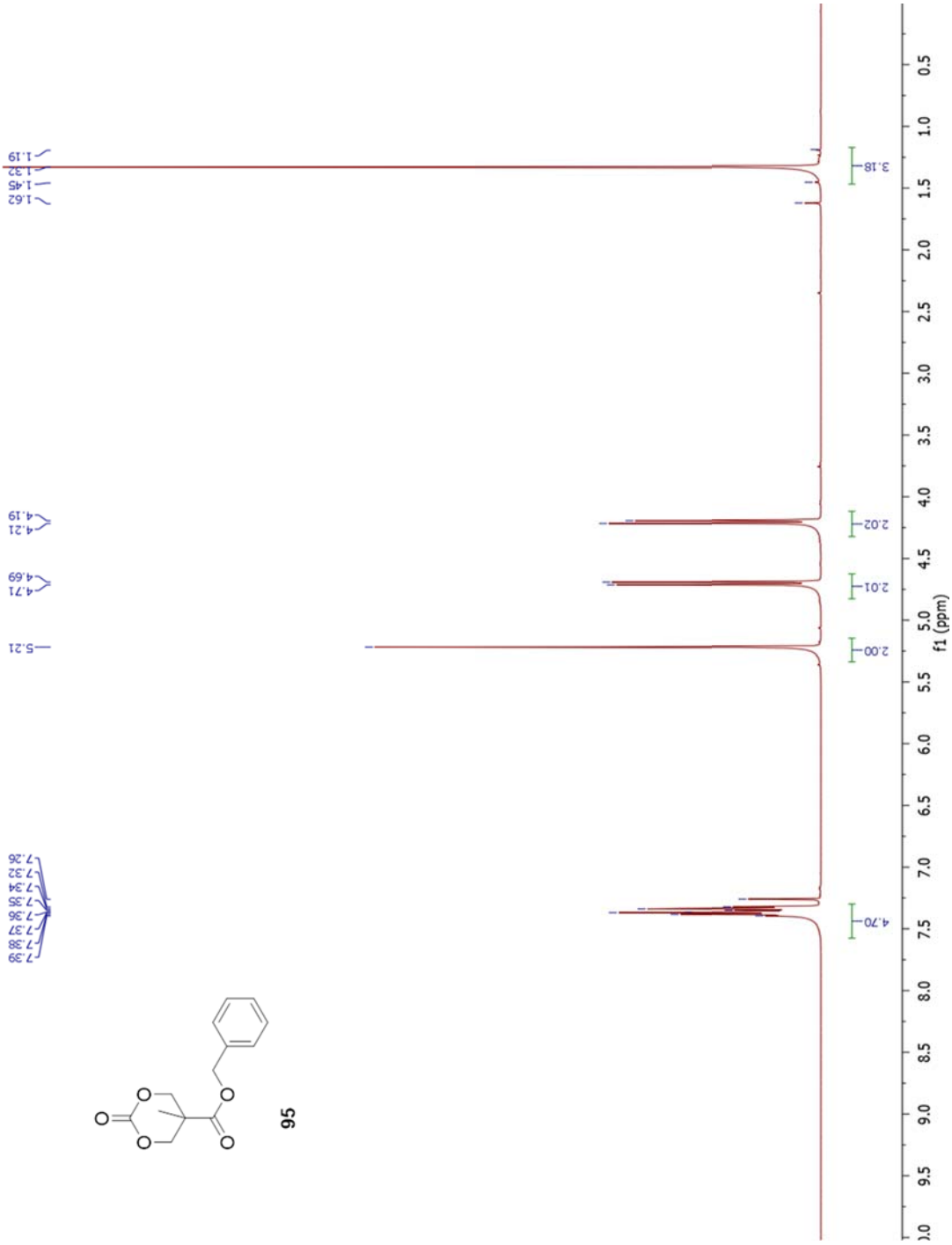

Figure A.102 ^{1}H-NMR of **95**

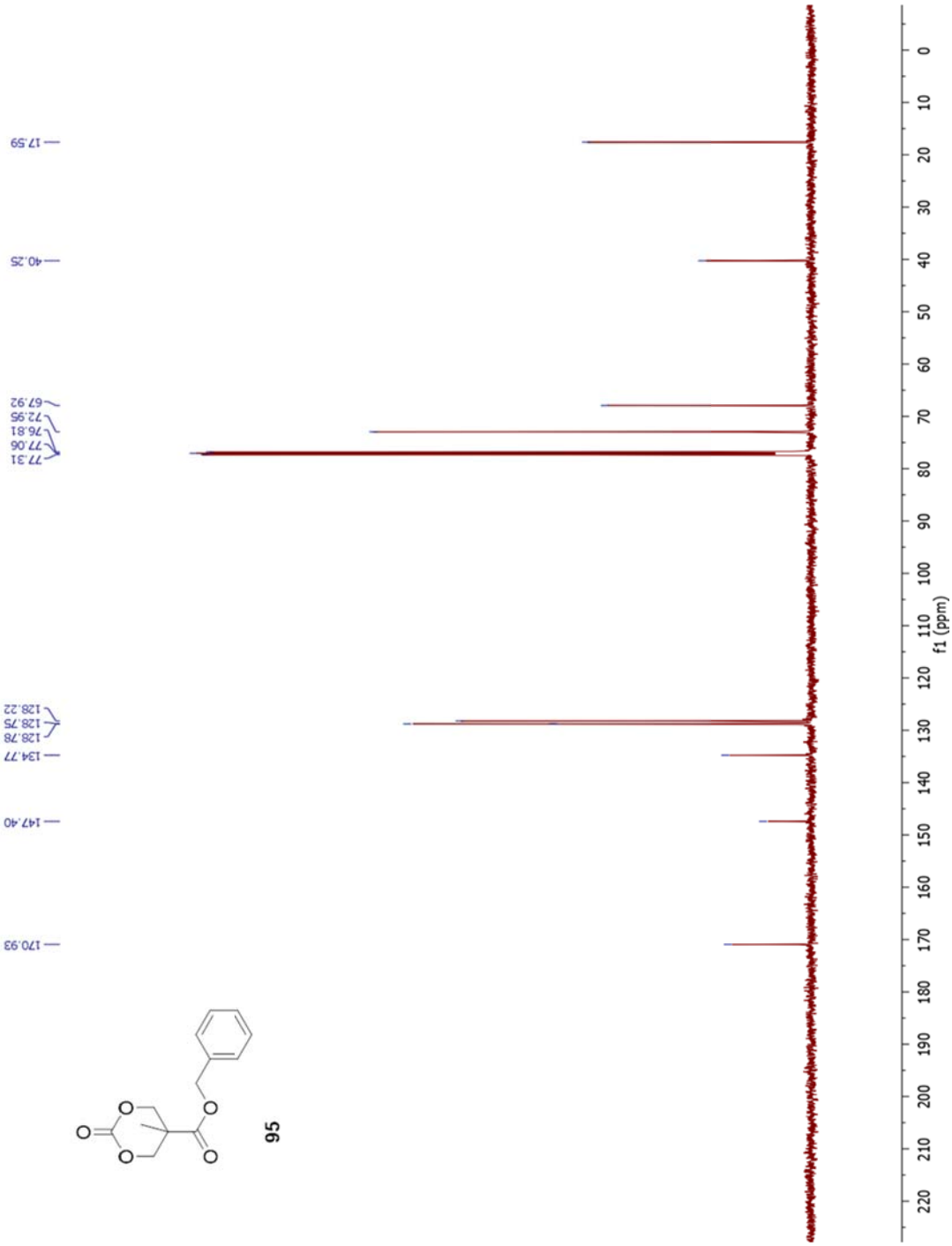

Figure A.103 ^{13}C-NMR of **95**

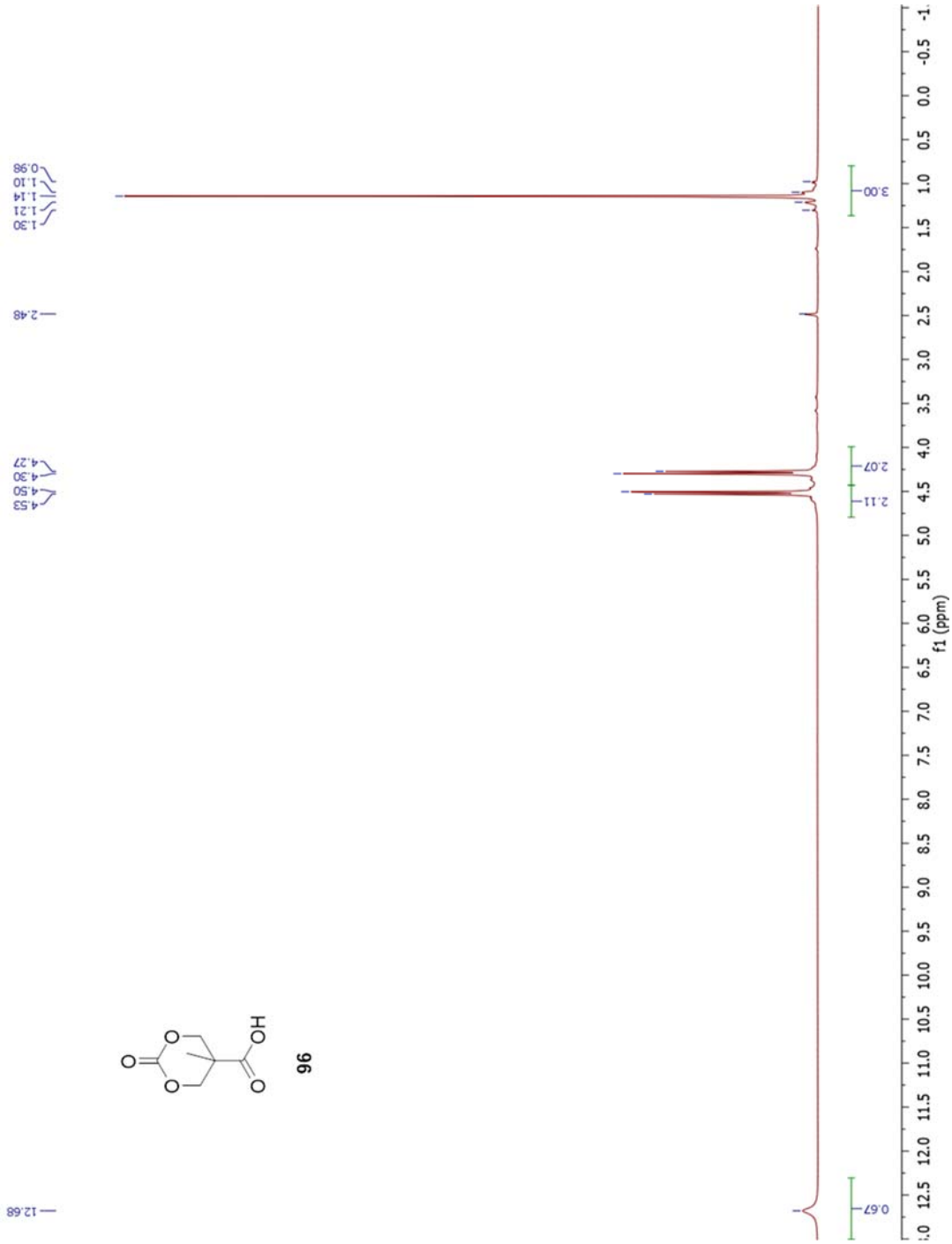

Figure A.104 ^{1}H-NMR of **96**

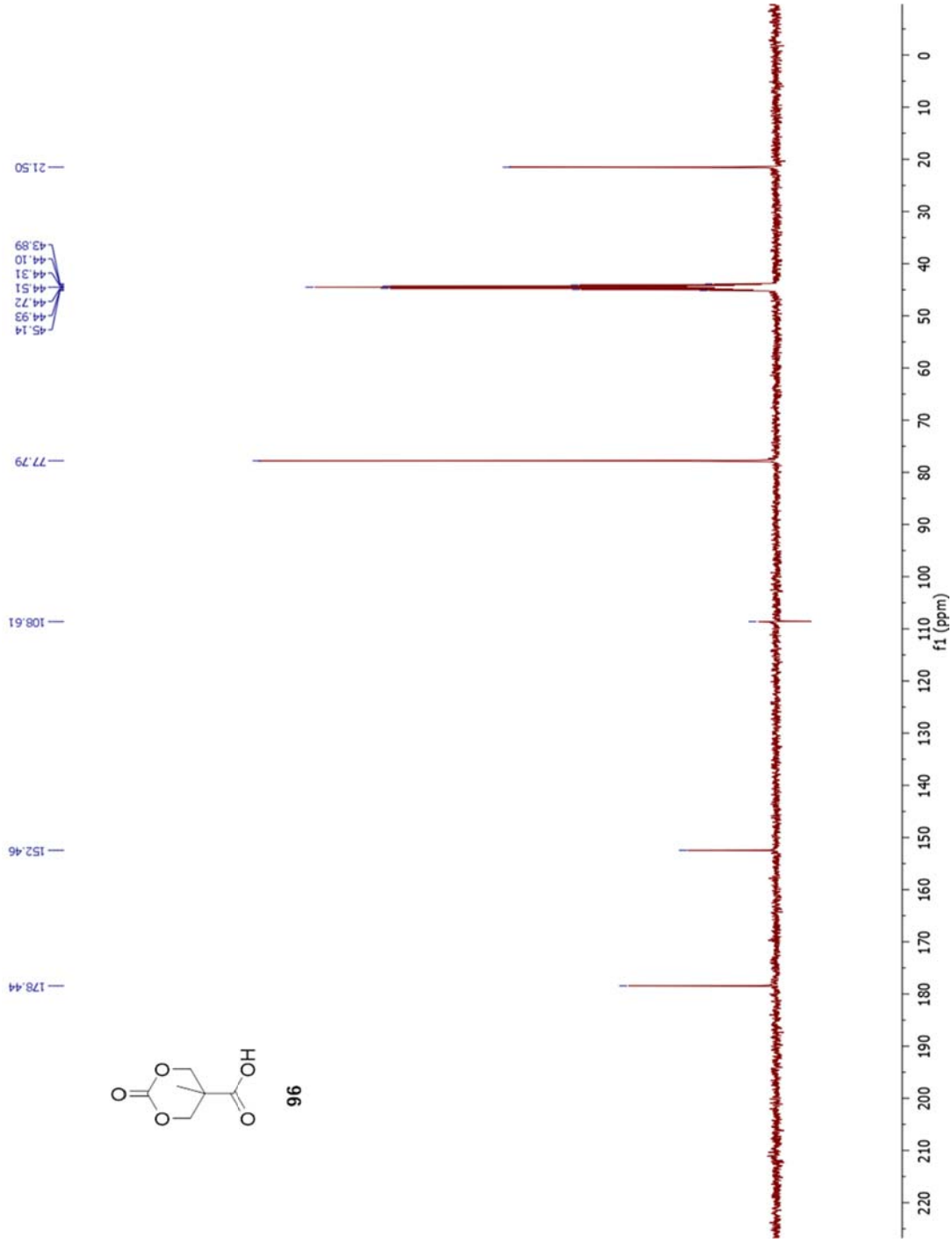

Figure A.105 ^{13}C-NMR of **96**

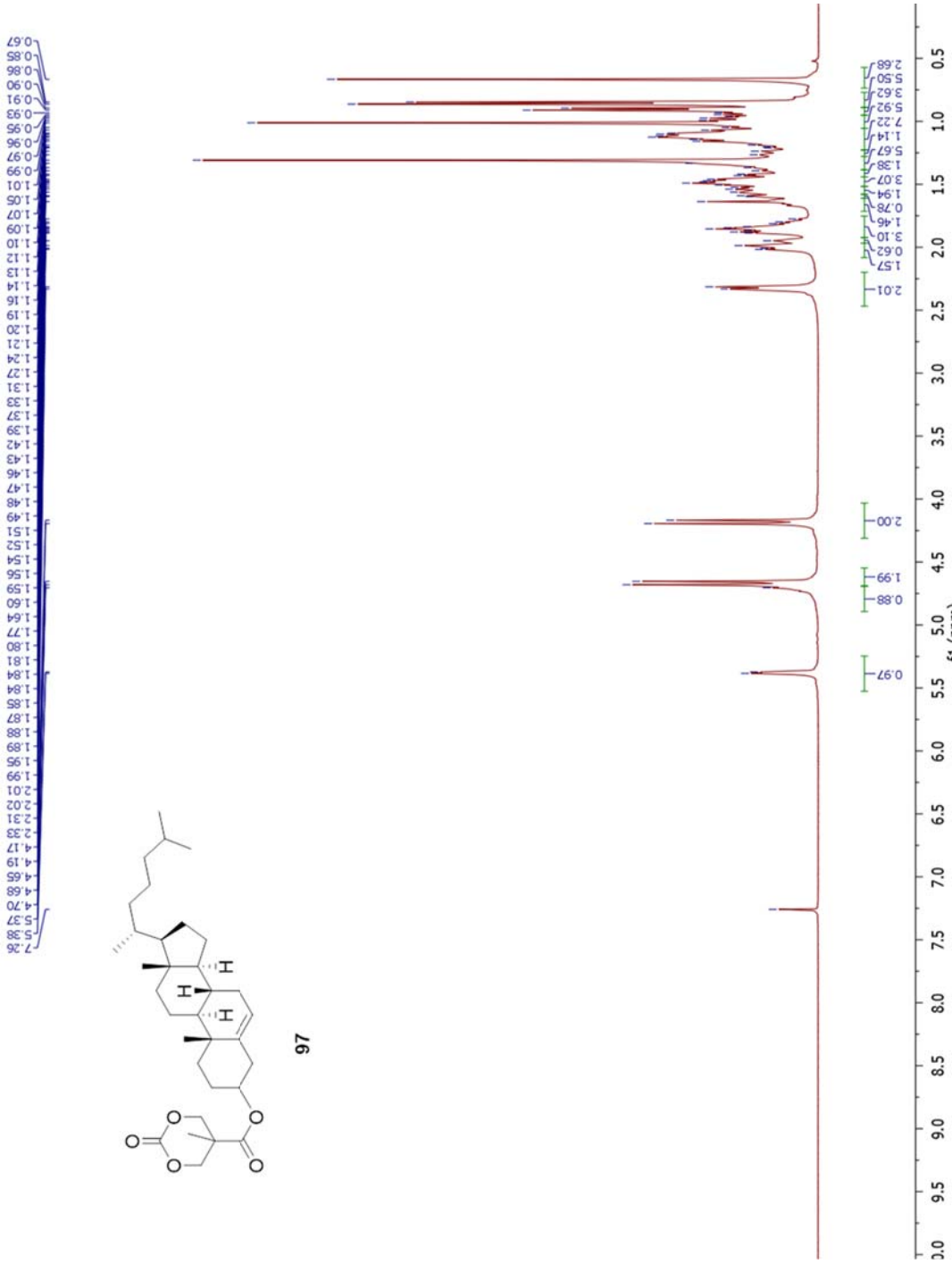

Figure A.106 ^{1}H-NMR of **97**

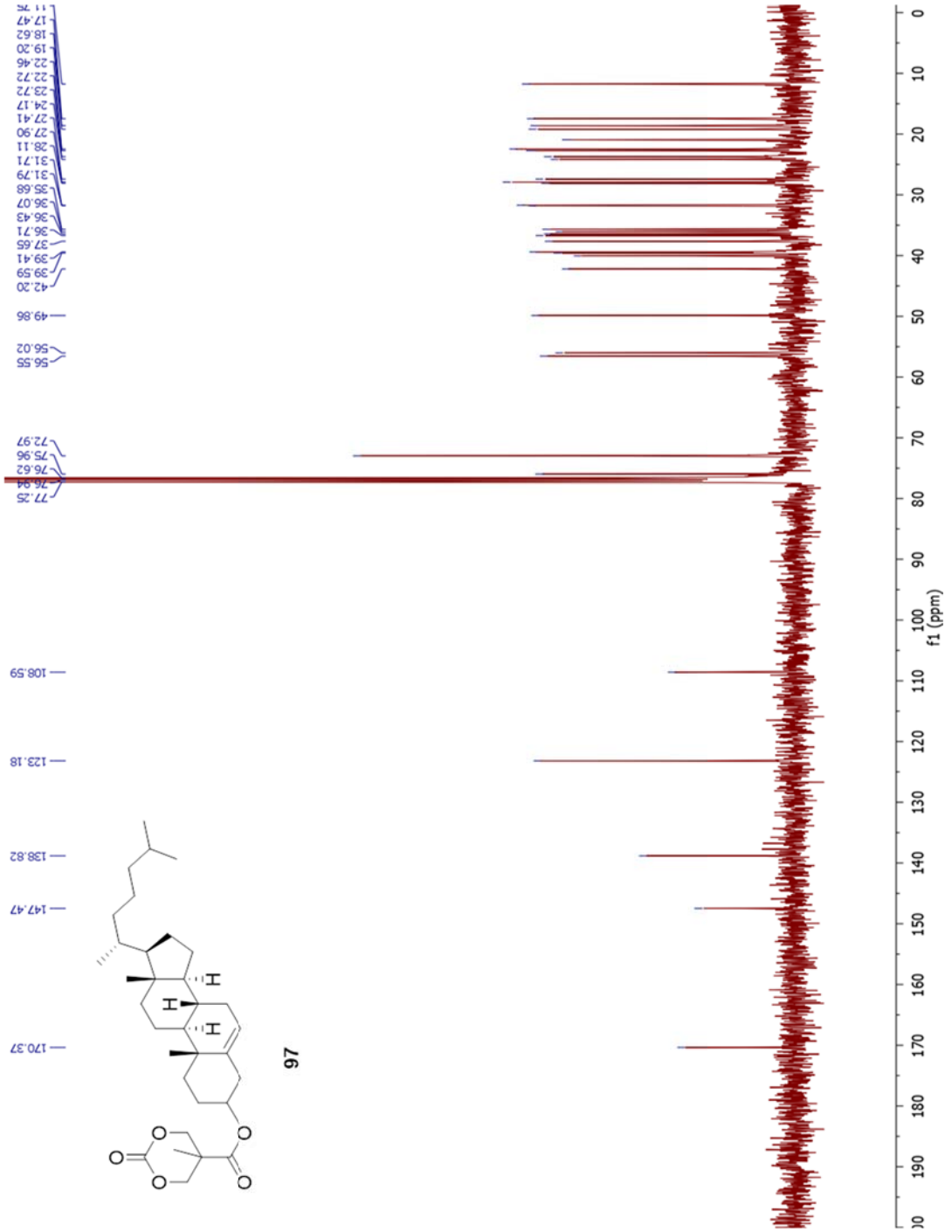

Figure A.107 ^{13}C-NMR of **97**

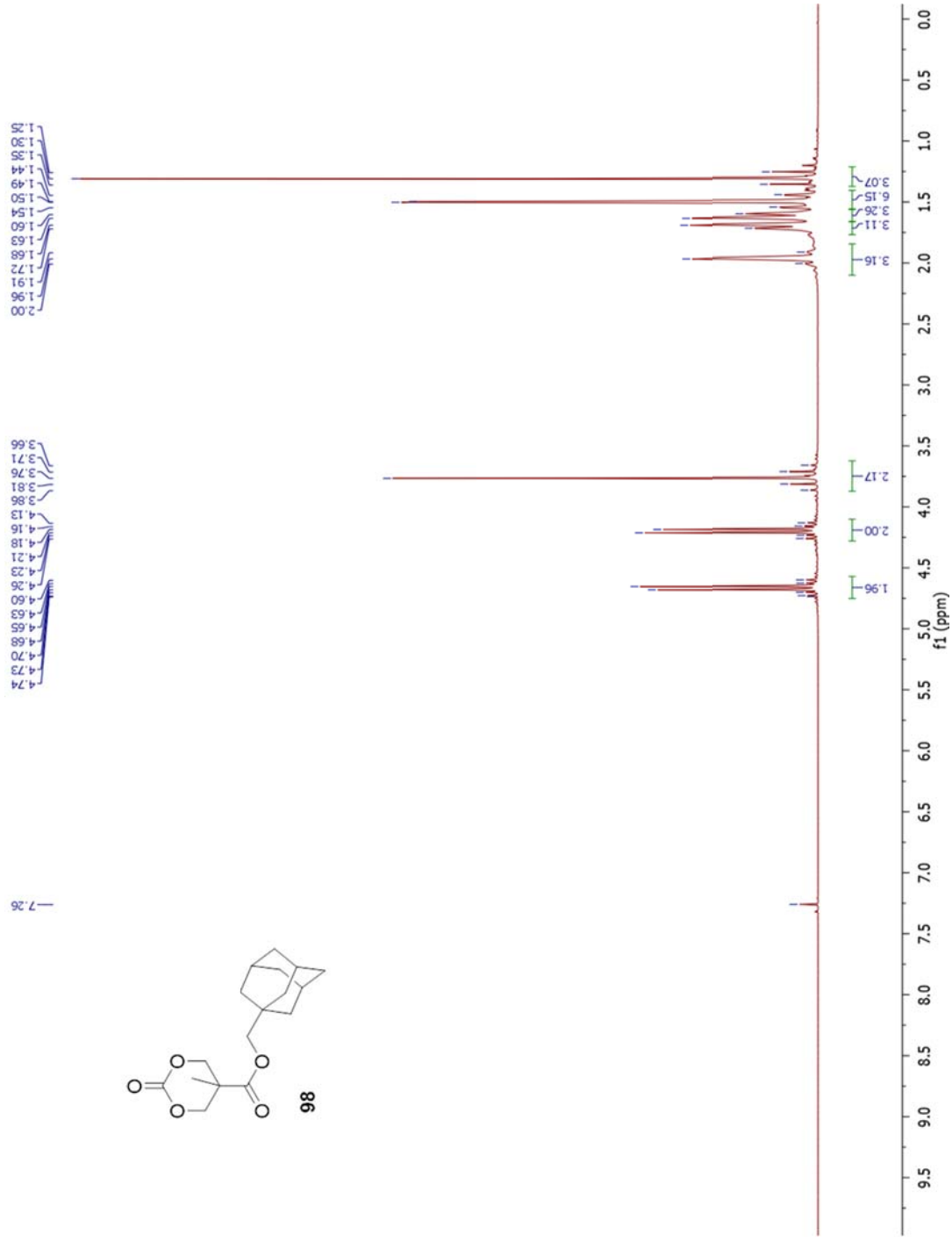

Figure A.108 ^{1}H-NMR of **98**

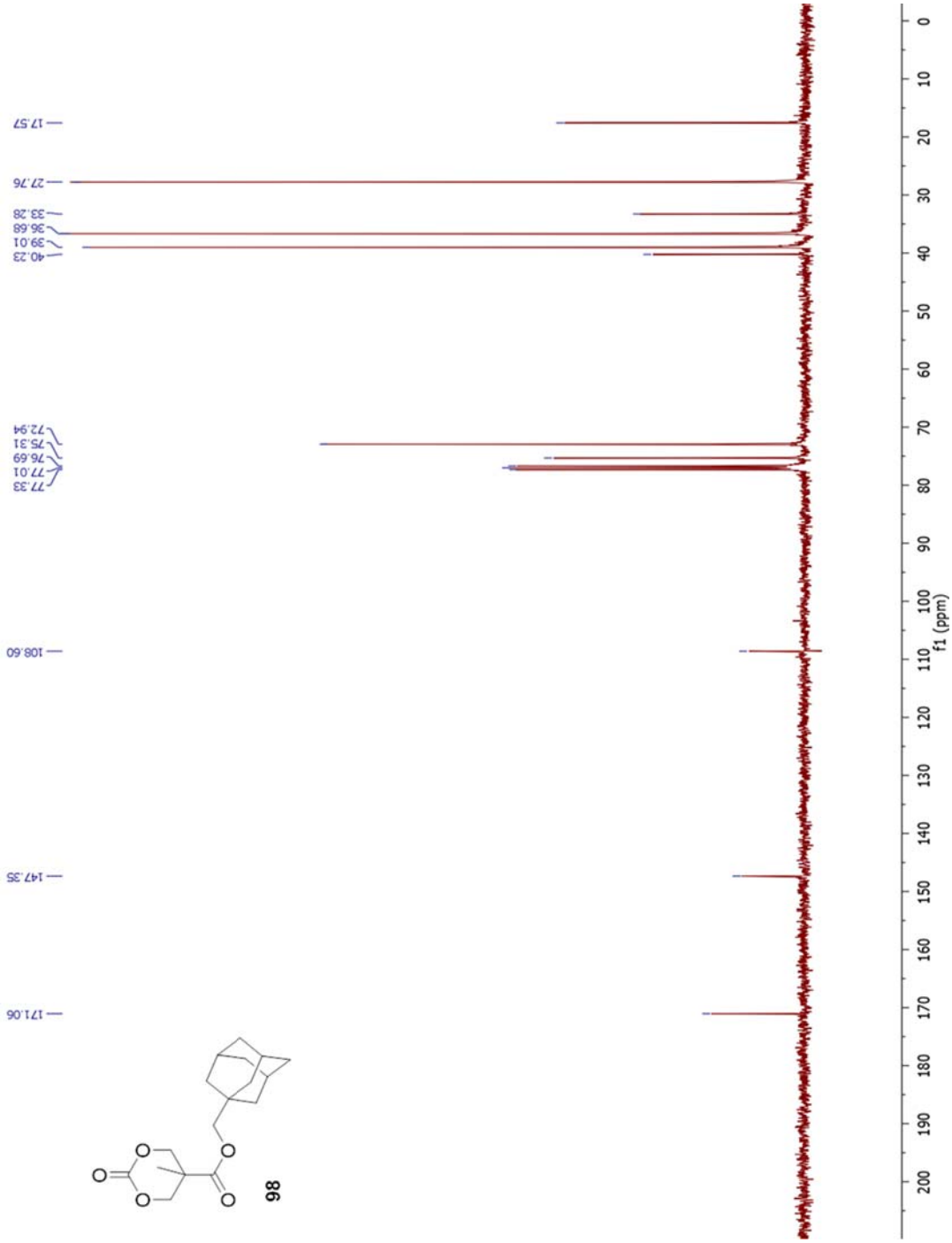

Figure A.109 ^{13}C-NMR of **98**

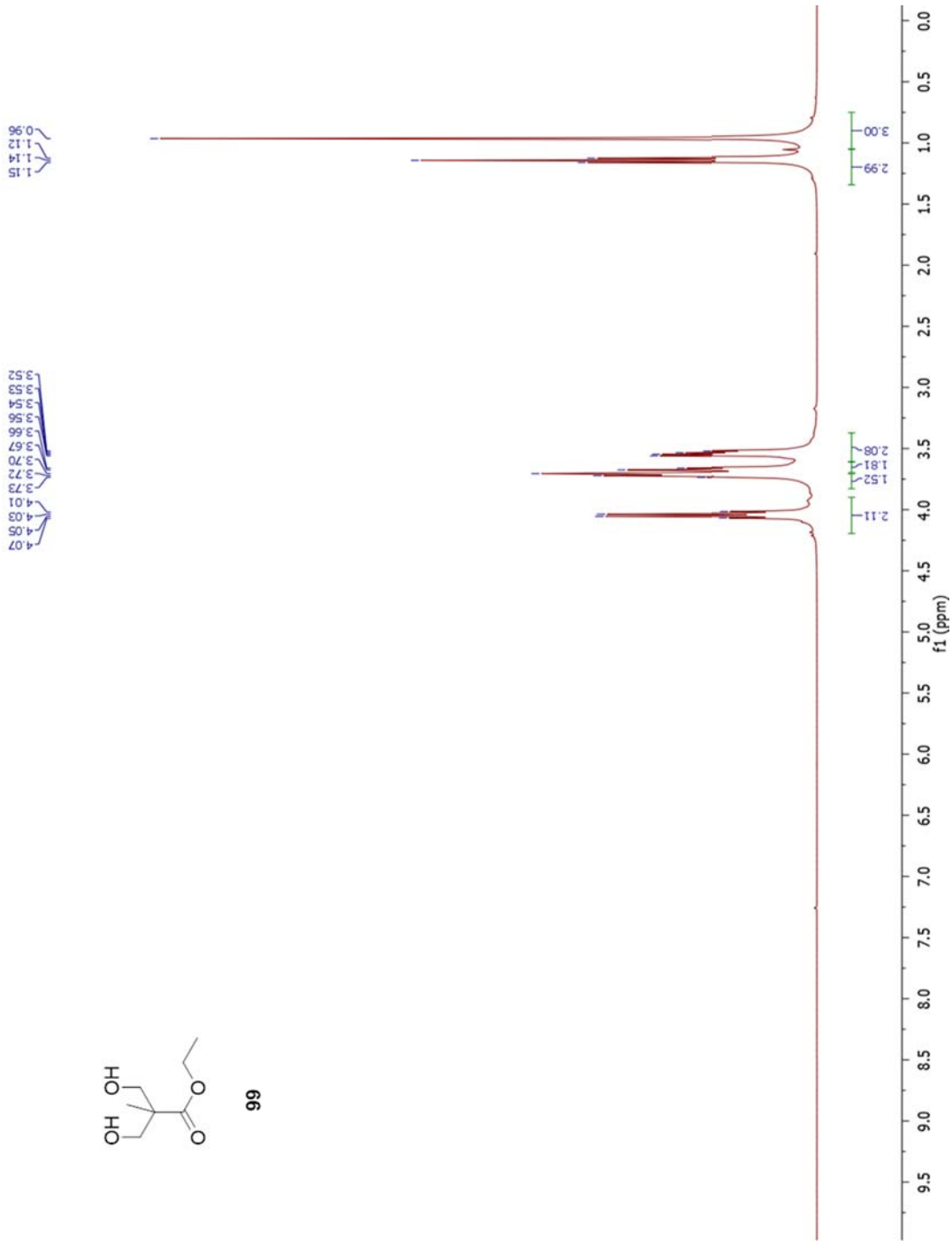

Figure A.110 ^{1}H-NMR of **99**

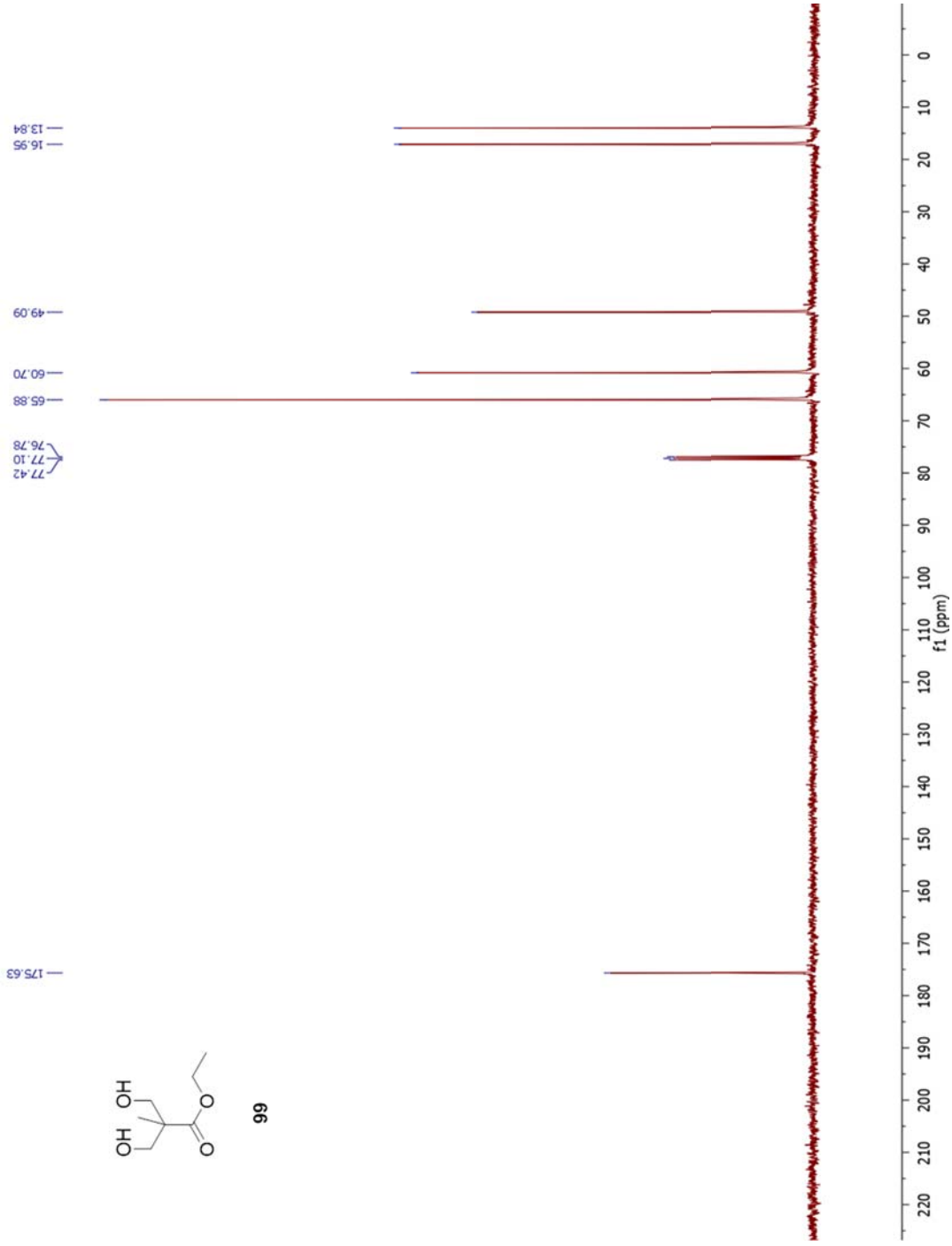

Figure A.111 ^{13}C-NMR of **99**

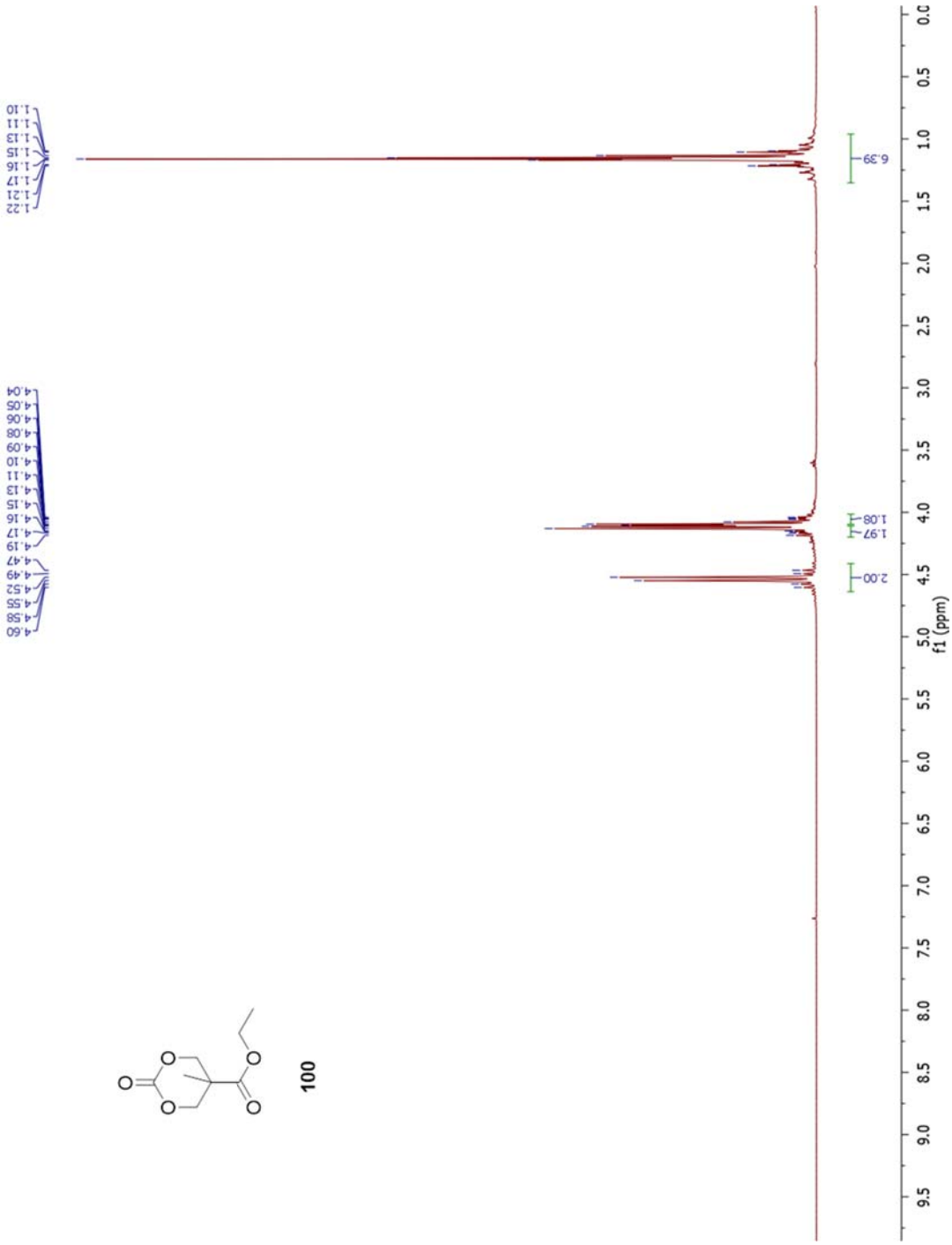

Figure A.112 ^{1}H-NMR of **100**

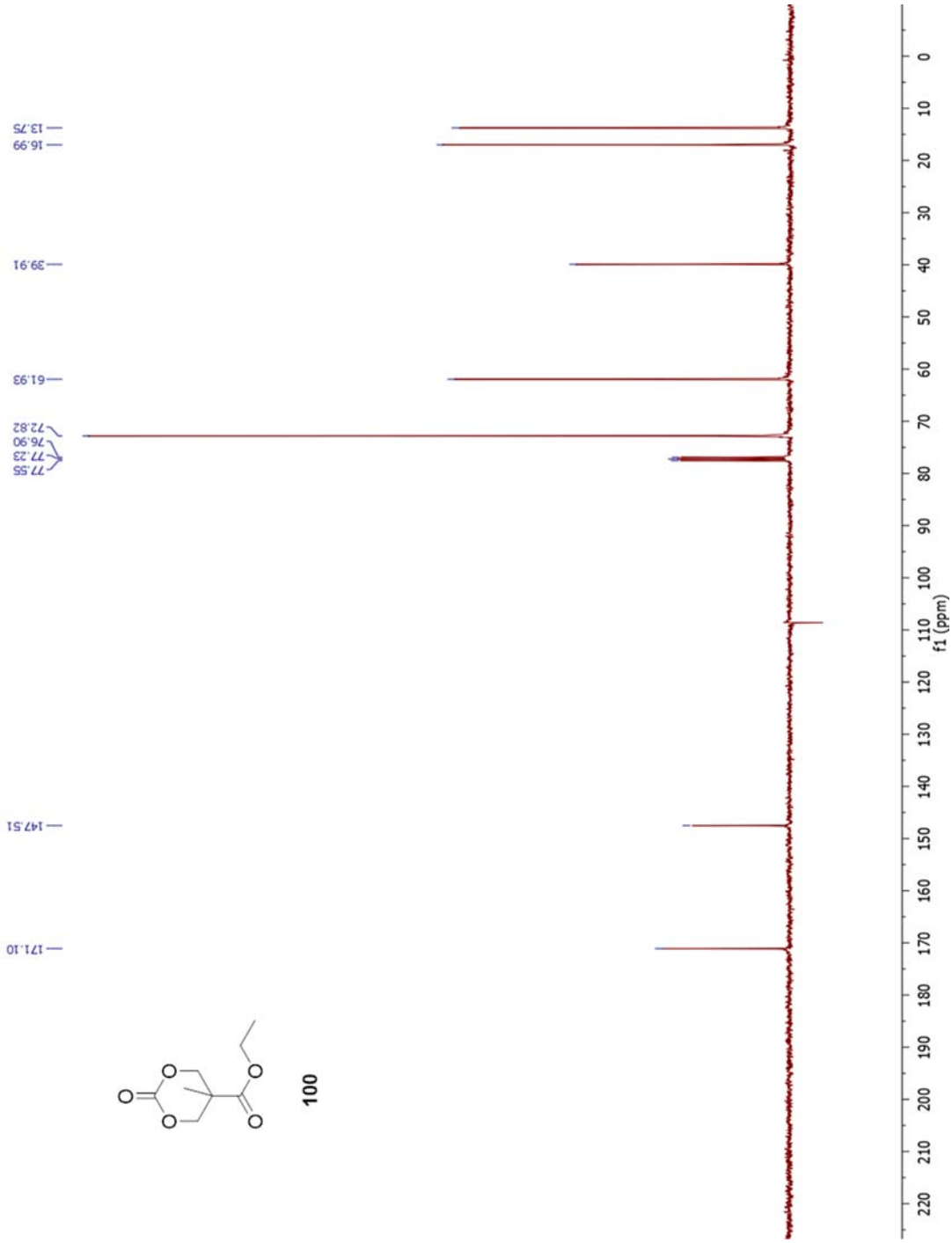

Figure A.113 ^{13}C-NMR of **100**

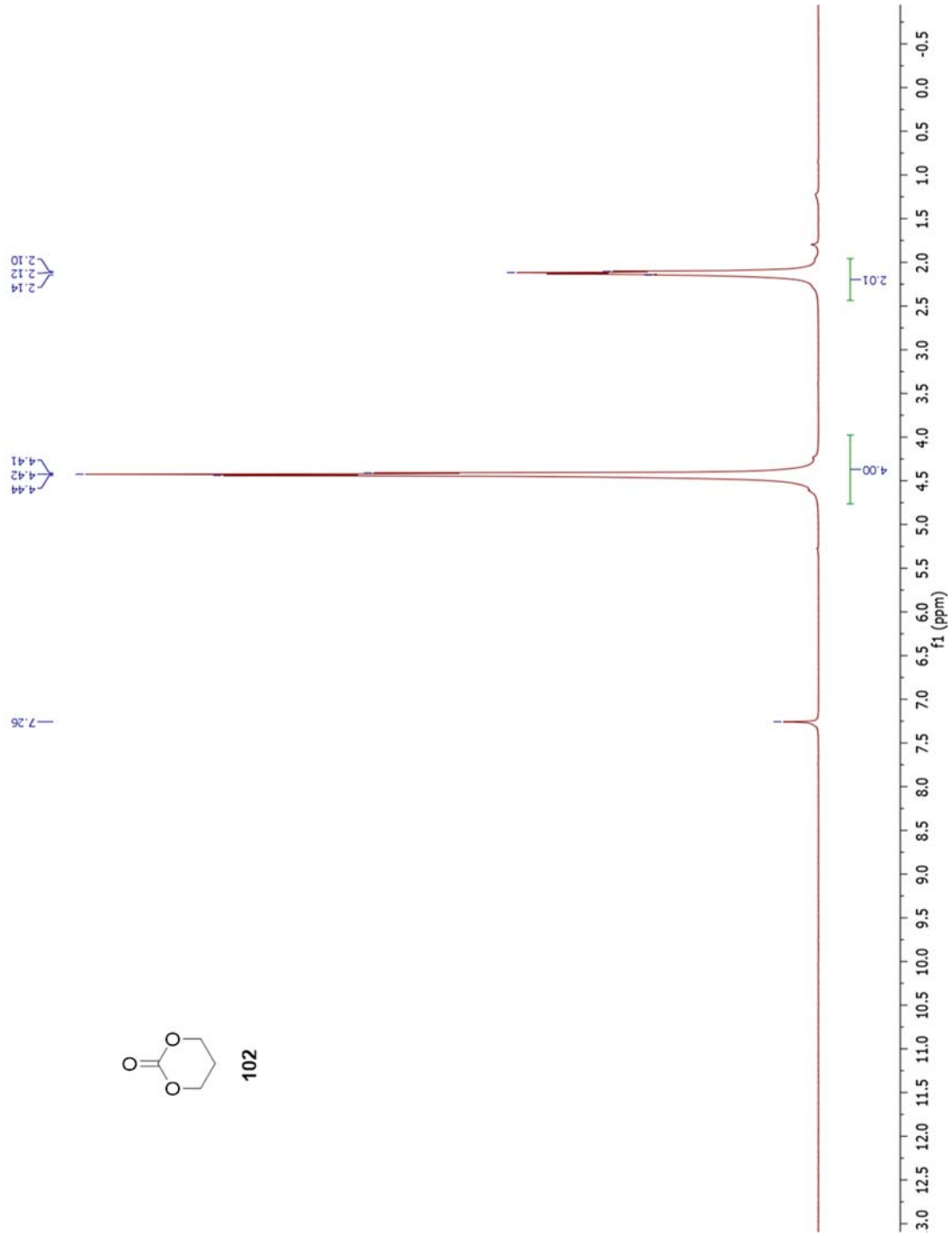

Figure A.114 ^{1}H-NMR of **102**

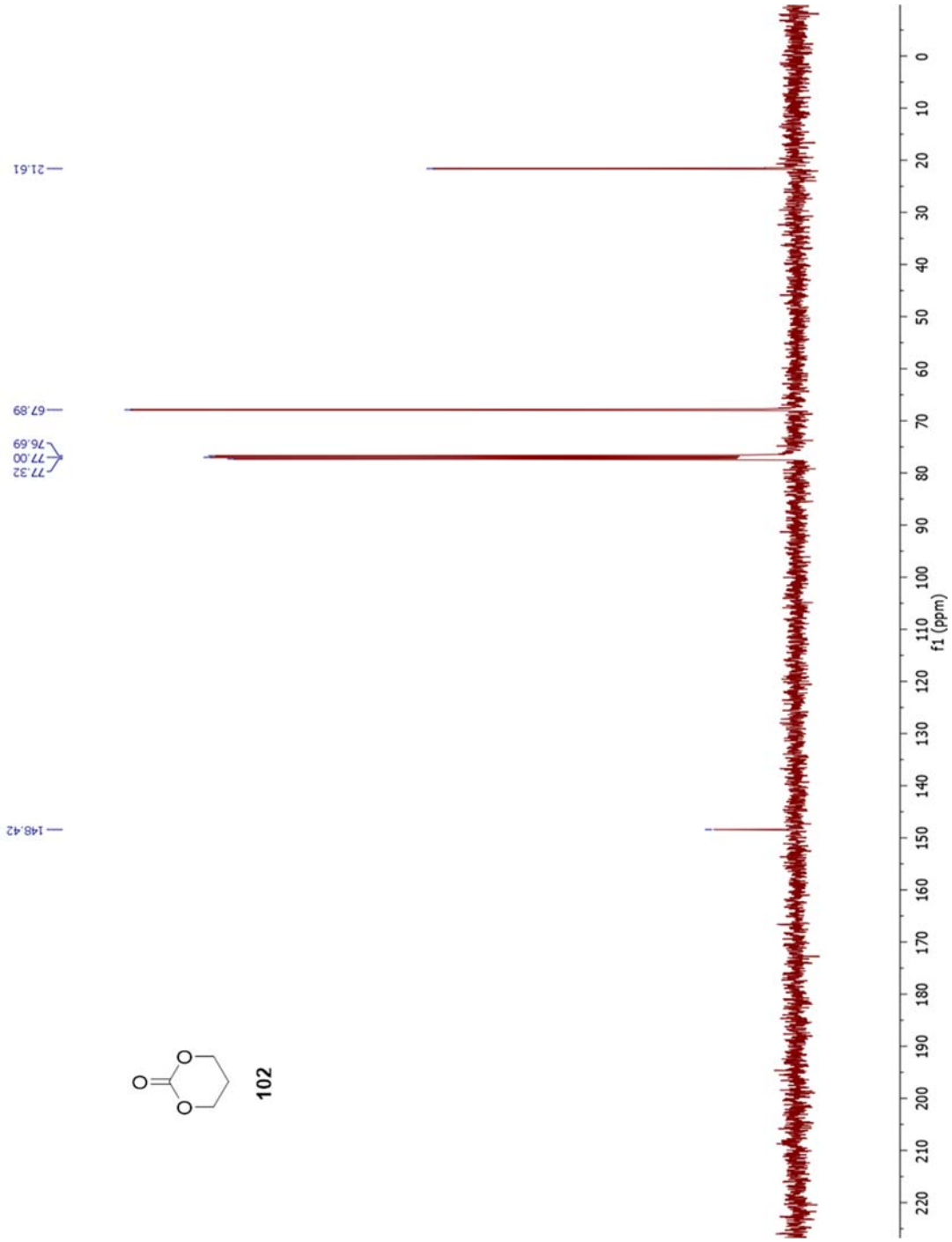

Figure A.115 ^{13}C-NMR of **102**

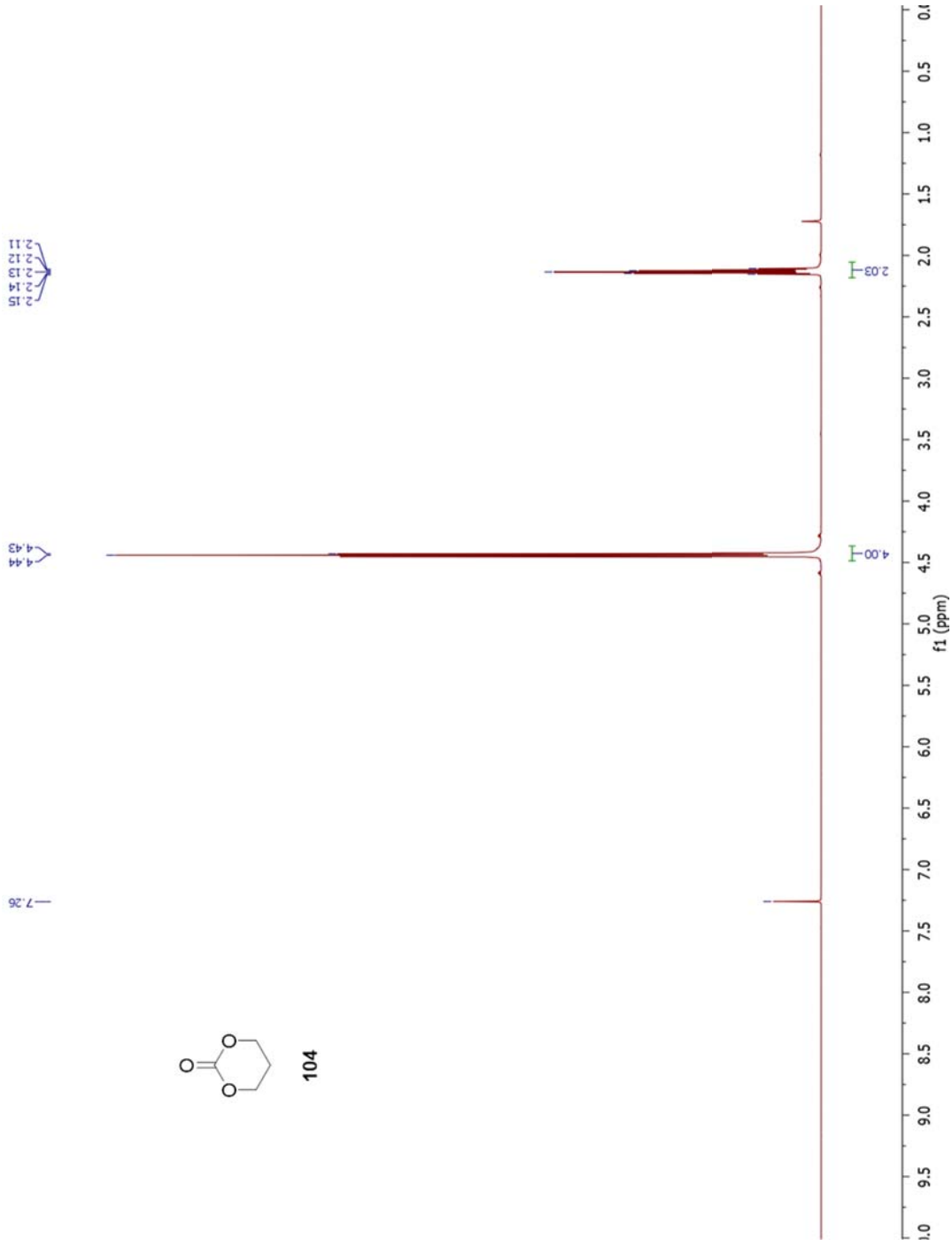

Figure A.116 ^{1}H-NMR of **104**

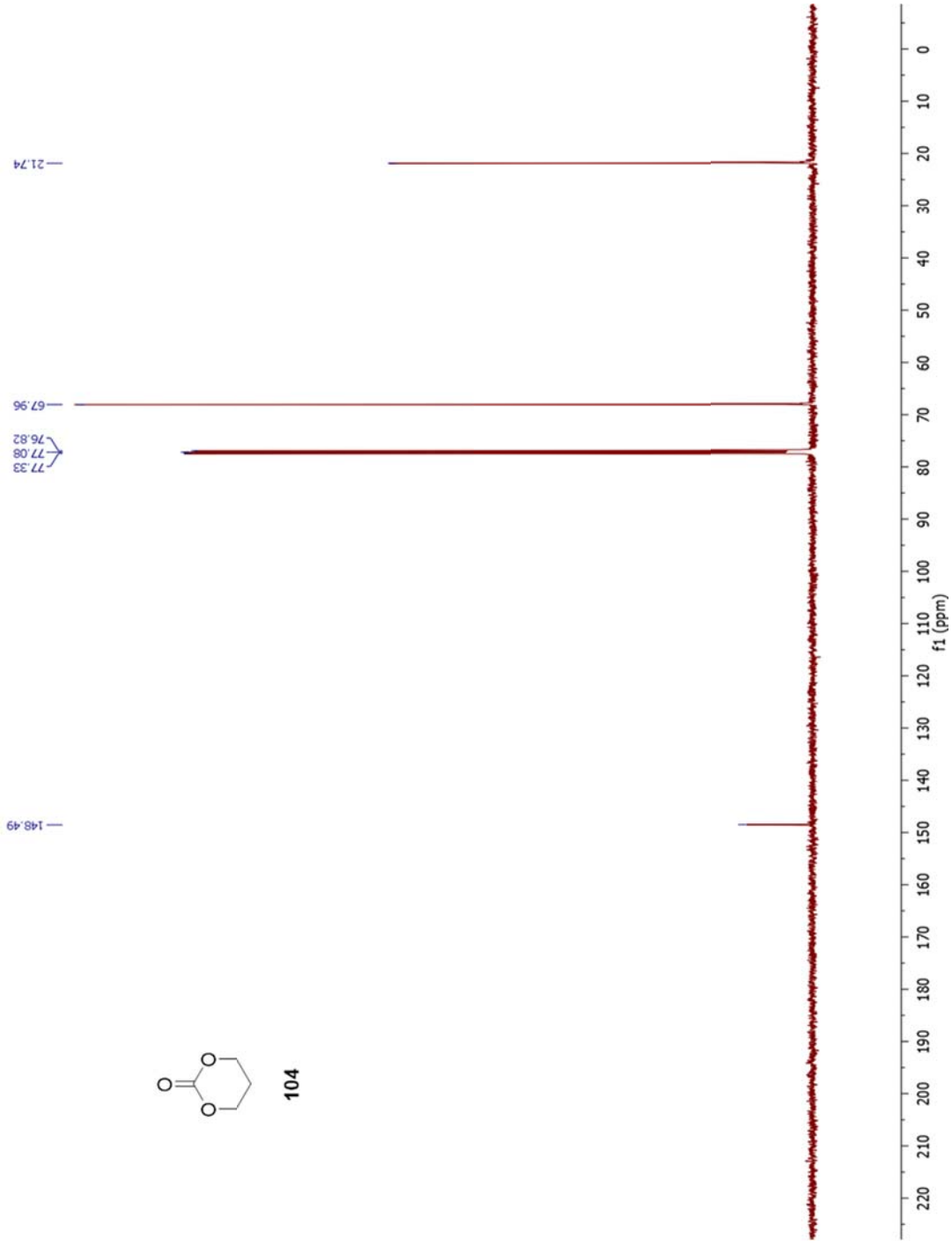

Figure A.117 ^{13}C-NMR of **104**

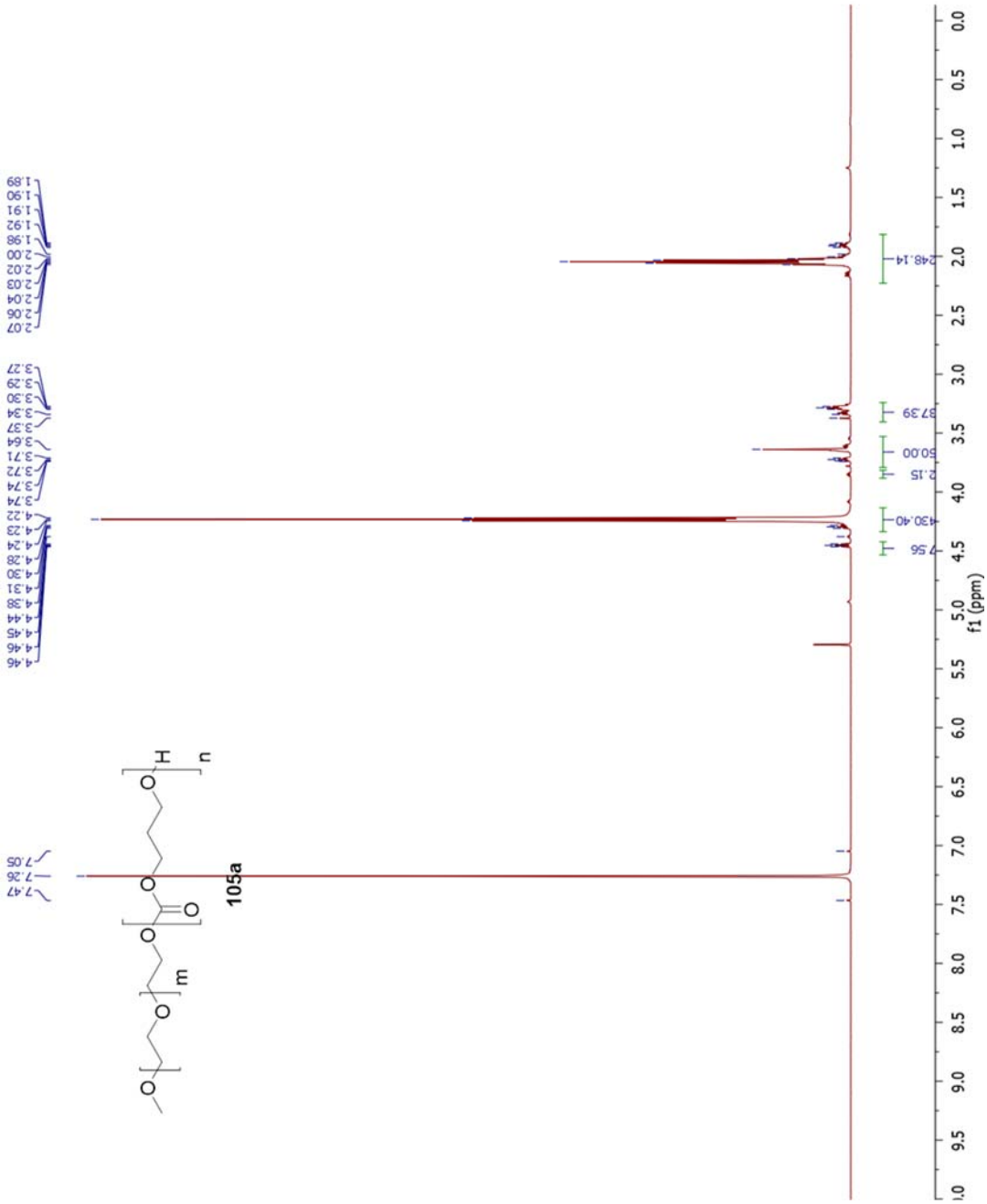

Figure A.118 ^{1}H-NMR of **105a**

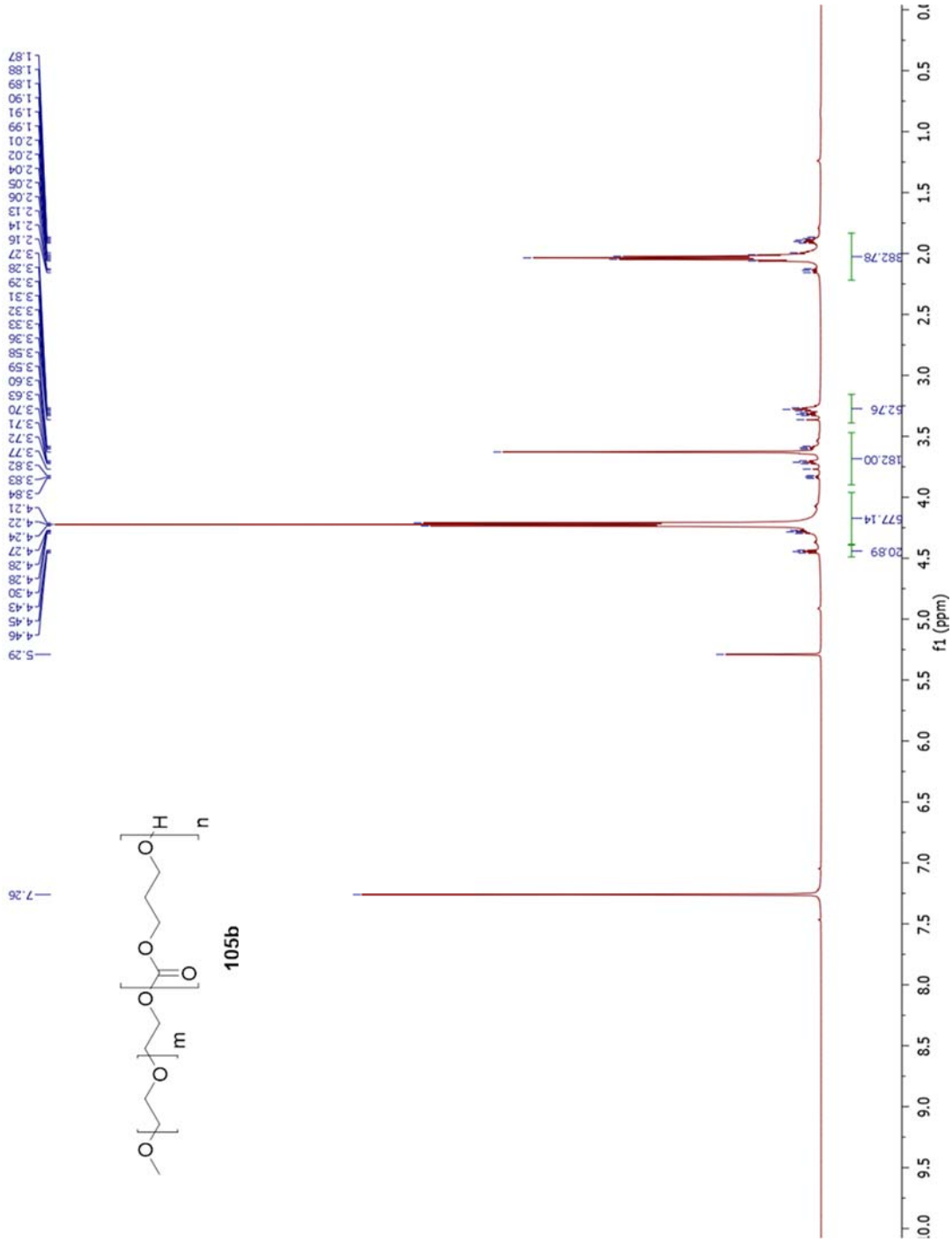

Figure A.119 ^{1}H-NMR of **105b**

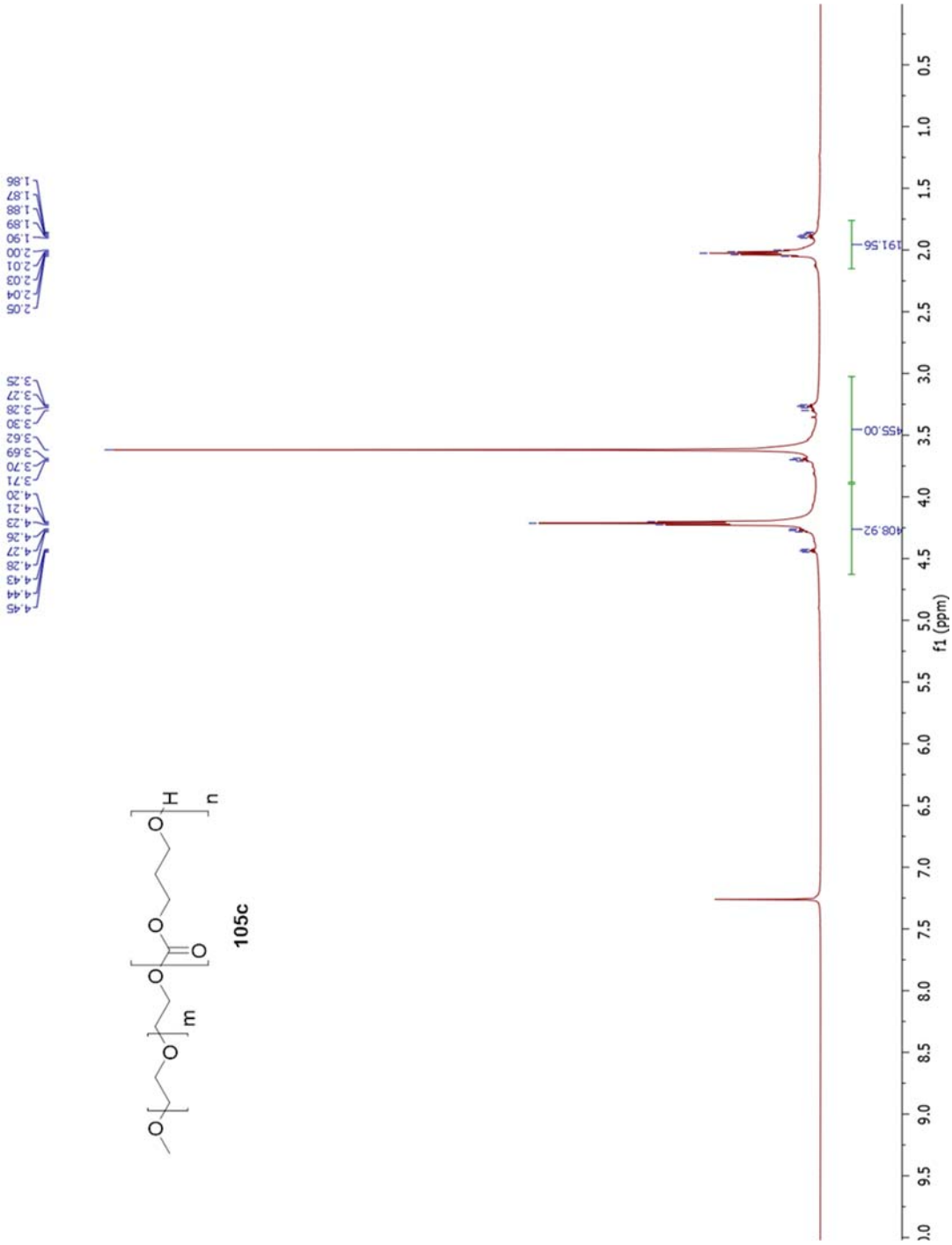

Figure A.120 ^{1}H-NMR of **105c**

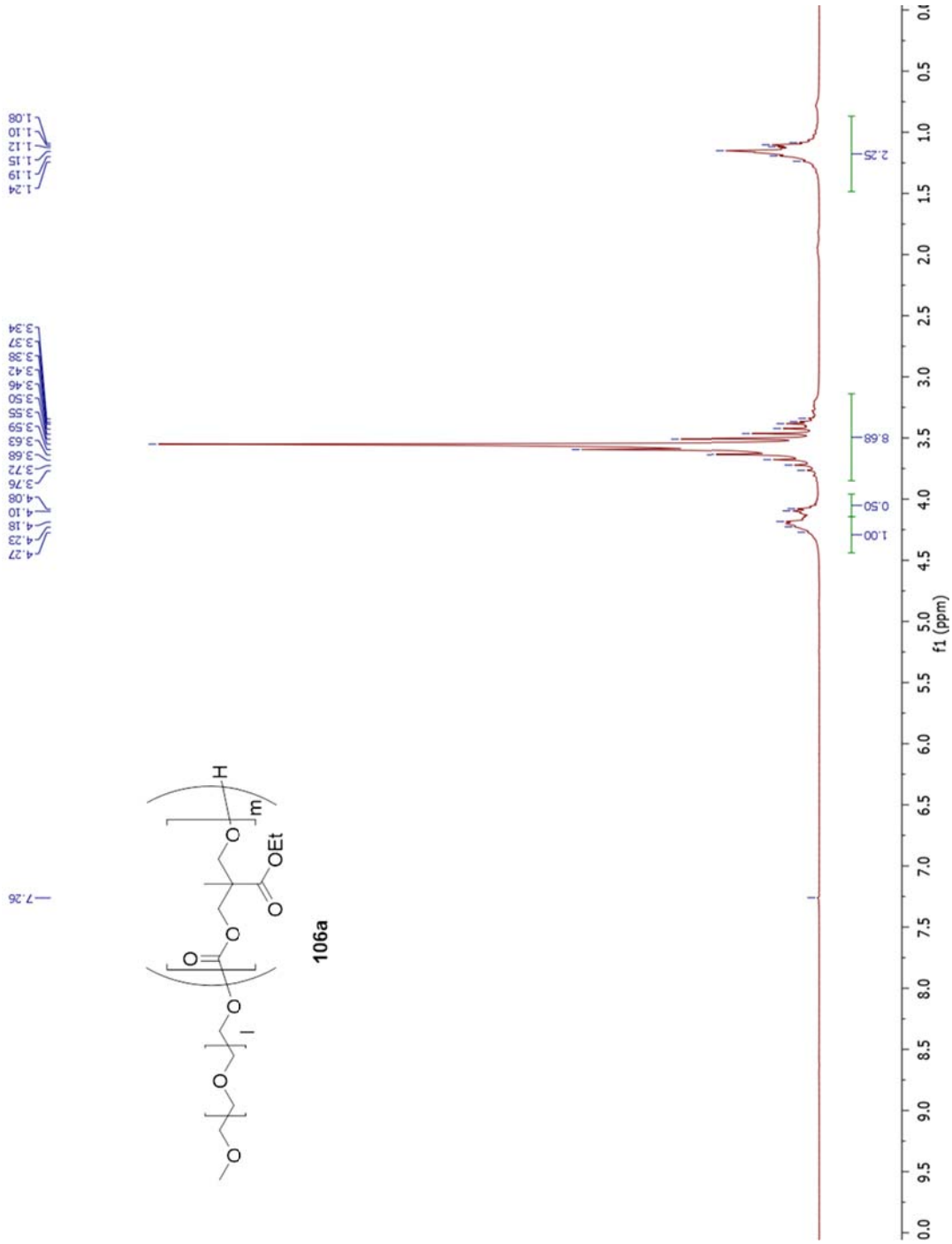

Figure A.121 ^{1}H-NMR of **106a**

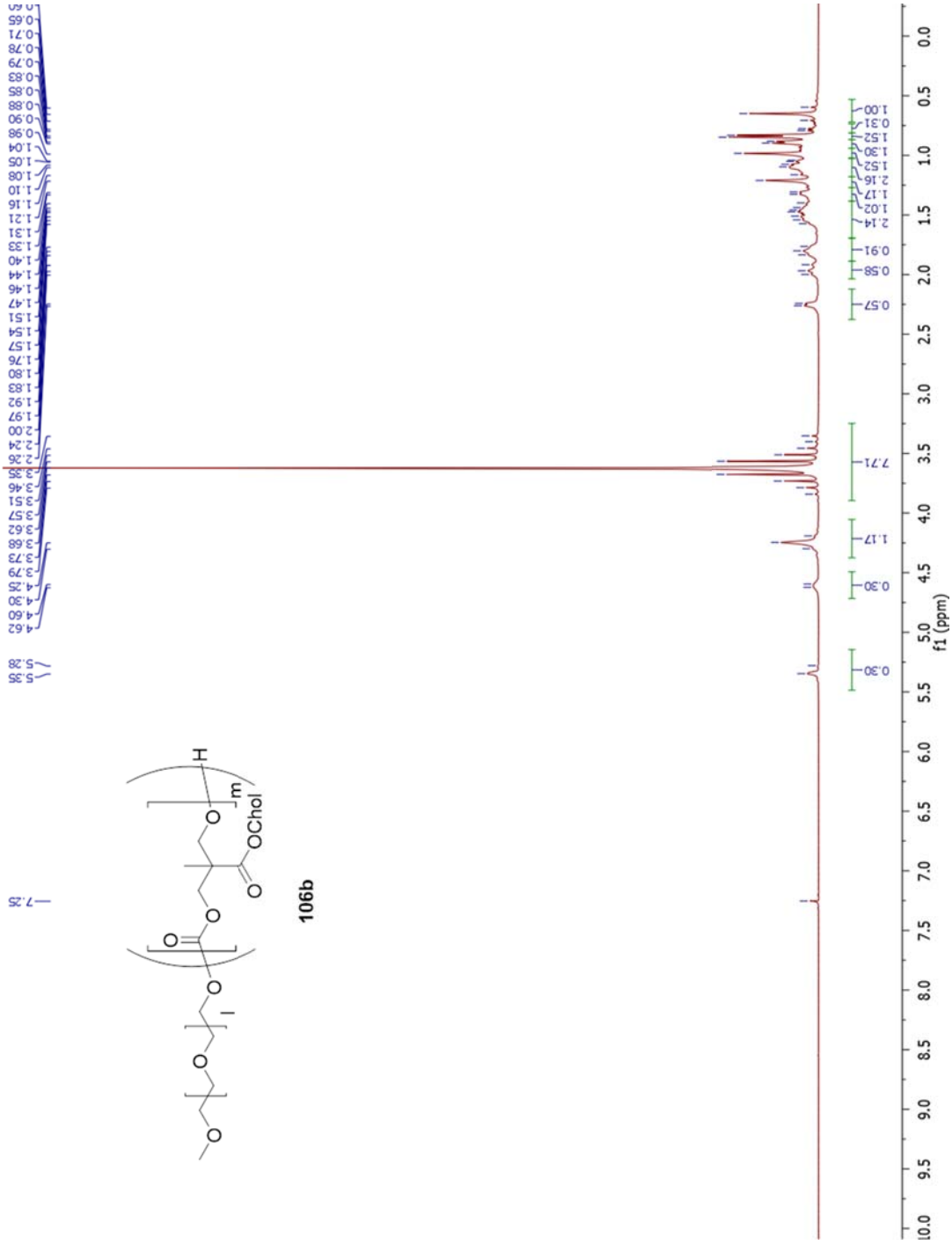

Figure A.122 ^{1}H-NMR of **106b**

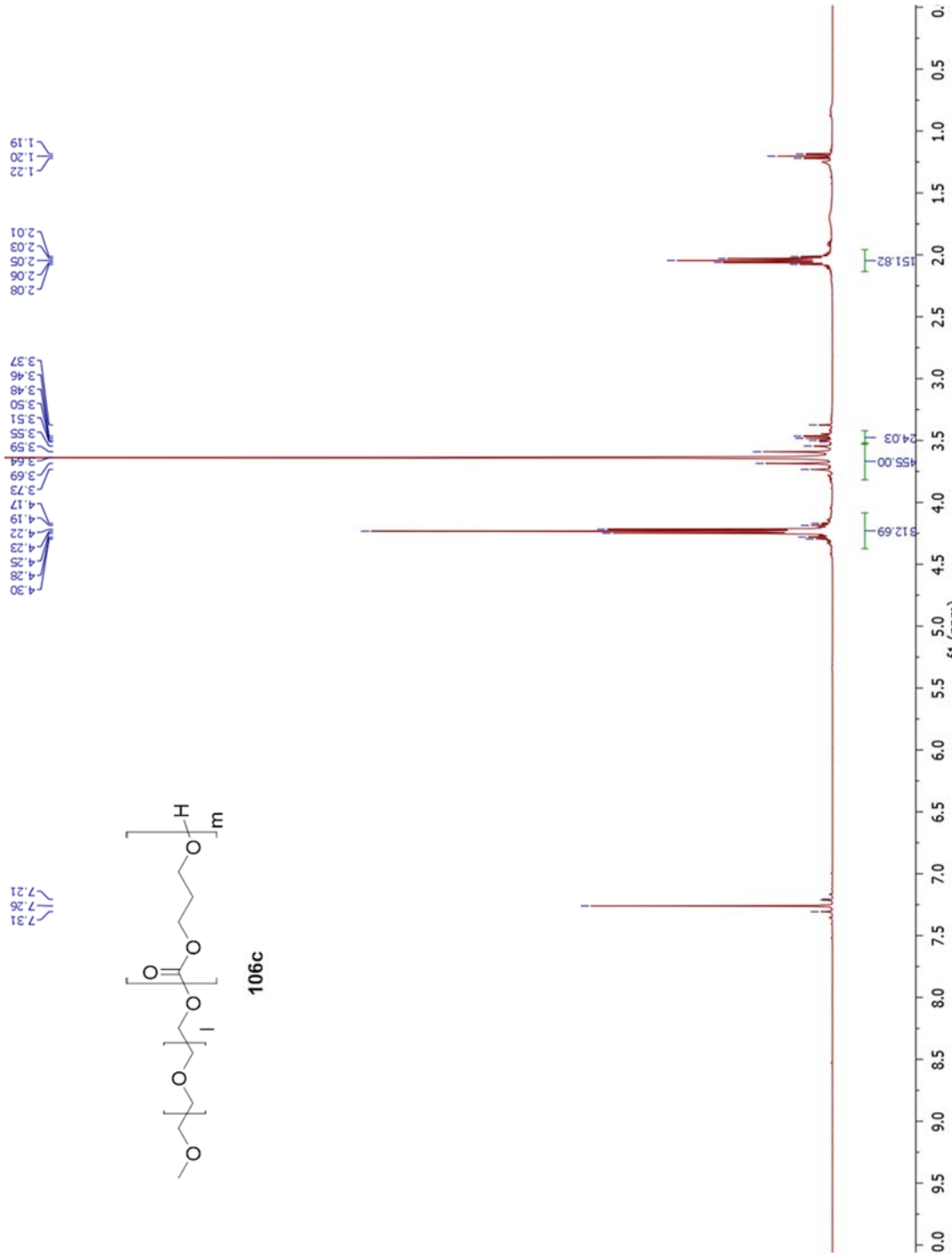

Figure A.123 ^{1}H-NMR of **106c**

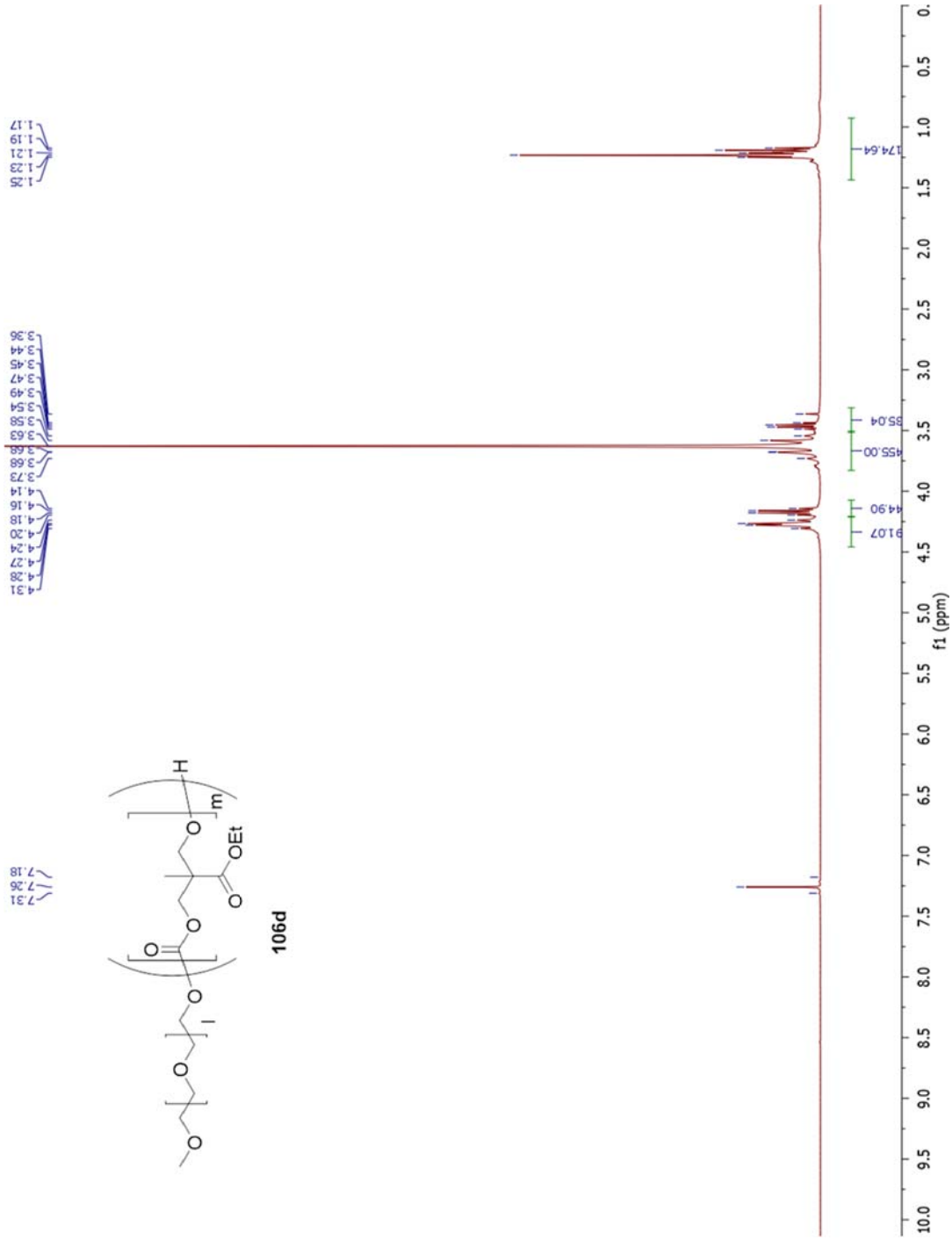

Figure A.124 ^{1}H-NMR of **106d**

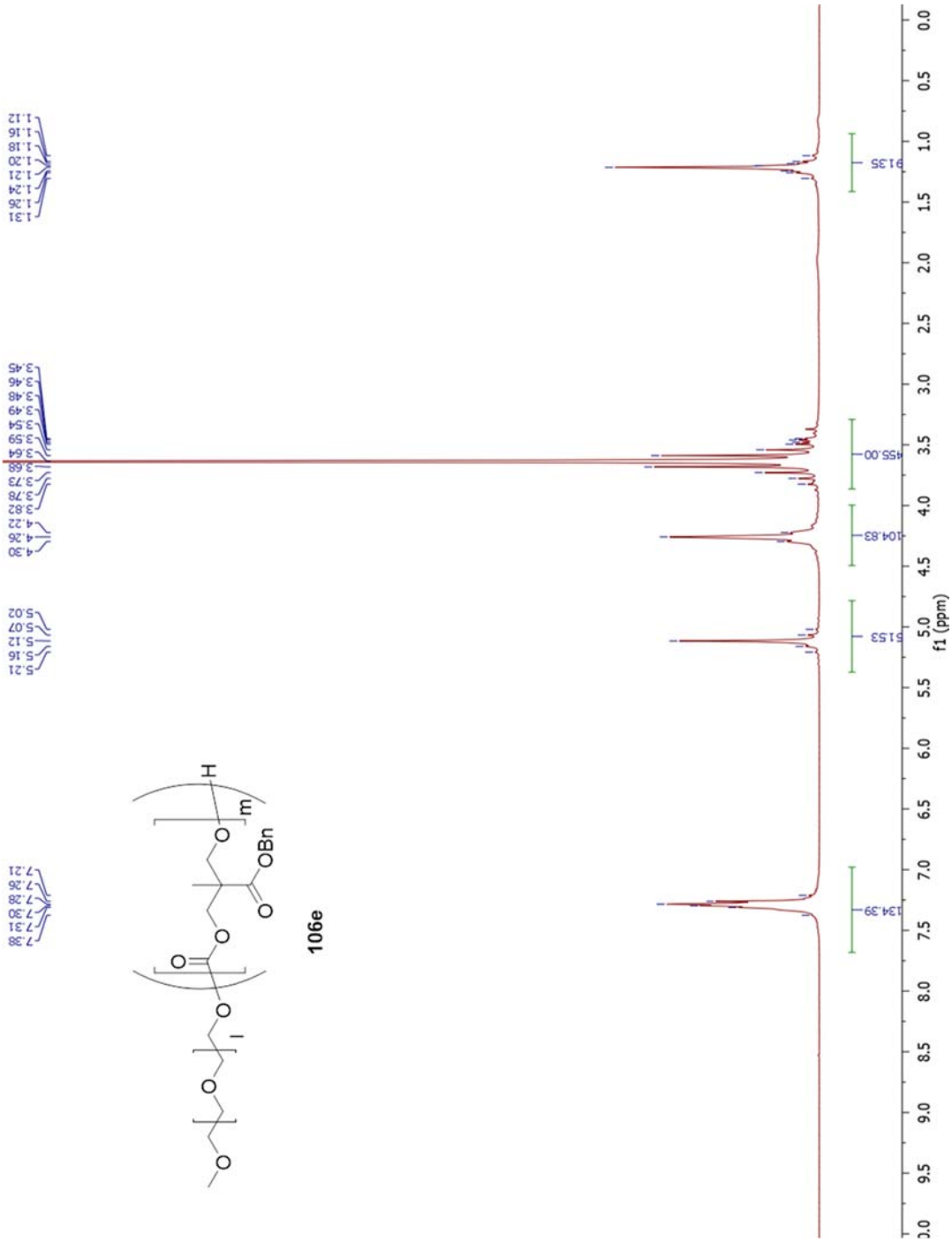

Figure A.125 ^{1}H-NMR of **106e**

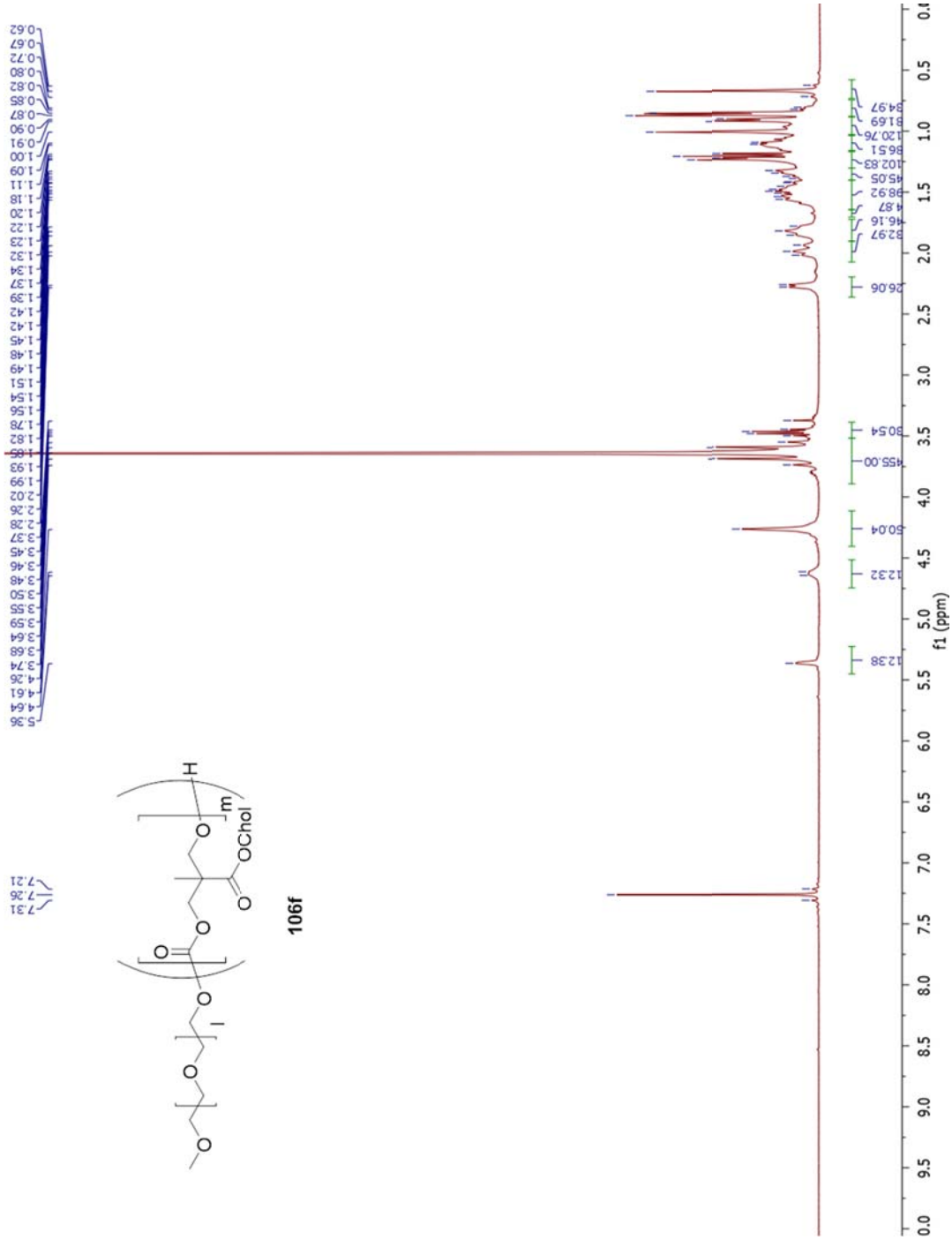

Figure A.126 ^{1}H-NMR of **106f**

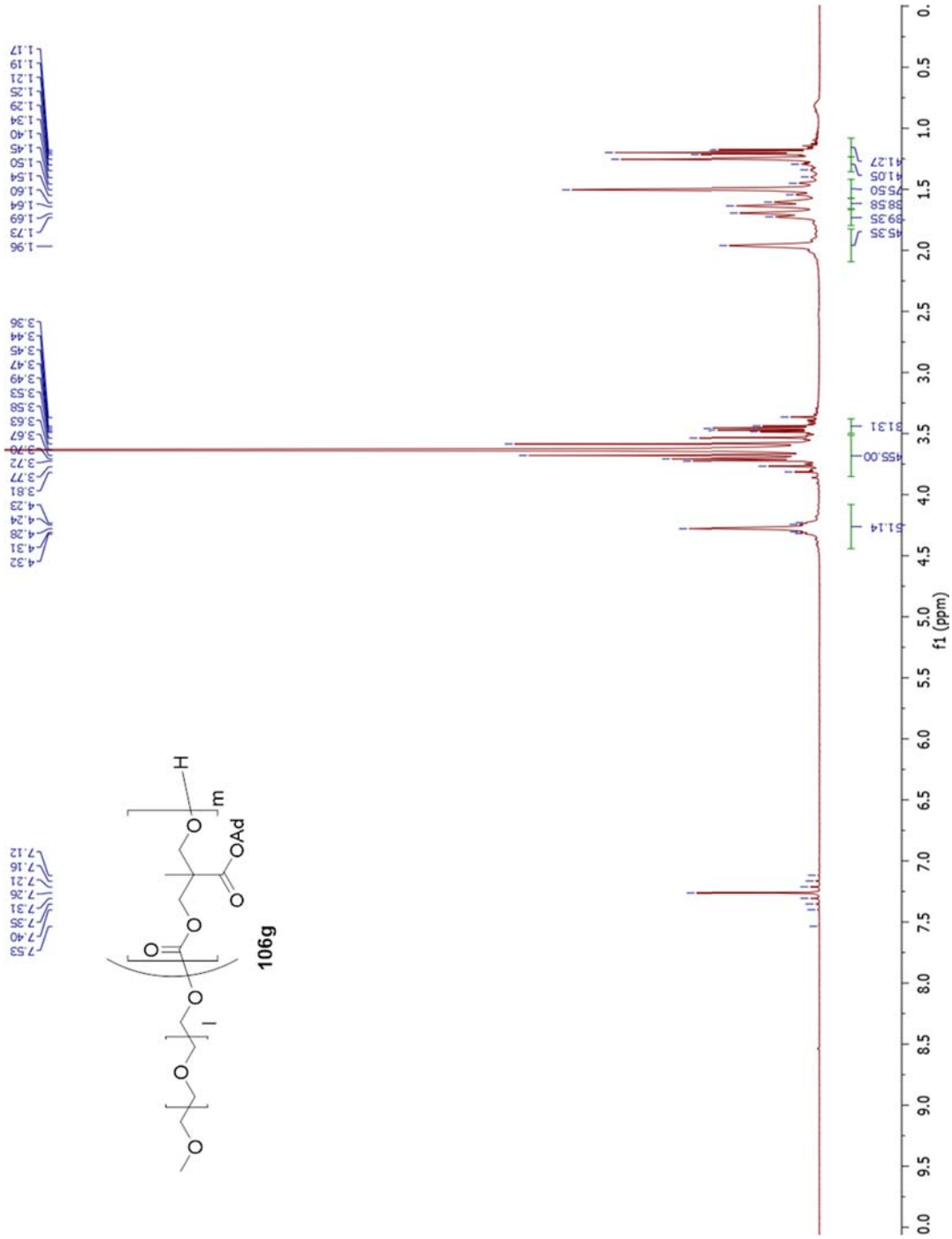

Figure A.127 ^{1}H-NMR of **106g**

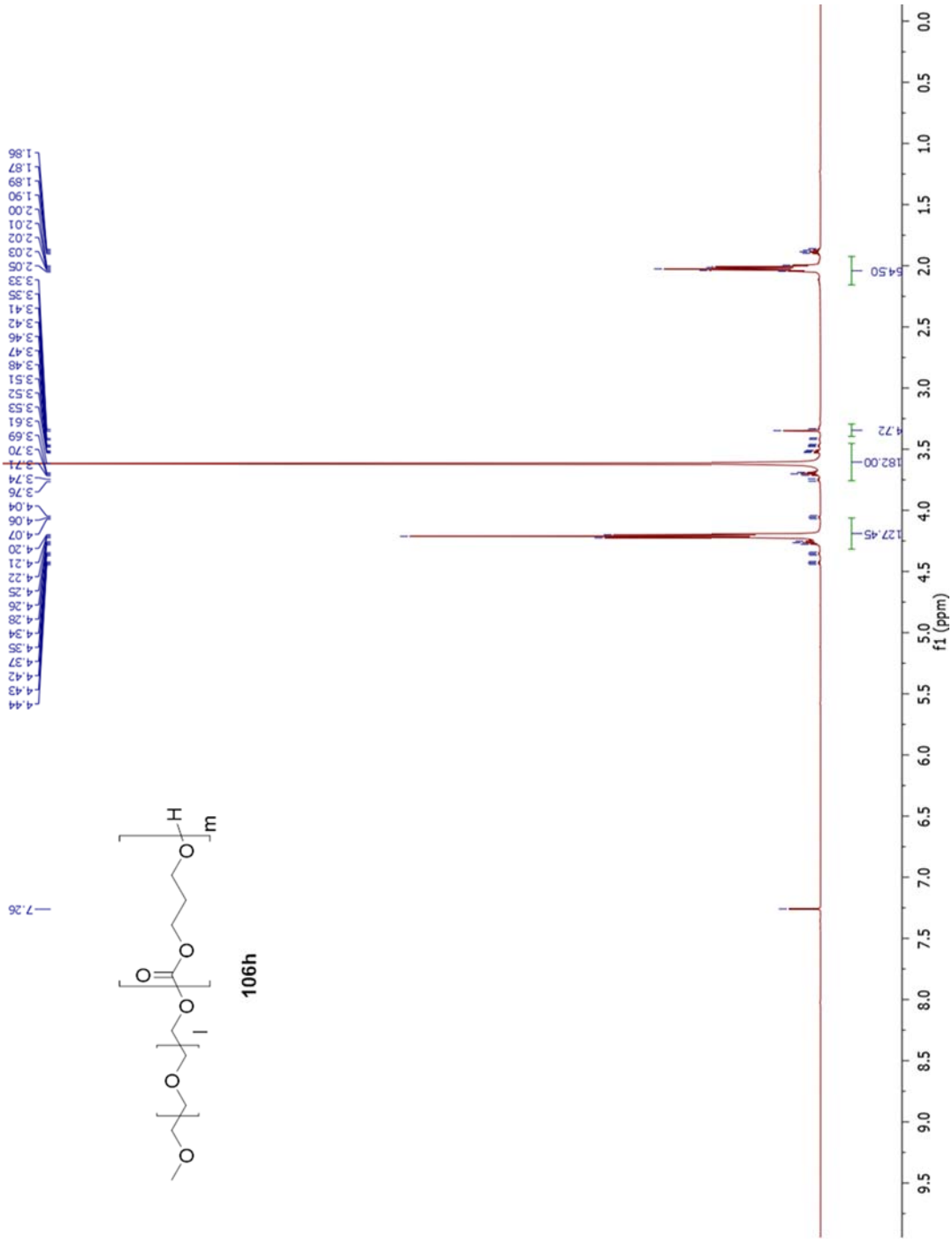

Figure A.128 ^{1}H-NMR of **106h**

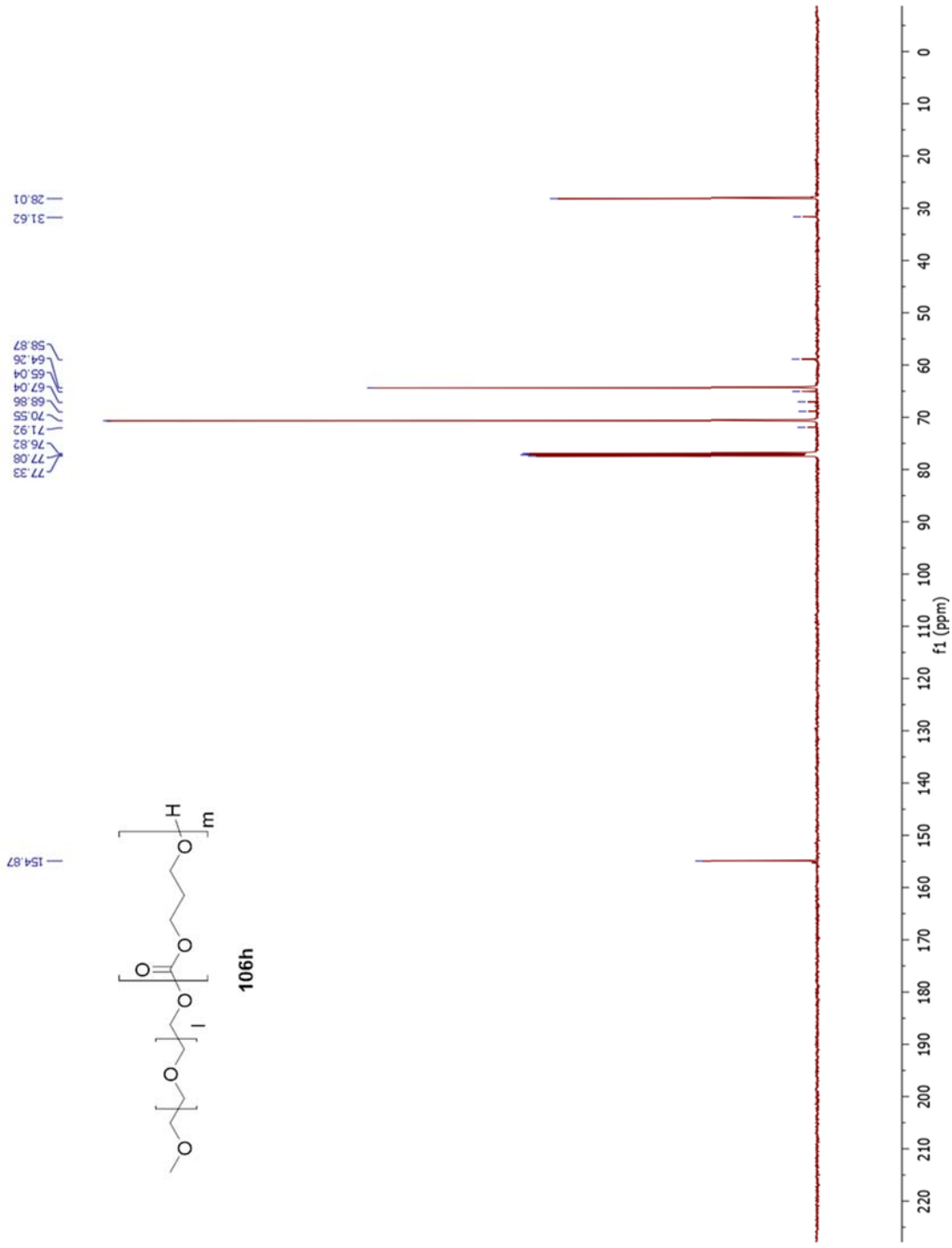

Figure A.129 ^{13}C-NMR of **106h**

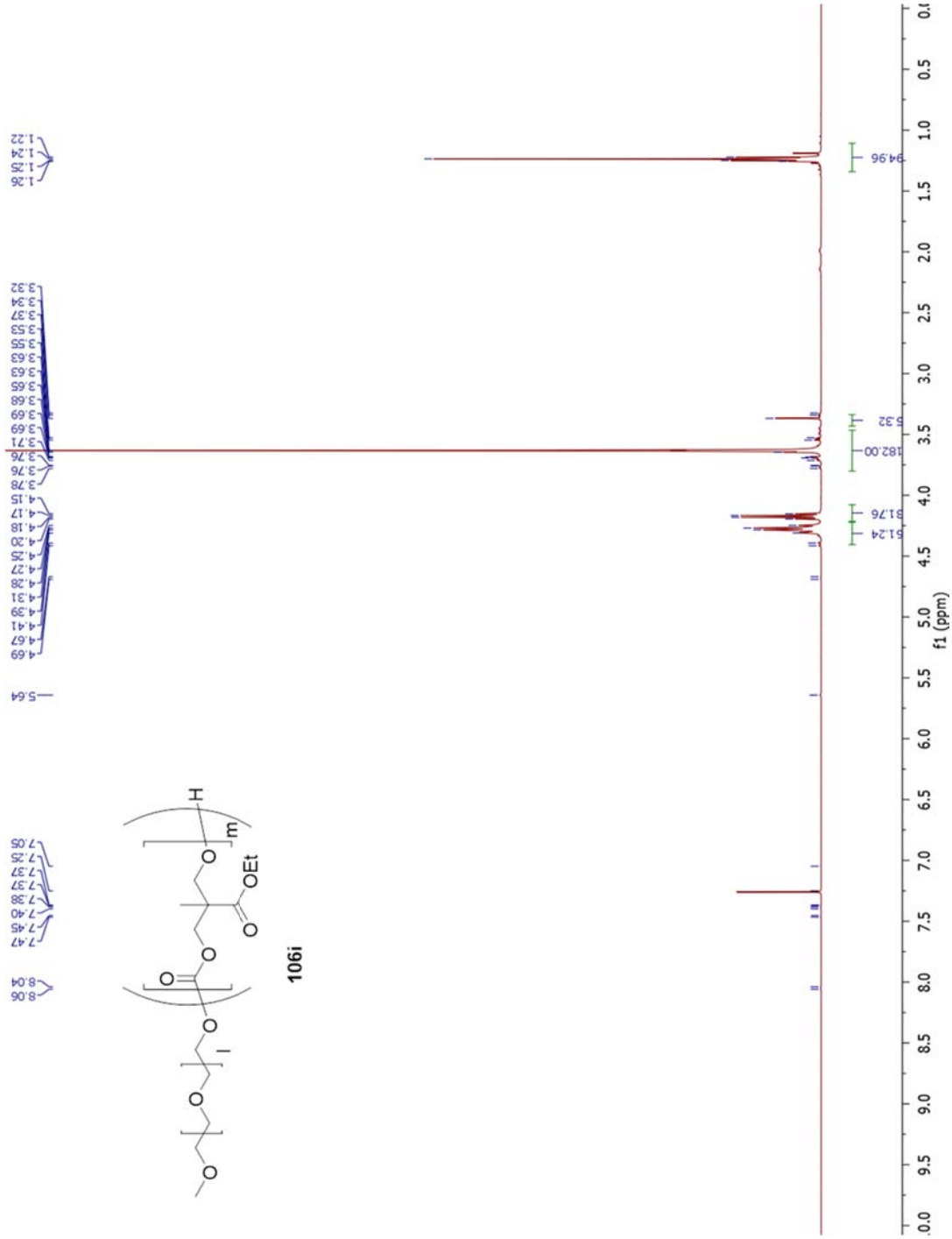

Figure A.130 ^{1}H-NMR of **106i**

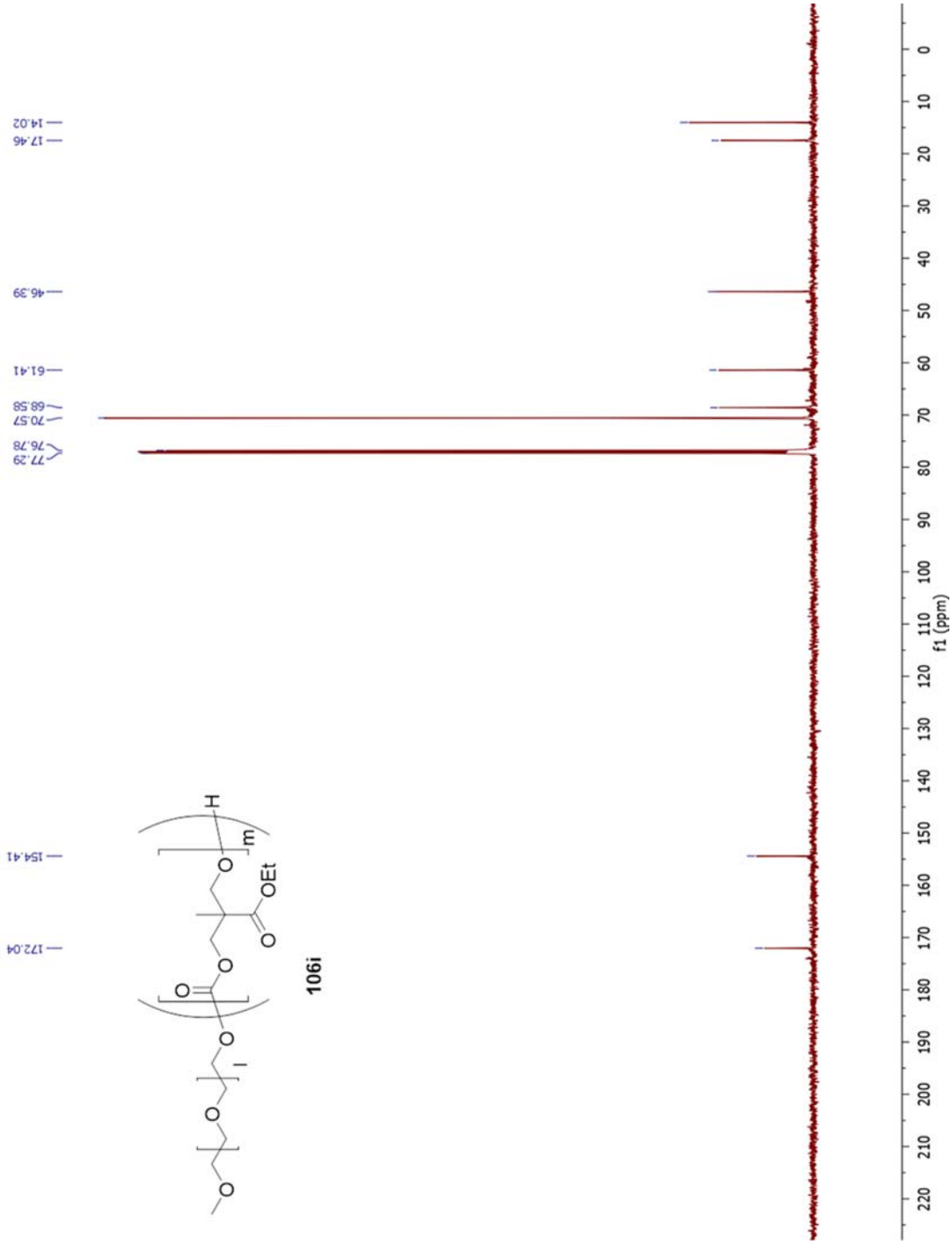

Figure A.131 ^{13}C-NMR of **106i**

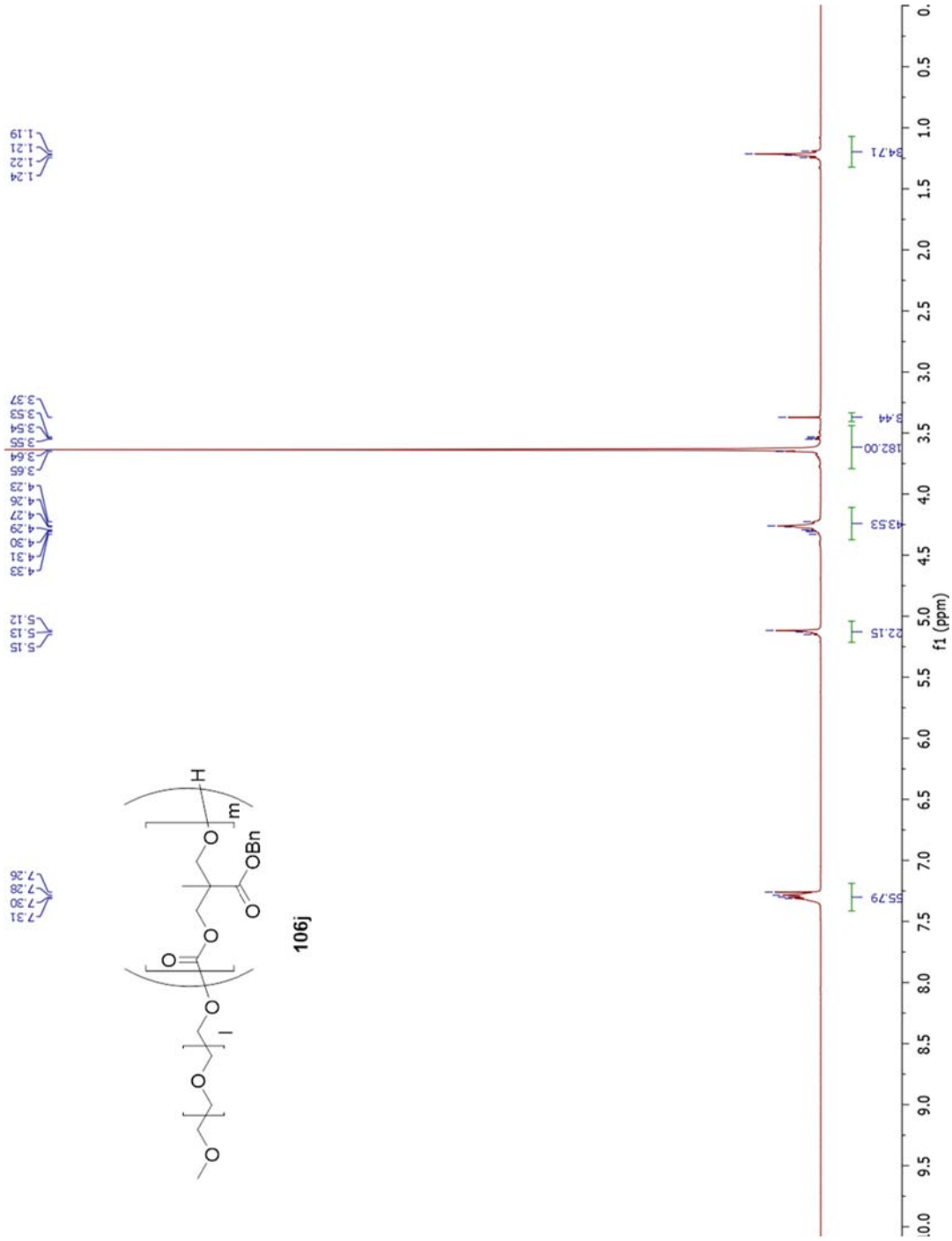

Figure A.132 ^{1}H-NMR of **106j**

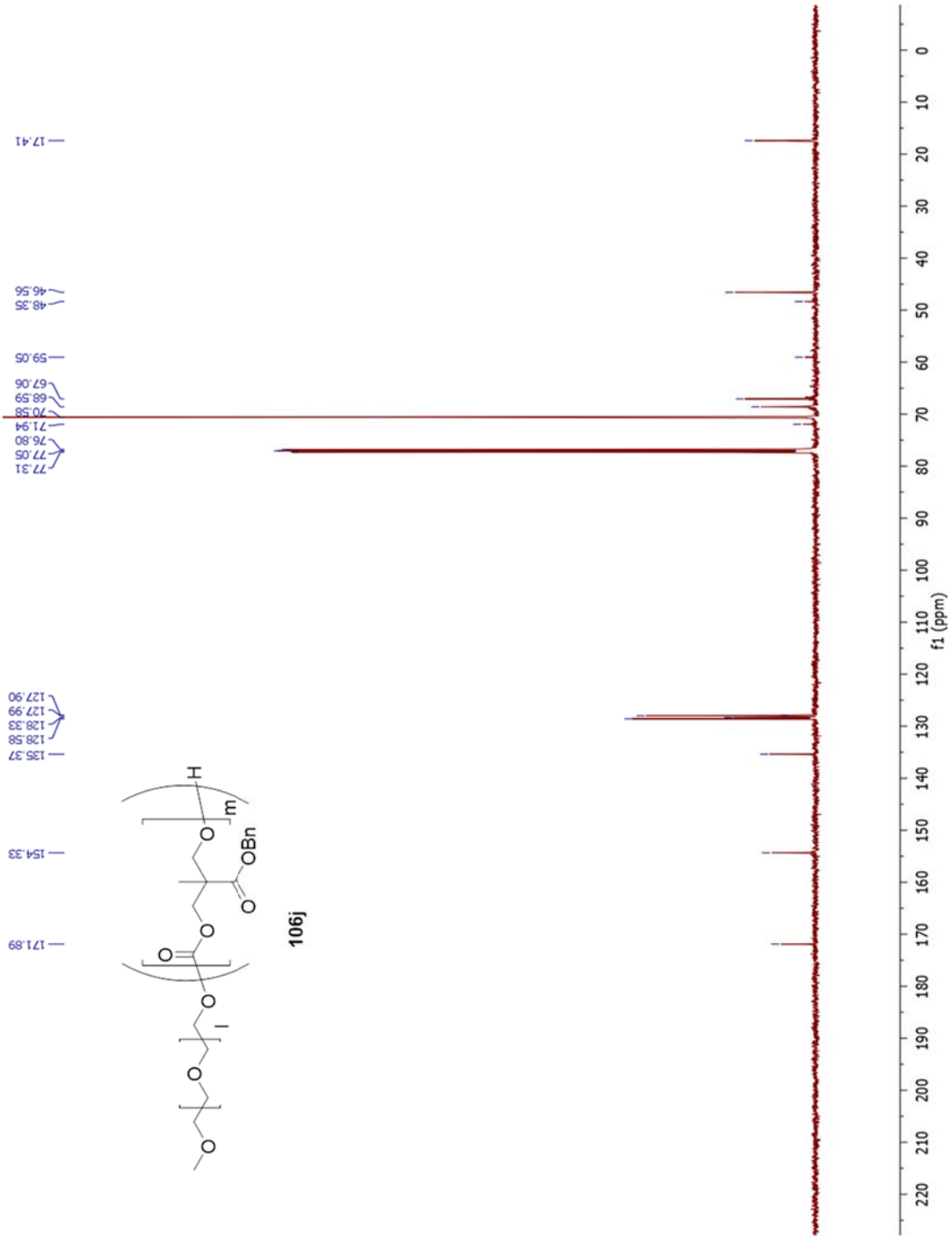

Figure A.133 ^{13}C-NMR of **106j**

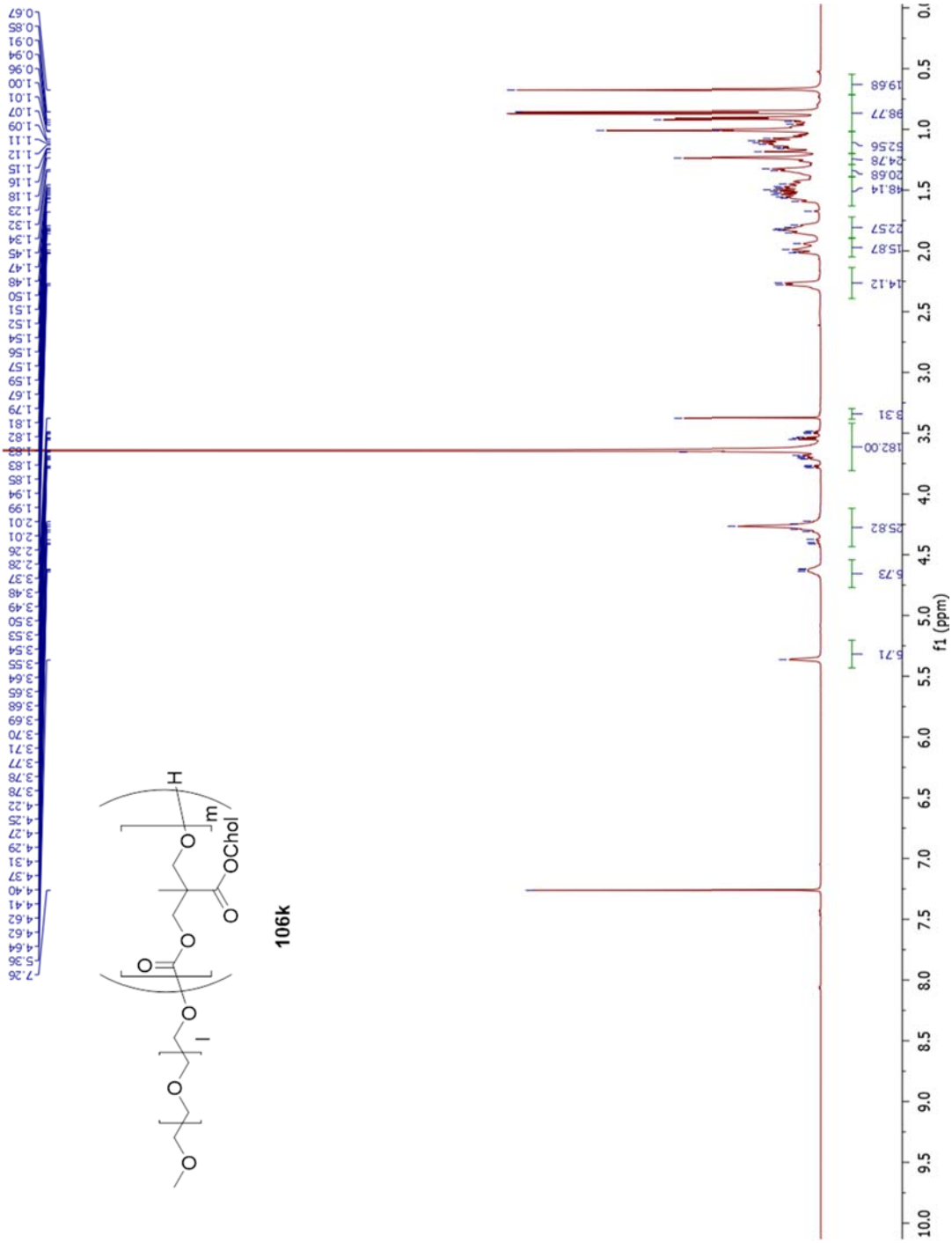

Figure A.134 ^{1}H-NMR of **106k**

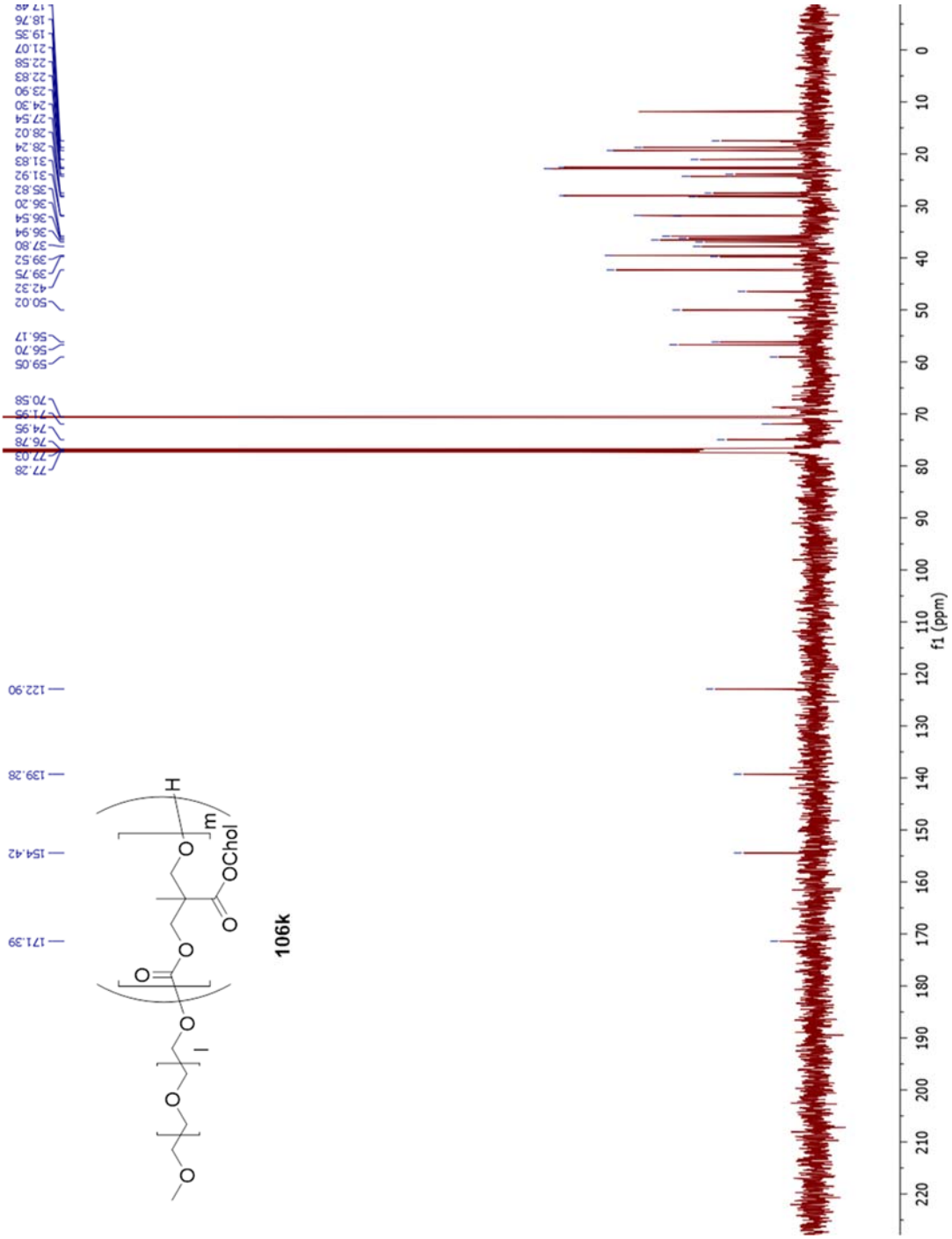

Figure A.135 ^{13}C-NMR of **106k**

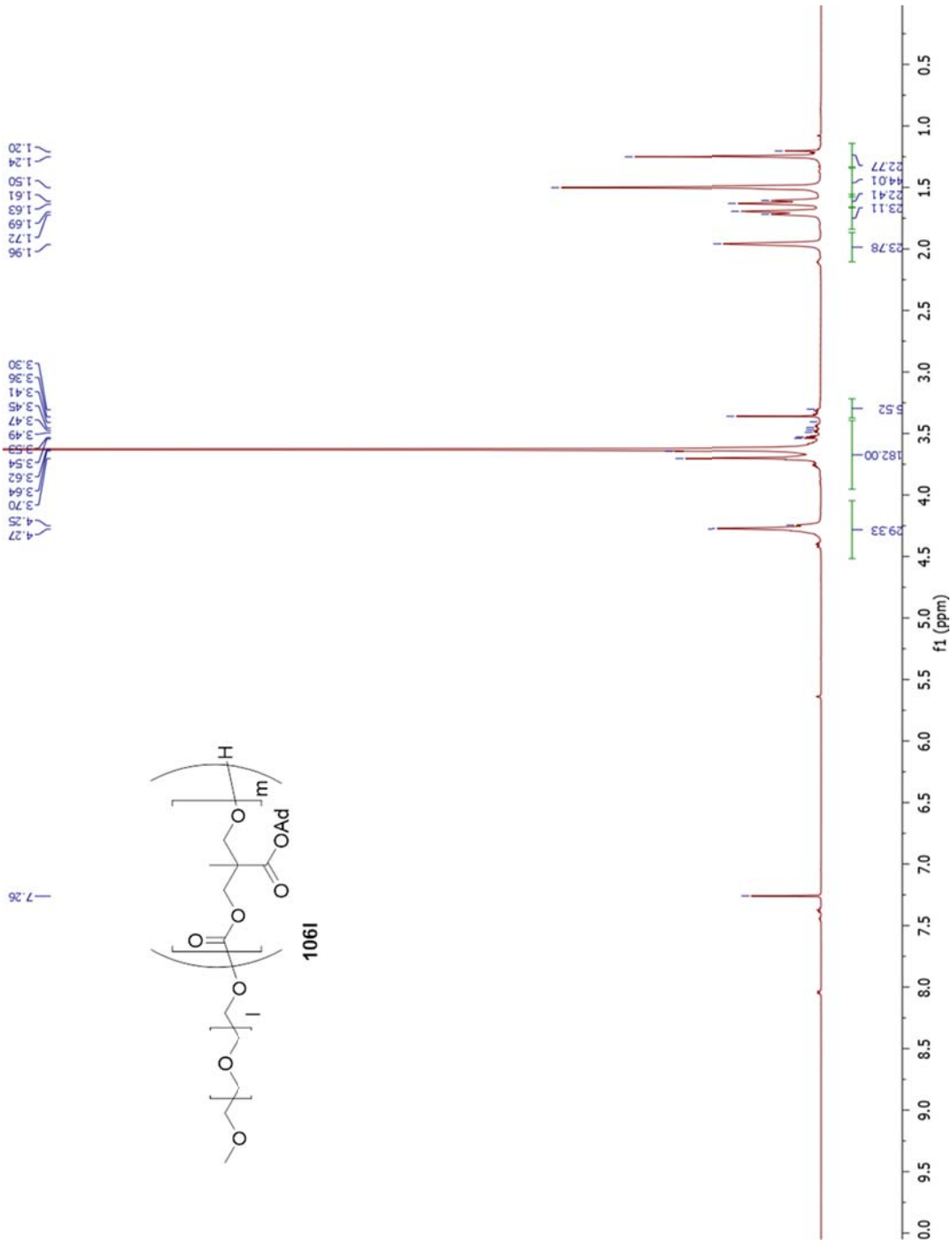

Figure A.136 ^{1}H-NMR of **106l**

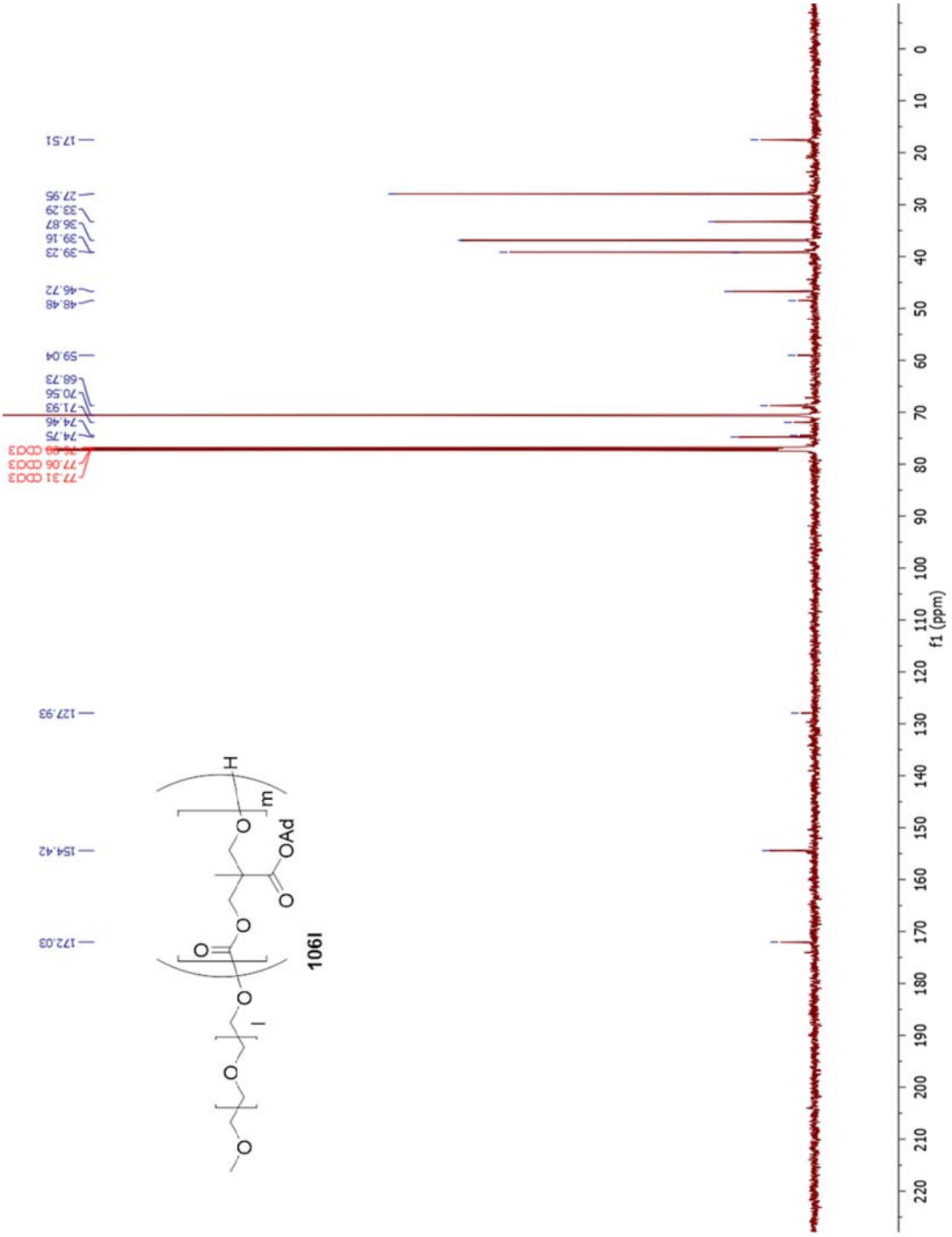

Figure A.137 ^{13}C-NMR of **106l**

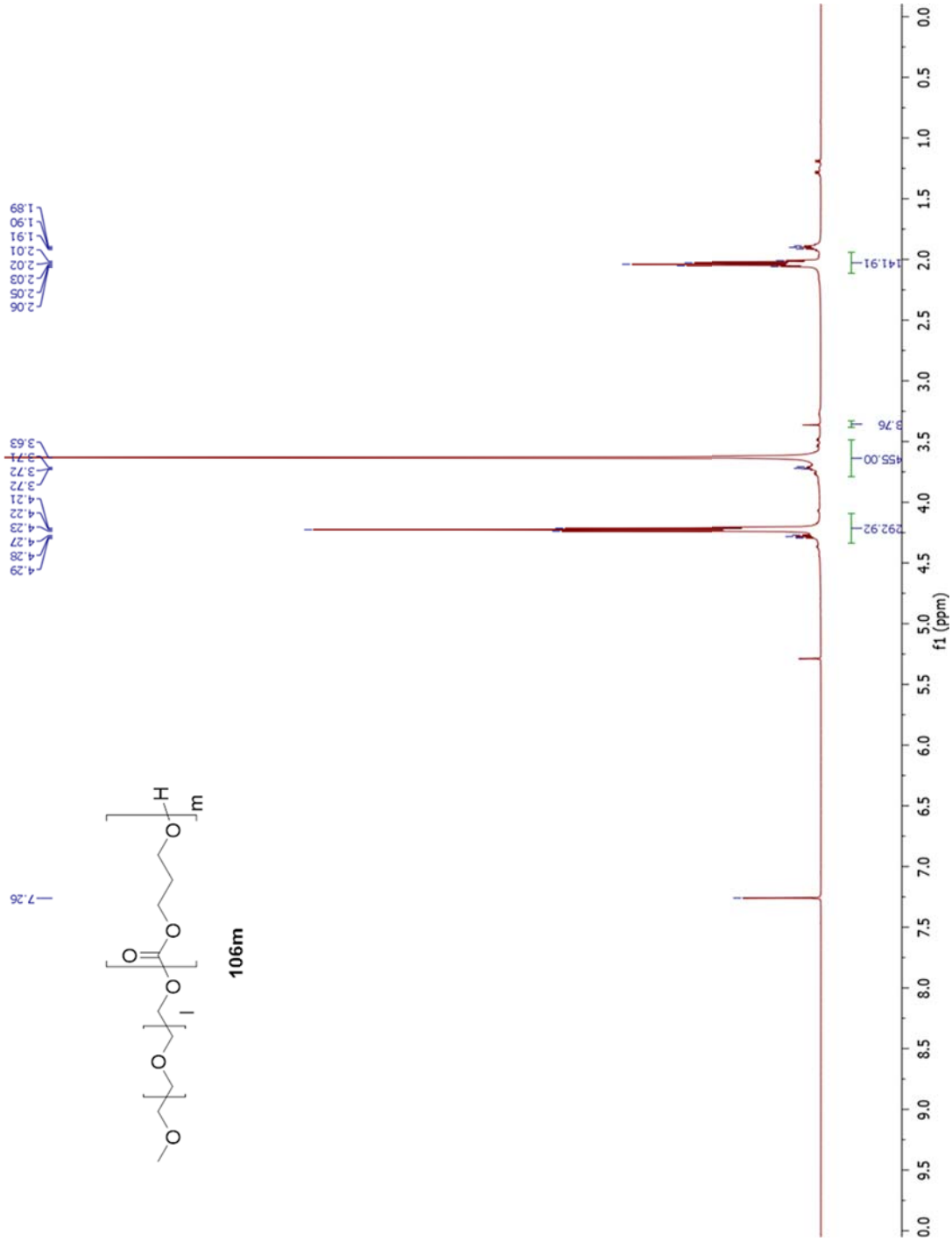

Figure A.138 ^{1}H-NMR of **106m**

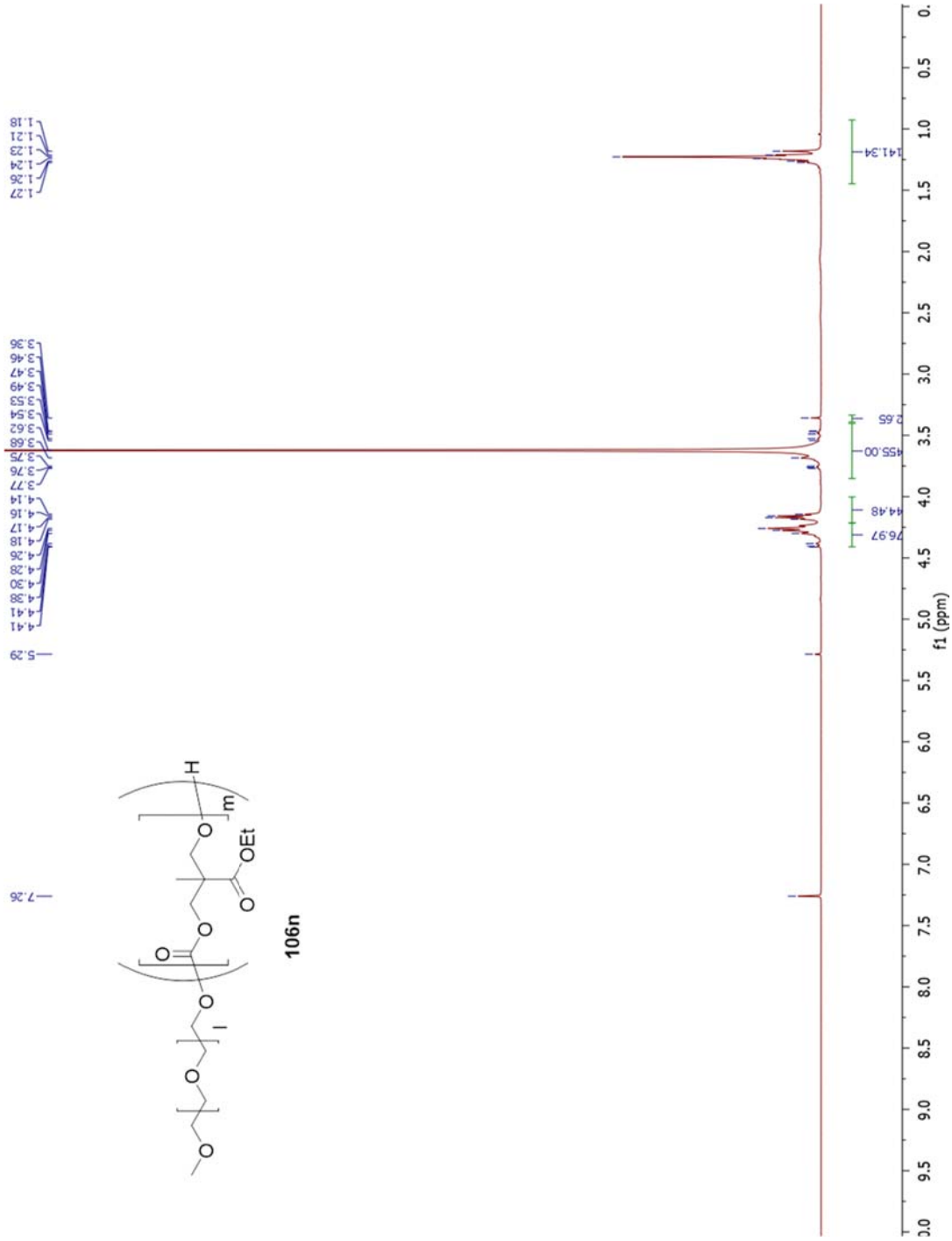

Figure A.139 ^{1}H-NMR of **106n**

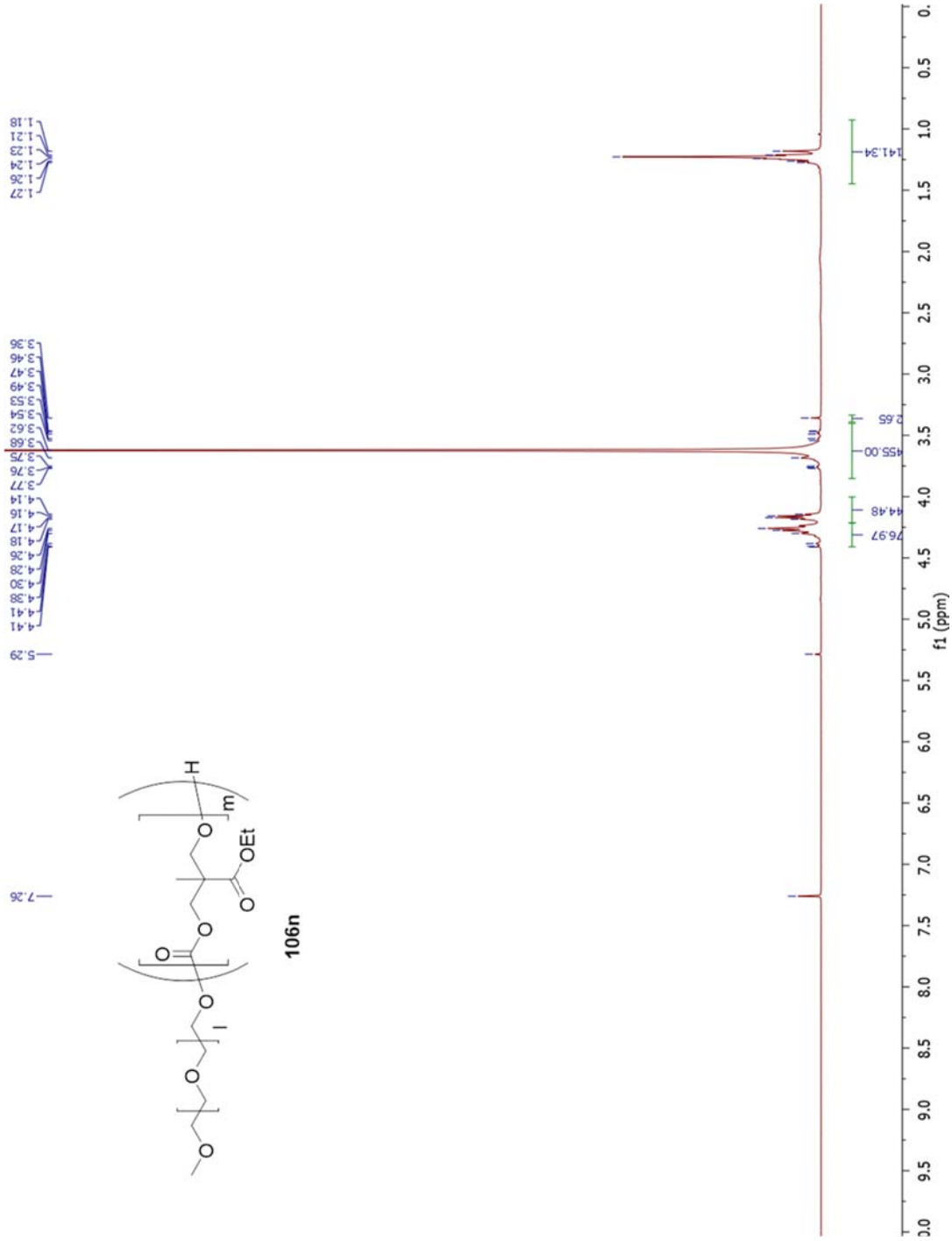

Figure A.140 ^{1}H-NMR of **106o**

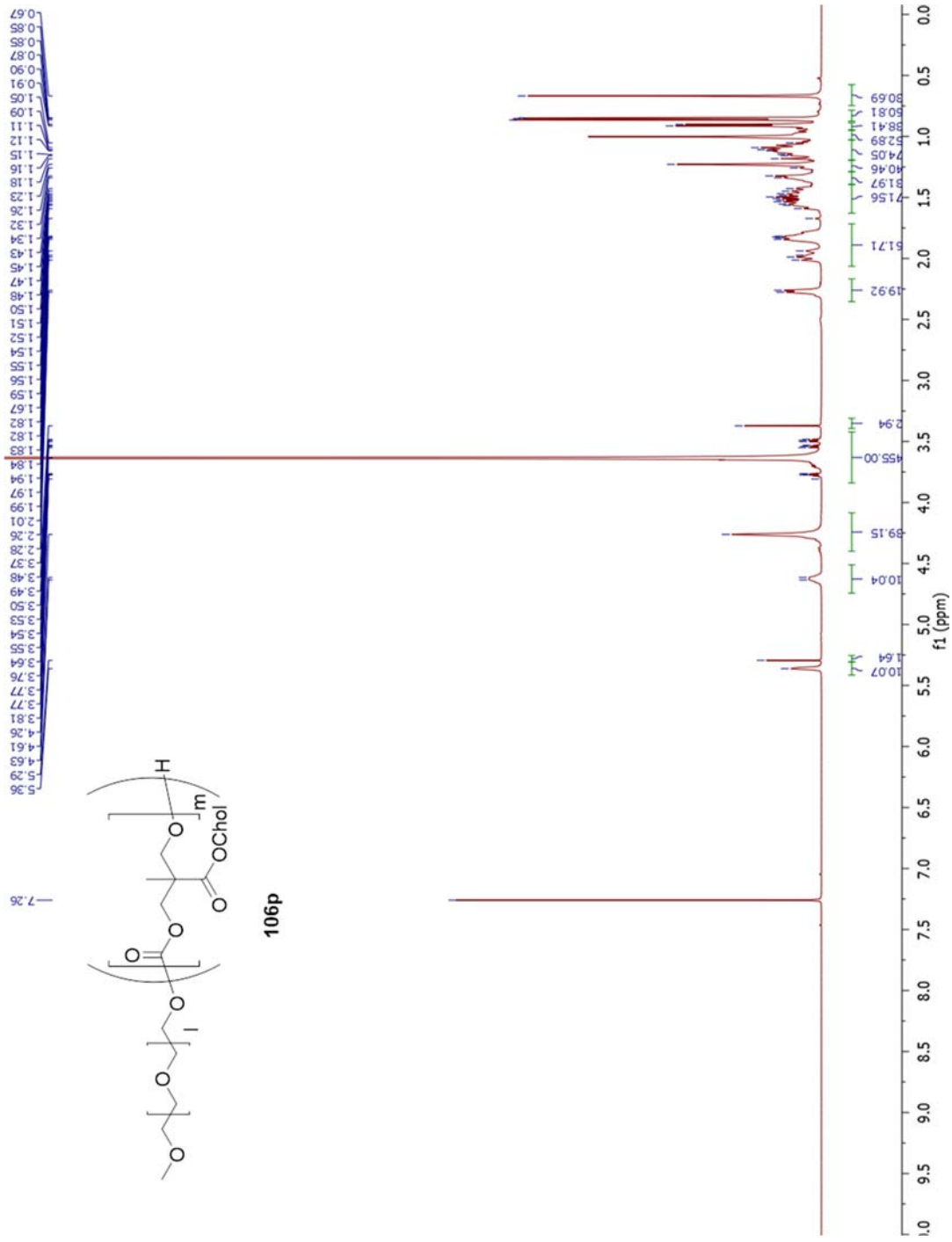

Figure A.141 ^{1}H-NMR of **106p**

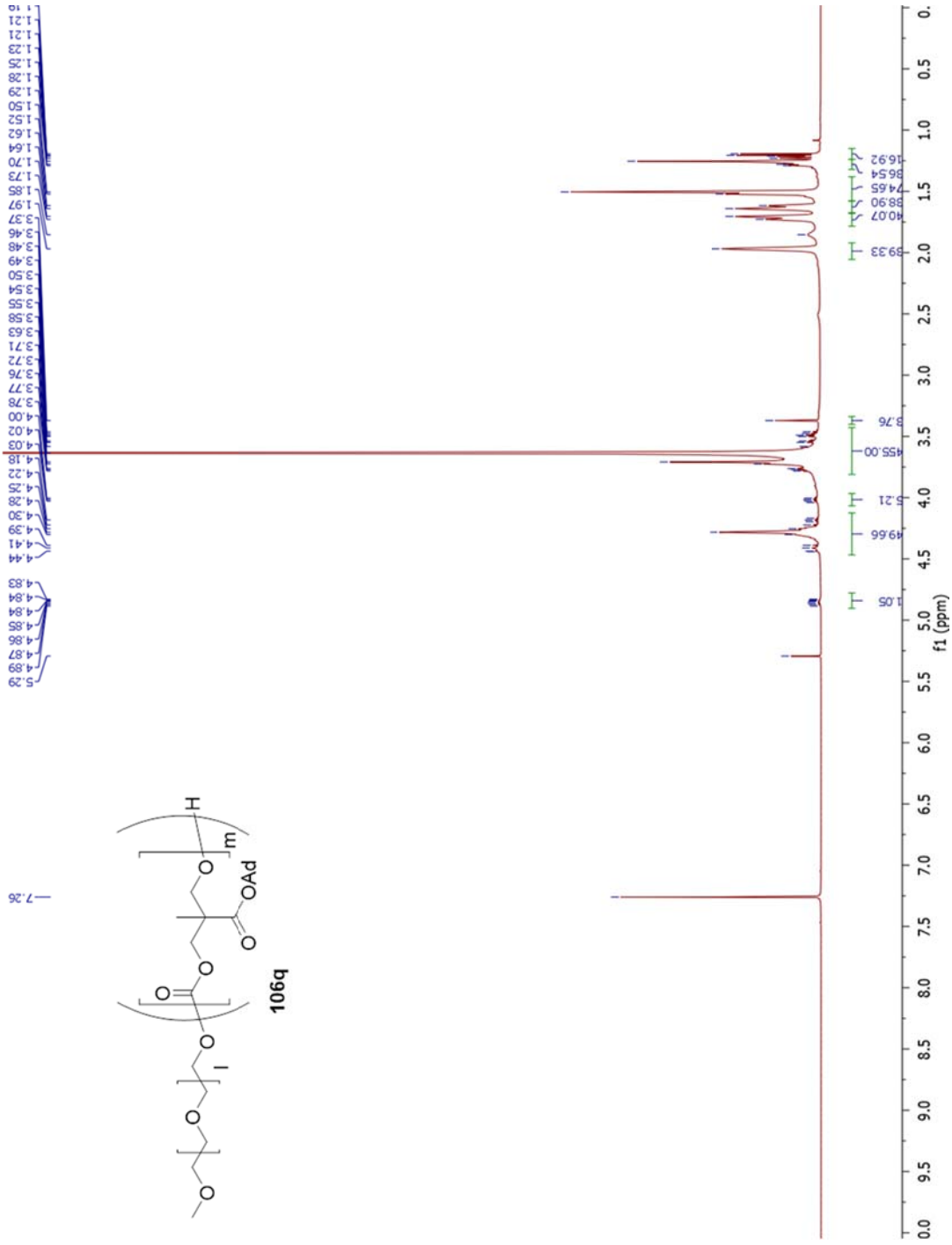

Figure A.142 ^{1}H-NMR of **106q**

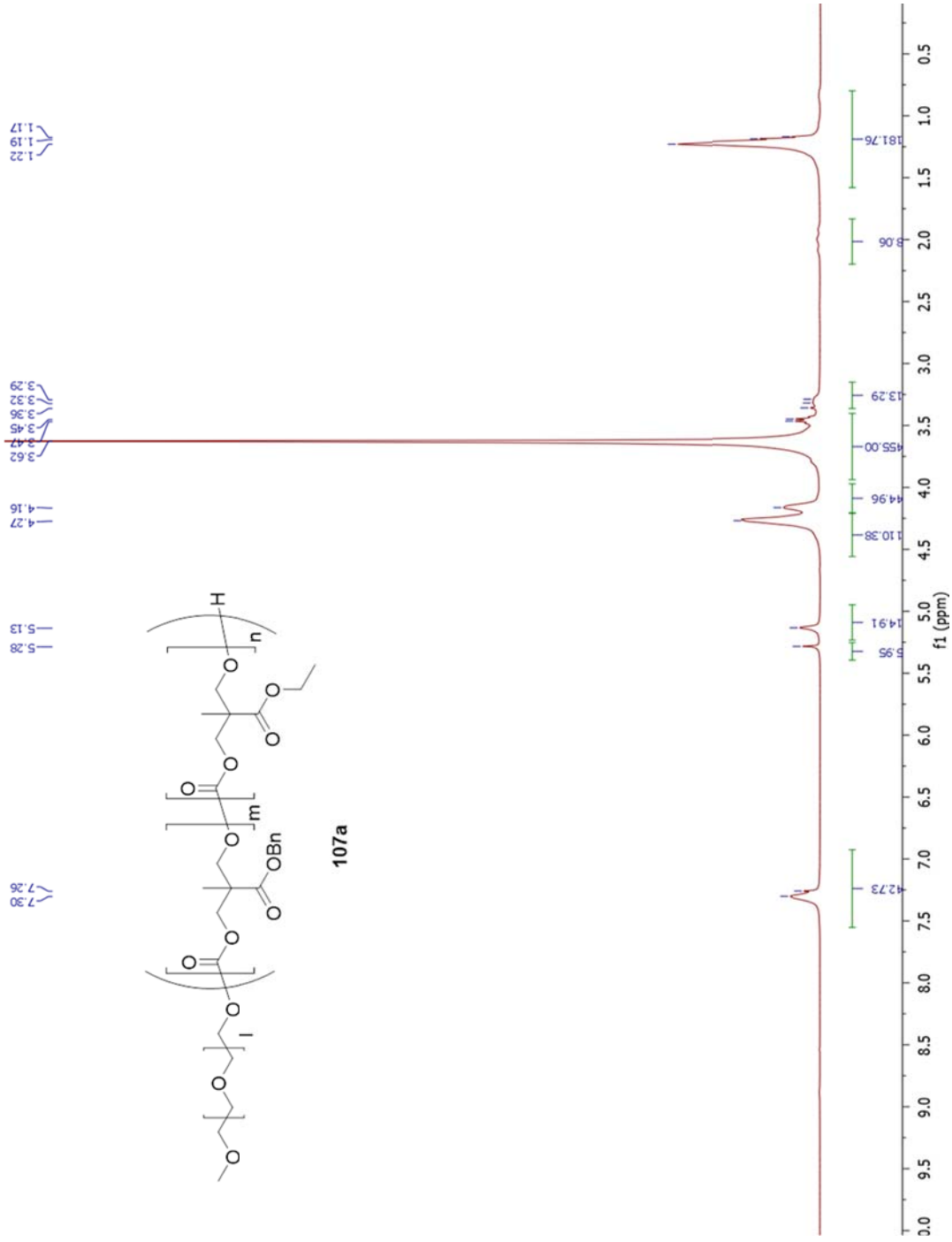

Figure A.143 ^{1}H-NMR of **107a**

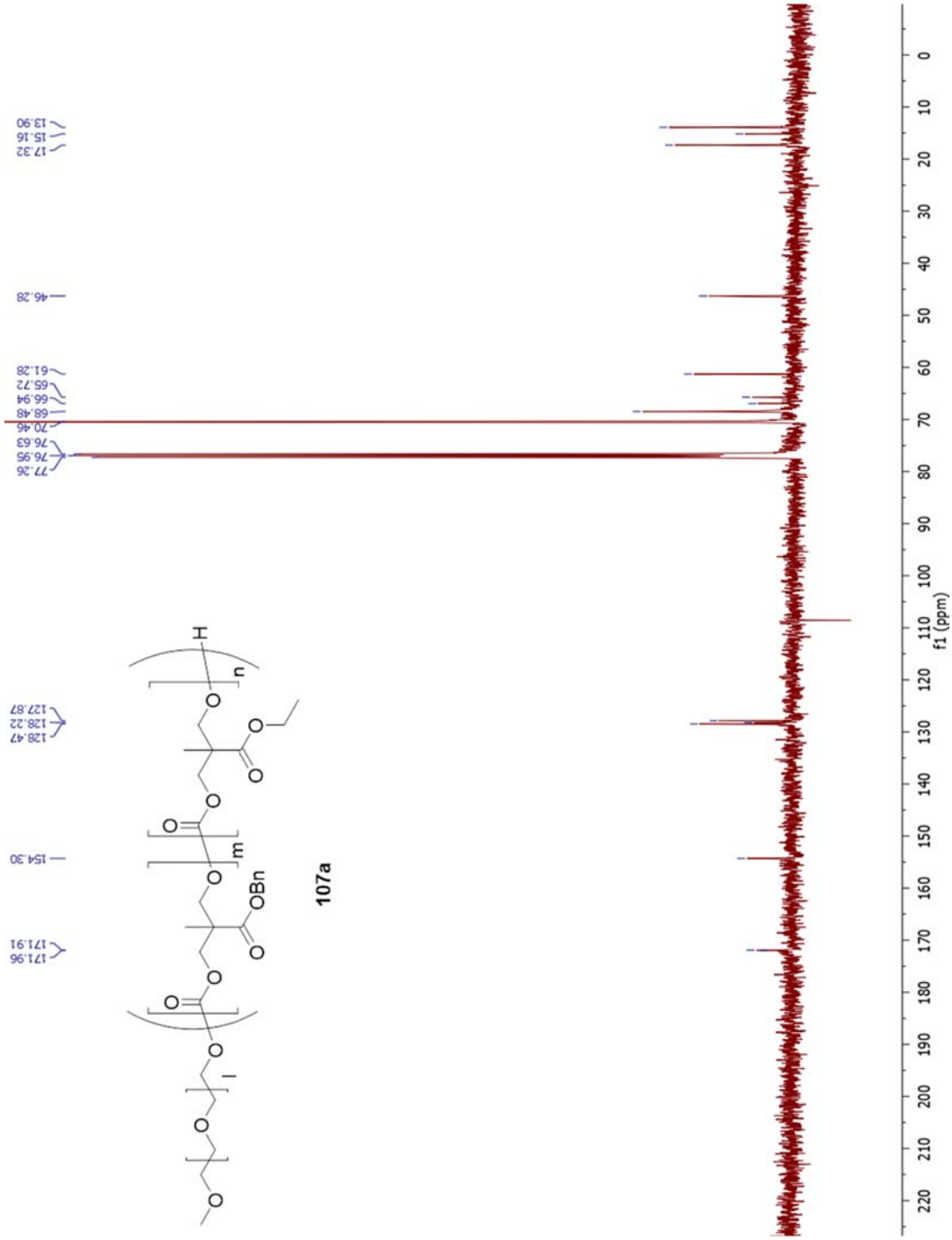

Figure A.144 ^{13}C-NMR of **107a**

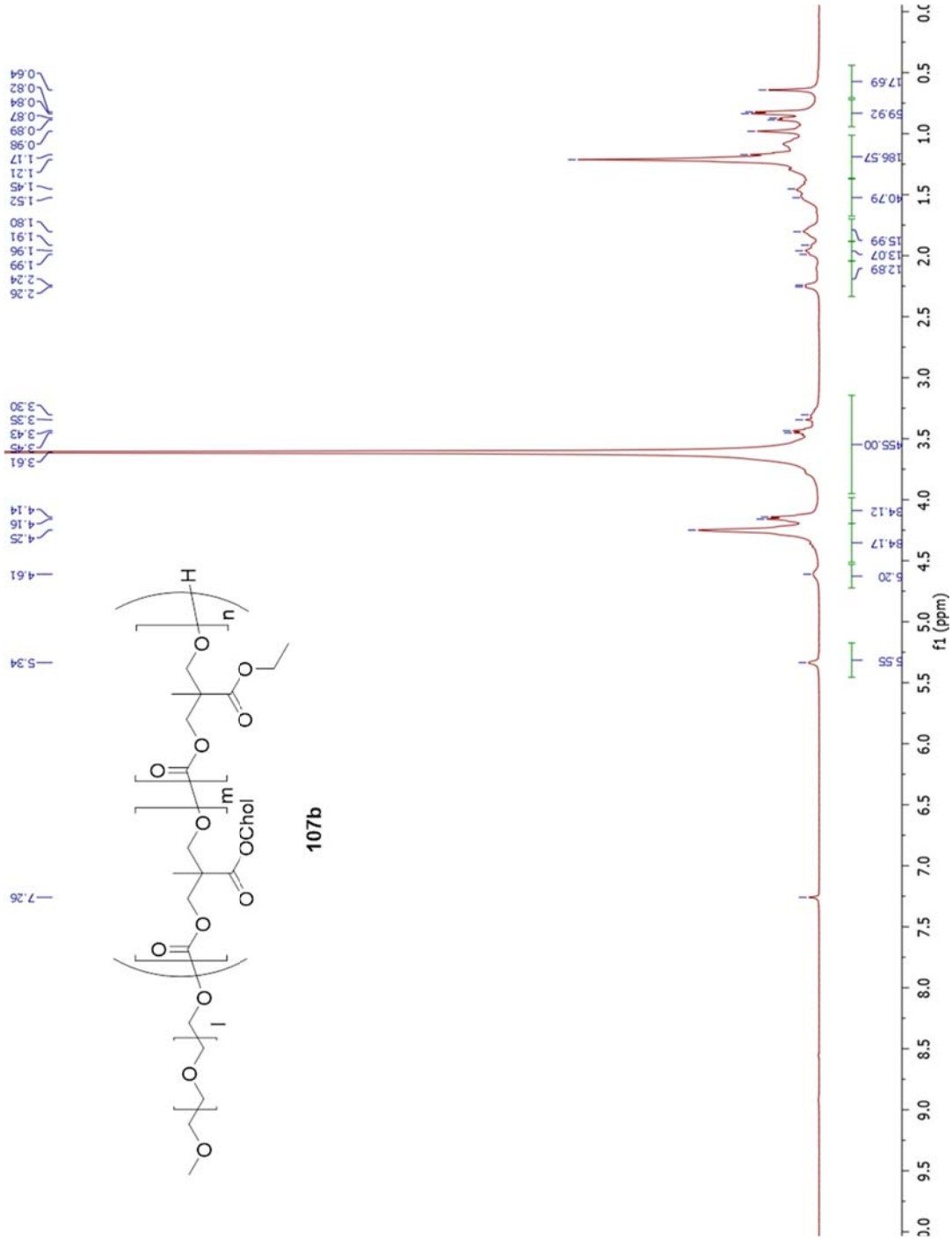

Figure A.145 ^{1}H-NMR of **107b**

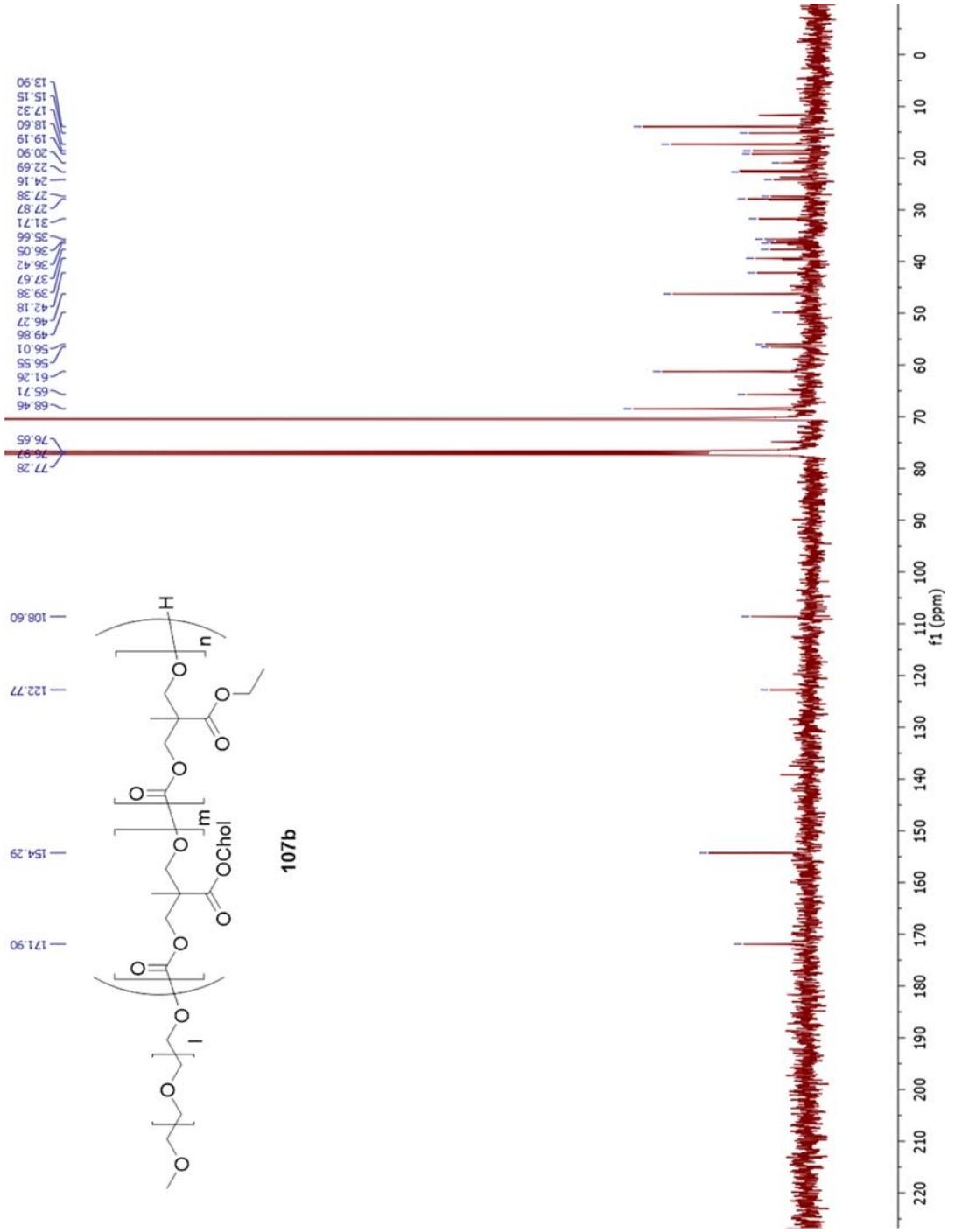

Figure A.146 ^{13}C-NMR of **107b**

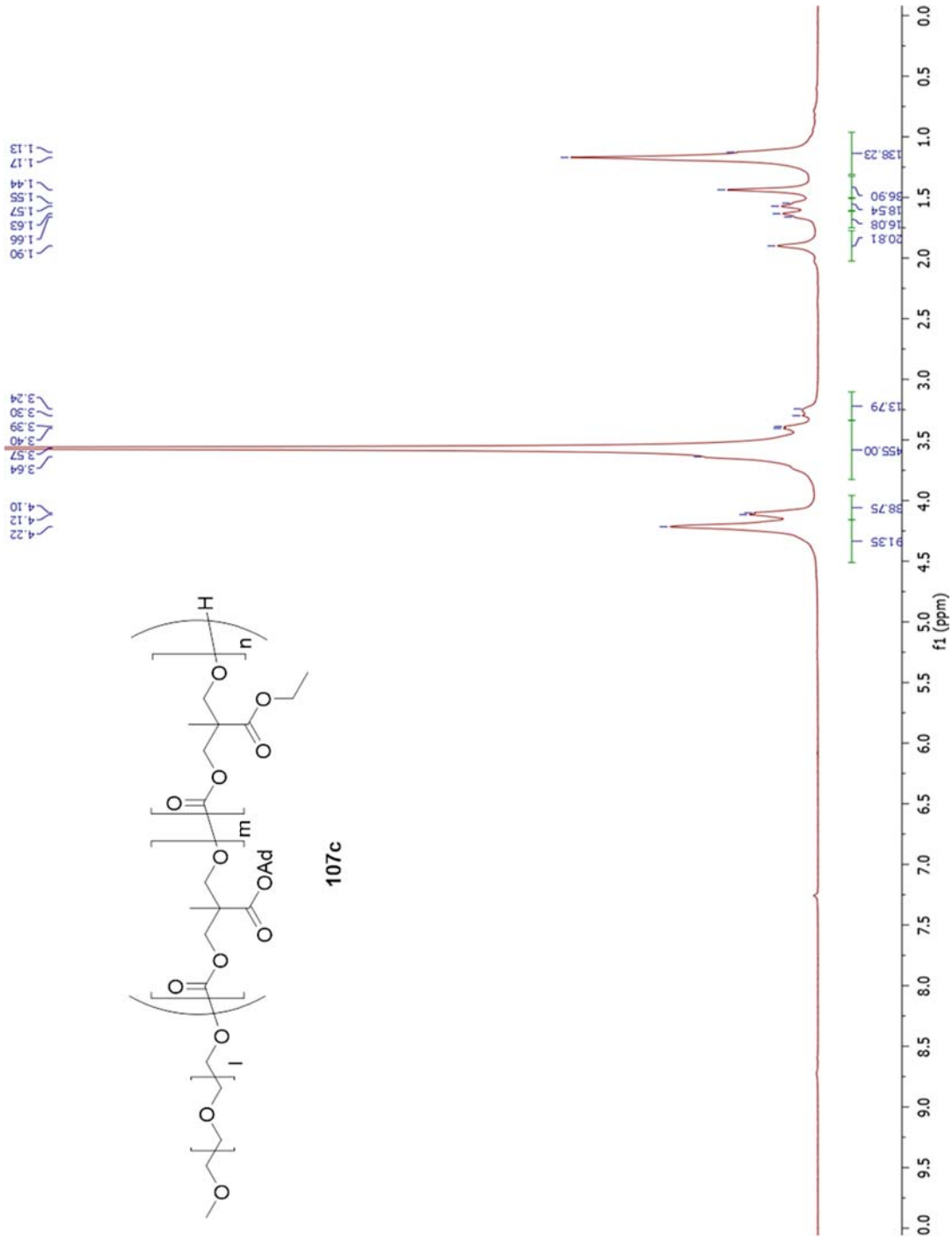

Figure A.147 ^{1}H-NMR of **107c**

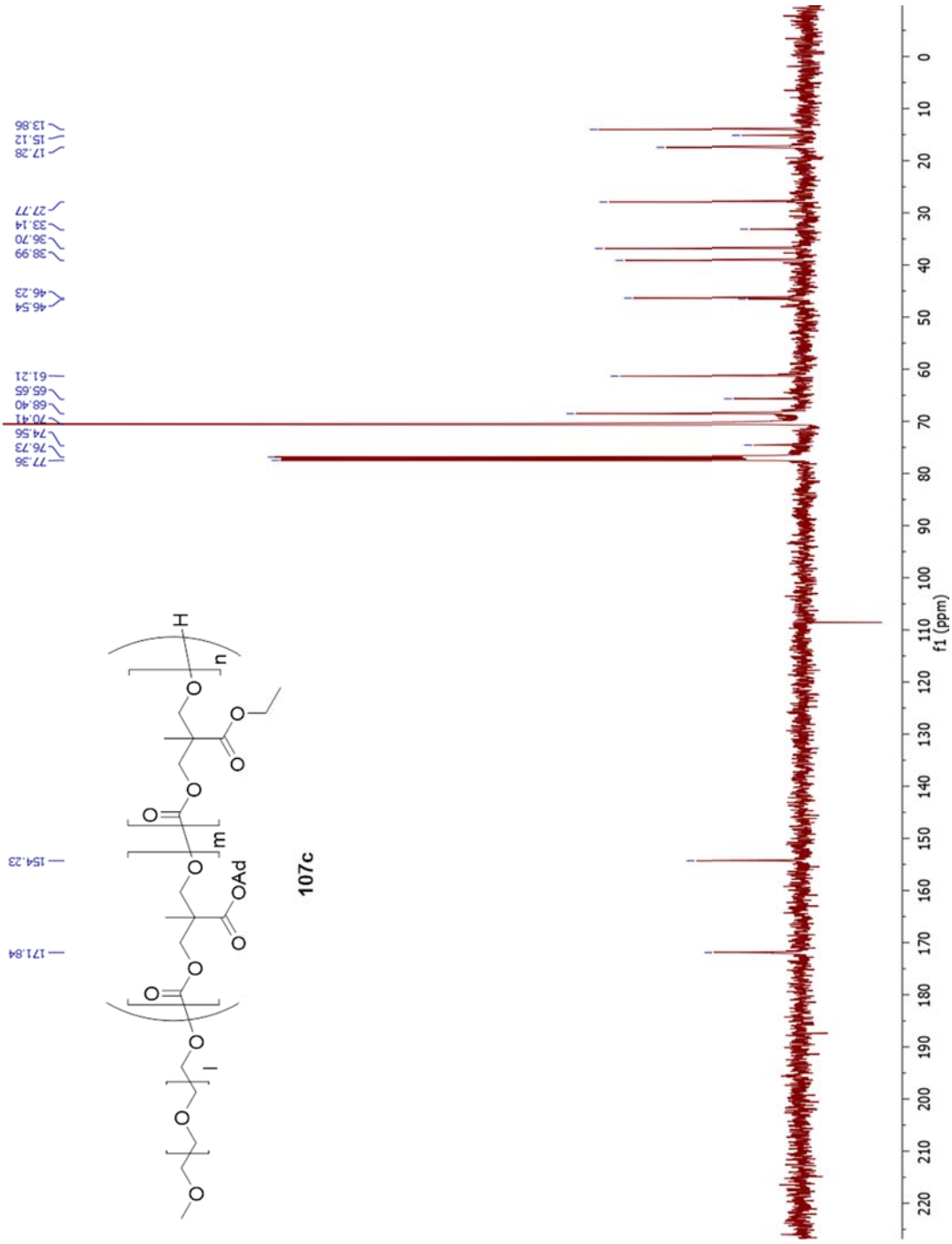

Figure A.148 ^{13}C-NMR of **107c**

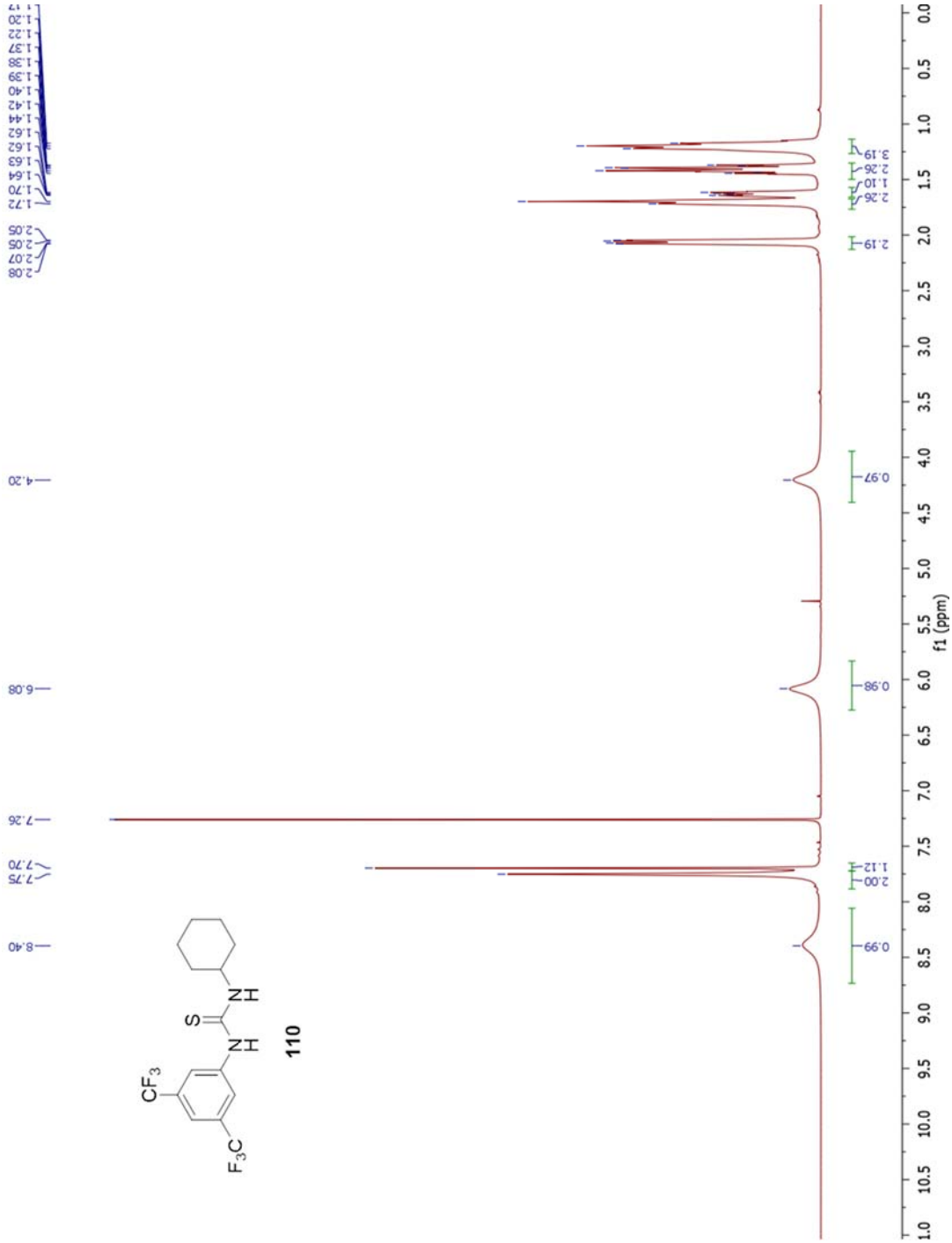

Figure A.149 ^{1}H-NMR of **110**

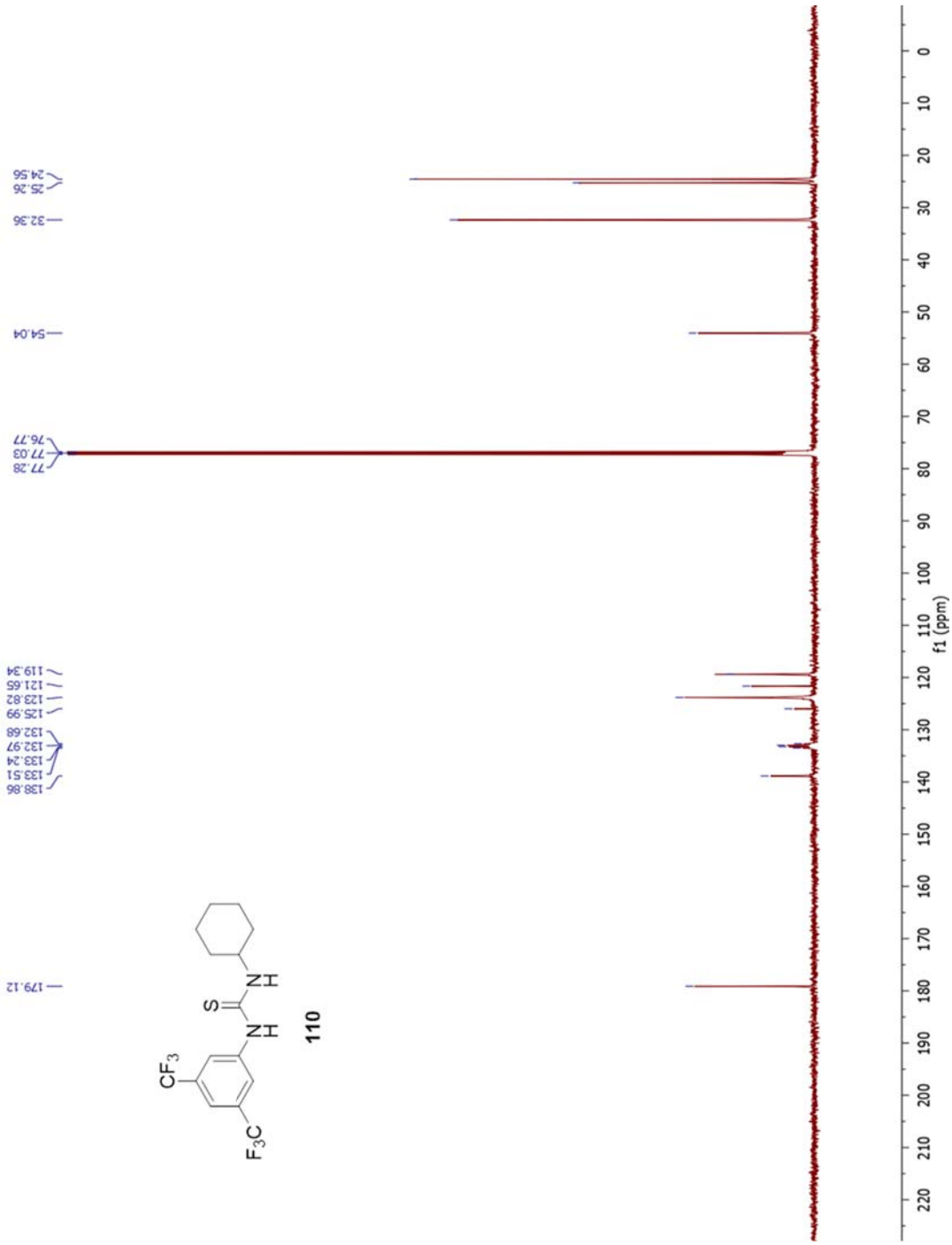

Figure A.150 ^{13}C-NMR of **110**

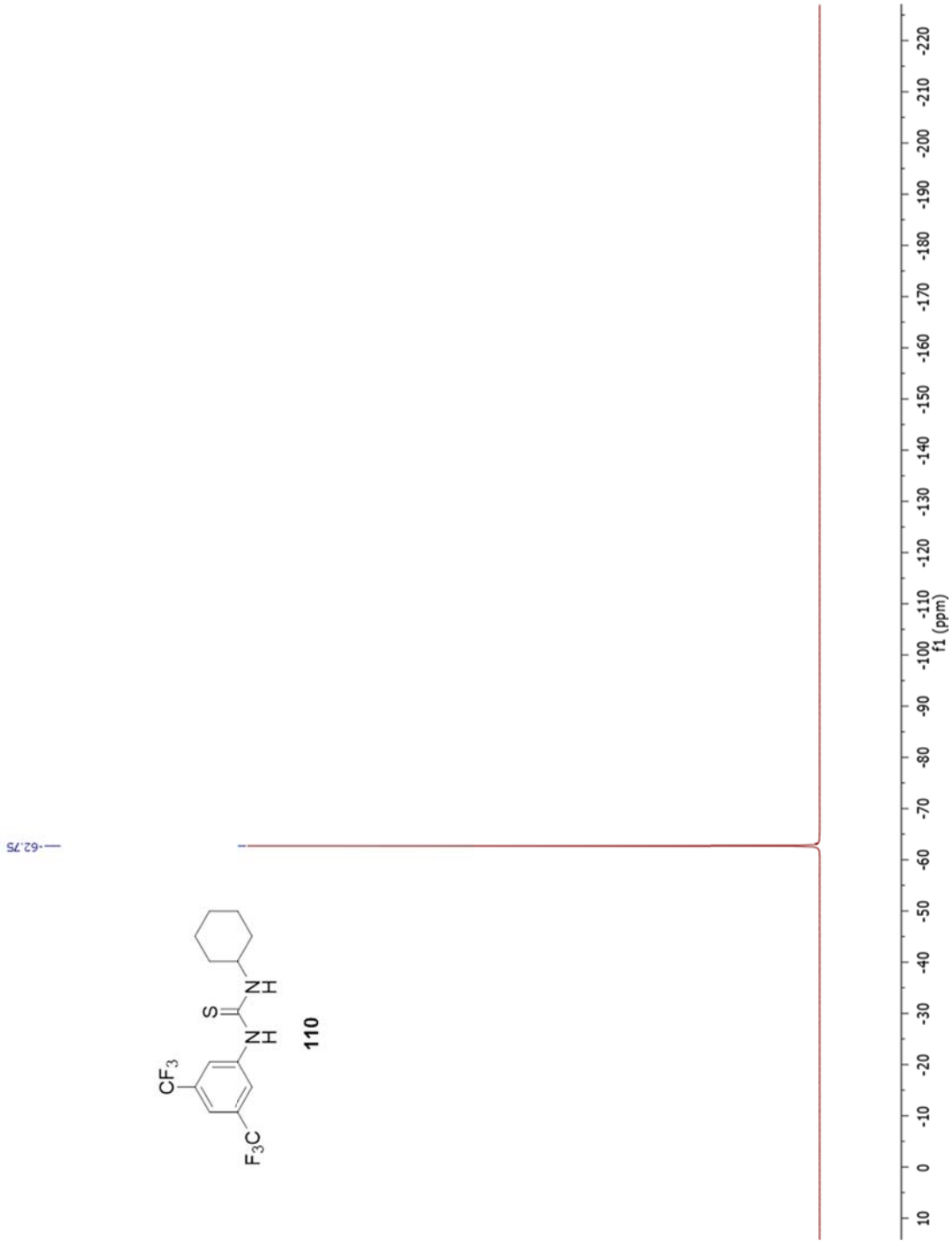

Figure A.151 ^{19}F-NMR of **110**

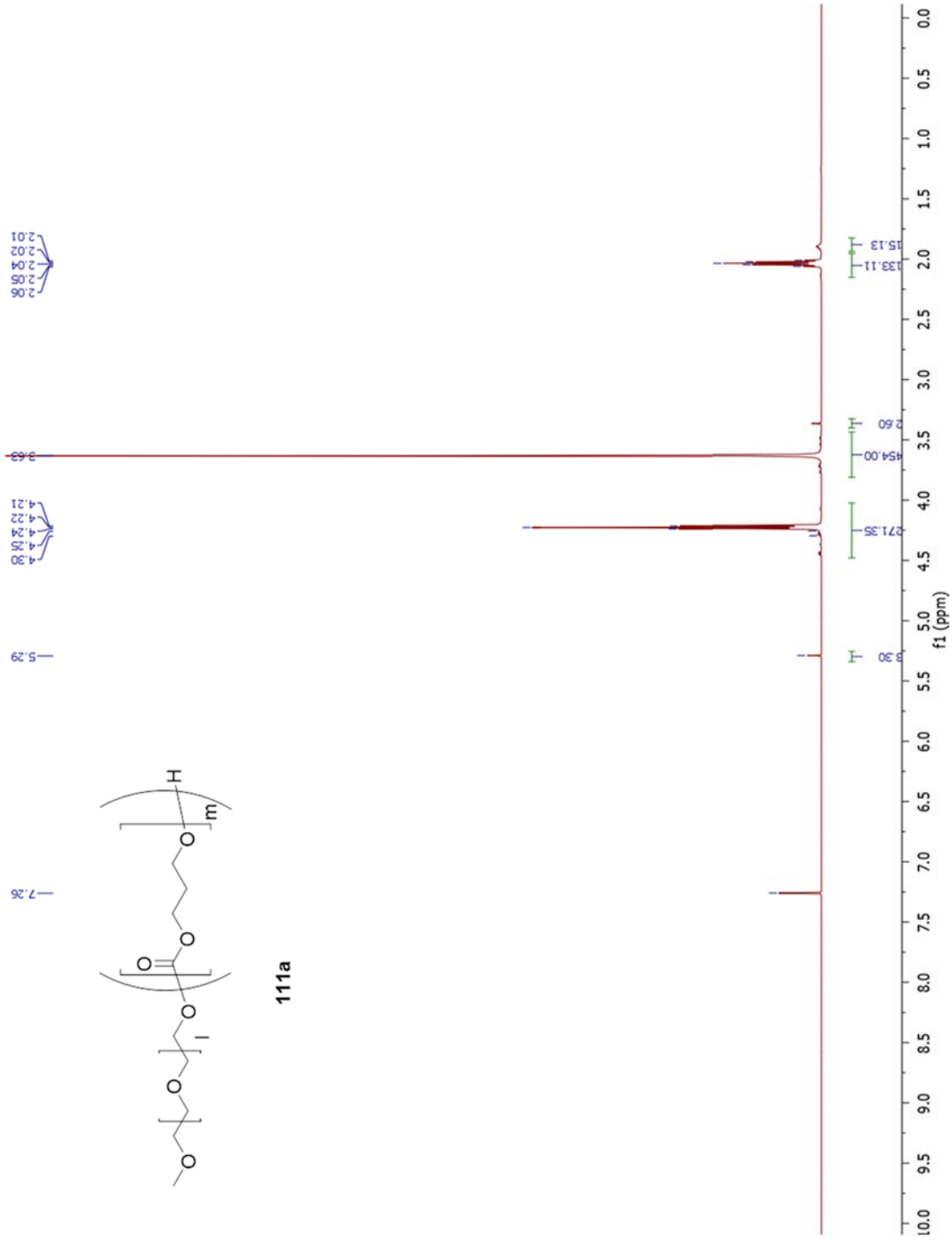

Figure A.152 ^{1}H-NMR of **111a**

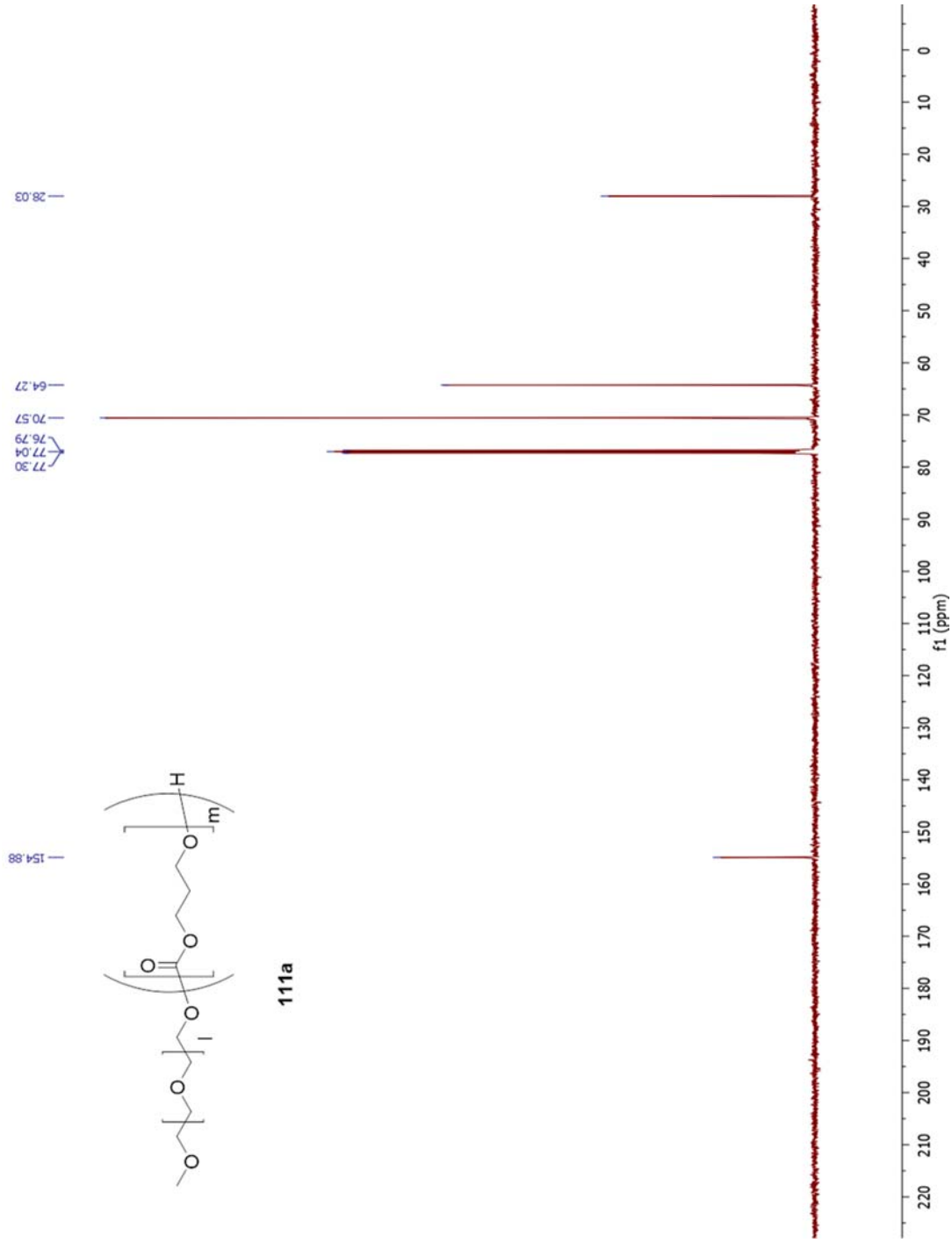

Figure A.153 ^{13}C-NMR of **111a**

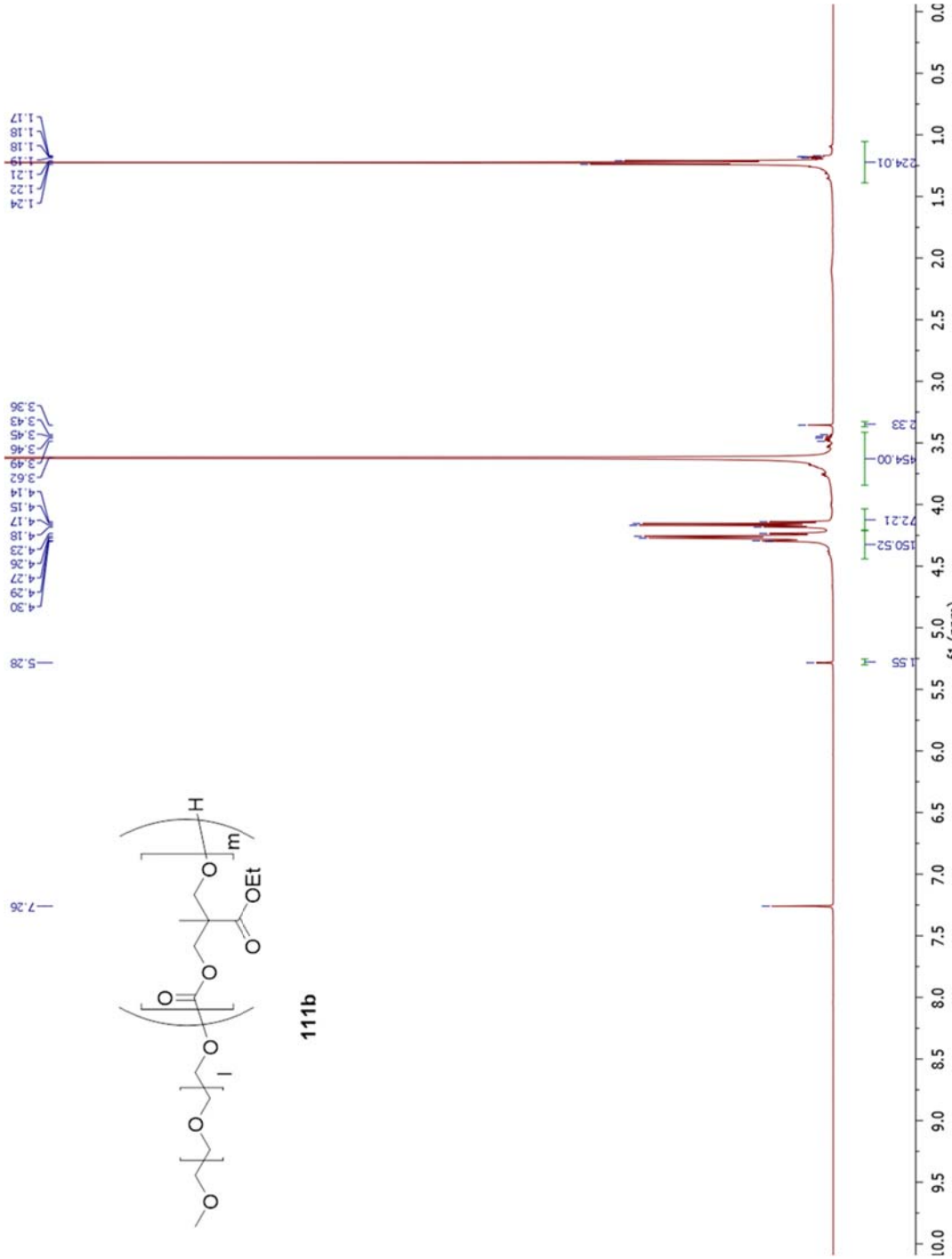

Figure A.154 ^{1}H-NMR of **111b**

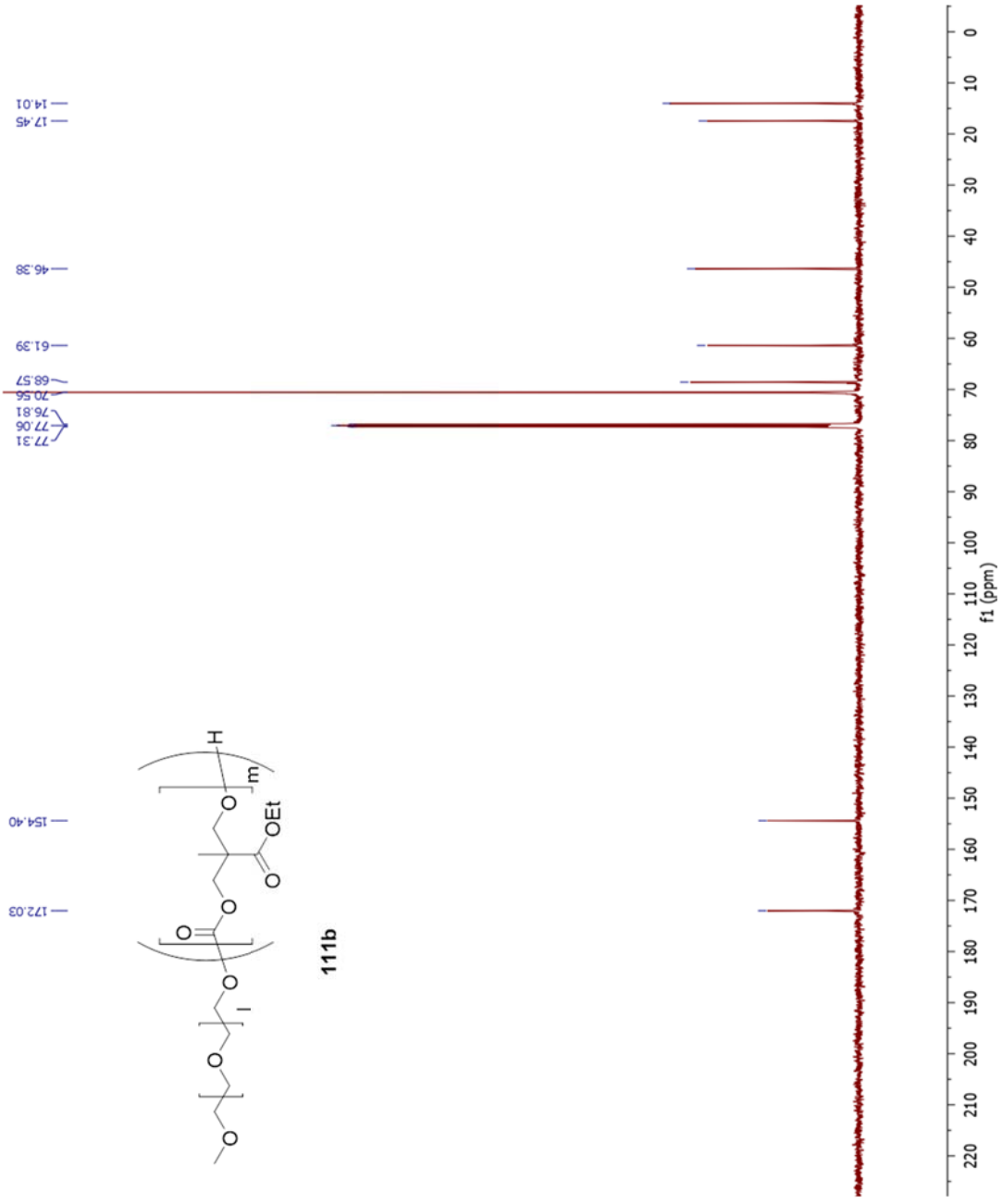

Figure A.155 ^{13}C-NMR of **111b**

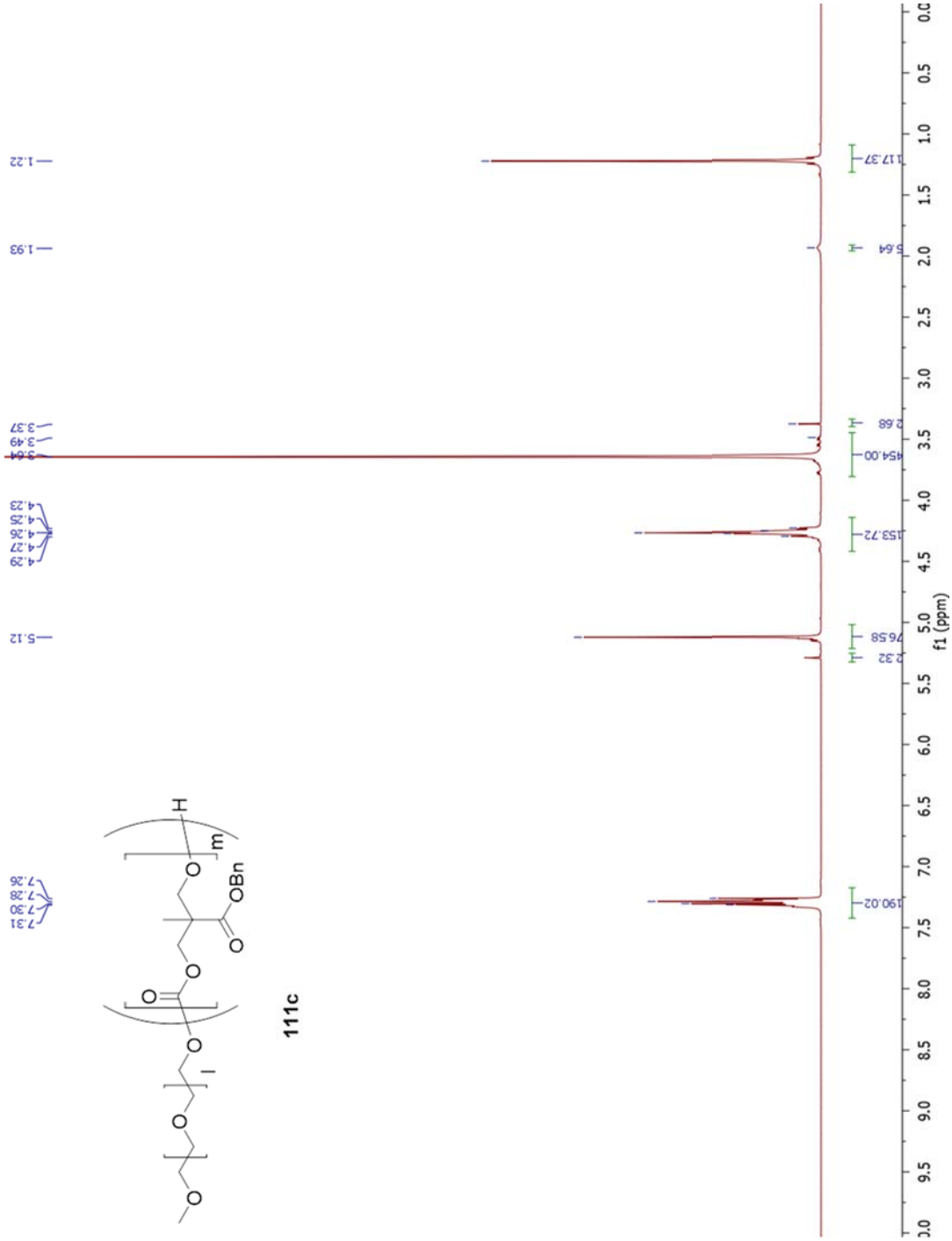

Figure A.156 ^{1}H-NMR of **111c**

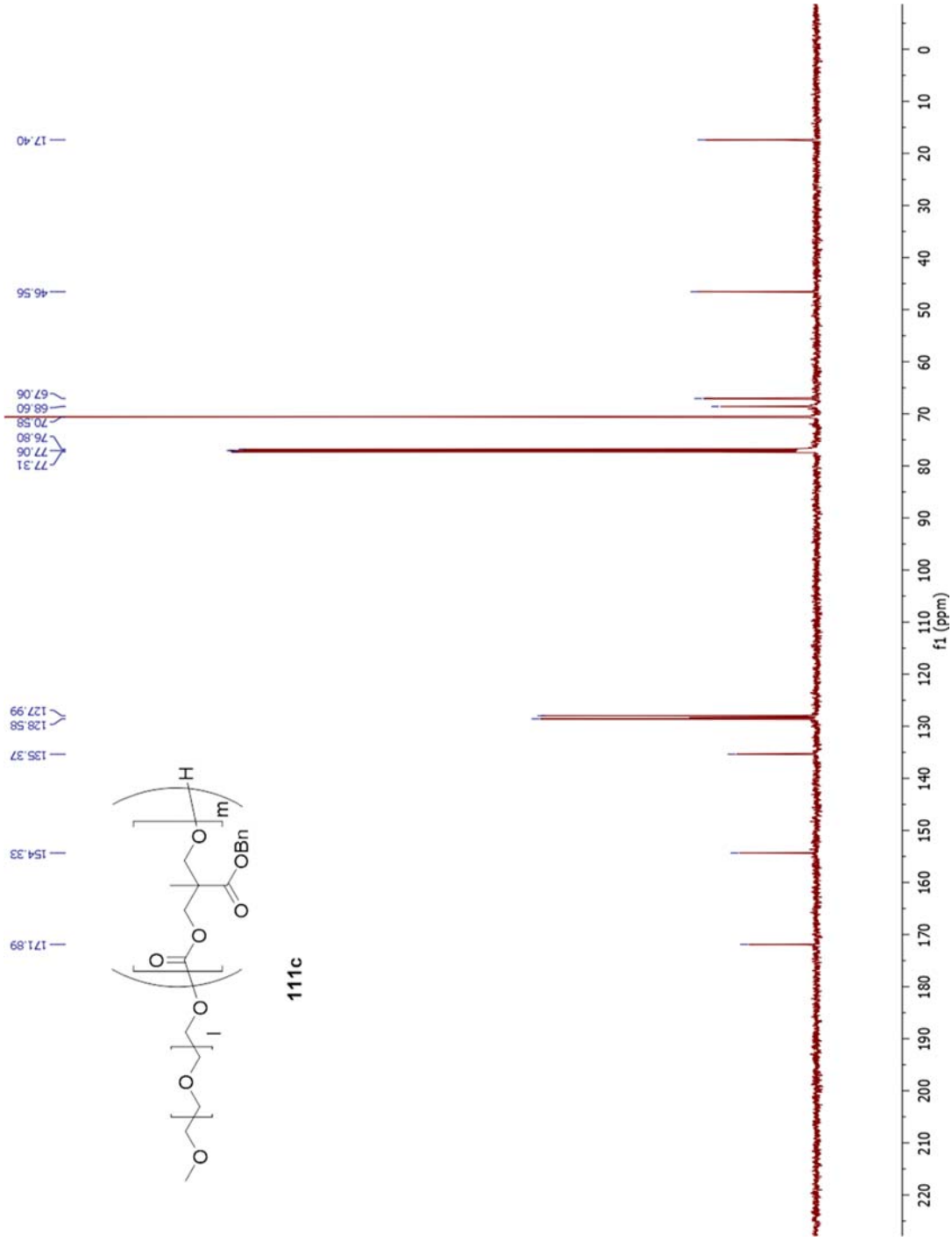

Figure A.157 ^{13}C-NMR of **111c**

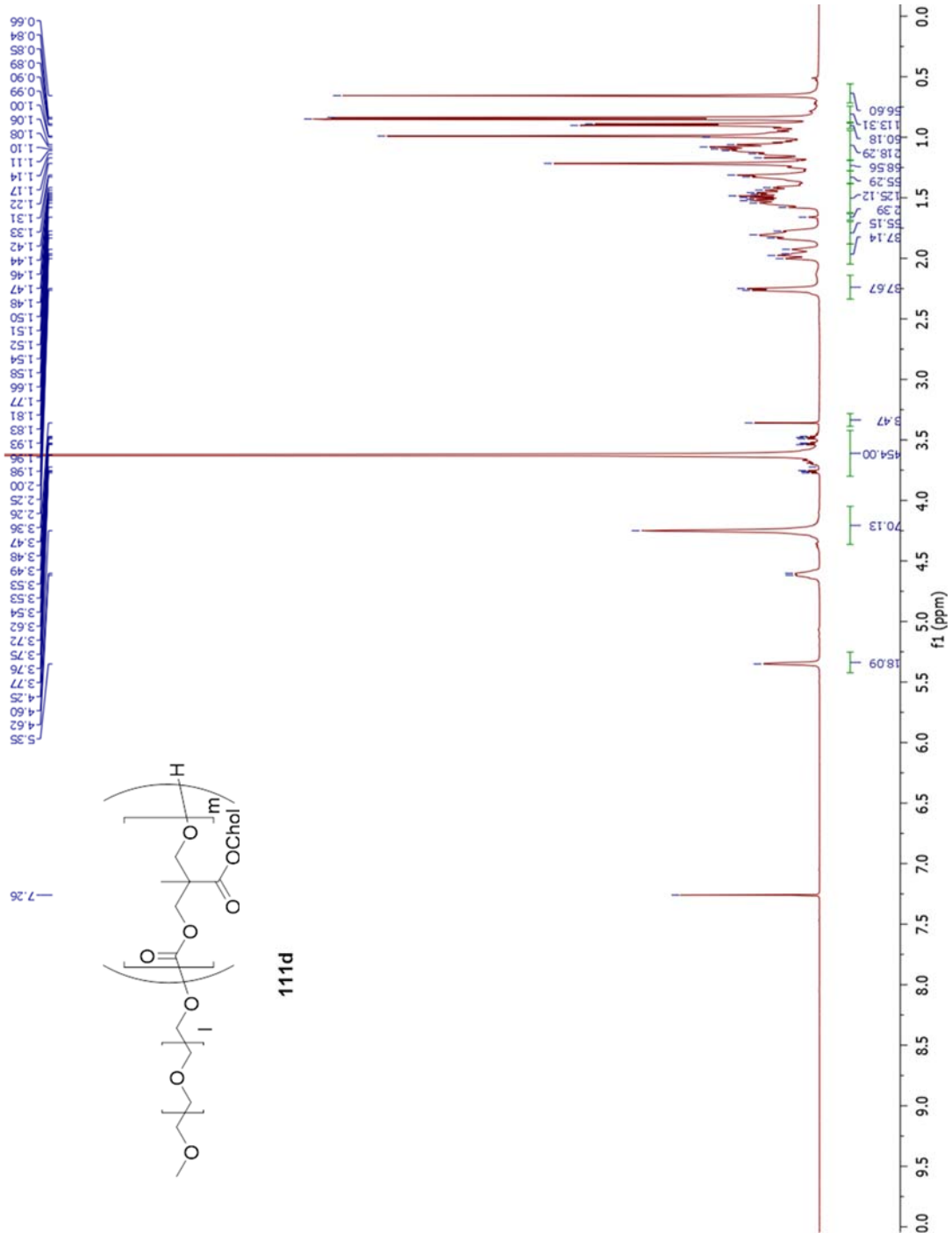

Figure A.158 ^{1}H-NMR of **111d**

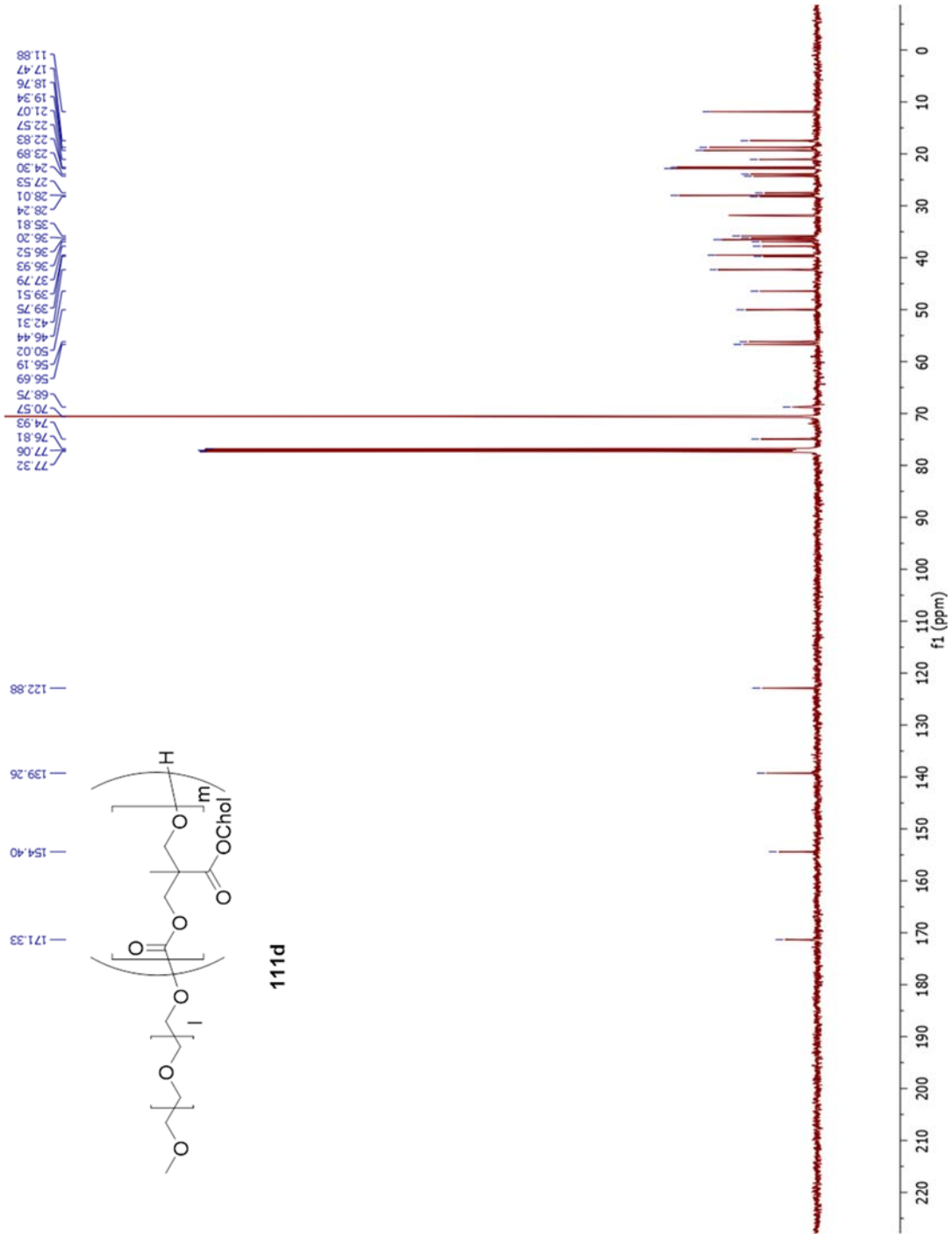

Figure A.159 ^{13}C-NMR of **111d**

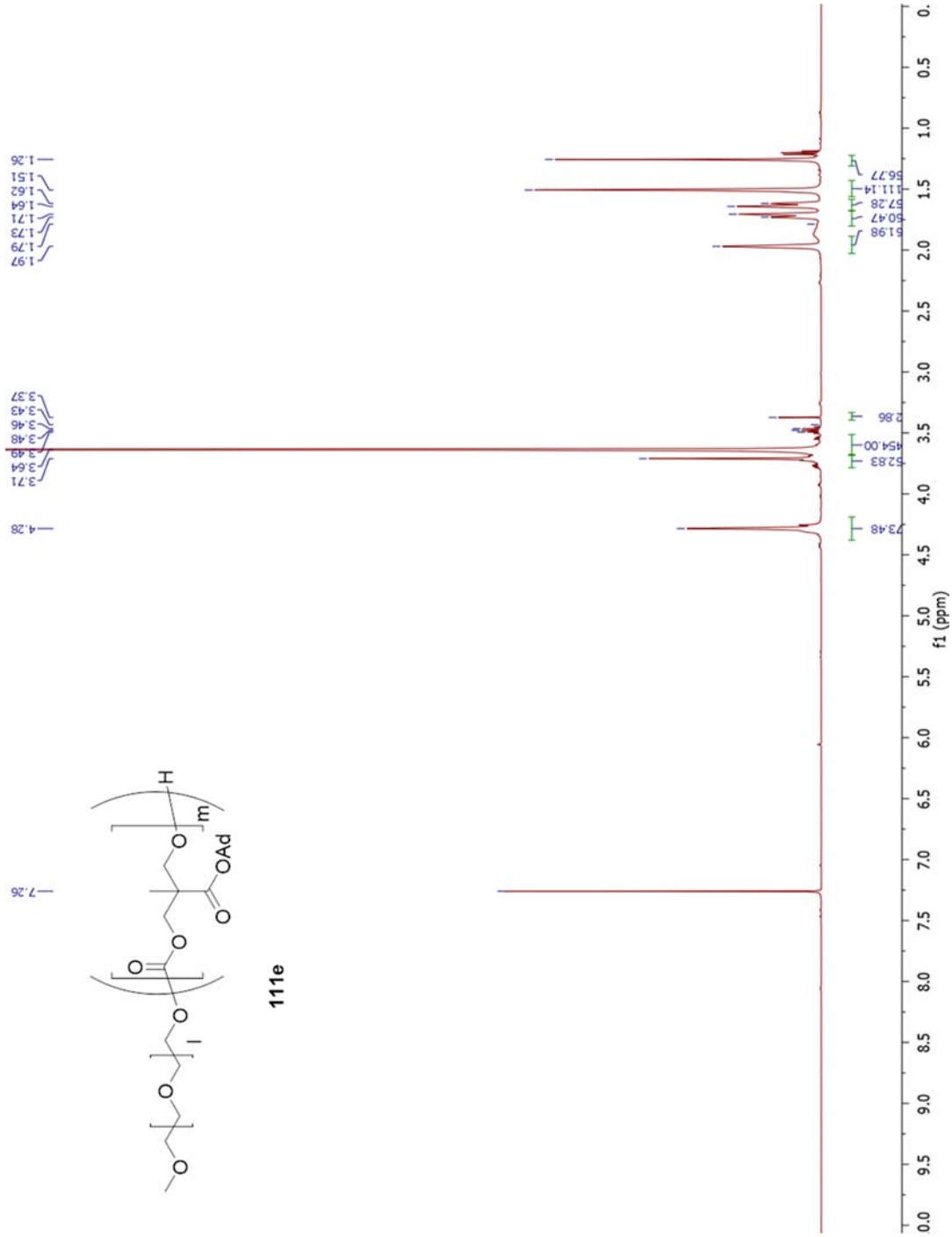

Figure A.160 ^{1}H-NMR of **111e**

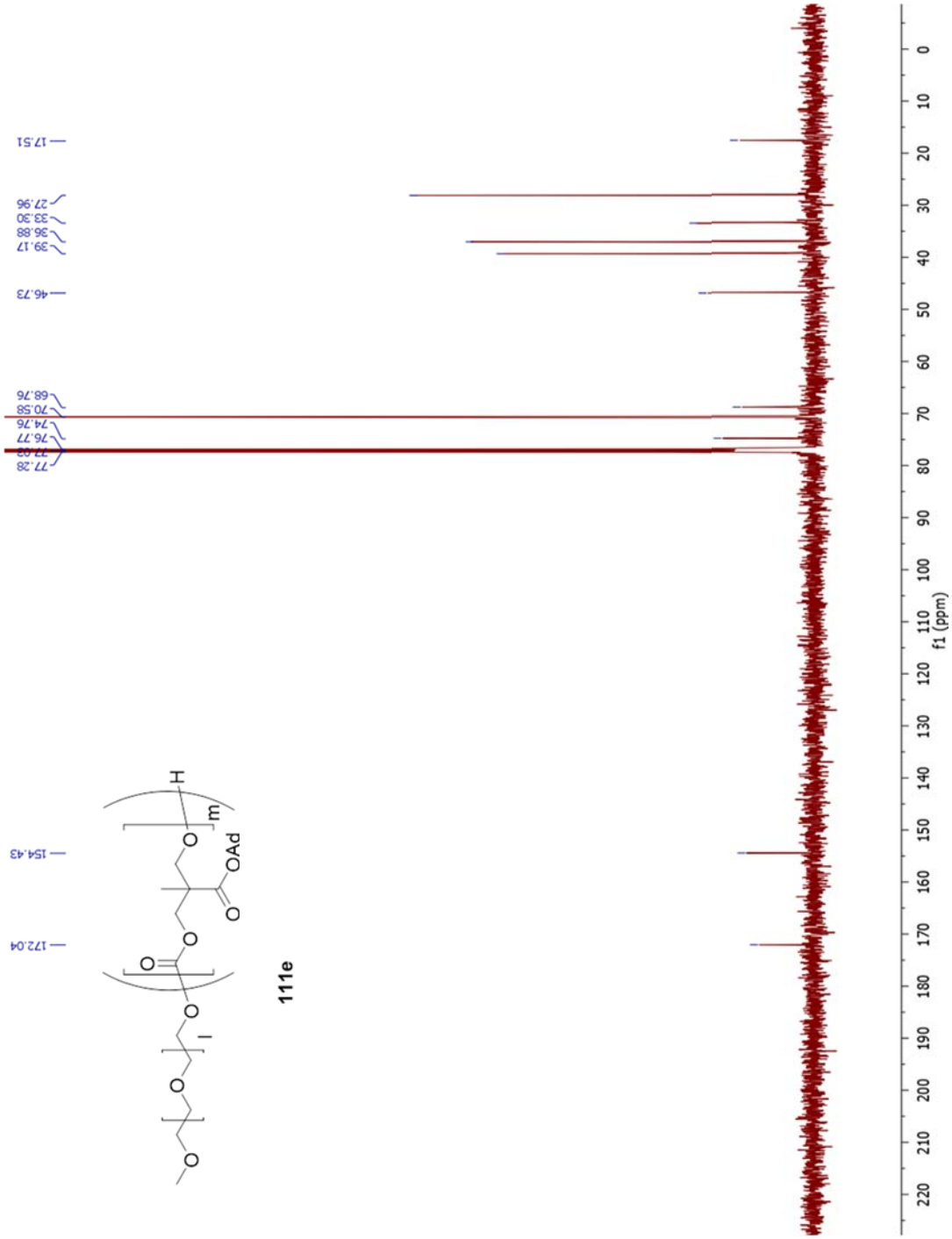

Figure A.161 ^{13}C-NMR of **111e**

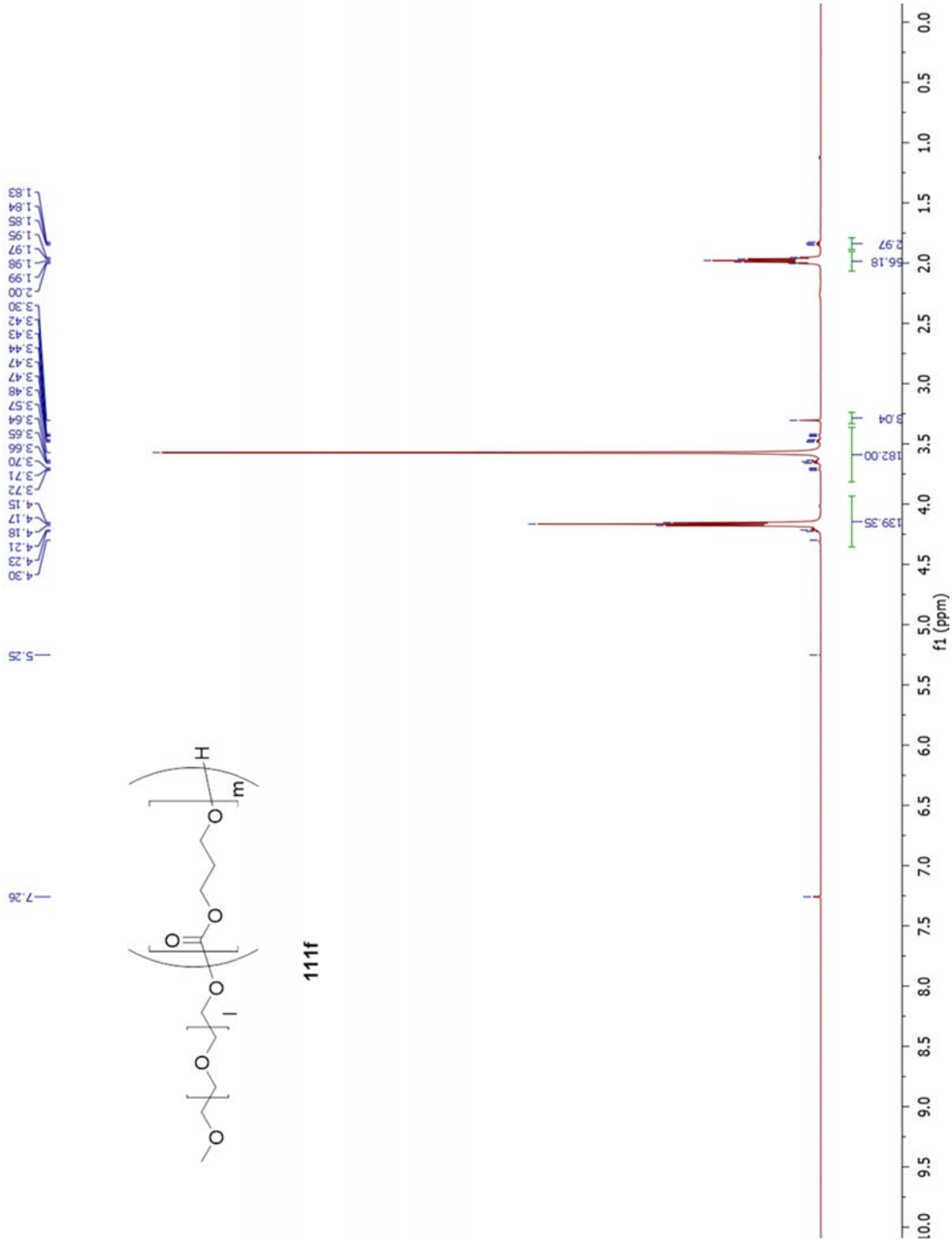

Figure A.162 ^{1}H-NMR of **111f**

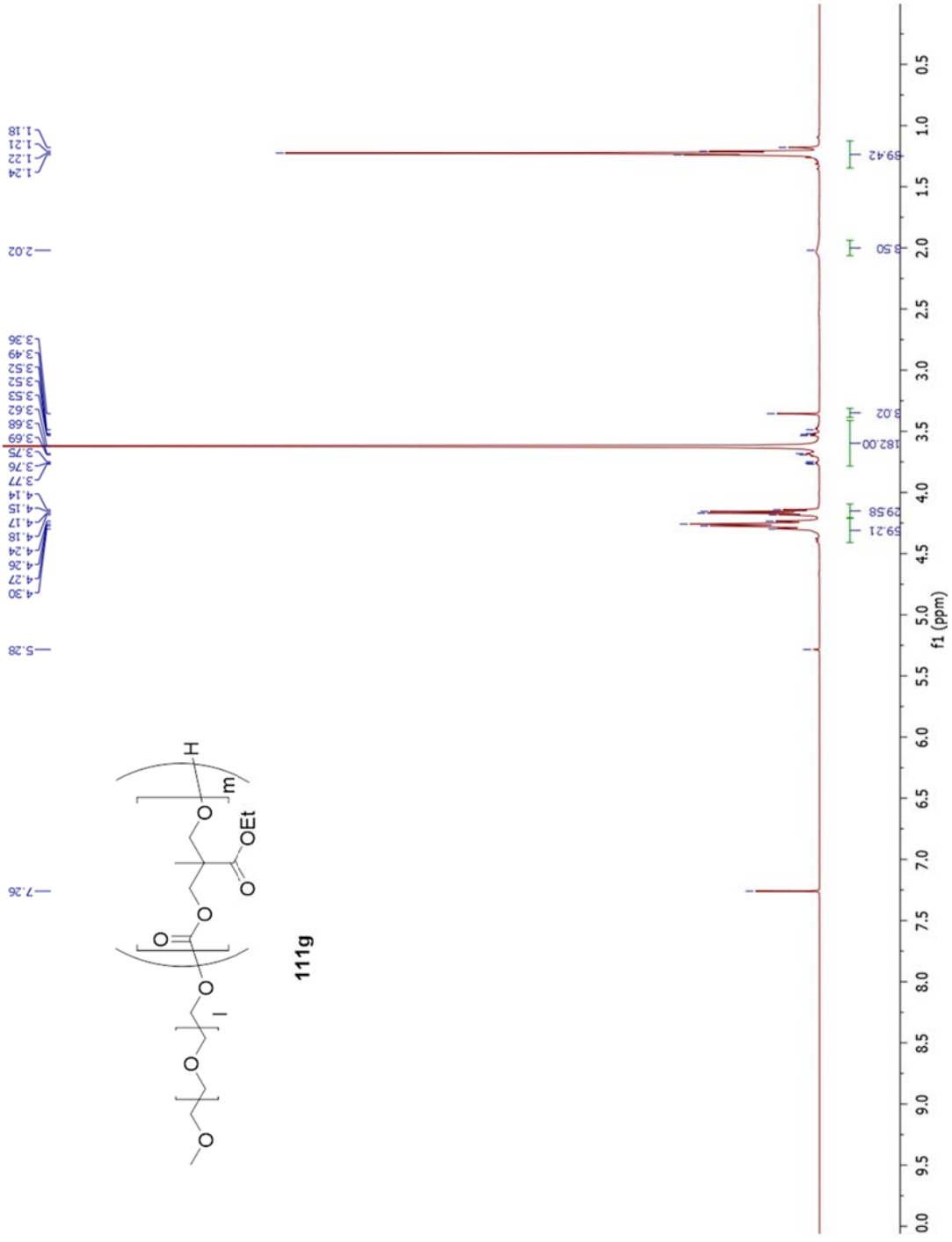

Figure A.163 ^{1}H-NMR of **111g**

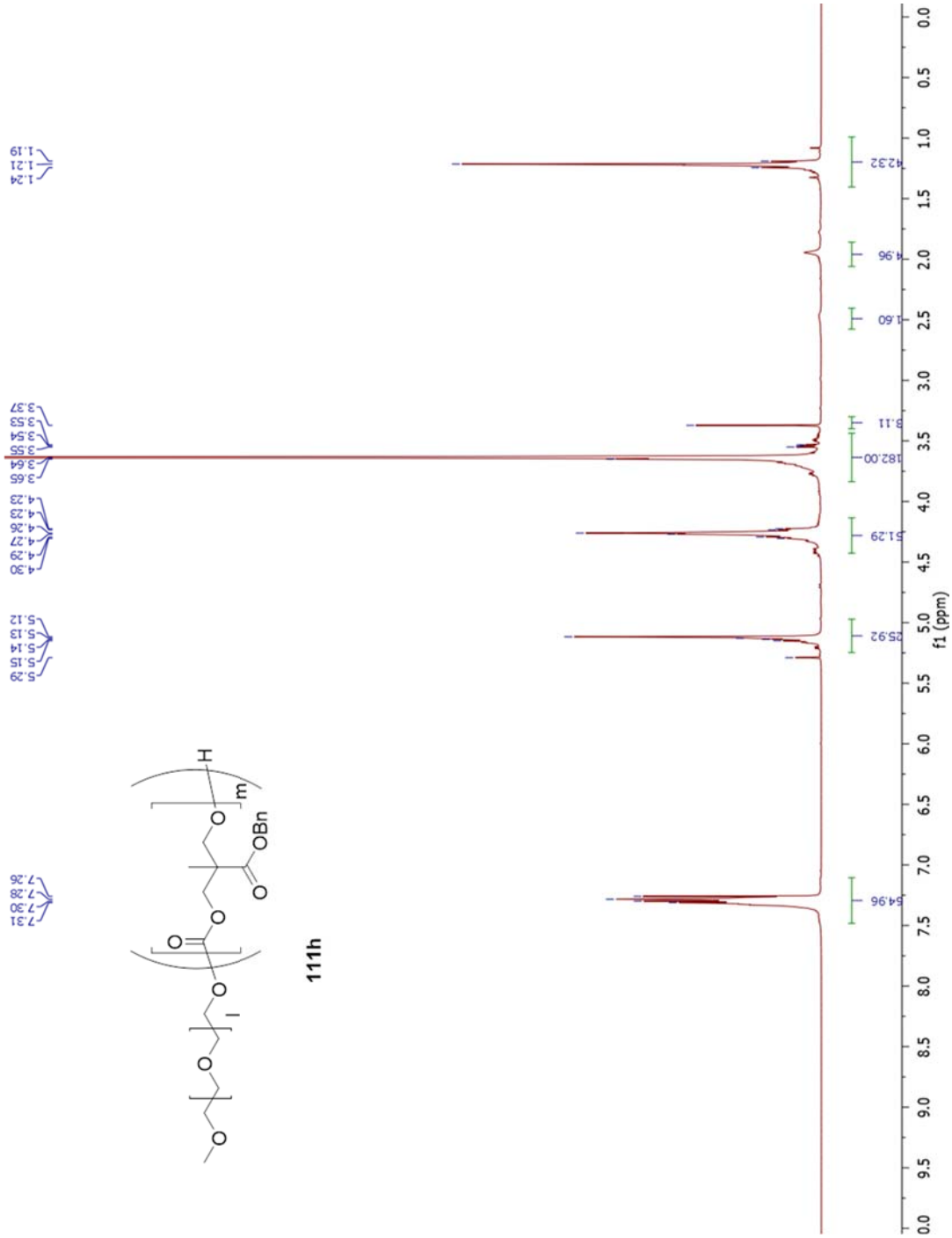

Figure A.164 ^{1}H-NMR of **111h**

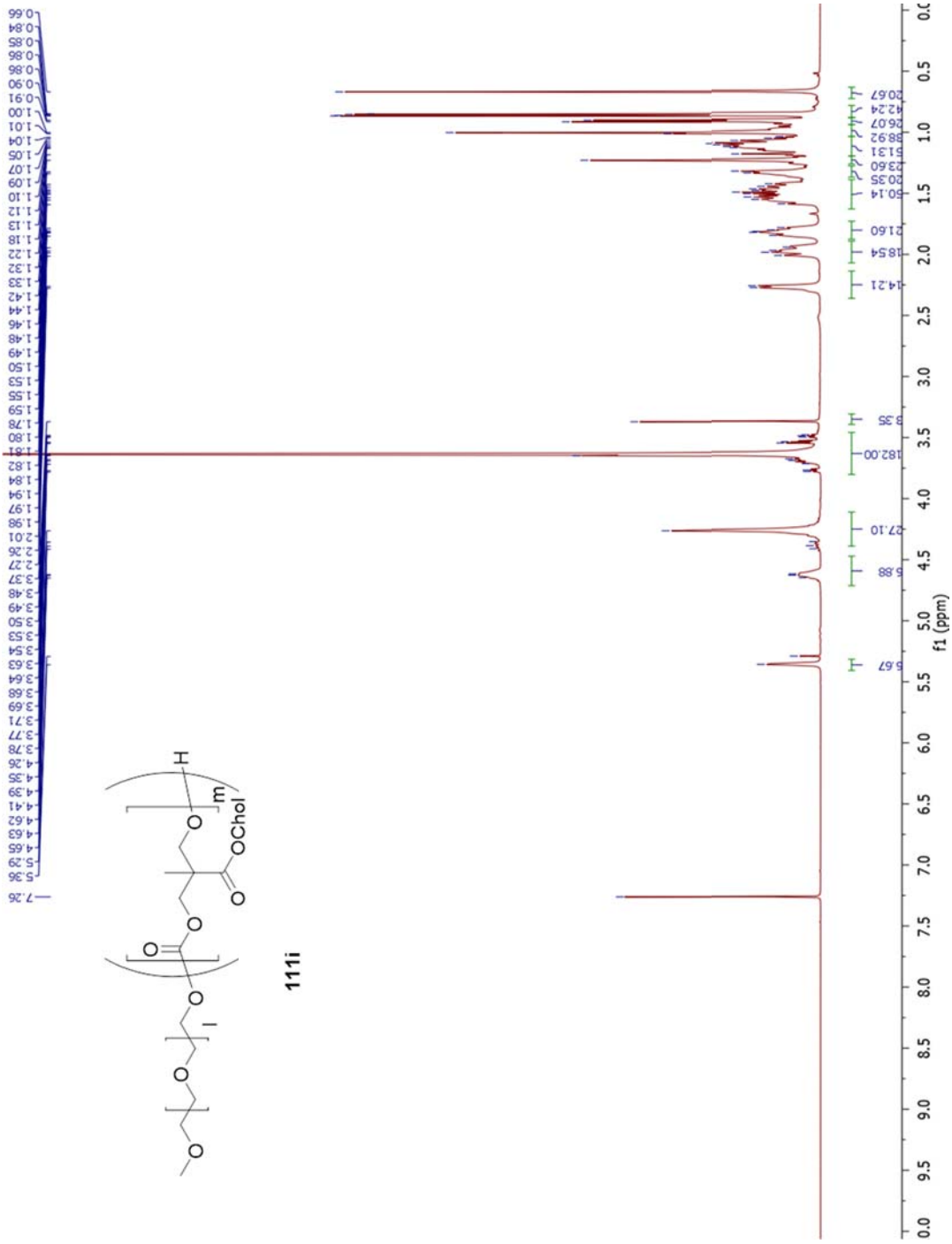

Figure A.165 ^{1}H-NMR of **111i**

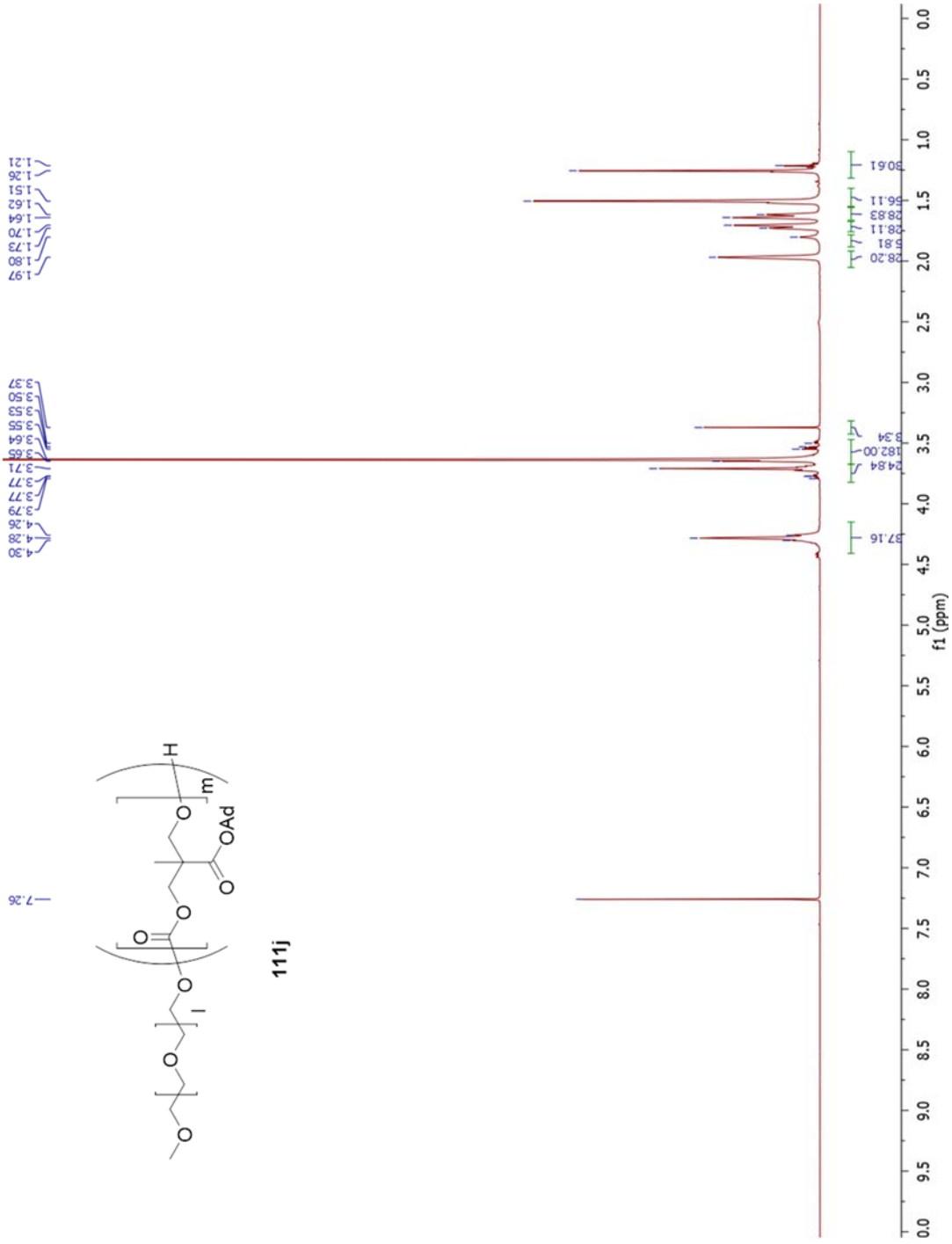

Figure A.166 ^{1}H-NMR of **111j**

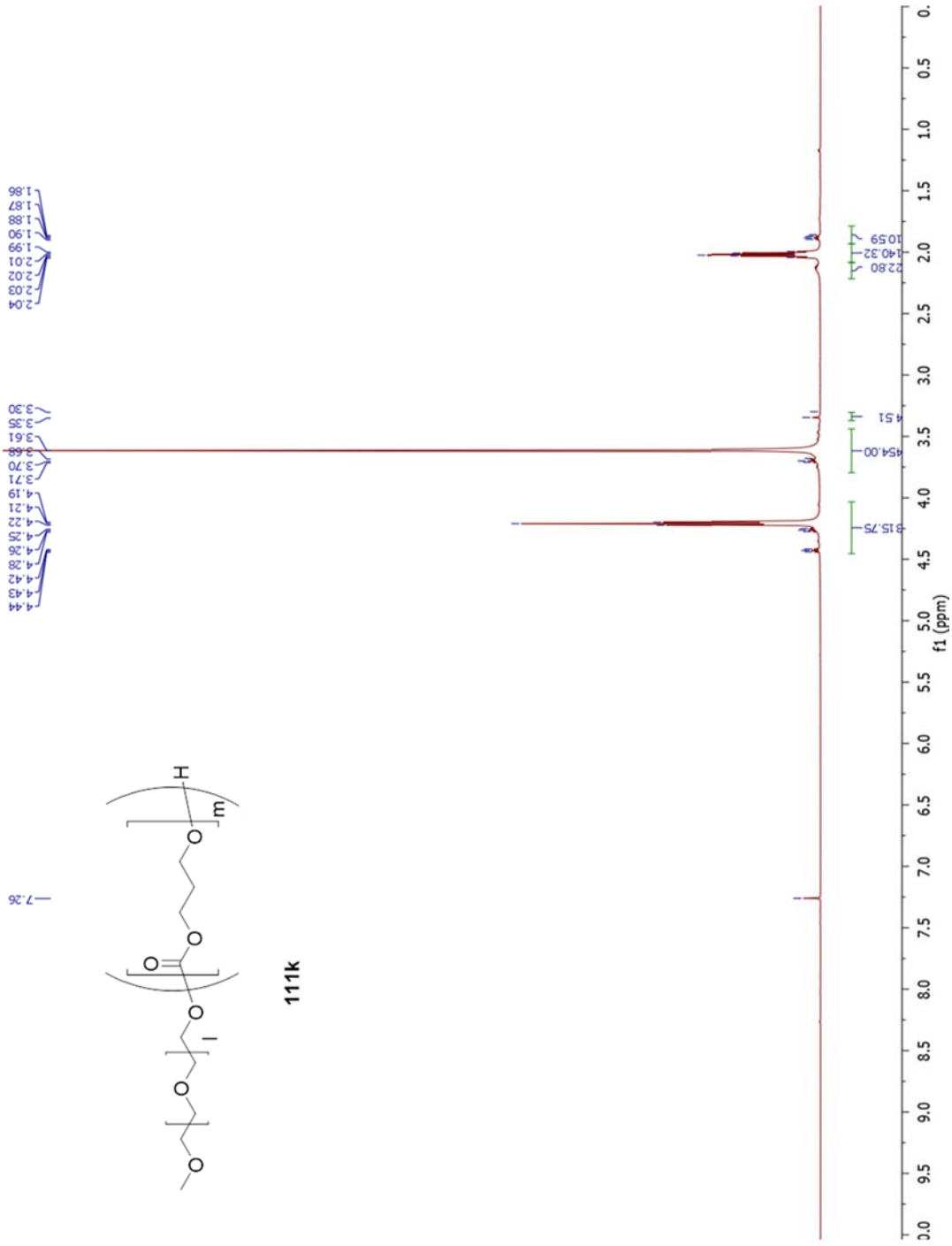

Figure A.167 ^{1}H-NMR of **111k**

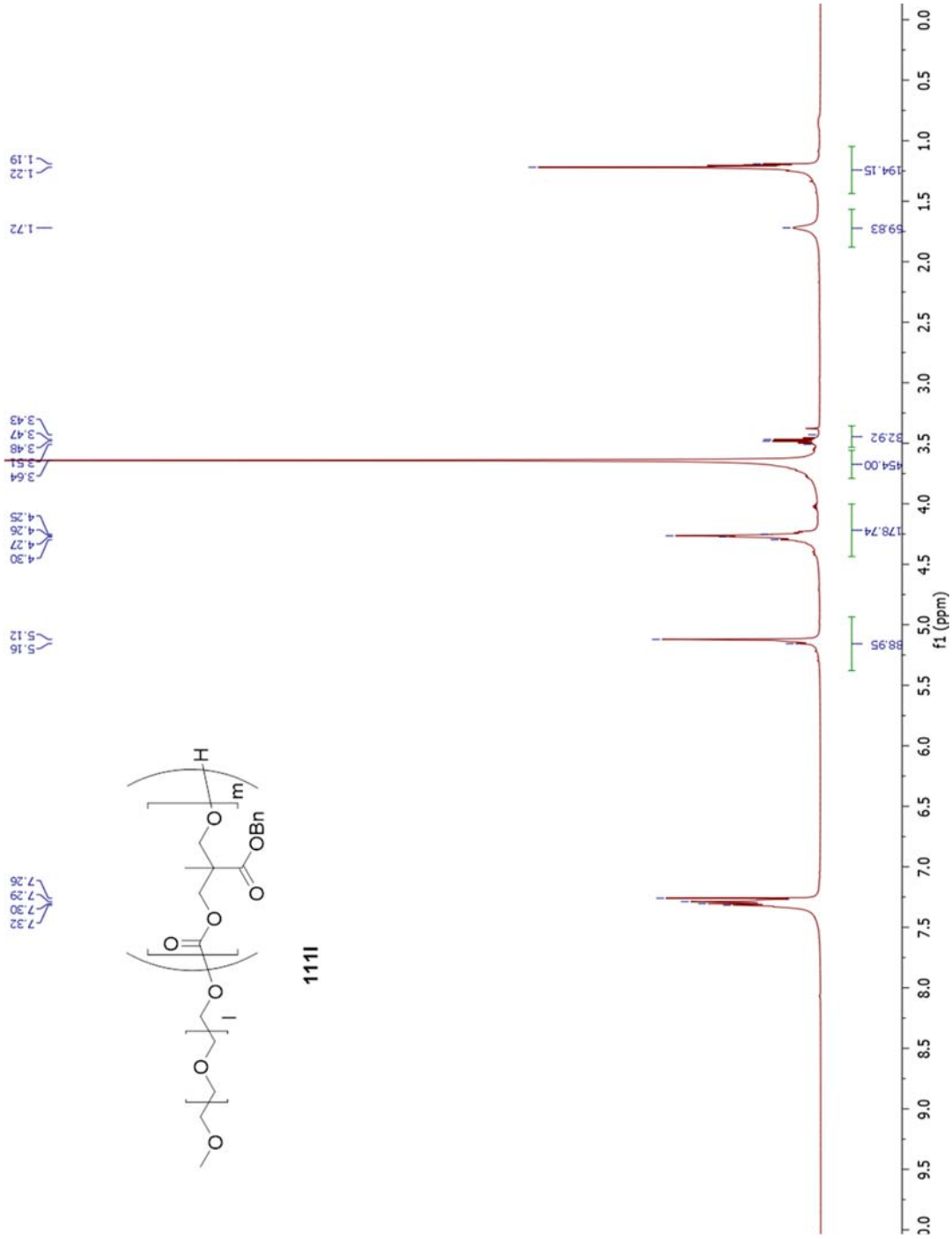

Figure A.168 ^{1}H-NMR of **111l**

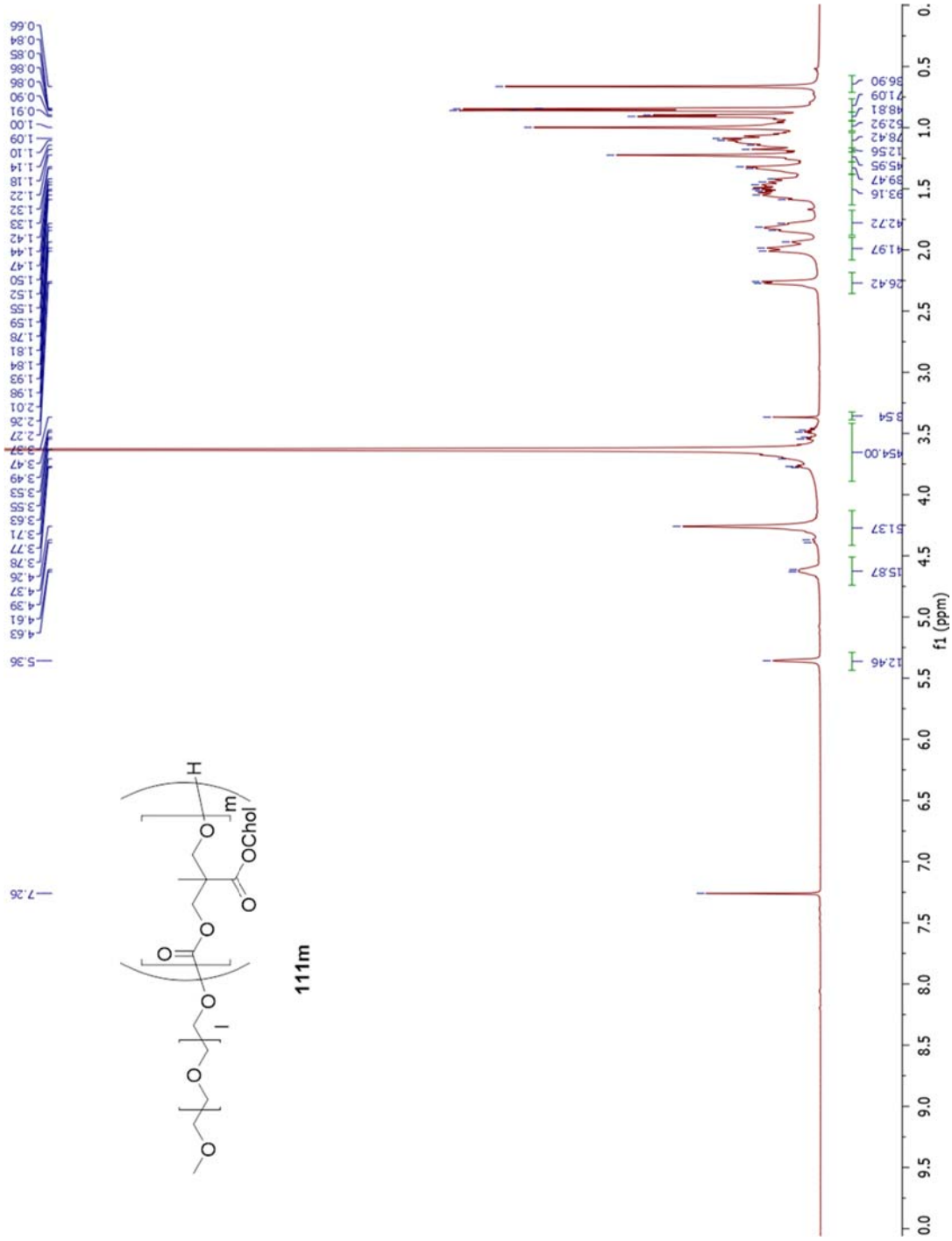

Figure A.169 ^{1}H-NMR of **111m**

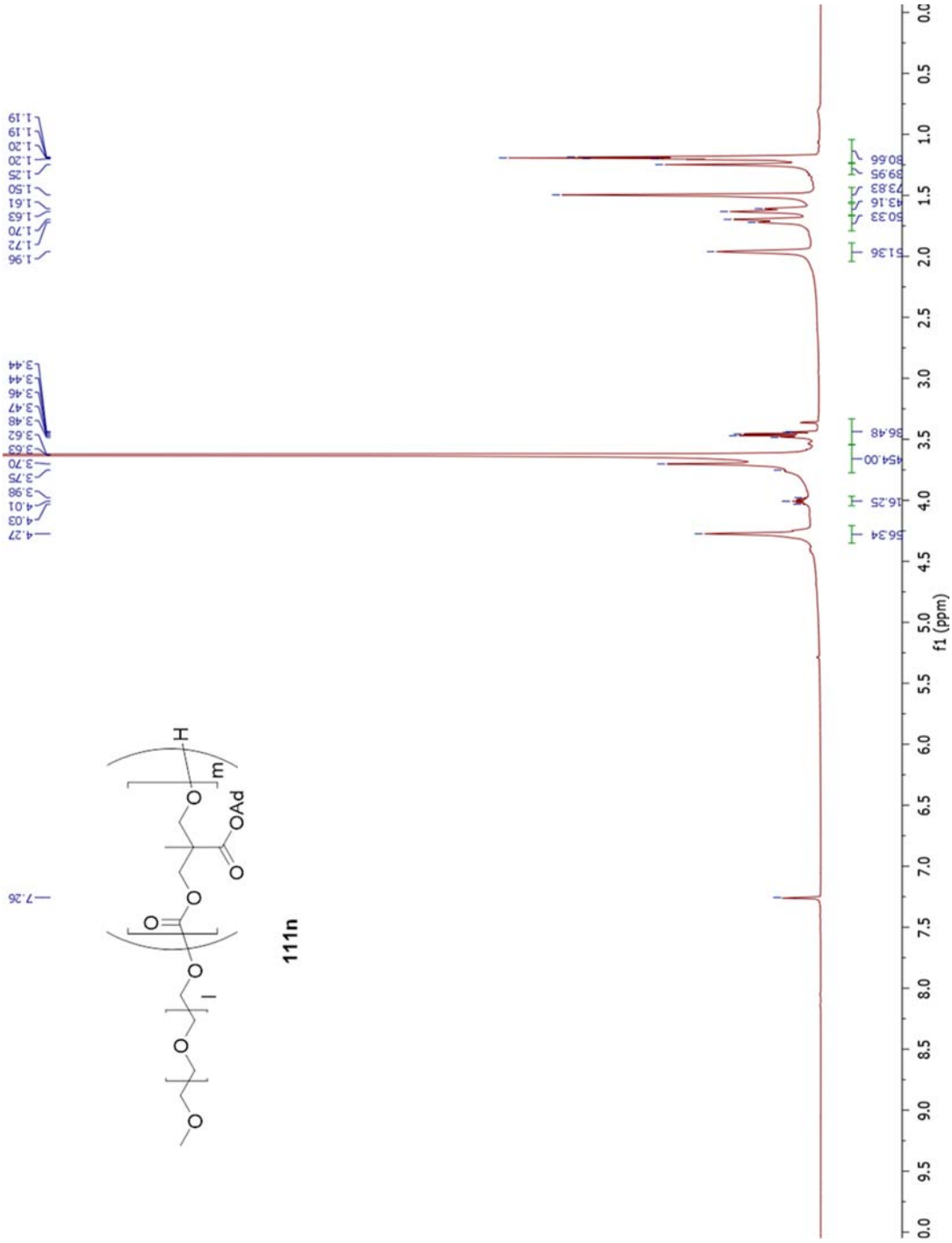

Figure A.170 ^{1}H-NMR of **111n**

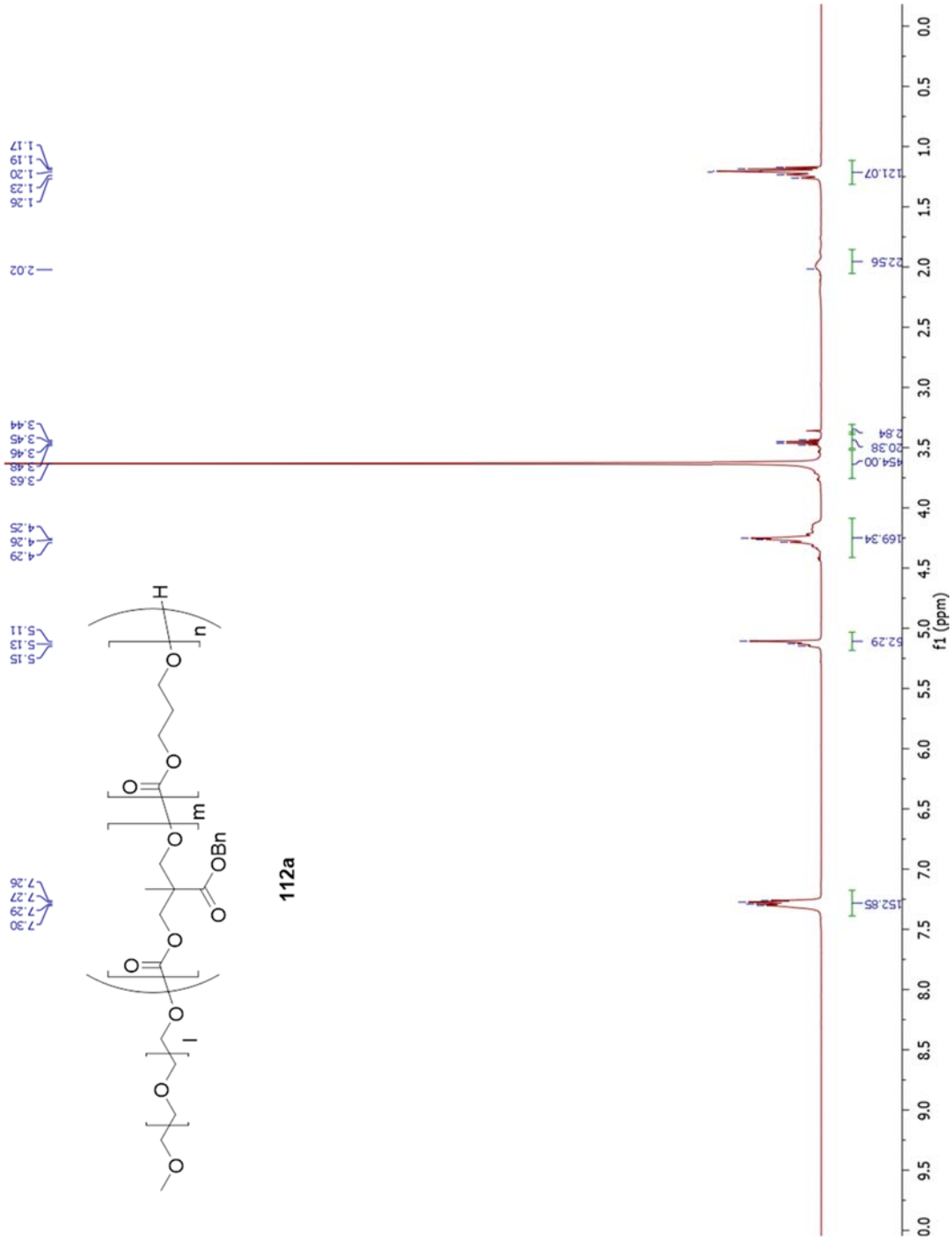

Figure A.171 ^{1}H-NMR of **112a**

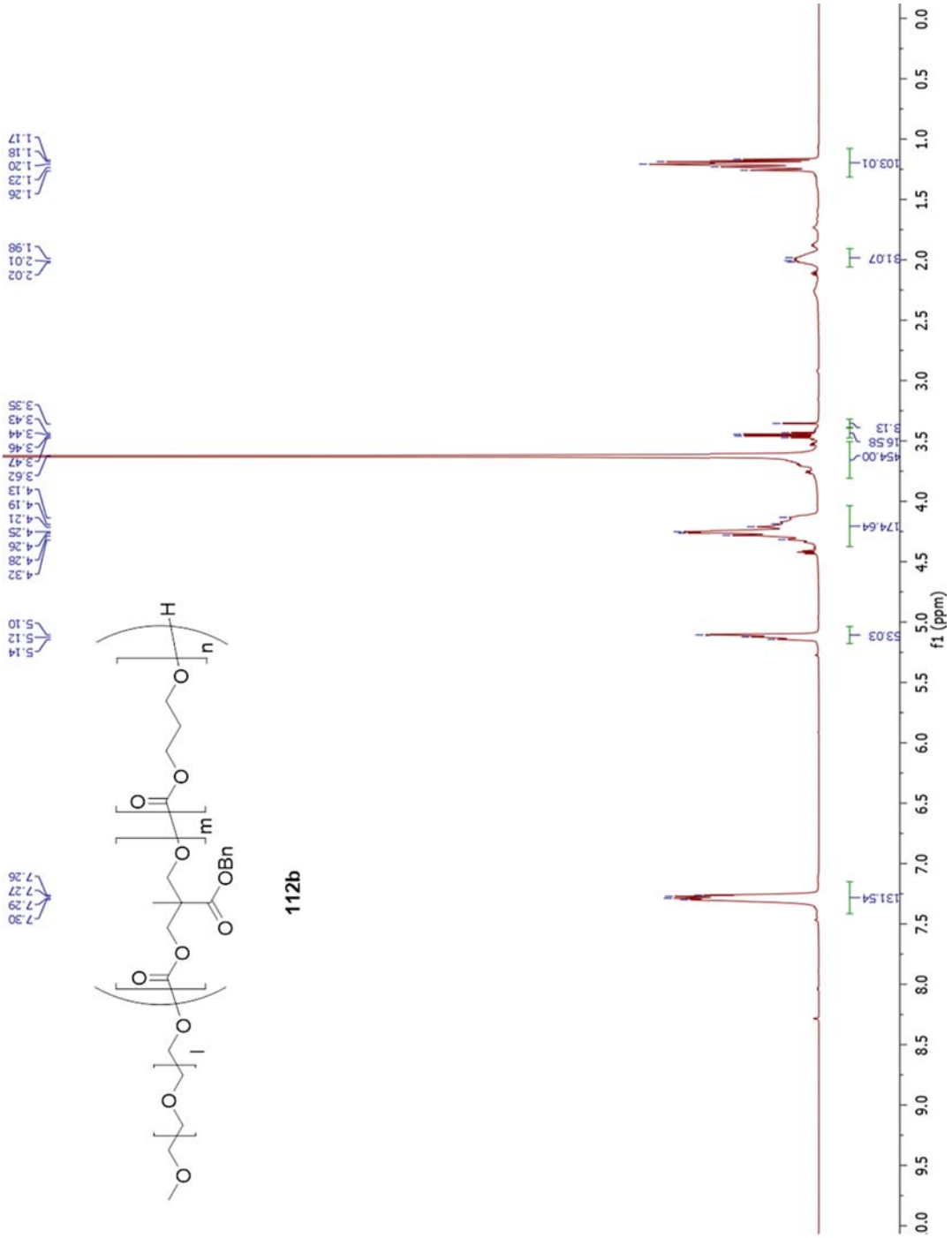

Figure A.172 ^{1}H-NMR of **112b**

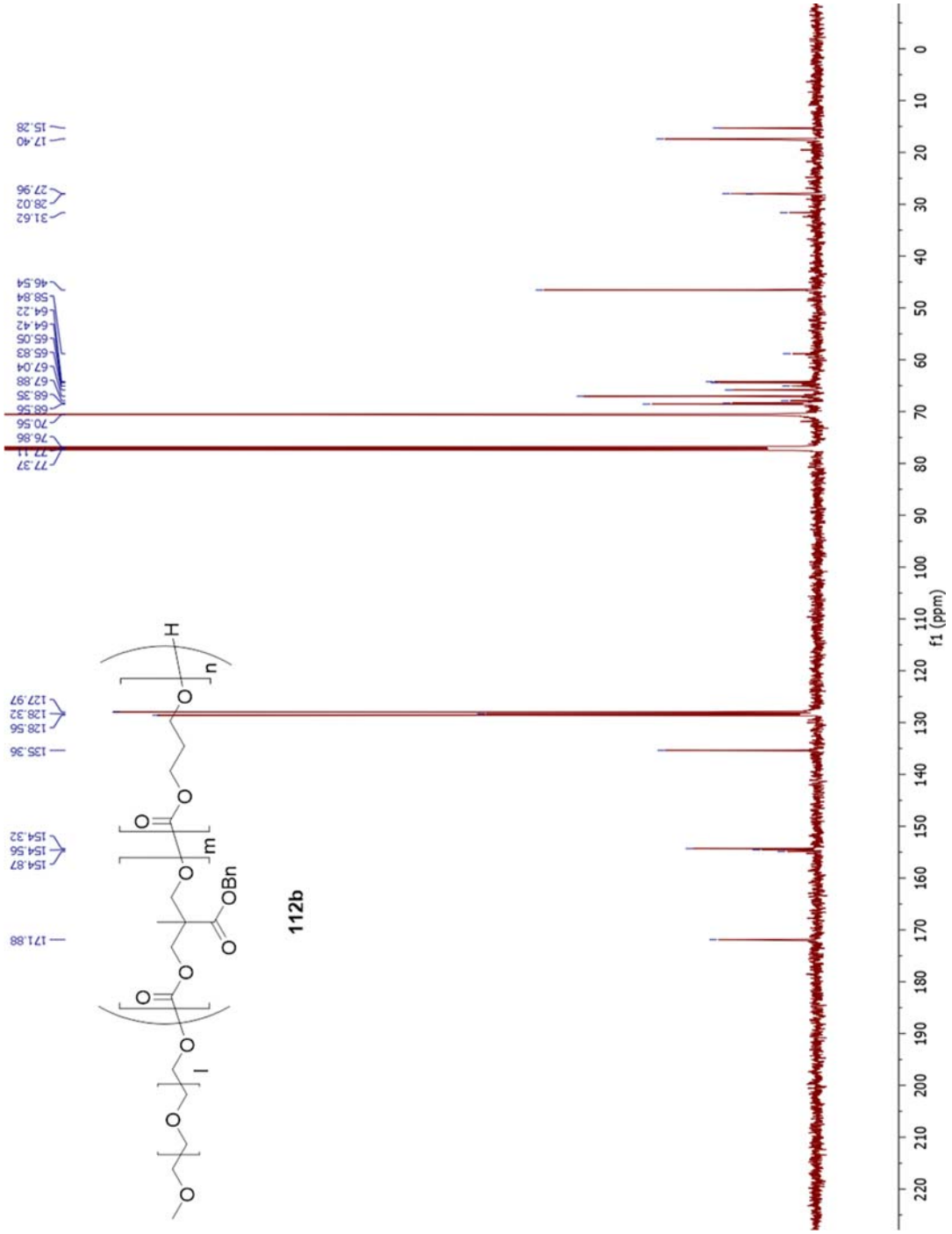

Figure A.173 ^{13}C-NMR of **112b**

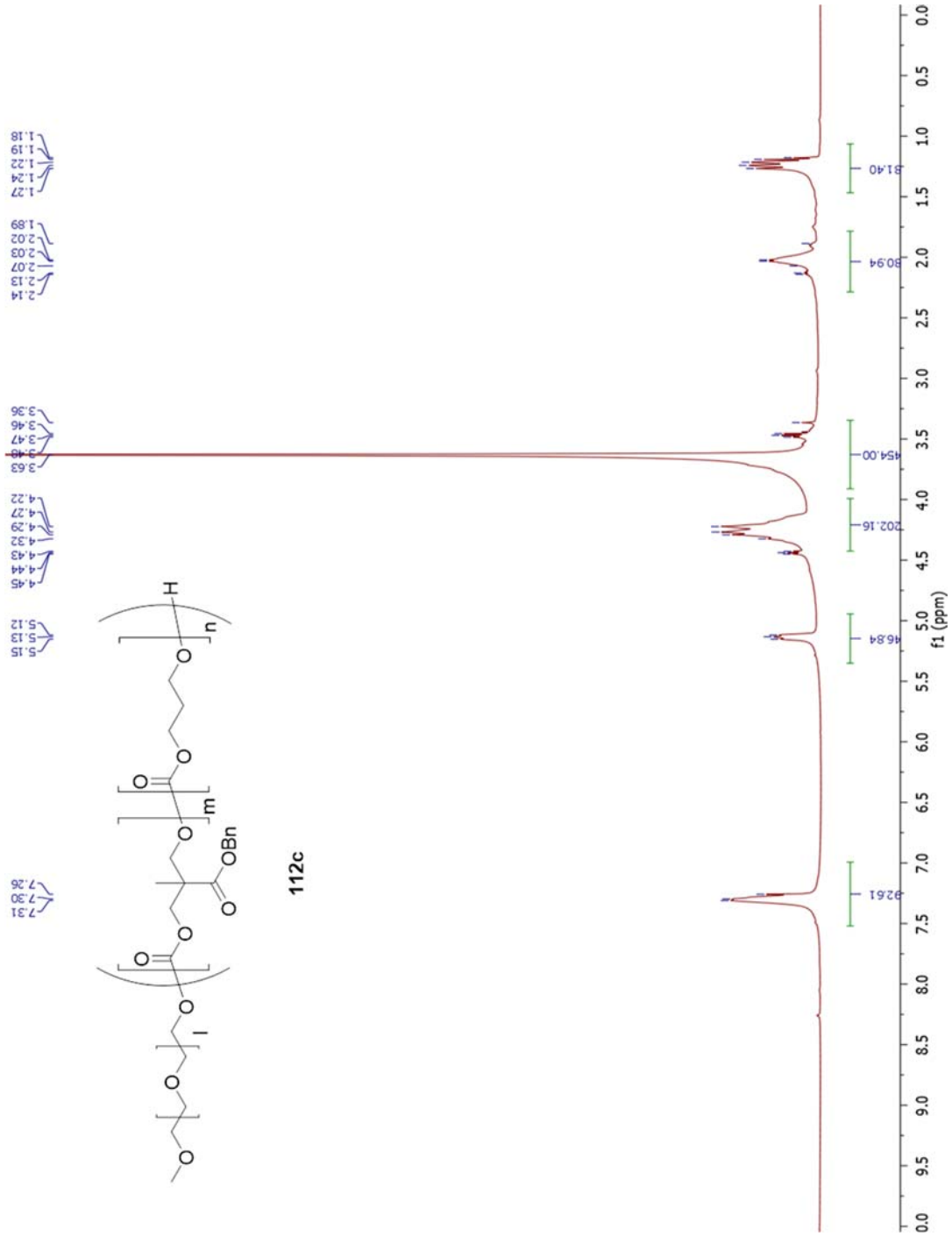

Figure A.174 ^{1}H-NMR of **112c**

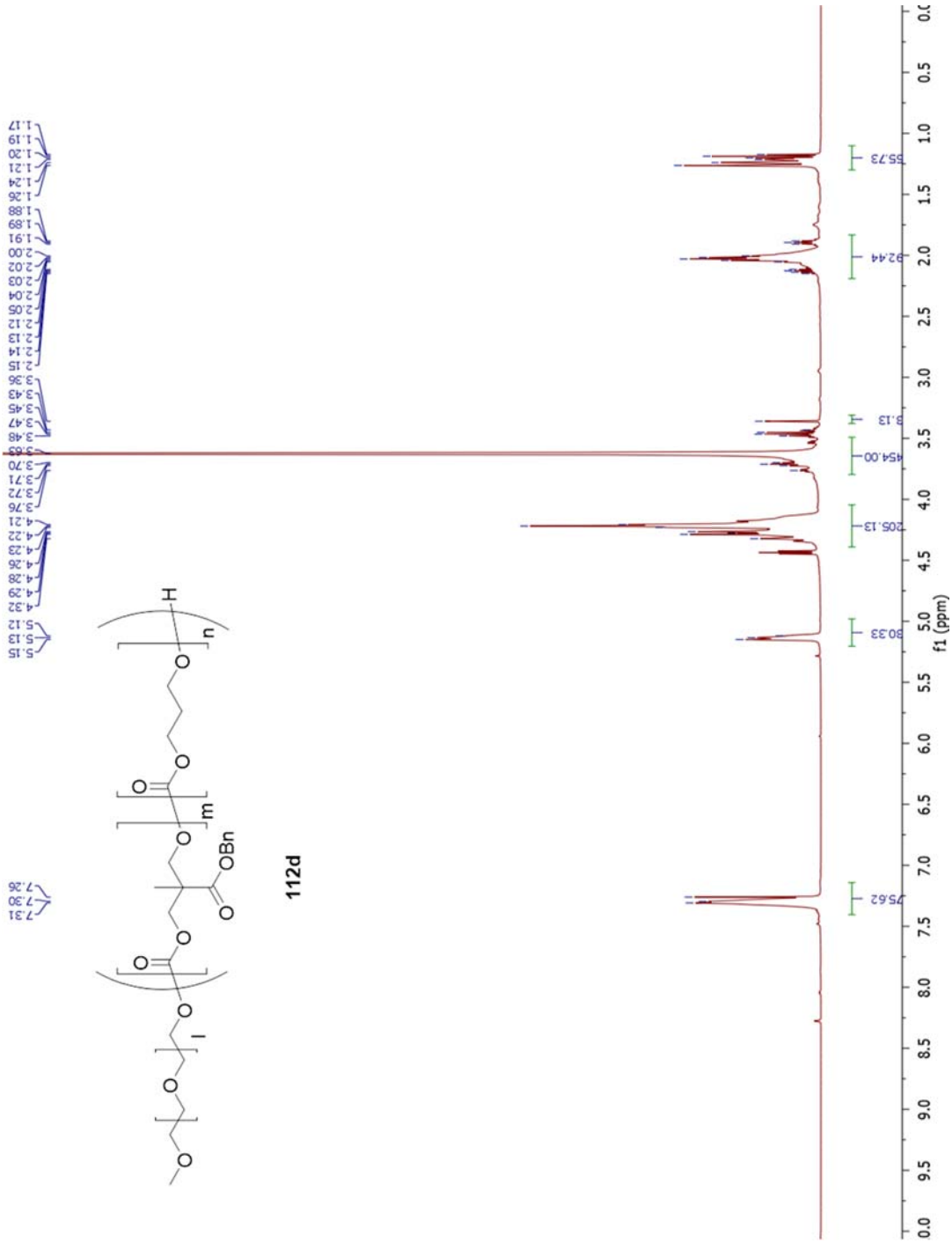

Figure A.175 ^{1}H-NMR of **112d**

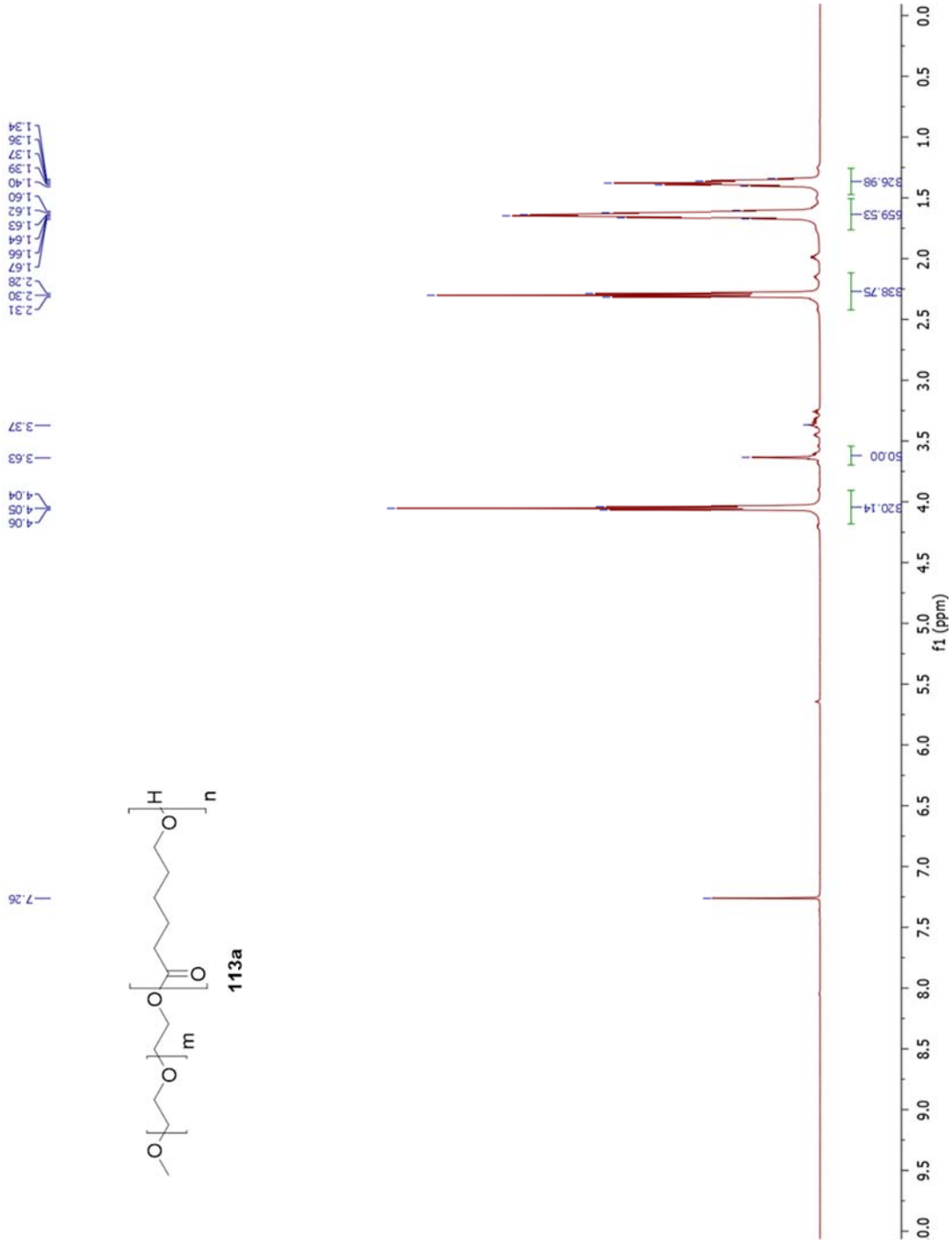

Figure A.176 ^{1}H-NMR of **113a**

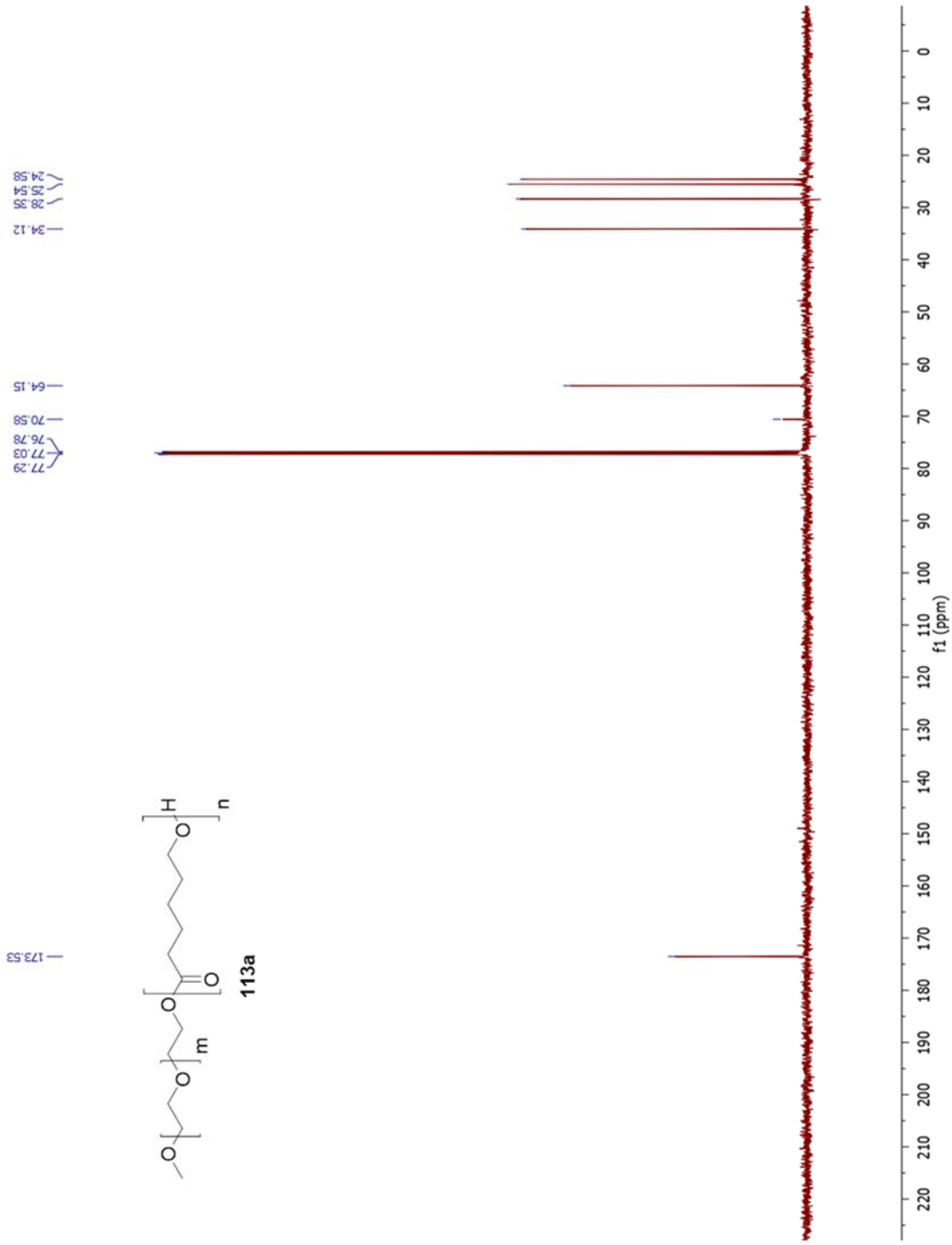

Figure A.177 ^{13}C-NMR of **113a**

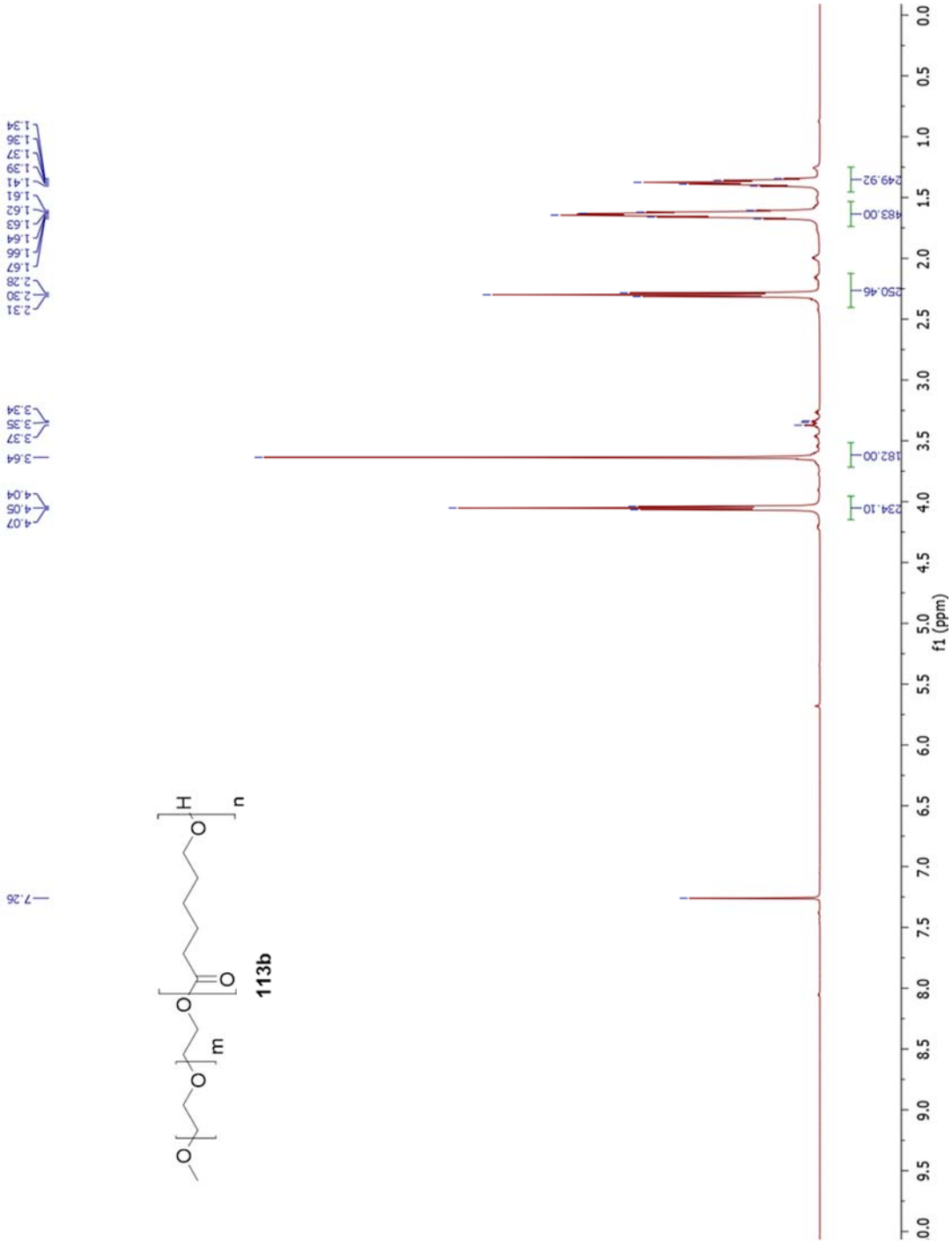

Figure A.178 ^{1}H-NMR of **113b**

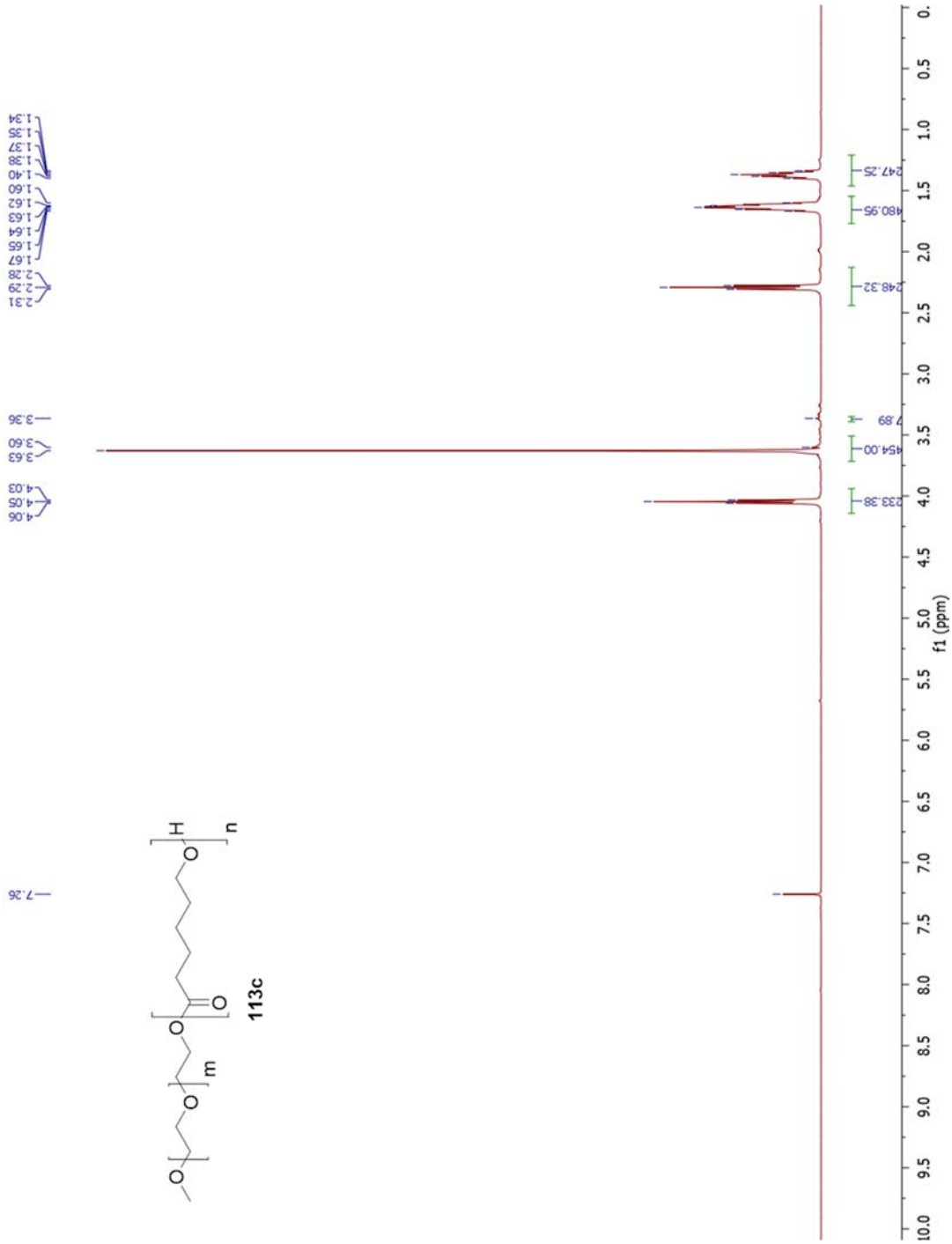

Figure A.179 ^{1}H-NMR of **113c**

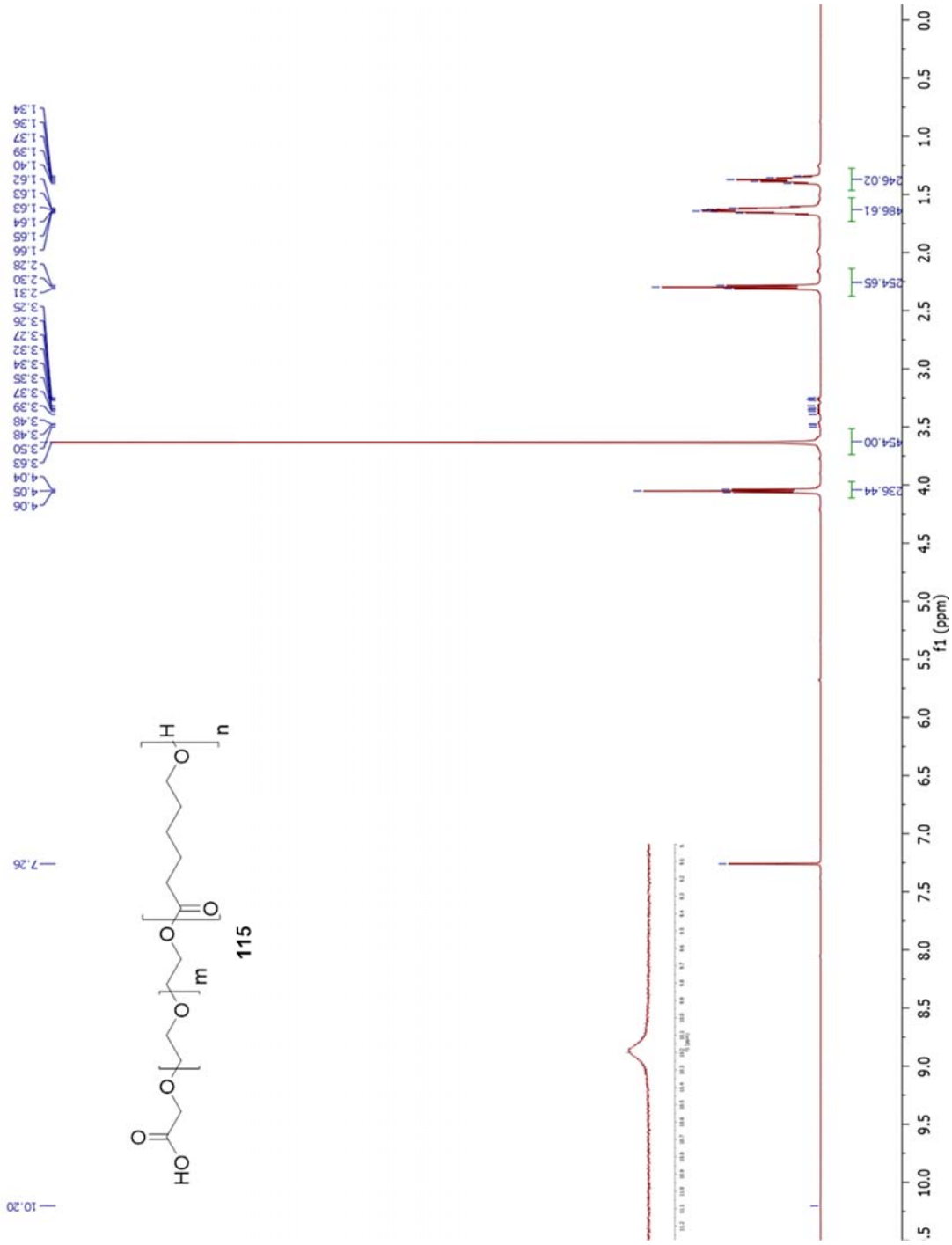

Figure A.180 ^{1}H-NMR of **115**

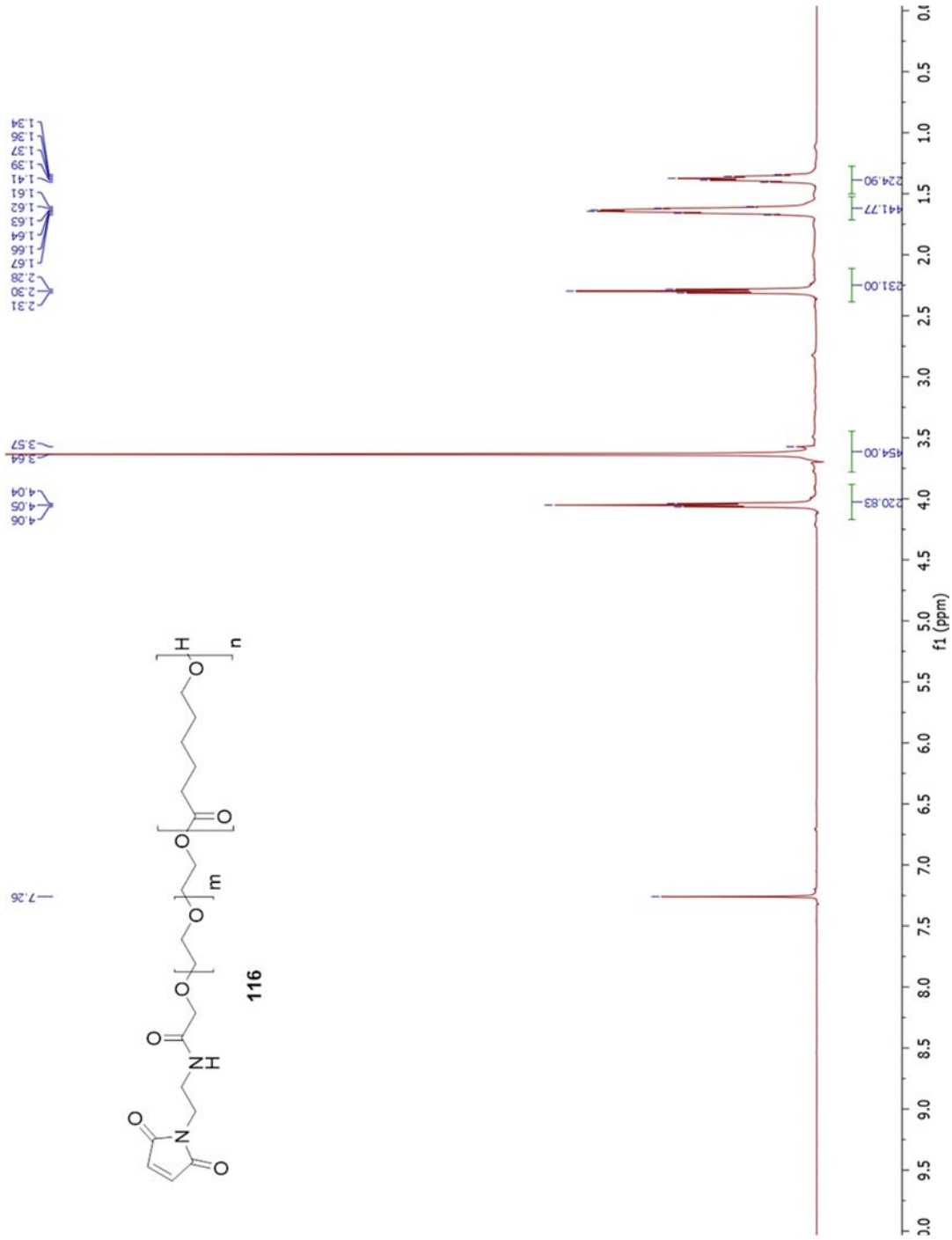

Figure A.181 ^{1}H-NMR of **116**

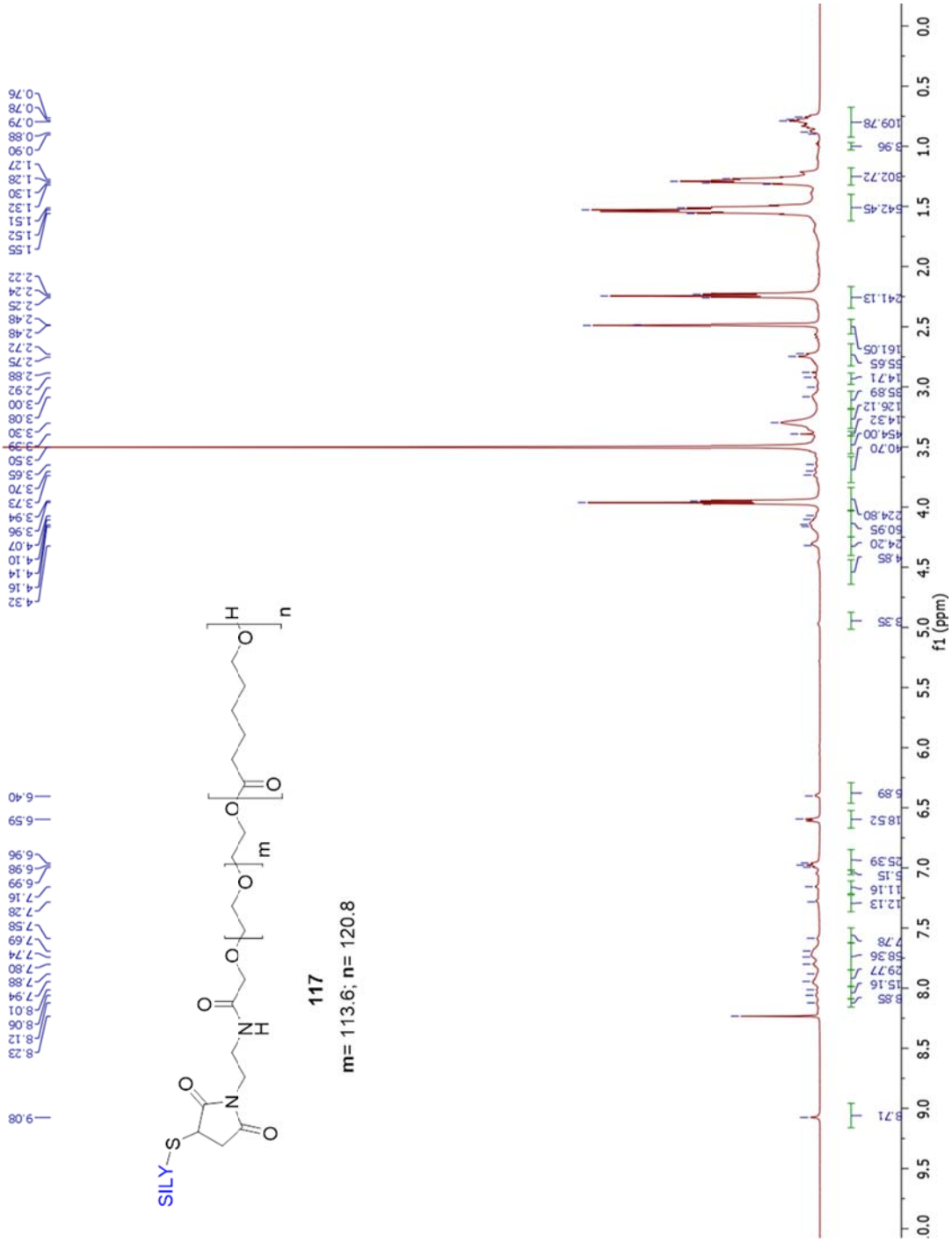

Figure A.182 ^{1}H-NMR of **117**

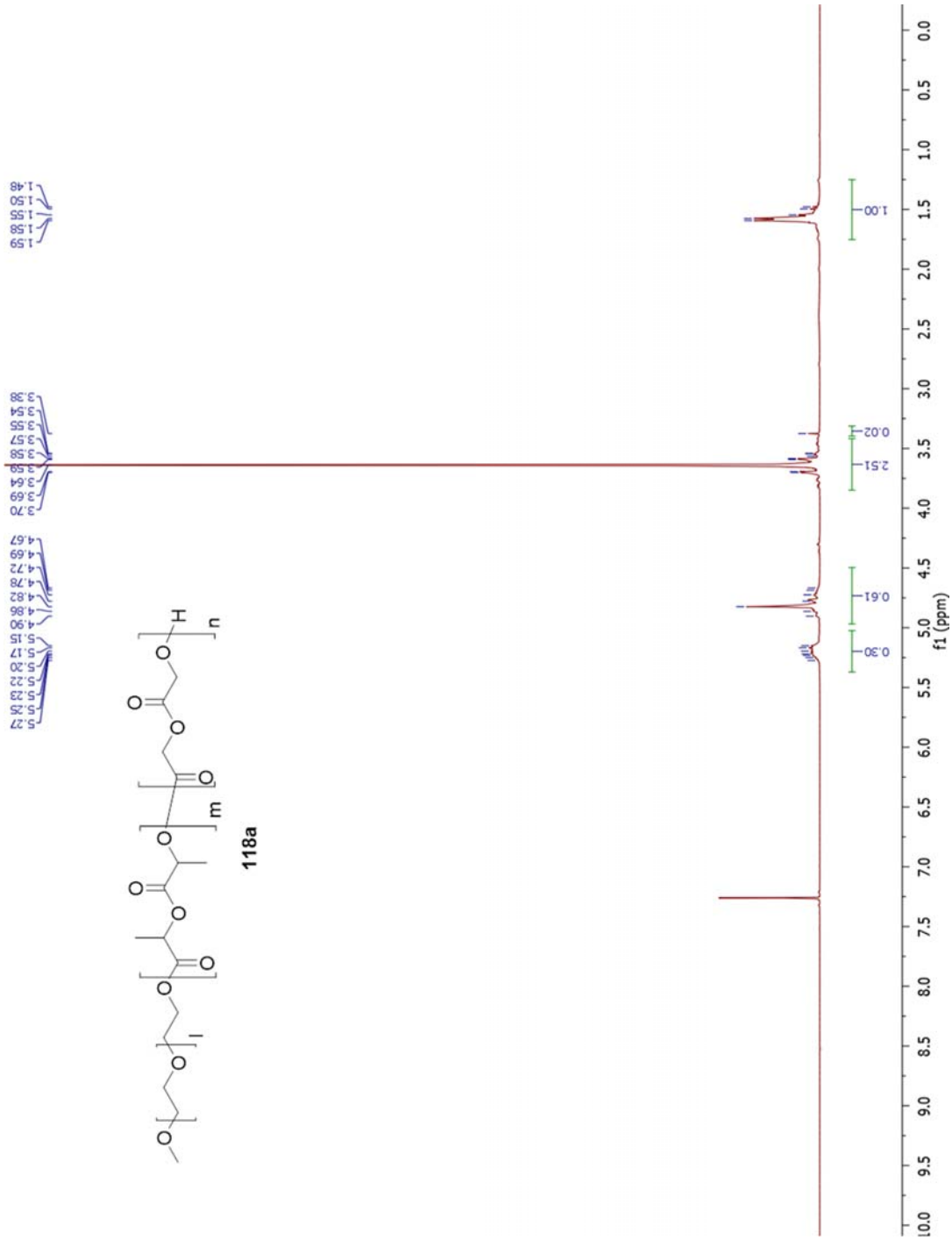

Figure A.183 ^{1}H-NMR of **118a**

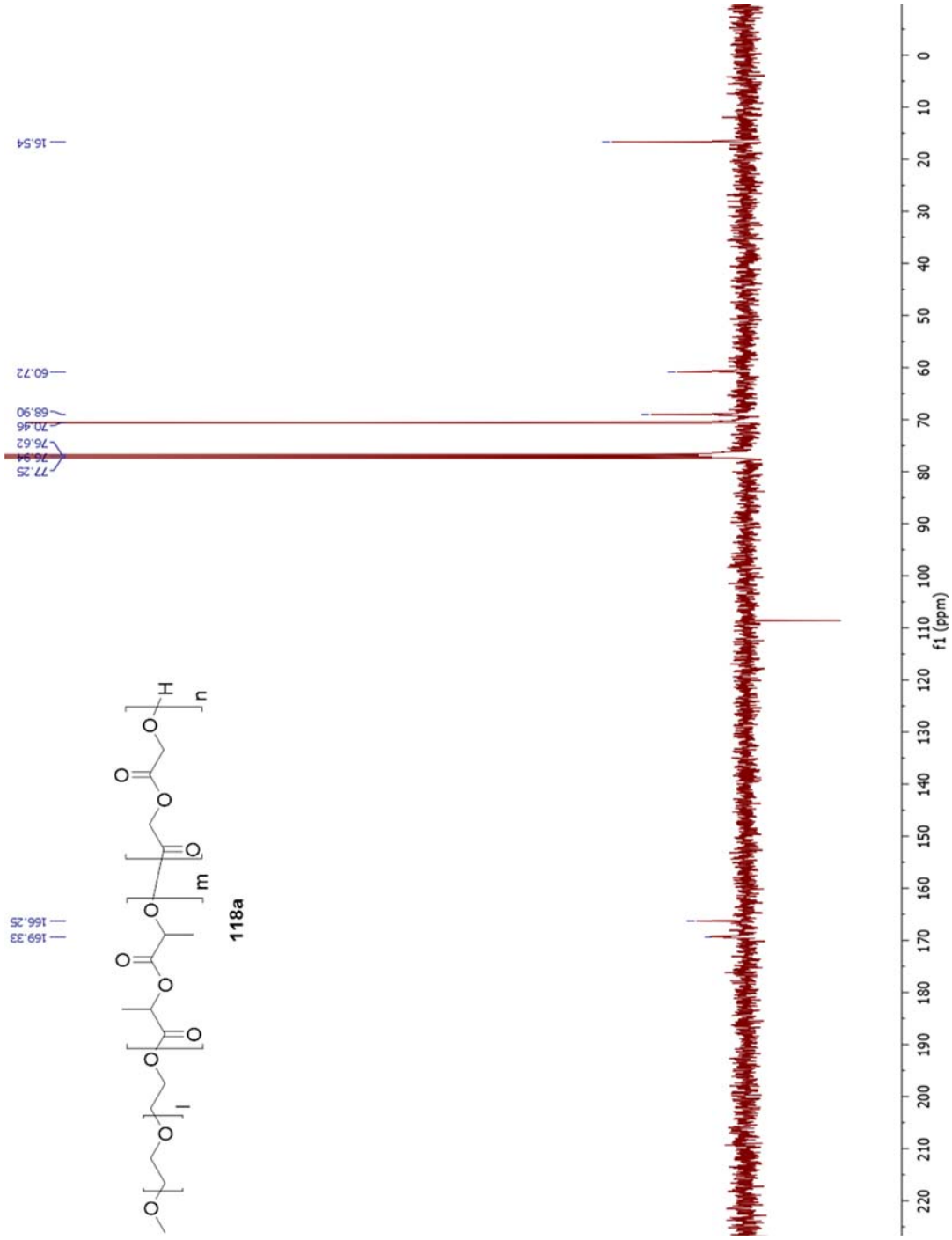

Figure A.184 ^{13}C-NMR of **118a**

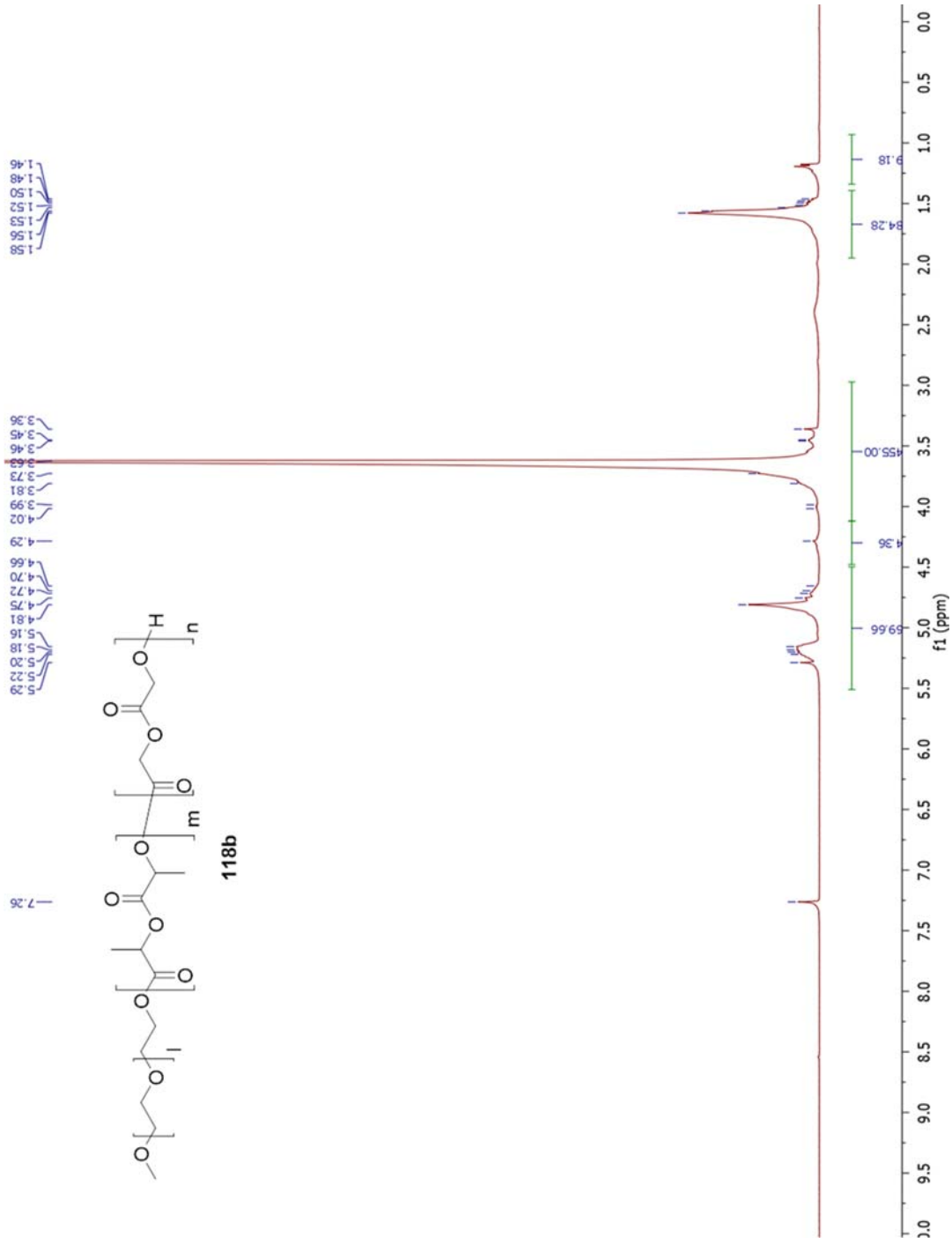

Figure A.185 ^{1}H-NMR of **118b**

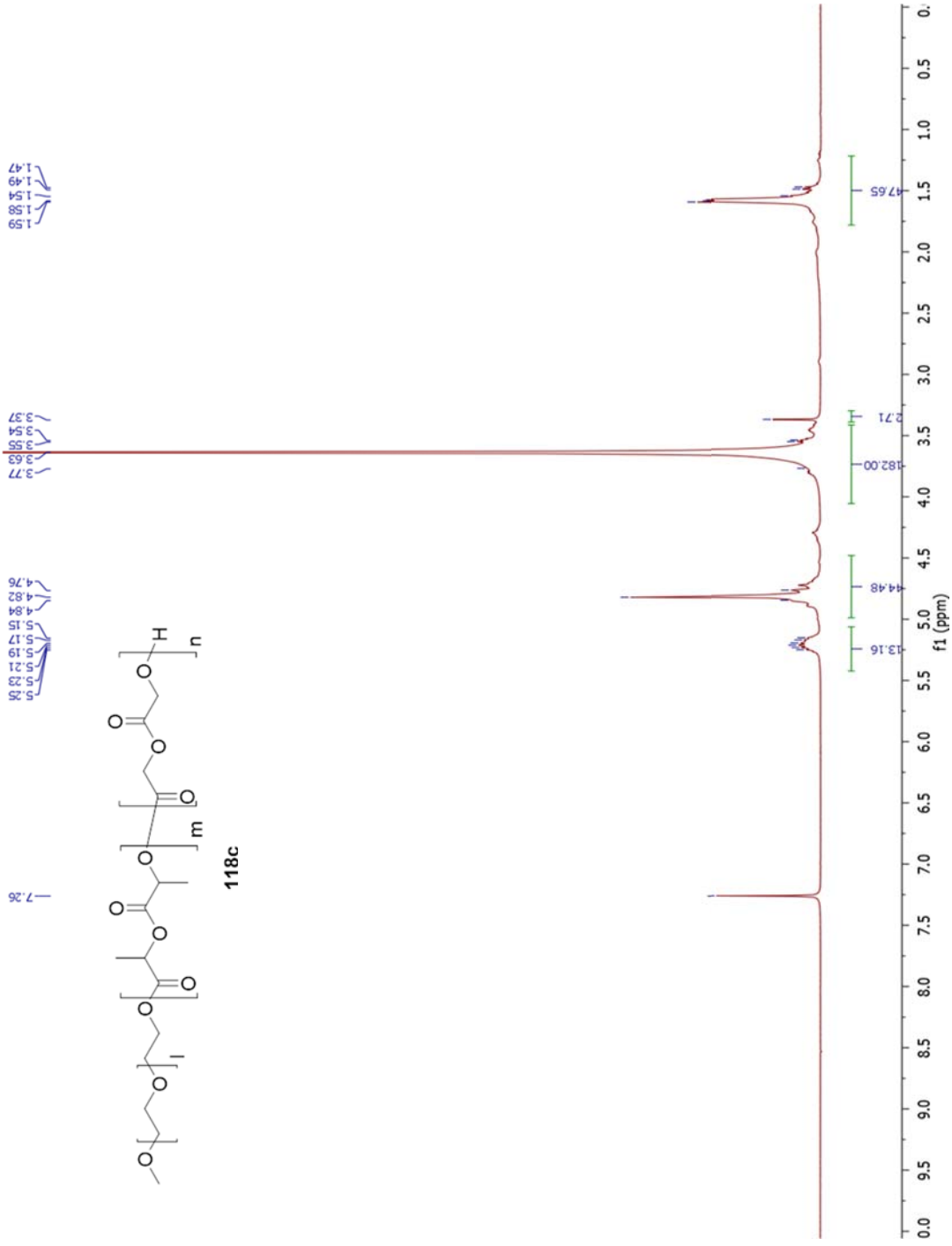

Figure A.186 ^{1}H-NMR of **118c**

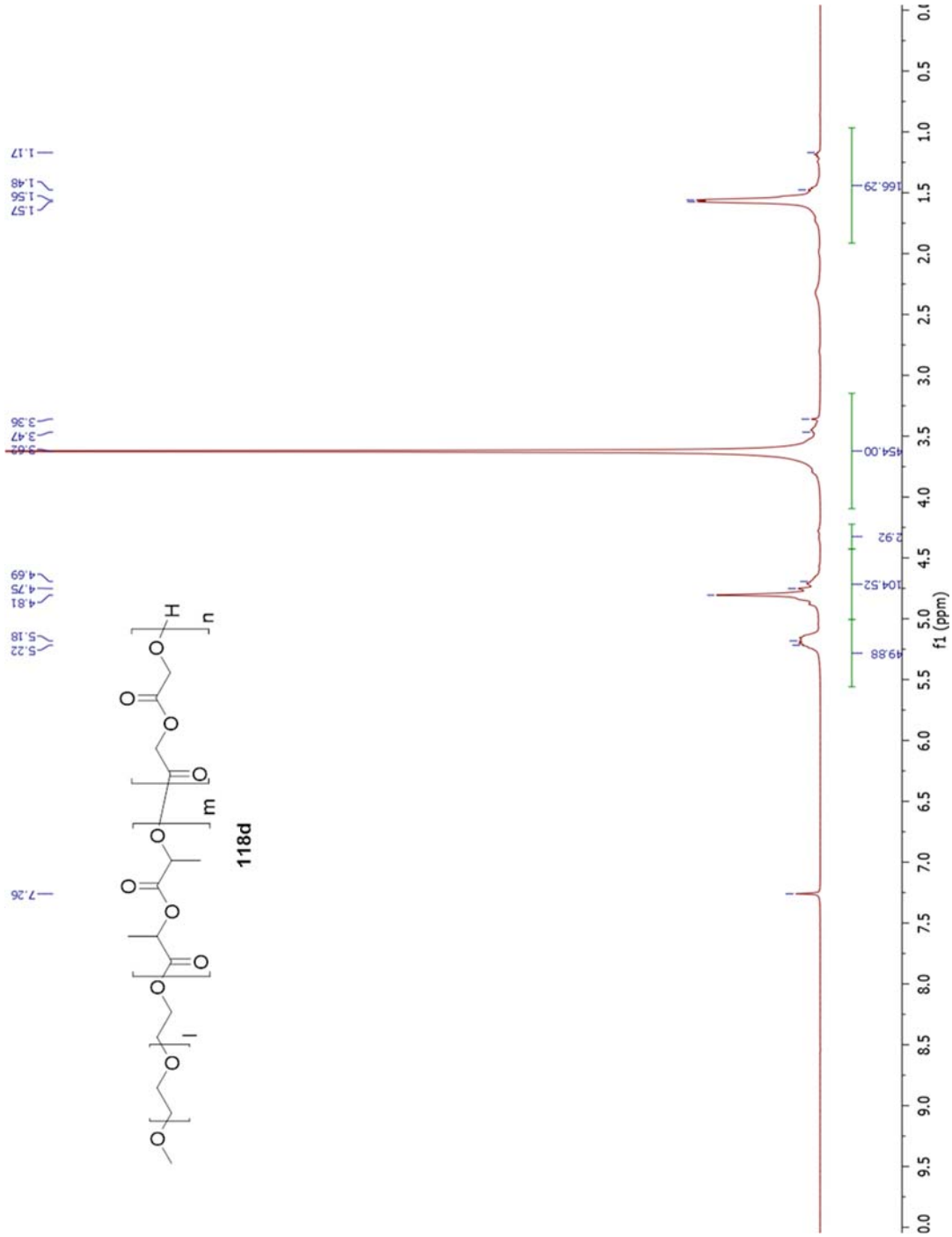

Figure A.187 ^{1}H-NMR of **118d**

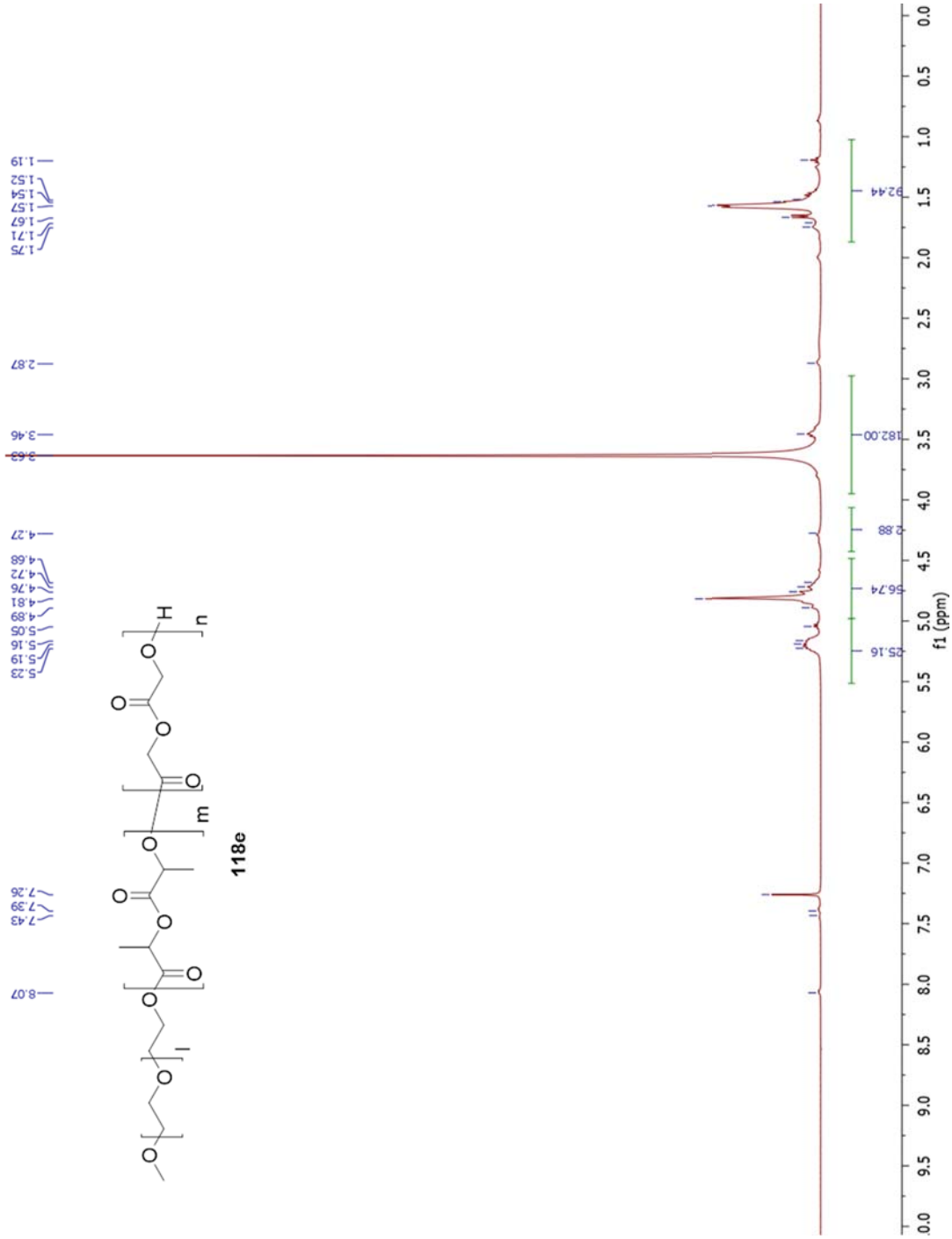

Figure A.188 ^{1}H-NMR of **118e**

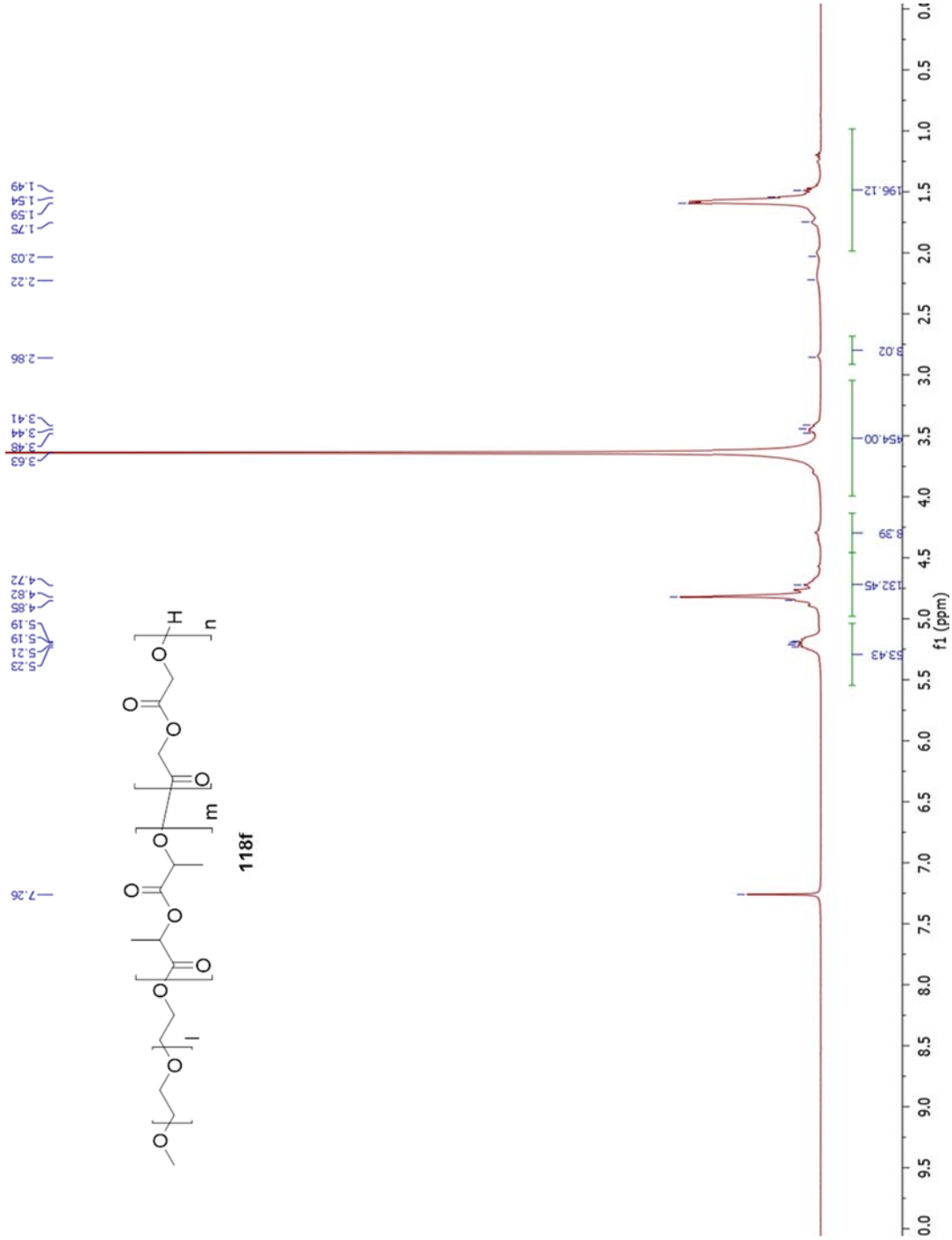

Figure A.189 ^{1}H-NMR of **118f**

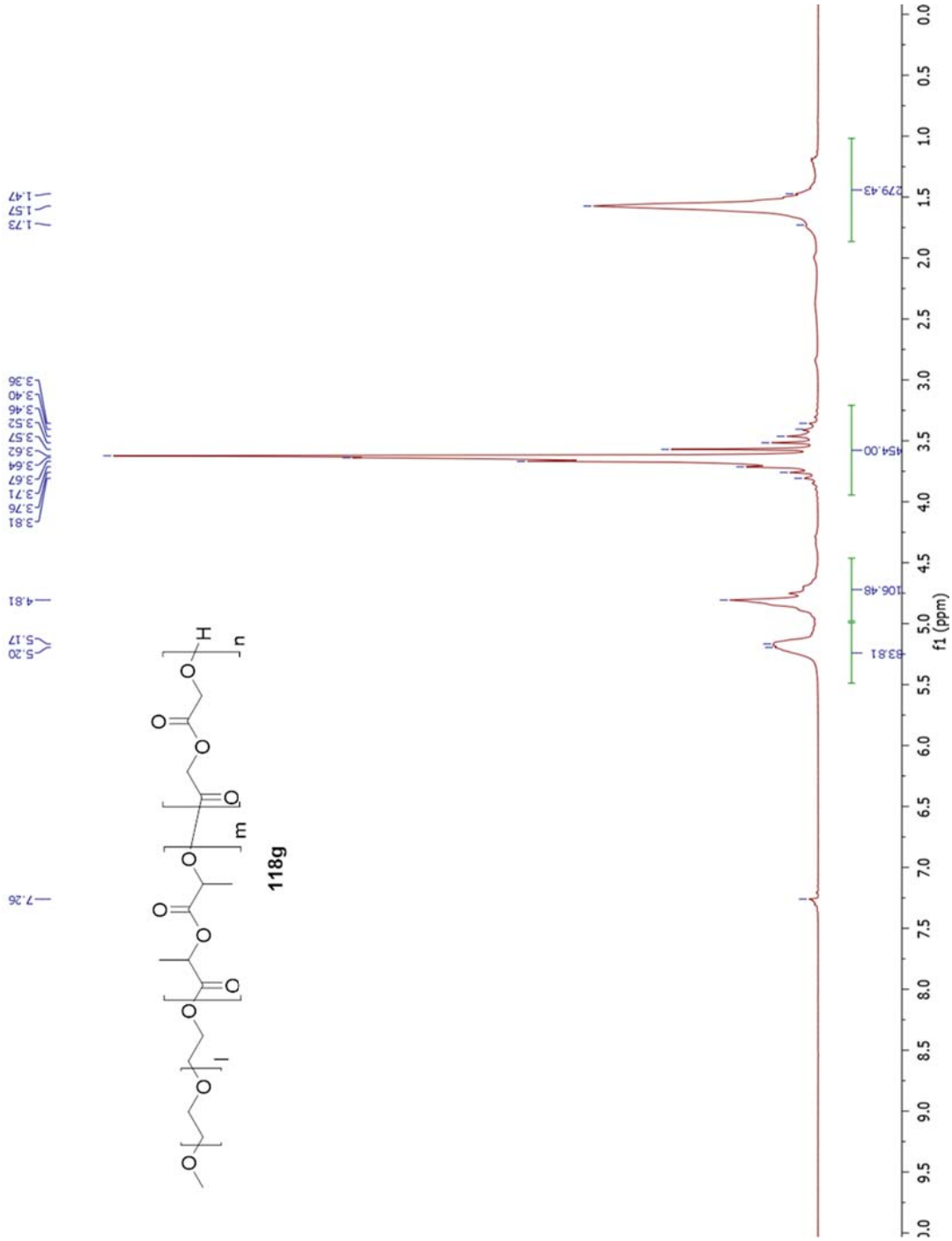

Figure A.190 ^{1}H-NMR of **118g**

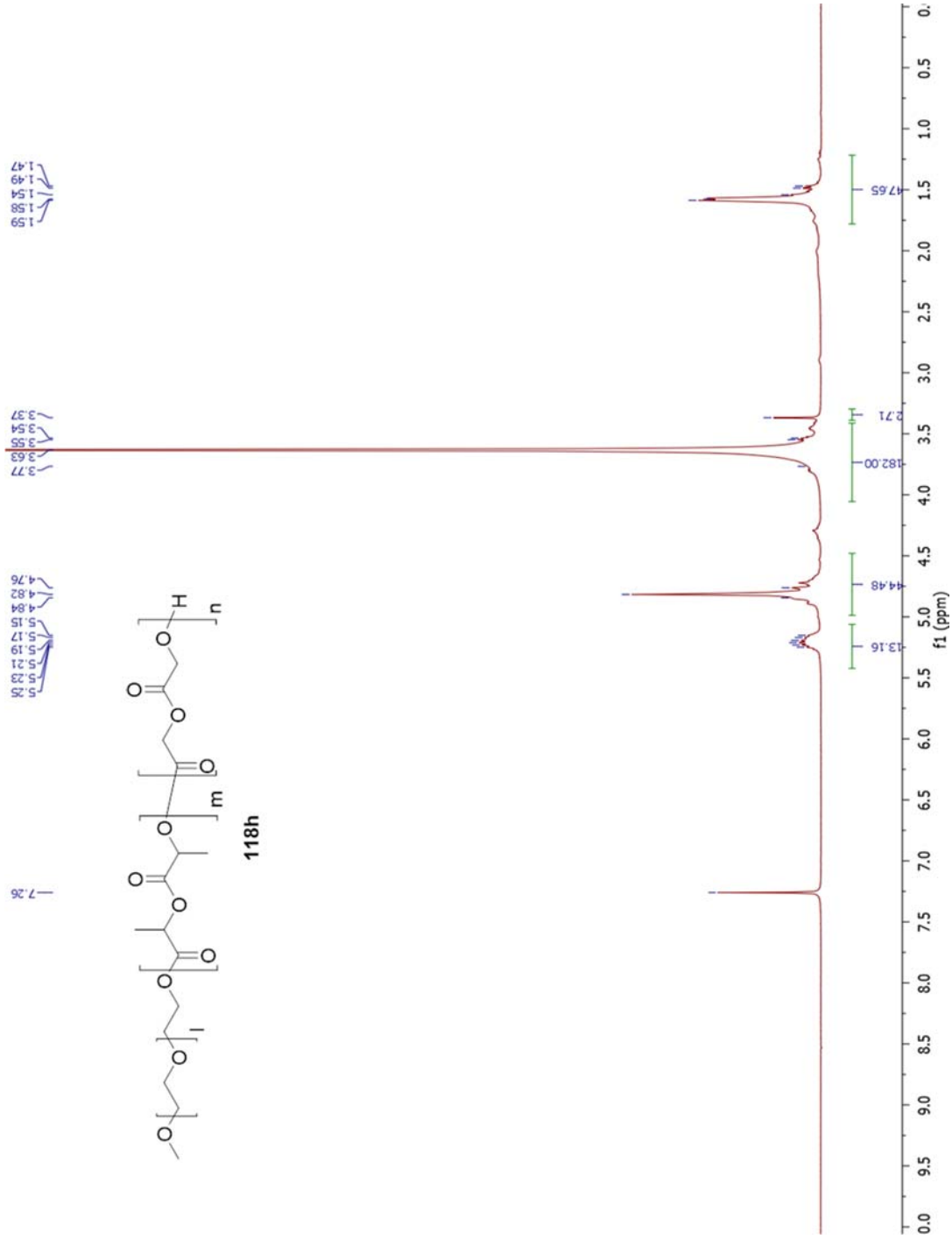

Figure A.191 ^{1}H-NMR of **118h**

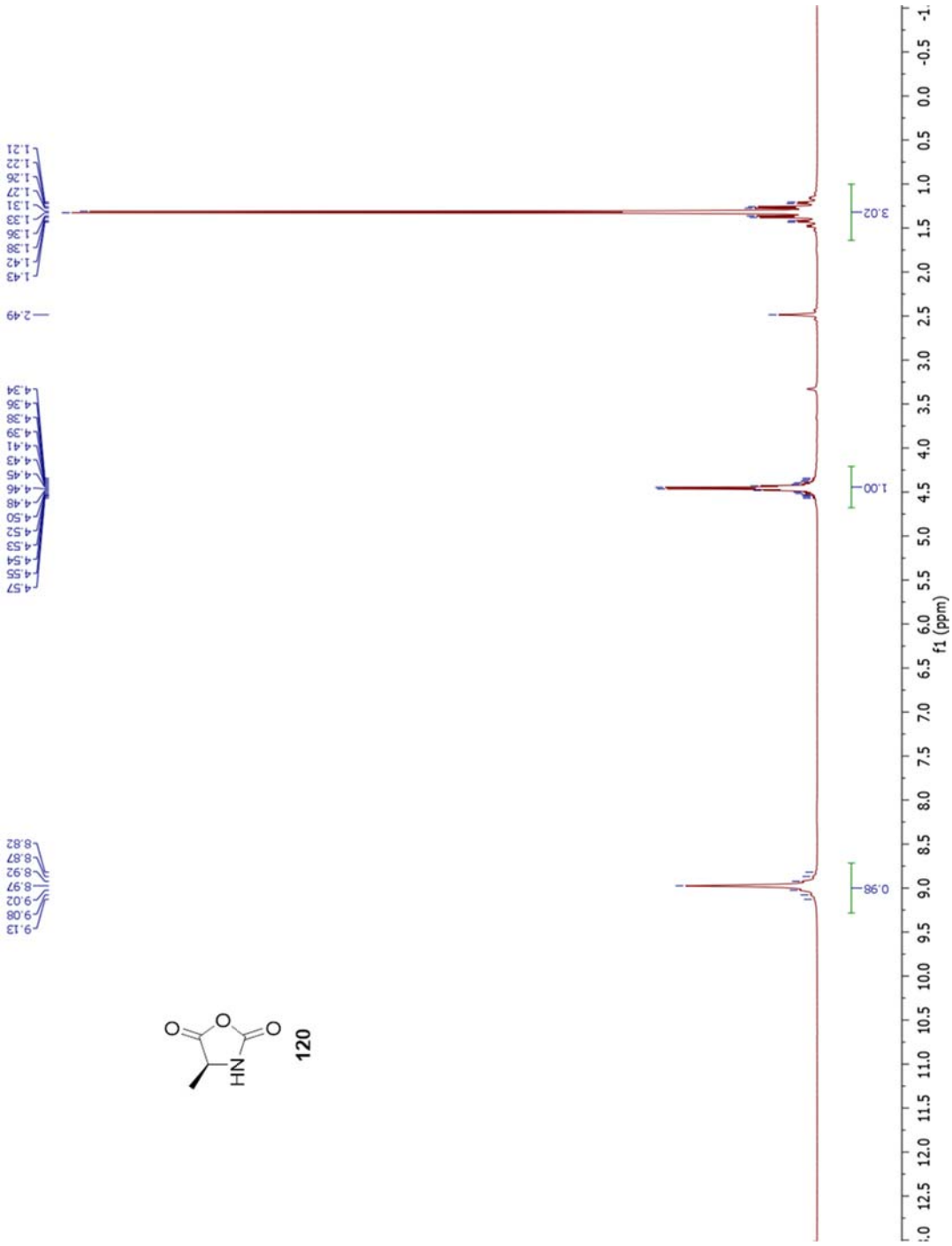

Figure A.192 ^{1}H-NMR of **120**

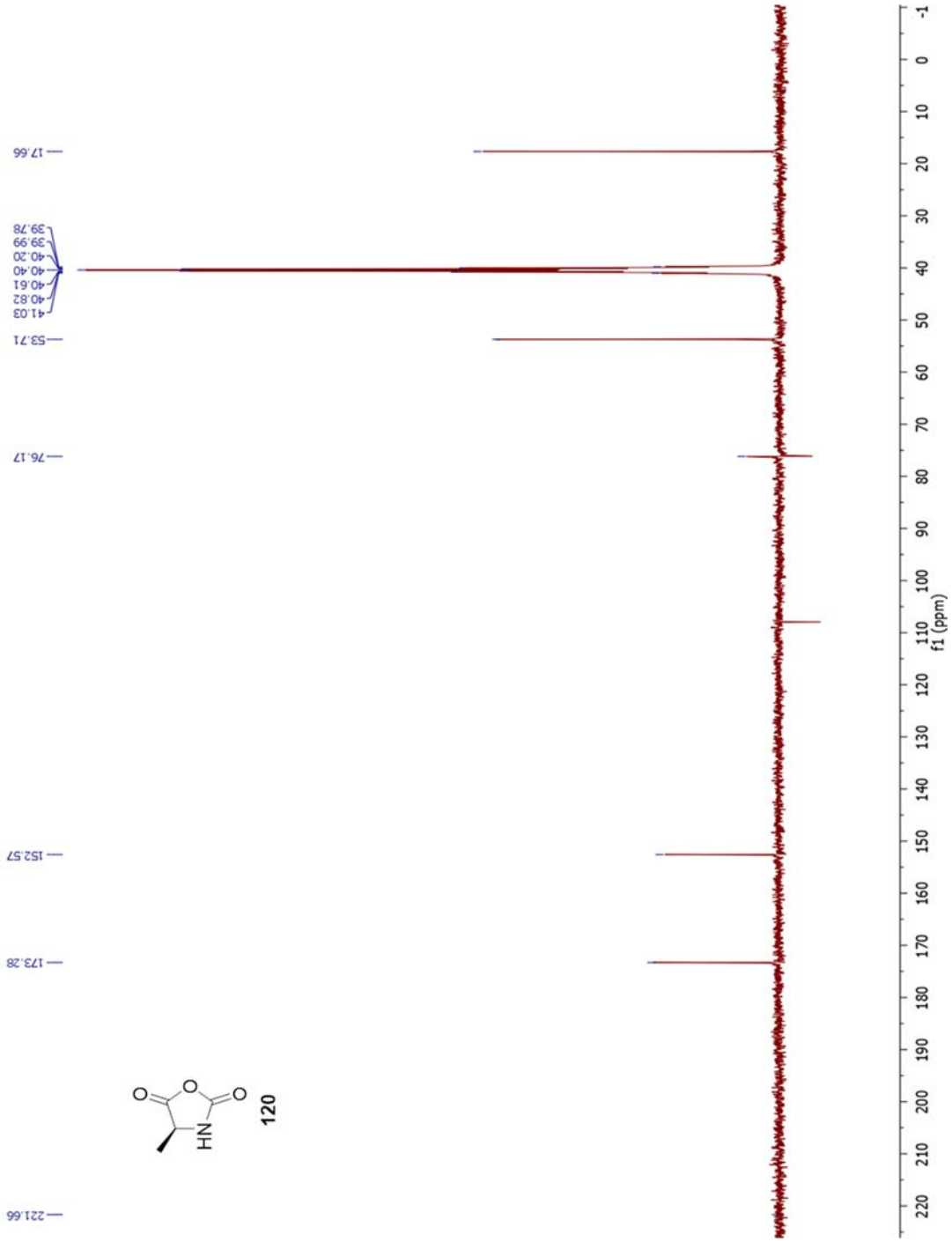

Figure A.193 ^{13}C-NMR of **120**

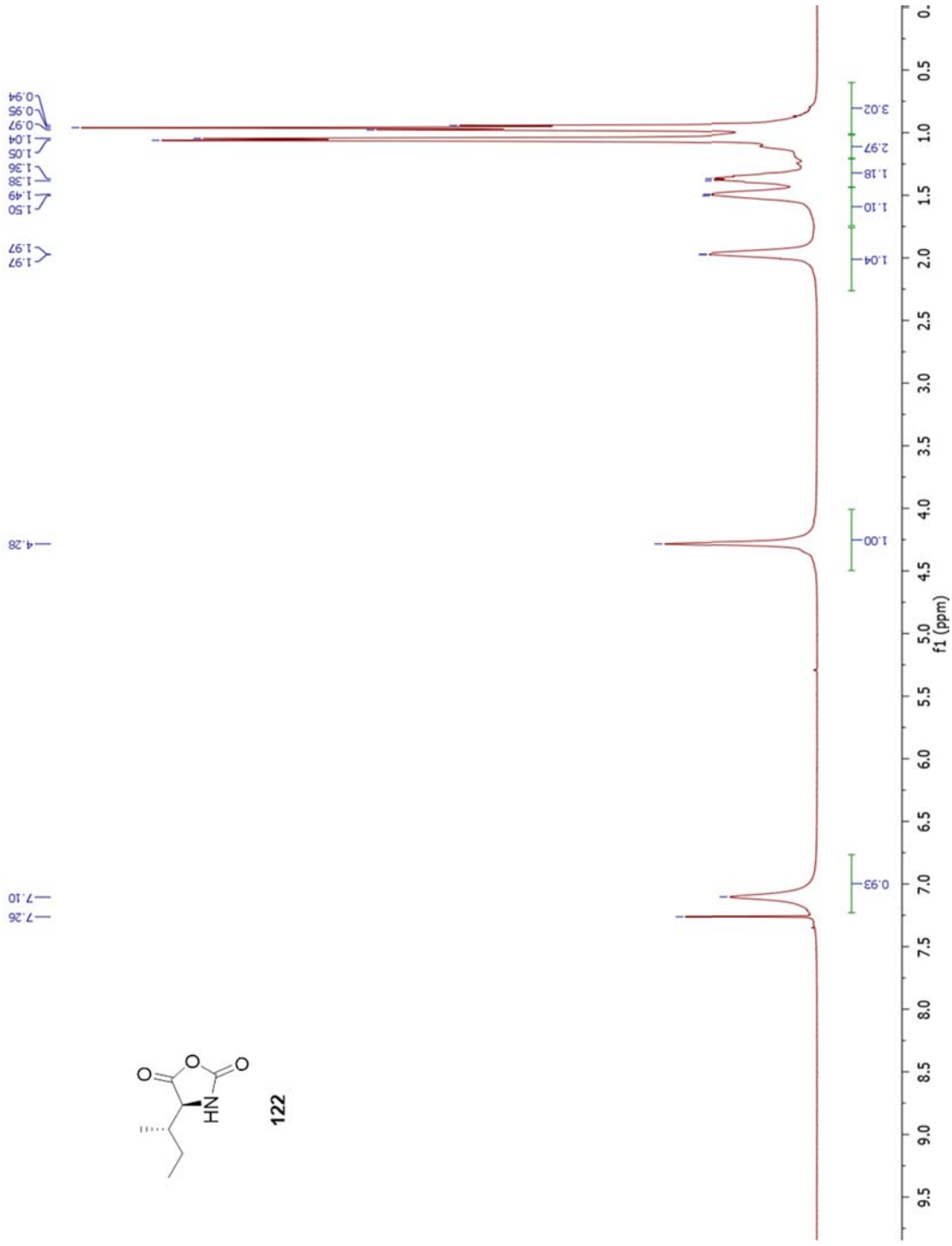

Figure A.194 ^{1}H-NMR of **122**

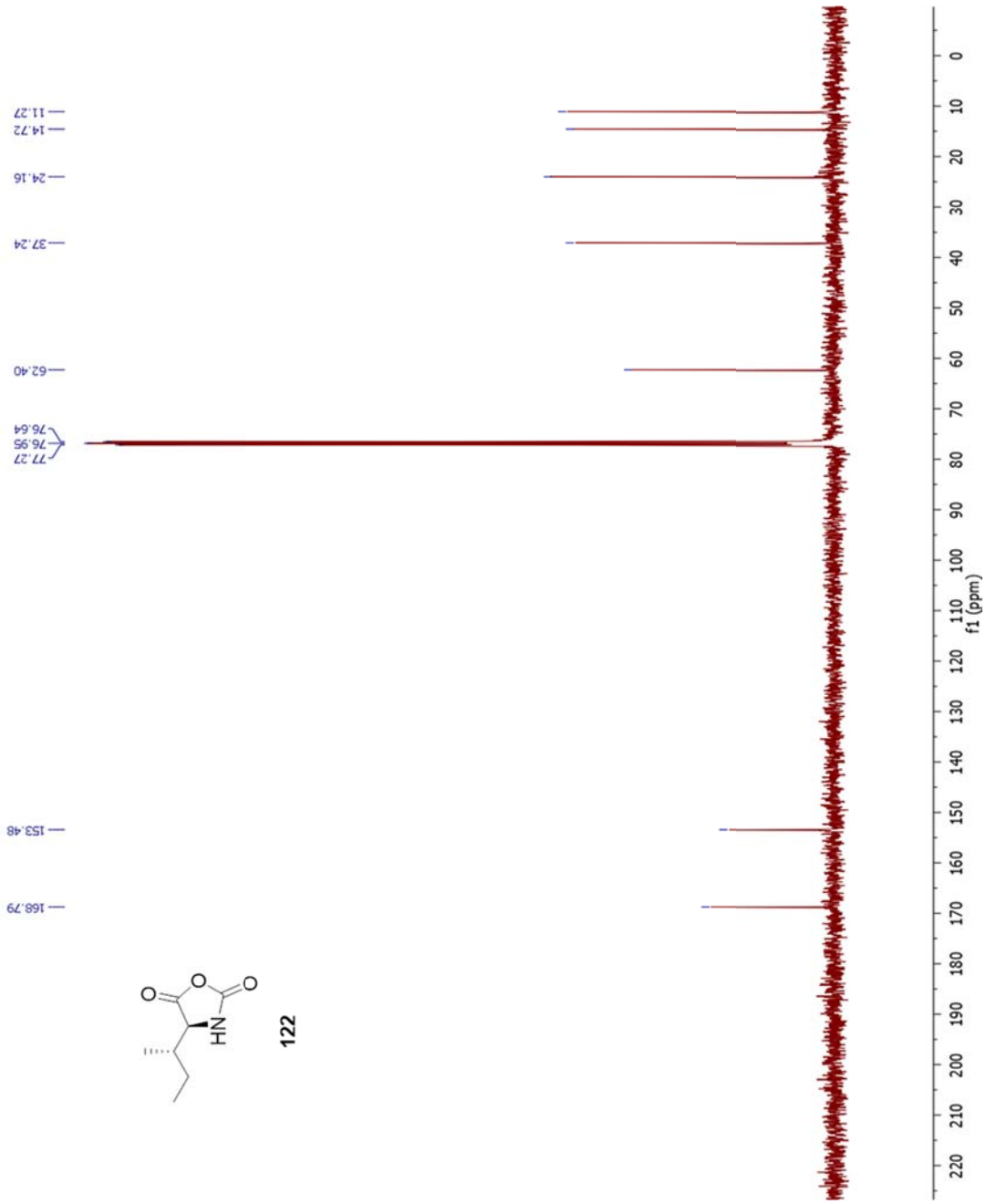

Figure A.195 ^{13}C-NMR of **122**

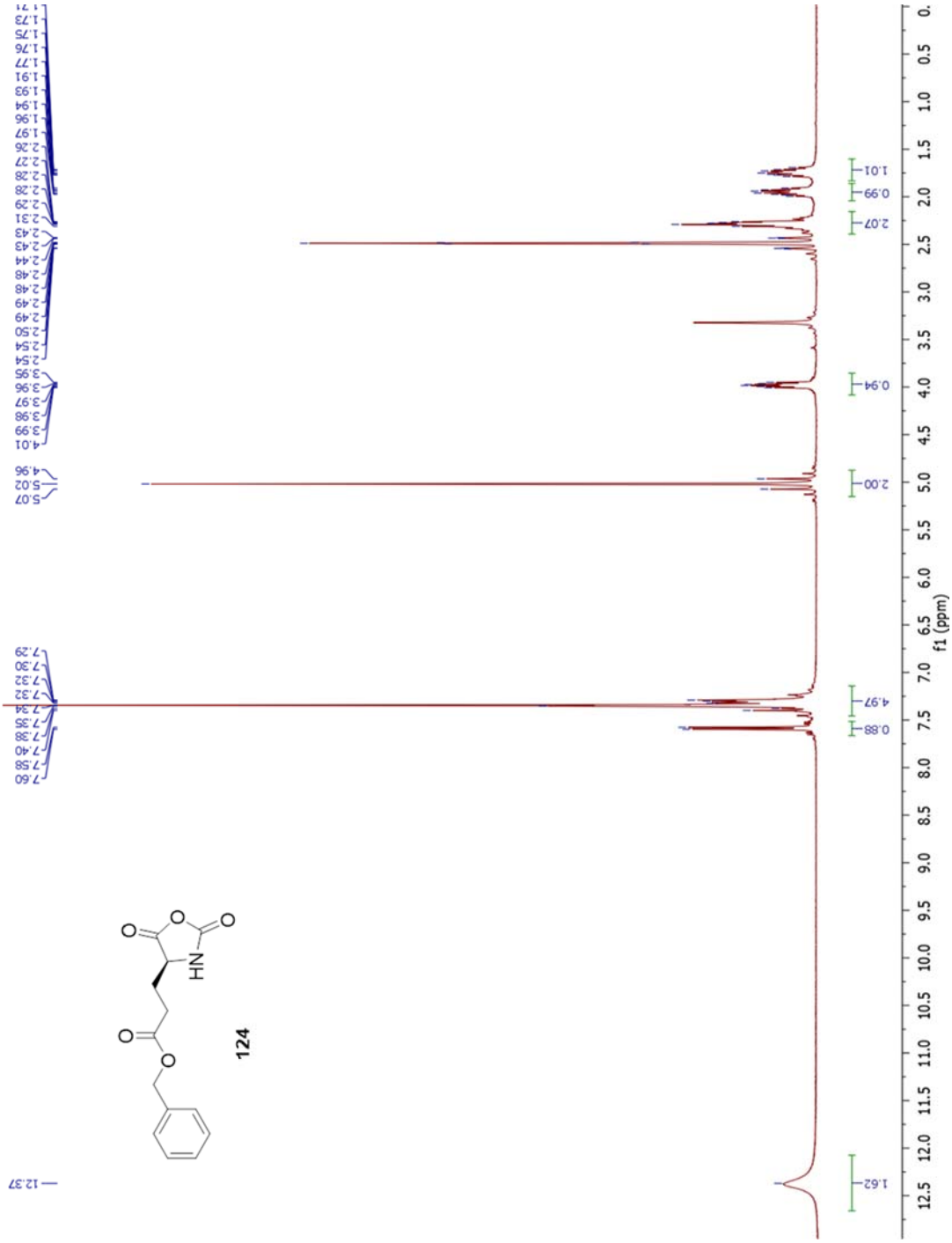

Figure A.196 ^{1}H-NMR of **124**

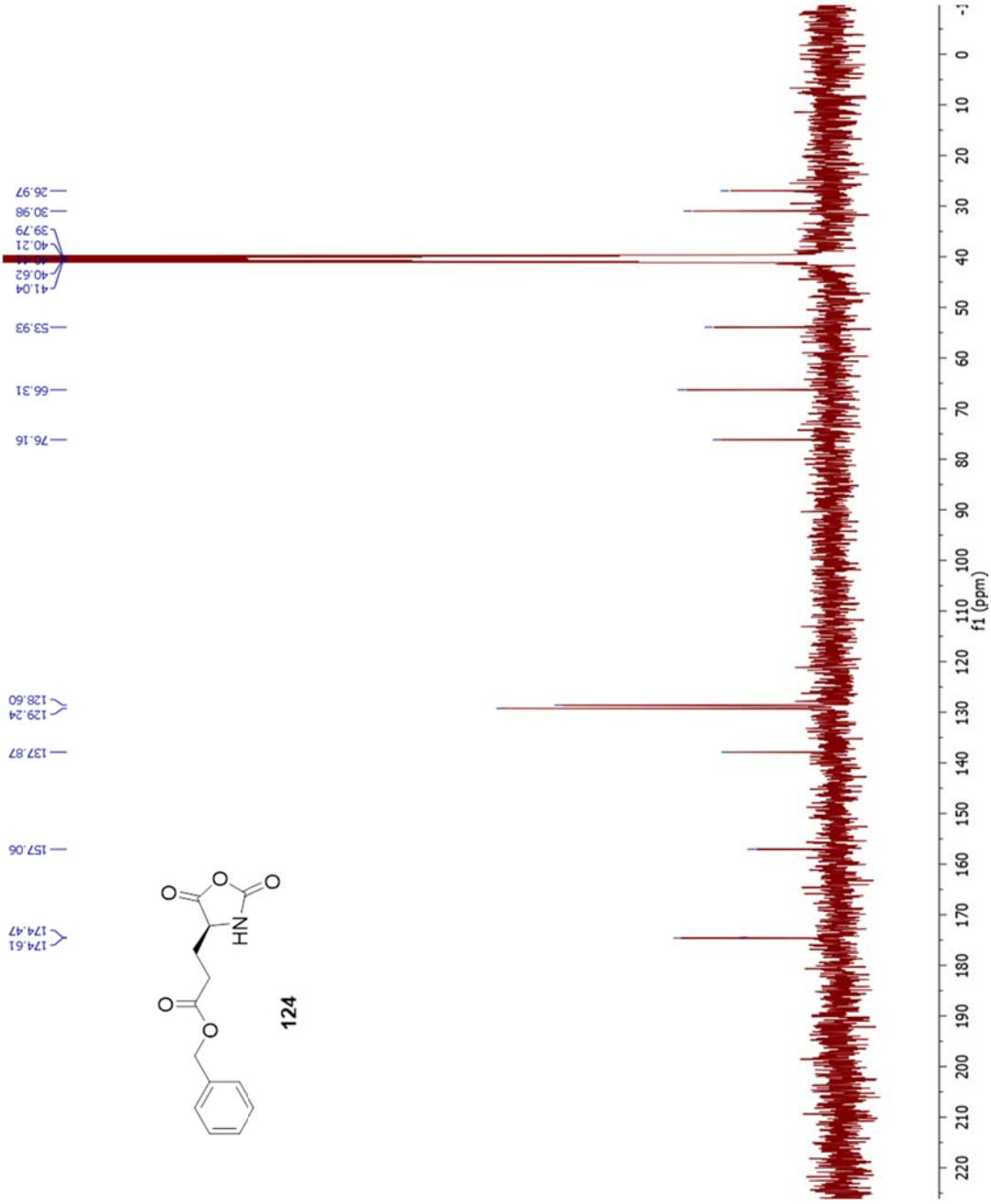

Figure A.197 ^{13}C-NMR of **124**

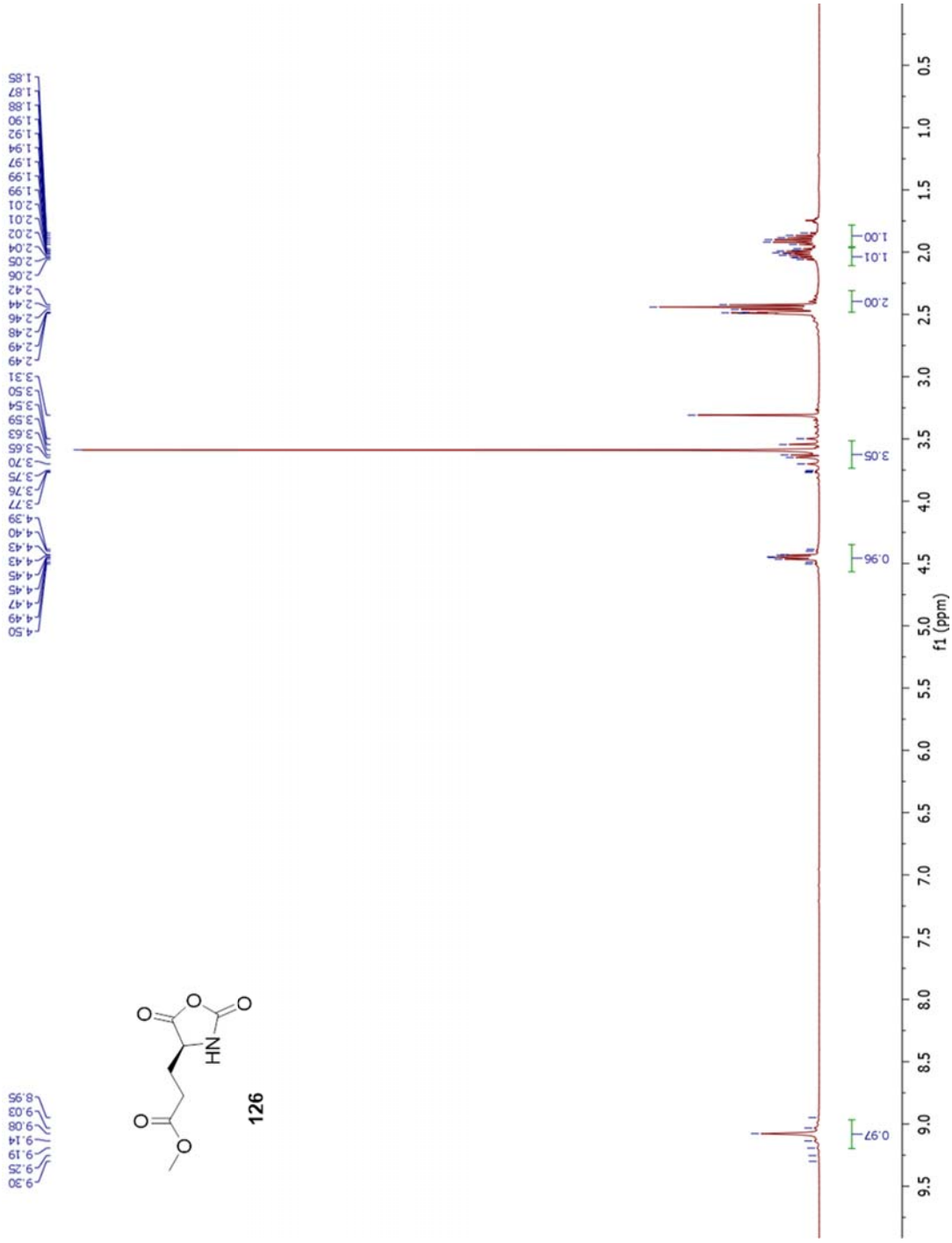

Figure A.198 ^{1}H-NMR of **126**

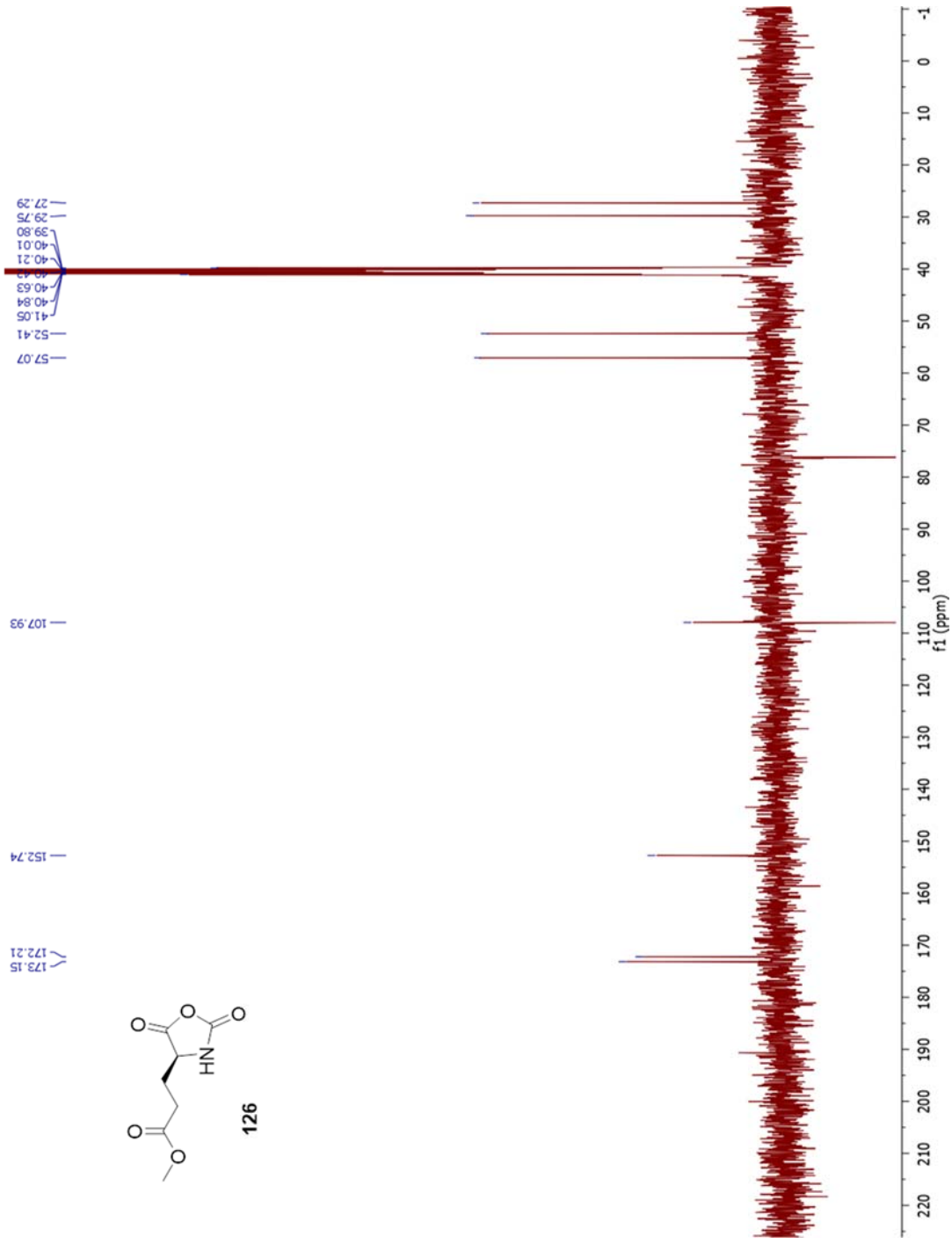

Figure A.199 ^{13}C-NMR of **126**

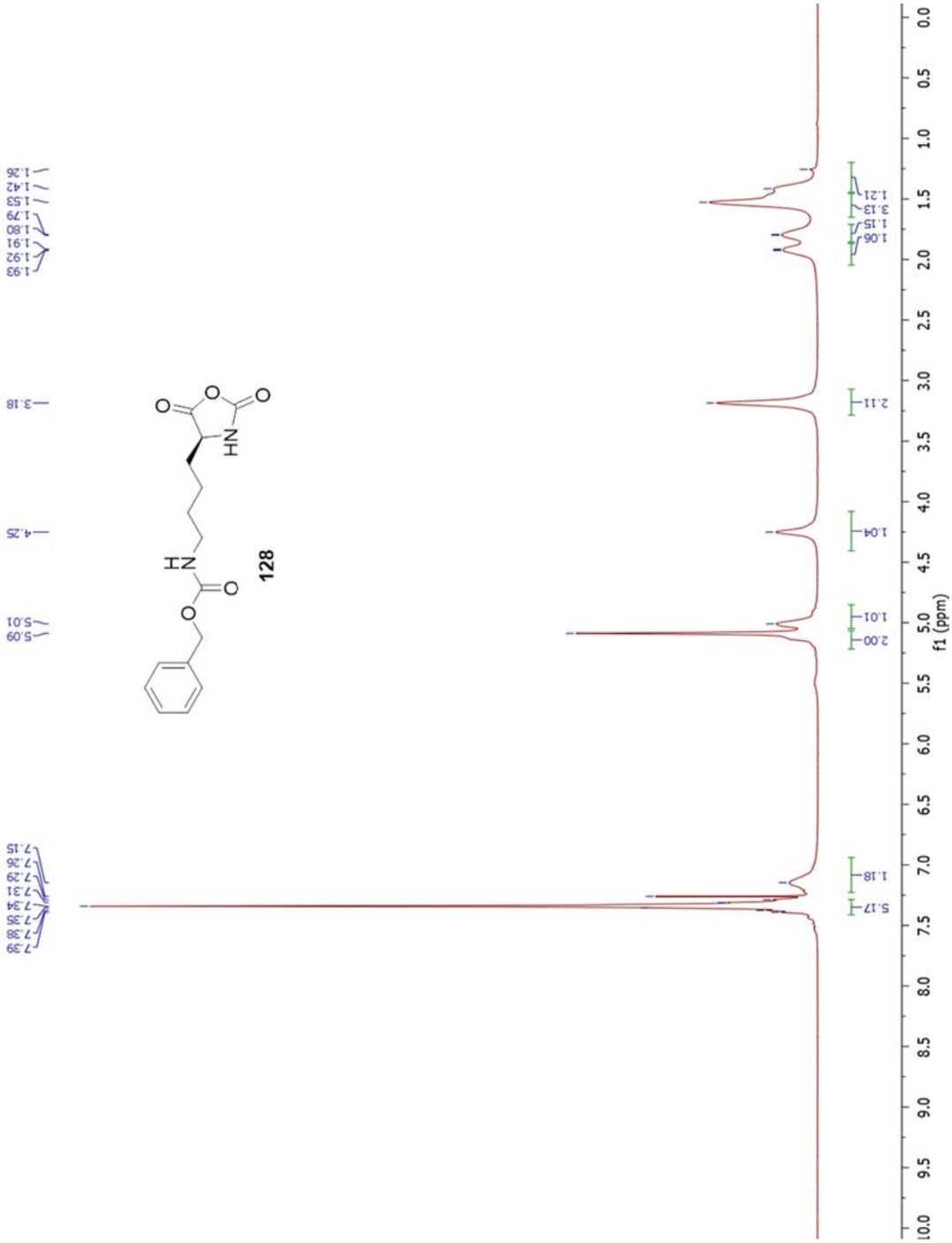

Figure A.200 ^{1}H-NMR of **128**

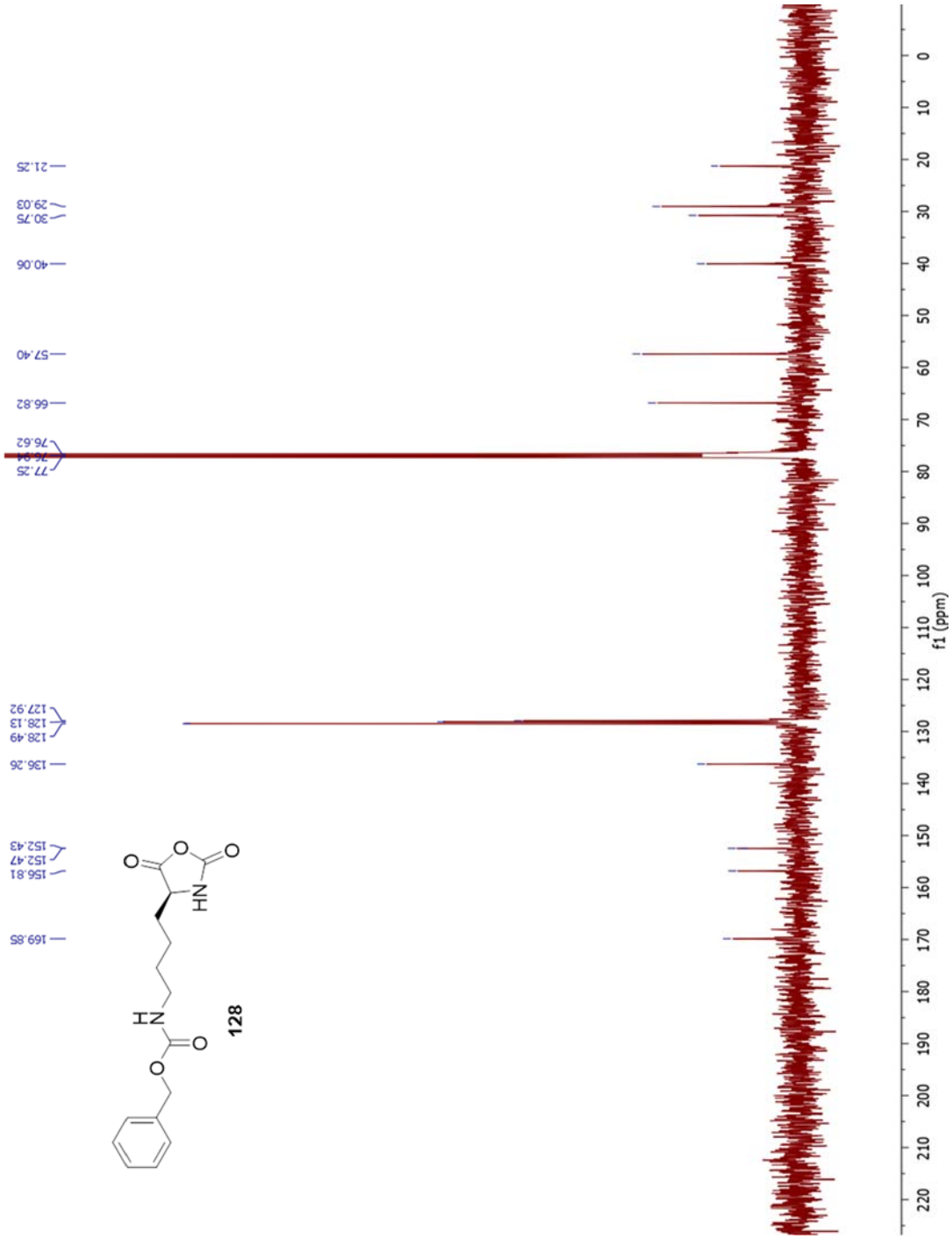

Figure A.201 ^{13}C-NMR of **128**

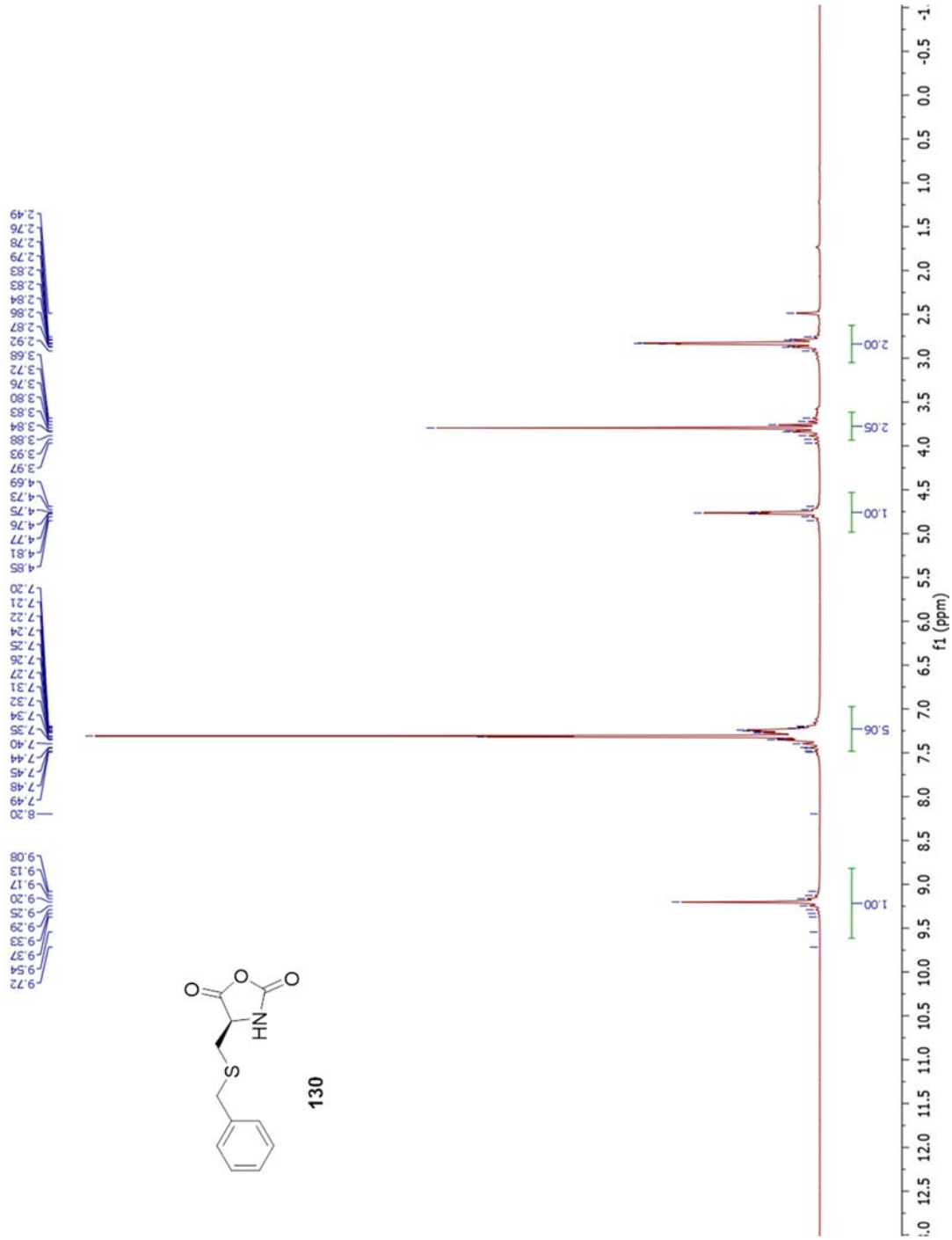

Figure A.202 ^{1}H-NMR of **130**

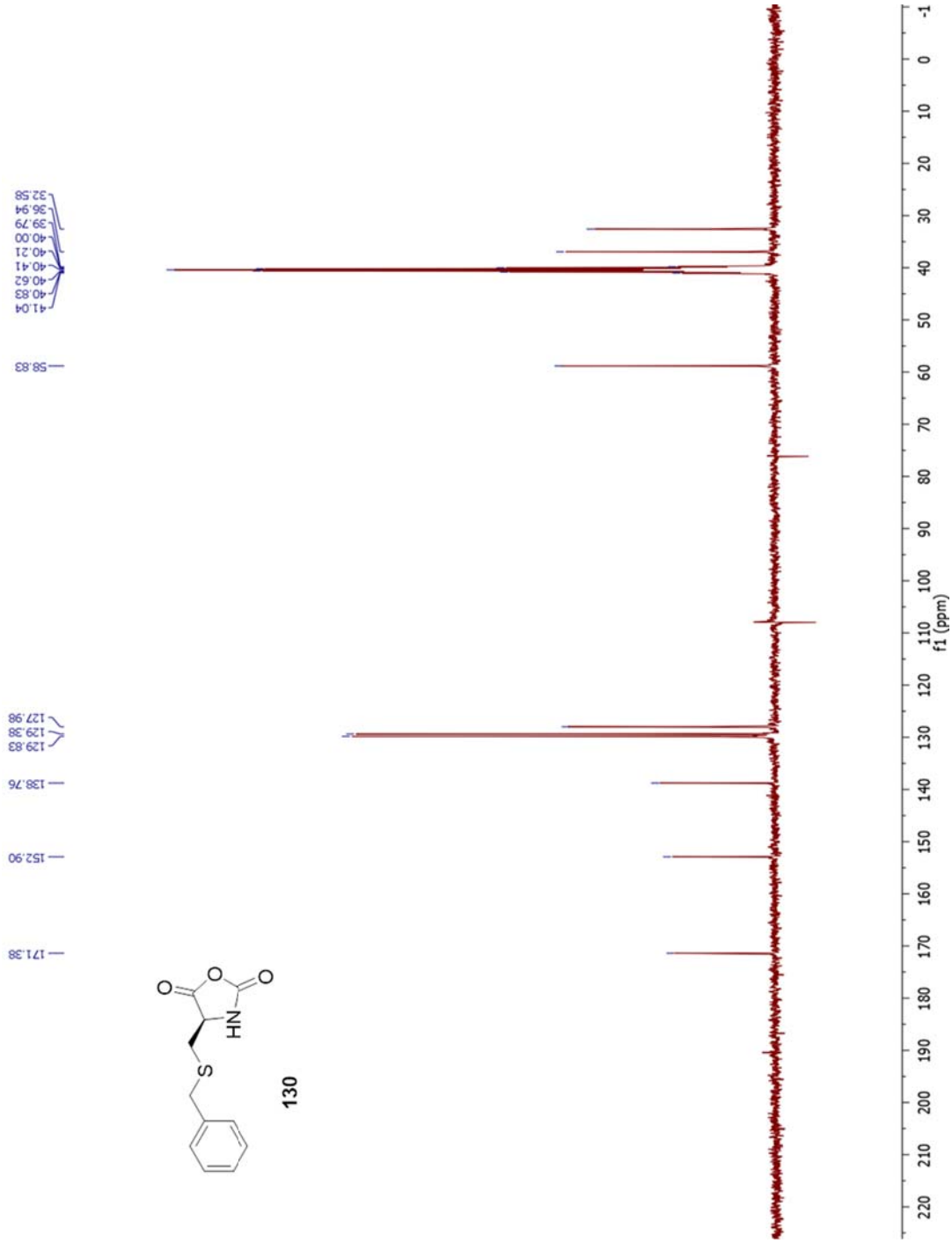

Figure A.203 ^{13}C-NMR of **130**

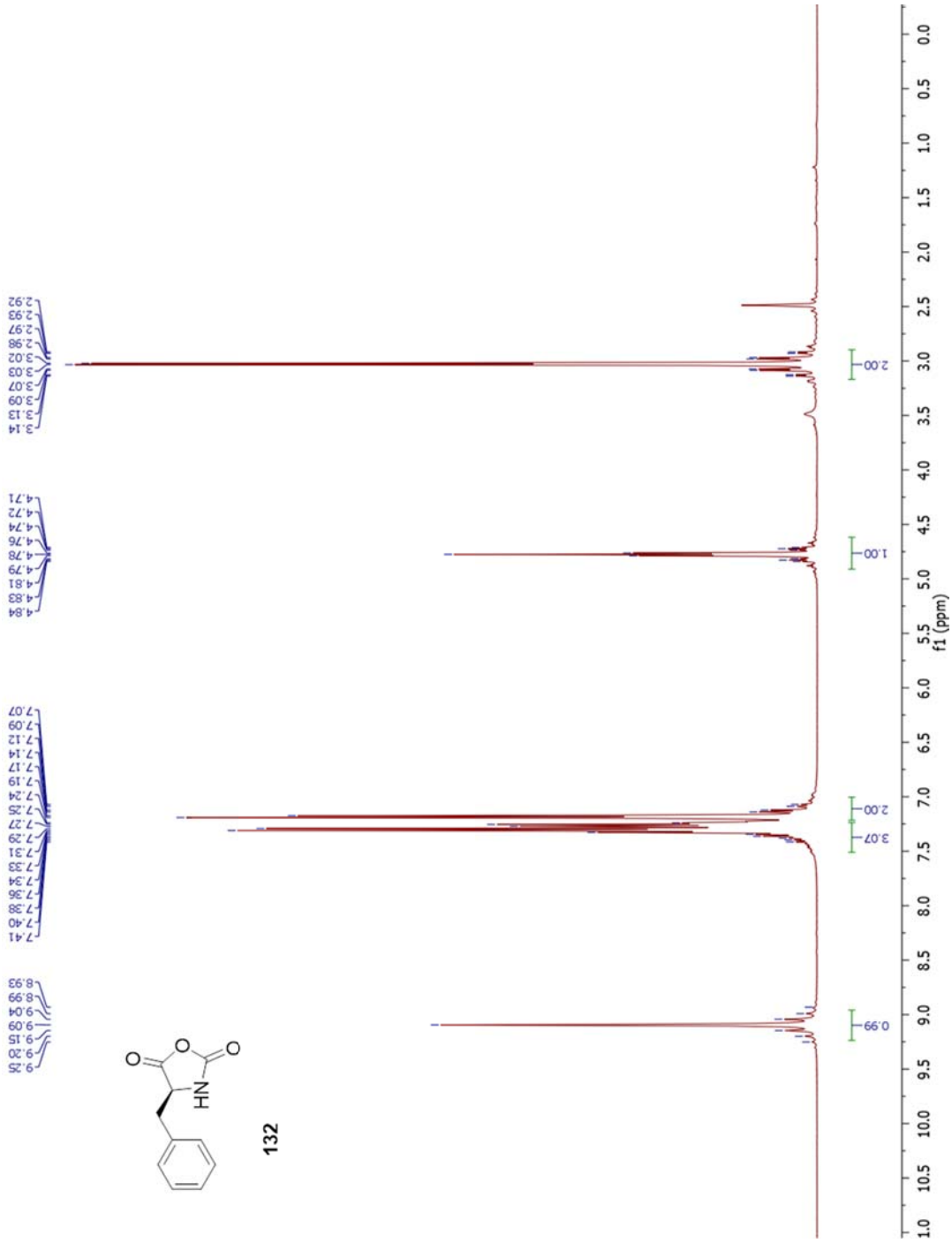

Figure A.204 ^{1}H-NMR of **132**

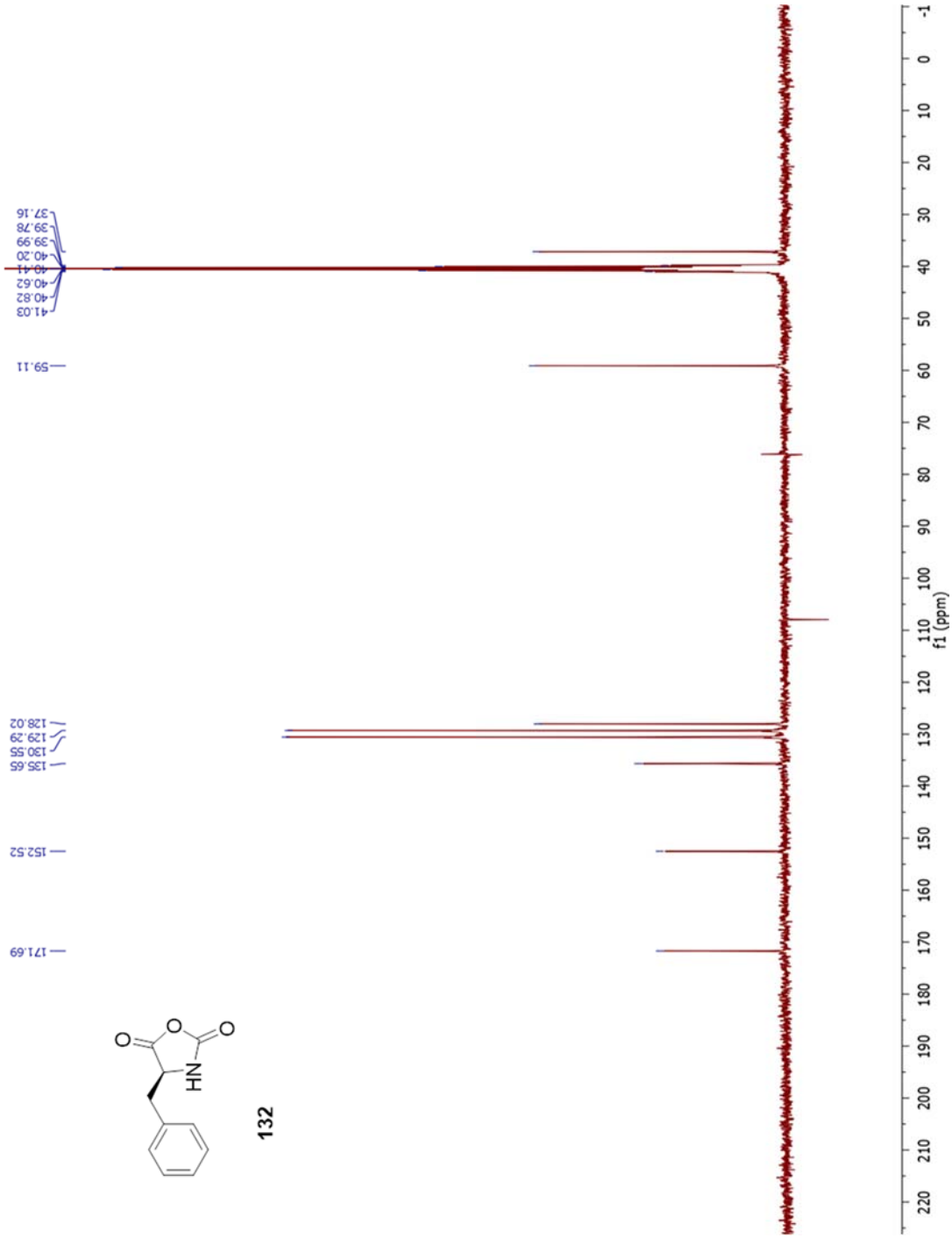

Figure A.205 ^{13}C-NMR of **132**

VITA

VITA

Kyle J. Wright was born in Sullivan, Indiana on June 12, 1988. In 2011, he received a B.S. degree in biochemistry with honors and a minor in biological sciences from Purdue University West Lafayette, Indiana. In 2011, he began his graduate studies at Purdue University, from which he graduated in December 2016 under the direction of Prof. David H. Thompson with research focus on the synthesis and applications of novel supramolecular materials for structural biology and drug and gene delivery.

PUBLICATIONS

LANGMUIR

Article

pubs.acs.org/Langmuir

Nonfouling NTA-PEG-Based TEM Grid Coatings for Selective Capture of Histidine-Tagged Protein Targets from Cell Lysates

Christopher J. Benjamin,[†] Kyle J. Wright,[†] Seok-Hee Hyun,[†] Kyle Krynski,[†] Guimei Yu,[‡] Ruchika Bajaj,[‡] Fei Guo,[‡] Cynthia V. Stauffacher,[‡] Wen Jiang,[‡] and David H. Thompson*[,†]

[†]Department of Chemistry and [‡]Department of Biological Sciences, Purdue University, West Lafayette, Indiana 47907, United States

Supporting Information

ABSTRACT: We report the preparation and performance of TEM grids bearing stabilized nonfouling lipid monolayer coatings. These films contain NTA capture ligands of controllable areal density at the distal end of a flexible poly(ethylene glycol) 2000 (PEG2000) spacer to avoid preferred orientation of surface-bound histidine-tagged (His-tag) protein targets. Langmuir−Schaefer deposition at 30 mN/m of mixed monolayers containing two novel synthetic lipids—1,2-distearoyl-*sn*-glycero-3-phosphoethanolamine-*N*-[(5-amido-1-carboxypentyl)iminodiacetic acid]polyethylene glycolamide 2000) (NTA-PEG2000-DSPE) and 1,2-(tricosa-10′,12′-diynoyl)-*sn*-glycero-3-phosphoethanolamine-*N*-(methoxypolyethylene glycolamide 350) (mPEG350-DTPE)—in 1:99 and 5:95 molar ratios prior to treatment with a 5 min, 254 nm light exposure was used for grid fabrication. These conditions were designed to limit nonspecific protein adsorption onto the stabilized lipid coating by favoring the formation of a mPEG350 brush layer below a flexible, mushroom conformation of NTA-PEG2000 at low surface density to enable specific immobilization and random orientation of the protein target on the EM grid. These grids were then used to capture His_6-T7 bacteriophage and RplL from cell lysates, as well as purified His_8-green fluorescent protein (GFP) and nanodisc solubilized maltose transporter, His_6-$MalFGK_2$. Our findings indicate that TEM grid supported, polymerized NTA lipid monolayers are capable of capturing His-tag protein targets in a manner that controls their areal densities, while efficiently blocking nonspecific adsorption and limiting film degradation, even upon prolonged detergent exposure.

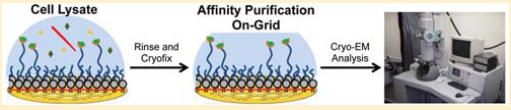

INTRODUCTION

Cryogenic electron microscopy (cryoEM) single particle reconstruction is a rapidly advancing method of protein structure elucidation that is now capable of producing structures with resolutions approaching 2.2 Å, provided that thousands of single particle images can be collected.[1] At present, this is achieved by collecting and class averaging images from many different carbon-coated grid preparations that randomly adsorb and present the protein target in multiple orientations for cryoEM imaging. Since many protein target candidates exist in low copy number, may be highly labile, and/or are derived from infectious agents that are in low supply, there is significant motivation for the development of new sample preparation methods to improve the throughput and predictability of this technique.

Lipid monolayers have been used to concentrate proteins at interfaces for structure determination, as first described by Uzgiris and Kornberg.[2] Subsequent affinity monolayer developments explored a variety of affinity lipid−ligand interactions such as biotin−streptavidin, ATP lipid−ATP binding protein, Ni^{2+}:nitrilotriacetic acid (NTA)-hexahistidine-tagged (His_6-tag) protein, or Cu^{2+}:iminodiacetic acid-His_6-tag protein.[3] Many of these efforts were focused on the development of two-dimensional crystallization methods using nitrilotriacetic acid (NTA)-modified lipid conjugates,[4−9] with some cases showing the potential of NTA lipids for structure elucidation with resolutions in the 10−25 Å regime.[5,8,9] NTA lipid monolayers were extended to the realm of cryoEM single particle reconstruction by Walz and co-workers, with the structures for 50S ribosomal subunits,[10] transferrin−transferrin receptor complex,[11,12] and human RNA polymerase II[13] reported using a commercially available NTA lipid conjugate, 1,2-dioleoyl-*sn*-glycero-3-[((*N*-(5-amino-1-carboxypentyl)iminodiacetic acid)-succinyl] (DGS-NTA), in mixed monolayers with DLPC. They also extended this technique to the retrieval of protein targets from cell lysates;[11,13] however, the potential of the approach is currently limited by the low stability,[10] nonspecific fouling,[11] and preferred orientation[14] limitations of DGS-NTA:DLPC monolayers.

We report our attempts to address these challenges by depositing nonfouling PEG-lipid[15−17] coatings containing common affinity ligands like NTA[3,8,9,18,19] onto TEM grids.[20] These coatings are prepared by compression of lipid films whose NTA surface density and PEG mushroom-brush conformational state can be controlled by initial film composition and applied surface pressures prior to Langmuir−-Schaefer (LS) deposition onto the EM grid. Brush conformation methoxypoly(ethylene glycol) (mPEG) coatings are highly nonfouling,[21−23] thereby enabling the application of cell lysates directly onto the grid and removal of the

Received: September 12, 2015
Revised: November 19, 2015
Published: January 4, 2016

DOI: 10.1021/acs.langmuir.5b03445
Langmuir 2016, 32, 551−559

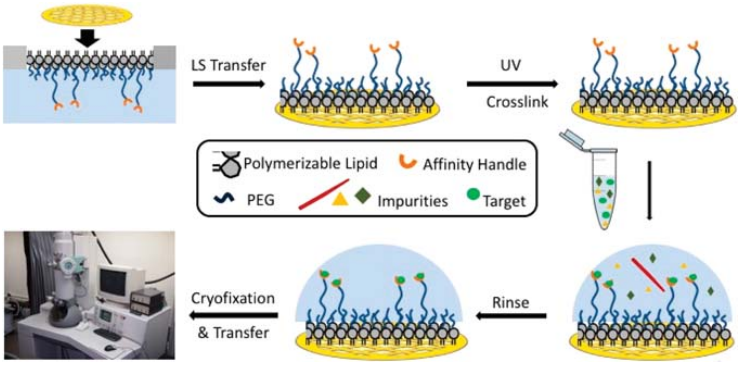

Figure 1. Conceptual diagram showing stabilized monolayer affinity grid fabrication and utilization. (top left) A fluid-phase mixed lipid monolayer comprised of Ni^{2+}:NTA-PEG2000-DSPE and mPEG350-DTPE (1:99 or 5:95 mol:mol) was compressed until the mPEG350-DTPE component entered the brush regime and the diyne lipid chains were fully condensed; (top center) the condensed lipid monolayer film was deposited onto carbon-coated TEM grids via Langmuir−Schaefer (LS) transfer; (top right) photopolymerization of the LS film, followed by Ni^{2+} activation, produces a grid with a stable affinity capture coating; (bottom right) solutions containing the His-tag protein of interest are deposited onto the coated grids, either as a clarified cell lysate or as a purified protein sample; (bottom center) blotting and rinsing of the sample removes nontarget material prior to (bottom left) cryofixation (or negative staining) and sample imaging.

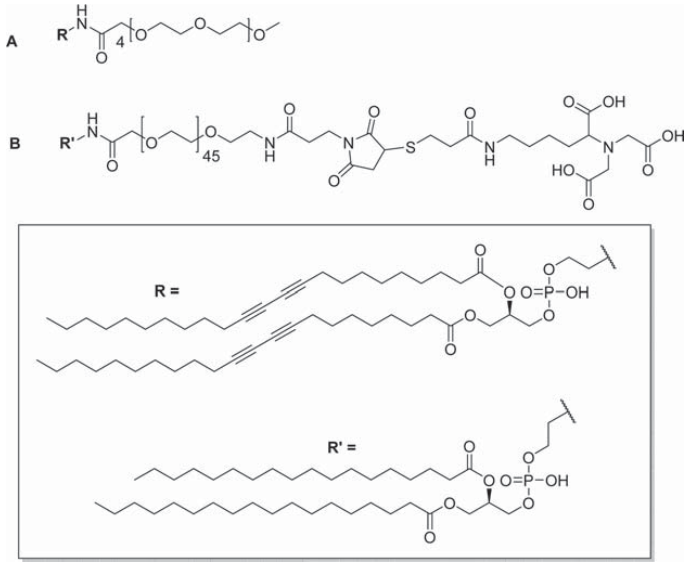

Figure 2. Structures of (A) mPEG350-DTPE and (B) NTA-PEG2000-DSPE.

nonspecifically bound material in subsequent buffer washing steps. In addition to the reduced sample quantity demands required for cryoEM analysis, the shortened sample processing times also limit the opportunities for proteolytic degradation and/or protein unfolding of the His_6-target that may occur during standard sample processing protocols. LS deposition of a mixed monolayer containing two synthetic polymerizable lipids—1,2-(tricosa-10′,12′-diynoyl)-*sn*-glycero-3-phosphoethanolamine-*N*-(methoxypolyethylene glycolamide 350) (mPEG350-DTPE) and 1,2-(tricosa-10′,12′-diynoyl)-*sn*-glycero-3-phosphoethanolamine-*N*-[(5-amido-1-carboxypentyl)-iminodiacetic acid]polyethylene glycolamide 2000) (NTA-PEG2000-DTPE)—prior to treatment with a 5 min, 254 nm light exposure was used to prepare stabilized affinity monolayers supported on carbon coated EM grids. These grids were then used to capture His_6-T7 bacteriophage and His_6-RplL from cell lysates, as well as purified histidine-tagged green fluorescent protein (His_8-GFP) and nanodisc embedded His_6-MalFGK$_2$ (Figure 1). Our findings indicate that polymerized NTA lipid monolayers are capable of capturing His_6-protein targets in a manner that controls their areal densities, while efficiently blocking nonspecific adsorption and limiting film degradation upon prolonged detergent exposure.

EXPERIMENTAL METHODS

Synthesis of mPEG350-DTPE, NTA-PEG2000-DSPE, and NTA-PEG2000-DTPE. The detailed synthesis procedures for mPEG350-DTPE, NTA-PEG2000-DSPE, and NTA-PEG2000-DTPE (Figure 2) are reported in Supporting Information.

DOI: 10.1021/acs.langmuir.5b03445
Langmuir 2016, 32, 551−559

Cell Lysate Preparations. The ASKA library, a complete *E. coli* K-12 ORF archive in which over 4000 bacterial proteins have been cloned into pCA24N expression vectors, was used. Each protein coding ORF has an N-terminal His_6 and a C-terminal green fluorescence protein (GFP); each protein coding ORF is also available without the GFP fusion (which are the strains used in these studies). Cells containing the RplL gene overexpression vector were grown to OD = 0.6 in 100 mL of LB broth using a 37 °C shaker/incubator and induced with a final concentration of 1.0 mM IPTG before allowing to grow for an additional 4 h. After centrifugation, the supernatant was discarded before resuspending the cell pellet in lysis buffer (20 mM Tris, 10 mM $MgCl_2$, 100 mM KCl, pH = 7.4, 100 μg aprotinin, 174 μg PMSF, 500 μg lysozyme) and incubation for 20 min. The cell membranes were disrupted by sonication (35 pulses, 1 s/pulse at 75 W) before centrifugation of the suspension at 11 000 *g* for 10 min. The supernatant containing His_6-RplL was diluted 10-fold before application to the TEM grid for analysis.

Purified C-terminal His_8-tag gp10 (capsid protein) of T7 bacteriophage was typically produced at concentrations of $\sim 1 \times 10^{12}$ particles/mL. BL21 bacteria cells in 1 mL of LB media were grown to OD = 0.8 before addition of T7 bacteriophage (1.0 μL, 1.0×10^{12} particles/mL) to the culture and shaking at 37 °C for 1 h. After centrifugation of the cells, the supernatant was used directly for TEM grid analysis.

His_8-GFP Purification. A glycerol stock of *E. coli* cells, transformed with the His_8-GFPuv pT7−7 plasmid, was shaken at 37 °C overnight before addition to 250 mL of LB media with shaking at 37 °C until an OD_{600} of 0.7 was reached. Then, a 1.0 M stock solution of isopropyl-β-D-thiogalactopyranoside (IPTG) was added, bringing the final concentration to 1.0 mM, before shaking continually at 37 °C for an additional 5 h. The cells were then centrifuged at 11 000 *g* for 10 min, the supernatant discarded, and the pellet resuspended in 10 mL of lysis buffer (50 mM NaH_2PO_4, 100 mM NaCl, pH = 8.0, 100 μg aprotinin, 174 μg phenylmethanesulfonyl fluoride (PMSF), and 500 μg of lysozyme). The suspension was allowed to stand for 20 min before the cell membranes were disrupted using 3 rounds of sonication (35 pulses of probe sonication, 1 s/pulse at 75 W with 1 s rest/pulse) and the debris pelleted by centrifugation at 11 000 *g* for 30 min. The supernatant was incubated with 100 μL of Ni-NTA agarose beads and gently rotated for 4 h. The beads were pelleted using a benchtop centrifuge operating at 5000 *g* for 2 min. The supernatant was discarded and the pellet was washed with PBS buffer containing imidazole (50 mM NaH_2PO_4, 100 mM NaCl, 10 mM imidazole, pH = 8.0). The same spin and wash sequence was repeated with 15 mM, 20 mM, and 30 mM imidazole in PBS. The protein was eluted from the resin after removal of the supernatant and incubation of the beads with 500 mM imidazole in PBS for 4 h. The removal of imidazole from the eluted protein was achieved by dialysis against PBS (50 mM NaH_2PO_4, 100 mM NaCl, 10 mM imidazole, pH = 8.0) overnight using a 10 000 MWCO Slide-A-Lyzer. The protein was characterized using 12.5% acrylamide SDS-PAGE gel electrophoresis.

Purified Maltose Transporter Solubilized in Lipid Nanodisc. The methods used to purify and insert His_6-$MalFGK_2$ maltose transporter in lipid nanodiscs derived from membrane scaffolding proteins (MSP) followed those described in a previously reported protocol.[24]

Langmuir−Schaefer Film Deposition onto TEM Grids. Stock solutions of two lipid mixtures (1:99 Ni^{2+}:NTA-PEG2000-DTPE:mPEG350-DTPE and 5:95 Ni^{2+}:NTA-PEG2000-DTPE:mPEG350-DTPE) were prepared in $CHCl_3$ at 2.0 mg/mL and stored at −80 °C. Each of these were spread via 10 μL microsyringe at the air−water interface of a Kibron μTrough and compressed to a final surface pressure of 30 mN/m (i.e., ~59 Å^2/molecule for 1:99 Ni^{2+}:NTA-PEG2000-DTPE:mPEG350-DTPE monolayers and ~66 Å^2/molecule for 5:95 Ni^{2+}:NTA-PEG2000-DTPE:mPEG350-DTPE monolayers). The compressed lipid monolayers were deposited onto TEM grids by Langmuir−Schaefer transfer using tabbed TEM grids (Ted Pella) to enable grid approach at 180° (and the transfer forceps at 90°) relative to the air−water interface. The LS film was immediately blotted with filter paper. (n.b.: Standard TEM grids and forceps produced extensive disruption of the interface during the LS transfer step, making it impossible to determine accurate grid transfer ratios under these conditions.) The supported monolayer films were then polymerized for 10 min using a hand-held 8 W/m^2 254 nm lamp that was placed 6−8 cm above the grid surface before transfer to a standard TEM grid box for later use.

Fluorescence Microscopy. Sessile drops of His_8-GFPuv solution (3.5 μL, 2.0 mg GFP/mL in PBS) were deposited onto 1:99 Ni^{2+}:NTA-PEG2000-DTPE:mPEG350-DTPE, 5:95 Ni^{2+}:NTA-PEG2000-DTPE:mPEG350-DTPE, 100% mPEG350-DTPE, or bare carbon coated grid surfaces for 2 min, followed by removal of excess sample using a microsyringe. Grids were then washed 3 times with 20 μL drops of Tris buffer before removal of the excess solution via microsyringe. For elution of Ni^{2+}:NTA-bound T7 bacteriophage from the surface of the grid, 500 mM imidazole was deposited on the grid surface for 5 min before washing twice with 20.0 μL of PBS. After preparation, the TEM grid was sandwiched between a microscope slide and coverslip and sealed with nail polish before recording the fluorescence images.

Negative-Staining Procedure. T7 bacteriophage and RplL cell lysate samples were prepared by incubating a 5.0 μL drop of cell lysate on the grid surface for 2.0 min before gentle removal by microsyringe. The grids were then washed 6 times with 20 μL drops of Tris buffer followed by a final wash with 20 μL of distilled water. A 5 μL drop of 2% uranyl acetate was placed on the grid for 1 min before removal of the excess solution with a wedge of filter paper. Ni^{2+}:NTA-immobilized samples were eluted from the grids by adding 5 μL of 500 mM imidazole in Tris buffer immediately after sample deposition (i.e., instead of 6 Tris buffer washes). Nanodisc solubilized $MalFGK_2$ and purified T7 bacteriophage samples were prepared in the same manner as the cell lysate samples, except that the incubation time of the samples on DLPC and mPEG350-DTPE modified grids was increased to 3 min. Negatively stained samples were imaged using a Tecnai TF20 transmission electron microscope operating at 200 kV.

Preparation of Frozen Hydrated Samples for Cryo-TEM. TEM grids modified with stabilized 5:95 Ni^{2+}:NTA-PEG2000-DTPE:mPEG350-DTPE monolayers were treated with His-tag protein samples as described above for negative-staining. After application of the protein solution, the excess sample was removed by blotting the grids twice for 3 s with an offset of −1 at 80% humidity using a Vitrobot (FEI Company). The grids were then cryo-fixed by plunging into liquid ethane and imaged at 200 kV on an FEI CM200 transmission electron microscope using low-dose techniques. Images were recorded using a Gatan Ultrascan CCD.

RESULTS AND DISCUSSION

mPEG350-DTPE was prepared in 24% yield by treatment of commercially available 1,2-(tricosa-10′,12′-diynoyl)-*sn*-glycero-3-phosphoethanolamine (DTPE) with the *N*-hydroxysuccinimidyl (NHS) active ester form of mPEG350 (Supporting Information, Scheme S1). NTA-PEG2000-DSPE was prepared in 40% yield by sequential modification of doubly activated NHS-PEG2000-maleimide with 1,2-distearoyl-*sn*-glycero-3-phosphoethanolamine (DSPE) and a thiol-modified lysine-NTA derivative (Figure 2; Supporting Information, Schemes S2−S4). NTA-PEG2000-DTPE was prepared in 13% yield in a similar manner as NTA-PEG2000-DSPE, except that DTPE was used for NHS displacement instead of DSPE.

$CHCl_3$ stock solutions of the lipid mixtures were prepared, spread at the air−water interface at 20 °C, a 5 min incubation period allowed for evaporation of the solvent, and the films compressed at a rate of 10 Å^2/molecule until collapse at 30−35 mN/m for the mixed monolayers and 40 mN/m for pure mPEG350-DTPE monolayers. The pressure−area isotherms shown in Figure S1 for 1:99 and 5:95 NTA-PEG2000-DTPE:mPEG350-DTPE lipid mixtures displayed gradually increasing surface pressures upon film compression, except

DOI: 10.1021/acs.langmuir.5b03445
Langmuir 2016, 32, 551−559

that the onset of surface pressure occurred at larger molecular areas as the NTA-PEG2000-DTPE composition in the film increased. We attribute this observation to the displacement of surface-adsorbed NTA-PEG2000 from the air−water interface as previously described[25] for mixed mPEG2000-lipid monolayers. As this desorption process progresses, the majority component, mPEG350, undergoes a mushroom−brush regime transition upon compression to 30 mN/m while the NTA-PEG2000 fraction remains in the mushroom configuration. The extension of the PEG2000 polymer mushroom conformation from the surface of the film can be calculated by $L_o = \alpha N(\alpha/D)^{2/3}$, where L_o = the length of PEG graft, α = length of PEG monomer (3.5 Å), N = number of ethylene glycol units in the PEG chain (i.e., 45), and D = the distance between grafting sites. For a lipid film containing 1% NTA-PEG2000-DTPE, the grafting site separation is estimated to be 47 Å and the L_o = 2.8 nm. Fully compressed 5:95 NTA-PEG2000-DTPE:mPEG350-DTPE monolayers are estimated to have a grafting site separation of 9.4 Å and a NTA-PEG2000 graft extension of 8.2 nm. As the lipid film is compressed below 113 Å^2/molecule, the mPEG350 fraction enters the brush regime, while the NTA-PEG2000 polymer chain accommodates further compression by extending farther away from the air−water interface in a concentration-dependent manner. Consequently, a longer NTA-PEG was prepared for these studies since it would confer greater conformational freedom to the immobilized histidine-tagged target and present it in a greater diversity of possible orientations for cryoEM single particle analysis.

Since the lipid films typically collapsed at surface pressures above 30 mN/m, the monolayers were compressed to 30 mN/m prior to Langmuir−Schaefer (LS) transfer onto carbon-coated grids that were not subjected to glow discharge before LS deposition. This method produced transfer ratios between 0.89 and 0.97 for the LS deposition step. Photopolymerization of the lipid monolayer was initiated by placing the grids ∼6−8 cm from a hand-held UV lamp and irradiating for 10 min. Grid performance as a function of varied irradiation time suggested that a 10 min exposure was most favorable.

After monolayer film transfer onto 400 mesh grids and staining with freshly prepared 1% $UO_2(OAc)_2$, TEM images revealed the presence of large continuous areas exceeding 900 μm^2 in size that were punctuated by much smaller zones of higher contrast (Figure S2). We infer from these findings that the large area regions were monolayer films with occasional, interspersed domains of bilayer and trilayer films arising from partial monolayer collapse during compression that were preserved by the photopolymerization process. Sufficiently large areas of the grid were coated by stabilized monolayer film structures to make them suitable for negative stain and cryoEM studies; however, the multilayer sections of the film were helpful for monitoring the stability of the film in the presence of detergents as described below.

The antifouling properties of the mPEG350 brush layer within the stabilized monolayer coating was probed qualitatively using fluorescence microscopy analysis of His_8-GFPuv adsorption onto these modified surfaces. Wide field and line scan fluorescence microscopy analysis revealed that glow discharged bare amorphous carbon surfaces possessed nearly 20-fold greater fluorescence intensities after exposure to His_8-GFPuv than grids bearing mPEG350 brush regime coatings (>8000 RFU and ∼400 RFU, respectively; Figure S3). Our data shows that the fluorescence distribution was uniform over both types of surfaces; however, in rare instances there were small variations in fluorescence observed. In those cases, we attribute the areas of decreased fluorescence to grid regions with an incomplete carbon coating, whereas zones of substantially increased fluorescence were ascribed to incomplete LS transfer of the brush layer mPEG350-DTPE. We infer from these findings that nonspecific binding of protein on the brush regime mPEG350-DTPE coated grids is much lower than that of glow discharged bare carbon films due to the combined effects of molecular weight, polymer hydration, excluded volume, elastic restoration, and grafting density on the surface that enhance the antifouling properties of the mPEG coating.[22,26,27] In some cases, low molecular weight PEG polymers such as mPEG350 display greater antifouling properties than their higher molecular weight counterparts since the shorter PEG chains are better able to form a more densely packed layer.[28,29] Based on these findings, we concluded that brush regime mPEG350-DTPE monolayers, deposited onto a carbon coated surface by LS transfer, would be a good candidate for blocking nonspecific adsorption of macromolecules onto EM grid surfaces. To test this assumption, we conducted a comparative study between DLPC monolayers and mPEG350-DTPE stabilized monolayers, both deposited via LS transfer, using bare carbon grids as a control.

His_8-GFPuv capture on grids bearing stabilized 1:99 and 5:95 Ni^{2+}:NTA-PEG2000-DTPE:mPEG350-DTPE monolayers was first demonstrated by fluorescence microscopy. Wide-field fluorescence images (Figure S4) of Ni^{2+}:NTA-PEG2000-DTPE:mPEG350-DTPE modified grids reveal a nonuniform, concentration-dependent GFP fluorescence. Some spots of bright fluorescence, suggestive of GFP aggregation, were also observed. The observed pixel intensities in the fluorescence line scan analyses were higher for the grids bearing a 5:95 Ni^{2+}:NTA-PEG2000-DTPE:mPEG350-DTPE coating than the grids coated with a 1:99 monolayer. In both cases, the bound His_8-GFPuv could be removed from the grid surface after a brief 5 min exposure to either 500 mM imidazole or 150 mM EDTA to remove Ni^{2+} from the His_8:Ni^{2+}:NTA complex to enable elution of the immobilized protein target from stabilized, Ni^{2+} activated 1:99 and 5:95 Ni^{2+}:NTA-PEG2000-DTPE:mPEG350-DTPE monolayers. These findings indicate that His-tag targets can be captured in an NTA concentration-dependent manner, with higher NTA loadings producing greater target protein concentrations on TEM grids coated with stabilized, Ni^{2+}-activated NTA-PEG2000-DTPE:mPEG350-DTPE monolayers.

Purified His_6-T7 bacteriophage (10^{11}−10^{12} particles/mL) was used to probe the nonspecific adsorption properties of DLPC and mPEG350-DTPE stabilized monolayer-coated grids at higher resolution, with carbon coated, glow-discharged grids serving as a control. The sample aggregated on grids lacking modified DLPC or mPEG350 monolayers (Figure 3A). We identified virus-like particles on these grids, as shown in Figure 3A (inset); however, the poor sample quality produced on unmodified, glow-discharged grids made accurate quantification of adsorbed virus particles impossible. Therefore, we only quantified virus adsorption onto DLPC and mPEG350 modified grids, as discrete particles could be discerned in both cases. DLPC coated grids were found to decrease the amount of T7 that was adsorbed to the grid relative to bare carbon grids (Figure 3B), indicating that interactions between T7 bacteriophage and the DLPC monolayer are not as favorable. Nonetheless, a significant amount of occult debris

DOI: 10.1021/acs.langmuir.5b03445
Langmuir 2016, 32, 551−559

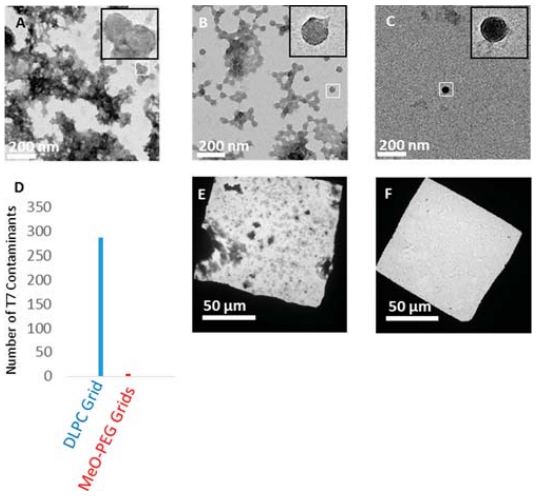

Figure 3. Comparative performance of uncoated (bare carbon, glow-discharge), DLPC, and mPEG350-DTPE coated grids toward nonspecific protein adsorption (i.e., lacking NTA groups to promote specific binding). The capacity of these grids to reject nonspecific protein adsorption was tested by negative stain TEM analysis using His_6-T7 bacteriophage in purified form or within cell lysates. (A) Purified His_6-T7 bacteriophage on glow-discharged bare carbon grid; (B) purified His_6-T7 bacteriophage on 100% DLPC monolayer coated grid; (C) His_6-T7 bacteriophage on stabilized 100% mPEG350-DTPE monolayer coated grid; (D) number of nonspecific contaminants adsorbed from purified His_6-T7 bacteriophage solution onto bare carbon grids (blue), DLPC coated grids (red), and mPEG350-DTPE coated grids (green) as determined by counting 60 randomly selected fields across 3 different grids for each grid type; (E) His_6-T7 bacteriophage in cell lysate applied to 100% DLPC coated grid; and (F) His_6-T7 bacteriophage in cell lysate applied to stabilized 100% mPEG350-DTPE coated grid.

remained on the DLPC monolayer coated grids. Grids coated with mPEG350-DTPE stabilized monolayers, however, displayed a greatly reduced accumulation of both T7 and debris (Figure 3C). The appearance of the virus particles in these samples included round-like objects as well as more familiar hexagonal projection of the mature icosahedral form of the virus. The T7 phage particles in these images represent the immature form where an absence of mature capsid shell protein gives results in the rounded appearance of these particles.[30] The low abundance of T7 phage particles highlights the antifouling opportunities of these PEGylated surfaces. Quantitative comparisons of the T7 particle densities on DLPC and mPEG350 monolayers revealed an accumulation of ~110 particle/1 μm^2, and 5 particle/1 μm^2, respectively. We infer from these findings that mPEG350-DTPE stabilized monolayers are the most effective toward blocking nonspecific adsorption of T7 bacteriophage (Figure 3D). Low magnification images of purified T7 deposited onto both DLPC and mPEG-DTPE stabilized monolayer coated grids reveal a substantially lower background in the case of mPEG350-DTPE coated grids (Figure 3E,F).

After evaluating the capacity of these grids to inhibit nonspecific adsorption, we next turned our attention to their ability to direct affinity-guided interactions with NTA-modified grids. First, we used fluorescence microscopy to monitor His_8-GFPuv capture on grids bearing stabilized 1:99 and 5:95 Ni^{2+}:NTA-PEG2000-DTPE:mPEG350-DTPE monolayers. Wide-field fluorescence images (Figure S4) of Ni^{2+}:NTA-PEG2000-DTPE:mPEG350-DTPE modified grids reveal a nonuniform, concentration-dependent GFP fluorescence. Occasional spots of bright fluorescence, suggestive of GFP aggregation, were also observed. The observed average pixel intensities in the fluorescence line scan analyses were higher for the grids bearing a 5:95 Ni^{2+}:NTA-PEG2000-DTPE:mPEG350-DTPE coating than the grids coated with a 1:99 monolayer. In both cases, the bound His_8-GFPuv could be removed from the grid surface after a brief 5 min exposure to either 500 mM imidazole or 150 mM EDTA to remove Ni^{2+} from the His_8:Ni^{2+}:NTA complex to enable elution of the immobilized protein target from stabilized, Ni^{2+} activated 1:99 and 5:95 Ni^{2+}:NTA-PEG2000-DTPE:mPEG350-DTPE monolayers. These findings indicate that histidine-tagged targets can be captured in an NTA concentration-dependent manner, with higher NTA loadings producing greater target protein concentrations on TEM grids coated with stabilized, Ni^{2+}-activated NTA-PEG2000-DTPE:mPEG350-DTPE monolayers.

Affinity capture of His_6-T7 bacteriophage from cell lysates was then tested by negative stain and cryoelectron microscopy using grids modified with mPEG350-DTPE stabilized monolayers, Ni^{2+}:NTA-PEG2000-DTPE:mPEG350-DTPE stabilized monolayers, and Ni^{2+}:NTA-PEG2000-DTPE:mPEG350-DTPE stabilized monolayers rinsed with 500 mM imidazole after lysate exposure (Figure 4). In the presence of mPEG350-DTPE stabilized monolayers, we observed minimal binding of His_6-T7 bacteriophage and very low levels of debris from the lysate onto the grid (Figure 4A). In some cases, T7 particles were not observed on the brush polymer surface even at low

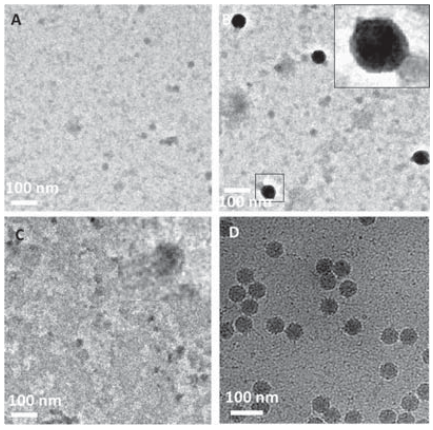

Figure 4. Effect of NTA surface density on His-T7 bacteriophage captured from cell lysates using negative stain and cryoEM analysis. (A) Negative stain TEM appearance of grid coated with stabilized 100% mPEG350-DTPE monolayer after 2 min exposure to cell lysate containing His-T7 bacteriophage; (B) same as in (A), except that the grid was coated with stabilized 1:99 Ni^{2+}:NTA-PEG2000-DSPE:mPEG350-DTPE monolayer; (C) same as in (B), except that the grid was rinsed with 500 mM imidazole, pH = 7.4, after the 2 min lysate exposure step; and (D) cryoEM appearance of grid coated with stabilized 5:95 Ni^{2+}:NTA-PEG2000-DSPE:mPEG-350-DTPE monolayer after 2 min exposure to cell lysate containing His-T7 bacteriophage.

DOI: 10.1021/acs.langmuir.5b03445
Langmuir 2016, 32, 551−559

magnification, suggesting a complete blockage of nonspecific adsorption. Grids bearing Ni^{2+}-charged 1:99 NTA-PEG2000-DTPE:mPEG350-DTPE stabilized monolayers were capable of capturing His_6-T7 bacteriophage from cell lysate while limiting the background adsorption of undesired nontarget cellular components (Figure 4B). It is worth noting that T7 viral particles often give mixed results of negative-stain and positive-stained particles since UO_2^{2+} salts may positively stain packaged nucleic acid within the capsid structure.[31] Exposure of these samples to 500 mM imidazole led to greatly decreased surface adsorption of His_6-T7 bacteriophage, suggesting that the interaction of phage particles with the supported NTA-lipid monolayer is Ni^{2+} specific (Figure 4C). We attribute the occurrence of the few remaining particles to either nonspecific adsorption to uncoated grid regions or particles that are avidly bound due to multivalent interactions between the phage particles and the NTA-PEG grafted surface. To compensate for particle capture efficiency limitations in samples prepared for cryogenic imaging[10] due to unfavorable kinetics and/or modest ligand−receptor affinities,[32] we examined 1:99 and 5:95 Ni^{2+}:NTA-PEG2000-DTPE:mPEG350-DTPE stabilized monolayer coated grids to determine whether the areal density of NTA ligands had a detectable influence on His_6-T7 bacteriophage capture efficiency. Using identical sample processing methods and incubation times, we qualitatively observed an increase in particle surface density with increasing Ni^{2+}:NTA-PEG2000-DTPE composition (unpublished data). Since this comparison was not performed in a side-by-side manner between 1:99 and 5:95 Ni^{2+}:NTA-PEG2000-DTPE:mPEG350-DTPE stabilized monolayers with the same lysate, it is conceivable that these findings may be the result of different virus titers in the His_6-T7 bacteriophage preparations. Nonetheless, these findings are consistent with the His_8-GFPuv experiments described above (Figure S4) showing that higher surface concentrations of affinity capture lipid produces greater areal densities of immobilized target on the NTA-modified surface, with the 5:95 Ni^{2+}:NTA-PEG2000-DTPE:mPEG350-DTPE stabilized monolayer coated grids being more suitable for cryoEM sample preparation (Figure 4D). The immobilization of both mature and immature T7 phage from lysate samples (Figure S8) highlights the potential of rapid purification using affinity grids toward studying dynamic processes, which may not be possible when visualizing purified samples generated using standard TEM sample preparations.

We next demonstrated the capture of the 50S *E. coli* ribosomal subunit,[10] His_6-RplL, directly from cell lysates onto grids coated with Ni^{2+}:NTA-PEG2000-DTPE:mPEG350-DTPE stabilized monolayers. Negative stain EM images of His_6-RplL lysate deposited onto grids coated with mPEG350-DTPE stabilized monolayers showed no appreciable target-specific adsorption onto the grid (Figure 5A). After LS deposition of 20:80 Ni^{2+}:NTA-PEG2000-DTPE:mPEG350-DTPE stabilized monolayers onto the grids, particles consistent with the size and various shapes of the 50S subunit were observed on the grid surface (Figure 5B). When 500 mM imidazole was added to samples containing the captured ribosomal particles on 20:80 Ni^{2+}:NTA-PEG2000-DTPE:mPEG350-DTPE stabilized monolayers, the previously adsorbed particles were eluted from the surface of the TEM grid (Figure 5C), consistent with the expectation that the interaction of His_6-RplL with the surface of the grid is Ni^{2+} specific. Using the same sample preparation procedure, cryoEM analysis revealed the capture of His_6-RplL from *E. coli* lysates (Figure 5D) as

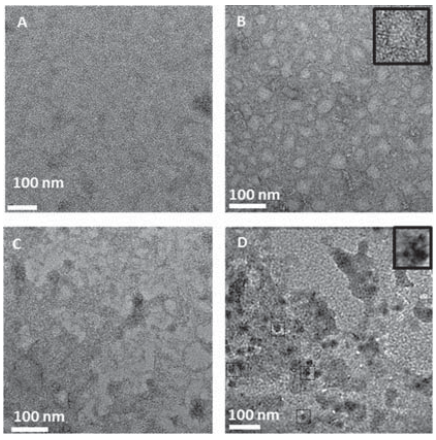

Figure 5. Affinity capture of His-RplL from cell lysates onto stabilized Ni^{2+}:NTA-PEG2000-DTPE:mPEG-350-DTPE monolayer coated grids. (A) Negative stain TEM of grid coated with stabilized 100% mPEG350-DTPE after 2 min exposure to cell lysate containing His-RplL; (B) negative stain TEM of grid coated with 20:80 Ni^{2+}:NTA-PEG2000-DSPE:mPEG350-DTPE after 2 min exposure to cell lysate containing His-RplL; (C) same as in (B), except that the grid was rinsed with 500 imidazole, pH = 7.4, after the 2 min exposure to cell lysate containing His-RplL; and (D) cryoEM image of grid coated with stabilized 5:95 Ni^{2+}:NTA-PEG2000-DSPE:mPEG-350-DTPE monolayer after 2 min exposure to cell lysate containing His-RplL.

crown-like projections in some images (Figure 5D). These have frequently been reported and are attributed to the 50S ribosomal subunit. The earliest reported TEM images of ribosomes were small, featureless bumps on the grid surface;[33] however, more powerful tools eventually led to the revelation of several features in the ribosomal units such as "crown-like" and "duck-like" projections for the 50S and 30S subunits, respectively.[34,35] Since the RplL protein carries the hexahistidine tag on the 50S subunit in our construct, we identified many more of these particles bound to the grid than the 30S subunit. Crown-like projections are clearly seen from the side view of the 50S particle with a central protuberance, a ridge, a stalk, and two groove-like features.

A key design feature of these stabilized affinity coatings is their utilization of two different types of poly(ethylene glycol)-modified lipids, one high molar ratio brush layer short segment to block nonspecific adsorption and facilitate stabilization via photopolymerization (i.e., mPEG350-DTPE) and a second low molar ratio component to enable multiple orientations of the captured protein target to avoid preferred orientations at the monolayer interface and provide a more representative single particle reconstruction analysis data set. We tested this hypothesis by preparing dozens of TEM grids bearing stabilized Ni^{2+}:NTA-PEG2000-DSPE:mPEG350-DTPE coatings that had been treated with His_6-RplL containing lysates. CryoEM evaluation of these grids confirmed that the NTA-PEG2000 tether is capable of both capturing and presenting multiple orientations of the bound His_6-RplL target as demonstrated by the overlay of the known 50S subunit and 70S complex structures in different rotational configurations (data not shown).

MSP have become an increasingly popular tool for stabilizing membrane protein dispersions since it provides a platform in

DOI: 10.1021/acs.langmuir.5b03445
Langmuir 2016, 32, 551−559

which the local environment of solubilized membrane proteins resemble the natural environment of the lipid bilayer in cells.[36] MSP are used to corral lipids and membrane proteins within disk-like structures containing a lipid bilayer interior that can host reconstituted membrane proteins for structure analysis by electron microscopy,[37,38] protein modification studies,[39] and protein activation analysis.[40] We used the purified hexahistidine-tagged maltose transporter, His_6-MalFGK$_2$, solubilized in MSP lipid nanodisc, for evaluating their affinity capture properties on NTA-modified stabilized affinity grids. Although His-tag MSP can be used for affinity purification,[41] we used a His_6-MalFGK$_2$ construct for nanodisc reconstitution to ensure that only nanodisc containing His_6-MalFGK$_2$ are surface immobilized. We found that mPEG350-DTPE stabilized monolayer coated grids treated with His_6-MalFGK$_2$ nanodisc appeared to have fewer particles bound to the grid surface (Figure 6A) than the grids coated with 1:99 Ni^{2+}:NTA-PEG2000-DTPE:mPEG350-DTPE stabilized monolayers (Figure 6B). Treatment of the His_6-MalFGK$_2$-immobilized grids with 500 mM imidazole produced a decrease in MSP nanodisc binding to the surface (Figure 6C), further suggesting that the interaction between nanodisc solubilized His_6-MalFGK$_2$ and the NTA-modified surface is Ni^{2+} specific. High magnification images of nanodisc solubilized His_6-MalFGK$_2$ immobilized onto 5:95 Ni^{2+}:NTA-PEG2000-DTPE:mPEG350-DTPE stabilized monolayers (Figure 6D) reveal a set of disc-like features in the size range of other lipid nanodisc dispersions (7−13 nm in diameter).[42] Although the His_6-MalFGK$_2$ within the MSP nanodiscs is not directly observed due to its small size relative to the nanodiscs, the fact that these features elute with 500 mM imidazole strongly corroborates the assumption that they contain His_6-MalFGK$_2$. In addition, our images show predominantly top/bottom views of the particles, i.e., a disk-like appearance in TEM micrographs (Figure 6D), suggesting that a longer PEG spacer is needed to collect a greater number of side views for this solubilized target.

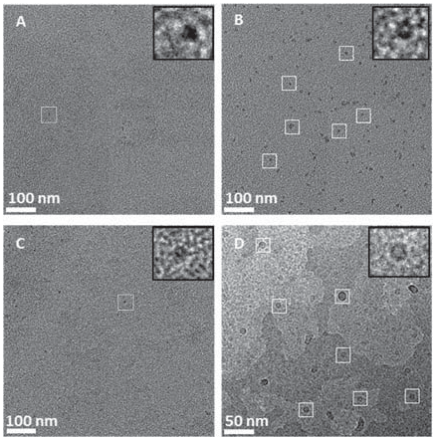

Figure 6. Affinity capture of MSP nanodisc containing purified His-MalFGK$_2$. (A) Negative stain TEM of stabilized 100% mPEG350-DTPE monolayer-coated grid after treatment with His-MalFGK$_2$ in nanodiscs; (B) negative stain TEM of His-MalFKG$_2$ in nanodisc captured on stabilized 1:99 Ni^{2+}:NTA-PEG2000-DSPE:mPEG350-DTPE monolayer-coated grid; (C) same as in (B), except that the grid was rinsed with 500 mM imidazole, pH = 7.4, after the His-MalFGK$_2$ in nanodisc exposure step; and (D) cryoEM of His-MalFGK$_2$ in nanodisc captured on stabilized 5:95 Ni^{2+}:NTA-PEG2000-DSPE:mPEG-350-DTPE monolayer-coated grid.

In order to test the durability of the stabilized monolayers toward detergent exposure, the modified grids were treated with either 0.03% Triton X-100 (CAC = 0.015%), 0.014% Tween 20 (CAC = 0.0072%), and 0.5% CHAPS (CMC = 0.49%) solutions for varying periods of time before TEM observation. Lipid monolayers adsorbed to solid substrates display better detergent resistance than lipid bilayers that are prone to disruption via lipid flip-flop.[43,44] Initial encounter of detergents with the outer bilayer leaflet results in fluidization and lipid flip-flop from the inner leaflet to the outer leaflet, eventually leading to complete solubilization of the bilayer structure.[44] Inhibition of flip-flop due to adsorption of a highly compressed monolayer onto the solid carbon substrate inhibits flip-flop processes, leading to improved detergent resistance.

Despite some evidence of enhanced detergent resistant of supported DLPC monolayers, prior attempts to produce TEM grids coated with mixed Ni^{2+}:NTA-DSG:DPLC monolayers showed that their exposure to harsher detergents such as Triton X-100, Tween-20, and CHAPS led to monolayer solubilization.[10] We tested the detergent resistance of our stabilized Ni^{2+}:NTA-PEG2000-DTPE:mPEG350-DTPE monolayer coatings under conditions where DLPC monolayers failed by using 0.03% Triton X-100, 0.014% Tween 20, and 0.5% CHAPS at 5, 15, and 30 min exposures to the detergent solutions. Negative stain TEM observation of the coatings after detergent exposure indicated that stabilized Ni^{2+}:NTA-PEG2000-DTPE:mPEG350-DTPE monolayer coatings remain intact after 30 min of incubation with Triton X-100, Tween-20, and CHAPS (Figure S6). In the case of Triton X-100, some holes in the monolayer were occasionally observed, but none were apparent in grids treated with Tween 20 or CHAPS. The capacity of these coatings to immobilize purified His_6-T7 bacteriophage after detergent exposure for 20 min indicated that a modest reduction in phage binding to the grid occurred; however, the immobilized His_6-T7 bacteriophage particles were bound specifically as indicated by their ability to be removed by elution with 500 mM imidazole (unpublished data).

Fluorescence microscopy analysis of detergent-treated Ni^{2+}:NTA-PEG2000-DTPE:mPEG350-DTPE monolayers revealed that the stabilized Ni^{2+} lipid monolayer coatings retained their ability to capture His_8-GFPuv. Pixel intensity data was collected over the entire fluorescence image (Figure 7) to best represent the overall specific capture capacity of the coating, regardless of whether it had been detergent compromised or not. In the case of Triton X-100 exposed samples, the fluorescence was occasionally enhanced near the grid edges, possibly as a result of solubilized or damaged monolayer near the center of the grid holes that were unable to capture His_8-GFPuv in those regions. We did not see this phenomenon with either CHAPS- or Tween 20-treated surfaces. These grids exhibited a uniform distribution of His_8-GFPuv fluorescence over the grid holes until the surfaces were treated with 500 mM imidazole to displace the immobilized protein. Despite the limitations of these stabilized Ni^{2+}:NTA-PEG2000-DTPE:mPEG350-DTPE monolayer coatings toward prolonged Triton X-100 exposure, our data indicates that histidine-tagged proteins can be reversibly immobilized even after detergent exposure. We infer from these findings that both the integrity of the stabilized lipid monolayer and the specific affinity capture of

DOI: 10.1021/acs.langmuir.5b03445
Langmuir 2016, 32, 551−559

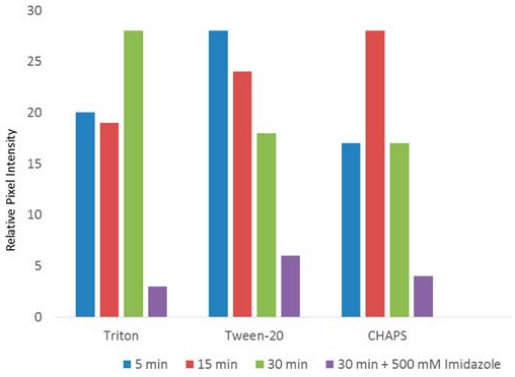

Figure 7. Effect of detergent exposure on 1:99 Ni^{2+}:NTA-PEG2000-DSPE:mPEG350-DTPE stabilized monolayer affinity grids as determined by fluorescence microscopy using His-GFP as a probe for NTA monolayer retention.

the grids remains intact after exposure to detergents that has proven detrimental to previously reported mixed Ni^{2+}:NTA-DGS:DLPC monolayers.[10]

CONCLUSIONS

Langmuir−Schaefer transfer of compressed, mixed lipid monolayers containing Ni^{2+}:NTA-PEG2000:mPEG350 headgroups in 1:99 and 5:95 molar ratios are capable of capturing His-tag protein targets from cell lysates with controllable areal densities and low degrees of nonspecific protein adsorption. Photopolymerization of the mPEG350-DTPE component in these monolayers by irradiating for 5 min at 254 nm produced EM grids with stabilized lipid coatings that were used to then used to capture His_6-T7 bacteriophage and His_6-RplL from cell lysates, purified His_8-GFPuv, and nanodisc embedded His_6-$MalFGK_2$. Our data indicate that the cross-linked lipid coating maintains the nonfouling properties of the monolayer and provides multiple orientations of the captured target on the surface, while also affording greater mechanical and detergent resistance than previously reported for EM grid-supported DLPC monolayers.

ASSOCIATED CONTENT

Supporting Information

The Supporting Information is available free of charge on the ACS Publications website at DOI: 10.1021/acs.langmuir.5b03445.

Pressure-area isotherms, negative stain TEM images, fluorescence microscopy, materials and experimental methods, and NMR spectra (PDF)

AUTHOR INFORMATION

Corresponding Author

*E-mail: davethom@purdue.edu.

Notes

The authors declare no competing financial interest.

ACKNOWLEDGMENTS

This paper is dedicated to the memory of Amy L. Davidson. The financial support of NIH Grant #R41GM098017 is gratefully acknowledged.

REFERENCES

(1) Bartesaghi, A. 2.2 A resolution cryo-EM structure of [beta]-galactosidase in complex with a cell-permeant inhibitor. *Science* **2015**, *348*, 1147−1151.
(2) Uzgiris, E. E.; Kornberg, R. D. Two-dimensional Crystallization Technique for Imaging Macromolecules, With Application to Antigen-Antibody Complement Complexes. *Nature* **1983**, *301*, 125−129.
(3) Thompson, D. H.; Zhou, M.; Grey, J.; Kim, H.-k. Design, Synthesis and Performance of NTA-Modified Lipids as Templates for Histidine-Tagged Protein Crystallization. *Chem. Lett.* **2007**, *36*, 956−975.
(4) Schmitt, L.; Dietrich, C.; Tampe, R. Synthesis and Characterization of Chelator-lipids for Reversible Immobilization of Engineered Proteins at Self-assembled Lipid Interfaces. *J. Am. Chem. Soc.* **1994**, *116*, 8485−8491.
(5) Kubalek, E. W.; Le Grice, S. F. J.; Brown, P. O. Two-dimensional Crystallization of Histidine-tagged, HIV-1 Reverse Transcriptase Promoted by a Novel Nickel-chelating Lipid. *J. Struct. Biol.* **1994**, *113*, 117−123.
(6) Dietrich, C.; Schmitt, L.; Tampe, R. Molecular Organization of Histidine-tagged Biomolecules at Self-assembled Lipid Interfaces Using a Novel Class of Chelator Lipids. *Proc. Natl. Acad. Sci. U. S. A.* **1995**, *92*, 9014−9018.
(7) Dietrich, C.; Boscheinen, O.; Scharf, K. D.; Schmitt, L.; Tampe, R. Functional Immobilization of a DNA-binding Protein at a Membrane Interface via Histidine Tag and Synthetic Chelator Lipids. *Biochemistry* **1996**, *35*, 1100−1105.
(8) Barklis, E.; McDermott, J.; Wilkens, S.; Schabtach, E.; Schmid, M.; Fuller, S.; Karanjia, S.; Love, Z.; Jones, R.; Zhao, X.; Rui, Y.; Thompson, D. H. Structural Analysis of Membrane-Bound Retrovirus Capsid Proteins. *EMBO J.* **1997**, *16*, 1199−1213.
(9) Barklis, E.; McDermott, J.; Wilkens, S.; Fuller, S.; Thompson, D. H. Organization of HIV-1 Capsid Proteins on a Lipid Monolayer. *J. Biol. Chem.* **1998**, *273*, 7177−7180.
(10) Kelly, D. F.; Abeyrathne, P. D.; Dukovski, D.; Walz, T. The Affinity Grid: A Pre-fabricated EM grid for Monolayer Purification. *J. Mol. Biol.* **2008**, *382*, 423−433.
(11) Kelly, D. F.; Dukovski, D.; Walz, T. Monolayer Purification: A Rapid Method for Isolating Protein Complexes for Single-particle Electron Microscopy. *Proc. Natl. Acad. Sci. U. S. A.* **2008**, *105*, 4703−4708.
(12) Dukovski, D.; Li, Z.; Kelly, D. F.; Mack, E.; Walz, T. Structural and Functional Studies on the Stalk of the Transferrin Receptor. *Biochem. Biophys. Res. Commun.* **2009**, *381*, 712−716.
(13) Kelly, D. F.; Dukovski, D.; Walz, T. Strategy for the Use of Affinity Grids to Prepare Non-His-Tagged Macromolecular Complexes for Single-Particle Electron Microscopy. *J. Mol. Biol.* **2010**, *400*, 675−681.
(14) Sharma, G.; Pallesen, J.; Das, S.; Grassucci, R.; Langlois, R.; Hampton, C. M.; Kelly, D. F.; des Georges, A.; Frank, J. Affinity Grid-based Cryo-EM of PKC Binding to RACK1 on the Ribosome. *J. Struct. Biol.* **2013**, *181*, 190−194.
(15) Boomer, J. A.; Inerowicz, H. D.; Zhang, Z.-Y.; Bergstrand, N.; Edwards, K.; Kim, J.-M.; Thompson, D. H. Acid-Triggered Release from Sterically-Stabilized Fusogenic Vesicles: A Novel DePEGylation Strategy. *Langmuir* **2003**, *19*, 6408−6415.
(16) Longo, G.; Thompson, D. H.; Szleifer, I. Ligand-Receptor Interactions Between Surfaces: The Role of Binary Polymer Spacers. *Langmuir* **2008**, *24*, 10324−10333.
(17) Shin, J.; Shum, P.; Grey, J.; Malhotra, G. S.; Fujiwara, S.; González-Bonet, A. M.; Moase, E.; Allen, T. M.; Thompson, D. H. Acid-labile PEG-Vinyl Ether-Lipids with Tunable pH Sensitivity: Synthesis and Structural Effects on Hydrolysis Rates, Calcein Release

Performance and Biodistribution of Their DOPE Dispersions. *Mol. Pharmaceutics* **2012**, *9*, 3266−3276.
(18) Zhou, M.; Haldar, S.; Franses, J.; Kim, J.-M.; Thompson, D. H. Synthesis and Self-Assembly Properties of Acylated Cyclodextrins and Nitrilotriacetic Acid (NTA)-Modified Inclusion Ligands for Interfacial Protein Crystallization. *Supramol. Chem.* **2005**, *17*, 101−111.
(19) Kang, E.; Park, J.-w.; McClellan, S.; Kim, J.-M.; Holland, D. P.; Lee, G. U.; Franses, E.; Park, K.; Thompson, D. H. Specific Adsorption of Histidine-Tagged Proteins on Silica Surfaces Modified with Ni2+:NTA-Derivatized Poly(ethylene glycol). *Langmuir* **2007**, *23*, 6281−6288.
(20) Yu, G.; Vago, F.; Zhang, D.; Snyder, J. E.; Yan, R.; Zhang, C.; Benjamin, C.; Jiang, X.; Kuhn, R. J.; Serwer, P.; Thompson, D. H.; Jiang, W. Single-step Antibody-based Affinity Cryo-Electron Microscopy for Imaging and Structural Analysis of Macromolecular Assemblies. *J. Struct. Biol.* **2014**, *187*, 1−9.
(21) Lee, J. H.; Kopecek, J.; Andrade, J. D. Protein-resistant Surfaces Prepared by PEO-containing Block Copolymer Surfactants. *J. Biomed. Mater. Res.* **1989**, *23*, 351−368.
(22) Jeon, S. I.; Andrade, J. D. Protein-Surface Interactions in the Presence of Polyethylene Oxide. *J. Colloid Interface Sci.* **1991**, *142*, 159−166.
(23) Malmsten, M.; Emoto, K.; Van Alstine, J. M. Effect of Chain Density on Inhibition of Protein Adsorption by Poly(ethylene glycol) Based Coatings. *J. Colloid Interface Sci.* **1998**, *202*, 507−517.
(24) Alvarez, F. J. D.; Orelle, C.; Davidson, A. L. Functional Reconstruction of an ABC Transporter in Nanodisc for use in Electron Paramagnetic Resonance Spectroscopy. *J. Am. Chem. Soc.* **2010**, *132*, 9513−9515.
(25) Boomer, J. A.; Qualls, M. M.; Inerowicz, H. D.; Haynes, R. H.; Patri, V. S.; Kim, J.-M.; Thompson, D. H. Cytoplasmic Delivery of Liposomal Contents Mediated by an Acid-labile Cholesterol-Vinyl Ether-PEG Conjugate. *Bioconjugate Chem.* **2009**, *20*, 47−59.
(26) Hansen, P. L.; Cohen, J. A.; Podgornik, R.; Parsegian, V. A. Osmotic Properties of Poly(Ethylene Glycols): Quantitative Features. *Biophys. J.* **2003**, *84*, 350−355.
(27) Ham, A. S. W.; Klibanov, A. L.; Lawrence, M. B. Action at a Distance: Lengthening Adhesion Bonds with Poly(ethylene glycol) Spacers Enhances Mechanically Stressed Affinity for Improved Vascular Targeting of Microparticles. *Langmuir* **2009**, *25*, 10038−10044.
(28) Nguyen, T. D. H.; Perrin, F.-X.; Nguyen, D. L. New Hybrid Materials Based on Poly(ethylene oxide)-Grafted Polysilazane by Hydrosilylation and Their Anti-fouling Activities. *Beilstein J. Nanotechnol.* **2013**, *4*, 671−677.
(29) Banerjee, I.; Pangule, R. C.; Kane, R. S. Antifouling Coatings: Recent Developments in the Design of Surfaces That Prevent Fouling by Proteins, Bacteria, and Marine Organisms. *Adv. Mater.* **2011**, *23*, 690−718.
(30) Agirrezabala, X.; Martin-Benito, J.; Caston, J. R.; Miranda, R.; Valpuesta, M.; Carrascosa, J. L. Maturation of phage T7 involves structural modification of both shell and inner core components. *EMBO J.* **2005**, *24*, 3820−3829.
(31) Ackermann, H. W.; Jolicoeur, P.; Berthiaume, L. Advantages and inconveniences of uranyl acetate in comparative virology: study of 4 tailed bacteriophages. *Can. J. Microbiol.* **1974**, *20*, 1093−1099.
(32) Kastner, B.; Fischer, N.; Golas, M. M.; Sander, B.; Dube, P.; Boehringer, D.; Hartmuth, K.; Deckert, J.; Hauer, F.; Wolf, E.; Uchtenhagen, H.; Urlaub, H.; Herzog, F.; Peters, J. M.; Poerschke, D.; Luhrmann, R.; Stark, H. Grafix: Sample Preparation for Single-particle Electron Microscopy. *Nat. Methods* **2007**, *5*, 53−55.
(33) Wittmann, H. G. Architecture of Prokaryotic Ribosomes. *Annu. Rev. Biochem.* **1983**, *52*, 35−65.
(34) Frank, J.; Zhu; Penczek, P.; Li, Y.; Srivastava, S.; Verschoor, A.; Radermacher, M.; Grassucci, R.; Lata, R. K.; Agrawal, R. K. A Model of Protein Synthesis Based on Cryo-electron Microscopy of the E. coli Ribosome. *Nature* **1995**, *376*, 441−444.
(35) Stark, H.; Mueller, F.; Orlova, E. V.; Schatz, M.; Dube, P.; Erdemir, T.; Zemlin, F.; Brimacombe, R.; van Heel, M. The 70S Escherichia coli Ribosome at 23Å Resolution: Fitting the Ribosomal RNA. *Structure* **1995**, *3*, 815−821.
(36) Baas, B. J.; Denisov, I. G.; Sligar, S. G. Homotropic Cooperativity of Monomeric Cytochrome P450 3A4 in a Nanoscale Native Bilayer Environment. *Arch. Biochem. Biophys.* **2004**, *430*, 218−228.
(37) Frauenfeld, J.; Gumbart, J.; van der Sluis, E. O.; Funes, S.; Gartmann, M.; ABeatrix, B.; Mielke, T.; Berninghausen, O.; Becker, T.; Schulten, K.; Beckman, R. Cryo-EM Structure of the Ribosome-SecYE Complex in the Membrane Environment. *Nat. Struct. Mol. Biol.* **2011**, *5*, 614−621.
(38) Pandit, A.; Shirzad-Wasei, N.; Wlodarczyk, L. M.; van Roon, H.; Boekema, E. J.; Dekker, J. P.; de Grip, W. J. Assembly of the Major Light-harvesting Complex II in Lipid Nanodiscs. *Biophys. J.* **2011**, *101*, 2507−2515.
(39) Leitz, A. J.; Bayburt, T. H.; Barnakov, A. N.; Springer, B. A.; Sligar, S. G. Functional Reconstitution of beta2-Adrenergic Receptors Utilizing Self-assembling Nanodisc Technology. *BioTechniques* **2006**, *40*, 601−612.
(40) Wang, Z.; Raines, L. L.; Hooy, R. M.; Roberson, H.; Leahy, D. J.; Cole, P. A. Tyrosine Phosphorylation of Mig6 Reduces its Inhibition of the Epidermal Growth Factor Receptor. *ACS Chem. Biol.* **2013**, *8*, 2372−2376.
(41) Shen, H.-H.; Lithgow, T.; Martin, L. L. Reconstitution of Membrane Proteins into Model Membranes: Seeking Better Ways to Retain Protein Activities. *Int. J. Mol. Sci.* **2013**, *14*, 1589−1607.
(42) Ly, S.; Bourguet, F.; Fischer, N. O.; Lau, E. Y.; Coleman, M. A.; Laurence, T. A. Quantifying Interactions of a Membrane Protein Embedded in a Lipid Nanodisc Using Fluorescence Correlation Spectroscopy. *Biophys. J.* **2014**, *106*, L5−L8.
(43) Ngassam, V. N.; Howland, M. C.; Sapuri-Butti, A.; Rosidic, N.; Parikh, A. N. A Comparison of Detergent Action on Supported Lipid Monolayers and Bilayers. *Soft Matter* **2012**, *8*, 3734−3738.
(44) Kragh-Hansen, U.; le Maire, M.; Moller, J. V. The Mechanism of Detergent Solubilization of Liposomes and Protein-Containing Membranes. *Biophys. J.* **1998**, *75*, 2932−2946.

DOI: 10.1021/acs.langmuir.5b03445
Langmuir 2016, 32, 551−559

www.nature.com/scientificreports

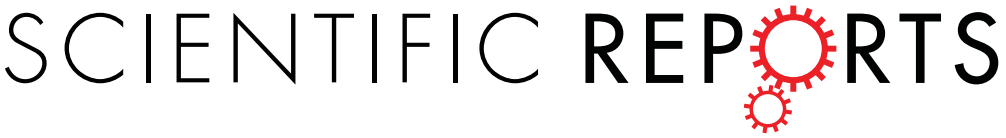

OPEN

Selective Capture of Histidine-tagged Proteins from Cell Lysates Using TEM grids Modified with NTA-Graphene Oxide

Received: 07 June 2016
Accepted: 08 August 2016
Published: 17 October 2016

Christopher J. Benjamin[1,*], Kyle J. Wright[1,*], Scott C. Bolton[1,*], Seok-Hee Hyun[1], Kyle Krynski[1], Mahima Grover[1], Guimei Yu[2], Fei Guo[2], Tamara L. Kinzer-Ursem[3], Wen Jiang[2] & David H. Thompson[1,3,4]

We report the fabrication of transmission electron microscopy (TEM) grids bearing graphene oxide (GO) sheets that have been modified with N^{α}, N^{α}-dicarboxymethyllysine (NTA) and deactivating agents to block non-selective binding between GO-NTA sheets and non-target proteins. The resulting GO-NTA-coated grids with these improved antifouling properties were then used to isolate His_6-T7 bacteriophage and His_6-GroEL directly from cell lysates. To demonstrate the utility and simplified workflow enabled by these grids, we performed cryo-electron microscopy (cryo-EM) of His_6-GroEL obtained from clarified *E. coli* lysates. Single particle analysis produced a 3D map with a gold standard resolution of 8.1Å. We infer from these findings that TEM grids modified with GO-NTA are a useful tool that reduces background and improves both the speed and simplicity of biological sample preparation for high-resolution structure elucidation by cryo-EM.

Single particle cryo-EM analysis (SPA) is a rapidly growing method for elucidating structure of biological materials at near atomic resolution[1,2] due to recent advances in instrumentation and computational algorithms[3]. One aspect of the SPA process that is not well optimized, however, is sample preparation. Traditionally, proteins targeted for structural analysis must be overexpressed and subjected to time-consuming purification and concentration steps, sometimes under harsh conditions that disrupt protein-protein interactions of interest. Recently, there have been efforts reported that seek to address these limitations, either by improving grid rigidity to reduce beam-induced motion[4–6] or by effecting on-grid purification with 'affinity grids'[7–10] that employ metal chelating lipids that were originally developed for two-dimensional protein crystallization at the lipid-water interface[11–14]. The latter approach seeks to selectively capture biological target molecules from complex mixtures such as cell lysates as an integral part of the TEM sample preparation process[10,15].

Although lipid monolayer affinity grids have shown some success in producing samples for cryo-EM reconstruction at 20 Å resolution[7], robust performance of the reported grid coatings may be limited by film instability and non-uniformity under the evaporative casting methods that are often employed. Additionally, these lipid films require a thin polymer layer or a holey carbon substrate layer to provide mechanical support of the deposited film. The electrical conductivity of monolayer graphene is six orders of magnitude higher than amorphous carbon, and although the level of conductivity in graphene decreases with the extent of oxidation, it has been shown to recover much of this conductivity upon reduction with H_2 plasma[9]. Additionally, unlike unsupported lipid monolayers, the elasticity of graphene makes it ideal to resist permanent deformation due to mechanical transfer techniques from the material-water interface. Our interest in utilizing graphene-based affinity substrates is focused on exploiting the superior mechanical strength and conductivity it offers. By conferring better target specificity to this substrate, affinity graphenic substrates have the potential to offer both improved stability and resistance to non-specific adsorption such that direct capture from cell lysates may be feasible.

[1]Department of Chemistry, Purdue University, West Lafayette, Indiana 47907, USA. [2]Department of Biological Sciences, Purdue University, West Lafayette, Indiana 47907, USA. [3]Weldon School of Biomedical Engineering, Purdue University, West Lafayette, Indiana 47907, USA. [4]Center for Cancer Research, Purdue University, West Lafayette, Indiana 47907, USA. *These authors contributed equally to this work. Correspondence and requests for materials should be addressed to D.H.T. (email: davethom@purdue.edu)

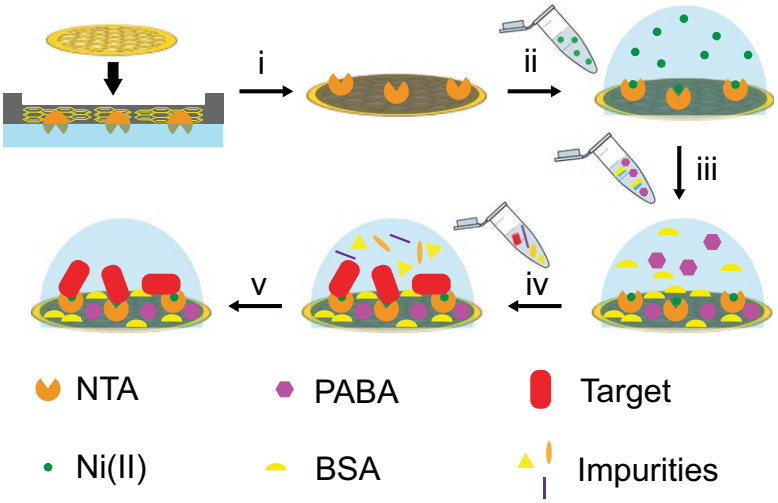

Figure 1. Conceptual diagram of sample preparation using a GO-NTA modified TEM grid. (i) GO-NTA monolayer deposition onto TEM grid via L-S transfer; (ii) activation of NTA with Ni^{2+}; (iii) blocking of non-specific reaction and/or adsorption sites with 4-aminobenzoic acid (PABA) and bovine serum albumin (BSA); (iv) incubation of clarified lysate with blocked grid; (v) washing of non-target molecules from grid, followed by cryo-fixation or staining.

We sought to address the limitations of lipid monolayer coated affinity grids by employing a GO derivative that minimizes background signal due to the single atom thickness and improved conductivity as a way to combat sample charging and instability during image capture[16]. Here we demonstrate the utility of affinity grids using Langmuir-Schaefer (L-S) transfer of GO monolayer sheets that have been functionalized with covalently linked N^{α}, N^{α}-dicarboxymethyllysine (GO-NTA). Using these affinity grids, we were able to selectively capture both His_6-T7 bacteriophage and His_6-GroEL. When the prepared grids were further modified with bovine serum albumin (BSA), a common antifouling agent that limits non-specific adsorption of non-targeted cellular debris, we were able to selectively capture these proteins directly from bacterial lysate while avoiding deposition of non-target proteins (Fig. 1).

Results and Discussion

Synthesis of GO Sheets Functionalized with NTA. GO was produced from graphene using Hummer's method[16]. Activation of the GO carboxylic acid groups with $SOCl_2$ prior to reaction with the tris-*t*-butyl ester of lysine NTA gave GO-NTA-(O-*t*-Bu)$_3$. TFA deprotection of this intermediate gave GO-NTA (Fig. 2A). Fourier transfer infrared spectroscopy was used to monitor these reactions as shown in Fig. 2B[17]. The spectra of GO displayed a broad absorption at 3236 cm^{-1} (O-H stretch) and a sharper absorption at 1648 cm^{-1} (C=O stretch)[16]. The NTA-GO tris-*t*-butyl ester displayed an additional absorption at 2933 cm^{-1} (C-H stretch) due to the incorporation of the lysine and *t*-butyl moieties. Following treatment of NTA-GO tris-*t*-butyl ester with TFA, the presence of the aliphatic C-H stretching was greatly reduced, indicating successful deprotection of the NTA chelator substituents[18].

Previous work has shown that the typical GO sheet absorption band at ~240 nm is shifted to ~270 nm when the GO sheets are dispersed in aqueous solution. The origin of this hypsochromic shift is due to n-π^* electronic transitions arising from the C=O bonds introduced by oxidation[19]. GO-NTA samples prepared in this manner exhibited a major absorption peak at ~280 nm (Figure S1), in good agreement with these reports.

GO-NTA Monolayer Formation. Most reports of Langmuir dispersions of GO at the air-water interface focus on surfactant-assisted dispersion methods to stabilize GO sheets dispersed in water[20]. Treatment of GO with surfactants in these cases; however, biases the interfacial activity towards water-surfactant activity rather than GO-NTA activity due to their high relative abundance. The planar structure and functional group distribution on GO-NTA confers edge amphiphilicity due to the distribution of hydrophilic carboxyl, ketone, aldehyde, amide, and alcohol groups around the periphery of the hydrophobic aryl GO-NTA core (Fig. 2A)[21]. Since GO-NTA becomes increasingly hydrophobic as displacement toward the core from the GO-NTA edge increases, larger sheets will tend to be more hydrophobic and migrate to the air-water interface, whereas smaller more hydrophilic GO-NTA sheets are displaced into the aqueous subphase by the larger GO-NTA sheets[22].

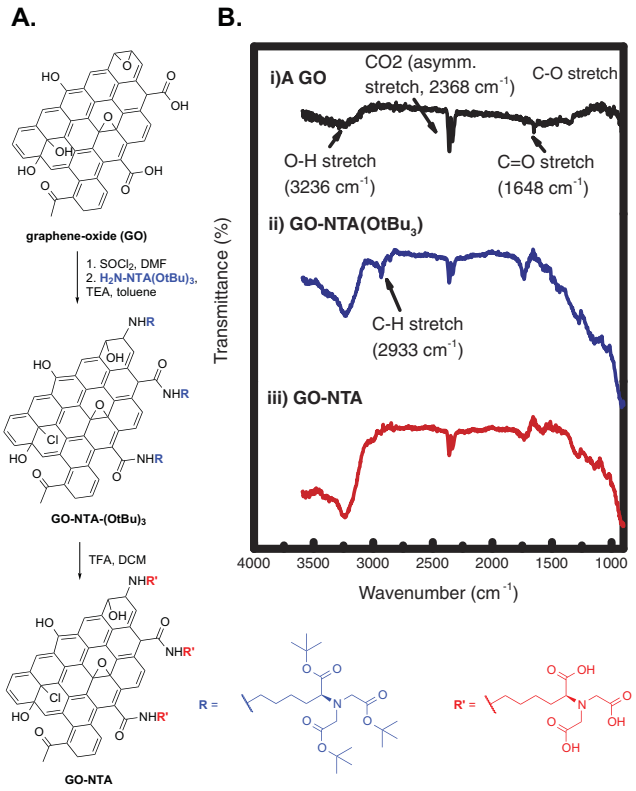

Figure 2. Synthesis and characterization of GO-NTA. (**A**) Reaction sequence for preparation of GO-NTA from GO. (**B**) FTIR spectra of (i) GO, (ii) GO-NTA (O-*t*-Bu)$_3$, and (iii) GO-NTA.

Previously, it was thought that the use of surface-active agents was needed to disperse GO sheets. More recent work; however, has shown that GO layers form at the air-water interface in the absence of surfactant molecules[23]. Brewster angle microscopy studies have shown that the interfacial refractive index of GO solutions change after a few hours of stirring pure GO dispersions in water[24]. This suggests a time-dependent mechanism for GO absorption at the air-water interface, with slower interfacial adsorption rates attributable to slower diffusion rates of large graphene sheets relative to typical surfactant molecules used for studies of the air-water interfaces. To increase the amount of surface-active graphene sheets present at the air-water interface while circumventing hours of stirring, studies using rising gas bubbles of CO_2 and N_2 as a way of transporting these sheets to the surface have proven successful[22]. These studies show that GO can migrate to the air-water interface, while other work suggests that the surface activity of GO sheets in water can be increased using volatile, polar protic solvents to enable their manipulation using Langmuir compression[23].

Compression of the GO-NTA material at the interface gave a characteristic surface pressure-area isotherm (Fig. 3A), suggesting a progression from isolated GO-NTA sheets to close edge-to-edge packing of GO-NTA sheets, followed by folding, wrinkling, and sliding of the nearest neighbor GO-NTA sheets atop one another upon further compression[25], in a manner analogous to pressure-induced collapse of Langmuir phospholipid monolayer films[23]. Repulsive electrostatic interactions and attractive van der Waals forces compete as GO-NTA sheets come into close contact. Previous work with GO monolayers has suggested that over-compression of GO causes irreversible coagulation above ~15 mN/m[23] due to the increasing participation of attractive van der Waals interactions once the repulsive electrostatic interactions between sheet edges has been overcome by lateral compression. Transfer of these films onto silicon substrates at multiple surface pressures enabled the transfer of single layer GO sheets at surface pressures above 15 mN/m.

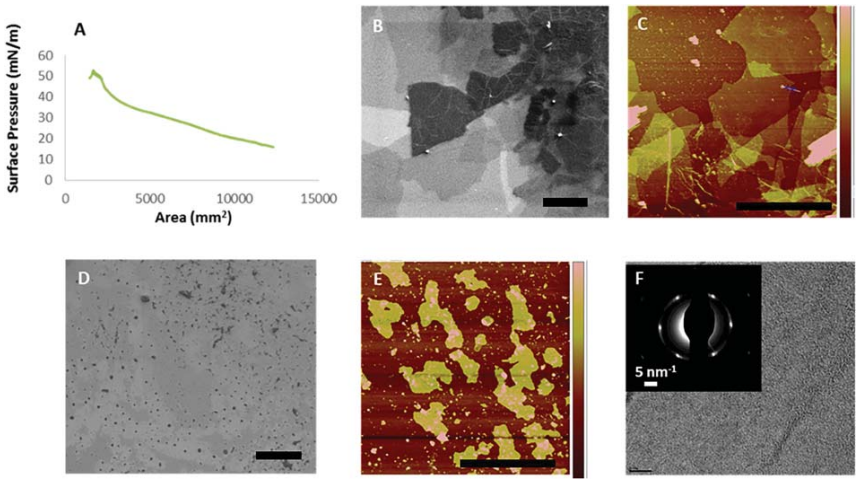

Figure 3. Characterization of GO-NTA surfaces. (**A**) Pressure-area isotherm for GO-NTA sheets at the air-water interface, dispersed at 67 ng/mL in water at 20 °C. GO-NTA sheets compressed at a rate of 500 mm^2/min. (**B**) SEM images taken 1.0 keV, with 5 μm scale bar and (**C**) AFM images of GO-NTA after LS-transfer onto Si wafers from a subphase of pure H_2O (5 μm scale bar). (**D**) SEM images taken at 0.5 keV (5 μm scale bar) and (**E**) AFM of GO-NTA after LS-transfer onto Si wafers from a subphase of IPA/H_2O (5 μm scale bar). (**F**) TEM image of GO-NTA monolayers after L-S transfer from a subphase of IPA/H_2O onto TEM grids; Inset: Selected area electron diffraction analysis of GO-NTA monolayer.

Characterization of GO-NTA Monolayers. Epifluorescence microscopy, AFM, and SEM was employed to determine the thickness and lateral distribution of GO-NTA sheets deposited onto solid substrates by L-S transfer from the air-water interface[26]. In particular, epifluorescence microscopy of F-PABA-GO-NTA monolayers proved useful because opacity of the graphene-based sheet is directly related to its thickness as revealed by analysis of monolayer-coated grid and negative control bare Cu TEM grid samples that showed significantly greater fluorescence intensity for grids coated with F-PABA-GO-NTA (Figure S2).

We then evaluated drop casting and L-S transfer deposition methods for the production of the thinnest films possible, while yielding films with the highest density of NTA capture ligands. Drop casting[26,27], followed by slow evaporation of solvent, resulted in a fluorescence signal that completely spanned the holes of Formvar-coated 400 mesh Cu grids (data not shown). Slow solvent evaporation enables GO sheets to settle on top of one another to form a multi-layered film covering the TEM grid holes. Although successful, our findings suggest that drop casting typically yields sheets that are too thick and heterogeneous for protein structure elucidation applications by cryoEM. L-S transfer in the presence of 2-propanol (IPA) proved successful for depositions onto 1500 mesh grids, both with and without Formvar coating; however, L-S transfers with pure water resulted in thicker heterogeneous coatings over a limited area of the holes. L-S transfer onto Si wafers under identical conditions confirmed the presence of multilayered films (Fig. 3B,D). We were not able to fabricate functional coatings with 400 mesh grids using L-S transfer, a finding we attribute to the mismatch between the average GO-NTA sheet size of ~16 μm × 16 μm and the 37 μm × 37 μm grid holes of these grids. It is worth noting that the GO-NTA sheet size can vary as a function of oxidation reaction duration and sonication time employed during GO synthesis[28].

To gain further insight into the structure of these GO-NTA films, SEM and AFM analyses were performed after compression to 15 mN/m and L-S transfer of GO-NTA monolayer sheets onto Si wafers. To prepare Si wafers for L-S transfer, ~2.25 cm^2 wafers were cut and glued (bottom side) onto a transfer tube. The surface pressure was maintained until the Si wafer contacted the monolayer; the film was then recompressed to 15 mN/m after the L-S transfer step. The area difference before and after L-S transfer indicated transfer efficiencies of 75–85%. Image analysis of the coated Si wafers revealed the presence of GO-NTA monolayer sheets transferred from IPA-containing subphases with ~1.3 nm thicknesses that were relatively uniform (Fig. 3D,E), in good agreement with previously reported values for single layer GO[29]. In the absence of IPA; however, data from SEM and AFM experiments revealed GO-NTA films comprised of overlapping sheets and undesirable layer thickness variations (Fig. 3B,C).

Selected area electron diffraction analysis of GO-NTA L-S films, deposited onto bare 2000 mesh grids from the air-IPA/H_2O interface, revealed a hexagonal diffraction pattern, indicative of a single layer of graphenic material (Fig. 3F). The measured intensity of the inner and outer peaks confirms the presence of a single GO-NTA layer (Figure S3)[27].

Affinity Capture of His_6-T7 Bacteriophage from *E. coli* Lysate Using GO-NTA Monolayer Purification and PABA + BSA as Antifouling Agents. The capacity of GO-NTA coated grids to capture His_6-T7 bacteriophage (His_6-T7) by affinity interaction was examined first by negative-stain TEM. After a 2 min exposure of purified His_6-T7 on GO-NTA modified 1500 mesh grids, dense clusters of phage particles were found on the GO-NTA surface in the absence of Ni^{2+} (Fig. 4A). Paradoxically, we observed fewer phage particles after charging the GO-NTA grids with Ni^{2+} (Fig. 4B). We attribute these findings to non-specific and random covalent coupling of lysine residues with epoxide and aldehyde residues on the GO sheets that are inactivated upon exposure to the metal ion[30]. To obviate this problem, we chemically deactivated these functional groups by treatment of GO-NTA with 4-aminobenzoic acid (PABA) after L-S transfer. The resulting PABA-GO-NTA grids showed a reduction in, but incomplete abrogation of, non-specific His_6-T7 binding under the same incubation conditions (Fig. 4C). When activated with Ni^{2+}, PABA-GO-NTA grids revealed a higher density of phage particles due to engagement of the NTA:Ni^{2+}:His_6 affinity interaction (Fig. 4D). To further enhance the anti-fouling properties of this material, we incubated the PABA-GO-NTA grids with BSA immediately before the affinity capture step. Under these conditions, BSA appears to complete the blockade of non-specific viral particle adsorption (Fig. 4E), suggesting that BSA inhibits non-specific binding more effectively than PABA modification. After Ni^{2+} activation of the BSA-blocked PABA-GO-NTA surfaces, we observed a recovery in His_6-T7 binding to the grids (Fig. 4F). To further demonstrate the Ni^{2+} dependence of this interaction, we treated the grid with 500 mM imidazole, leading to the elution of His_6-T7 from the grid (data not shown). Taken together, these findings demonstrate the importance of deactivating highly reactive chemical functionalities on the surface of GO prior to use in affinity capture experiments.

Next, we sought to capture His_6-T7 directly from clarified *E. coli* lysate. The engineered His-tag does not interfere with His_6-T7 infectivity, thereby enabling the infection of BL21 cells and viral replication *in vitro*. A negative control experiment demonstrated that Ni^{2+}-free BSA-PABA-GO-NTA grids resulted in little or no capture of phage and minimal background adsorption from non-targeted cellular material (Figure S4); however, Ni^{2+} activation prompted selective His_6-mediated binding of bacteriophage to the grid surface (Fig. 4G). As an additional control, the grid was washed with 500 mM imidazole after Ni^{2+}, but prior to incubation with lysate, to demonstrate that imidazole stripping of the metal ion results in the abrogation of His_6-T7 binding (Fig. 4H). These results indicate that BSA-PABA-GO-NTA coated grids are able to effectively purify His_6-T7 directly from clarified lysate on the grid using the reversible NTA:Ni^{2+}:His_6 affinity interaction.

Affinity Capture of GroEL From *E. coli* Lysate Using BSA-PABA-GO-NTA Monolayer Purification. The performance of antifouling BSA-PABA-GO-NTA coatings for high-resolution single particle reconstruction analysis was then evaluated by performing on-grid affinity capture of His_6-GroEL from *E. coli* lysates. As observed for His_6-T7 capture, specific binding of His_6-GroEL occurred only with Ni^{2+}-activated (Fig. 5B), but not Ni^{2+}-free (Fig. 5A) or 500 mM imidazole treated grids (Fig. 5C). Next, we obtained cryo-EM images of His_6-GroEL deposited onto BSA-PABA-GO-NTA coated grids (Fig. 5D). Initial attempts at His_6-GroEL capture and cryofixation on 1500 mesh grids coated with BSA-PABA-GO-NTA generated unacceptably thick sample vitrification; however, high quality samples of His_6-GroEL captured from lysate were afforded by BSA-PABA-GO-NTA films deposited by L-S transfer onto lacey carbon-supported 400 mesh copper grids.

Single Particle Analysis of His_6-GroEL. EMAN 2.1[31] was used for single particle analysis of His_6-GroEL deposited onto BSA-PABA-GO-NTA coated grids since this protein target is often used for gauging workflow performance and data processing robustness[32–34]. The reconstruction effort followed the usual steps from within the application, except that the particles were manually picked. Background signal contributions by the BSA blocking layer may have contributed to the difficulties encountered during attempts at automated particle picking. Nonetheless, 5363 particles were hand-picked from 217 micrographs and the particles rapidly converged into coherent classes displaying high contrast (Fig. 6A).

Of 50 total class averages, 12 were chosen to produce an initial model with imposed D7 symmetry (Fig. 6A). After 12 refinement iterations with an angular sampling of 1.76 degrees, we were able to produce a gold standard (0.143 criteria) density map having 8.1 Å resolution using conservative masking (Fig. 6B–D). There were visible nodes in the FSC curve at regular intervals that resulted from an uneven distribution of micrograph defocuses.

To probe the accuracy of our model, we performed a comparison with published 4.2 Å resolution cryo-EM map EMD-5001[34] that was also produced by EMAN using D7 symmetry. Chimera[35] was used to fit the volumes before calculating the FSC, yielding a 9 Å resolution using 0.5 criteria (Fig. 6D–F).

A substantial difference between our map and the published structure was observed, wherein additional electron density within the inner pore of the protein was found in the case of our His_6-GroEL map. We attribute this finding to the extended amino acid sequences at the N- and C-termini (i.e., MRGSHHHHHHTDPALRA and GLCGR, respectively) of our His_6-GroEL construct derived from the ASKA Library.

Wild type N- and C-termini of the protomers are located at the surface of the inner pore lining the assembled tetradecameric complex. Thus, the 14 engineered subunits comprising our His_6-GroEL complex yield an additional 308 residues that occupy the pore, of which 84 are histidines. Given the large number of potential metal chelation regioisomers and topoisomers, as well as the high potential for conformational flexibility in the N- and C-terminal sequences, we believe that this density is unlikely to adopt a defined structure and instead appears as a filled "droplet" within each ring. Also, there is a noticeable decrease in density in the flexible apical region that suggests less structural coherency. We infer from these findings that the additional pore residues, along with NTA chelation, may create dynamic distortions to the structure of GroEL that could vary for each particle, reducing coherency and map density at the apical ends. Further experiments that vary the length and number of his-tag linkers per particle may allow for a better model convergence with improved resolution, and potentially improved resemblance to wild type GroEL.

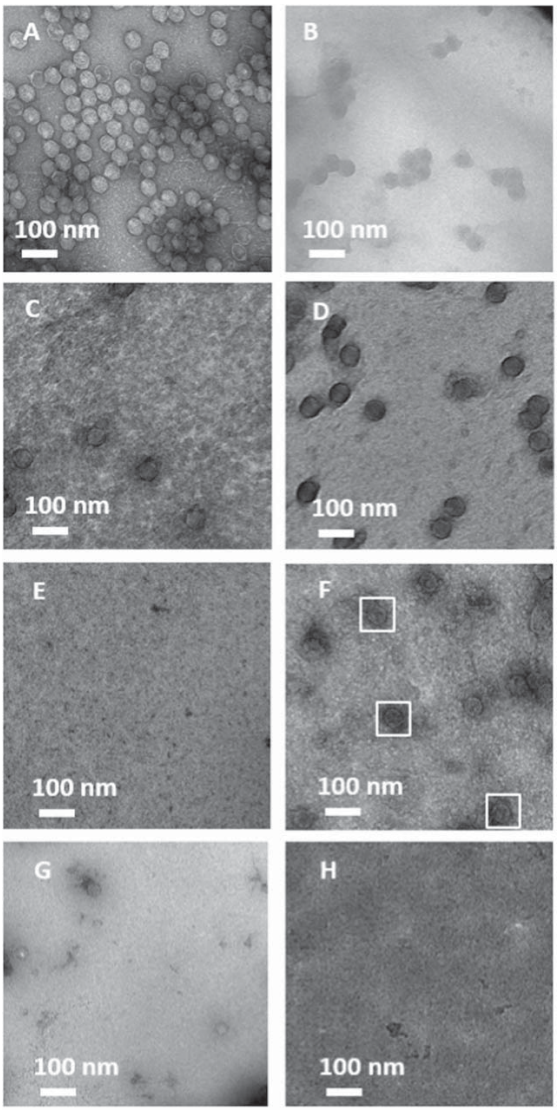

Figure 4. Micrographs of negatively stained his_6-T7 bacteriophage using various TEM grid coatings: (**A**,**B**) GO-NTA; (**C**,**D**) PABA-GO-NTA; and (**E**–**H**) BSA-PABA-GO-NTA. Negative controls (**A**,**C**,**E**) demonstrate no capture of purified phage when Ni^{2+} is absent, whereas coatings treated with Ni^{2+} (**B**,**D**,**F**) show capture of purified phage. Affinity capture of phage from lysate (**G**) can be reversed by incubation of (**G**) with 500 mM imidazole (**H**) that removes the Ni^{2+} from the coating and abrogates the affinity interaction between the phage and the grid surface.

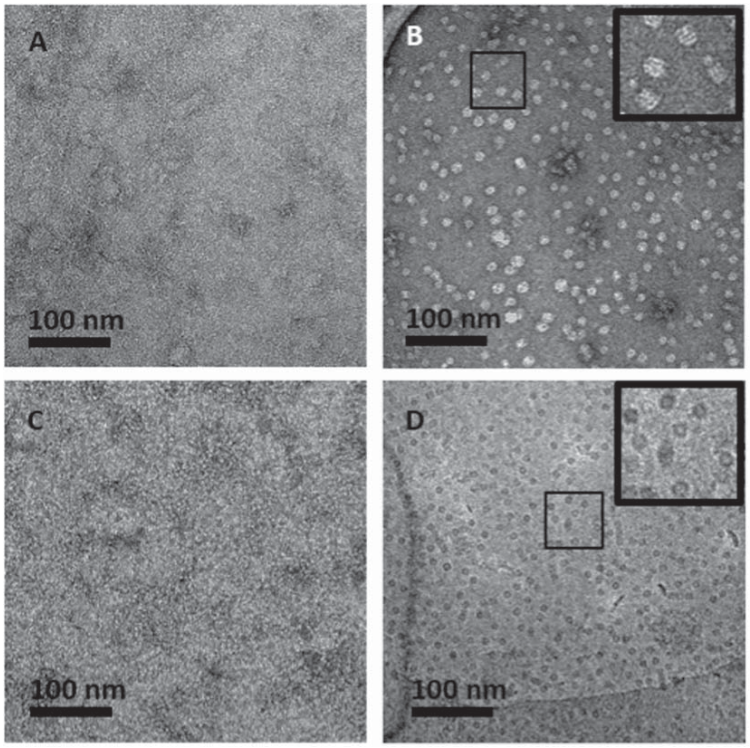

Figure 5. Micrographs of his_6-GroEL lysate affinity capture using BSA-PABA-GO-NTA TEM grid coating. Micrographs (**A–C**) are negatively stained. (**A**) Negative control showing no capture of his_6-GroEL when Ni^{2+} is absent. (**B**) Affinity coating activated with Ni^{2+} displays specific capture of his_6-GroEL from lysate. Treatment of the grid in (**B**) with 500 mM imidazole (**C**) leads to Ni^{2+} stripping from the coating and abrogation of his_6-GroEL capture. (**D**) Representative cryo-EM image of affinity captured his_6-GroEL from lysate.

Conclusions

Our findings show that a new functionalized GO-NTA monolayer sheet can be used as a coating to facilitate on-grid affinity purification from clarified cell lysates for negative stain TEM and cryo-EM single particle reconstruction analysis. GO sheets were successfully functionalized with lysine-NTA affinity ligands and compressed monolayer films at the air-water interface were prepared by employing an IPA/H_2O mixture to lower surface tension before L-S transfer onto EM grids. SEM, AFM, fluorescence spectroscopy, and TEM analysis of these films suggests that single monolayer sheets of GO-NTA can be transferred onto Si wafers, bare copper grids, and holey carbon grids using this method. Since GO films are thinner than amorphous carbon substrates and offer better electron dissipation than lipid-based affinity grids, we believe these two benefits will yield improved contrast for cryo-EM image acquisition of biological molecules.

Two blocking techniques, PABA coupling and BSA adsorption, were needed to deactivate the reactive GO surface towards non-specific adsorption of occult impurities present in complex samples such as cell lysates. Our data shows that further investigations into blocking agents that minimize background noise and improve cryofixation reliability are needed. Nonetheless, this grid coating approach showed good specificity for capture of His-tagged T7 bacteriophage and GroEL from highly complex cell lysates, while limiting background adsorption of non-targeted cellular material.

The utility of these grids for on-grid purification from cell lysates and single particle reconstruction was demonstrated using His_6-GroEL. Capture of this target onto the surface of GO-NTA affinity grids from clarified cell lysates was then used as the key step to enable selection of 5363 particles for reconstruction analysis, yielding a map with a gold standard resolution of 8.1 Å. The presence of additional His-tag and linker amino acids in our

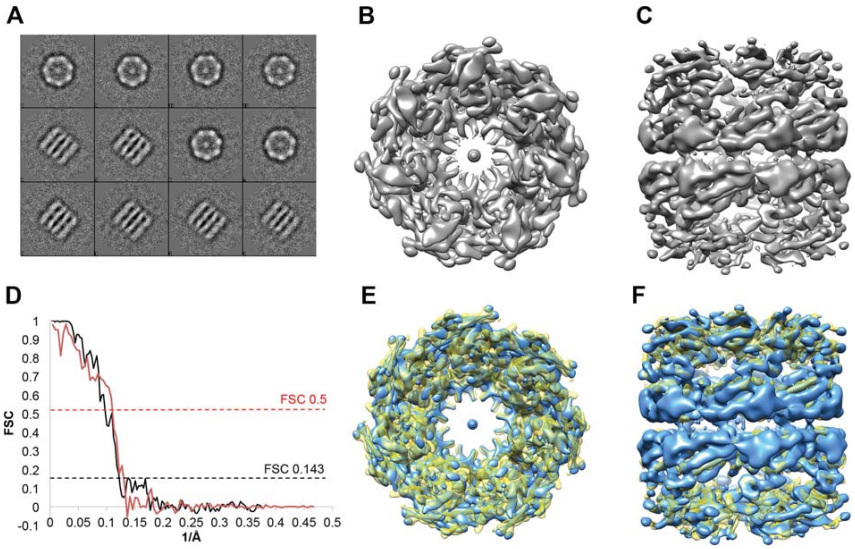

Figure 6. SPA of his6-GroEL captured from lysate. (**A**) Class averages of his_6-GroEL images captured from BSA-PABA-GO-NTA coated grids that were used to build the initial model; (**B**) Top and (**C**) side views of refined his_6-GroEL EM map at 8.1 Å resolution (gold standard, 0.143 criteria); (**D**) Fourier Shell Correlations: gold standard using conservative masking (black), and cross-validation between published GroEL map EMD-5001 and our map (red); (**E**) Top and (**F**) side views of overlay with our his_6-GroEL EM map (blue) and EMD-5001 (yellow)[34].

engineered GroEL was distinctly visible in our density map, but our final map could still be fit to a published high-resolution EM map to 9 Å resolution using 0.5 criteria. We conclude based on these findings that affinity capture-based graphenic materials offer great potential for simplified and accelerated cryo-EM sample preparation for high-resolution structure elucidation. These coatings possess many advantages over NTA-lipid-modified grids[7,8] or other grid coatings that lack protection from non-specific binding[4–6], thereby offering substantial improvements in sample preparation time and reduced sample volumes needed to acquire high resolution structural information of a given protein target and, potentially, its interaction partners.

Experimental Methods

Graphene-Oxide-NTA Synthesis. GO was synthesized as described by Marcano *et al.*[16]. This intermediate (335 mg) was stirred in a mixture of $SOCl_2$ (60 mL) and DMF (1.5 mL) at 70 °C for 3 d before evaporating the $SOCl_2$ and DMF and washing the residue with dry DCM (3 × 50 mL). ACN (50 mL) and Et_3N (3 mL) were then added and the mixture stirred for 30 min. Tris(O-*t*-butyl)-N^{α},N^{α}-dicarboxymethyllysine ester (533 mg) was then added and the mixture stirred at 100 °C for 3 d before washing with THF and H_2O (9,000 rpm for 15 min, 3 times for each solvent), and vacuum drying at 60 °C for 24 h. TFA (10 mL) in THF (30 mL) was added to the dried *t*-butyl-NTA ester intermediate (180 mg) and stirred at 60 °C for 5 h before washing with THF and H_2O (11,000 rpm × 15 min, 3 times for each solvent)[29,36].

GO-NTA Exfoliation. The GO-NTA sheets were ultrasonically exfoliated at 1 mg/mL by suspension of the powder in 5:1 MeOH:H_2O using probe sonication at 150 watts for five cycles (45 s sonication followed by 45 s of rest in each cycle). The product was centrifuged at 1200 g for 10 min, after which the supernatant of exfoliated GO-NTA sheets was removed from the sediment of aggregated sheets and subjected to another 5 rounds of sonication. A final centrifugation at 1200 g for 10 min was performed prior to removal of the supernatant to yield a GO-NTA solution that was stored for subsequent grid coating experiments.

Langmuir-Trough Setup. Exfoliated GO-NTA was deposited at the air-water interface of a Kibron μTrough via a syringe pump fitted with a 20 mL syringe. The GO-NTA dispersion was loaded into the syringe and slowly introduced at the air-water interface at a rate of 100 μL/min until the surface pressure reached 15 mN/m. The film was then allowed to relax for 5 min, followed by slow compression of the film to 15 mN/m. IPA was then added

to the subphase and the film transferred to either Si wafers, bare 1500 mesh TEM grids, or holey carbon grids by Langmuir-Schaefer (L-S) transfer.

4-Aminobenzoic acid (PABA) Modification of GO-NTA. GO-NTA (1 mg/mL) was partially deactivated by adding PABA (30 mg) to a 10 mL GO-NTA dispersion. This mixture was probe sonicated at 150 W for 30 sec of continuous sonication, followed by shaking for 24 h on a rotary mixer. The PABA-GO-NTA was then exfoliated and washed as described above for GO-NTA exfoliation.

Fluorescein Modification. Fluorescein modification of GO-NTA was performed by adding 2 mg of aminofluorescein to an aqueous solution of PABA-GO-NTA (10 mL at 1 mg/mL). This mixture was probe sonicated for 30 s at 150 W of continuous sonication and then placed on a rotary mixer in the dark for another 24 h. The material was then centrifuged to pellet the GO species before re-suspending in water, addition of 5:1 MeOH:H_2O, re-pelleted, and decanted a total of 10 times before exfoliation of the Fluorescein-PABA-GO-NTA (F-PABA-GO-NTA) product as described above for GO-NTA.

Bovine Serum Albumin (BSA) Modification. Following L-S transfer of GO-NTA or PABA-GO-NTA onto EM grids and overnight drying in a desiccator, the grids were placed on a strip of Teflon before addition of BSA (10 μL of 0.1 mg/mL) and incubation for 5 min, followed by 3 × 20 μL double deionized H_2O washes. The modified grids were then stored in a desiccator until use.

Fluorescence Microscopy Sample Preparation. F-PABA-GO-NTA was deposited onto 1500 mesh grids in the dark by L-S transfer as described above. After transfer, the grids were allowed to dry in the dark for 1 d before sandwiching them between a glass and cover slip with 5 μL of double deionized H_2O and the sandwich sealed with nail polish. The glass slide was then mounted on a light microscope for epifluorescence imaging.

GO Concentration Measurements. The concentrations of the GO-NTA dispersions were measured at different steps of the synthesis by monitoring the UV-vis spectra of the products. The extinction coefficient data used for one batch of GO-NTA is shown (Fig. S1A). Since each batch of GO-NTA has minor differences in concentration, each preparation was evaluated for its own experimentally determined extinction coefficient for subsequent concentration measurements. Standard solutions used to determine the extinction coefficients were prepared by dispersing a weighed amount of dry GO-NTA into known volumes of 5:1 MeOH:H_2O and measuring the absorbance at 280 nm across a series of dilutions with 5:1 MeOH:H_2O. The extinction coefficient was derived from the slope of these concentration-dependent absorption plots.

GO-NTA Grid Treatment with Purified His_6-T7 Bacteriophage. Purified C-terminal gp10 His_6-T7 bacteriophage was initially prepared at a concentration of 10^{12} particles/mL, with dilution to 10^{10} particles/mL in HEPES buffer (pH = 7.4), before application to the affinity grid surface. GO-NTA modified grids were placed on a Teflon strip, 1 mM $NiSO_4$ (10 μL) added, and the grids incubated for 5 min before washing with double deionized H_2O (2 × 20 μL) and HEPES buffer (1 × 20 μL). Purified phage (3.5 μL) was then applied to the surface and incubated for 2 min before washing with HEPES (2 × 20 μL), double deionized H_2O (1 × 20 μL), and staining with 2% uranyl acetate (5 μL).

GO-NTA Grid Treatment with His_6-T7 Bacteriophage Lysate. BL21 bacterial cells in 1 mL of LB media were grown to an OD of 0.8 before adding 1.0 μL of His_6-T7 bacteriophage (1 × 10^{12} particles/mL) to the media and shaking the culture for 1 h. After bench top centrifugation of the cells, the supernatant was withdrawn for use in His_6-T7 bacteriophage particle capture studies. The grids were Ni^{2+}-activated as described above, except that His_6-T7 lysate (5 μL) was applied to the surface before incubation for 2 min. The grids were then washed with HEPES (2 × 20 μL), double deionized H_2O (1 × 20 μL), and then stained with 2% uranyl acetate (5 μL).

GO-NTA Grid Treatment with His_6-GroEL Lysate. The ASKA Library was used to express N-terminal His_6-GroEL. Cells containing N-His_6-GroEL gene overexpression vector were grown to OD = 0.6 (in 100 mL of LB broth using a 37 °C shaker/incubator) and induced with a final concentration of 1.0 mM IPTG, before allowing the cells to grow for an additional 4 h. After centrifugation and removal of the supernatant, the cell pellet was re-suspended in lysis buffer (20 mM HEPES, 100 mM NaCl, pH = 7.4, 100 μg aprotinin, 174 μg phenylmethanesulfonyl fluoride (PMSF), and 500 μg of lysozyme) and allowed to sit for 20 min. Further disruption of the cell membranes was effected by 110 W probe sonication (35 pulses at 1 second/pulse), followed by centrifugation at 11,000 g for 10 min. The supernatant containing His_6-GroEL was diluted 10-fold and assayed for affinity binding using the Ni^{2+}-activation procedure described above, except that N-His_6-GroEL lysate (5 μL) was applied to the surface and incubated for 2 min. The grids were then washed and stained with 2% uranyl acetate as described above.

Affinity Capture of His_6-GroEL from *E. coli* Lysates onto BSA-PABA-GO-NTA Grids for Cryo-EM Imaging. Samples were prepared as described above for negative stain TEM imaging, except that BSA-PABA-GO-NTA modified grids were exposed to His_6-GroEL lysate, after which the excess solution was removed by blotting twice for 6 s per blot using an offset setting of −1 at 80% humidity using a Vitrobot device (FEI Company). The grids were then plunged into liquid ethane for cryofixation and imaged at 300 kV on an FEI Titan Krios equipped with a Gatan K2 Summit direct electron detection camera using low-dose techniques. Integrated microscope automation software (Leginon)[37] was used to acquire a large set of micrographs at 11,000x magnification with an exposure time of 7.6 sec.

Single Particle Analysis of His_6- GroEL. Direct electron detector movie frames were processed in Appion[38] to produce a set of averaged, motion-compensated micrographs to be used in subsequent steps. The micrographs had a 1.32 $Å^2$/pixel resolution across a 4096 Å × 4096 Å array. EMAN 2.1 software[31] was used for reconstruction of 5363 particles that were manually picked from 217 micrographs using a box size of 256. Automatic contrast transfer function (CTF) estimation and structure factor were determined from the incoherent sum of particles using e2ctf and phase-flipped to generate high-pass CTF-corrected particle stacks. Defocus was estimated to range between 0.4 μm–4 μm, but 55% of the particles were defocused between 2 μm–3 μm which resulted in a somewhat jagged CTF slope. Particles were binned 2X for class averaging and 12 classes were chosen to create an initial model with imposed D7 symmetry. The classes contained a mix of top and side views. In the refinement steps, the input set of particles was divided into even/odd halves, each containing 2682 particles. Two independent refinements were generated, producing a gold standard of 8.1 Å (using 0.143 criteria) after 12 iterations over two refinements with an angular sampling of 1.76 degrees. Additionally, we performed Fourier shell correlation against an existing high-resolution cryo-EM map, EMD-5001[34]. The maps were rotated and translated using Chimera[35] to fit the volumes together. The correlation of our model against EMD-5001 (4.2 Å) gave an approximate resolution of 9 Å.

References

1. Bartesaghi, A. *et al.* 2.2 A resolution cryo-EM structure of beta-galactosidase in complex with a cell-permeant inhibitor. *Science* **348,** 1147–1151, doi: 10.1126/science.aab1576 (2015).
2. Banerjee, S. *et al.* 2.3 A resolution cryo-EM structure of human p97 and mechanism of allosteric inhibition. *Science* **351,** 871–875, doi: 10.1126/science.aad7974 (2016).
3. Cheng, Y., Grigorieff, N., Penczek, Pawel A. & Walz, T. A primer to single-particle cryo-electron microscopy. *Cell* **161,** 438–449, doi: 10.1016/j.cell.2015.03.050 (2015).
4. Russo, C. J. & Passmore, L. A. Controlling protein adsorption on graphene for cryo-EM using low-energy hydrogen plasmas. *Nature Methods* **11,** 649–652, doi: 10.1038/nmeth.2931 (2014).
5. Meyerson, J. R. *et al.* Self-assembled monolayers improve protein distribution on holey carbon cryo-EM supports. *Scientific Reports* **4,** 7084, doi: 10.1038/srep07084 (2014).
6. Russo, C. J. & Passmore, L. A. Ultrastable gold substrates: Properties of a support for high-resolution electron cryomicroscopy of biological specimens. *Journal of Structural Biology* **193,** 33–44, doi: 10.1016/j.jsb.2015.11.006 (2016).
7. Kelly, D. F., Dukovski, D. & Walz, T. Monolayer purification: a rapid method for isolating protein complexes for single-particle electron microscopy. *Proceedings of the National Academy of Sciences of the United States of America* **105,** 4703–4708, doi: 10.1073/pnas.0800867105 (2008).
8. Kelly, D. F., Dukovski, D. & Walz, T. Strategy for the use of affinity grids to prepare non-His-tagged macromolecular complexes for single-particle electron microscopy. *Journal of Molecular Biology* **400,** 675–681, doi: 10.1016/j.jmb.2010.05.045 (2010).
9. Kutsay, O. *et al.* Surface properties of amorphous carbon films. *Diamond and Related Materials* **17,** 1689–1691, doi: 10.1016/j.diamond.2008.02.020 (2008).
10. Kelly, D. F., Abeyrathne, P. D., Dukovski, D. & Walz, T. The affinity grid: a pre-fabricated EM grid for monolayer purification. *Journal of Molecular Biology* **382,** 423–433, doi: 10.1016/j.jmb.2008.07.023 (2008).
11. Kubalek, E. W., Le Grice, S. F. & Brown, P. O. Two-dimensional crystallization of histidine-tagged, HIV-1 reverse transcriptase promoted by a novel nickel-chelating lipid. *Journal of Structural Biology* **113,** 117–123, doi: 10.1006/jsbi.1994.1039 (1994).
12. Schmitt, L., Dietrich, C. & Tampe, R. Synthesis and characterization of chelator-lipids for reversible immobilization of engineered proteins at self-assembled lipid interfaces. *Journal of the American Chemical Society* **116,** 8485–8491, doi: 10.1021/ja00098a008 (1994).
13. Barkļis, E. *et al.* Structural analysis of membrane-bound retrovirus capsid proteins. *The EMBO Journal* **16,** 1199–1213, doi: 10.1093/emboj/16.6.1199 (1997).
14. Thompson, D. H., Zhou, M., Grey, J. & Kim, H.-k. Design, synthesis, and performance of NTA-modified lipids as templates for histidine-tagged protein crystallization. *Chemistry Letters* **36,** 956–975, doi: 10.1246/cl.2007.956 (2007).
15. Benjamin, C. J. *et al.* Nonfouling NTA-PEG-based TEM grid coatings for selective capture of histidine-tagged protein targets from cell lysates. *Langmuir* **32,** 551–559, doi: 10.1021/acs.langmuir.5b03445 (2016).
16. Marcano, D. C. *et al.* Improved synthesis of graphene oxide. *ACS Nano* **4,** 4806–4814, doi: 10.1021/nn1006368 (2010).
17. Zhang, J., Yu, J. G., Jaroniec, M. & Gong, J. R. Noble metal-free reduced graphene oxide-$Zn_xCd_{1-x}S$ nanocomposite with enhanced solar photocatalytic H-2-production performance. *Nano Letters* **12,** 4584–4589, doi: 10.1021/Nl301831h (2012).
18. Wang, G. X. *et al.* Synthesis of enhanced hydrophilic and hydrophobic graphene oxide nanosheets by a solvothermal method. *Carbon* **47,** 68–72, doi: 10.1016/j.carbon.2008.09.002 (2009).
19. Paredes, J. I., Villar-Rodil, S., Martínez-Alonso, A. & Tascón, J. M. D. Graphene oxide dispersions in organic solvents. *Langmuir* **24,** 10560–10564, doi: 10.1021/la801744a (2008).
20. Gengler, R. Y. *et al.* Large-yield preparation of high-electronic-quality graphene by a Langmuir-Schaefer approach. *Small* **6,** 35–39, doi: 10.1002/smll.200901120 (2010).
21. Kim, J. *et al.* Graphene oxide sheets at interfaces. *Journal of the American Chemical Society* **132,** 8180–8186, doi: 10.1021/ja102777p (2010).
22. Cote, L. J. *et al.* Graphene oxide as surfactant sheets. *Pure and Applied Chemistry* **83,** 95–110, doi: 10.1351/Pac-Con-10-10-25 (2011).
23. Cote, L. J., Kim, F. & Huang, J. Langmuir-Blodgett assembly of graphite oxide single layers. *Journal of the American Chemical Society* **131,** 1043–1049, doi: 10.1021/ja806262m (2009).
24. Kim, J., Cote, L. J. & Huang, J. Two dimensional soft material: new faces of graphene oxide. *Accounts of Chemical Research* **45,** 1356–1364, doi: 10.1021/ar300047s (2012).
25. Zheng, Q. *et al.* Structure control of ultra-large graphene oxide sheets by the Langmuir-Blodgett method. *RSC Advances* **3,** 4680–4691, doi: 10.1039/C3RA22367A (2013).
26. Ni, Z. H. *et al.* Graphene thickness determination using reflection and contrast spectroscopy. *Nano Letters* **7,** 2758–2763, doi: 10.1021/nl071254m (2007).
27. Wilson, N. R. *et al.* Graphene oxide: structural analysis and application as a highly transparent support for electron microscopy. *ACS Nano* **3,** 2547–2556, doi: 10.1021/Nn900694t (2009).
28. Pan, S. Y. & Aksay, I. A. Factors controlling the size of graphene oxide sheets produced via the graphite oxide route. *ACS Nano* **5,** 4073–4083, doi: 10.1021/Nn200666r (2011).
29. Song, J. P., Qiao, J., Shuang, S. M., Guo, Y. J. & Dong, C. Synthesis of neutral red covalently functionalized graphene nanocomposite and the electrocatalytic properties toward uric acid. *Journal of Materials Chemistry* **22,** 602–608, doi: 10.1039/C1jm13233d (2012).

30. Ema, T., Miyazaki, Y., Koyama, S., Yano, Y. & Sakai, T. A bifunctional catalyst for carbon dioxide fixation: cooperative double activation of epoxides for the synthesis of cyclic carbonates. *Chemical Communications* **48,** 4489–4491, doi: 10.1039/c2cc30591g (2012).
31. Tang, G. *et al.* EMAN2: an extensible image processing suite for electron microscopy. *J of Structural Biology* **157,** 38–46, doi: 10.1016/j.jsb.2006.05.009 (2007).
32. Ludtke, S. J., Jakana, J., Song, J. L., Chuang, D. T. & Chiu, W. A 11.5 A single particle reconstruction of GroEL using EMAN. *Journal of Molecular Biology* **314,** 253–262, doi: 10.1006/jmbi.2001.5133 (2001).
33. Ludtke, S. J., Chen, D. H., Song, J. L., Chuang, D. T. & Chiu, W. Seeing GroEL at 6 A resolution by single particle electron cryomicroscopy. *Structure* **12,** 1129–1136, doi: 10.1016/j.str.2004.05.006 (2004).
34. Ludtke, S. J. *et al.* De novo backbone trace of GroEL from single particle electron cryomicroscopy. *Structure* **16,** 441–448, doi: 10.1016/j.str.2008.02.007 (2008).
35. Pettersen, E. F. *et al.* UCSF Chimera–a visualization system for exploratory research and analysis. *Journal of Computational Chemistry* **25,** 1605–1612, doi: 10.1002/jcc.20084 (2004).
36. Cote, L. J., Kim, J., Zhang, Z., Sun, C. & Huang, J. X. Tunable assembly of graphene oxide surfactant sheets: wrinkles, overlaps and impacts on thin film properties. *Soft Matter* **6,** 6096–6101, doi: 10.1039/C0sm00667j (2010).
37. Suloway, C. *et al.* Automated molecular microscopy: the new Leginon system. *Journal of Structural Biology* **151,** 41–60, doi: 10.1016/j.jsb.2005.03.010 (2005).
38. Lander, G. C. *et al.* Appion: an integrated, database-driven pipeline to facilitate EM image processing. *Journal of Structural Biology* **166,** 95–102, doi: 10.1016/j.jsb.2009.01.002 (2009).

Acknowledgements

The authors gratefully acknowledge support from the Purdue University Center for Cancer Research NIH Grant P30 CA023168 and NIH Grant R21 NS095218.

Author Contributions

C.J.B., K.J.W., S.C.B. and D.H.T. wrote the manuscript. K.J.W. completed the work in section Synthesis of GO Sheets Functionalized with NTA and prepared Figures 1 and 2. C.J.B. and K.K. completed the work in section GO-NTA Monolayer Formation. S.-H.H., C.J.B. and K.K. completed the work in section Characterization of GO-NTA Monolayers and prepared Figures 3, S1, S2 and S3. C.J.B. completed the work for section Affinity Capture of His_6-T7 Bacteriophage and prepared Figures 4 and S4. C.J.B., M.G., G.Y. and F.G. completed the work for section Affinity Capture of His_6-GroEL and prepared Figure 5. S.C.B. completed the work in section Single Particle Analysis of His_6-GroEL and prepared Figure 6. T.L.K.-U., W.J. and D.H.T. provided technical guidance, review and editing of the manuscript.

Additional Information

Supplementary information accompanies this paper at http://www.nature.com/srep

Competing financial interests: The authors declare no competing financial interests.

How to cite this article: Benjamin, C. J. *et al.* Selective Capture of Histidine-tagged Proteins from Cell Lysates Using TEM grids Modified with NTA-Graphene Oxide. *Sci. Rep.* **6**, 32500; doi: 10.1038/srep32500 (2016).